ISSN 2188-5001

MATERIALS DESIGN AND
CHARACTERIZATION LABORATORY

SUPERCOMPUTER CENTER

ACTIVITY REPORT 2023

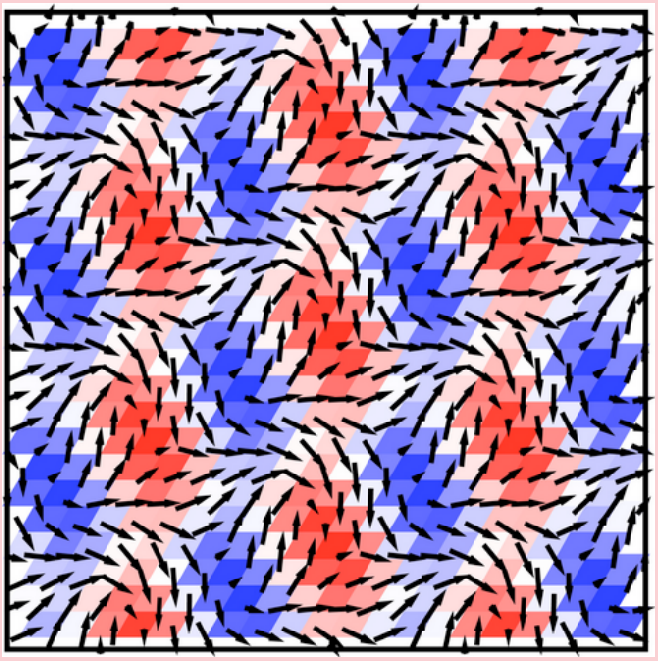

THE UNIVERSITY OF TOKYO

Materials Design and Characterization Laboratory (MDCL)

The MDCL was established as the third research facility of the Institute for Solid State Physics (ISSP) when the latter was reorganized in May 1996. Its aim is to promote material science with an emphasis on the "DSC cycle", where DSC stands for design, synthesis and characterization, three processes for developing new materials.

The MDCL consists of two sections, Materials Design (MD) section and Materials Synthesis and Characterization (MSC) section. The Supercomputer Center of the ISSP (SCC-ISSP) is placed in the MD section, while in the MSC section there are seven laboratories for joint use; Materials Synthesis Laboratory, Chemical Analysis Laboratory, X-ray Diffraction Laboratory, Electron Microscope Laboratory, Electromagnetic Measurement Laboratory, Spectroscopy Laboratory, and High-Pressure Synthesis Laboratory.

Almost all the facilities of the MDCL are open to scientists in Japan through the User Programs conducted by two steering committees of the MDCL. One is the steering committee of the SCC-ISSP, under which the Supercomputer Project Advisory Committee is placed for reviewing proposals. The other is the steering committee of the MSC facilities. More than half of the members of these committees are from the outside of ISSP.

COVER FIGURE

Snapshot during microwave-induced topology switching in the triangular Kondo-lattice model.

See Page 23–36, M. Mochizuki, and R. Eto, "Theoretical studies on the spin-charge dynamics in Kondo-lattice models".

PREFACE

The Supercomputer Center (SCC) is a part of the Materials Design and Characterization Laboratory (MDCL) of ISSP. Its mission is to serve the whole community of computational condensed-matter physics of Japan providing it with high performance computing environment. In particular, the SCC selectively promotes and supports large-scale computations. For this purpose, the SCC invites proposals for supercomputer-aided research projects and hosts the Steering Committee, as mentioned below, that evaluates the proposals.

The ISSP supercomputer system consists of two subsystems: System B, which was last replaced in Oct. 2020, is intended for larger total computational power and has more nodes with relatively loose connections whereas System C is intended for higher communication speed among nodes. System B (ohtaka) consists of 1680 CPU nodes of AMD EPYC 7702 (64 cores) and 8 FAT nodes of Intel Xeon Platinum 8280 (28 cores) with total theoretical performance of 6.881 PFlops. System C was replaced in June 2022 and the current system (kugui) consists of 128 CPU nodes of AMD EPYC 7763 (64 cores) and 8 ACC nodes of AMD EPYC 7763 (64 cores) NVIDIA A100 40GB for HGX with total theoretical performance of 0.973 PFLOPS.

In addition to the hardware administration, the SCC puts increasing effort on the software support. Since 2015, the SCC has been conducting “Project for advancement of software usability in materials science (PASUMS).”In this project, for enhancing the usability of the ISSP supercomputer system, we conduct several software-advancement activities: developing new application software that runs efficiently on the ISSP supercomputer system, adding new functions to existing codes, help releasing private codes for public use, creating/improving manuals for public codes, etc. Two target programs were selected for fiscal year 2023: (1) TeNeS (proposal made by T. Okubo (Univ. Tokyo)), and (2) HTP tools (proposal made by K. Yoshimi (ISSP)). In addition, since 2021, we have been maintaining the data repository service for secure storage and enhanced usability of results of numerical calculation.

All staff members of university faculties or public research institutes in Japan are invited to propose research projects (called User Program). The proposals are evaluated by the Steering Committee of SCC. Peer-reviewing is done by the Supercomputer Project Advisory Committee. In fiscal year 2023, totally 320 projects were approved including the ones under the framework of Supercomputing Consortium for Computational Materials Science (SCCMS), which specially supports FUGAKU and other major projects in computational materials science.

The research projects are roughly classified into the following three (the number of projects approved):

First-Principles Calculation of Materials Properties (160)
Strongly Correlated Quantum Systems (36)
Cooperative Phenomena in Complex, Macroscopic Systems (112)
SCCMS projects (12)

In all the three categories, most proposals involve both methodology and applications. The results of the projects are reported in 'Activity Report 2023' of the SCC. Every year 3-4 projects are selected for “invited papers” and published at the beginning of the Activity Report. In the Activity Report 2023, the following four invited papers are included:

``Density functional theory calculations of H_2O adsorption monolayer on a Pt(111) surface", Jun HARUYAMA, Osamu SUGINO (ISSP), and Toshiki SUGIMOTO (Institute for Molecular

Science, JST)

``Theoretical studies on the spin-charge dynamics in Kondo-lattice models",
Masahito MOCHIZUKI, and Rintaro ETO (Waseda Univ.)

``Mixing Free Energy and Molecular Dynamics Simulations",
Naoko NAKAGAWA and Akira YOSHIDA (Ibaraki Univ.)

``*Ab initio* optical calculation by RESPACK",
Kazuma NAKAMURA (Kyutech)

June 11, 2024

Naoki Kawashima
(Chairman of the steering committee, SCC, ISSP)

CONTENTS

1 OUTLINE

1.1 Supercomputer System

In School year 2023 (SY 2023), the ISSP supercomputer center provided users with System B - Dell PowerEdge C6525/R940 system named "ohtaka" and System C - HPE Apollo 2000 Gen10 Plus/HPE Apollo 6500 Gen10 Plus system named "kugui". System B is a massively-parallel supercomputer with two types of compute nodes: 8 "Fat" nodes and 1680 "CPU" nodes. "Fat" nodes are each comprised of four Intel Xeon Platinum 8280 CPUs (28 cores/CPU) and 3 TB of memory per node. "CPU" nodes have two AMD EPYC 7702 CPUs (64 cores/CPU) and 256 GB of memory per node. System B achieves about 6.881 PFLOPS in theoretical peak performance with high power efficiency. The subsystem comprised of only CPU nodes ranks 87st in the Nov. 2020 Top 500 List, which is a ranking based on total performance measured by the HPL benchmark. The compute nodes communicate to each other through HDR100 Infiniband and are connected in fat tree topology. SY 2023 was the fourth year of the operation of the current System B. System C is a massively-parallel supercomputer with two types of compute nodes: 128 "CPU" nodes and 8 "ACC" nodes. "CPU" nodes are each comprised of two AMD EPYC 7763 CPUs (64 cores/CPU) and 256 GB of memory. The compute nodes communicate to each other through HDR200 Infiniband and are connected in fat tree topology. "ACC" nodes are each comprised of one AMD EPYC 7763 CPUs (64 cores/CPU), four NVIDIA A100 40GB for HGX GPUs and 256 GB of memory. System C achieves 973 TFLOPS in theoretical peak performance. SY 2023 was the second year of the operation of the current System C. As shown in Fig. 1, users can access both systems via the Internet using SSH public key authentication. For further details, please contact ISSP Supercomputer Center (SCC-ISSP).

[Correspondence: center@issp.u-tokyo.ac.jp]

1.2 Project Proposals

The ISSP supercomputer system provides computation resources for scientists working on condensed matter sciences in Japan. All scientific staff members (including post-docs) at universities or public research institutes in Japan can submit proposals for projects related to research activities on materials and condensed matter sciences. These proposals are peer-reviewed by the Advisory Committee members (see Sec. 1.3), and then the computation resources are allocated based on the review reports. The leader of an approved project can set up user accounts for collaborators. Other types of scientists, including graduate students, may also be added. Proposal submissions, peer-review processes, and user registration are all managed via a web system.

The computation resources are distributed in a unit called "point", determined as a function of available CPU utilization time and consumed disk resources. There

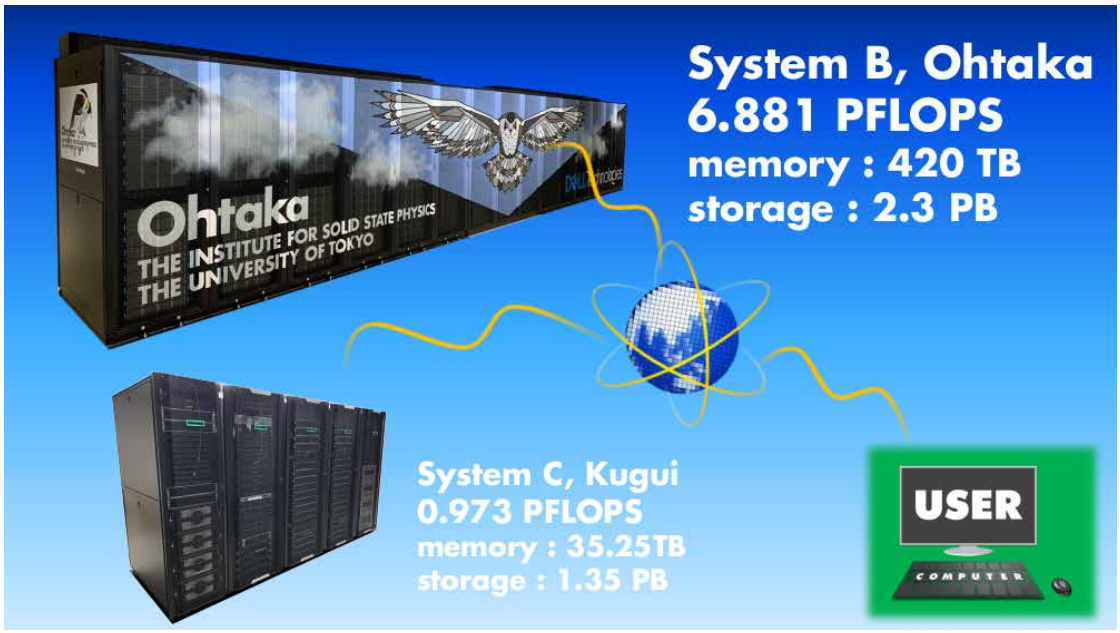

Figure 1: Supercomputer System at the SCC-ISSP

were calls for six classes of research projects in SY 2023. The number of projects and the total number of points that were applied for and approved in this school year are listed in Table 1.

- Class A is for trial use by new users; proposals for Class A projects are accepted throughout the year.
- Proposals for projects in Classes B (small), C (mid-size), E (large-scale), and S (exceptional) can be submitted twice a year. Approved projects in Classes A, B, C, and E continue to the end of the school year.
- In Class D, projects can be proposed on rapidly-developing studies that need to perform urgent and relatively large calculations. An approved project continues for 6 months from its approval.
- Class S is for projects that are considered extremely important for the field of condensed matter physics and requires extremely large-scale computation. The project may be carried out either by one research group or cooperatively by several investigators at different institutions. A project of this class should be applied with at least 10,000 points; there is no maximum. We require group leaders applying for Class S to give a presentation on the proposal to the Steering Committee of the SCC-ISSP. Class S projects are carried out within one year from its approval.
- Project leaders can apply for points so that the points for each system do not exceed the maximum point shown in this table.

Table 1: Classes of research projects in SY 2023. Total points listed in this table are rounded. In Class D, we collect information about the projects ended in each semester.

Class	Maximum Points		Application	# of Proj.	Total points			
					Applied		Approved	
	Sys–B	Sys–C			Sys–B	Sys–C	Sys–B	Sys–C
A	100	50	any time	24	2.4k	1.2k	2.4k	1.2k
B	650	100	twice a year	99	58.1k	7.3k	38.5k	6.5k
C	6.5k	500	twice a year	185	996.9k	58.4k	513.6k	45.8k
D	10k	500	any time	7	43.5k	1.5k	39.6k	1.5k
E	20k	1.5k	twice a year	17	317.0k	25.5k	185.0k	20.7k
S	–	–	twice a year	0	0	0	0	0
SCCMS				12	27.0k	2.6k	27.0k	2.6k
Total				344	1444.9k	96.6k	806.1k	78.3k

In addition, from SY 2016, ISSP Supercomputer has been providing 20% of its computational resources for Supercomputing Consortium for Computational Materials Science (SCCMS), which aims at advancing parallel computations in condensed matter, molecular, and materials sciences on the 10-PFlops K Computer and the exascale post-K project. From SY 2020, up to 10% of the computational resources have been provided for SCCMS. Computational resources have also been allotted to Computational Materials Design (CMD) workshops, as well as CCMS hands-on workshops.

1.3 Committees

In order to fairly manage the projects and to smoothly determine the system operation policies, the Materials Design and Characterization Laboratory (MDCL) of the ISSP has organized the Steering Committee of the MDCL and the Steering Committee of the SCC-ISSP, under which the Supercomputer Project Advisory Committee (SPAC) is formed to review proposals. The members of the committees in SY 2023 were as follows:

Steering Committee of the MDCL

OKAMOTO, Yoshihiko	ISSP (Chair person)
KAWASHIMA, Naoki	ISSP
YAMAURA, Jun-ichi	ISSP
OZAKI, Taisuke	ISSP
NOGUCHI, Hiroshi	ISSP
UWATOKO, Yoshiya	ISSP
SUGINO, Osamu	ISSP
KUBO, Momoji	Tohoku Univ.

HUKUSHIMA, Koji	Univ. of Tokyo
HONDA, Fuminori	Kyushu Univ.
SHIMAKAWA, Yuichi	Kyoto Univ.
OTSUKI, Junya	Okayama Univ.
OBA, Fumiyasu	Tokyo Tech.
KUDO, Kazutaka	Osaka Univ.
MATSUDA, Tatsuma	Tokyo Metropolitan Univ.

Steering Committee of the SCC-ISSP

KAWASHIMA, Naoki	ISSP (Chair person)
NOGUCHI, Hiroshi	ISSP
OZAKI, Taisuke	ISSP
SUGINO, Osamu	ISSP
TSUNETSUGU, Hirokazu	ISSP
KATO, Takeo	ISSP
KIMURA, Takashi	ISSP
FUKUDA, Masahiro	ISSP
IDO, Kota	ISSP
NAKANO, Hiroyoshi	ISSP
NAKAJIMA, Kengo	Univ. of Tokyo
OTSUKI, Junya	Okayama Univ.
MOTOME, Yukitoshi	Univ. of Tokyo
ONO, Tomoya	Kobe Univ.
TODO, Synge	Univ. of Tokyo
KUBO, Momoji	Tohoku Univ.
OBA, Fumiyasu	Tokyo Tech.
WATANABE, Hiroshi	Keio Univ.
HUKUSHIMA, Koji	Univ. of Tokyo
KITAO, Akio	Tokyo Tech.
HAMADA, Ikutaro	Osaka Univ.
YOSHIMI, Kazuyoshi	ISSP
YATA, Hiroyuki	ISSP
FUKUDA, Takaki	ISSP
MOTOYAMA, Yuichi	ISSP

Supercomputer Project Advisory Committee

KAWASHIMA, Naoki	ISSP (Chair person)
OZAKI, Taisuke	ISSP
NOGUCHI, Hiroshi	ISSP
SUGINO, Osamu	ISSP
TSUNETSUGU, Hirokazu	ISSP
KIMURA, Takashi	ISSP
KATO, Takeo	ISSP

FUKUDA, Masahiro	ISSP
IDO, Kota	ISSP
NAKANO, Hiroyoshi	ISSP
NAKAJIMA, Kengo	Univ. of Tokyo
MOTOME, Yukitoshi	Univ. of Tokyo
TODO, Synge	Univ. of Tokyo
KUBO, Momoji	Tohoku Univ.
OBA, Fumiyasu	Tokyo Tech.
WATANABE, Hiroshi	Keio Univ.
HUKUSHIMA, Koji	Univ. of Tokyo
ONO, Tomoya	Kobe Univ.
OTSUKI, Junya	Okayama Univ.
KITAO, Akio	Tokyo Tech.
HAMADA, Ikutaro	Osaka Univ.
IKUHARA, Yuichi	Univ. of Tokyo
SHIBATA, Naokazu	Tohoku Univ.
AKAGI, Kazuto	Tohoku Univ.
YANASE, Yoichi	Kyoto Univ.
HATSUGAI, Yasuhiro	Univ. of Tsukuba
OKADA, Susumu	Univ. of Tsukuba
KOBAYASHI, Nobuhiko	Univ. of Tsukuba
HOTTA, Takashi	Tokyo Metropolitan Univ.
MATSUKAWA, Hiroshi	Aoyama Gakuin Univ.
YAMAUCHI, Jun	Keio Univ.
HAGITA, Katsumi	National Defense Academy
KONTANI, Hiroshi	Nagoya Univ.
YUKAWA, Satoshi	Osaka Univ.
SUGA, Seiichiro	Univ. of Hyogo
YASUDA, Chitoshi	Univ. of the Ryukyus
KIM, Kang	Osaka Univ.
MORIKAWA, Yoshitada	Osaka Univ.
KOGA, Akihisa	Tokyo Tech.
SHIMOJO, Fuyuki	Kumamoto Univ.
TAKETSUGU, Tetsuya	Hokkaido Univ.
TSURUTA, Kenji	Okayama Univ.
HAMAGUCHI, Satoshi	Osaka Univ.
NISHIDATE, Kazume	Iwate Univ.
KAGESHIMA, Hiroyuki	Shimane Univ.
ISHII, Fumiyuki	Kanazawa Univ.
TATETSU, Yasutomi	Meio Univ.
YANAGISAWA, Susumu	Univ. of the Ryukyus
SHUDO, Ken-ichi	Yokohama Natl. Univ.
OHMURA, Satoshi	Hiroshima Inst. Tech.
NOGUCHI, Yoshifumi	Shizuoka Univ.
NAKAMURA, Kazuma	Kyushu Inst. Tech.

GOHDA, Yoshihiro	Tokyo Tech.
RAEBIGER, Hannes	Yokohama Natl. Univ.
KAWARABAYASHI, Tohru	Toho Univ.
KATO, Yusuke	Univ. of Tokyo
NASU, Joji	Tohoku Univ.
HOTTA, Chisa	Univ. of Tokyo
ISOBE, Masaharu	Nagoya Inst. Tech.
TANAKA, Shu	Keio Univ.
KOBAYASHI, Kazuaki	NIMS
TATEYAMA, Yoshitaka	NIMS
TAMURA, Ryo	NIMS
HIGUCHI, Yuji	Kyushu Univ.
KAWAMURA, Mitsuaki	Univ. of Tokyo
TADA, Tomofumi	Kyushu Univ.
HATANO, Naomichi	Univ. of Tokyo
YOSHINO, Hajime	Osaka Univ.
OKUMURA, Hisashi	NINS-ExCELLS
HOSHI, Takeo	NIFS-PQP
TSUNEYUKI, Shinji	Univ. of Tokyo
SUZUKI, Takafumi	Univ. of Hyogo
YOSHIMOTO, Yoshihide	Univ. of Tokyo
TOHYAMA, Takami	Tokyo Univ. of Sci.
ARITA, Ryotaro	Univ. of Tokyo
OGATA, Masao	Univ. of Tokyo
WATANABE, Satoshi	Univ. of Tokyo
YABANA, Kazuhiro	Univ. of Tsukuba
FURUKAWA, Nobuo	Aoyama Gakuin Univ.
KUROKI, Kazuhiko	Osaka Univ.
TANAKA, Yukio	Nagoya Univ.
KUSAKABE, Koichi	Univ. of Hyogo
SAKAI, Toru	Univ. of Hyogo
ISHIBASHI, Shoji	AIST
OTANI, Minoru	Univ. of Tsukuba
TOMITA, Yusuke	Shibaura Inst. Tech.
SHIRAISHI, Kenji	Nagoya Univ.
OGUCHI, Tamio	Osaka Univ.
KAWAKATSU, Toshihiro	Tohoku Univ.
OTSUKI, Tomi	Sophia Univ.
ODA, Tatsuki	Kanazawa Univ.
ARAI, Noriyoshi	Keio Univ.
UNEYAMA, Takashi	Nagoya Univ.

1.4 Staff

The following staff members of the SCC-ISSP usually administrate the ISSP Supercomputer.

KAWASHIMA, Naoki	Professor (Chair person)
NOGUCHI, Hiroshi	Associate Professor
OZAKI, Taisuke	Professor
SUGINO, Osamu	Professor
IDO, Kota	Research Associate
FUKUDA, Masahiro	Research Associate
NAKANO, Hiroyoshi	Research Associate
YOSHIMI, Kazuyoshi	Project Researcher
AOYAMA, Tatsumi	Project Researcher
MOTOYAMA, Yuichi	Technical Specialist
YATA, Hiroyuki	Technical Specialist
FUKUDA, Takaki	Technical Specialist
ARAKI, Shigeyuki	Project Academic Specialist

2 STATISTICS (SCHOOL YEAR 2023)

2.1 System and User Statistics

In the following, we present statistics for operation time taken in the period from April 4th 2023 to March 31th 2024 (SY 2023). In Table 2, we show general statistics of the supercomputer system in SY 2023. The total numbers of compute nodes in System B "ohtaka" and System C "kugui" are 1688 and 136, respectively. Consumed disk points amount to about a few percent of the total consumed points in both System B and System C.

Table 2: Overall statistics of SY 2023

	System B ohtaka	System C kugui
total service time ($\times 10^3$ node·hours)	13944	1135
number of executed jobs	509541	132715
total consumed points ($\times 10^3$ point)	472	26
CPU points ($\times 10^3$ point)	456	25
disk points ($\times 10^3$ point)	16	1
total exec. time ($\times 10^3$ node·hours)	12929	1008
availability	94.81%	95.77%
utilization rate	92.70%	88.83%

In Fig. 2, availabilities, utilization rates, and consumed points in Systems B and C are plotted for each month. Throughout the school year, the availability and the utilization rates were very high : the availability and the utilization rates exceed about 90% and 80% throughout most of the year, respectively. In this SY, we stopped the operation of System B for one week in August for power saving. This affects the availability of System B in August below 80%, as shown in Fig. 2. The other declines in the availabilities are due to maintenance of the systems, a planned power outage at ISSP, or equipment failure.

The user statistics are shown in Fig. 3. The horizontal axis shows the rank of the user/group arranged in the descending order of the execution time (hour×nodes). The execution time of the user/group of the first rank is the longest. The vertical axis shows the sum of the execution time up to the rank. From the saturation points of the graphs, the numbers of "active" users of Systems B and C are around 400 and 100, respectively. The maximum ranks in the graphs correspond to the number of the users/groups that submitted at least one job.

2.2 Queue and Job Statistics

Queue structures of Systems B and C in SY 2023 are shown in Tables 3 and 4, respectively. In System B "ohtaka", users can choose from two types of compute nodes; jobs submitted to queues with "cpu" and "fat" at the end of their queue names are submitted to CPU and Fat nodes, respectively. In System C, there are two types of compute nodes: CPU and ACC nodes. Jobs submitted to queues with "cpu" and "acc" at the end of their queue names are submitted to CPU and ACC nodes, respectively, If users submit a job to queues with "accs" at the end of their queue names, the job runs in the ACC node shared by other jobs of "accs" queues. See Sec. 1.1 for a description of each type of compute node. The user then has to choose the queue according to the number of nodes to use and the duration of their calculation jobs. Queue names starting with "F" are for jobs taking 24 hours or less, while those starting with "L" can run much longer up to 120 hours. More nodes are allotted to "F" queues in order to maximize the turnaround time of user jobs. The queue names starting with "i" are used for interactive debugging of user programs and the elapsed time limit is 30 minutes. The number following "F", "L", or "i" correspond to the number of nodes that can be used by one user job. Although we do not mention here in detail, to promote utilization of the massively parallel supercomputer, background queues (queue name starting with "B") for Systems B and C which charge no points for the jobs have also been open.

To prevent overuse of the storage, points are charged also for usage of disk quota in the systems, as shown in Table 5. Disk points are revised often for optimal usage of the resources by examining usage tendencies each year.

The number of jobs, average waiting time, and total execution time in each queue are shown in Tables 6 and 7. In Systems B and C, a large portion of jobs have been executed in "F" queues. The largest amount of the execution time has been consumed in "F72cpu" and "F1cpu" queues for Systems B and C, respectively. However, substantial number of jobs were run in every queue,

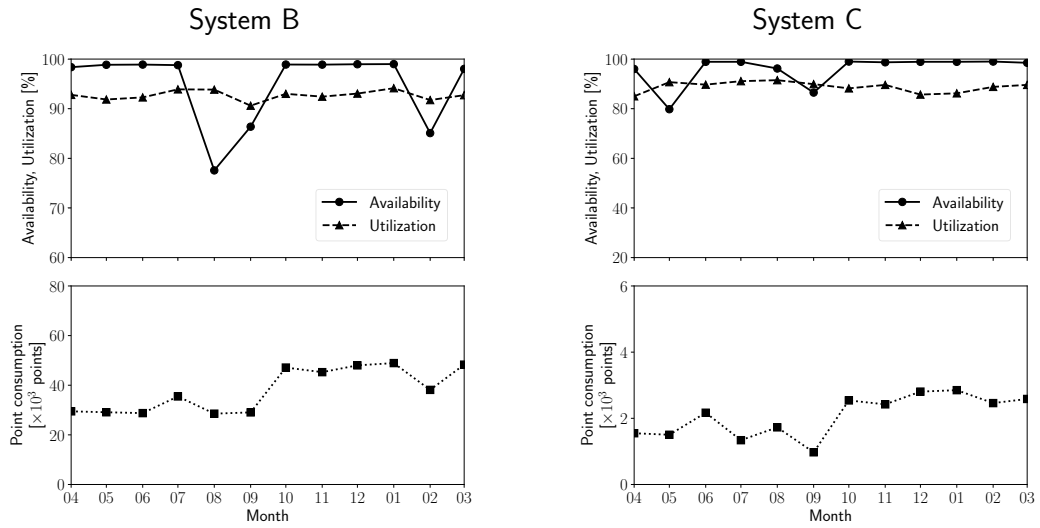

Figure 2: Availabilities, utilization rates and point consumptions of each month during SY 2023.

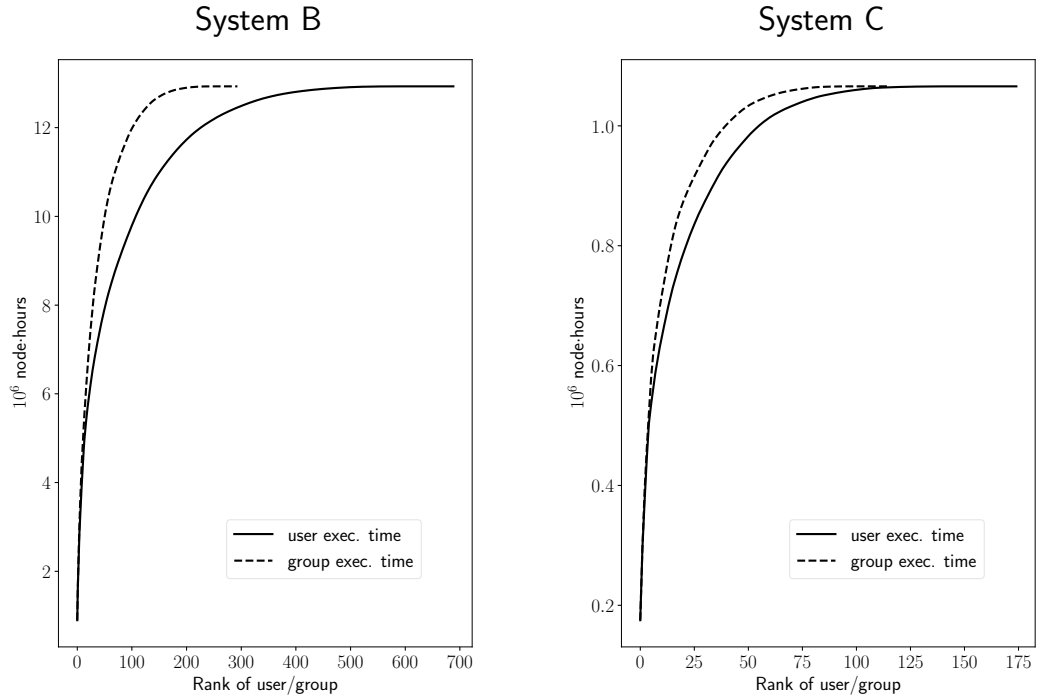

Figure 3: User statistics. The horizontal axis shows the rank of the user/group arranged in the descending order of the execution time (hour×nodes). The vertical axis shows the sum of the execution time up to the rank.

Table 3: Queue structures of System B in SY 2023

System B, ohtaka

queue name	Elapsed time limit (hr)	# of nodes /job	# of nodes /queue	Memory limit (GB)	job points /(node·day)
F1cpu	24	1	600	230/node	1
L1cpu	120	1	300	230/node	1
F4cpu	24	2–4	216	230/node	1
L4cpu	120	2–4	108	230/node	1
F16cpu	24	5–16	288	230/node	1
L16cpu	120	5–16	144	230/node	1
F36cpu	24	17–36	72	230/node	1
L36cpu	120	17–36	36	230/node	1
F72cpu	24	72	576	230/node	1
L72cpu	120	72	288	230/node	1
F144cpu	24	144	432	230/node	1
L144cpu	120	144	144	230/node	1
i8cpu	0.5	1–8	72	230/node	1
F2fat	24	1–2	7	2900/node	4
L2fat	120	1–2	3	2900/node	4
i1fat	0.5	1	1	2900/node	4

suggesting that a wide variety of user needs are met by this queuing scheme. In most of these queues, the queue settings meet the user's tendencies in that the waiting times are on the order of the elapsed-time limit.

2.3 Project for Advancement of Software Usability in Materials Science

From School Year 2015, the supercomputer center (SCC) has started "Project for advancement of software usability in materials science". In this project, for enhancing the usability of the supercomputer system in ISSP, we perform some software-advancement activity such as implementing a new function to an existing code, releasing a private code on Web, writing manuals. Target programs are publicly offered in December and selected in the review by the Steering Committee of SCC. The projects are carried out by the software development team composed of three members in ISSP. In SY 2023, two projects were selected as listed in Table 8.

Table 4: Queue structures of System C in SY 2023

System C, kugui

queue name	Elapsed time limit (hr)	# of nodes /job	# of nodes /queue	Memory limit (GB)	job points /(node·day)
i2cpu	0.5	1–2	8	240/node	1
F1cpu	24	1	120	240/node	1
L1cpu	120	1	60	240/node	1
F4cpu	24	2–4	32	240/node	1
L4cpu	120	2–4	16	240/node	1
F16cpu	24	5–16	64	240/node	1
L16cpu	120	5–16	32	240/node	1
F1accs	24	1	3	$60\times N_{\mathrm{GPU}}$	1
L1accs	120	1	1	$60\times N_{\mathrm{GPU}}$	1
i1accs	0.5	1	1	$60\times N_{\mathrm{GPU}}$	1
F2acc	24	1–2	4	240/node	1
L2acc	120	1–2	2	240/node	1

* N_{GPU} in ACC queues denotes the number of occupied GPUs.

2.4 ISSP Data Repository

From School Year 2021, the supercomputer center (SCC) has started to operate ISSP Data Repository (ISSP-DR) for accumulating and utilizing research data in materials science. GitLab is used as the data management system, and a portal site is provided as a data registration and search system for the registered data. By using ISSP-DR, it is possible to store and publish research data used in papers and datasets useful in the field of condensed matter science. Users of ISSP Supercomputer are welcome to apply for and use ISSP-DR.

Table 5: Disk points of Systems B and C

		point/day
System B ohtaka	`/home`	$0.001 \times \theta(q - 600)$
	`/work`	$0.0001 \times \theta(q - 6000)$
System C kugui	`/home`	$0.001 \times \theta(q - 150)$
	`/work`	$0.0001 \times \theta(q - 1500)$

* q is denoted in unit of GB.
* $\theta(x)$ is equal to the Heaviside step function $H(x)$ multiplied by x, i.e., $xH(x)$.

Table 6: Number of jobs, average waiting time, total execution time, and average number of used nodes per job in each queue of System B.

System B, ohtaka

queue	# of Jobs	Waiting Time (hour)	Exec. Time ($\times 10^3$ node·hour)	# of nodes
F1cpu	96782	57.70	220.70	1.00
L1cpu	5186	87.32	161.97	1.00
F4cpu	181422	14.96	1277.01	2.39
L4cpu	4151	26.33	411.48	3.24
F16cpu	47965	19.67	1631.91	8.57
L16cpu	1548	50.60	596.13	9.46
F36cpu	1211	50.05	278.68	26.97
L36cpu	92	109.00	129.81	24.86
F72cpu	5331	34.57	3201.14	72.00
L72cpu	115	287.42	256.11	72.00
F144cpu	1847	59.32	2209.31	144.00
L144cpu	86	24.30	299.44	144.00
i8cpu	149334	0.13	104.29	4.32
F2fat	5144	42.50	39.17	1.26
L2fat	345	56.03	15.28	1.28
i1fat	850	1.13	0.06	1.00

Table 7: Number of jobs, average waiting time, total execution time, and average number of used nodes per job in each queue of System C.

System C, kugui

queue	# of Jobs	Waiting Time (hour)	Exec. Time ($\times 10^3$ node·hour)	# of nodes
i2cpu	9431	0.59	1.38	1.33
F1cpu	46089	4.16	153.28	1.00
L1cpu	6005	5.16	75.33	1.00
F4cpu	4059	10.18	100.33	2.87
L4cpu	461	11.89	32.65	3.22
F16cpu	1366	13.98	112.34	11.41
L16cpu	97	17.99	36.88	12.25
i1accs	11431	0.80	1.64	1.00
F1accs	5934	25.48	43.34	1.00
L1accs	477	87.64	23.07	1.00
F2acc	2738	10.19	13.81	1.05
L2acc	413	39.05	10.07	1.11

Table 8: List of Project for advancement of software usability in materials science for SY 2023.

Project Proposer	Project Name
Tsuyoshi Okubo University of Tokyo	Finite temperature support in tensor network solver TeNeS for quantum lattice models
Kazuyoshi Yoshimi ISSP, University of Tokyo	Development of a tool to create a database of first-principles calculations using high-throughput calculations

3 RESEARCH REPORTS

3.1 Invited Articles

Density functional theory calculations of H_2O adsorption monolayer on a Pt(111) surface

Jun HARUYAMA and Osamu SUGINO

The Institute for Solid State Physics, The University of Tokyo, Kashiwa-no-ha, Kashiwa, Chiba 277-8581

Toshiki SUGIMOTO

Department of Materials Molecular Science, Institute for Molecular Science, Myodaiji, Okazaki, Aichi, 444-8585, Japan

Precursory Research for Embryonic Science and Technology, Japan Science and Technology Agency, Saitama 332-0012, Japan

Abstract

From a theoretical point of view, the estimation of intermediate state free energy is essential for finding more efficient electrocatalyst. To investigate the accuracy of density functional theory functionals at the metal/water interface, we focus on an ideal metal/ice system: the H_2O adsorption monolayer on a Pt(111) surface. Three DFT functionals (PBE, vdW-DF, and vdW-DF2-B86R) are used to compare the adsorption energies of √39×√39 (and √37×√37) 5·7-member ring structure with the experimental activation energy of desorption. It is found that the vdW-DF2-B86R functional slightly overestimates the Pt–H_2O interaction while others seriously underestimate it.

Furthermore, we develop a first-principles methodology for analyzing the second-order nonlinear susceptibility $\chi^{(2)}_{zzz}$ applicable for metal/adsorption systems. The calculated Im $\chi^{(2)}_{zzz}$ spectra show negative double peaks in the high-frequency region, consistent with those obtained from the measured sum-frequency generation spectra. This study provides a fundamental basis for analyzing the structure of H_2O adsorbed on metal surfaces.

1 Introduction

In electrochemistry, a metal/water interface has general importance and continued interest because of the applicability of fuel cells, water electrolysis, and so on. The conversion efficiency of an electrochemical reaction depends on the free energy landscape of its rate determining step, e.g., the oxygen reduction reaction (ORR). Therefore, to estimate the free

energy of reaction intermediate states, accurate description of the interactions between H2O molecules and a metal surface is beneficial. In this study, we focus on an experimentally well-confirmed system, i.e., H_2O adsorption monolayer on a Pt(111) surface. [1, 2] In order to investigate how accurate the interaction description of density functional theory (DFT) calculations, we compare the properties obtained by first-principles calculations and previous experiments.

At low temperatures (≈ 100 K), the growth of layered structure of adsorbed H_2O molecules (in other words, crystalline ice film) was observed on a Pt(111) surface, [3] and structural analysis methods in surface science have been applied to investigate the Pt(111)/H_2O structure. In 1997, Glebov et al. observed He-atom scattering (HAS) diffraction patterns of the H_2O adsorbed molecules on Pt(111) surface and found a well-ordered 2D ice layer with a $(\sqrt{37}\times\sqrt{37})R25.3°$ or $(\sqrt{39}\times\sqrt{39})R16.1°$ symmetry. [4] They suggested possible lateral H_2O arrangements, in which the hydrogen bonds construct 6-member rings. As well as the HAS measurement, Haq et al. obtained an equivalent low-energy electron diffraction (LEED) pattern on the first layer of H_2O adsorption molecules on Pt(111). [5] In the same study, Haq et al. showed the activation energy of desorption, $E_a = 52 \pm 2$ kJ/mol, for the adsorption layers by temperature programmed desorption (TPD) analysis. [5] Daschbach measured the desorption rates of the H_2O layers on Pt(111) by HAS and estimated the activation energy $E_a = 54.2 \pm 3$ kJ/mol, by the Arrhenius equation. [6]

In 2010, Nie et al. obtained scanning tunneling microscope (STM) images on the H_2O first layer. Inferred from an observed triangular depression, the authors proposed the first layer structure as a hexagon of H_2O molecules surrounding 5- and 7-member rings. [7, 8] From the consistency between the experimental observation and DFT calculations, we consider the structure suggested by Nie to be thermodynamically stable at low temperatures. Thus, the detailed structure and activation energy of desorption can be compared with first-principles calculations in the Pt/water system.

In this study, we confirmed the stable structure for H_2O adsorption monolayer on Pt(111) by comparing the DFT calculated adsorption energies of several model structures. The zero-point vibration energies of stable structures were considered. We further discuss the prediction accuracy of the DFT calculation for this Pt/water system.

2 Ice Ih and H_2O monolayer models

For the discussion of functional accuracies, we evaluated the lattice energy E_{lat} in bulk ice (Ih phase), which is defined using the DFT total energy E_{DFT}:

$$E_{lat} = -\{E_{DFT}(n\mathrm{H_2O}) - nE_{DFT}(\mathrm{H_2O})\}/n \quad (1),$$

where $n\mathrm{H_2O}$ and $\mathrm{H_2O}$ represent the systems of ice Ih and an isolated H_2O molecule,

respectively. Here, the Bernal–Fowler periodic model was employed as the structure of Ih phase. [9] The resulted values by using three DFT functionals, PBE, [10] vdW-DF, [11] and vdW-DF2-B86R, [12] are listed in Table 1.

Table 1. Lattice parameter ratios c/a, cell volumes V (Å^3/H_2O), and lattice energies E_{lat} (meV/H_2O). Experimental values are taken from refs. [13, 14].

Functional	c/a	V_0	E_{lat}
PBE	1.634	29.90	655
vdW-DF	1.635	33.19	582
vdW-DF2-B86R	1.632	29.41	697
Experiment	1.629	32.55	580

The lattice parameters and energies of PBE and vdW-DF are consistent with those of previous DFT studies. [15, 16] The lattice energy of vdW-DF is good agreement with the experimental value, and those of PBE and vdW-DF2-B86R are overestimated it c.a. 100 meV/H_2O. It is worth noting that these estimated accuracies of the H_2O–H_2O interaction cannot be invoked for the Pt–H_2O interaction.

In addition to the H_2O–H_2O interaction, it is also ambiguous whether the metal–H_2O interaction can be correctly described by DFT calculations. Here, considering the adsorption of H_2O monolayer on Pt(111), the difference in Pt–H_2O interactions obtained by the selected functionals is discussed. The adsorption energy E_{ad} is defined as

$$E_{ad} = -\{E_{DFT}(\mathrm{Pt}/n\mathrm{H_2O}) - E_{DFT}(\mathrm{Pt}) - nE_{DFT}(\mathrm{H_2O})\}/n \quad (2),$$

where Pt/$n$$H_2O$ and Pt represent the systems of $n$$H_2O$ adsorption on the Pt(111) and pristine Pt(111) surface, respectively. We conducted DFT calculations and evaluated E_{ad} of several model monolayer structures, i.e., simple H-down configurations with $(\sqrt{3}\times\sqrt{3})R30°$ symmetry (called √3 H-up/down), realistic 6- and 5·7-ring configurations with $(\sqrt{39}\times\sqrt{39})R16.1°$ symmetry (called √39 6-ring and √39 5·7-ring) as shown in Figs. 1 (a), (b), and (c), respectively. We further considered the adsorption model with 5·7-ring with $(\sqrt{37}\times\sqrt{37})R25.3°$ symmetry. We evaluated the zero-point vibrational correction ΔE_{ZPE} and the heat of adsorption H_{ad} defined as

$$\Delta E_{ZPE} = -\{E_{ZPE}(\mathrm{Pt}/n\mathrm{H_2O}) - E_{ZPE}(\mathrm{Pt}) - nE_{ZPE}(\mathrm{H_2O})\}/n \quad (3),$$

$$H_{ad} = E_{ad} + \Delta E_{ZPE} \quad (4).$$

The zero-point vibrational energy E_{ZPE} within the harmonic approximation is evaluated by the summation of the vibrational (phonon) eigen-frequencies.

2.1 Computational details for H_{ad}

A four-layer slab of Pt(111) was constructed by cutting face-centered cubic (fcc) crystals. We fixed the lattice constant of the Pt(111) surface at an experimental value of 3.924 Å. The Pt atom positions in the first and second bottom layers were fixed in the crystal positions. The VESTA

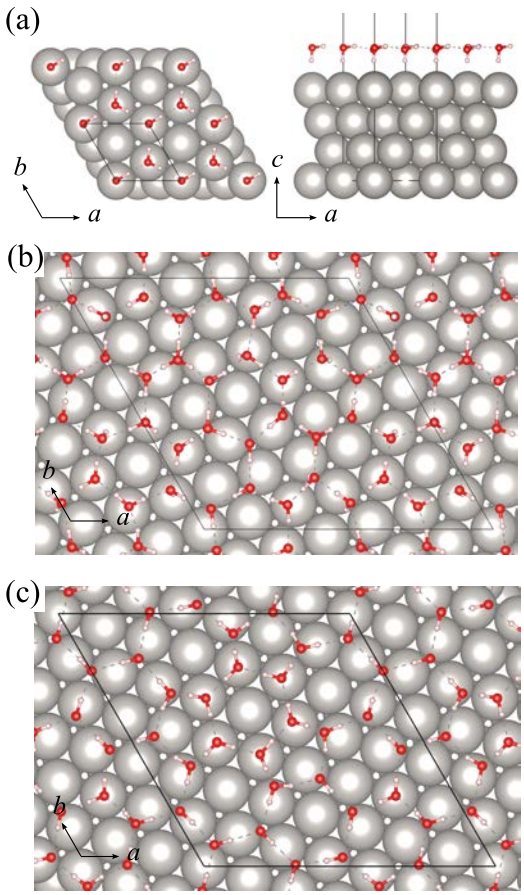

Fig 1. Structures of H_2O monolayer: (a) √3 H-down, (b) √39 6-ring, and (c) √39 5·7-ring. Adapted with permission from ref. [17]. Copyright 2024 American Physical Society.

package was used for visualization of atom coordinates. [18] Quantum ESPRESSO (QE) code [19] was used to perform spin-unpolarized DFT calculations. The cutoff energies were set to 40 and 320 Ry for the wave functions and the augmented charge, respectively. In surface slab calculations, converged k-point samplings of 12×12×1, 4×4×1, and 4×4×1 were adopted for the √3, √39, and √37 cells, respectively. Vibrational frequencies and modes were obtained from the diagonalization of dynamical matrix implemented in QE. Non-shifted k-point (q-point) samplings for electronic states of 8×8×1 (4×4×1), 1×1×1 (1×1×1), and 1×1×1 (1×1×1) were adopted for √3, √39, and √37 cells, respectively. The raw data of the structures obtained are made available in the ISSP data repository. [20]

3 Results of adsorption energies

Table 2 shows the obtained adsorption energies E_{ad} in this study. E_{ad} of the √39 6-ring was larger than that of √3 H-down by 10–25 meV/H_2O in the PBE and vdW-DF2-B86R functionals. The opposite result was obtained using vdW-DF functional. The √39 5·7-ring structure had highly ordered H_2O configurations, with perfect hydrogen bonds along surface parallel direction. In addition, 6 H_2O molecules in the √39 cell were close to the surface ($d_{Pt–O}$ = 2.21–2.25 Å), while the other H_2O molecules were located away by one step ($d_{Pt–O}$ = 3.3–4.0 Å). The latter molecules tend to point a H atom toward the surface. These features and adsorption energies indicate that the 5·7-ring structure has the largest advantage from the Pt-H_2O interaction.

Table 2 also lists the heats of adsorption H_{ad} of the √39 5·7-ring and √37 5·7-ring structures. The zero-point vibration corrections ΔE_{ZPE} of the two structures were c.a. −100 meV/H_2O. Considering a typical physisorption process of H_2O adsorption, the activation energy of the desorption can be approximated by H_{ad}.

Compared with the experiment, H_{ad} obtained by the PBE, and vdW-DF functionals underestimated the experimental value (c.a. 110–160 meV), while that obtained by vdW-DF2-B86R slightly overestimated (c.a. 40 meV). In addition, the wetting condition was satisfied by vdW-DF2-B86R only; this functional is optimal among the three functional. However, going back to the estimated errors of E_{lat} in ice Ih (see Table 1), this agreement come from the accidental cancellation about overestimation of interaction between H_2O–H_2O and underestimation between Pt–H_2O. Therefore, more accurate functional will be required to satisfy the thermodynamic condition of multilayer H_2O on Pt(111).

Table 2. Adsorption energies E_{ad}, and the heats of adsorption H_{ad}. Adapted from ref. [17].

Functional	PBE	vdW-DF	vdW-DF2-B86R
Structure	E_{ad} [meV/H_2O]		
√3 H-down	486	502	640
√39 6-ring	511	476	654
√39 5·7-ring	556	529	710
√37 5·7-ring	558	537	709
	H_{ad} [meV/H_2O]		
√39 5·7-ring	447	403	589
√37 5·7-ring	446	404	605

4 Second-order non-linear susceptibility

Recently, sum frequency generation (SFG) vibrational spectroscopy has become a frequently used method to determine the configuration of adsorbed H_2O on various metal surfaces. The heterodyne-detected SFG spectroscopy can be applied to the ice film on Pt(111) to obtain the imaginary part of the second-order nonlinear susceptibility, Im $\chi^{(2)}$, revealing the structure. [21, 22] In this study, we develop a DFT-based method for calculating $\chi^{(2)}$.

We use the sum-over-states representation of $\chi^{(2)}$ derived from perturbation theory: [23, 24]

$$\chi^{(2)}_{\alpha\beta\gamma}(\omega_{IR}) = \sum_{v} \frac{A_{\alpha\beta\gamma,v}}{\omega_v - \omega_{IR} - i\Gamma_v} \qquad (5),$$

where ω_{IR}, ω_v, and Γ_v represent the infrared (IR) frequency, vibrational frequency of the eigenmode v, and dephasing rate, respectively. The components of α, β, and γ are x-, y-, or z-direction. The numerator is defined as

$$A_{\alpha\beta\gamma,v} = \left(\sum_{\kappa,\gamma'} R_{\kappa,\alpha\beta\gamma'} U_v(\kappa,\gamma') \right) \times \left(\sum_{\kappa,\gamma'} Z^*_{\kappa,\gamma\gamma'} U_v(\kappa,\gamma') \right) \qquad (6),$$

where $U_v(\kappa,\alpha)$, $Z^*_{\kappa,\alpha\beta}$, and $R_{\kappa,\alpha\beta\gamma}$ represent the displacements of vibrational eigenmodes, the Born effective-charge tensor, and the Raman tensor on an atom index κ, respectively. For the calculations of $Z^*_{\kappa,\alpha\beta}$ and $R_{\kappa,\alpha\beta\gamma}$, we used the representation of response tensors with respect to electric field $\mathcal{E}_\alpha$:

$$Z^*_{\kappa,\alpha\beta} = \frac{\partial F_{\kappa,\beta}}{\partial \mathcal{E}_\alpha} \qquad (7),$$

$$R_{\kappa,\alpha\beta\gamma} = \frac{\partial^2 F_{\kappa,\gamma}}{\partial \mathcal{E}_\alpha \partial \mathcal{E}_\beta} \qquad (8),$$

where $F_{\kappa,\alpha}$ is the Hellman-Feynman force. By modifying the effective-screening medium (ESM) method to apply $\mathcal{E}_z$ along surface normal

direction, [25] eqs. (7) and (8) can be evaluated using the finite difference method.

4.1 Computational details for $\chi^{(2)}$

The ESM boundary condition of the metal/vacuum/metal system was used under a finite electric field. [25] $Z^*_{\kappa,\alpha\beta}$ and $R_{\kappa,\alpha\beta\gamma}$ were obtained using the 4- and 5-point central-finite-difference formulae, respectively. $\Delta\mathcal{E}_z$ was set to 0.005 Ry/e·bohr. The dephasing rate Γ_ν was set to 30 cm^{-1} in eq. (5).

5 Results of second-order non-linear susceptibility: H_2O monolayer on Pt(111)

Figure 2 shows $\mathrm{Im}\,\chi^{(2)}_{zzz}$ of the √39 5·7-ring structure. The PBE and vdW-DF2-B86R functionals gave qualitatively similar results. The intensity at greater than 3000 cm^{-1} region was significantly higher than that at lower region. The large negative amplitude of $\mathrm{Im}\,\chi^{(2)}_{zzz}$ at this region can be attributed to the stretching modes of the H-down molecules. This trend is consistent with those of water and ice surfaces. [21–24]

We compared the calculated spectra of $\mathrm{Im}\,\chi^{(2)}_{zzz}$ with the √39 5·7-ring structure by vdW-DF2-B86R functional with the heterodyne-detected SFG spectroscopy. [21, 22] The first-highest amplitude peak located around 3430 cm^{-1} is in good agreement with the SFG peak positions of 0.8 and 1.4 BL samples (~ 3370 cm^{-1}). The second-highest peak at 3250 cm^{-1} is also in reasonable agreement with the peak positions of 0.8 and 1.4 BL samples (3290–3300 cm^{-1}). The results suggest that the experimental peak at

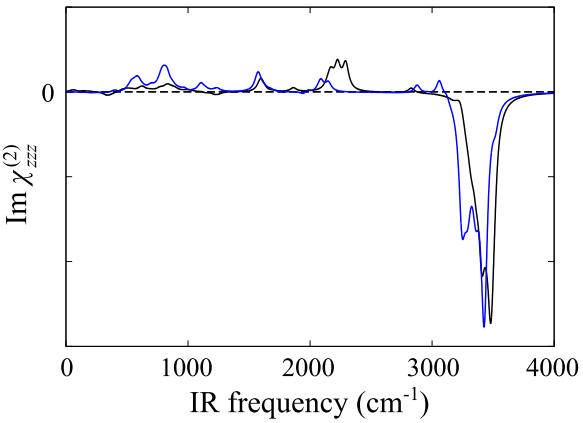

Fig 2. $\mathrm{Im}\,\chi^{(2)}_{zzz}$ as a function of IR frequency ω_{IR}. The amplitudes obtained by PBE and vdW-DF2-B86R functionals are shown as black and blue lines, respectively. Adapted with permission from ref. [17]. Copyright 2024 American Physical Society.

3280 cm^{-1} of 2.6 BL could be come from the OH stretching mode of bulky surface layers. To determine which vibrational mode contributes to the negative amplitude, the vibrational density of states of √39 5·7-ring structures were projected onto center 6-ring, upper 5-ring, and the other 6·7-ring H_2O molecules. The DOSs of the two structures at 3250 cm^{-1} are exclusively composed of the 5-ring and 6·7-ring H_2O molecules. Such analysis is useful to attribute $\chi^{(2)}$ spectral to characteristic modes and atoms.

To the best of our knowledge, $\mathrm{Im}\,\chi^{(2)}_{zzz}$ of Pt(111)/ice system at low-frequency region (ω_{IR} < 3000 cm^{-1}) has not been observed by SFG measurements; however, the first-principles

method developed in this study can provide all frequency region. The small positive amplitude of Im $\chi^{(2)}_{zzz}$ in the low-frequency region was predicted as shown in Fig. 2. For the stretching modes at ω_{IR} = 1800–2400 cm^{-1}, the connected 5-ring H_2O molecules include H-up H_2O molecules, which results in a positive amplitude. For the bending and libration modes at 1600 and 600–1200 cm^{-1}, respectively, a qualitative one-molecule description can be used to explain the sign of Im $\chi^{(2)}_{zzz}$, as follows; we consider the bending and libration (rotation around *y*-axis) motions of one H-down H_2O molecule as shown in Fig. 3. For the bending motion, the *z*-component amplitude of H1 atom is negligible. On the other hand, the *z*-component amplitude of H2 atom is finite. Because the OH direction of the contributed H atom are upward, the positive sign of Im $\chi^{(2)}_{zzz}$ is expected. In the same way, for the libration motion, the downward H1 and upward H2 atoms have no and positive contributions to Im $\chi^{(2)}_{zzz}$, respectively.

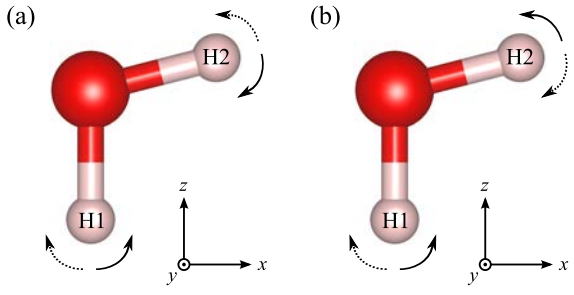

Fig 3. Schematic images of (a) bending and (b) libration motions of one H-down H_2O molecule. Reprinted with permission from ref. [17]. Copyright 2024 American Physical Society.

6 Conclusions

The adsorbed H_2O monolayers on Pt(111) surface were treated within first-principles methods. The adsorption energies E_{ad} of √3 H-down, √39 6-ring, √39 (and √37) 5·7-ring structures were calculated by three (PBE, vdW-DF, and vdW-DF2-B86R) functionals. It is indicated that the 5·7-ring structure has great advantage of the interaction energies between Pt–H_2O and H_2O–H_2O. The heats of adsorption H_{ad} of √3 H-down, √39 5·7-ring, and √37 5·7-ring structures show that the vdW-DF2-B86R functional is the most reliable one among them. In addition, the second-order nonlinear susceptibility $\chi^{(2)}_{zzz}$ was obtained by developing the ESM + applied field approach. The negative and positive amplitudes of Im $\chi^{(2)}_{zzz}$ were obtained in the high and low frequency regions, respectively. The spectra calculated with the √39 5·7-ring structure were consistent with SFG spectroscopy. This study paved the way for the understanding of metal-adsorbed water and electrochemical interfacial systems.

References

[1] J. Carrasco, A. Hodgson, and A. Michaelides, Nat. Mater. **11**, 667 (2012).

[2] A. Groβ and S. Sakong, Chem. Rev. **122**, 10746 (2022).

[3] N. Materer, U. Starke, A. Barbieri, M A. Van Hove, G. A. Somorjai, G.-J. Kroes, and C. Minot, J. Chem. Phys. **99**, 6267 (1995).

[4] A. Glebov, A. P. Graham, A. Menzel, and J.

P. Toennies, J. Chem. Phys. **106**, 9382 (1997).
[5] S. Haq, J. Harnett, and A. Hodgson, Surf. Sci. **505**, 171 (2002).
[6] J. L. Daschbach, B. M. Peden, R. S. Smith, and B. D. Kay, J. Chem. Phys. **120**, 1516, (2004).
[7] S. Nie, P. J. Feibelman, N. C. Bartelt, and K. Thümer, Phys. Rev. Lett. **105**, 026102, (2010).
[8] P. J. Feibelman, N. C. Bartelt, S. Nie, and K. Thümer, J. Chem. Phys. **133**, 154703 (2010).
[9] D. R. Hamann, Phys. Rev. B **55**, R10157 (1997).
[10] J. P. Perdew, K. Burke, and M. Ernzerhof, Phys. Rev. Lett. **77**, 3865 (1996).
[11] M. Dion, H. Rydberg, E. Schröder, D. C. Langreth, and B. I. Lundqvist, Phys. Rev. Lett. **92**, 246401 (2004).
[12] I. Hamada, Phys. Rev. B **89**, 121103(R) (2014).
[13] V. R. Brill and A. Tippe, Acta Cryst. **23**, 343 (1967).
[14] E. Whalley, Trans. Faraday Soc. **53**, 1578 (1957).
[15] P. J. Feibelman, Phys. Chem. Chem. Phys. **10**, 4688 (2008).
[16] I. Hamada, J. Chem. Phys. **133**, 214503 (2010).
[17] J. Haruyama, T. Sugimoto, and O. Sugino, Phys. Rev. Materials **7**, 115803 (2023).
[18] K. Momma and F. Izumi, J. Appl. Crystallogr. **44**, 1272 (2011).
[19] P. Giannozzi *et al*., J. Phys.: Condens. Matter **21**, 395502 (2009); *ibid.* **29**, 465901 (2017).
[20] https://isspns-gitlab.issp.u-tokyo.ac.jp/j-haruyama/Pt111_H2O-monolayer
[21] T. Sugimoto, N. Aiga, Y. Otsuki, K. Watanabe, and Y. Matsumoto, Nature Phys. **12**, 1063 (2016).
[22] T. Sugimoto and Y. Matsumoto, Phys. Chem. Chem. Phys. **22**, 16453 (2020).
[23] A. Morita and J. T. Hynes, Chem. Phys. **258**, 371, (2000).
[24] A. Morita and J. T. Hynes, J. Phys. Chem. B **106**, 673, (2002).
[25] M. Otani and O. Sugino, Phys. Rev. B **73**, 115407 (2006).

Theoretical studies on the spin-charge dynamics in Kondo-lattice models

Masahito MOCHIZUKI, and Rintaro ETO
Department of Applied Physics, Waseda University
Okubo, Shinjuku-ku, Tokyo 169-8555

Abstract

The Kondo-lattice model describes a typical spin-charge coupled system in which localized spins and itinerant electrons are strongly coupled via exchange interactions and exhibits a variety of long-wavelength magnetic orders originating from the nesting of Fermi surfaces. Recently, several magnetic materials that realize this model have been discovered experimentally, and they have turned out to exhibit rich topological magnetic phases including skyrmion crystals and hedgehog lattices. Our recent theoretical studies based on the large-scale spin-dynamics simulations have revealed several interesting nonequilibrium phenomena and excitation dynamics in the Kondo-lattice model, e.g., dynamical magnetic topology switching and peculiar spin-wave modes of the skyrmion crystals and the hedgehog lattices under irradiation with electromagnetic waves such as microwaves and light [1, 2, 3]. These achievements are expected to open a new research field to explore novel nonequilibrium topological phenomena and related material functions of the spin-charge coupled magnets.

1 Introduction

Since the discovery of magnetic skyrmions in chiral magnets in 2009 [4, 5], topological spin textures such as skyrmions, merons, biskyrmions, hedgehogs, and hopfions have attracted a great deal of research interest from the viewpoints of both fundamental science and technical applications [6, 7, 8, 9, 10]. A variety of physical phenomena and material functions of the topological magnetism have been intensively studied and explored, which include magnetic memory device functions based on their current-driven motion [11, 12, 13, 14, 15], various anomalous quantum transport phenomena induced by emergent magnetic fields through the Berry phase mechanism, unique optical and microwave device functions arising from their peculiar excitation dynamics [16, 17, 18, 19, 20], and potentially useful power generation functions originating from coupling with electric charges [21, 22, 23, 24].

Many of the topological magnetic textures with spatially modulated magnetizations are manifested and stabilized by the Dzyaloshinskii-Moriya interaction (DMI) [31, 32, 33], which becomes active in magnets with broken spatial inversion symmetry, e.g., chiral magnets [4, 5, 25, 26, 27], polar magnets [28, 29, 30], and magnetic heterojunctions [11]. The DMI has a relativistic origin and favors a helical alignment of magnetizations with a 90-degree rotation angle. This interaction competes with the ferromagnetic exchange interaction, which favors parallel alignment of magnetizations. Their competition results in the formation of topological magnetic textures with moderate pitch angles.

In such DMI magnets, the skyrmions can appear not only as isolated defects in the fer-

romagnetic background but also as a long-range order with a hexagonally crystallized form. However, other topological magnetic textures mostly appear as isolated defects only, and they are usually not stable energetically. In addition, in the DMI magnets, the spatial configurations of magnetizations are governed by structures of the DM vectors, which is predominantly determined by crystal symmetry [34, 35]. As a result, the internal degrees of freedom such as helicity, chirality, and vorticity are generally frozen and cannot be changed.

Recently, in addition to the DMI magnets, the Kondo-lattice system, in which itinerant electrons and localized spins are coupled via exchange interactions, has been theoretically proposed as a new host of topological magnetism stabilized by different physical mechanisms [36, 37, 38]. Specifically, various novel topological magnetic textures stabilized by the RKKY-type long-range spin-spin interactions mediated by itinerant electrons have been theoretically proposed, which include not only usual skyrmion crystals with a topological charge of $|Q|$=1 but also nontrivial skyrmion crystals with a larger topological charge of $|Q| \geq 2$, meron crystals with a half-integer topological charge $|Q|$=1/2, and hedgehog lattices with periodically aligned hedgehog and antihedgehog pairs [39].

These topological magnetisms are realized as superpositions of magnetic helices with multiple propagation vectors ($\boldsymbol{Q}$ vectors) governed by Fermi-surface nesting. This indicates possible realizations of more diverse topological magnetic textures by tuning the Fermi-surface geometry and the $\boldsymbol{Q}$ vectors through variations in material parameters, external fields, and element substitutions. Indeed, recent experiments have observed three-dimensional hedgehog lattices in MnGe [40], $MnSi_{1-x}Ge_x$ [41] and $SrFeO_3$ [42], triangular skyrmion crystals in Gd_2PdSi_3 [43], $Gd_3Ru_4Al_{12}$ [44] and EuPtSi [45], and square skyrmion crystals in $GdRu_2Si_2$ [46].

More importantly, in the Kondo-lattice magnets, the topological magnetic textures do not require breaking of spatial inversion symmetry and the resulting DMI for their emergence and stabilization because they are realized by the exchange interactions between itinerant electrons and localized spins. As a consequence, the helicity, chirality, and vorticity of the magnetic textures remain unfrozen as internal degrees of freedom in this system, which enables us their low-energy excitations and continuous modulations. This aspect provides a unique opportunity to control and switch magnetic topology by various external stimuli.

It is known that skyrmions and skyrmion tubes in chiral magnets exhibit interesting physical phenomena and potential device functions originating from their unique spin-wave modes in the microwave regime. We expect that the topological magnetism manifested in Kondo lattice magnets also exhibits interesting phenomena and functionalities associated with possible collective excitation modes peculiar to the Kondo-lattice system. However, nature and properties of the spin-charge dynamics have not been elucidated sufficiently.

In this paper, we overview the following three topics associated with our recent theoretical studies in this direction.

(1) Microwave-induced magnetic topology switching [1]: It is discovered that application of circularly polarized microwave magnetic field can switch the magnetic topology among three topological magnetic phases characterized by different topological numbers ($|N_{\rm sk}|$=0, 1, and 2) in a triangular Kondo-lattice model.

(2) Low-energy excitation modes and spin-charge segregation [2]: It is discovered that a zero-field skyrmion crystal phase in a triangular Kondo-lattice model has three linearly dispersive Goldstone modes associated with spin excitations and one quadratically dispersive pseudo-Goldstone mode associated with charge excitations. Surprisingly they turn

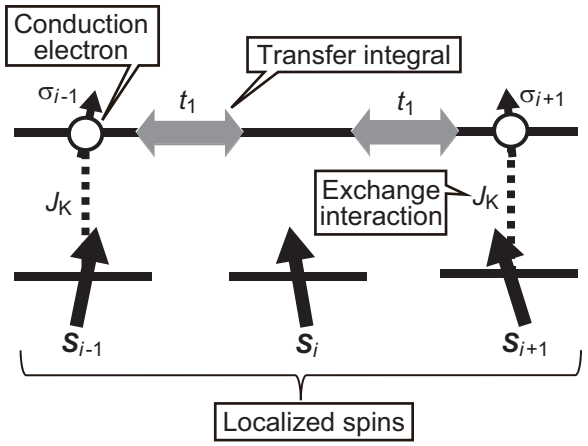

Figure 1: Schematics of the Kondo-lattice model. Itinerant electrons and localized spins are coupled via the Kondo exchange coupling $J_{\rm K}$. The localized spins are not necessarily interacting directly, but indirect interactions mediated by the itinerant electrons exist, which realize long-range ordering of the localized spins.

out to be perfectly decoupled in contrast to our naive expectation of strong spin-charge coupling in the Kondo-lattice model.

(3) Spin-wave modes associated in the quadratic hedgehog lattices [3]: It is discovered that quadratic hedgehog lattice phases in the cubic Kondo-lattice model have collective excitation modes associated with translational oscillation of Dirac strings connecting a hedgehog and an antihedgehog. One of the two modes turn out to vanish upon a field-induced topological phase transition where one of the two types of Dirac-string sublattices undergoes pair annihilations and disappears.

2 Model and Method

The Hamiltonian of the Kondo-lattice model is given by,

$$\mathcal{H}_{\rm KLM} = \sum_{i,j,\sigma} t_{ij}\hat{c}^{\dagger}_{i\sigma}\hat{c}_{j\sigma} - \mu\sum_{i\sigma}\hat{c}^{\dagger}_{i\sigma}\hat{c}_{i\sigma}, - \frac{J_{\rm K}}{2}\sum_{i,\sigma,\sigma'}\hat{c}^{\dagger}_{i\sigma}\boldsymbol{\sigma}_{\sigma\sigma'}\hat{c}_{i\sigma'}\cdot\boldsymbol{S}_i. \quad (1)$$

Here $\hat{c}^{\dagger}_{i\sigma}$ ($\hat{c}_{i\sigma}$) is a creation (annihilation) operator of an itinerant electron with spin $\sigma(=\uparrow,\downarrow)$ on site i. The first and second terms describe kinetic energies and a chemical potential of itinerant electrons. The third term describes the Kondo exchange coupling between the itinerant electron spins and the localized classical spins $\boldsymbol{S}_i$ ($|\boldsymbol{S}_i|=1$).

We also consider the Zeeman-coupling term,

$$\mathcal{H}_{\rm Zeeman} = -\sum_i [\boldsymbol{H}_{\rm ext} + \boldsymbol{H}(t)]\cdot\boldsymbol{S}_i, \quad (2)$$

where $\boldsymbol{H}_{\rm ext} = (0,0,H_z)$ is a static magnetic field, and $\boldsymbol{H}(t)$ is a time-dependent magnetic field acting on the localized spins. The total Hamiltonian is given by $\mathcal{H} = \mathcal{H}_{\rm KLM} + \mathcal{H}_{\rm Zeeman}$. The coupling between the magnetic fields and the itinerant electrons is neglected, since we have confirmed that it does not affect the results even quantitatively in the microwave and sub-terahertz frequency regimes.

Time evolutions of the localized spins are numerically simulated using the Landau-Lifshitz-Gilbert (LLG) equation,

$$\frac{d\boldsymbol{S}_i}{dt} = -\boldsymbol{S}_i\times\boldsymbol{H}_i^{\rm eff} + \frac{\alpha_{\rm G}}{S}\boldsymbol{S}_i\times\frac{d\boldsymbol{S}_i}{dt}. \quad (3)$$

The equation is composed of two contributions. The first term describes precession of localized spins around the effective local magnetic field $\boldsymbol{H}_i^{\rm eff}$. The second term phenomenologically describes a dissipation effect where $\alpha_{\rm G}$ is the dimensionless Gilbert-damping coefficient. The effective field $\boldsymbol{H}_i^{\rm eff}$ is calculated by,

$$\boldsymbol{H}_i^{\rm eff} = -\frac{\partial\Omega}{\partial\boldsymbol{S}_i} + \boldsymbol{H}_{\rm ext} + \boldsymbol{H}(t). \quad (4)$$

The thermodynamic potential Ω for $\mathcal{H}_{\rm KLM}$ is given by,

$$\Omega = \int \rho(\varepsilon,\{\boldsymbol{S}_i\})\, f(\varepsilon-\mu)\, d\varepsilon, \quad (5)$$

with

$$\rho(\varepsilon,\{\boldsymbol{S}_i\}) = \frac{1}{2N}\sum_{\nu=1}^{2N}\delta(\varepsilon-\varepsilon_\nu(\{\boldsymbol{S}_i\})), \quad (6)$$

$$f(\varepsilon-\mu) = -\frac{1}{\beta}\ln\left[1+e^{-\beta(\varepsilon-\mu)}\right], \quad (7)$$

where $\rho(\varepsilon, \{\boldsymbol{S}_i\})$ is the density of states of the itinerant electrons for a given set of the localized spins $\{\boldsymbol{S}_i\}$, and $f(\varepsilon - \mu)$ is the free energy density of the system. We use the kernel polynomial method based on the Chebyshev polynomial expansion to calculate Ω and the automatic differentiation technique to calculate its magnetization-derivative $\partial\Omega/\partial\boldsymbol{S}_i$ [47, 48]. We solve the LLG equation using the fourth-order Runge-Kutta method to obtain the spatiotemporal profiles of the dynamics of localized spins. This methodology assumes that in the low-frequency regimes of gigahertz or sub-terahertz considered here, the itinerant electrons smoothly follow the localized-spin dynamics and are immediately relaxed to a ground state for a given localized-spin configuration at each moment.

All the numerical simulations discussed below are performed at zero temperature with no thermal fluctuations in order to investigate pure effects of microwave/light irradiation for dynamical phenomena in the Kondo-lattice models. For more details of the simulations, see references indicated in each section.

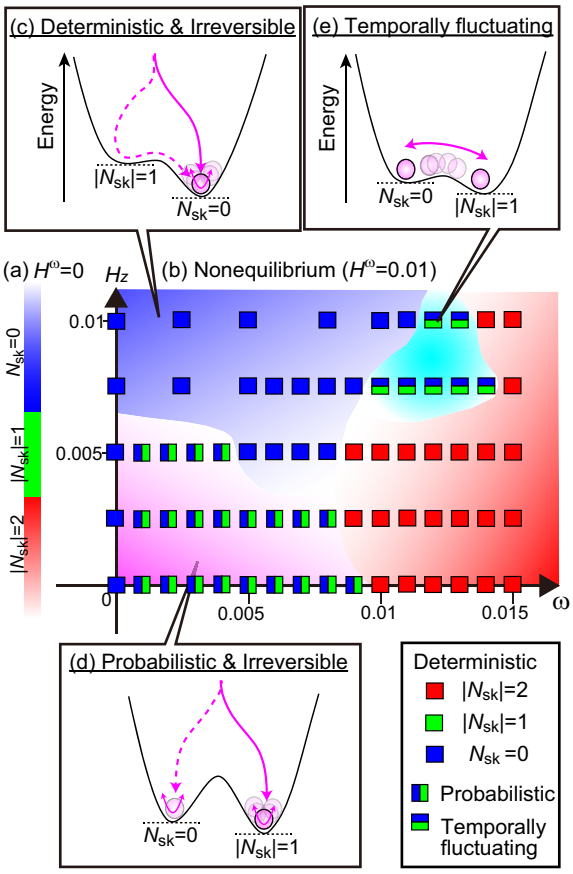

Figure 2: (a) Equilibrium phase diagram of the triangular Kondo-lattice model in a static magnetic field $H_{\rm ext} = (0, 0, H_z)$ without microwave (H^ω=0). (b) Nonequilibrium phase diagram in plane of microwave frequency ω and H_z under irradiation with circularly polarized microwave field. The microwave amplitude is fixed at H^ω=0.01. (c)-(e) Schematic energy landscapes for different switching behaviors.

3 Microwave-Induced Switching of Magnetic Topology

First, we discuss microwave-induced dynamical switching of magnetic topology in a triangular Kondo-lattice model [1]. We adopt $t_1 = -1$ for the nearest-neighbor hopping, $t_3 = 0.85$ for the third-neighbor hopping, $J_{\rm K} = 1$ for the Kondo exchange coupling, and $\mu = -3.5$ for the chemical potential. With this parameter set, the model is known to exhibit two types of skyrmion crystals with different skyrmion numbers as superpositions of three magnetic helices [38].

The noncoplanar spin structures generally have finite local scalar spin chirality χ_i, which is defined by a solid angle spanned by three neighboring spins. On the triangular lattice, it is defined by

$$\chi_i = \boldsymbol{S}_i \cdot (\boldsymbol{S}_{i+\hat{\boldsymbol{a}}} \times \boldsymbol{S}_{i+\hat{\boldsymbol{b}}})/4\pi, \tag{8}$$

where $\hat{\boldsymbol{a}}$ and $\hat{\boldsymbol{b}}$ are primitive translation vectors of the triangular lattice. This quantity is related with a topological invariant called the skyrmion number $N_{\rm sk}$ as,

$$N_{\rm sk} = N_{\rm muc} \sum_{i=1}^{N} \chi_i / N, \tag{9}$$

where $N_{\rm muc}$ is the number of sites in a magnetic unit cell.

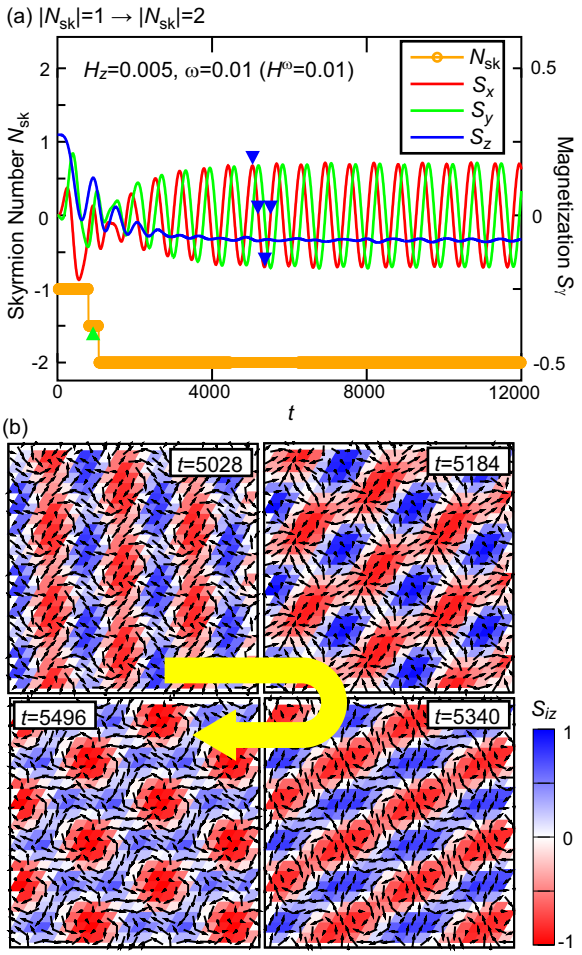

Figure 3: Time profiles of the net spin $\boldsymbol{S} = (S_x, S_y, S_z)$ and the skyrmion number $N_{\rm sk}$ during a process of the microwave-induced topology switching from $N_{\rm sk} = -1$ to $N_{\rm sk} = -2$ in the triangular Kondo-lattice model at H_z=0.005 irradiated with circularly polarized microwave field with a frequency of ω=0.01.

Figure 2(a) shows an equilibrium phase diagram as a function of H_z, in which three magnetic phases, i.e., a skyrmion crystal phase with $|N_{\rm sk}|$=2, another skyrmion crystal phase with $|N_{\rm sk}|$=1, and a nontopological phase with $|N_{\rm sk}|$=0, successively appear with increasing H_z. Importantly, several internal degrees of freedom, e.g., helicity, chirality, and vorticity, remain unfrozen in this system because of the spatial inversion symmetry, and the spin structures in these phases have infinite degeneracy. This is in striking contrast to the skyrmion crystals in chiral magnets stabilized by DMI.

The continuous degeneracy due to these internal degrees of freedom enables us to realize the transformation of spin structures by application of external stimuli. To demonstrate it, we have simulated spatiotemporal dynamics of localized spins induced by an applied microwave field $\boldsymbol{H}(t) = H^{\omega}\beta(t)(\cos\omega t, \sin\omega t, 0)$ with a time-dependent factor $\beta(t)$ introduced for a gradual increase of the microwave amplitude.

The numerical simulations have indeed revealed that spin excitations induced by irradiation with circularly polarized microwave can switch the magnetic topology, e.g., from the skyrmion crystal with $|N_{\rm sk}|$=1 to another skyrmion crystal with $|N_{\rm sk}|$=2 or to a nontopological magnetic state with $|N_{\rm sk}|$=0 depending on the microwave frequency. The induced nonequilibrium spin phases are summarized in the nonequilibrium phase diagram in plane of ω and H_z when the microwave amplitude is fixed at H^{ω}=0.01 [Fig. 2(b)].

The magnetic topology switching shows various behaviors, that is, deterministic irreversible switching, probabilistic irreversible switching, and temporally random fluctuation depending on the microwave frequency and the strength of external magnetic field, variety of which is attributable to different energy landscapes in the dynamical regime.

We show a few examples of the observed topology-switching phenomena below. In Fig. 3, we present simulated time profiles of the net spin $\boldsymbol{S} \equiv (1/N)\sum_i \boldsymbol{S}_i$ and the skyrmion number $N_{\rm sk}$ in a system irradiated with circularly polarized microwave field with a frequency of ω=0.01 when $H_z = 0.005$. Starting with the skyrmion crystal with $N_{\rm sk} = -1$ as a ground state at $H_z = 0.005$, we observe a microwave-induced switching of the magnetic topology from $N_{\rm sk} = -1$ to $N_{\rm sk} = -2$. Here the skyrmion crystal with $N_{\rm sk} = -2$ appears as a nonequilibrium steady state where the total spin oscillates in a steady manner. Interest-

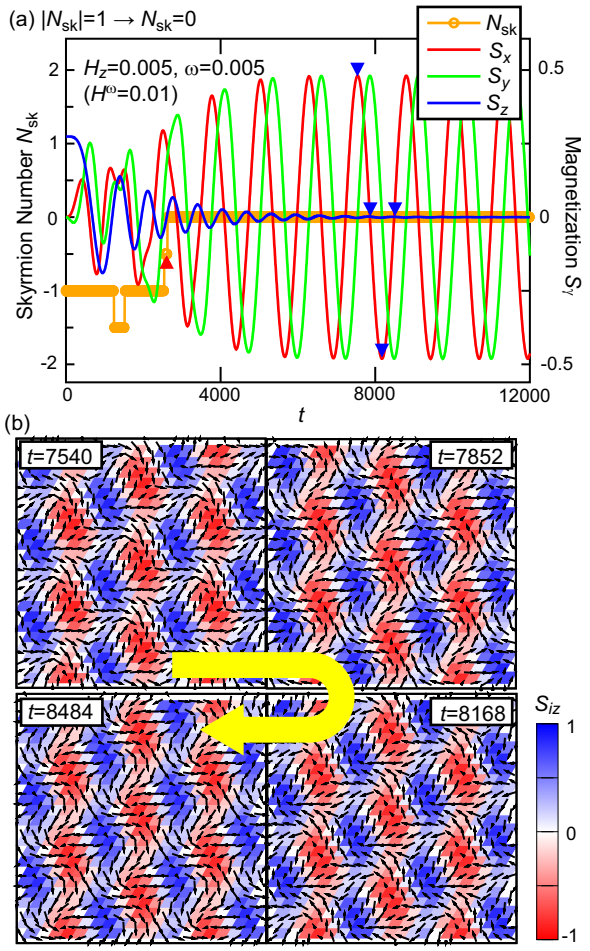

Figure 4: Time profiles of the net spin $\boldsymbol{S}$ and the skyrmion number $N_{\rm sk}$ during a process of the microwave-induced topology switching from $N_{\rm sk} = -1$ to $N_{\rm sk}$=0 in the triangular Kondo-lattice model at H_z=0.005 irradiated with circularly polarized microwave with a relatively slower frequency of ω=0.005.

ingly, a transient magnetic state with a half-integer skyrmion number ($N_{\rm sk} = -1.5$) is observed during the switching process.

On the other hand, Fig. 4 shows simulated time profiles of the total spin $\boldsymbol{S}$ and the skyrmion number $N_{\rm sk}$ when the system is irradiated with a relatively slower circularly polarized microwave field with ω=0.005. Starting with the a skyrmion crystal state with $N_{\rm sk} = -1$ as a ground state at $H_z = 0.005$, the nontopological state with $N_{\rm sk} = 0$ appears as a nonequilibrium steady state with steady oscillation of $\boldsymbol{S}$. Again, a nonequilibrium transient state with a half-integer skyrmion number is observed during the switching process.

4 Low-Energy Spin and Charge Excitations in Skyrmion Crystals

Next we discuss our theoretically study on the spin and charge excitations of skyrmion crystals in centrosymmetric Kondo-lattice magnets [2]. As we have discussed, long-range spin interactions mediated by itinerant electrons stabilize various skyrmion-crystal phases as different patterns of superpositions of multiple spin helices whose propagation vectors are governed by the Fermi-surface nesting. Hence, we naively expect that nature of strong spin-charge coupling should appear in their low-energy excitations. However, it is not always the case in reality as argued in this section.

We again employ the Kondo-lattice model on a triangular lattice given by Eq. (1). Figure 5(a) shows the ground-state phase diagarm in plane of H_z and $J_{\rm K}$ when $t_1 = -1$, $t_3 = 0.85$ and $\mu = -3.5$. A skyrmion crystal phase with $|N_{\rm sk}|$=2 [Fig. 5(b)], another skyrmion crystal phase with $|N_{\rm sk}|$=1 [Fig. 5(c)], and a nontopological phase with $|N_{\rm sk}|$=0 appear in this order as H_z increases in the broad range of the Kondo exchange coupling $J_{\rm K}$. We set $J_{\rm K} = 1(\sim |t_1|)$, for which the system is in the weak-coupling regime and, thus, is metallic with no finite exchange gap.

To study the spin and charge excitation spectra in each phase, we simulate spatiotemporal dynamics of the localized spins $\boldsymbol{S}_i(t)$ after locally applying a short magnetic-field pulse using the Landau-Lifshitz equation. The equation is obtained by setting $\alpha_{\rm G} = 0$ in Eq. (3). The effective local magnetic field $\boldsymbol{H}_i^{\rm eff}$ is calculated again using the kernel polynomial method combined with the automatic differentiation technique [47, 48]. The wavefunction of itinerant electrons $|\Psi(t)\rangle$ at each moment t is composed of eigenstates $|\psi_\nu(t)\rangle$ of the Hamil-

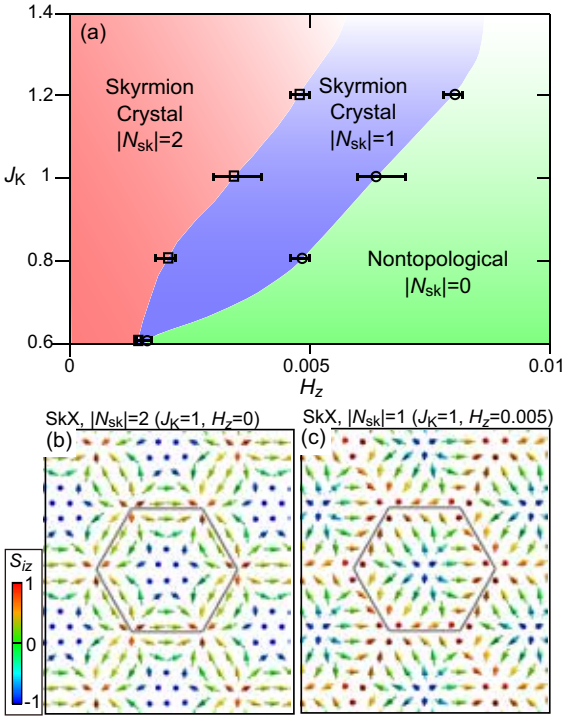

Figure 5: (a) Ground-state phase diagram in plane of H_z and $J_{\rm K}$ for the triangular Kondo-lattice model. (b), (c) Spatial spin configurations $\{\boldsymbol{S}_i\}$ for two kinds of skyrmion crystal states with (b) $|N_{\rm sk}|$=2 and (c) $|N_{\rm sk}|$=1. For the parameter values, see text.

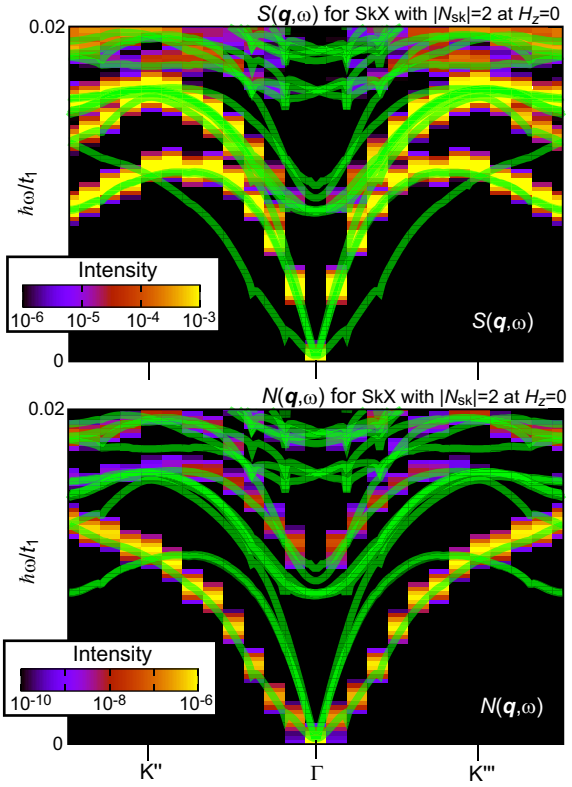

Figure 6: Dynamical spin and charge structure factors, $S(\boldsymbol{q},\omega)$ and $N(\boldsymbol{q},\omega)$, near the Γ point for the skyrmion crystal with $|N_{\rm sk}| = 2$ at $H_z = 0$. The spectra calculated by the spin dynamics simulations are presented by square dots, while the dispersion relations calculated by the linear spin-wave theory are presented by thick lines.

tonian $\mathcal{H}_{\rm KLM}$.

Dynamical spin and charge structure factors $S(\boldsymbol{q},\omega)$ and $N(\boldsymbol{q},\omega)$ are calculated from the simulated time profiles of $\boldsymbol{S}_i(t)$ and $|\Psi(t)\rangle$ as,

$$S(\boldsymbol{q},\omega) \propto \sum_{i,j=1}^{N} e^{-i\boldsymbol{q}\cdot(\boldsymbol{r}_i-\boldsymbol{r}_j)} \sum_{n=1}^{N_t} e^{i\omega t_n} \langle \boldsymbol{S}_i(t)\cdot\boldsymbol{S}_j(0)\rangle$$

$$N(\boldsymbol{q},\omega) \propto \sum_{i,j=1}^{N} e^{-i\boldsymbol{q}\cdot(\boldsymbol{r}_i-\boldsymbol{r}_j)} \sum_{n=1}^{N_t} e^{i\omega t_n} \langle n_i(t)\cdot n_j(0)\rangle,$$

where $n_i(t) = \sum_\sigma \langle\Psi(t)|\, \hat{c}^\dagger_{i\sigma}\hat{c}_{i\sigma}\, |\Psi(t)\rangle$ is the expectation value of the electron number on site i at time t. We also calculate dispersion relations of the excitation spectra by using the linear spin-wave theory.

Figure 6 shows calculated $S(\boldsymbol{q},\omega)$ and $N(\boldsymbol{q},\omega)$ for the skyrmion crystal with $|N_{\rm sk}| = 2$ at $H_z = 0$. Noticeably, the spin-excitation spectrum $S(\boldsymbol{q},\omega)$ has large intensities on the three linearly dispersive gapless modes (Goldstone modes), whereas no intensity is observed on the quadratically dispersive mode. These three Goldstone modes are associated with three generators of the SO(3) group in the spin space and originates from spontaneous breaking of the SO(3) symmetry.

On the other hand, the charge-excitation spectrum $N(\boldsymbol{q},\omega)$ has a large intensity on the quadratic mode, whereas no intensity is observed on the three linearly dispersive Goldstone modes. This quadratic mode is associated with translational symmetry. Because of the discreteness of the lattice, this mode has a finite gap but it is negligibly small. This nearly gapless mode (pseudo-Goldstone mode) origi-

nates from spontaneous breaking of the pseudo continuous translational symmetry.

Surprisingly, it is found that the spin and charge excitations appear in different modes, which are separated and totally independent of each other in contrast to our naive expectation of the strong spin-charge coupling in the Kondo-lattice model. This spin-charge segregation in the low-energy excitations is attributable to a fact that the global SO(3) symmetry of the spin rotation and the global translation symmetry of the skyrmion-crystal spin configuration are independent and thus are decoupled. This fact may enable us selective activations of spin and charge degrees of freedom in this system as a unique property of spin textures in the centrosymmetric Kondo-lattice magnets.

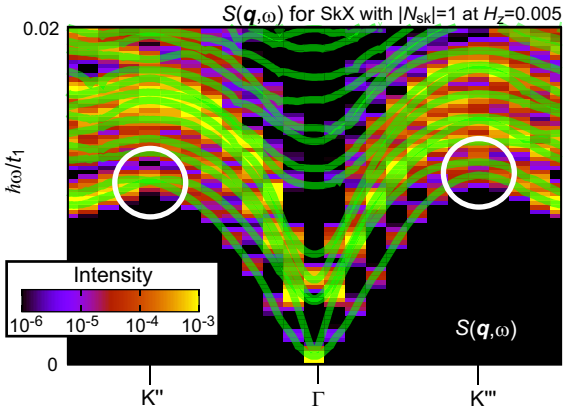

Figure 7: Dynamical spin structure factor $S(\boldsymbol{q},\omega)$ near the Γ point for the skyrmion crystal with $|N_{\rm sk}| = 1$ at $H_z = 0.005$. Nonreciprocal nature of the spin-wave propagation appears in the dispersion relations at the momenta indicated by circles.

However, the spin and charge degrees of freedom are not always decoupled in excitations of the Kondo-lattice magnets. In fact, the spin-charge coupling is manifested in the excitation of scalar spin chirality. The dynamical structure factor of the scalar spin chirality $C_\chi(\boldsymbol{q},\omega)$ has dominant spectral weight on the quadratic mode (not shown) similar to the charge structure factor $N(\boldsymbol{q},\omega)$. The dynamics of noncollinear spin texture with nonzero scalar spin chirality can induce the charge dynamics through generating emergent electromagnetic fields acting on the itinerant electrons via the Berry phase mechanism. The coincidence of charge and chirality excitation channels comes from this coupling.

Figure 7 shows the calculated dynamical spin structure factor $S(\boldsymbol{q},\omega)$ for another skyrmion crystal phase with $|N_{\rm sk}| = 1$ in a finite magnetic field of $H_z = 0.005$. The application of magnetic field reduces the symmetry in the spin space from SO(3) to U(1). As a result, two of the three linearly dispersive Goldstone modes become gapped, and only one mode remains to be gapless. Accordingly, only one linearly dispersive Goldstone mode is observed in the spectra. On the contrary, the quadratic pseudo-Goldstone mode survives even under the application of magnetic field because the pseudo continuous translational symmetry remains even in the magnetic field. It is also found that the applied magnetic field causes mixing of the spin and charge excitations so that the spin-charge segregation observed in the $|N_{\rm sk}|$=2 phase is obscure in the $|N_{\rm sk}|$=1 phase.

The nonreciprocal nature of the spin-wave excitations, i.e., $S(\boldsymbol{q},\omega) \neq S(-\boldsymbol{q},\omega)$, in the skyrmion crystal phase with $|N_{\rm sk}| = 1$ is worth noting as a striking feature of this system, which can be seen in comparison between the spin-wave dispersions indicated by two circles in Fig. 7. This nonreciprocity comes from symmetry of the electronic structure governed by symmetry of the skyrmion-crystal spin configuration in the magnetic field. Indeed, the Fermi surface in this phase does not have the C_2 point-group symmetry, and thus the symmetry of the system is reduced to C_{3h} from original D_{6h} for the triangular lattice. This nonreciprocal nature might be detected experimentally by e.g., neutron-scattering experiments, angle-resolved photoemission spectroscopies, and several transport measurements.

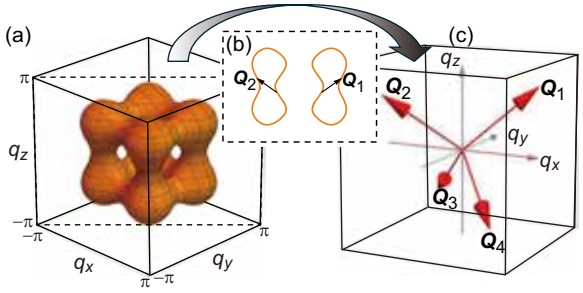

Figure 8: Fermi surface for the kinetic term in Eq. (1). (b) Cross section of the Fermi surface with nesting vectors $\boldsymbol{Q}_1$ and $\boldsymbol{Q}_2$. (c) Four propagation vectors $\{\boldsymbol{Q}_\nu\}$ of magnetic helices constituting the quadratic hedgehog-lattice ($4Q$-HL) states.

5 Collective Modes in Quadratic Hedgehog Lattices

Finally, we discuss a theoretical study on the spin-wave modes of magnetic hedgehog lattices in the Kondo-lattice model in three dimensions [3]. The monopole and antimonopole are conceptual particles which were originally proposed by Paul Dirac in 1931 as isolated positive and negative magnetic charges [49]. The magnetic hedgehog and antihedgehog are spin textures in magnets, which can be regarded as emergent monopole and antimonopole as they behave as source and sink of emergent magnetic fields acting on itinerant electrons through the Berry-phase mechanism.

The magnetic hedgehog lattices are three-dimensional magnetic structures in which the hedgehogs and antihedgehogs are aligned in a periodic manner, which have been recently discovered in several itinerant magnets, e.g., MnGe [40], $MnSi_{1-x}Ge_x$ [41], and $SrFeO_3$ [42]. The hedgehog lattice in MnGe is described by a superposition of three spin helices with cubic propagation vectors and, thus, is referred to as the triple-Q hedgehog lattice ($3Q$-HL). On the other hand, the hedgehog lattices in $MnSi_{1-x}Ge_x$ and $SrFeO_3$ are described by superpositions of four spin helices with tetrahedral propagation vectors, which is, thus, referred to as the quadruple-Q hedgehog lattice ($4Q$-HL).

There are several kinds of $4Q$-HL states with different number of hedgehogs and antihedgehogs in the magnetic unit cell. Possible transformations among them by application of magnetic field have been experimentally proposed. This proposal provides us with an opportunity to study the tunability of material properties via the field-induced topological phase transitions of the hedgehog lattices in $MnSi_{1-x}Ge_x$ and $SrFeO_3$. Under these circumstances, clarification of the collective spin-charge dynamics of the hedgehog lattices is a subject of essential importance because they are deeply related with responses to electromagnetic waves (e.g., microwaves and light) as sources of rich magnetic/optical device functions, dynamical topological phase transitions, and optical control of topology-related material properties.

To study collective excitation modes in the $4Q$-HL states in itinerant chiral magnets $MnSi_{1-x}Ge_x$, we start with the Kondo-lattice model on a chiral cubic lattice. The following two terms are newly added to the original Hamiltonian in Eq. (1),

$$\mathcal{H}_{\rm DMI} = -D \sum_{<i,j>} \boldsymbol{e}_{ij} \cdot (\boldsymbol{S}_i \times \boldsymbol{S}_j), \qquad (10)$$

$$\mathcal{H}_{\rm AFM} = \sum_{<i,j>} J_{\rm AFM} \boldsymbol{S}_i \cdot \boldsymbol{S}_j. \qquad (11)$$

The term $\mathcal{H}_{\rm DMI}$ describes the DMI, while the term $\mathcal{H}_{\rm AFM}$ describes antiferromagnetic exchange interaction, both of which work between the nearest-neighbor localized spins. Here $\boldsymbol{e}_{ij}$ denotes the normalized bond-directional vector from site i to site j. We adopt $J_{\rm K}$=0.8, $J_{\rm AFM}$=0.0008 and examine both cases with and without DMI (i.e., $D = 0$ and $D = 0.0002$). Note that the DMI generally originates from the spin-orbit coupling, but its effects on the itinerant electrons are neglected here for simplicity, which is justified from an experimental insight for $MnSi_{1-x}Ge_x$ [41].

The chemical potential is set to be μ =

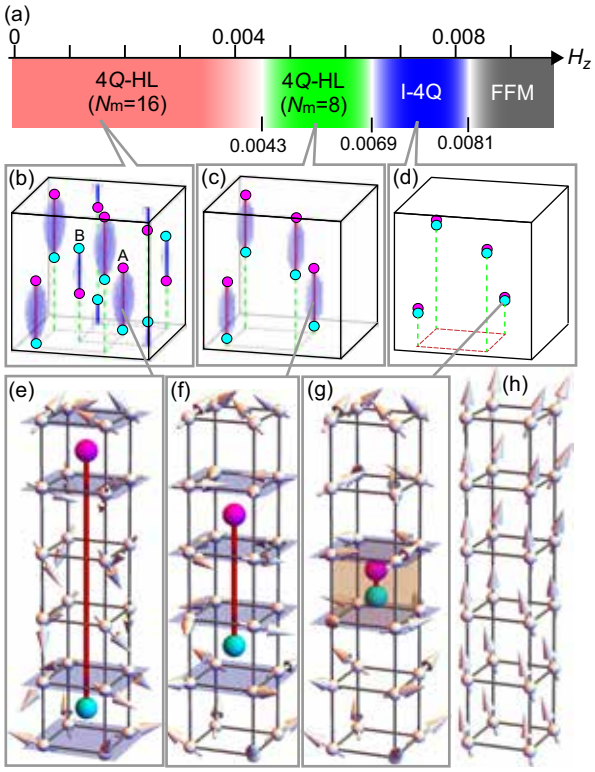

Figure 9: (a) Phase diagram of the cubic Kondo-lattice model as a function of H_z, which contains two $4Q$-HL phases, the intermediate $4Q$ (I-$4Q$) phase, and the forced ferromagnetic (FFM) phase. (b)-(d) Spatial configurations of the Bloch points of hedgehogs (magenta) and antihedgehogs (cyan) in the $4Q$-HL and I-$4Q$ phases. (e)-(g) Spin configurations around the Dirac string A in respective phases. (h) Spin configurations after the Dirac string A vanishes in the FFM phase.

-3.79, which reproduces a wavenumber of $Q \approx \pi/4$ and a spatial period of $\lambda = 2\pi a/\sqrt{3}Q \approx 2.15$ nm in agreement with the experimental value of λ =1.9-2.1 nm for $MnSi_{1-x}Ge_x$ [41]. Here the lattice constant is assumed to be $a = 0.465$ nm. In Figs. 8, the Fermi surface and its cross section associated with the nesting vectors $\boldsymbol{Q}_1$ and $\boldsymbol{Q}_2$ are shown.

Figure 9(a) shows a ground-state phase diagram as a function of magnetic field H_z. In the absence of magnetic field (H_z=0), a $4Q$-HL state composed of eight hedgehogs and eight antihedgehogs in the magnetic unit cell appears where the total number of the hedgehogs and antihedgehogs is N_m=16. This $4Q$-HL state contains two inequivalent Dirac strings (A and B), each of which connects a hedgehog and an antihedgehog along the z axis. There are eight strings in total, four each for strings A and B.

The Dirac strings A and B have the same length in the $4Q$-HL phase with N_m=16 at $H_z = 0$. As H_z increases, both strings A and B gradually shrink. Importantly, the strings B shrink faster than the strings A. Thereby, the strings B disappear first as a result of the hedgehog-antihedgehog pair annihilation when H_z reaches 0.0043, which is a topological phase transition from the $4Q$-HL with N_m=16 to another $4Q$-HL with N_m=8. Subsequently, the system enters the intermediate $4Q$ (I-$4Q$) state at H_z=0.0069 in which the hedgehog and antihedgehog collide to be merged and share the same cubic unit of the lattice. With further increasing H_z, the merging or the pair annihilation of the hedgehog and antihedgehog connected by strings B complete, and the system enters the forced ferromagnetic phase at H_z=0.0081.

In Fig. 10, we show calculated spectra of $\mathrm{Im}\chi_z(\omega)$ where $\chi_z(\omega)$ is the longitudinal dynamical magnetic susceptibility. Noticeably, we observe three excitation modes in the $4Q$-HL phase with $N_m = 16$, which are named L1, L2, and L3 modes, respectively. These modes are expected to appear in the subterahertz regime because ω=0.004 in Fig. 10 corresponds to 1 THz approximately when we assume $t_1 = 1$ eV. Calculated spatial profiles of oscillation amplitudes for respective phases inidcate that the L2 mode is associated with Strings B, whereas the L3 mode is with Strings A. Namely, the L2 and L3 modes are localized around the respective Dirac strings. On the contrary, the L1 mode is a nonlocalized mode whose oscillation amplitude is broadly distributed in space.

Importantly, the L2 mode disappears when

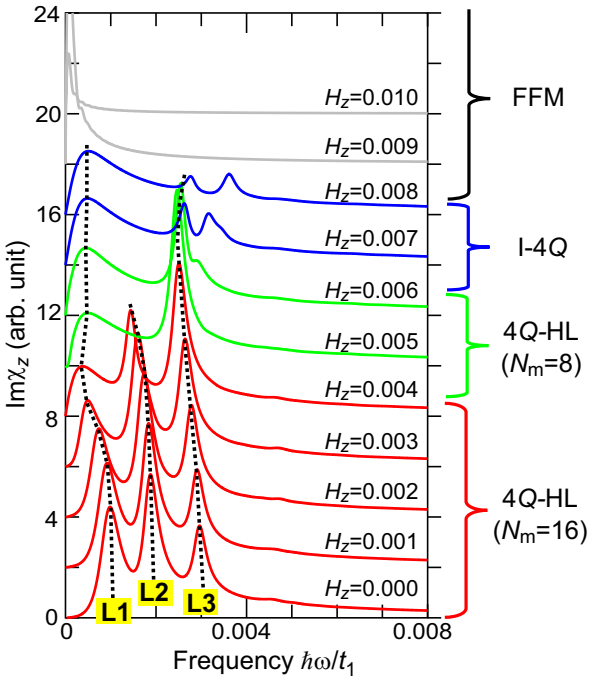

Figure 10: Calculated microwave/light absorption spectra for various values of H_z.

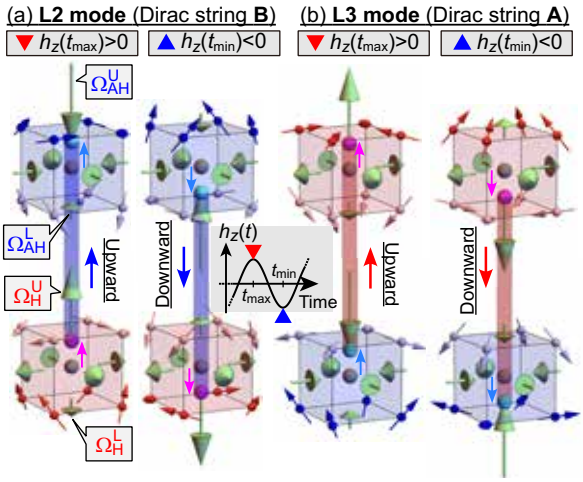

Figure 11: Schematics of the translational oscillations of (a) the Dirac string B in the L2 mode and (b) the Dirac string A in the L3 mode.

the system enters the $4Q$-HL phase with $N_{\rm m} = 8$ because the Strings B vanish upon this phase transition, which indicates that this topological transition can be detected in the magnetic resonance measurements. On the contrary, the L3 mode survives after this phase transition because the Strings A still exist in the $4Q$-HL phase with $N_{\rm m} = 8$. Moreover, the L3 mode is observed in the $N_{\rm m} = 8$ $4Q$-HL phase and even in the subsequent I-$4Q$ phase in which the merging hedgehog-antihedgehog pair has nonzero scalar spin chirality as a residue of the magnetic topology. The L3 mode disappears when the system enters the forced ferromagnetic phase at $H_z \approx 0.0081$, in which the scalar spin chirality vanishes because of the collinear spin configuration.

The L2 and L3 modes can be regarded as translational modes of Dirac strings B and A, respectively. The ac magnetic field of applied electromagnetic wave dynamically modulates the hedgehog and antihedgehog spin configurations, which results in asymmetric distribution of their emergent magnetic fields on a cubic cell composed of eight spins at its corners. More specifically, the solid angles spanned by four-spin plaquettes on the upper and lower cube faces, which is originally symmetric, becomes asymmetric when the ac magnetic field is applied in the z direction. Thereby, an oscillatory shift of the center-of-mass position of the spin solid angles occurs along the z axis at each hedgehog and antihedgehog. The shifts occur with the same phase in each mode, and the resulting in-phase oscillations can be regarded as coherent translational modes of the Dirac strings [Figs. 11(a) and (b)]. It is found that the oscillation phases are the same between L2 and L3 modes, whereas the oscillation phase of the L1 mode is opposite to those of the L2 and L3 modes.

6 Summary

In summary, we have overviewed our recent theoretical studies on the spin-charge dynamics and related microwave/light induced dynamical phenomena in the Kondo-lattice models, which exhibit rich long-wavelength magnetic orders including topological magnetism. Several kinds of skyrmion crystals and hedge-

hog lattices are realized by long-range interactions among the localized spins mediated by itinerant electrons. The long-wavelength magnetic orders in the Kondo-lattice models are usually described by superpositions of multiple helices whose propagation vectors are determined by the nesting of Fermi surfaces. By the large-scale spin-charge dynamics simulations using the Kernel polynomial method, we have revealed a variety of interesting phenomena including (1) microwave-induced switching of magnetic topology for the skyrmion crystal states in the triangular Kondo-lattice model, (2) three linearly dispersive Goldstone modes associated with SO(3) symmetry of the localized spins and one quadratic pseudo-Goldstone mode associated with itinerant-electron charges governed by the discrete translational symmetry of the skyrmion crystal, and unexpected spin-charge segregation in the low-energy excitations of the zero-field skyrmion crystal in the triangular Kondo-lattice model, and (3) two translation modes associated with Dirac strings and disappearance of one of these two modes upon the field-induced topological phase transition with hedgehog-antihedgehog pair annihilations in the quadratic hedgehog lattices in the cubic Kondo-lattice model for real materials of $MnSi_{1-x}Ge_x$ and $SrFeO_3$. Recently, new magnetic materials that realize the Kondo-lattice models have been successively discovered and synthesized experimentally. Furthermore, a variety of topological magnetic phases have been observed in these materials. We expect that the phenomena predicted in our studies will be experimentally observed and confirmed in near future. Moreover, we hope that this article could help to open a new research field on fundamental physics and even engineering of rich dynamical magnetic topology in the spin-charge coupled magnets.

7 Acknowledgements

The studies associated with this article have been supported by JSPS KAKENHI (Grants No. 20H00337, No. 23H04522, and No. 24H02231), JST CREST (Grant No. JPMJCR20T1), and Waseda University Grant for Special Research Projects (2023C-140, 2024C-153). R.E. was supported by a Grant-in-Aid for JSPS Fellows (Grant No. 23KJ2047). Most of the numerical calculations were performed using the supercomputers in Institute for Solid State Physics (ISSP), the University of Tokyo.

References

[1] R. Eto, and M. Mochizuki, Phys. Rev. B **104**, 104425 (2021).

[2] R. Eto, R. Pohle, and M. Mochizuki, Phys. Rev. Lett. **129**, 017201 (2022).

[3] R. Eto, and M. Mochizuki, Phys. Rev. Lett. **132**, 226705 (2024).

[4] S. Mühlbauer, B. Binz, F. Jonietz, C. Pfleiderer, A. Rosch, A. Neubauer, R. Georgii, and P. Böni, Science **323**, 915 (2009).

[5] X. Z. Yu, Y. Onose, N. Kanazawa, J. H. Park, J. H. Han, Y. Matsui, N. Nagaosa, and Y. Tokura, Nature **465**, 901 (2010).

[6] S. Seki and M. Mochizuki, *Skyrmions in Magnetic Materials* (Springer, Berlin, 2016).

[7] N. Nagaosa and Y. Tokura, Nat. Nanotech. **8**, 899 (2013).

[8] K. Everschor-Sitte, J. Masell, R. M. Reeve, and M. Kläui, J. Appl. Phys. **124**, 240901 (2018).

[9] B. Göbel, I. Mertig, and O. A. Tretiakov, Phys. Rep. **895**, 1 (2021).

[10] Y. Tokura and N. Kanazawa, Chem. Rev. **121**, 2857 (2021).

[11] A. Fert, V. Cros, and J. Sampaio, Nat. Nanotech. **8**, 152 (2013).

[12] J. Iwasaki, M. Mochizuki, and N. Nagaosa, Nat. Commun. **4**, 1463 (2013).

[13] J. Iwasaki, M. Mochizuki, and N. Nagaosa, Nat. Nanotechnol. **8**, 742 (2013).

[14] G. Finocchio, F. Buttner, R. Tomasello, M. Carpentieri, and M. Kläui, J. Phys. D: Appl. Phys. **49**, 423001 (2016).

[15] *Topological Structures in Ferroic Materials: Domain Walls, Skyrmions and Vortices* (Springer, 2016) edited by J. Seidel, Chapter 3, "Current-Driven Dynamics of Skyrmions" pp. 55-81, by M. Mochizuki.

[16] M. Mochizuki, Phys. Rev. Lett. **108**, 017601 (2012).

[17] M. Mochizuki, and S. Seki, Phys. Rev. B **87**, 134403 (2013).

[18] Y. Okamura, F. Kagawa, M. Mochizuki, M. Kubota, S. Seki, S. Ishiwata, M. Kawasaki, Y. Onose, and Y. Tokura, Nat. Commun. **4**, 3391 (2013).

[19] M. Mochizuki, Phys. Rev. Lett. **114**, 197203 (2015).

[20] M. Mochizuki, and S. Seki, J. Phys.: Cond. Mat. 27, 503001 (2015).

[21] J. Ohe and Y. Shimada, Appl. Phys. Lett. **103**, 242403 (2013).

[22] Y. Shimada and J. I. Ohe, Phys. Rev. B **91**, 174437 (2015).

[23] T. Koide, A. Takeuchi, and M. Mochizuki, Phys. Rev. B **100**, 014408 (2019).

[24] J. Matsuki and M. Mochizuki, Phys. Rev. B **107**, L100408 (2023).

[25] X. Z. Yu, N. Kanazawa, Y. Onose, K. Kimoto, W. Z. Zhang, S. Ishiwata, Y. Matsui, and Y. Tokura, Nat. Mater. **10**, 106 (2011).

[26] S. Seki, X. Z. Yu, S. Ishiwata, and Y. Tokura, Science 336, 198 (2012).

[27] S. Seki, S. Ishiwata, and Y. Tokura, Phys. Rev. B 86, 060403(R) (2012).

[28] I. Kézsmárki, S. Bordács, P. Milde, E. Neuber, L. M. Eng, J. S. White, H. M. Rønnow, C. D. Dewhurst, M. Mochizuki, K. Yanai, H. Nakamura, D. Ehlers, V. Tsurkan, and A. Loidl, Nat. Mater. **14**, 1116 (2015).

[29] T. Kurumaji, T. Nakajima, V. Ukleev, A. Feoktystov, T.-h. Arima, K. Kakurai, and Y. Tokura, Phys. Rev. Lett. **119**, 237201 (2017).

[30] T. Kurumaji, , T. Nakajima, , A. Feoktystov, E. Babcock, Z. Salhi, V. Ukleev, T.-h. Arima, K. Kakurai, and Y. Tokura, J. Phys. Soc. Jpn. **90**, 024705 (2021).

[31] I. Dzyaloshinsky, J. Phys. Chem. Solids **4**, 241 (1958).

[32] T. Moriya, Phys. Rev. **120**, 91 (1960).

[33] T. Moriya, Phys. Rev. Lett. **4**, 228 (1960).

[34] A. N. Bogdanov and D. A. Yablonskii, Sov. Phys. JETP **68**, 101 (1989).

[35] A. Bogdanov and A. Hubert, J. Magn. Magn. Mater. **138**, 255 (1994).

[36] R. Ozawa, S. Hayami, K. Barros, G.-W. Chern, Y. Motome, and C. D. Batista, J. Phys. Soc. Jpn. **85** 103703 (2016).

[37] S. Hayami, R. Ozawa, and Y. Motome, Phys. Rev. B **95**, 224424 (2017).

[38] R. Ozawa, S. Hayami, and Y. Motome, Phys. Rev. Lett. **118**, 147205 (2017).

[39] S. Hayami and Y. Motome, J. Phys.: Cond. Mat. **33**, 443001 (2021).

[40] N. Kanazawa, Y. Nii, X.-X. Zhang, A. S. Mishchenko, G. De Filippis, F. Kagawa, Y. Iwasa, N. Nagaosa, and Y. Tokura, Nat. Commun. **7**, 11622 (2016).

[41] Y. Fujishiro, N. Kanazawa, T. Nakajima, X. Z. Yu, K. Ohishi, Y. Kawamura, K. Kakurai, T. Arima, H. Mitamura, A. Miyake, K. Akiba, M. Tokunaga, A. Matsuo, K. Kindo, T. Koretsune, R. Arita, and Y. Tokura, Nat. Commun. **10**, 1059 (2019).

[42] S. Ishiwata, T. Nakajima, J.-H. Kim, D. S. Inosov, N. Kanazawa, J. S. White, J. L. Gavilano, R. Georgii, K. M. Seemann, G. Brandl, P. Manuel, D. D. Khalyavin, S. Seki, Y. Tokunaga, M. Kinoshita, Y. W. Long, Y. Kaneko, Y. Taguchi, T. Arima, B. Keimer, and Y. Tokura, Phys. Rev. B **101**, 134406 (2020).

[43] T. Kurumaji, T. Nakajima, M. Hirschberger, A. Kikkawa, Y. Yamasaki, H. Sagayama, H. Nakao, Y. Taguchi, T. Arima, and Y. Tokura, Science **365**, 914 (2019).

[44] M. Hirschberger, T. Nakajima, S. Gao, L. Peng, A. Kikkawa, T. Kurumaji, M. Kriener, Y. Yamasaki, H. Sagayama, H. Nakao, K. Ohishi, K. Kakurai, Y. Taguchi, X. Yu, T.-h. Arima, and Y. Tokura, Nat. Commun. **10**, 5831 (2019).

[45] K. Kaneko, M. D. Frontzek, M. Matsuda, A. Nakao, K. Munakata, T. Ohhara, M. Kakihana, Y. Haga, M. Hedo, T. Nakama, and Y. Ōnuki, J. Phys. Soc. Jpn. **88**, 013702 (2019).

[46] N. D. Khanh, T. Nakajima, X. Yu, S. Gao, K. Shibata, M. Hirschberger, Y. Yamasaki, H. Sagayama, H. Nakao, L. Peng, K. Nakajima, R. Takagi, T. Arima, Y. Tokura, and S. Seki, Nat. Nanotech. **15**, 444 (2020).

[47] A. Weiße, G. Wellein, A. Alvermann, and H. Fehske, Rev. Mod. Phys. **78**, 275 (2006).

[48] K. Barros and Y. Kato, Phys. Rev. B **88**, 235101 (2013).

[49] P. A. M. Dirac, Proc. R. Soc. A **133**, 60 (1931).

Mixing Free Energy and Molecular Dynamics Simulations

Naoko NAKAGAWA and Akira YOSHIDA
Department of Physics, Ibaraki University
2-1-1 Bunkyo, Mito, Ibaraki 310-8512

1 Introduction

Mixing free energy determines the properties of a solution, while theories for its estimation are limited to rather dilute solutions [1, 2, 3]. A simpler numerical method applicable to the general mole fraction and valid regardless of the system size would be valuable. Alchemical free energy calculation is one of the free energy calculation methods often used in the numerical study of drug discovery [4, 5, 6, 7, 8, 9, 10, 11, 12, 13]. Extending the idea, we create a solution from a pure substance, which may provide a formula for calculating the mixing free energy. We thus propose a method for molecular dynamics simulations that estimates the mixing free energy. The details of the derivation and numerical confirmations are in the reference [14].

2 Mixing free energy and activity coefficients

The important quantity that determines the thermodynamic properties for the mixture is the mixing free energy $\Delta_{\rm mix}G$. This corresponds to the work required for quasistatic mixing at constant temperature and constant pressure, which is the sum of the enthalpy change in mixing and the mixing entropy $\Delta_{\rm mix}S$. The change in the thermodynamic properties of each substance is represented by excess chemical potential; i.e., the deviation of chemical potential from that of each pure substance. The excess chemical potential is written as

$$\beta\mu_{\rm A}^{\rm ex}(T,p,c) = \ln c + \ln\gamma_{\rm A}, \tag{1}$$
$$\beta\mu_{\rm B}^{\rm ex}(T,p,c) = \ln(1-c) + \ln\gamma_{\rm B}, \tag{2}$$

with the activity coefficients $\gamma_{\rm A}(T,p,c)$ and $\gamma_{\rm B}(T,p,c)$. c is the mole fraction in the mixture. The mixing Gibbs free energy is given by $\Delta_{\rm mix}G = N[c\mu_{\rm A}^{\rm ex} + (1-c)\mu_{\rm B}^{\rm ex}]$, where N is the total amount of molecules. When $\gamma_{\rm A} = \gamma_{\rm B} = 1$, the mixture is ideal; i.e., a molecule of substance A does not interact with a molecule of B. Then, $\Delta_{\rm mix}G^{\rm id} = -T\Delta_{\rm mix}S^{\rm id}$ with

$$\Delta_{\rm mix}S^{\rm id} = N[c\ln c + (1-c)\ln(1-c)]. \tag{3}$$

The activity coefficients $\gamma_{\rm A}$ and $\gamma_{\rm B}$ represent the intrinsic properties of the mixture that result from the interaction of the two pure substances. Determining $\Delta_{\rm mix}G$ identifies such intrinsic properties as

$$\Delta_{\rm mix}G + T\Delta_{\rm mix}S^{\rm id} = N[c\ln\gamma_{\rm A} + (1-c)\ln\gamma_{\rm B}], \tag{4}$$

because the ideal entropic effects $T\Delta_{\rm mix}S^{\rm id}$ has already known as (3).

3 Difficulty of numerical determination

In textbooks on thermodynamics [15, 16], a standard protocol for determining $\Delta_{\rm mix}S$ and $\Delta_{\rm mix}G$ for two pure substances is the quasistatic shift of two semi-permeable membranes

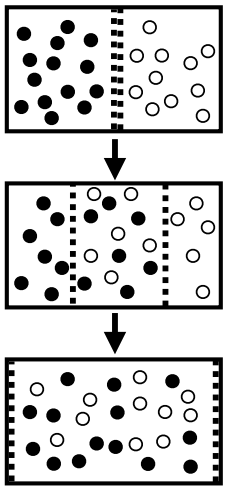

Figure 1: Quasi-static mixing process using two permeable membranes.

as shown in Fig. 1. Initially, two substances are spatially separated by two semi-permeable membranes. Then, shift the two membranes slowly enough as it is regarded as quasi-static. When each membrane reaches the left or right boundary wall, the container is filled with a mixture of the two substances.

We emphasize that this mixing process is difficult in computation involving huge computational resources. The speed of the shift of the membranes should be much slower than the velocity of molecules, as the process needs to be performed quasi-statically. Moreover, because the distance between each membrane and boundary wall is macroscopic, the process requires at least $O(N)$ time steps per trajectory. Thus, this number could be more such as $O(N^2)$. Such a high-cost calculation is hard to complete with a large enough system, and this is likely the reason that such processes are not usually used in the numerical investigation of the mixing entropy.

4 Work relation for determining mixing free energy

We consider microscopic operations called alchemical processes, which change the attributes, such as mass and size, of molecules. Alchemical methods are usually used to estimate the effect of substituting some groups into a large single molecule [6, 7]. We note that an alchemical method itself is not necessarily limited to single molecules but can be applied to multi-molecule systems to create a mixture from a pure substance. Below, we set alchemical protocols for creating a mixture taking care of the distinguishability of the molecules of the same species. Using the protocols we formulate the relation useful for the numerical determination of mixing free energy.

4.1 Setup

We deal with classical systems of N molecules packed in a cobid of volume V. The surrounding environment is at a constant temperature T. We write the Hamiltonian of the system as

$$H(\Gamma;\boldsymbol{\alpha}) = \sum_{i=1}^{N} \frac{\boldsymbol{p}_i^2}{2m_i} + \Phi(\{\boldsymbol{r}_i\};\boldsymbol{\alpha}_\Phi), \qquad (5)$$

where $\Gamma = (\{\boldsymbol{r}_i\},\{\boldsymbol{p}_i\})$ with the position $\boldsymbol{r}_i$ and momentum $\boldsymbol{p}_i$ for the ith molecule, and $(\{a_i\})$ is an abbreviation of $(a_1, a_2, \cdots, a_N)$. m_i is the mass of the ith molecule and the potential Φ comprises the interaction among molecules and the interaction between molecules and walls of the container, which are parameterized by the set $\boldsymbol{\alpha}_\Phi$. The whole of the opearational parameters are $\boldsymbol{\alpha} = (\{m_i\}, \boldsymbol{\alpha}_\Phi)$.

For investigating fixed pressure systems, we replace the Hamiltonian as

$$H_p(\Gamma, V;\boldsymbol{\alpha}) = H(\Gamma;\boldsymbol{\alpha}) + pV, \qquad (6)$$

by replacing a certain wall of the container with a movable wall at a constant pressure of p.

Suppose that an external operator changes the value of $\boldsymbol{\alpha}$ in the period $0 \le t \le \tau$. For

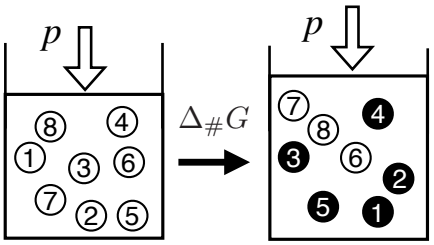

Figure 2: Alchemical processes for determining $\Delta_{\#}G$. The first n particles are changed from a species A to another species B.

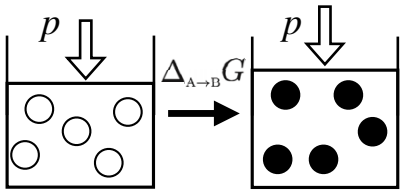

Figure 3: Alchemical processes for determining $\Delta_{\mathrm{A}\to\mathrm{B}}G$. All n particles are changed from a species A to another species B.

a protocol $\hat{\boldsymbol{\alpha}} = (\boldsymbol{\alpha}(t))_{t\in[0,\tau]}$, where $\boldsymbol{\alpha}_0 = \boldsymbol{\alpha}(0)$ and $\boldsymbol{\alpha}_1 = \boldsymbol{\alpha}(\tau)$, the work done by the external operator is written as

$$\hat{W}(\hat{\Gamma}) = \int_0^\tau ds\ \frac{d\boldsymbol{\alpha}}{ds}\cdot\left.\frac{\partial H(\Gamma(s);\boldsymbol{\alpha})}{\partial\boldsymbol{\alpha}}\right|_{\boldsymbol{\alpha}=\boldsymbol{\alpha}(s)}, \tag{7}$$

where $\hat{\Gamma} = (\Gamma(t))_{t\in[0,\tau]}$ is a trajectory in the phase space. We assume below that the system is in equilibrium at $\boldsymbol{\alpha}_0$ for $t \le 0$. For constant pressure systems, the volume V becomes a microscopic variable, and a trajectory in phase space is replaced by $(\hat{\Gamma}, \hat{V}) = (\Gamma(t), V(t))_{t\in[0,\tau]}$.

4.2 Alchemical protocols

We concentrate on a mixture of two species A and B, whose numbers of molecules are n and $N-n$, respectively. The mole fraction is $c \equiv n/N$.

We put N molecules of species A in a container and index all N molecules in order. After relaxing the system to equilibrium, we change the attributes of the first n molecules, $1 \le i \le n$, alchemically as they become another species B as depicted in Fig. 2. We write the work for completing the alchemical process as $\hat{W}_{\#}(\hat{\Gamma}, \hat{V})$. The resulting system is similar to a typical two-component mixture except that all molecules are indexed.

Let $G_{\mathrm{AB}^{\#}}$ be the free energy for the mixture of the indexed molecules, while G_{AB} be that for the usual mixture. We note that

$$G_{\mathrm{AB}}(T,p,n,N-n) \neq G_{\mathrm{AB}^{\#}}(T,p,n,N-n), \tag{8}$$

because the molecules are indexed. We can determine the difference from the pure substance A by measuring the work $\hat{W}_{\#}$ as

$$\begin{aligned}\Delta_{\#}G &\equiv G_{\mathrm{AB}^{\#}}(T,V,n,N-n) - G_{\mathrm{A}}(T,V,N),\\ &= -k_{\mathrm{B}}T\ln\left\langle e^{-\beta\hat{W}_{\#}}\right\rangle\end{aligned} \tag{9}$$

where $\langle\cdot\rangle$ is the average over trajectories $(\hat{\Gamma}, \hat{V})$.

We are also possible to determine the Gibbs free energy difference between the pure substances of A and B

$$\begin{aligned}\Delta_{\mathrm{A}\to\mathrm{B}}G &\equiv G_{\mathrm{B}}(T,V,n) - G_{\mathrm{A}}(T,V,n)\\ &= -k_{\mathrm{B}}T\ln\left\langle e^{-\beta\hat{W}_{\mathrm{A}\to\mathrm{B}}}\right\rangle,\end{aligned} \tag{10}$$

with the work in the alchemical process changing all n molecules from A into B as shown in Fig. 3.

4.3 Formula for the mixing Gibbs free energy

We have shown in [14] that the mixing free energy satisfies

$$\begin{aligned}\Delta_{\mathrm{mix}}G + T\Delta_{\mathrm{mix}}S^{\mathrm{id}} &= \Delta_{\#}G - \Delta_{\mathrm{A}\to\mathrm{B}}G\\ &= -k_{\mathrm{B}}T\ln\frac{\left\langle e^{-\beta\hat{W}_{\#}}\right\rangle}{\left\langle e^{-\beta\hat{W}_{\mathrm{A}\to\mathrm{B}}}\right\rangle}\end{aligned} \tag{11}$$

with errors smaller than $\ln N$. We emphasize that $\Delta_{\mathrm{mix}}G$ in (11) is determined just from two alchemical processes in Fig. 2 and Fig. 3.

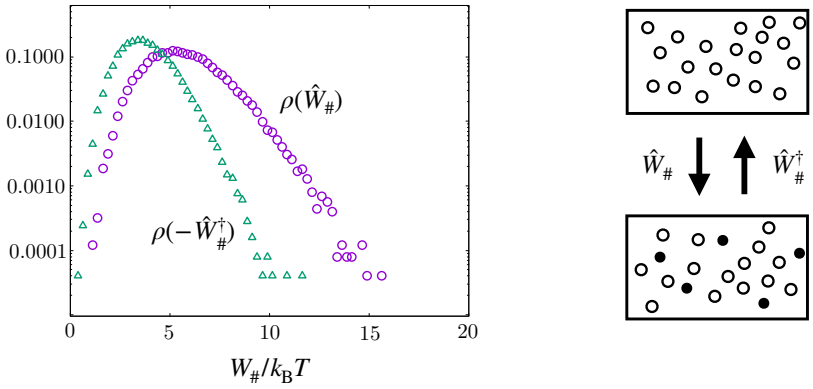

Figure 4: Work distributions in the left figure for the forward and backward protocols for creating a mixture. Here, operation time is $1000\tau_{\rm MD}$. The shape of the distribution depends on the operation time. The sketch of the protocols is shown in the right figures.

process	operation time
textbook	30000 $\tau_{\rm MD}$
A $\to$ B	400 $\tau_{\rm MD}$
#	400 $\tau_{\rm MD}$

Table 1: Comparison of operation times for calculating $\Delta_{\rm mix}G$ for the mixture of two substances of mass m and $2m$ with $c = 0.5$.

process	operation time
textbook	15000 $\tau_{\rm MD}$
A $\to$ B	2050 $\tau_{\rm MD}$
#	2050 $\tau_{\rm MD}$

Table 2: Comparison of operation times for calculating $\Delta_{\rm mix}G$ for the mixture of two substances of diameter σ and 2σ with $c = 0.5$.

The estimates of activity coefficients are a major issue in the research of mixtures, especially from the point of chemical engineering. The relation (11) may offer a new method of estimating the activity coefficients for various mixtures and solutions, which involves only a molecular dynamics simulation with two types of the alchemical process. Moreover, (11) can be applicable not only to dilute mixtures but rather to the mixture showing unstable and dynamic collective behaviors appeared in the first-order transitions. The formula (11) provides a general work relation giving the mixing free energy $\Delta_{\rm mix}G$ at constant pressure.

4.4 Advantage of (11) for numerical determination of $\Delta_{\rm mix}G$.

Compared with the mixing free energy calculation along the standard textbook process in Fig. 1, the numerical cost to calculate (11) is not expensive. We show comparison examples for the calculation costs in Tables 1 and 2 provided in constant temperature and volume. The first example is the mixture of two isotopes whose components differ only in mass. The computation time for completing the process in Fig. 1 takes about 37 times longer than the sum of the computation times for the alchemical processes in Fig. 2 and Fig. 3. In the second example, two components are different in size. The computation time required for the two alchemical processes is about 25% of the time for the textbook process in Fig. 1.

We show the work distribution $\rho(\hat{W}_\#)$ and $\rho(-\hat{W}^\dagger_\#)$ for the second example. Here, $\hat{W}_\#$ is the work measured in the alchemical process from the pure substance to a mixture, while $\hat{W}^\dagger_\#$ is the work for the backward protocol for creating the pure substance from the mixture. We find a cross point of the two dis-

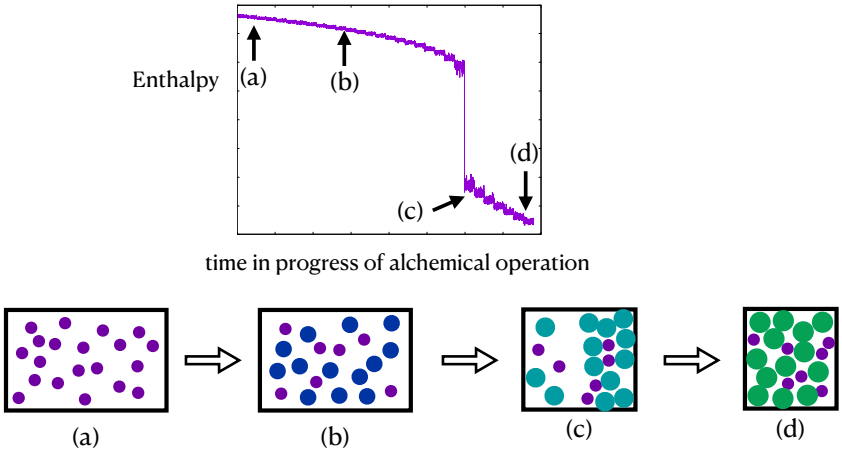

Figure 5: (a)(b)(c)(d) Schematic snapshots during the protocol from (a) an initial pure argon gas state to (b) the final target mixture of argon and krypton. Each argon molecule is depicted by a purple circle and each krypton molecule by a green circle. The other colored circles represent intermediate hypothetical molecules existing during the alchemical process. (Top) Time evolution of enthalpy during the process from (a) to (d). The jump in enthalpy suggests a transition from gas to liquid.

tributions, which confirms the convergence of the free energy difference $\Delta_{\#}F$. We check such work distributions for various operation times. We then determine the operation time for obtaining plausible free energy difference, which are depicted in Tables 1 and 2.

In the above examples, we took constant volume conditions. This is an essential point for the computation. The two alchemical processes in Fig. 2 and Fig. 3 are well-defined in constant pressure protocols while the mixing process with two semi-permeable membranes in Fig. 1 cannot be performed quasi-statically while keeping constant pressure. This is due to the osmotic pressure. Once the mid-region surrounded by the two semi-permeable membranes appears, all molecules tend to flow into the mid-region.

5 Example of a dense mixture with a first-order transition

We present an example of $\Delta_{\mathrm{mix}}G$ determined from the molecular dynamics simulation for a mixture of argon and krypton at constant temperature and constant pressure. The mixture is modeled as three-dimensional Lennard–Jones liquids. We use the LAMMPS package in this demonstration. The molecules are packed in a cuboid whose volume can fluctuate while keeping an aspect ratio of $21:5:5$ to fix the value of pressure. The container is periodic in y and z directions whereas two boundary walls are set perpendicularly to the x axis.

In detail, the interaction of any two molecules, argon or krypton, is given by the Lennard–Jones potential,

$$\phi(r;\epsilon,\sigma) = 4\epsilon\left[\left(\frac{\sigma}{r}\right)^{12} - \left(\frac{\sigma}{r}\right)^{6}\right], \qquad (12)$$

with a cutoff length $r_{\mathrm{c}} = 3\sigma_{\mathrm{Kr}}$. For the argon pair, $\sigma_{\mathrm{Ar}} = 3.401$ Å and $\epsilon_{\mathrm{Ar}} = 0.2321$ kcal/mol, whereas $\sigma_{\mathrm{Kr}} = 3.601$ Å, $\epsilon_{\mathrm{Kr}} = 0.3270$ kcal/mol for the krypton pair [17]. For the pair of argon and krypton, $\sigma_{\mathrm{ArKr}} = (\sigma_{\mathrm{Ar}} + \sigma_{\mathrm{Kr}})/2 = 3.501$ Å and $\epsilon_{\mathrm{ArKr}} = \sqrt{\epsilon_{\mathrm{Ar}}\epsilon_{\mathrm{Kr}}} = 0.2755$ kcal/mol according to the Lorentz–Berthelot law [18, 19]. The masses of argon and krypton are $m_{\mathrm{Ar}} = 39.95$ g/mol and $m_{\mathrm{Kr}} = 83.80$ g/mol. We perform the molecular dynamics simulations of

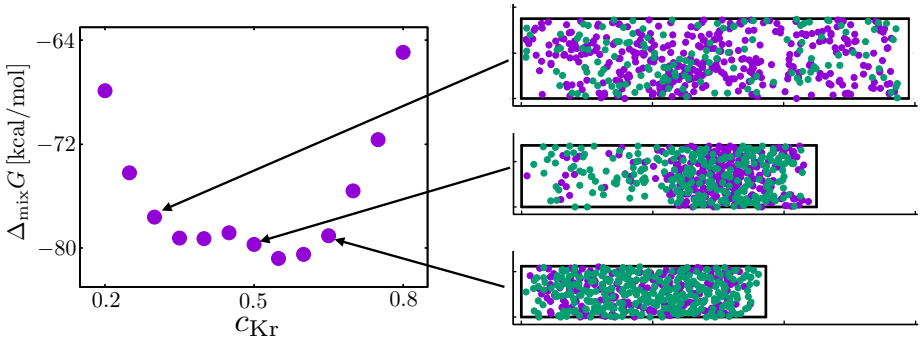

Figure 6: (Left) $\Delta_{\mathrm{mix}}G$ for the binary mixture of argon and krypton with $N = 500$ determined using (11). (Right) Snapshots of the particle distribution for the mixture of argon (purple) and krypton (green) for $c_{\mathrm{Kr}} = 0.3$, 0.5, and 0.65. The three-dimensional space is projected onto the two-dimensional space. The original figures are Figs. 7 and 9 in reference [14].

the constant temperature and pressure in $T = 163.15\,\mathrm{K}$ and $p = 4\,\mathrm{MPa}$ by adopting the Nose–Hoover chain and Martyna–Tobias–Klein barostat [20].

Liquid–vapor transition is observed with an increasing molar fraction $c_{\mathrm{Kr}} = N_{\mathrm{Kr}}/N$ of the krypton [21]. The right figures in Fig. 6 show snapshots of the system's configuration in $N = 500$ after sufficient relaxation for $c_{\mathrm{Kr}} = 0.3$, 0.5, and 0.65. The volume differs greatly among the three values of c_{Kr}. The number density at $c_{\mathrm{Kr}} = 0.65$ is approximately 5 times that at $c_{\mathrm{Kr}} = 0.3$, and dense and dilute regions coexist at $c_{\mathrm{Kr}} = 0.5$. Such behaviors exhibit the characteristics of liquid–vapor transition. These observations are consistent with the previous report in [21].

The alchemical protocol for calculating $\Delta_{\#}G$ is designed as follows: We take the initial pure substance as being argon in Fig. 5(a). Then, change the value of (m, σ, ϵ) related to the first n molecules from those of argon to krypton gradually in time. The snapshots of the system may be observed as Fig. 5(b) and (c). Here, the molecules during the protocol are hypothetical, not argon or krypton. Even in a single trajectory, we observe a sudden decrease in enthalpy and volume as shown in Fig. 5. The equilibrium state for the hypothetical system changes to liquid as shown in Fig. 5(d).

Calculating both $\Delta_{\#}G$ and $\Delta_{\mathrm{Ar}\to\mathrm{Kr}}G$, the resulting mixing free energy $\Delta_{\mathrm{mix}}G$ is shown in Fig. 6 for $N = 500$. The curve has a double-well shape and is convex upwards in the approximate range of $0.35 < c_{\mathrm{Kr}} < 0.55$ showing the liquid–vapor coexistence. We thus conclude that the functional shape of $\Delta_{\mathrm{mix}}G$ well characterizes the liquid–vapor transition for the argon–krypton mixture. Our formula (11) works as a quantitative method for determining the mixing Gibbs free energy.

The main term of the finite-size effects is of $\ln N$, which is about 1% of N at $N = 500$. This may affect thermodynamic properties. Indeed, the upward convexity in $\Delta_{\mathrm{mix}}G$ is not expected in the thermodynamic limit. To examine the system size dependence of $\Delta_{\mathrm{mix}}G$, we have performed the same calculations for $N = 4,000$ and $N = 13,000$. As the system size becomes larger, we find longer relaxation time. Especially when the trajectory passes through a transition from gas to liquid or from liquid to gas as demonstrated in Fig. 5, the relaxation time becomes significantly longer.

In the present temperature and pressure, the pure argon behaves as gas while the pure krypton does as liquid. Depending on the mole

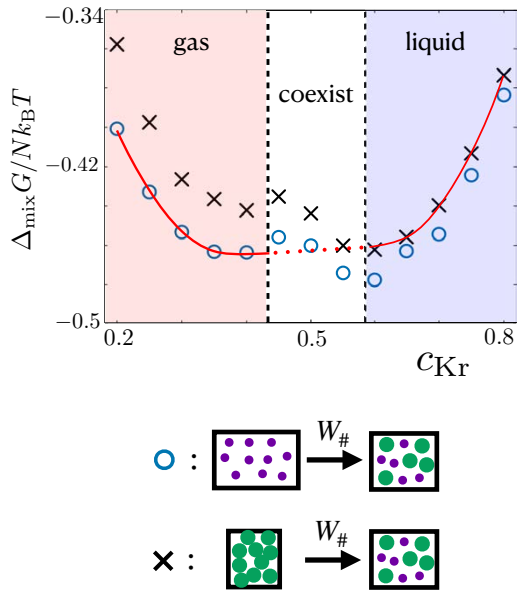

Figure 7: $\Delta_{\rm mix}G$ for the binary mixture of argon and krypton with $N = 4,000$ determined using (11). The circle points are calculated adopting the initial pure material as argon gas, whereas the initial pure material is chosen as krypton liquid in the cross points.

fraction $c_{\rm Kr}$ of the target mixture, the final state is different, i.e., gas, liquid, or liquid-gas coexistence. Suppose we choose the initial pure material as krypton when the target mixture is gas. Each trajectory shows a transition from liquid to gas as in Fig. 5, which may induce hysteresis. This transition may depend on the trajectory and is likely to show hysteresis. Then, the calculated results may not belong to equilibrium properties. To examine such a possibility, we compare two initial conditions; one starts from the pure argon and the other is from the pure krypton. The former is from gas and the latter is from liquid. As shown in Fig. 7, the obtained $\Delta_{\rm mix}G$ depends on the initial condition in $N = 4,000$.

Such differences do not appear in $N = 500$. This is because the fluctuations seem large enough to pass all typical equilibrium configurations when $N = 500$. By choosing the initial pure material properly, i.e., as the initial material is in the same phase as the target mixture, we avoid the difficulty due to the hysteresis. The red line in Fig.7 is drawn by choosing the results without experiencing transition. Comparing with Fig. 6, we find that $\Delta_{\rm mix}G$ in small $c_{\rm Kr}$ is slightly smaller with increasing N. As a result, the upward convexity seems to become flattened with increasing the system size N. The obtained $\Delta_{\rm mix}G$ would be reliable.

Acknowledgment

The present work was supported by KAKENHI (Nos. 17H01148, 19K03647, 20K20425). A. Y. was supported by JST and the Establishment of University Fellowships Towards the Creation of Science Technology Innovation under Grant Number JPMJFS2105. The numerical simulations in this work were done using the facilities of the Supercomputer Center, the Institute for Solid State Physics, The University of Tokyo.

References

[1] R. E. Skyner, J. L. McDonagh, C. R. Groom, T. Van Mourik, and J. B. O. Mitchell, A review of methods for the calculation of solution free energies and the modelling of systems in solution, Phys. Chem. Chem. Phys. **17**, 6174 (2015).

[2] M. Kohns, S. Reiser, M. Horsch, and H. Hasse, Solvent activity in electrolyte solutions from molecular simulation of the osmotic pressure, J. Chem. Phys. **144**, 084112 (2016).

[3] P. W. Debye and E. Huükel, Zur Theorie der Elektrolyte, Phys. Z. **24**, 185 (1923).

[4] C. Chipot and A. Pohorille (Eds.), *Free Energy Calculations: Theory and Applications in Chemistry and Biology*, Springer Series in Chemical Physics Vol. 86 (Springer-Verlag, Berlin, 2007).

[5] B. Cheng and M. Ceriotti, Computing the absolute Gibbs free energy in atomistic simulations: Applications to defects in solids, Phys. Rev. B **97**, 054102 (2018).

[6] P. Kollman, Free energy calculations: Applications to chemical and biochemical phenomena, Chem. Rev. **93**, 2395 (1993).

[7] P. A. Kollman, Advances and continuing challenges in achieving realistic and predictive simulations of the properties of organic and biological molecules, Acc. Chem. Res. **29**, 461 (1996).

[8] T. Simonson, G. Archontis, and M. Karplus, Free energy simulations come of age: Protein-ligand recognition, Acc. Chem. Res. **35**, 430 (2002).

[9] D. L. Mobley, J. D. Chodera, and K. A. Dill, On the use of orientational restraints and symmetry corrections in alchemical free energy calculations, J. Chem. Phys. **125**, 084902 (2006).

[10] D. L. Mobley and P. V. Klimovich, Perspective: Alchemical free energy calculations for drug discovery, J. Chem. Phys. **137**, 230901 (2012).

[11] T. Steinbrecher, C. Zhu, L. Wang, R. Abel, C. Negron, D. Pearlman, E. Feyfant, J. Duan, and W. Sherman, Predicting the effect of Amino Acid single-point mutations on protein stability-Large-scale validation of MD-based relative free energy calculations, J. Mol. Biol. **429**, 948 (2017).

[12] M. Kuhn, S. Firth-Clark, P. Tosco, A. S. J. S. Mey, M. MacKey, and J. Michel, Assessment of binding affinity via alchemical free-energy calculations, J. Chem. Inf. Model. **60**, 3120 (2020).

[13] J. Scheen, W. Wu, A. S. J. S. Mey, P. Tosco, M. Mackey, and J. Michel, Hybrid alchemical free energy/machine-Learning methodology for the computation of hydration free energies, J. Chem. Inf. Model. **60**, 5331 (2020).

[14] A. Yoshida and N. Nakagawa, Work relation for determining the mixing free energy of small scale mixtures, Phys. Rev. Res. **100**, 125125 (2022).

[15] J. W. Gibbs, On the equilibrium of heterogeneous substances, Trans. Conn. Acad. Arts Sci. **3**, 343 (1875-1878).

[16] E. Fermi, *Thermodynamics* (Dover, New York, 1956).

[17] S. K. Oh, Modified Lennard-Jones potentials with a reduced temperature-correction parameter for calculating thermodynamic and transport properties: Noble gases and their mixtures (He, Ne, Ar, Kr, and Xe), J. Thermodyn. **1**, 29 (2013).

[18] H. A. Lorentz, Ueber die Anwendung des Satzes vom Virial in der kinetischen Theorie der Gase, Ann. Phys. **248**, 127 (1881).

[19] D. Berthelot, Sur le mèlange des gaz, C. R. Acad. Sci. **126**, 1703 (1889).

[20] G. J. Martyna, D. J. Tobias, and M. L. Klein, Constant pressure molecular dynamics algorithms, J. Chem. Phys. **101**, 4177 (1994).

[21] A. E. Nasrabad, R. Laghaei, and U. K. Deiters, Prediction of the thermophysical properties of pure neon, pure argon, and the binary mixtures neon-argon and argon-krypton by Monte Carlo simulation using ab initio potentials, J. Chem. Phys. **121**, 6423 (2004).

Ab initio optical calculation by RESPACK

Kazuma NAKAMURA
Graduate School of Engineering, Kyushu Institute of Technology
1-1 Sensui-cho, Tobata, Kitakyushu, Fukuoka, 804-8550

1 Introduction

In this report, we present optical-response calculations of materials using first-principles calculation software RESPACK [1]. *Ab initio* optical-response calculations have been performed for a long time, and have contributed to the understanding of materials through quantitative comparisons between theoretical and experimental spectra. However, since the calculation is heavier than normal band calculations, it was often performed for small systems containing a small number of atoms. In recent years, with advances in computers and the spread of open software, the calculation has become possible even for large systems. RESPACK is one of such software and is increasingly being used to understand the optical response of complex and large systems. In this report, we would like to introduce some recent results of the optical response calculations using RESPACK.

2 Method

In this section, we briefly describe a calculation detail. The symmetric dielectric function [2] can be written with using the polarization function as

$$\begin{aligned}&\epsilon_{\mathbf{GG}'}(\mathbf{q},\omega)\\ =\ &\delta_{\mathbf{GG}'}-\frac{4\pi}{\Omega}\frac{1}{|\mathbf{q}+\mathbf{G}|}\chi_{\mathbf{GG}'}(\mathbf{q},\omega)\frac{1}{|\mathbf{q}+\mathbf{G}'|},\end{aligned} \tag{1}$$

where $\chi_{\mathbf{GG}'}(\mathbf{q},\omega)$ is the Fourier transform of the polarization function, and the explicit expression can be found in Ref. [1]. $\mathbf{q}$ and ω are wavevector in the Brillouin zone and frequency, respectively, and $\mathbf{G}$ is reciprocal vector. Ω is the volume of the unit cell.

The optical response is related to $\mathbf{q}\sim\mathbf{0}$, and in the calculation of $\epsilon_{\mathbf{GG}'}(\mathbf{q},\omega)$, the head component which corresponds to the $\mathbf{G}=\mathbf{G}'=\mathbf{0}$ component in the $\mathbf{q}\to\mathbf{0}$ limit must be treated carefully. For the head component, we calculate the following [3]

$$\lim_{\mathbf{q}\to\mathbf{0}}\epsilon_{\mathbf{00}}(\mathbf{q},\omega)=1-\frac{4\pi}{\Omega}\frac{\partial^2\chi_{\mathbf{00}}(\mathbf{q},\omega)}{\partial q^2}-\frac{(\omega_{pl}^{\mu\nu})^2}{\omega(\omega+i\delta)}. \tag{2}$$

Here, the last term results from the intraband transition, and δ is a smearing factor. ω_{pl} is the bare plasma frequency calculated via the Fermi-surface integral as

$$\omega_{pl}^{\mu\nu}=\frac{1}{N_k}\sum_{\mathbf{k}}^{N_k}\sum_{\alpha}p_{\alpha\alpha\mathbf{k}}^{\mu}p_{\alpha\alpha\mathbf{k}}^{\nu}\delta(E_{\alpha\mathbf{k}}-E_F), \tag{3}$$

where E_F is the Fermi energy determined in the density functional band calculation, and $p_{\alpha\alpha\mathbf{k}}^{\nu}$ is the diagonal element of the transition-moment matrix with respect to the bands as

$$\begin{aligned}p_{\alpha\beta\mathbf{k}}^{\mu}&=-i\Big\langle\psi_{\alpha\mathbf{k}}\Big|\frac{\partial}{\partial x_\mu}+[V_{NL},x_\mu]\Big|\psi_{\beta\mathbf{k}}\Big\rangle\\ &\sim-i\Big\langle\psi_{\alpha\mathbf{k}}\Big|\frac{\partial}{\partial x_\mu}\Big|\psi_{\beta\mathbf{k}}\Big\rangle\end{aligned} \tag{4}$$

with x_μ being the Cartesian coordinate. On the above evaluation, we ignore the contribution from the non-local part of the pseudopotential, V_{NL}. We note that, in the optical response, the non-local pseudopotential contribution may sometimes manifest itself as a significant effect, especially for the transition metals [4].

The optical properties such as the macroscopic dielectric function $\epsilon_{\mathrm{M}}(\omega)$, the real part of the optical conductivity $\sigma(\omega)$, and the reflectance spectrum $R(\omega)$ are calculated from the inverse of the matrix $\epsilon_{\mathbf{GG}'}(\mathbf{q},\omega)$ in Eqs.(1) and (2) as

$$\epsilon_{\mathrm{M}}(\omega)=\lim_{\mathbf{q}\to0}\frac{1}{\epsilon^{-1}_{\mathbf{00}}(\mathbf{q},\omega)}, \tag{5}$$

$$\mathrm{Re}\big[\sigma(\omega)\big]=\frac{\omega}{4\pi}\mathrm{Im}\lim_{\mathbf{q}\to0}\frac{1}{\epsilon^{-1}_{\mathbf{00}}(\mathbf{q},\omega)}, \tag{6}$$

and

$$R(\omega)=\left|\frac{1-\sqrt{\lim_{\mathbf{q}\to0}\epsilon^{-1}_{\mathbf{00}}(\mathbf{q},\omega)}}{1+\sqrt{\lim_{\mathbf{q}\to0}\epsilon^{-1}_{\mathbf{00}}(\mathbf{q},\omega)}}\right|, \tag{7}$$

respectively.

3 Results and Discussions

Below, we show some applications of RESPACK. We performed *ab initio* density function calculations using Quantum Espresso [5, 6] in which the wave functions were expanded on a plane-wave basis. We employed norm-conserving pseudopotentials, and the generalized-gradient approximation for the exchange-correlation energy. The cutoff energies for the wave function and charge density are 100 Ry and 400 Ry, respectively. The calculation condition of the optical calculations is as follows: The energy cutoff for the polarization function was set to 10 Ry. The total number of bands considered in the polarization calculation was determined to cover unoccupied states up to 10-15 eV above E_F. The details of the k-point sampling vary depending on the system, so we will describe it in each section of materials.

3.1 WC

The first example is tungsten carbide WC. Recently, we found that the WC can be a good candidate for solar selective absorber [7]. Sunlight absorption and its efficient use of energy is an important topic and is being actively studied worldwide. The sunlight energy range is from 0.5 to 4.1 eV, and the important problem is to find materials that can selectively absorb light in this energy range. As a basis for the material design, we focus on plasma excitations, especially in a low energy [8]. The plasma excitation is the collective excitation of electrons in metals, and some materials have the plasma excitation with an excitation energy of 0.1-1.0 eV around the cutoff of the sunlight energy. The WC is one of the main components in a TiCN-based cermet widely used as a cutting tool. Through the *ab initio* electronic-structure analysis for the wasted TiCN-based cermet, we found that the WC has a low-energy plasma excitation of 0.6 eV exactly corresponding to the sunlight cutoff [7].

Figure 1(a) is our calculated band structures (red solid curves) of the WC being a hexagonal closed pack (hcp) structure and containing 2 atoms in the unit cell. The k-point sampling is $32 \times 32 \times 32$. A spin-orbit interaction (SOI) of tungsten is known to be nearly 0.4 eV, then we calculated the SOI band structure and compared it with that without the SOI (black solid curves). The SOI can bring about a splitting of the low-energy bands, but the effect

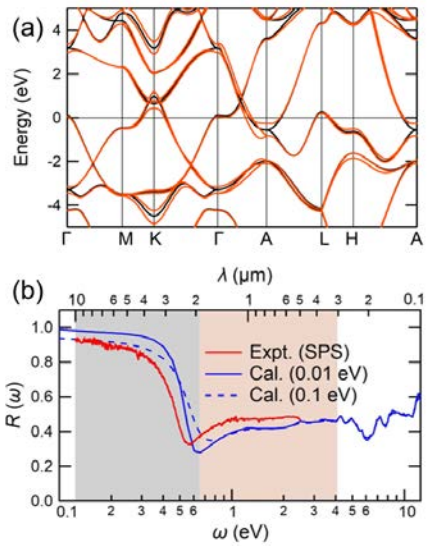

Figure 1: (a) Comparison between *ab initio* density functional band structure of WC with (red solid curves) and without (black solid curves) the SOI. The energy zero is the Fermi level. Dispersions of the WC are plotted along the high symmetry points in the Brillouin zone, where Γ= (0, 0, 0), M = (1/2, 0, 0), K = (1/3, 1/3, 0), A = (0, 0, 1/2), L = (−1/2, 0, 1/2), and H = (1/3, 1/3, 1/2), where the coordinates are represented in terms of basic vectors of the reciprocal lattice of the hcp lattice. (b) Comparison of experimental (red-solid line) and *ab initio* (blue-solid line) reflectance spectra with a smearing of 0.01 eV. We also show an *ab initio* result (blue dashed line) with smearing of 0.1 eV. In the figure, the bright orange shadow represents the spectral range of sunlight, and the gray shadow represents the range of radiation.

is basically small. Figure 1(b) is the comparison of the experimental (red-solid line) and our calculated *ab initio* (blue-solid line) reflectance spectra with a smearing of 0.01 eV. The WC sample was prepared as a polycrystalline obtained with the spark plasma sintering (SPS) method. The spectrum with the SOI was calculated with the spinor version of RESPACK [9]. We see a clear plasma edge around 0.6 eV (2.0 μm) corresponding to the cutoff energy of the sunlight spectrum. Around the low-energy (0.1-0.5 eV), we see the lowering of the experimental reflectance compared with the theoretical spectrum, which would be due to the multiple scattering in the pores on the polycrystalline WC surface. To consider this point, we calculated an *ab initio* reflection spectra with a smearing factor of 0.1 eV, denoted by the blue-dashed line, where the smearing size qualitatively represents the strength

of scattering by impurities. As can be seen by comparing the result with the smearing factor of 0.01 eV, increasing the smearing broadens the spectrum.

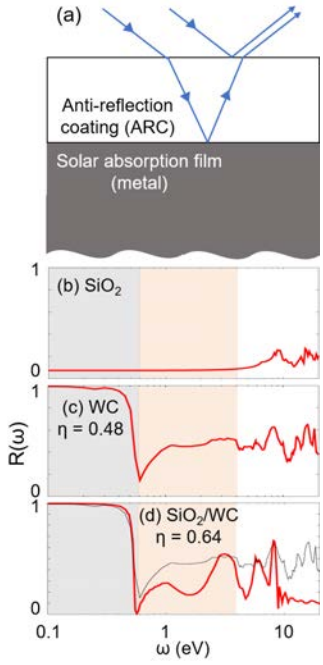

Figure 2: (a) Reflectance property of the WC system including anti-reflection coating (ARC). (b) *Ab initio* reflectance of SiO_2 as ARC and (c) WC as solar absorption film. (d) A film-interference simulation result with the *ab initio* inputs.

We next discuss the discrepancy in the high energy region (0.6-4.0 eV). In this region, the reflectance is large as ~ 0.5, which must be reduced for the preferable solar absorption. The figure of merit η for the solar absorption of the bulk WC was estimated as 0.48 [7], which is not so high and the origin is the high reflectance in the region of 0.6-4.0 eV. In this case, anti-reflection coating (ARC) is effective to suppress the higher-energy reflectance [Fig. 2(a)]. To evaluate the suppression effect by the ARC, we perform a film-interference simulation with insulator SiO_2 for the ARC.

The calculation proceeds as follows: We first consider a reflection coefficient of Air and ARC as

$$r_{\mathrm{Air-ARC}}(\lambda) = \frac{N_{\mathrm{Air}} - N_{\mathrm{ARC}}(\lambda)}{N_{\mathrm{Air}} + N_{\mathrm{ARC}}(\lambda)}, \tag{8}$$

where N_{Air} and $N_{\mathrm{ARC}}(\lambda)$ are reflective index of Air and ARC, respectively. The λ is the wavelength of light. Similarly, a reflection coefficient of WC and ARC is given as

$$r_{\mathrm{ARC-WC}}(\lambda) = \frac{N_{\mathrm{ARC}}(\lambda) - N_{\mathrm{WC}}(\lambda)}{N_{\mathrm{ARC}}(\lambda) + N_{\mathrm{WC}}(\lambda)} \tag{9}$$

with $N_{\mathrm{WC}}(\lambda)$ being a reflective index of the WC. By using these quantities, the reflectance spectrum of the total system is calculated as

$$R(\lambda) = \frac{r_{\mathrm{Air-ARC}}(\lambda) + r_{\mathrm{ARC-WC}}(\lambda)e^{i\Delta(\lambda)}}{1 + r_{\mathrm{Air-ARC}}(\lambda)r_{\mathrm{ARC-WC}}(\lambda)e^{i\Delta(\lambda)}} \tag{10}$$

with

$$\Delta(\lambda) = \frac{4\pi d_{\mathrm{ARC}} N_{\mathrm{ARC}}(\lambda)}{\lambda}. \tag{11}$$

Here d_{ARC} is a thickness of ARC. We note that all the parameters can be calculated from first-principles.

Figure 2 summarizes the results about the WC system. The panels (b) and (c) display *ab initio* reflectance spectra of the bulk SiO_2 as an ARC and WC as a solar absorber, respectively. With these *ab initio* data , the reflectance spectrum of the total ARC/WC system is obtained in Fig. 2(d), where we found a significant improvement of η from 0.48 to 0.64.

3.2 Interface system

The second example is the transition-metal oxide $SrVO_3$ (SVO). SVO is a famous strongly correlated metal and an important benchmark in studying electronic correlations in materials. We found that the SVO also exhibits the low-energy plasma excitation of 1.6 eV [8] somewhat higher than the solar absorption range. We found that, based on *ab initio* calculations, by depositing SVO films on $SrTiO_3$ (STO) substrate, the plasma excitation energy can be reduced from 1.6 to 0.7 eV. Thus, the STO/SVO system is a fascinating system as the solar absorbing device. Here, we show the electronic structure and reflectance spectrum of the interface system of the STO/SVO hetero structure.

Figure 3 shows our structure models to be analyzed, where we consider a multilayer model consisting of SVO and STO blocks [panel (a)] and a symmetric slab model [(b)]. The slab model includes a vacuum region with 20 Å, and has a mirror symmetry with respect to the central TiO_2 plane. Then, artificial electric fields due to asymmetry in the both ends of the slab do not occur. The structural models include several SVO blocks, where we specify the number of the blocks as n. In the

present study, we consider the structural models until $n = 4$. The number of the STO blocks was fixed to 5 for the multilayer and 8.5 for the slab (0.5 indicates an additional central TiO_2 layer).

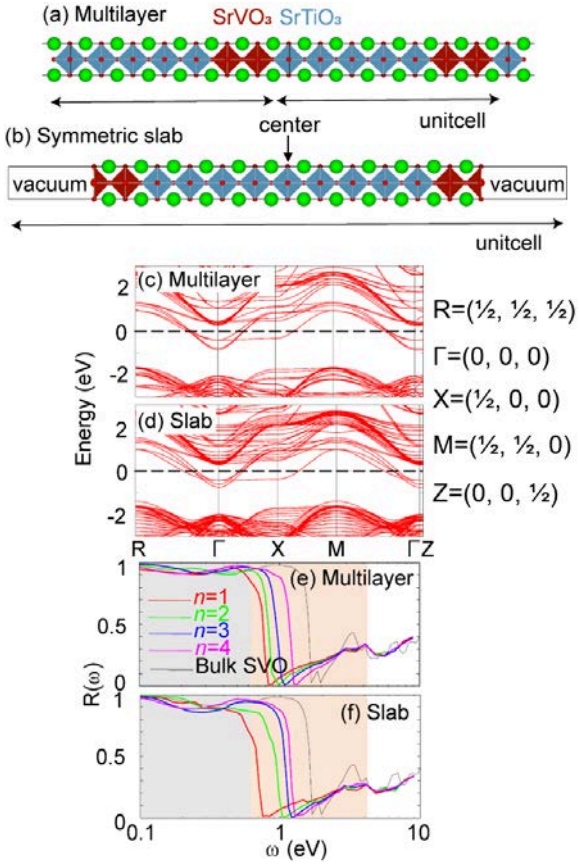

Figure 3: Two structural model: (a) Multilayer consisting of $SrTiO_3$ and $SrVO_3$ blocks. (b) Symmetric slab having a mirror symmetry with respect to the center TiO_2 plane. Our calculated band structures of (c) multilayer and (d) slab model where we show the $n = 2$ case. Panels (e) and (f) show our calculated reflectance spectra of multilayer and slab models, respectively.

Figure 3 shows our calculated band structures of the multilayer (c) and slab (d) with the $k = 10 \times 10 \times 2$ sampling, where the band structures for the $n = 2$ model are displayed. From the band structures, we see that both two systems are metal; the SVO t_{2g} bands cross E_F, and the STO t_{2g} band is about 1 eV above from E_F. Figures 3(e) and (f) show our calculated reflectance spectra for the multilayer and slab models, respectively. We see that the both spectra exhibit a lowering of the plasma edge compared to the bulk SVO one. We also see the appreciable n dependence of the plasma edge; by reducing the SVO thickness, the plasma edge becomes lower. The difference between the multilayer and slab results seems to be small. We estimate the $n = 1$ slab gives $\eta = 0.73$ clearly improving the bulk SVO of $\eta = 0.46$.

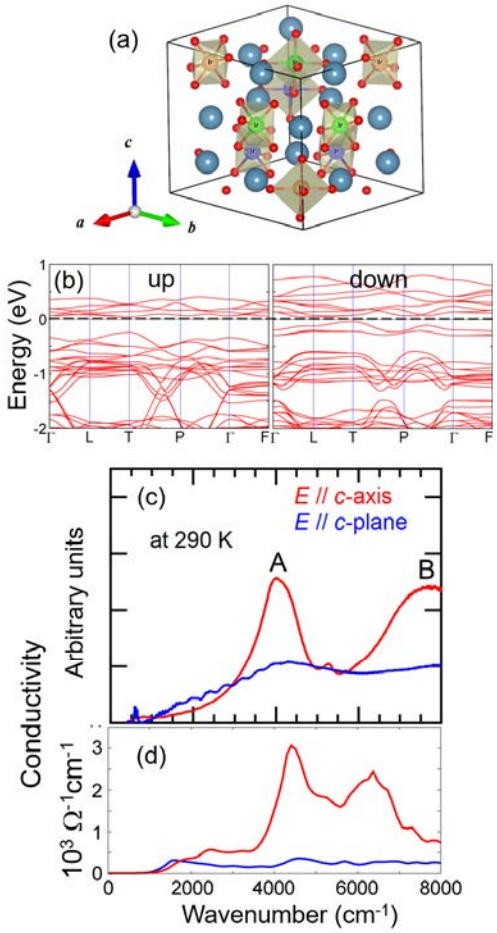

Figure 4: (a) Crystal structure of $\sqrt{3}a \times \sqrt{3}a \times 3c$ superlattice of $Ca_5Ir_3O_{12}$ (space group: R_3). Red, green, and blue spheres are nonequivalent Ir atoms which are the center of an IrO_6 octahedron. (b) *Ab initio* spin density functional band structure, where Γ= (0, 0, 0), L = (1/2, 0, 0), T = (1/2, −1/2, 1/2), P = (0.24, −0.76, 0.24), and F = (1/2, −1/2, 0), and the coordinates are represented in terms of basic vectors of the reciprocal lattice of trigonal lattice. (c) Experimental optical conductivity with polarization parallel to the c-axis (red line) and the c-plane (blue line) at 290 K. (d) Our calculated *ab initio* optical conductivity.

3.3 $Ca_5Ir_3O_{12}$

The third example is $Ca_5Ir_3O_{12}$. This material undergoes two phase transition at 105 K and 7 K [10], and the mechanisms related to so-called hidden or-

der have been very actively debated recently. Experimentally, this is an insulator from above room temperature [11], but *ab initio* density functional calculations predict a metal. Recently, the optical conductivity was measured, and no Drude-like behavior was observed, indicating that it is also the insulator with the optical probe [12]. Thus, the *ab initio* calculation and the experiments do not match, and the origin of the insulation remains unclear. Inelastic X-ray diffraction experiments have detected the superlattice reflection [13] indicating that the structure after the first transition at 105 K changes a $3a \times 3a \times 3c$ superlattice [Fig. 4(a)], and the space group is R_{3m}. Here, we perform *ab initio* spin density functional calculations for the superlattice and investigate the origin of the insulating gap.

Figure 4(b) is our calculated spin density functional band structure for the superlattice containing 60 atoms with the $k = 4 \times 4 \times 4$ sampling, where we see an insulating gap of near 0.2 eV. Also, Figs. 4(c) and (d) shows a comparison of experimental and theoretical optical conductivity. The red lines are the spectra for light with an electric field parallel to the c-axis, and the blue lines are the spectra for light with an electric field parallel to the c-plane. In the experiment, we see two-peak structure denoted by A and B in the spectrum of $E \parallel c$-axis, which are well reproduced with the *ab initio* calculations.

3.4 Ta_4SiTe_4

The fourth example is Ta_4SiTe_4. Recently, a single crystal of one-dimensional telluride Ta_4SiTe_4 and its Mo-doped samples were reported to exhibit a very large $|S|$ with sufficiently small ρ for thermoelectric materials over wide temperatures from 50 K to room temperature [14]. Ta_4SiTe_4 has a one-dimensional crystal structure with the orthorhombic *Pbam* space group, consisting of Ta_4SiTe_4 chains loosely bounded by van der Waals interactions between Te atoms, in Fig. 5(a). The Ta_4SiTe_4 chains lie parallel to the c-axis, forming an almost perfect triangular lattice in the ab plane, and making the material almost isotropic in this plane. The insulating gap is estimated as 0.1-0.15 eV.

Figure 5(b) is the experimental optical conductivity of Ta_4SiTe_4 at room temperature [15]. Blue and red lines are the optical conductivity for $E \parallel c$ $[\sigma_{\parallel}(\omega)]$ and $E \perp c$ $[\sigma_{\perp}(\omega)]$. $\sigma_{\parallel}(\omega)$ has peaks at 2.5, 1.9, 1.3, and 0.2 eV. The first three peaks in the near-infrared to visible region most likely correspond to the interband transition. The last peak at 0.2 eV corresponds to the band gap at E_F. In contrast, $\sigma_{\perp}(\omega)$ also has a small peak at around 0.2 eV, but does not show a clear peak due to the interband transition. These behaviors are well reproduced by the *ab initio* calculation with the $k = 4 \times 2 \times 9$ sampling, shown in Fig. 5(c). The theoretical spectrum for $E \parallel c$ has four prominent peaks at 2.5, 2.0, 1.4, and 0.4 eV, and the spectra of $E \parallel a$ and $E \parallel b$ are almost identical and have no significant structure other than a strong decrease below 0.2–0.4 eV. These are totally consistent with the experiments.

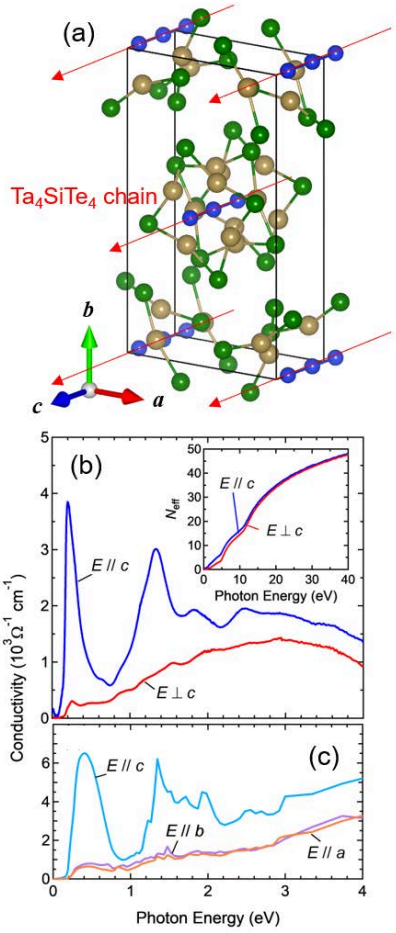

Figure 5: (a) Crystal structure of Ta_4SiTe_4 with orthorhombic unit cell (space group: *Pbam*). Blue, green, and brown spheres are Si, Te, and Ta atoms, respectively. (b) Experimental optical conductivity of a Ta_4SiTe_4 single crystal parallel and perpendicular to the c-axis at room temperature. The inset shows the effective number of electrons per formula unit. (c) *Ab initio* optical conductivity spectra of Ta_4SiTe_4 parallel to the a-, b-, and c-axes.

3.5 Ruby

For remaining parts, we introduce applications of RESPACK other than optical property. The first example is an excitation-energy calculation of the impurity system of ruby (Al_2O_3:Cr). Figure 6(a) is the atomic geometry and the panel (b) is our calculated band structure with the $k = 3 \times 3 \times 3$ sampling, where we see two impurity bands near E_F due to the Cr impurity. Blue dotted lines are the Wannier interpolated band obtained from RESPACK-wannier program. By using RESPACK, we derived an *ab initio* effective low-energy model for the five d orbitals of the Cr impurity.

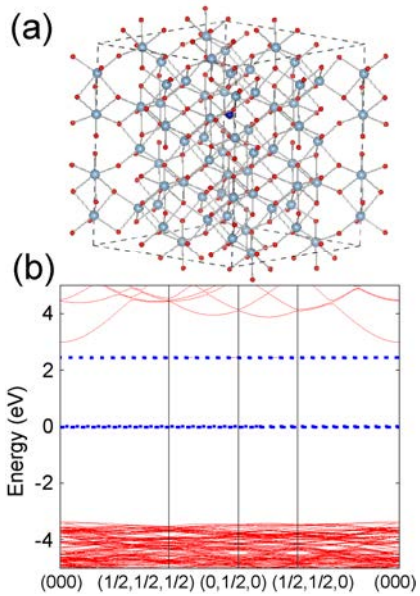

Figure 6: (a) Atomic geometry for impurity system: $Al_{47}CrO_{72}$ (2×2×1 supercell containing 120 atoms). (b) Our calculated band structure with the $k = 3\times3\times3$ sampling using xTAPP [16]. Blue dotted lines represent the Wannier interpolated bands for the impurity levels.

When the RESPACK job is executed, a directory `dir-mvmc` is generated under the calculation directory, and the files necessary for model-analysis softwares mVMC [17] and $\mathcal{H}\Phi$ [18] are output. Using these data and a standard-mode input for mVMC and $\mathcal{H}\Phi$, all inputs of the model calculations are automatically generated under the following command:

```
HPhi -s stan.in (or vmc.out -s stan.in)
```

Here, `HPhi` and `vmc.out` are execution files of $\mathcal{H}\Phi$ and mVMC, respectively, and `stan.in` is an input file for standard mode. This interface code has the lattice conversion function; when the user moves from *ab initio* calculation to model one, the lattice adopted at the *ab initio* calculation can be flexibly changed. Also, the code has an option for avoiding the Hartree-term double count; user can adjust one-body correction $\Delta_{i\mathbf{0}}$ by optional parameter α,

$$\begin{aligned}\Delta_{i\mathbf{0}} &= \alpha U_{i\mathbf{0},i\mathbf{0}} D^{\mathrm{KS}}_{i\mathbf{0},i\mathbf{0}} \\ &+ \sum_{\mathbf{R}\neq\mathbf{0}} \sum_{k} D^{\mathrm{KS}}_{k\mathbf{0},k\mathbf{0}} \Big(U_{i\mathbf{0},k\mathbf{R}} - (1-\alpha) J_{i\mathbf{0},k\mathbf{R}} \Big),\end{aligned} \tag{12}$$

where U, J, and D are the direct integral, exchange integrals, and density matrix with the Kohn-Sham orbital, respectively.

Table 1 shows our calculated excitation energy diagram of the impurity model. The excitation energy depends on α in Eq. (12), and the results correcting of the Hartree-term double counting ($\alpha = 1$) reasonably reproduce the experimental result.

Table 1: Calculated energy diagram of impurity model from RESPACK + $\mathcal{H}\Phi$. The unit is eV. Values of the ground state (GS) are the total energy.

Expt	Theory		
	$\Delta_{i\mathbf{0}} = 0$	$\alpha = 0.5$	$\alpha = 1$
GS(^4A)	47.9(^4A)	5.60(^4A)	−3.04(^4A)
1.79(^2E)	1.67(^2E)	1.61(^2E)	1.62(^2E)
1.87(^2T)	1.78(^2T)	1.73(^2T)	1.84(^2T)
2.23(^4T)	2.29(^4T)	1.79(^4E)	2.32(^2A)
2.62(^2T)	2.46(^4T)	2.23(^4T)	2.56(^4T)
3.10(^4T)	2.69(^2T)	2.60(^4A)	2.78(^4T)

3.6 La_2CuO_4

Next example is La_2CuO_4, where we would like to introduce Wannier function analysis to understand piezosuperconductivity with a bending strain. It is known that a superconducting transition temperature T_c can be changed with pressure and strain. An epitaxial strain is one of well-known mechanisms of changing T_c by strain. In this treatment, however, the T_c is not changed after sample preparation is completed. Recently, Horide et. al. have developed a new-type strain-processing method that can control material properties adiabatically and continuously by bending strain [19].

We have applied the method to superconducting $La_{2-x}Sr_xCuO_4$ (LSCO), where the structure is freely controlled to be compressed or stretched. From the experiment, they found that the compressive strain for LSCO leads to increasing T_c, while the tensile strain brings about decreasing T_c. In the present study, to understand this trend microscopically, we perform electronic-structure analysis for La_2CuO_4 being a mother compound of the LSCO from first principles.

Figures 7(d) and (e) display our calculated Cu-d_{z^2} and Cu-$d_{x^2-y^2}$ Wannier orbitals, respectively. By using these two orbitals, we performed a fat-band analysis for original density functional band structure. These results are summarized in Fig. 7(f). We see that the fat band due to the Cu-$d_{x^2-y^2}$ (blue) is almost constant for all the strained configurations, while that from the Cu-d_{z^2} (green) appreciably increases from compressive-bent to tensile-bent configurations. This trend is well correlated with the experimental T_c trend with bending strain. It is known that the T_c of the cuprate can increase with purification of the Cu-$d_{x^2-y^2}$ orbital in the Fermi surface (FS) [20]. The present result is consistent with this view; the compressive strain brings about suppressing the Cu-d_{z^2} weight in the FS, leading to increasing T_c.

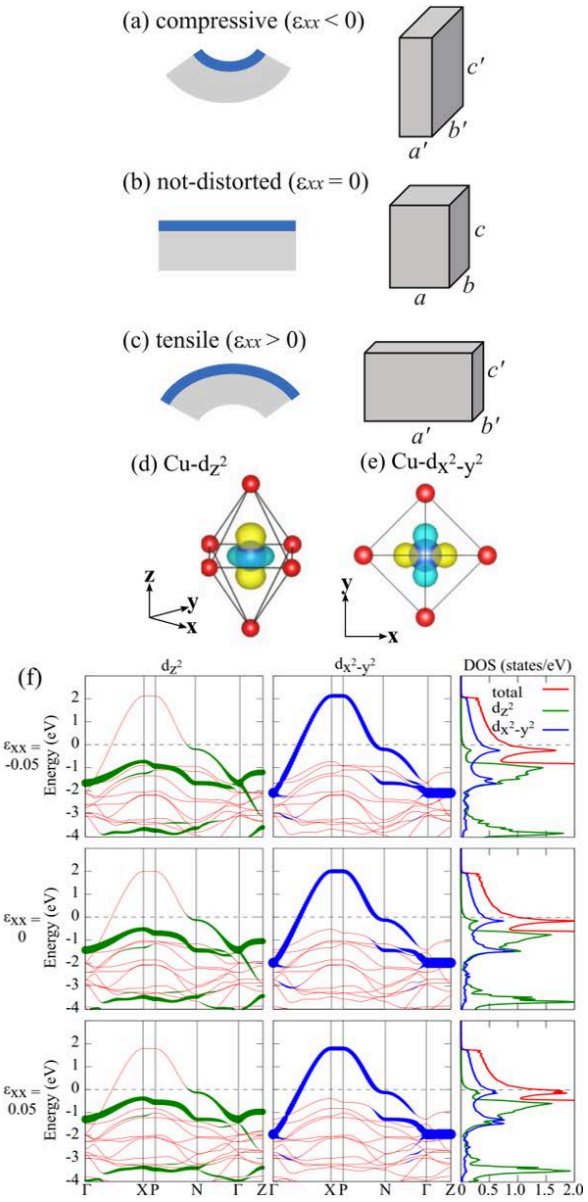

Figure 7: (a)-(c): Schematic figure of strained configurations and corresponding unit cells: (a) compressive-bent, (b) unbent, and (c) tensile-bent structures. Left panels show schematic strained samples, and right panels show deformed unit cells with strain ϵ_{xx}. Maximally localized Wannier orbitals of (d) Cu-d_{z^2} and (e) Cu-$d_{x^2-y^2}$ calculated with RESPACK. (f) Fat-band plots with Cu-d_{z^2} (left) and Cu-$d_{x^2-y^2}$ (center) contributions, and density of states (DOS) (right) for strain $\epsilon_{xx} = -0.05$, 0, and 0.05. Dispersions are plotted along the high symmetry points in the Brillouin zone, where Γ= (0, 0, 0), X = (1/2, 0, 0), P = (1/4, 1/4, 1/4), N = (0, 1/2, 0), Z = (1/2, 1/2, −1/2), where the coordinates are represented in terms of basic vectors of the reciprocal lattice of the body-centered tetragonal lattice.

Acknowledge

We thank Toshiharu Chono, Tatsuro Aikawa, Shota Hayakawa, Hiroki Hanate, Shoya Kawano, Takumi Hasegawa, Tomoya Horide, Koji Miyazaki, Kazuyuki Matsuhira, Yoshihiko Okamoto, Koshi Takenaka, Takahiro Misawa, Yoshihide Yoshimoto, and Shinji Tsuneyuki for helpful discussions. We acknowledge the financial support of JSPS Kakenhi Grant JP19K03673, JP22H01183, and JP23H01126. A part of the computation was done at Supercomputer Center, Institute for Solid State Physics, University of Tokyo.

References

[1] Kazuma Nakamura et al. RESPACK: An *ab initio* tool for derivation of effective low-energy model of material. *Computer Physics Communications*, 261:107781, 2021.

[2] Mark S. Hybertsen and Steven G. Louie. *Ab initio* static dielectric matrices from the

density-functional approach. I: formulation and application to semiconductors and insulators. *Phys. Rev. B*, 35:5585–5601, Apr 1987.

[3] Claudia Ambrosch-Draxl and Jorge O. Sofo. Linear optical properties of solids within the full-potential linearized augmented planewave method. *Computer Physics Communications*, 175(1):1–14, 2006.

[4] Andrea Marini, Giovanni Onida, and Rodolfo Del Sole. Plane-wave dft-lda calculation of the electronic structure and absorption spectrum of copper. *Phys. Rev. B*, 64:195125, Oct 2001.

[5] Paolo Giannozzi et al. Quantum espresso: a modular and open-source software project for quantum simulations of materials. *Journal of Physics: Condensed Matter*, 21(39):395502 (19pp), 2009.

[6] Paolo Giannozzi et al. Advanced capabilities for materials modelling with quantum espresso. *Journal of Physics: Condensed Matter*, 29(46):465901, 2017.

[7] Shota Hayakawa et al. *Ab initio* calculation for electronic structure and optical property of tungsten carbide in a TiCN-based cermet for solar thermal applications. *Scientific Reports*, 13(1):9407, 2023.

[8] Kazuma Nakamura, Yoshiro Nohara, Yoshihide Yosimoto, and Yusuke Nomura. Ab initio GW plus cumulant calculation for isolated band systems: Application to organic conductor $(TMTSF)_2PF_6$ and transition-metal oxide $SrVO_3$. *Phys. Rev. B*, 93:085124, Feb 2016.

[9] Maxime Charlebois et al. *Ab initio* derivation of low-energy hamiltonians for systems with strong spin-orbit interaction: Application to $Ca_5Ir_3O_{12}$. *Phys. Rev. B*, 104:075153, Aug 2021.

[10] Makoto Wakeshima, Nobuyuki Taira, Yukio Hinatsu, and Yoshinobu Ishii. Electrical and magnetic properties of pseudo-one-dimensional calcium iridium oxide $Ca_5Ir_3O_{12}$. *Solid State Communications*, 125(6):311 – 315, 2003.

[11] Kazuyuki Matsuhira et al. Nonlinear conductivity of geometrically frustrated iridate $Ca_5Ir_3O_{12}$. *Journal of the Physical Society of Japan*, 87(1):013703, 2018.

[12] Hiroki Hanate et al. Insulating nature of iridium oxide $Ca_5Ir_3O_{12}$ probed by synchrotron-radiation-based infrared spectroscopy. *Journal of the Physical Society of Japan*, 92(6):064705, 2023.

[13] Hiroki Hanate et al. First observation of superlattice reflections in the hidden order at 105 k of spin–orbit coupled iridium oxide $Ca_5Ir_3O_{12}$. *Journal of the Physical Society of Japan*, 90(6):063702, 2021.

[14] Takumi Inohara, Yoshihiko Okamoto, Youichi Yamakawa, Ai Yamakage, and Koshi Takenaka. Large thermoelectric power factor at low temperatures in one-dimensional telluride Ta_4SiTe_4. *Applied Physics Letters*, 110(18):183901, 05 2017.

[15] Fumiya Matsunaga et al. Anisotropic optical conductivity accompanied by a small energy gap in the one-dimensional thermoelectric telluride Ta_4SiTe_4. *Phys. Rev. B*, 109:L161105, Apr 2024.

[16] Jun Yamauchi, Masaru Tsukada, Satoshi Watanabe, and Osamu Sugino. First-principles study on energetics of *c*-BN(001) reconstructed surfaces. *Phys. Rev. B*, 54:5586–5603, Aug 1996.

[17] Takahiro Misawa and otherso. mVMC: open-source software for many-variable variational monte carlo method. *Computer Physics Communications*, 235:447–462, 2019.

[18] Mitsuaki Kawamura et al. Quantum lattice model solver HPhi. *Computer Physics Communications*, 217:180–192, 2017.

[19] Tatsuro Aikawa, Tomoya Horide, and Kazuma Nakamura. *Ab initio* wannier analysis for cuprate la_2cuo_4 with bending strain. In *PROCEEDINGS OF 11th SYMPOSIUM ON APPLIED ENGINEERING AND SCIENCES 2023*.

[20] Hirofumi Sakakibara, Hidetomo Usui, Kazuhiko Kuroki, Ryotaro Arita, and Hideo Aoki. Two-orbital model explains the higher transition temperature of the single-layer Hg-cuprate superconductor compared to that of the La-cuprate superconductor. *Phys. Rev. Lett.*, 105:057003, Jul 2010.

3.2 First-Principles Calculation of Material Properties

Development of database of anharmonic phonon properties using first-principles calculation

Masato OHNISHI

Department of Mechanical Engineering,

The University of Tokyo, Hongo, Bunkyo-ku, Tokyo 113-8656

Materials Informatics (MI) technology has rapidly developed in recent years. In materials science, limited data availability often hampers the development of materials using MI, making data expansion a critical challenge. Previous studies have led to the development of databases such as the Materials Project, AFLOW, and AtomWork, which focus on inorganic materials. However, these databases primarily feature data on electronic properties, such as band gaps and electronic band structures, and lack data on anharmonic phonon properties like thermal conductivity, crucial for developing thermo-functional materials. Therefore, since 2022, we have been developing a database dedicated to anharmonic phonon properties, utilizing first-principles calculations. In the fiscal year of 2023, our focus has primarily been on calculations that consider three-phonon scattering, excluding other factors such as four-phonon scattering, phonon renormalization, and electron-phonon interactions.

In this project, we developed computational software that automates the analysis of anharmonic phonon properties in inorganic materials using first-principles calculations. We employed VASP [1] for first-principles calculations and ALAMODE [2] for phonon calculations. Additionally, we utilized various Python libraries to enhance our processes: ASE [3] and Pymatgen [4] for handling crystal structures, Spglib [5] for crystal symmetry, and Custodian [4] for managing VASP job submissions and fine-tuning parameters. Currently, our software targets approximately 20,000 materials listed in the Phonondb (A. Togo) database of harmonic phonon properties, as well as non-metallic and non-magnetic materials from the Materials Project. Our process primarily considers three-phonon scattering, focusing mainly on stable structures. Automatic calculations for these materials are currently underway.

The calculations conducted in fiscal years 2022 and 2023 led to the determination of thermal conductivity (anharmonic phonon properties) for approximately 4,500 materials and harmonic phonon properties for over 10,000 materials, as illustrated in Fig. 3. This database now represents an unprecedentedly large collection of anharmonic phonon properties for inorganic materials based on first-principles

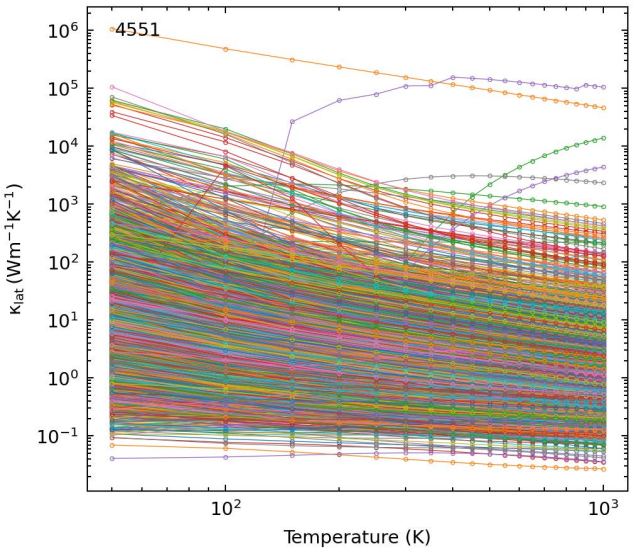

Fig. 3 Temperature-dependent thermal conductivity for approximately 4,500 analyzed materials.

calculations. Previously, publications related to MI typically discussed datasets encompassing no more than 100 materials. For the next step, our plans include expanding our calculations to metallic materials and approximately 48,000 stable materials that were recently announced by DeepMind at the end of 2023 [6].

As mentioned above, we have calculated the thermal conductivities for a large number of materials. However, as shown in Figure 3, some results indicate thermal conductivities exceeding 10,000 Wm-1K-1 at room temperature, and some exhibit a rapid increase in thermal conductivity with rising temperature. These unrealistic results can be attributed to the omission of four-phonon scattering and an insufficient density of the k-mesh in reciprocal lattice space, which lowers the accuracy of calculations, especially for materials with high thermal conductivity. Conversely, the data on materials with low thermal conductivity appears more reliable and is expected to be valuable for future predictions of thermal conductivity using machine learning.

References

[1] G. Kresse and J. Furthmüller, Phys. Rev. B 54, 11169 (1996).

[2] T. Tadano, Y. Gohda, and S. Tsuneyuki, J. Phys.: Condens. Matter 26, 225402 (2014).

[3] H. Larsen et al., J. Phys.: Condens. Matter 29, 273002 (2017).

[4] S. P. Ong, W. D. Richards, A. Jain, G. Hautier, M. Kocher, S. Cholia, D. Gunter, V. L. Chevrier, K. A. Persson, and G. Ceder, Comput. Mater. Sci. 68, 314 (2013).

[5] A. Togo and I. Tanaka, ArXiv. 1808.01590 (2018).

[6] N. J. Szymanski et al., Nature 624, 86 (2023).

Theoretical Study on Dynamical Processes in Heterogeneous Catalysis using Density Functional Theory and Machine Learning Methods

Thanh Ngoc PHAM, Harry Handoko HALIM, John Isaac G. ENRIQUEZ, Yuelin WANG, Muhammad Rifqi AL FAUZAN and Yoshitada MORIKAWA
Department of Precision Engineering, Graduate School of Engineering, Osaka University
2-1 Yamadaoka, Suita, Osaka 565-0871

Although first-principles electronic structure calculation methods have high prediction accuracy and have been used to elucidate various reaction processes, the spatial scale is limited to about nm and the time scale is limited to about several tens of ps because of the high computational cost. Recently, it has become possible to overcome this limit by combining DFT with machine learning methods. Using multi-scale simulations, we have been able to achieve large spacial scale and long time scale simulations on surfaces and interfaces that were previously impossible. We aim to elucidate the heterogeneous catalytic reaction process through multi-scale simulations and to identify factors that govern catalyst reactivity and provide guidelines for designing more efficient catalysts.

In this fiscal year, we investigated several systems which are important in both fundamental science and applications. Self-regenerative materials are keys to the development of stable catalysts used under high temperature condition, e.g., three-way catalyst converters in automobiles. Among others, metal nanoparticles supported on perovskite oxides are promising ones. However, little is known about their atomistic details, which are crucial for understanding and development of thermally stable catalysts. Therefore, we investigated a machine-learning enhanced density functional theory study of Pd_xO_y nanoparticles supported on a $Sr_3Ti_2O_7$ (001) surface and demonstrate that supported oxidized Pd particles fulfill the conditions for the self-regenerative catalysts [1].

We investigated the influence of CO to the formation of Cu clusters on Cu(111) surface by doing a set of MD simulations driven by machine-learning force-field [2]. By using the Cu island deposited on the Cu surface as the model, the simulations show that the CO-decorated Cu clusters are formed within a hundred of ns at 450 K and 550 K given the exposure to CO molecules. On the other hand, no cluster is formed on clean Cu surface even at 550 K. CO-decorated Cu clusters ranging from dimer to hexamer are detected within a hundred of ns at 450 K. Lowering the temperature to 350 K doesn't result in the formation of clusters due to the scarce detachments of adatom. Raising the temperature to 550 K results in the formation of bigger clusters, ranging from dimer to heptamer, but with shorter lifetime. The clusters can be formed directly through simultaneous detachment of a group of stepatoms or indirectly by agglomeration of wandering $Cu1(CO)_1$ and smaller clusters on the surface terrace. The statistical analysis on the evolution of the clusters shows the $Cu(CO)_1$ significantly involved in the formation and decomposition of the clusters due to their high mobility.

We also elucidated the surface facet depen-

dence on the oxygen adsorption and oxidized surface morphology of the diamond (111) and (100) surfaces to give insights that will improve the polishing, etching, and fabrication of diamond devices [3]. We used spin-polarized density functional theory to systematically simulate the O adsorption and CO and CO2 desorption reactions from pristine and etched diamond (111) and (100) surfaces. The results show that the surface facet dependence is caused by two factors: (1) the difference in the reactivity of the O_2 and (2) the difference in the carbonyl orientation of the O-terminated surfaces. The O_2 adsorption and activation energies on the C(111)-(2 × 1) surface are weaker and higher, respectively, compared to those on the C(100)-(2 × 1) surface. Moreover, the O_2 adsorption energy on the C(111)-(2 × 1) weakens with O_2 coverage. At monolayer O coverage, the carbonyl groups on the C(111)-(1 × 1):O surface have an inclined orientation which causes high steric repulsion between adjacent O atoms. The repulsion decreases with less neighboring molecules, leading to staggered etching, formation of islands, and loss of well-defined crystallographic orientation of the surface atoms. For the C(100)-(1 × 1):O surface, the carbonyl groups have an upright orientation and have low steric repulsion. The CO desorption activation energy is lower near an existing vacancy, leading to row-wise etching, which preserves the crystallographic orientation of the surface atoms.

We further performed DFT calculations and AIMD simulations to investigate the ORR mechanism on the sp-N1GDY/G and Pyri-NGDY/G with and without the solvation effect [4]. We found that under both vacuum and water conditions, ORR firstly proceeds on sp-N1GDY/G via dissociative mechanism because O_2 can be chemisorbed on a clean surface and easily dissociated rather than protonated to OOH*. However, OH* is strongly adsorbed on the sp-N1GDY/G surface, resulting in the weakening of the second O_2 adsorption, and ORR takes place via the ET-OHP associative mechanism. Pyri-NGDY/G also prefers ET-OHP associative mechanism.

We theoretically investigated the NO reduction reaction on Cu(100), Cu(111), Cu(110), Cu(211), and Cu(221) surfaces using a microkinetic analysis based on DFT energetics. [5]. We show that monomer dissociation requires high activation energies of more than 1 eV on almost all of the Cu surfaces we have considered. On the other hand, the existence of the flat-ONNO intermediate significantly lowered the activation energies, suggesting that the dimer-mediated pathway is preferred for NO dissociation, particularly at lower temperatures. Through this study, we provide an in-depth understanding of the NO reduction reaction on Cu surfaces over a wide temperature range.

References

[1] T.N. Pham, B.A.C. Tan, Y. Hamamoto, K. Inagaki, I. Hamada, and Y. Morikawa: ACS Catal. **14**, 1443 (2024).

[2] H.H. Halim, R. Ueda, and Y. Morikawa: J. Phys. Condens. Matter, **35**, 495001 (2023).

[3] J. I. G. Enriquez, T. Yamasaki, M. Michiuchi, K. Inagaki, M. Geshi, I. Hamada, and Y. Morikawa: J. Phys. Chem. C, **128**, 6294-6308 (2024).

[4] Y. Wang, T. N. Pham, H. H. Halim, L. Yan, Y. Morikawa: Materials Advances, **4**, 6542-6552 (2023).

[5] M. R. Al Fauzan, T. N. Pham, H. H. Halim, Y. Hamamoto, K. Inagaki, I. Hamada, and Y. Morikawa: J. Phys. Chem. C, **127**, 19451-19467 (2023).

Clarification of Microscopic Mechanisms of Semiconductor Epitaxial Growth and Device-Interface Formation by Large-Scale Quantum-Theory-Based Computations

Atsushi Oshiyama

Institute of Materials and Systems for Sustainability, Nagoya University

Furo-cho, Chikusa-ku, Nagoya 464-8601

In the fiscal year of 2023, on the basis of the total-energy electronic-structure calculations and molecular dynamics simulations within the density-functional theory (DFT), we have studied the epitaxial growth of wide-gap semiconductors, atomic and electronic structures of semiconductor-insulator interfaces, and mechanisms of atomic diffusion in semiconductors. The main computational tools are our RSDFT (Real Space DFT) code and RS-CPMD (Car-Parrinello Molecular Dynamics) code as well as VASP code. Specifically, we have studied 1) microscopic origin of hole traps at GaN/SiO_2 MOS device interfaces [1], 2) microscopic mechanism of the acceptor doping during epitaxial growth of GaN [2], and 3) possibility of recombination-enhanced migration of Mg acceptor in GaN [3]. The below is the explanation of the issue 1) above.

Identification of Hole Traps at GaN/SiO_2 MOS Device Interfaces

Power devices necessary to convert energies on the earth to electric power are crucial to sustain our energy-saving society in future. Currently, power devices based on silicon, are widely used, and overwhelming in the market. However, achieving higher efficiency and miniaturization of Si power devices is limited. In contrast, wide band gap semiconductors are obviously beneficial to energy conversion processes in power devices, and silicon carbide (SiC) and gallium nitride (GaN) indeed emerge in the market typically as MOSFET in power electronics.

In GaN-MOSFET devices, SiO_2 is usually used as a gate oxide. However unidentified hole traps emerge in such devices, and deteriorate the device performance. Recently, spontaneous formation of a Ga-oxide (GaO_x) intermediate layer with 1-2 nm thickness at the GaN/SiO_2 interface has been reported. We envisage that this nanometer-scale Ga oxide plays a role and have performed melt-quench calculations and explored the origin of the hole traps.

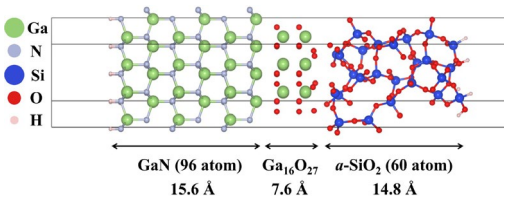

Fig. 1: Initial structure of GaN/GaO_x/SiO_2 interface in our slab model before the melt-quench calculations in the first-principles MD scheme. The thickness of the vacuum layer at the right and left sides is 12 Å

The GaO_x amorphous layer sandwiched by amorphous SiO_2 and GaN is simulated by atomic slabs separated from its images by vacuum regions as in Fig. 1.

Starting from the initial structure (Fig. 1), we perform melt-quench calculation and obtain stable GaN/a-GaO_x/a-SiO_2 structures. By adopting distinct heating and annealing procedures, we have prepared 4 distinct amorphous samples as shown in Fig. 2. Details of the heating and annealing procedures are found in our JAP paper [1].

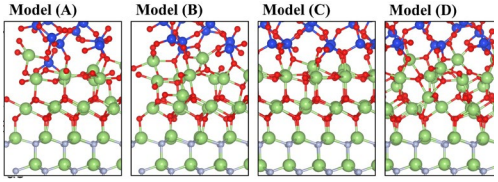

Fig. 2: Four distinct structures near the GaN/a-GaO_x/a-SiO_2 interfaces obtained by the first-principles MD calculations with the melt-quench technique. The color code is the same as in Fig. 1.

The local structures in the a-GaO_x layers obtained by our melt-quench calculations exhibit certain diversity. The Ga atoms are 4-, 5- or 6-fold coordinated with O atoms, whereas the O atoms are 2-, 3-, or 4-fold coordinated with either Ga or Si atoms. One of the important features in the local structures is the presence of the 2-fold coordinated O such as the -GaOSi- and the absence of the -GaOGa-. The presence of the 2-fold coordinated O is common in many oxides. However, what we have found for the nanometer-scale GaO_x sandwiched by GaN and SiO_2 is the sole presence of the -GaOSi- structure.

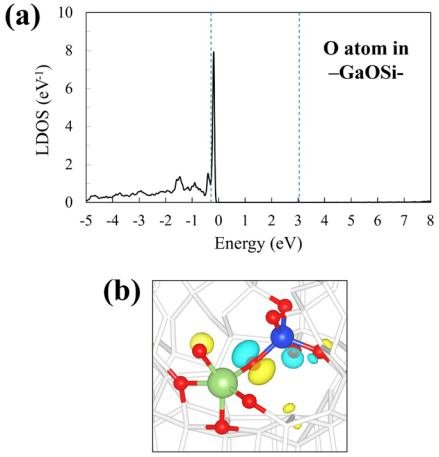

Fig. 3: Local density of states (LDOS) of the O atom in the -GaOSi- structure (a) and Kohn-Sham orbital at the LDOS peak (b). The blue dashed lines in the figure show the VBM and CBM of the GaN layer.

Figure 3 shows the local density of states contributed from this -GaO-Si local structure. We have found that this local structure induces a localized electron state just above the valence-band maximum, thus becoming a hole trap. The calculated Kohn-Sham orbital [Fig. 3(b)] unequivocally shows that this hole trap is the O lone pair state between Ga and Si atoms.

(The group id for this work is k0042)

Related publications

[1] S. Hattori, A. Oshiyama, and K. Shiraishi, J. Appl. Phys. to be published (2024).
[2] S. Yamauchi, I. Mizushima, T. Yoda, A. Oshiyama, and K. Shiraishi, Appl. Phys. Exp. to be published (2024).
[3] Y. Zhao, K. Shiraishi, T. Narita, and A. Oshiyama, App. Phys. Lett. to be published (2024).

Development of first-principles calculation code RSPACE and design of highly functional interface

Tomoya ONO
Graduate School of Engineering, Kobe University
Rokkodai-cho, Nada, Kobe 657-8501

SiC attracts much attention because it is one of the most promising wide-bandgap semiconductors for developing next-generation switching devices operating in high-power and high-frequency applications. However, the high channel resistance of SiC-MOSFETs hampers their performance. This high resistance is expected to be attributed to the low field-effect mobility in SiC-MOSFETs, which is much lower than the ideal electron mobility (~ 1000 $cm^2V^{-1}s^{-1}$). n-type MOSs, in which the inversion layers are composed by the conduction band edge (CBE) states, are more commonly used than p-type MOSs in the SiC-MOSFETs. The behavior of the CBE states of a SiC bulk is similar to that of free electrons and sensitive to the local atomic structure at the interface. In addition, in practical devices, off-oriented 4H-SiC(0001) surfaces by 4 degree are widely used. Thus, the SiC-MOS intrinsically possesses atomic-scale step and terrace structures even for the atomically flat surfaces. It is reported that the maximum field-effect mobility can be increased from 1-7 $cm^2V^{-1}s^{-1}$ to 25-40 $cm^2V^{-1}s^{-1}$ for 4H-SiC(0001) MOSFETs by interface nitridation by post-oxidation annealing with nitric oxide (NO). The microscopic information of the effect of NO annealing on a decrease of channel resistance of the SiC-MOSFET with atomic-scale steps is not fully clear although a lot of efforts have been made thus far.

In this study, the DFT calculation for the electronic structures of 4H-SiC(0001)/SiO_2 interfaces with atomic-scale steps is performed and the interface electronic structures before and after NO annealing are compared.[1]The computational models where the trench structure models are employed to imitate the step model are shown in Fig. 1 as an example. Owing to the excellent computation ability of supercomputer, such large models can be treated. In a 4H-SiC(0001) substrate, h and k site SiC bilayers are alternately stacked. The structure in which the Si atoms at the topmost h-site bilayer of the SiC substrate is bonded to the O atoms in the SiO_2 one-bond coordination is called the h1 model. The h3, k1, and k3 models were named similarly. The interface model with steps, in which the k1 and h3 interfaces are the upper and lower terraces, respectively, is named the k1/h3 model. The RSPACE code,[2] which uses the real-space finite-difference approach for the DFT, is employed.

Table 1: Partial charge density calculated in units of electron per supercell for flat interface before annealing. Data taken from Ref. 1.

Layer	k1	k3	h1	h3
1st-2nd	—	—	0.26	0.41
2nd-3rd	0.43	0.46	—	—
3rd-4th	—	—	0.44	0.43
4th-5th	0.43	0.44	—	—
5th-6th	—	—	—	—

The partial charge densities, which are projected on the wavefunction of the CBE states

Table 2: Partial charge density calculated in units of electron per supercell for step interface before annealing. Data taken from Ref. 1.

Layer	k1/h3	k3/h1	h1/k3	h3/k1
1st-2nd	—	—	0.14	0.02
2nd-3rd	0.39	0.23	—	—
3rd-4th	—	—	0.42	0.42
4th-5th	0.42	0.42	—	—
5th-6th	—	—	0.43	0.42

Table 3: Partial charge density calculated in units of electron per supercell for step interface after annealing. Data taken from Ref. 1.

Layer	k1/h3	k3/h1	h1/k3	h3/k1
1st-2nd	—	—	0.03	0.06
2nd-3rd	0.01	0.01	—	—
3rd-4th	—	—	0.14	0.12
4th-5th	0.39	0.40	—	—
5th-6th	—	—	0.43	0.43

of thin SiC bilayers, are defined as

$$\rho_{PC} = \Sigma_{i,k} \left| \int \Psi^*_{i,k}(\boldsymbol{r})\phi_k(\boldsymbol{r})d\boldsymbol{r} \right|^2 \times\theta(\epsilon_{i,k}-\epsilon_F)\theta(\epsilon_{max}-\epsilon_{i,k})\Delta_k, \quad (1)$$

where ϵ_F is the Fermi level, θ is the Heaviside function, and $\phi_k(x,y,z)$ is the wavefunction of the CBE states obtained by the thin film models. ϵ_{max}(=ϵ_F+1.65 eV), which is the maximum energy of the energy window, is chosen so that the energy window contains the CBE states inside the SiC substrate.

Table 1 lists the partial charge densities of the flat interface. We find that the partial charge density at the first bilayer in the h1 model is smaller than those at the other bilayers, which is consistent with the conclusion derived in the previous studies. The partial charge densities of the interfaces with steps before (after) NO annealing are also shown in Table 2 (Table 3). Our results indicate that the CBE states are absent below the upper terrace in some models before NO annealing owing to the finite-size effect and the Coulomb interaction of the O atom in the SiO_2 region. On the other hand, the effect of atomic configuration of the SiO_2 region is screened by the nitrided layer after NO annealing.

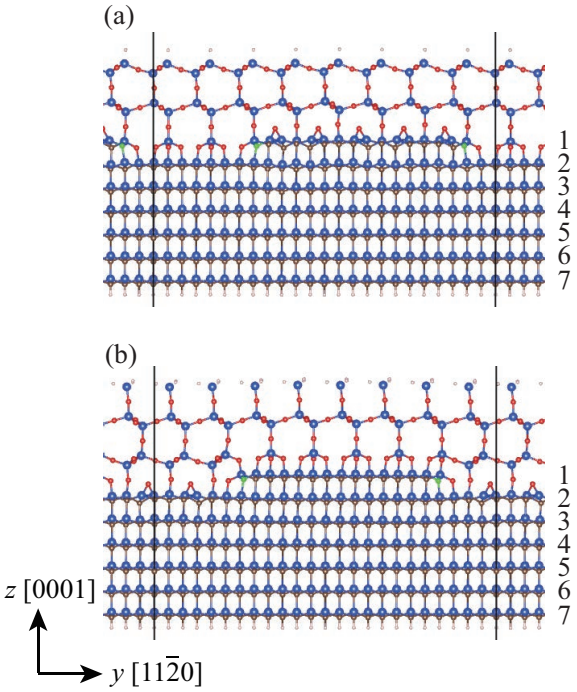

Figure 1: Interface atomic structure with steps for (a) k1/h3 (h1/k3) and (b) k3/h1 (h3/k1) models. Green, blue, red, and white balls represent N, Si, C, and O atoms, respectively. Black lines are the boundaries of supercells. The numbers written on the right-hand-side of the atomic structures are the indices of the atomic layers counted from the upper terrace.

References

[1] M. Uemoto, N. Funaki, K. Yokota, T. Hosoi, and T. Ono, Appl. Phys. Express **17**, 011009 (2024).

[2] K. Hirose, T. Ono, Y. Fujimoto, and S. Tsukamoto, *First-Principles Calculations in Real-Space Formalism, Electronic Configurations and Transport Properties of Nanostructures* (Imperial College, London, 2005).

First-principles study of functional materials

Fumiyuki ISHII, Naoya YAMAGUCHI, Rifky SYARIATI,
Hana Pratiwi KADARISMAN, Kaiki SHIBATA, Shohei MIURA,
Yaotang ZHANG, Yedija Yusua Sibuea TEWENG, Jin INOUE, Sota, YAMATE
Yume MORISHIMA, Khusnul YAKIN, Wardah AMALIA, Shigetomo YANASE,
Syifa Fauzia Hariyanti PUTURI, Ahmad GHIFFARI, Salsabila Amanda PUTRI
Nanomaterials Research Institute, Kanazawa University
Kanazawa, 920-1192, Japan

1. *Thermoelectric effect enhanced at van Hove singularity*[1]
The thermoelectric effect is a phenomenon where a temperature gradient generates an electric field, allowing for the effective harnessing of waste heat. There are two primary types of thermoelectric effects: the longitudinal Seebeck effect and the transverse Nernst effect. While the Seebeck effect generally results in higher thermoelectric conductivity, the Nernst effect is advantageous due to its simplicity and durability in thermoelectric devices.

In our research, we performed model calculations on a kagome lattice with a chiral spin state, focusing on the density of states (DOS) and its impact on thermoelectric conductivity. The DOS in this context shows singularities known as van Hove singularities (VHS). Our results indicate that these VHS enhance thermoelectric conductivity, leading to the prediction of a significant anomalous Nernst coefficient, approximately 10 μV/K at 50 K.

2. *Anomalous Nernst effect in Cr-doped Bi_2Se_3 singularity*[2]
We have investigated the electronic and thermoelectric properties of Cr-doped Bi_2Se_3 with six quintuple layers, modeling it as a quantized anomalous Hall insulator. Cr doping induces long-range ferromagnetism in Bi2Se3, a phenomenon confirmed both theoretically and experimentally. This magnetization leads to the experimental observation of the anomalous Hall effect in Bi_2Se_3, indicating that Cr-doped Bi2Se3 may exhibit Chern insulator characteristics. As a Chern insulator, it could serve as an outstanding transverse thermoelectric material, demonstrating a significant anomalous Nernst effect through the intrinsic contribution of the anomalous Hall effect and a pronounced Seebeck effect.

Using the rigid band approximation, we conducted first-principles density functional calculations to analyze the carrier-dependent anomalous Nernst coefficients. To enhance thermoelectric performance, we examined the origins of the anomalous Nernst effect, separating the contributions of the pure Nernst and Seebeck terms. Our study revealed a substantial contribution from the Seebeck term in Cr-doped Bi_2Se_3, attributed to the finite Chern number (C=-1). This finite Chern number is generated by the band splitting caused by out-of-plane magnetization from Cr doping. Consequently, we predict that Chern insulator materials, due to their Seebeck-induced effects, show great potential as transverse thermoelectric materials.

3. *Dirac electrons in graphene flake*[3]
Using the band unfolding method, we calculated the Dirac states of a finite graphene piece, referred to as a graphene flake. In a 15×15 rhombohedral graphene flake with an

approximate size of 3.7 nm, we clearly observed the Dirac states characteristic of pristine graphene, indicating the emergence of bulk-like electronic properties in this relatively small structure. To quantify these electronic properties, we determined the Fermi velocity by fitting the spectral weights using a weighted least-squares method. The approximated $E(k)$ and Fermi velocity for the 3×3 central region within the 15×15 graphene flake closely match those of pristine graphene. Our results highlight that the atomic arrangement and local periodicity in a small portion of the sample provide valuable insights into the system's electronic properties. The computational techniques used in this study may also be valuable for examining other finite or aperiodic systems, such as incommensurate twisted bilayer graphene.

4. *Proton Transfer in Triazole Molecules*[4] Triazole is an effective proton carrier because it features one proton donor and two proton acceptors. To investigate the proton transfer mechanism in triazole molecules, we performed density functional theory calculations in both gas and solvent phases. Our results indicate that 1,2,4-triazole molecules are more stable than 1,2,3-triazole molecules in both their neutral and protonated states. In the gas phase, proton transfer occurs only between symmetric molecular pairs. However, in solvent phases, proton transfer can also occur between some asymmetric molecular pairs as the proton donor-acceptor distance increases. The presence of solvents influences proton transfer by modifying the distance between proton donors and acceptors in triazole molecules.

References

[1] K. Shibata, N. Yamaguchi, H. Sawahata, and F. Ishii, J. Phys. Soc. Jpn. **92**, 124704(2023).

[2] R. Syariati, V. Saraswati, H. Sawahata, N. Yamaguchi, and F. Ishii, Jpn. J. Appl. Phys. **63** 01SP26 (2024).

[3] W. Amalia, N. Yamaguchi, S. Yunitasari, and F. Ishi, *submitted.*

[4] K. Yakin, N. Yamaguchi, T. Nakajima, M. Mizuno, F. Ishii, *submitted.*

Phonon effects in phase equilibria

Yoshihiro GOHDA
Department of Materials Science and Engineering, Tokyo Institute of Technology
J1-3, Nagatsuta-cho 4259, Midori-ku, Yokohama 226-8502, Japan

One of the most significant characteristic of metallic materials is the microstructure consisting of a few phases. Hence, many properties of metals cannot be understood from single crystals. The microstructure can be designed from the phase diagram that is determined from free energies of multiple phases. The free energy is decomposed into a few contributions, where the most important ones include the phonon effects and the configrational entropy. One of the problem in calculating the phonon free energy is the existence of the martensitic phase transition, where a high temperature phase is not stable at zero temperature exhibiting imaginary phonons. The self-consistent phonon (SCPh) method [1] can cure this problem.

In this project, we performed first-principles phonon calculations to evaluate free energies of metallic materials. Figure 1 shows calculated free-energy differences between the bcc and hcp phases for pure Ti and a Ti-Nb alloy. Since the bcc phase of Ti-based alloys exhibits martensitic phase transition, we performed SCPh calculations with the ALAMODE code [2]. In addition, we included effects of the electronic free energy, because we found it non-negligible. Even though binary Ti-Nb alloys has two-phase equilibrium regions in the phase diagram due to the digree of freedom in the composition variation, we fixed the composition so that the phase equilibrium occurs at a single temperature. The phase transition of the Ti-Nb alloy occurs at a lower temperature compared with pure Ti, consistent with an experimental fact that Nb is known as a bcc stabilizer in Ti-based alloys [3]. In addition, phase equilibria in permanent magnets were discussed through the CALPHAD approach with the first-principles cluster-expansion method [4].

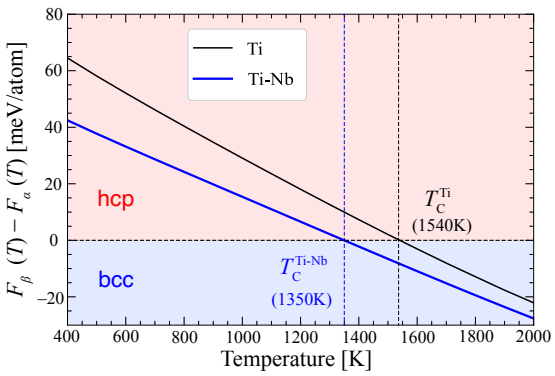

Figure 1: Calculated free-energy differences between the bcc and hcp phases for pure Ti and a Ti-Nb alloy as functions of the temperature T. $F_\alpha(T)$ indicates the free energy of the α phase, i.e., the hcp phase, whereas $F_\beta(T)$ is for the β phase, i.e., the bcc phase.

[1] T. Tadano and S. Tsuneyuki, Phys. Rev. B **92**, 054301 (2015).
[2] T. Tadano, Y. Gohda, and S. Tsuneyuki, J. Phys.: Condens. Matter **26**, 225402 (2014).
[3] K. Hashimoto, T. Tanaka, and Y. Gohda, in preparation.
[4] S. Enomoto, S. Kou, T. Abe, and Y. Gohda, J. Alloys Compd. **950**, 169849 (2023).

Analyses on local properties at complex structures via ab-initio-based methods

Satoshi WATANABE
Department of Materials Engineering, the University of Tokyo
7-3-1 Hongo, Bunkyo-ku, Tokyo, 113-8656

1 Introduction

The understanding of local properties in complex structures such as amorphous, surfaces, interfaces, and defects is becoming increasingly important as research and development of new information devices and energy-related systems progress. Nanoscale simulations with high prediction accuracy are a powerful means to gain this understanding, but those for local properties in complex structures are often still challenging due to the high computational cost. We have been addressing this issue not only using first-principles calculations but also employing machine learning potentials constructed based on data from first-principles calculations. In the following, two of our results from fiscal year 2023 are described.

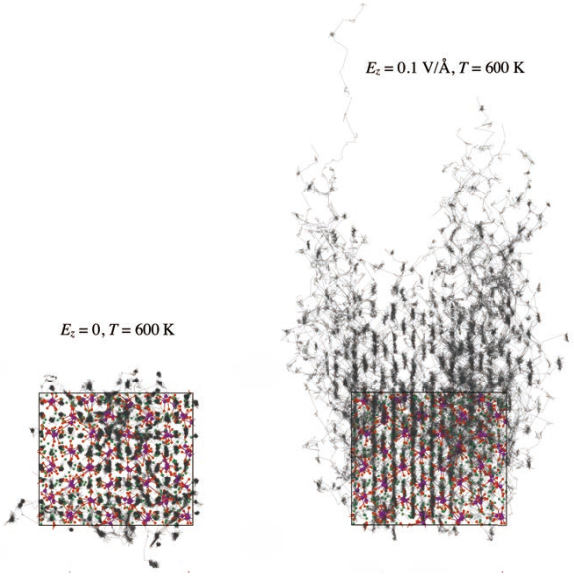

Figure 1: Calculated MD trajectories of Li in the amorphous Li_3PO_4 model for 300 ps at 600 K (left) without and (right) with the electric field. The z direction is upward one in the figure. Reprinted from Ref. [1].

2 Ion migration under electric fields

Understanding the ionic behavior under external electric fields is significant for the development of electronic and energy-related devices that utilize ion transport. To investigate such behavior, we developed a neural network (NN) model to predict the Born effective charges of ions [1]. By conducting molecular dynamics (MD) simulations that combine this NN model with a high-dimensional NN potential [2], we examined the migration of Li ions in Li_3PO_4 under a uniform electric field.

The prediction error of the constructed NN model, compared with the data from density functional perturbation theory, is 0.0376 e/atom. In MD simulations of a crystalline structure with a Li vacancy under a uniform electric field of 0.1 V/Å, we observed an enhanced mean square displacement of Li ions along the electric field, which appears to be physically reasonable. Furthermore, we obtained two interesting results. First, we found that the off-diagonal terms of the Born effective charges have a nonnegligible effect on Li migration under the electric field. Second,

in MD simulations of an amorphous structure without a Li vacancy, Li migration occurs in various areas despite the absence of explicitly introduced defects as can be seen in Fig. 1. We anticipate that the proposed NN method can be applied to any ionic material, facilitating the atomic-scale elucidation of ion behavior under electric fields.

3 Ion conduction in partially crystallized glass

Glass-ceramics, which crystallize from a glass state, often exhibit unique properties, including enhanced ionic conductivities compared to both the original crystalline and glass forms. However, details regarding the behavior of ion conduction in glass-ceramics, particularly the conduction pathways, remain elusive. We constructed a high-dimensional NN potential for Li_3PS_4 and examined the crystallization process of glass as well as ionic conduction through MD simulations.

First, we successfully reproduced experimentally observed crystallization from Li_3PS_4 glass. Next, we revealed that the diffusion barriers of Li decrease as the crystallinity in Li_3PS_4 glass-ceramics increases. Furthermore, we found that Li displacements predominantly occur in the precipitated crystalline portion, suggesting that percolation conduction plays a significant role in enhancing Li conduction. These findings provide valuable insights for the future utilization of glass-ceramic materials.

References

[1] K. Shimizu, R. Otsuka, M. Hara, E. Minamitani and S. Watanabe: Sci. Technol. Adv. Mater. Methods **3** (2023) 2253135.

[2] J. Behler and M. Parrinello: Phys. Rev. Lett. **98** (2007) 146401.

[3] K. Shimizu, P. Bahuguna, S. Mori, A. Hayashi, and S. Watanabe: J. Phys. Chem. C, submitted.

First Principles Design of GaN/Insulator Interface for GaN MOSFET

Kenji SHIRAISHI

Institute of Materials and Systems for Sustainability,

Nagoya University, Furo-cho, Chikusa-ku, Nagoya, Aichi 464-8601

Power devices necessary to convert energies on the earth to electric power are crucial to sustain our energy-saving society in future. The efficiency and also the compactness of such devices are essential to promote power electronics. GaN-based MOSFETs are promising power devices with high-speed operations owing to high mobility of carriers of GaN in addition to the high breakdown voltage. Many experiments have been conducted to investigate the GaN/SiO_2 interface properties. However, a high density of hole traps at the GaN/SiO_2 interface has been reported in experiments in the past [1]. This result obviously indicates that there are unidentified hole traps which make the carriers immobile at the GaN/SiO interface. Physical origins of those hole traps are totally unresolved.

We unveil atomic and electronic structures of the interface and identify the microscopic origin of the hole trap which has been a puzzle in GaN technology. The electron density of states (DOS) of the obtained GaN/a-GaOx/a-SiO_2 interface are shown in Fig. 1. A characteristic feature is the absence of electron states in midgap region of GaN. However, near to the valence-band maximum (VBM), within the energy region of about 1 eV. Those states appear in the energy gap at the edge of the valence bands [2].

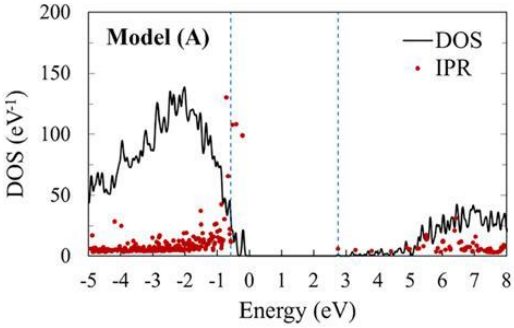

Fig.1: Calculated Density of State of GaN/a-GaOx/a-SiO_2 interface

These results indicate that O lone pairs in Ga-O-Si bonds are the atomistic origin of hole traps. Thus, to avoid these hole traps, the elimination of interfacial GaOx layers are inevitable.

References

1. Y. Wada, H. Mizobata, M. Nozaki, T. Kobayashi, T. Hosoi, T. Kachi, T. Shimura, and H. Watanabe, Appl. Phys. Lett. 120, 082103 (2022). (2020
2. S. Hattori, A. Oshiyama, and K. Shiraishi, J. Appl. Phys. 135, 175303 (2024).

Theoretical Studies on New Types of Point Defects Originated from Floating States in a-SiN towards Flash Memories Applications

Kenji SHIRAISHI

Institute of Materials and Systems for Sustainability,

Nagoya University, Furo-cho, Chikusa-ku, Nagoya, Aichi 464-8601

The a-SiN known as a useful hard material is now indispensable in current semiconductor technology: It is placed near the interface of Si-based metal-oxide-semiconductor structures and utilized as a nonvolatile flash memory which sustains our current data-driven society [1].

We performed first principles calculations to clarify the atomistic origin of charge traps in a-SiN which play crucial role in memory functions of recent flash memories.

In the actual a-SiN, H atoms are incorporated with its concentration of 10^{20}-10^{21}cm^{-3}. To clarify the role of the H atom, we have prepared H-incorporated a-SiN by our melt-quench scheme using $Si_{48}N_{63}H_3$ supercells. We have forged 4 distinct samples by varying heat treatments. By examining all the 4 samples, we have found, iour H-related local structures, NSi_2H, SiN_3H, NSi_3H and NSi_2H_2. We have found that these four H-related structures account for 92 % of all the H-related structures. This indicates that the under-coordinated or the wrong bond structures which induce mid-gap states are mostly passivated by H atoms. On the other hand, the SiN_4 configurations are not attached with H atoms. Hence the localized floating states (LFS) remain even in the H-incorporated amorphous samples (Fig. 1) [2]. As shown in Fig.1, LFS is hindered in the conduction band in case of neutral state, however it emerges as a charge trap state when electrons are captured. From these observation, LFS is the atomistic origin of a-SiN based flash memories.

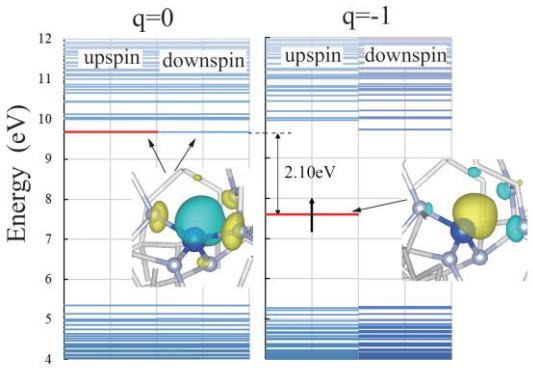

Fig.1: Energy levels and wave function of H incorporated a-SiN. (a) Neutral state. (b) Electron captured states.

References

1. K. Yamaguchi, A. Otake, K. Kobayashi, and K. Shiraishi, IEDM Tech. Dig. , pp. 275 (2009)..
2. Y. Nagaya, Master thesis, 2024, Nagoya University.

Identifying the Charge-Transition State in SiC/SiO_2 interfaces through a Combination of Ab-Initio Calculations and EDMR Experiments

Yu-ichiro MATSUSHITA

Laboratory for Materials and Structures,

Tokyo Institute of Technology, Yokohama 226-8503

In semiconductor physics, a quantitative understanding of interface properties is an extremely important research activity in device design. In particular, detailed analysis of defect levels is essential to understand interface defects and their effects on devices. In this article, we focus on the SiC-MOS (metal-oxide-semiconductor) interface, which is attracting attention as a next-generation power device, and present the results of our collaborative work with experiments to accurately understand the defect structure and its electronic levels.

In particular, it is known that the surface polarity of the SiC surface degrades the computational accuracy due to the ionic nature of the parent material. In this study, we first selected an electronic structure calculation method for SiC surface defects and confirmed the accuracy of the method. The electronic structure calculations for PbC centers were carried out using the high precision electronic structure approximation (HSE approximation) in combination with the finite size correction, as shown in Figure 1. The calculations show the existence of a (0/-) level 1.2 eV above the upper valence band (VBM). On the other hand, the latest experimental results from EDMR (electronically detected-magnetic-resonance spectroscopy) also confirm the location of the (0/-) level 1.2 eV above the VBM, and the combination of the HSE approximation and the finite-size correction allows us to calculate the electronic structure of interface defects with high quantitative accuracy. Considering the energy level, the P_{bC} center must impact both p- and n-channel devices, which is closely related to previously reported channel features. [1]

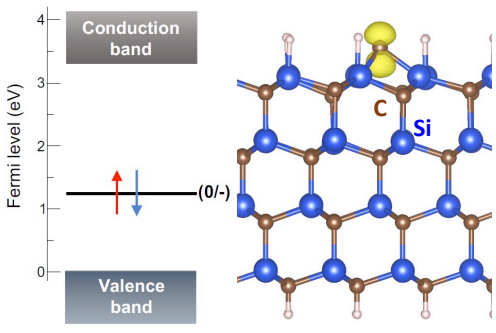

Figure 1. Results of elecgtronic structure calculations for Pbc centers. The calculated electronic levels (left) and their defect wavefunctions (isosurfaces at 15% of the maximum applitude of the wavefunction) (right).

In this study, we have used the RSDFT(Real-Space DFT) code on an ISSP Ohtaka Supercomputer.

References

[1] M. Sometani, APL Mater. **11**, 111119 (2023).

First-principles calculation of adsorption on electrode surfaces

Osamu SUGINO

Institute for Solid State Physics,

The University of Tokyo, Kashiwa-no-ha, Kashiwa, Chiba 277-8581

We have performed first-principles calculations of adsorbates on metal surfaces together with magnetic structure of a cuprate material. These calculations were based on the Generalized Gradient Approximation (GGA) or meta-GGA augmented with van der Waals functions scheme. This is because previous studies using GGA were often inconsistent with experiments and, on that basis, necessity of much more expensive functionals was argued. The simulated temperature programed desorption (TPD) spectra of an oxygen molecule and the distribution of the desorbed CO_2 were both consistent with experiment indicating accuracy of the functionals in describing the dynamics on Pt(111). These stringent benchmark calculations would prompt further simulation of the oxygen reduction reaction (ORR), CO oxidation, and other electrocatalytic reactions. The calculation scheme was also applied to water overlayers on Pt(111); although some inconsistencies in adsorption structure and energy remain, a serious comparison with experimental sum frequency generation (SFG) spectra has confirmed that the water molecules are arranged in such a way as to orient the hydrogen atoms towards the platinum surface. The computational scheme was moreover combined with the ring-polymer molecular dynamics simulation to study the quantum diffusion of H on Pd(111). By accelerating the simulation using the machine learning potential technique, the diffusing property of H atom was captured even at low temperatures where tunneling dominates. Simulation could explain how tunneling behavior differs between surface and bulk. We have further studied oxide materials, a pristine anatase TiO_2 surface, defective ZrO_2 surfaces and bulk $Sr_{1-x}La_xCuO_2$. The TPD spectra of O_2 were found to be consistent with the experiment for TiO_2; based on this result, we discussed the possible ORR efficiency on oxide-based electrocatalysts. The meta-GGA (SCAN) functional, which is able to describe the Mott transition of the cuprate, we discussed magnetic structure of this material.

Not only were these simulations time consuming, but the results needed to be provided in a timely manner to allow for collaboration with experiments. The ISSP supercomputer were found extremely useful for this purpose.

Analysis of thermal transport in disordered systems

Junichiro SHIOMI

Department of Mechanical Engineering,

The University of Tokyo, Hongo 7-3-1, Bunkyo-ku, Tokyo 113-8656, Japan

We have studied about thermal transport in complex systems. This year, we focused on the heat transport property of $FeCl_3$-graphite intercalation compounds and surface-disordered Si thin-film.

1. $FeCl_3$-graphite intercalation compounds

This research explores graphite and its intercalation with $FeCl_3$, aiming to uncover the mechanisms underlying the extremely low cross-plane thermal conductivity observed in GICs' experiments. In this study, we employed non-equilibrium molecular dynamics simulations to investigate the thermal conductivity of $FeCl_3$-graphite intercalation compounds (GIC) with various nanostructures, including different stages, thickness, and filling factor. Stage-'n' refers to the number of graphene layers sandwiched between neighboring intercalate layers, as shown in Fig. 1(a). Fixed boundary conditions were applied for cross-plane calculations (as shown in Fig 1(b)), and periodic boundary conditions were implemented for in-plane thermal conductivity analyses. By emulating superlattice, we observed decreasing-increasing trend in thermal conductivity, as shown in Fig. 2. We found that the cross-plane thermal conductivity increased with an increase in stage in a manner consistent with incoherent phonon interface scattering from $FeCl_3$ layers. However, at low stage (characterized by shorter periodic thickness), the decrease of cross-plane thermal conductivity as long-wavelength coherent phonon modes were expected to play a dominant role in the thermal transport, and the thermal conductivity values reached a saturated value of 0.3 W/m·K at stage5. The present work provides valuable insights into modulating the thermal properties of graphite by tuning phonon wave nature at room temperature with intercalated layered material. The observed decreasing-increasing thermal conductivity trend affirm the existence of coherent phonon transport at low stages.

2. surface-disordered Si thin-film

In this study, we investigated atomic-scale mechanisms underlying the reduction in thermal conductivity due to surface disorder by applying anharmonic lattice dynamics analysis to silicon thin-film structures with surface roughness. In this study, we fabricated ultra-thin silicon film structures with thicknesses ranging from 1 to 10 nm and introduced

disorder to the crystal structure of the surfaces to replicate surface roughness. The effect of surface roughness on suppressing thermal conductivity was usually estimated using the formula derived by Ziman[1]. However, the thermal conductivities of the thin films calculated in this study were lower than those estimated based on Ziman's formula (Fig. 3). Further analysis, separating the results into harmonic effects (phonon group velocity) and anharmonic effects (phonon relaxation time), revealed that while the harmonic effects suppressed thermal conductivity regardless of film thickness, the anharmonic effects were significant in suppressing thermal conductivity in extremely thin films of less than 5 nm. The insights from this study are useful for understanding the role of surfaces in materials with reduced thermal conductivity due to nanostructuring.

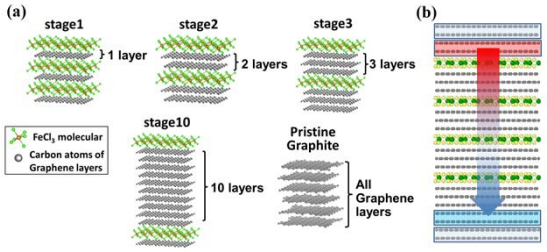

Fig. 1 Schematic illustration of the (a) main subject of this research, depicting various stages Graphite Intercalation Compounds (GICs) (b) setup for GIC's cross-plane thermal conductivity calculation, where the heat source and sink are positioned on the upper and lower sides.

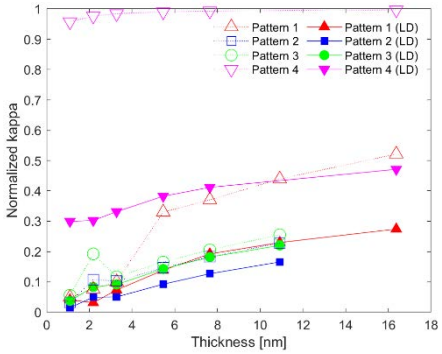

Fig. 3 Thermal conductivity of films with surface roughness. Normalized using the bulk thermal conductivity at T = 300 K. The empty markers represent the estimated thermal conductivity based on Ziman's formula[1], while the solid markers show the actual calculated results. Patterns 1-4 correspond to films with varying degrees of roughness.

References

[1] J. M. Ziman, Electrons and Phonons(Clarendon Press, Oxford,1960).

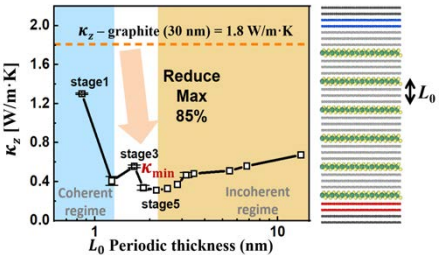

Fig. 2 Stage dependence of cross-plane thermal conductivity in GIC, with a constant total number of layers. Higher stages correspond to shorter periodic distances L_0 (the height of the smallest repeating unit) and more interfaces.

First-principles analysis of hydrogen-evolution semiconductor photocatalysts

Seiichiro L. TEN-NO
Graduate School of System Informatics, Kobe University
Rokkodai-Cho, Nada-Ku, Kobe 657-8501

Efficient dopants for high-performance photocatalytic $SrTiO_3$

Perovskite $SrTiO_3$ (STO) is a typical semiconductor photocatalyst for overall water splitting under ultraviolet. Similar to other photocatalysts, structural defects during synthesis should be controlled to promote photocatalytic activities. According to the recent experiment [1], it is observed that Al-doped STO can enable a quantum efficiency of almost unity at wavelengths between 350 and 360 nm.

To explore more efficient dopants for higher-performance photocatalysts, we have studied the dopant effects on the electronic structures of STO using the first-principles analysis based on the density functional theory (DFT). We use the supercell method to describe point defects including anion defects and substitutional doping, where several supercell models, namely, $2 \times 2 \times 3$, $2 \times 2 \times 4$, $3 \times 3 \times 3$, and $3 \times 3 \times 4$ supercell of the primitive cell of STO, are considered to take into account the finite size effects. The DFT calculations were performed within the PBE+U functional using PAW method as implemented in VASP [2]. The Hubbard U parameter was set to be $U =$ 4.36 eV for the 3d orbitals at the Ti sites, which reproduces the relative position of defect levels to the valence and conduction band.

Here we focus on the oxygen-site vacancy (V_O) and substitutional doping for the nearest Ti site. Since the O-defect works as the n-type doping and introduces 2 electron carriers, we also choose divalent and trivalent cations (namely, D^{2+} and T^{3+}) with a similar ionic radius to Ti^{4+} to introduce hole carriers. Then, we consider $D =$ Mg, Ni, Zn, and $D =$ B, Al, Ga, In, Tl, Sc.

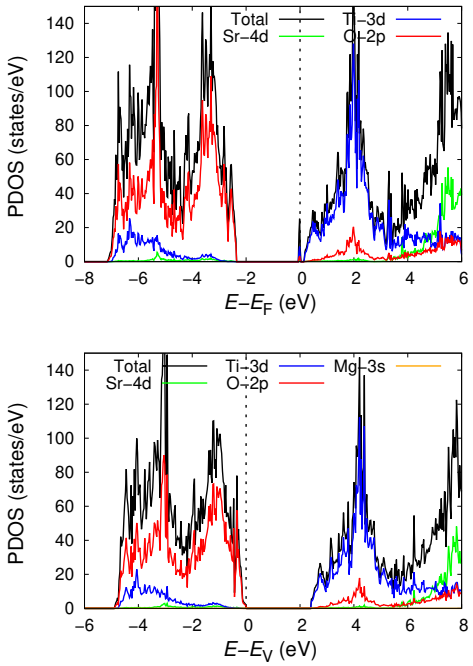

Figure 1: PDOS for (top) V_O and (bottom) Mg_{Ti}.

Figure 1 shows the projected density of states (PDOS) for V_O and Mg substitutional doping for the Ti, namely, Mg_{Ti}. Here the results of the $3 \times 3 \times 4$ supercell calculations are shown. In the presence of V_O, the defect level appears just below the conduction band minimum as a donor level. This defect level can

degrade the photocatalytic activities since it works as a recombination center. On the other hand, the Mg_{Ti} doping remove the defect level owing to the p-type doping, so that the photocatalytic degradation is expected to be prevented. We have also investigated whether the defect level can disappear in the other doping cases, namely, D_{Ti} and $2T_{Ti}$ doping.

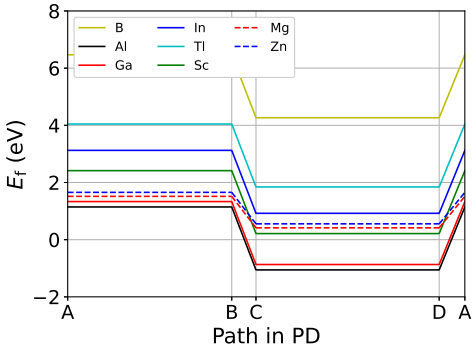

Figure 2: Dopant formation energy for each D_{Ti} and $2T_{Ti}$ doping.

Furthermore, we calculate the dopant formation energy for the D_{Ti} and $2T_{Ti}$ doping, which shown in Figure 3. Here each chemical potential is evaluated from the phase equilibrium of STO, and dopant chemical potentials are evaluated from the phase equilibrium of their oxides. Mg/Zn_{Ti} and $2Ga/Sc_{Ti}$ doping are easy to form according to the formation energy. Therefore, Mg/Zn_{Ti} and $2Ga/Sc_{Ti}$ doping can be expected to be efficient dopants for high-performance photocatalytic STO.

Hydrogen peroxide evolution on SnOx cocatalyst at hematite surface

Recent experiments have reported that when hematite (Fe_2O_3) is doped with Sn and Ti, the dopants diffuse to the particle surface to form a composite oxide ($SnTiO_x$) cocatalyst with hydrogen peroxide (H_2O_2) selectivity [3].

To investigate the water oxidation reaction on the SnO_x surface, we perform energy calculations of the adsorbates in each step of the

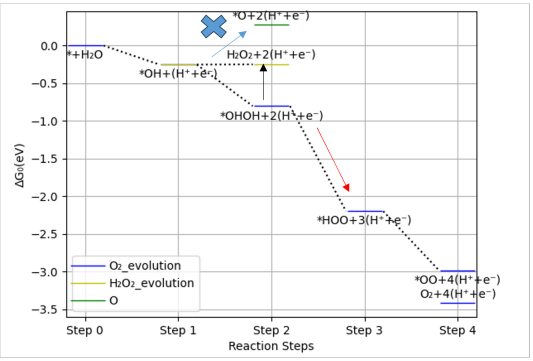

Figure 3: Energy diagram of water oxidation reaction added solvent effect.

predicted O_2 and H_2O_2 evolution reaction and perform a thermodynamic discussion. We find that both H_2O_2 and O_2 evolution reactions occur in structures without oxygen defects and with oxygen defects inside the bulk, while O_2 evolution reaction occurs in structures with oxygen defects near the surface. This result also suggests that there is a pathway for oxygen evolution other than the four-electron oxidation reaction. Furthermore, the numerical calculations including the solvent effect revealed that the 4-electron oxidation reaction and the O_2 evolution via 2-electron oxidation do not compete in real solvents.

Calculation conditions

We have performed hybrid (MPI+OpenMP) parallel computing using, where the parallelization over bands and k-points is used by VASP version 6.4.2.

References

[1] T. Takata *et. al.*: Nature **581**, 413 (2020).

[2] G. Kresse *et. al.*: Phys. Rev. B **47**, 558 (1993); Phys. Rev. B **49**, 14251 (1994); Computational Materials Science **6** (1996) 15–50; Phys. Rev. B **54**, 11169 (1996).

[3] Z. Zhang *et. al.*: Nat. Commun. **13**, 1499 (2022).

Improvement of accuracy and software development for the first-principles wave function theory

Masayuki OCHI
Forefront Research Center, Osaka University
1-1 Machikaneyama-cho, Toyonaka, Osaka 560-0043

April 1, 2024

We have developed a first-principles electronic structure calculation software using the transcorrelated (TC) method [1, 2]. The TC method is a many-body wave function theory, where Hamiltonian is similarity-transformed with the Jastrow correlation factor. By this transformation, electron correlation effects are efficiently considered. In particular, one-electron orbitals in the Jastrow-Slater-type wave function can be optimized in the same manner as the Hartree–Fock (HF) method, to say, by solving a one-body self-consistent-field (SCF) equation. It is advantageous that the computational cost for this process is the same order as that for the HF method [3].

In this year, we have published our study on isolated atoms [4]. In this study, we have tried several kinds of the Jastrow factor and checked the accuracy of fully-self-consistent TC+variational Monte Carlo (VMC) calculations. We found that the variance minimization in VMC is better compatible with TC than the energy minimization. In addition, an inclusion of the one-body Jastrow factor in VMC calculation gives better convergence of the self-consistency loop between TC and VMC calculations.

We have also studied condensed matter systems using our computational code TC++, which was published on github [5, 6] in the last year. One can perform TC calculations using TC++ by reading some output files dumped by DFT calculation using the Quantum-Espresso package [7]. TC++ supports the following functionalities: HF, TC, and biorthogonal TC (BITC) calculations, SCF and band calculations, solids and homogeneous electron gas, a plane-wave-basis set, and norm-conserving pseudopotentials. Calculation is MPI-parallelized for the k-point and band indices.

In this year, we have implemented the crystal-structure optimization using the Hellmann-Feynman force in the HF and BITC calculations. We note that the Hellmann-Feynman theorem holds for BITC but not for TC. We found that the lattice constants of bulk silicon is well reproduced by our (BI)TC calculations. We have also (internally) implemented the polynomial Jastrow factorsin (BI)TC calculations. The accuracy check is ongoing using supercomputers of ISSP.

References

[1] S. F. Boys and N. C. Handy, Proc. R. Soc. London Ser. A **309**, 209 (1969); *ibid.* **310**, 43 (1969); *ibid.* **310**, 63 (1969); *ibid.* **311**, 309 (1969).

[2] N. C. Handy, Mol. Phys. **21**, 817 (1971).

[3] M. Ochi, K. Sodeyama, R. Sakuma, and S. Tsuneyuki, J. Chem. Phys. **136**, 094108 (2012).

[4] M. Ochi, Phys. Rev. A **108**, 032806 (2023).

[5] https://github.com/masaochi/TC

[6] M. Ochi, Comput. Phys. Commun. **287**, 108687 (2023).

[7] https://www.quantum-espresso.org/

Density functional theory study of adsorption and reaction of molecules on metal surfaces

Ikutaro Hamada

Department of Precision Engineering, Graduate School of Engineering,

Osaka University, 2-1 Yamadaoka, Suita, Osaka 565-0871

To mitigate global warming and climate change, there is an urgent need to reduce fossil fuel usage and greenhouse gas emissions, particularly carbon dioxide. Considerable effort has been directed towards developing energy conversion devices like solar cells and proton exchange membrane fuel cells (PEMFC) based on renewable resources. Central to this effort is the development of molecules and materials for membranes and electrodes that facilitate efficient ion and electron transport and conversion.

Graphene has garnered significant attention due to its fascinating structural, mechanical, and electronic properties. Nitrogen-doped graphene, in particular, has demonstrated catalytic activity for the oxygen reduction reaction (ORR), crucial in PEMFC. Moreover, single transition metal atoms such as Fe and Co embedded in nitrogen-doped graphene have shown comparable catalytic activity to platinum, a highly active catalyst for ORR. However, to enhance the catalytic activity and durability of these single atom catalysts (SACs) within nitrogen-doped graphene, understanding the origin of their catalytic activity is imperative.

Computational studies, predominantly based on density functional theory (DFT), have been extensively conducted for this purpose. Yet, estimated catalytic activities, represented by limiting potentials—a measure of cell voltage in PEMFC—vary widely across the literature and do not consistently align with experimental results. Thus, further refinement of theoretical modeling for SACs is essential.

In this work [1], we performed DFT calculations of ORR on Fe and Co SACs embedded in nitrogen-doped graphene (Fe-N_4-C and Co-N_4-C), in which Fe and Co atoms are surrounded by 4 nitrogen atoms in graphene. We employed effective screening medium method combined with the reference interaction site mode (ESM-RISM) [2,3,4] that allows the systematic investigation of the roles of solvation, pH, and electrode potential, which are essential in the electrochemical reactions at the electrode-electrolyte interface. We used aqueous HCl as a solution with different electrolyte ion concentration (pH) using SPC and TIP5P models. All the calculations were performed using the projector augmented wave method [5] and revised Perdew-Burke Ernzerhof functional with dispersion correction (RPBE-D3) [6,7,8] as implemented in the Quantum-ESPRESSO package [9].

We investigated the oxygen reduction reaction (ORR) via the 4-electron associative mechanism. Initially, we calculated the limiting potentials with and without the electrolyte solution under neutral conditions using the computational hydrogen electrode method. The obtained limiting potentials were 0.66 V (Fe-N_4-C) and 0.51 V (Co-N_4-C) without the electrolyte solution, and 0.93 V (Fe-N_4-C) and 0.72 V (Co-N_4-C) with the electrolyte solution. These results did not align well with experimental observations. Particularly, we were unable to reproduce the trend where Fe-N_4-C and Co-N_4-C exhibited comparable limiting potentials.

However, by conducting calculations at a constant electrode potential, we obtained more accurate limiting potentials of 0.78 V (Fe-N_4-C) and 0.80 V (Co-N_4-C), which better matched experimental data. Through electronic structure analyses, we determined that the discrepancy between the results obtained under neutral conditions and those at constant electrode potential stems from differences in the charge states. Notably, in simulations at constant electrode potential, the active sites exhibit

significant charging.

This study highlights the critical role of surface charge/charge state in simulating electrochemical interfaces, indicating that accounting for that factor is essential for accurate predictions in such systems.

References

[1] A. F. Z. Abidin and I. Hamada, J. Phys. Chem. C **127**, 13623 (2023).
[2] M. Otani and O. Sugino, Phys. Rev. B **73**, 115407 (2006).
[3] N. Bonnet, T. Morishita, O. Sugino, and M. Otani, Phys. Rev. Lett. **109**, 266101 (2012).
[4] S. Nishihara and M. Otani, Phys. Rev. B **96**, 115429 (2017).
[5] P. E. Blöchl, Phys. Rev. B **50**, 17953 (1994).
[6] J. P. Perdew, K. Burke, and M. Ernzerhof, Phys. Rev. Lett. **77**, 3865 (1996).
[7] B. Hammer, L. B. Hansen, and J. K. Norskøv, Phys. Rev. B **59**, 7413 (1999).
[8] S. Grimme, J. Antony, S. Ehrlich, and H. Krieg, J. Chem. Phys. **132**, 154104 (2010).
[9] P. Giannozzi, *et al*. J. Phys.: Condens. Matter **29**, 465901 (2017).

Contributions of Second-Order Exchange Interactions in GW Electron-Hole Interaction Kernel

Yoshifumi NOGUCHI

Department of Applied Chemistry and Biochemical Engineering, Graduate School of Engineering, Shizuoka University, Johoku 3-5-1, Hamamatsu, Shizuoka 432-8561, Japan

The electron-hole interaction kernel, defined as the functional derivative of the one-electron self-energy operator using the one-particle Green's function, describes exciton binding energies and plays an important role in the determination of optical gaps. Within a GW approximation, four terms appear in the electron-hole interaction kernel including a first-order screened Coulomb interaction, a first-order bare Coulomb interactions, and two second-order interactions. The conventional GW+Bethe-Salpeter simulations have neglected the two second-order exchange terms based on the assumption that they are negligible small contributions, however the assumption has never been verified. In our previous study [1, 2], we implemented the full GW electron-hole interaction kernel, which includes not only the first-order direct and exchange terms but also the two second-order exchange terms, in our original all-electron mixed basis program and applied it to typical organic molecules [1]. In this study, we applied our method to the inter- and intra-molecular charge transfer excitations and discussed the contributions of the two second-order exchange terms. The significant

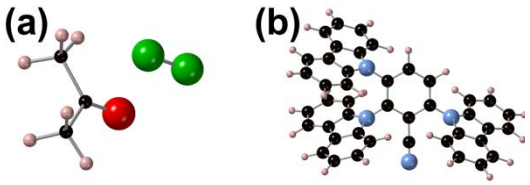

Fig. 1 Molecular geometries of (a) inter- and (b) intra-molecular charge transfer systems.

contributions were observed for thermally activated delayed fluorescence (TADF) molecules, in contrast to the typical organic molecules and the two-molecular systems. The two second-order exchange terms are several times larger than the first-order exchange term for the intra-molecular charge transfer excitations of TADF molecules. Our results suggest that the previous GW+Bethe-Salpeter simulations for TADF molecules should be reconsidered by considering the full GW electron-hole interaction kernel.

References

[1] Satoka Yamada, Yoshifumi Noguchi, Kohei Ishii, Daichi Hirose, Osamu Sugino, and Kaoru Ohno, Phys. Rev. B., **106**, 045113 (2022).

[2] Satoka Yamada and Yoshifumi Noguchi, J. Chem. Phys., **159**, 234105 (2023)

Equilibrium/nonequilibrium electrochemistry of disordered solid-state interfaces

Shusuke KASAMATSU

Academic Assembly (Faculty of Science),

Yamagata University, Kojirakawa, Yamagata-shi, Yamagata 990-8560

Simulation of solid-state electrochemical systems from first principles is challenging due to several factors including control of the chemical potential and handling of the combinatorial explosion in the possible number of ion configurations. To tackle these issues, we coded several new features into our original abICS framework for combination of high-throughput ab initio calculations (VASP, Quantum Espresso, or OpenMX), machine learning surrogate model training (aenet, nequip/allegro, MLIP3), and ensemble sampling [1].

To speed up the sampling for large-scale many-component systems, we implemented the population annealing Monte Carlo method for massively parallel ensemble sampling. We were also careful to cut back on file IO to minimize the impact on the network file system.

We also enabled calculation and control of the chemical potential through the implementation of free energy integration and grand canonical Monte Carlo sampling at fixed chemical potential. Figure 1 shows the state of charge in LiCoO2, an active material for Li-ion batteries, as a function of the Li chemical potential, which we calculated as a first test using the newly implemented grand canonical sampling. The results are in good general agreement with experiment. Further calculations on metal/solid electrolyte interfaces and electrocatalyst surfaces [2] are under way.

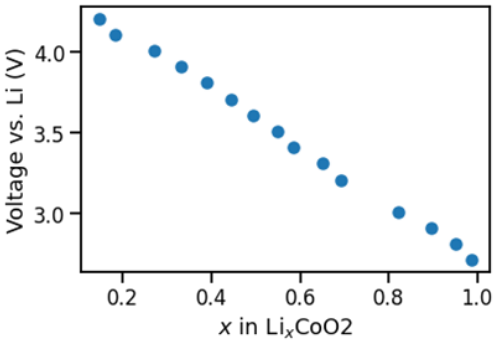

Fig. 1: Calculated state of charge vs. Li potential.

References

[1] S. Kasamatsu et al., Sci. Technol. Adv. Mater. Meth. 3, 2284128 (2023)

[2] A. Nakanishi et al., in preparation. arXiv:2307.11296

Large-scale simulations for magnetic nanopaticles

Hung Ba TRAN
Advanced Institute for Materials Research (WPI-AIMR), Tohoku University,
Email: *tran.ba.hung.a6@tohoku.ac.jp*,

Our previous works studied the effect of magnetic anisotropy on magnetocaloric properties by combining first-principles calculations and Monte Carlo simulations[1, 2, 3, 4]. The magnetic parameters, such as isotropic exchange coupling constants J_{ij}, the antisymmetric exchange also known as the Dzyaloshinskii–Moriya vector $\overrightarrow{D_{ij}}$, and magnetocrystalline anisotropy constants in uniaxial k_u and cubic k_c, are calculated from first–principles calculations. Then, the Monte-Carlo simulations are performed to estimate the magnetic properties at finite temperatures and external magnetic fields. We calculated the temperature dependence of magnetocrystalline anisotropy energy for uniaxial and cubic anisotropy. The Callen-Callen power law is widely used to determine the temperature dependence of magnetic anisotropy energy in the experiment, such as m^3 for uniaxial anisotropy and m^{10} for cubic anisotropy. Based on this power law, the magnetic anisotropy energy should be downed to zero at Curie temperature, where the magnetization disappears. However, we found that the magnetic anisotropy energy is not negligible even above Curie temperature in the case of uniaxial anisotropy. It comes from the magnetization anisotropy and anisotropic magnetic susceptibility. The evidence of finite magnetic anisotropy energy above Curie temperature from experimental works can be seen from the difference of isothermal magnetic anisotropy change when applying the magnetic field along the easy or hard axis in bulk CrI_3 and $AlFe_2B_2$[1, 2].

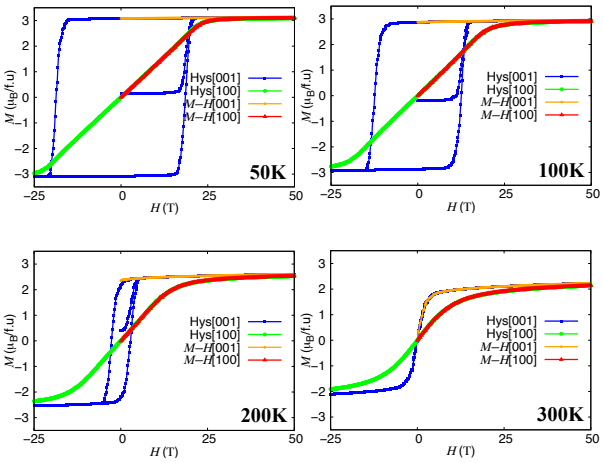

Figure 1: Temperature dependence of hysteresis loops and magnetization versus magnetic field M–H curves of $L1_0$ FePt nanoparticle.

In magnetic nanoparticles case, the magnetic anisotropy energy is the primary source of stabilizing magnetization against thermal fluctuation. The temperature dependence of the energy barrier in magnetic flips of the nanoparticles can be used to estimate the relaxation time of magnetic nanoparticles. In this study, we perform a large-scale simulation for $L1_0$ FePt nanoparticles by combining first-principles calculations and Monte Carlo simulations. Significantly, we found that the estimation of magnetocrystalline anisotropy energy of nanoparticles by using a hysteresis loop is not correct at finite temperatures due to the finite energy barrier of nanoparticles (Figure 1). In such cases, the magnetization versus magnetic field M–H curves are more reliable in estimating the temperature dependence of

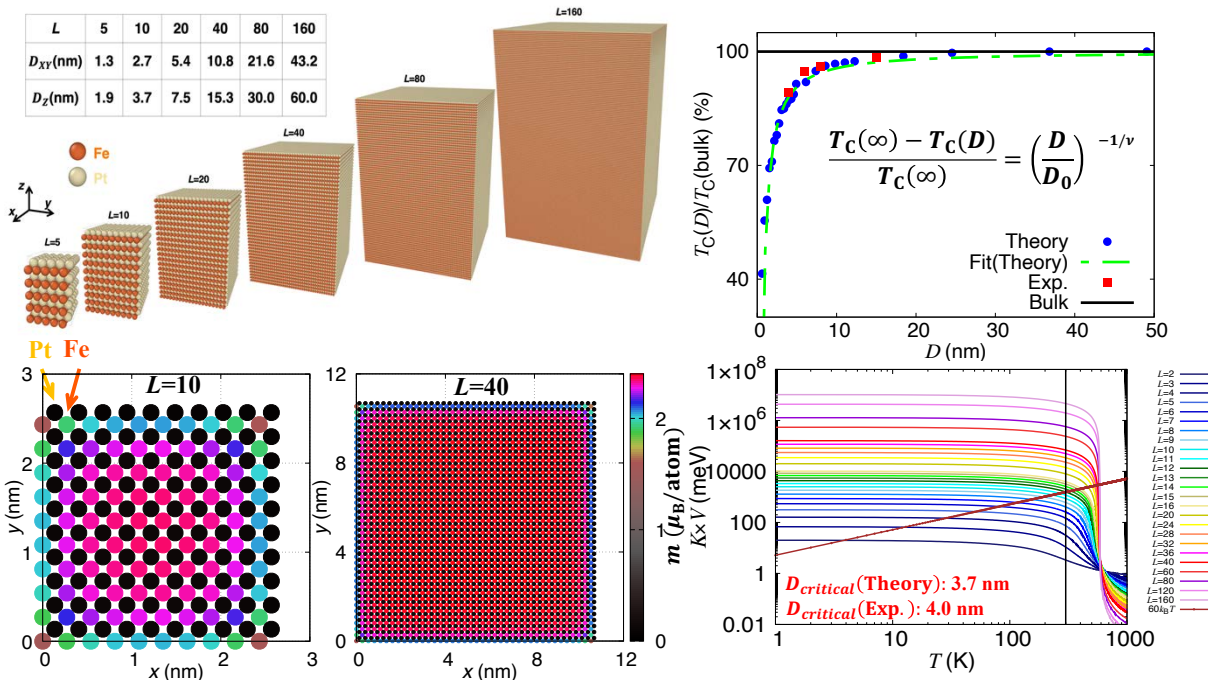

Figure 2: Size dependence of magnetic properties, such as Curie temperature, magnetic resolved, and energy barrier, of $L1_0$ FePt nanoparticle.

magnetic anisotropy energy.

The exponential behavior of the Curie temperature of various nanoparticle sizes is quantitatively reproduced compared with the data observed in the experimental works (Figure 2). The ferromagnetic order of nanoparticles will be absent at critical diameter D_0 due to the loss of the pairs in the exchange interaction at the surface. Moreover, the surface effect on the magnetic properties of $L1_0$ FePt nanoparticles is clarified by considering the magnetic profile in atomistic Monte Carlo simulations (Figure 2). Furthermore, the temperature and size dependence of the energy barrier for magnetic flips of $L1_0$ FePt nanoparticles is obtained in this work, demonstrating that the critical diameter of nanoparticles for long-term storage in hard-disk driver applications (10 years) is 3.7 nm, which is in good agreement with experimental work as 4.0 nm (Figure 2). Our work can be used as a guide to the experiment on developing the magnetic properties of nano-material applicable for magnetic recording.

References

[1] H. B. Tran, H. Momida, Y. Matsushita, K. Sato, Y. Makino, K. Shirai, and T. Oguchi, Phys. Rev. B **105**, 134402 (2022).

[2] H. B. Tran, H. Momida, Y. Matsushita, K. Shirai, and T. Oguchi, Acta Mater. **231**, 117851 (2022).

[3] H. B. Tran, Y. Matsushita, Appl. Mater. Today **32**, 101825 (2023).

[4] H. B. Tran, Y. Matsushita, Scr. Mater. **239**, 115799 (2024).

[5] H. B. Tran, Y. Matsushita, Scr. Mater. **242**, 115947 (2024).

Analyses on electronic/magnetic structuresinhigh-performance spintronics magnetic materials and parallelizationdevelopment/application in quasi-particleself-consistent *GW*code

Tatsuki ODA[1,2], Kazuki MURANAKA[2], Rinku MAJUMDER[2], Chandro PARDEDE[2], Jakub LUTSINEC[2], Ko HYODO[2], Masao OBATA[1,2]

[1]*Institute of Science and Engineering, Kanazawa University, Kanazawa, Ishikawa 920-1192*

[2]*Graduate School of Natural Science and Technology, Kanazawa University, Kanazawa, Ishikawa, 920-1192*

We have studied electronic structure in several systems of non-magnetic or magnetic material by means of density functional theory (DFT) approach or the quasi-particles self-consistent GW (QSGW) approach. Concerned with the latter calculation, we have successfully parallelized the corresponding part of computational code for the polarization function (PF), which is one of the most time-consuming parts in QSGW [1]. As a result, the computational time of PF was reduced by one order in the elapsed time using the ISSP computer for the system containing 16 atoms in the unit cell [2]. We have also developed the density functional theory (DFT) code optimized for GPU architecture [3].

(A) Migration of twin boundary

Migration of the twin boundary in a modulated martensite phase of the magnetic shape memory alloy Ni_2MnGa is significant to understand the magnetic shape memory effects. This work explored the migration mechanism of the nanotwin boundaries among the layers by first-principles calculations. We systematically analyzed intermediate structures throughout the migration path using the DFT approach [4]. We identified some key factors using the systems of 10M and 14M modulated phase. As a result, we obtained a concise barrier energy formula as empirical one. The resulting energy for barriers was found to be enough so low as a permission of the transition by the thermal energy.

(B) Ni_2MnX (X=Al, In) by QSGW

According to the QSGW, our group has found the Ni e_g orbitals appear just on the Fermi level in the cubic (austenite) phase of Ni_2MnGa, which leads to martensite phase transition by band Jahn-Teller effect. In addition, the generalized susceptibility provides the Fermi surface nesting vector, which coincides the experimental modulation for the

10M and 14M martensite phases [5]. These new achievements encourage several studies as revisit investigation. We investigated the electronic structures of Ni2MnX (X=Al, In) series using the QSGW [6].

(C) MAE in the alloy containing Pt element

Promising candidates for recording media, such as FePt alloys, have large magnetic anisotropy energy. This calculation aims to analyze the origin of magnetic anisotropy energy in a multilayer system of Pt/Fe/Pt. For this aim, in addition to a procedure of direct total energy calculation, the analysis for seeking the origins of anisotropy has been required. We are devoting the computational resources to set up a series of approach. It is one of the methods like the force theorem method. That will be completed in very near feature.

(D) Application to gallium oxide by QSGW

Wide band gap semiconductors are important materials for the power electronics applications. The beta-Ga_2O_3 has been fascinated recently because such material has a larger band gap and larger breakdown electric field compared with those of Si, SiC, and GaN, while it does not promote the removal of waste heat due to a shortcoming of its small thermal conductivity. To improve such heat removal, the interface with the sapphire substrate which promotes thermal conductivity has been studied in the experimental works. The final goal is of studies in such an interface, however, we calculated the band structures in the bulk and small slab systems using the QSGW at the present. We also used a hybrid exchange-correlation energy of QSGW and DFT for investigation. Using the hybrid method, the band gap energy was estimated to be the value obtained in the experiment within 1% accuracy [7]. We tried to investigate slab system of beta-Ga_2O_3. Using the effective screened medium approach, we successfully obtained a theoretical dielectric constant similar to the experimental values. Unfortunately, the calculations did not reach to an enough width of slab thickness for containing the layers of both tetrahedral and octahedral Ga atoms within the slab system due to its complexity of crystal structure and computational memory problems.

References

[1] T. Kotani, J. Phys. Soc. Jpn. **83**, 094711 (2014); *ecalj*: https://github.com/tkotani/ecalj/.

[2] K. Hyodo et al., accepted in the proceedings CCP2023.

[3] C. Pardede et al., accepted in the proceedings CCP2023.

[4] R. Majumder et al., accepted in the proceedings CCP2023.

[5] M. Obata, T. Kotani, and T. Oda, Phys. Rev. Mater. **7**, 024413 (2023).

[6] J. Luštinec et al., preparing for publication.

[7] JSAP Spring Meeting 2024: 24p-P16-27.

Development of Ceramic Protective Coating for High Corrosion Resistance of Metallic Materials

Yuji Kunisada

Center for Advanced Research of Energy and Materials, Faculty of Engineering, Hokkaido University, Sapporo, Hokkaido 060-8628

In order to develop efficient hydrogen permeation barriers, we investigated the adsorption and diffusion properties of hydrogen isotopes in the vicinity of the interface between different ceramic materials,[1] with the aid of the first-principles calculation based on the density functional theory (DFT). We also investigated the diffusion properties of hydrogen atoms at the grain boundaries of nanocrystalline ceramic materials.

We investigated the absorption energies and diffusion barriers of hydrogen isotopes in the vicinity of the α-Al_2O_3/α-Cr_2O_3 interface using The Vienna Ab initio Simulation Package (VASP). We installed a parallelized VASP with Intel® MPI Library and Intel® Math Kernel Library. We found that hydrogen atoms can form chemical bonds with coordinated oxygen atoms at the stable sites in the α-Al_2O_3 region as well as in the α-Cr_2O_3 region due to interfacial effects. On the other hand, in the transition state, hydrogen atoms cannot form chemical bonds with coordinating atoms. As a result, the diffusion barrier for hydrogen atoms is largest in the α-Al_2O_3 region adjacent to the interface rather than at the interface site. Obtained diffusion barrier is larger than that of the bulk α-Al_2O_3.

We also investigated the diffusion properties of hydrogen atoms at the grain boundaries of nanocrystalline TiN to reveal the effects of the grain boundaries. In grain boundaries, hydrogen atoms are negatively charged and become hydride ions. We found that the diffusion barrier of hydride ions varies significantly depending on the width of the grain boundary. Considering the grain boundary widths observed in the nanocrystalline TiN films prepared by RF magnetron sputtering, it is clear that the nanocrystalline TiN films have higher hydrogen permeability properties than conventional Pd hydrogen permeable films.

These results indicate that the hydrogen permeability of ceramic materials can be significantly changed by controlling the interface.

References

[1] Y. Kunisada, R. Sano, N. Sakaguchi, submitted.

[2] Y. Kunisada, C. Kura, N. Sakaguchi, C. Zhu, H. Habazaki, Y. Aoki, ACS Omega 9 (2024) 13738.

Analysis of incoherent interfaces by DFT calculations

Kazutoshi INOUE[1], Qian CHEN[2], Mitsuhiro SAITO[2], and Yuichi IKUHARA[1,2,*]
[1] *Advanced Institute for Materials Research, Tohoku University, Sendai, Miyagi, 980-8577*
[2] *Institute of Engineering Innovation, The University of Tokyo, Yayoi, Tokyo, 113-8656*

Materials interfaces are two-dimensional defects that significantly affect macroscopic properties due to their local atomic structures. Therefore, it is especially important to identify the stable atomic structure including interfaces, which strongly depends on the misorientation in both ionic and metallic materials. Coherent grain boundaries are classified by the coincidence-site lattice theory. However, it is necessary to effectively approximate the ratio of lattice constants by a rational number for modeling and prediction of incoherent interfaces. For a pair of lattices with a rational ratio of lattice constants, the CSL theory can be easily extended to give a possible pair of commensurate lattices. In this study, atomic models for incoherent grain boundaries were built with a 3D periodic boundary condition. The translation models are systematically constructed by the 0.1 Å steps within the Displacement-Shift-Complete lattice to screen the stable atomic structures. Each model was firstly calculated to obtain grain boundary energy to screen the translation states. The grain boundary energy is the interfacial excess free energy calculated by

$$\Delta E = \frac{1}{2A}\left(E_{\mathrm{total}} - N\sigma_i\right),$$

where E_{total} is the total energy of the system including grain boundaries, σ_i is the energy of the unit cell of the bulk crystal, N is the number of unit cells contained in the supercell, and A is the area of the grain bondary. We applied the first-principles DFT calculations with the plane-wave basis projector-augmented wave method included in VASP to screen and determine the stable atomic structure by using CPU nodes in System B. The generalized gradient approximation was used for the exchange-correlation potentials in the Perdew-Burke-Ernzerhof form, employing an ultrasoft pseudopotential. The cutoff energy was set 600 eV for all plane-wave basis sets. The Brillouin-zone integrations were performed over a $4\times4\times1$ k-point mesh generated by the Monkhorst-Pack scheme. Then, the atomic positions and supercell volumes of the most stable structures among those screened were fully relaxed to ensure that all forces on each relaxed atom were 1.0×10^{-5} eV/Å, and the residual force on each relaxed atom was 0.05 eV/Å under a constant pressure of 0 Pa and a constant temperature of 0 K.

It was anticipated that the longer the periodicity, the more precise the model would be. However, a comparison of the models with long and short periodicity revealed that the grain boundary energy and bandgaps were not dependent on the periodicity, contrary to expectations. Our findings indicate that the long periodicity model can be approximated by a summation of a few short periodicity models, which obeys the rule of approximation of the ratio of lattice constants by a rational number [1].

References

[1] K. Inoue, Q. Chen, K. Kawahara, M. Saito, M. Kotani, Y. Ikuhara: to be submitted (2023).

First-principles study on electron transport properties of heteroatom-doped graphene with adsorbed NO molecules

Yoshiyuki EGAMI
Division of Applied Physics, Faculty of Engineering, Hokkaido University
Kita 13, Nishi 8, Kita-ku, Sapporo, Hokkaido 060-8628

Adsorption of gas molecules on two-dimensional (2D) materials gives rise to significant modifications to atomic and electronic structures of the materials, affecting their electrical conductivity. Graphene is one of the typical 2D materials and shows high conductivity. On the other hand, a pristine graphene is not so suitable as a gas sensor material because the adsorption of gas molecules on the graphene is physisorption which is difficult to modulate the electronic structure of the graphene. Doping graphene with heteroatoms is expected to be the one of promising techniques to increase the detection sensitivity of graphene for adsorbed molecules. Several theoretical studies have shown that nitrogen-containing gas molecules such as NO can chemisorb with the doped heteroatoms and significantly affect the electronic structures of graphene.

In this study, we performed a first-principles study on the modulation in electronic structures and electron transport properties of the doped graphene with molecular adsorption. Here, Al, Si, or N atoms are doped into graphene, in which the ratio of dopant atoms X(=Al, Si, or N) to carbon atoms is 1:3, and NO molecules are adsorbed on the doped atoms. First-principles simulations were carried out using the "RSPACE" code based on the real-space finite-difference formalism[1, 2].

As the results of electronic structure calculations, it was confirmed that the density of states (DOS) near the Fermi level is lower for X=Si than that for X=N or Al. In all systems, the DOS increased in the vicinity of the Fermi level due to the NO molecular adsorption. On the other hand, the electron transport properties were slightly modified for SiC_3, whereas significant modifications in the transport properties were observed for AlC_3 or C_3N. In addition, the influence of the coverage of NO molecules over the graphene on the transport properties was evaluated. For example, in the C_3N system, significant differences in the transport properties were found even when a single NO molecule was adsorbed on the surface consisting of ∼1,000 atoms. This demonstrated the high detection accuracy of adsorbed molecules in the doped graphene.

This work has been performed on System B of the Supercomputer Center, the Institute for Solid State Physics, the University of Tokyo.

References

[1] K. Hirose *et al.*: First-principles calculations in real-space formalism (Imperial College Press, 2005).

[2] Y. Egami, S. Tsukamoto and T. Ono: Phys. Rev. Res. **3**, 013038 (2021).

Electronic properties of the supra-atomic-molecular-orbital-derived band in a solid C_{60}: Theoretical investigation with the GW approximation

Susumu YANAGISAWA
Faculty of Science, University of the Ryukyus
Senbaru 1, Nishihara, Okinawa 903-0213

Fullerenes such as C_{60} have attracted considerable attention as electron transport materials originating from their n−type semiconducting nature. C_{60}, with its soccer-ball molecular shape and thus its spherically high symmetry, has characteristic electronic properties, such as the Supra Atomic Molecular Orbital (SAMO). The SAMO originates from the spherical electronic potential due to the spherical molecular shape, which leads to the Rydberg-like electronic states. The spatial distribution of the wave function with few nodes leads to high electron mobility and free-electron-like nature of the band[1].

In this study, we theoretically estimated the electron mobility of the SAMO-derived band with the first-principles bandstructure calculation. To investigate the nature of the electronic band, we used the GW approximation for bandstructure calculation.

The Projector Augmented Wave (PAW) potential was used, as implemented in the VASP program code, and the valence wave function was expanded by the plane wave basis set with energy cutoff of 1000 eV. The atomic positions and the lattice constants of the C_{60} fcc crystal was optimized with the van der Waals density functional[2]. The 4×4×4 **k**-points were sampled in the Brillouin zone. The spatial distribution of the Kohn-Sham wave function was calculated with the STATE program code.

To calculate the band structure within the GW approximation, the GW space-time code[3] was used. The cutoff energy for the plane wave was 734 eV, and the unoccupied bands for calculating the Green's functions encompassed 440 eV above the Fermi level. The program code allows to calculate the GW band energies of arbitrary **k**-points without the Wannier interpolation. Inclusion of the many-body effect based on the zeroth-order wave functions and band energies, *i.e.* the one-shot GW, was conducted, by using the one-particle solutions obtained with the generalized gradient approximation (GGA) level of theory.

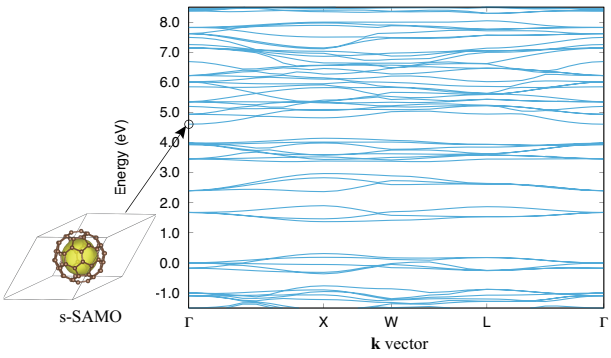

Figure 1: Band dispersion of C_{60} obtained with GGA, along with the spatial distribution of the s-SAMO wave function.

The optimized lattice constant of the C_{60} fcc crystal structure was 14.12 Å, in good

agreement with the experimental value of 14.3 Å measured at room temperature[4]. The band dispersion obtained with GGA level of theory indicates the parabolic band structure of the s-SAMO-derived band (Fig. 1), implying the suggested free-electron-like nature of the band. The effective electron mass estimated with the curvature of the band was 0.71, relative to the electron rest mass.

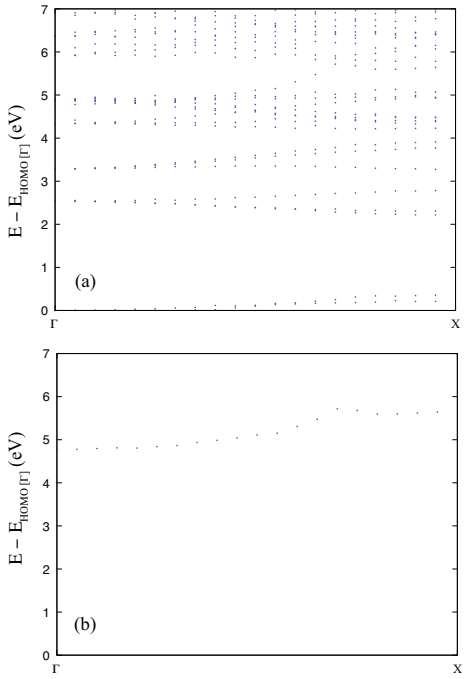

Figure 2: Band dispersion of C_{60} obtained with GW: (a) overall band structure, (b) s-SAMO derived band only.

By the many-body effect within the GW approximation, the calculated band gap was 2.0 eV, in fair agreement with the experimental value of 2.4 eV[5] (Fig. 2). It was found that compared to the band dispersion obtained with GGA the s-SAMO derived band shifted down relative to the other bands. The s-SAMO derived band obtained within GW (see Fig. 2 (b)) showed a parabolic band structure around the Γ-point, similarly to that obtained with GGA. The effective mass was estimated to be 1.13. The larger effective electron mass than that of GGA is consistent with the free-electron nature of the band: the polarization cloud attracts back the injected charge, which decreases the mobility of the charge compared to the free electron[6].

While the effective mass estimated within GW was consistently elucidated, the downward shift of the s-SAMO band by inclusion of the many-body effect needs consideration. Further investigation is in progress, *i.e.* further consistent inclusion of the many-body effect by the evGW approach.

References

[1] J. O. Johansson, E. Bohl, and, E. E. B. Campbell: Phil. Trans. R. Soc. A **374**, 20150322 (2016).

[2] I. Hamada: Phys. Rev. B **89**, 121103 (2014).

[3] M. M. Rieger et al., Comput. Phys. Commun. **117**, 211 (1999); L. Steinbeck et al., Comput. Phys. Commun. **125**, 105 (2000); C. Freysoldt et al., Comput. Phys. Commun. **176**, 1 (2007).

[4] K.-D. Tsuei et al., Phys. Rev. B **56**, 15412 (1997).

[5] A. Sugie et al., J. Phys. Chem. Lett. **14**, 11412 (2023).

[6] C. Friedrich, S. Blügel, and D. Nabok, Nanomaterials **12**, 3660 (2022).

Non-adiabatic excited-state time-dependent *GW* molecular dynamics simulation of photolysis of methane using TOMBO

Kaoru OHNO[1] and Aaditya MANJANATH[2]

[1]*Graduate School of Engineering, Yokohama National University*

79-5 Tokiwadai, Hodogaya-ku, Yokohama, Kanagawa 240-8501

[2]*Research Center for Structural Materials, National Institute for Materials Science*

1-2-1 Sengen, Tsukuba, Ibaraki 305-0047

There is a longstanding difficulty that time-dependent density functional theory relying on adiabatic local density approximation is not applicable to electron dynamics of an initially excited state such as in photochemical reactions. To overcome this, we developed non-adiabatic excited-state time-dependent *GW* (TD*GW*) molecular dynamics on the basis of the extended quasiparticle (QP) theory. Replacing Kohn-Sham energies with QP energies allows the full correspondence to excited-state surfaces and corresponding total energies, with satisfying extended Koopmans' theorem. Besides our other work [1-4], we demonstrated the power of TD*GW* using methane photolysis, $CH_4 \rightarrow CH_3^{\cdot} + H$, an important initiation reaction for combustion/ pyrolysis and hydrogen production of methane [5]. We successfully explored several possible pathways and showed how this reaction dynamics is captured accurately through simultaneously tracing all QP levels and orbitals (Fig. 1). TDGW scales as $O(N_B{}^{3-4})$, where N_B is the number of basis functions, which is distinctly advantageous to performing dynamics using configuration interaction and coupled cluster methods.

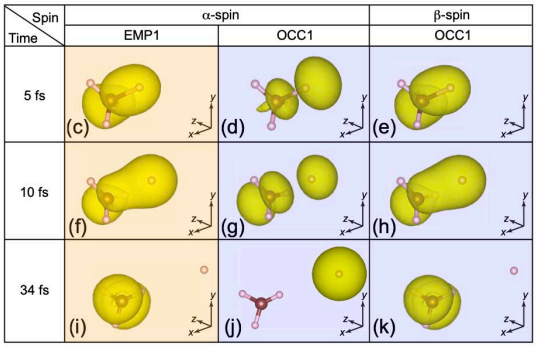

Fig. 1: Temporal change of QP orbitals in the reaction $CH_4 \rightarrow CH_3^{\cdot} + H$ at the excited state [5].

References

[1] T. Ohtsuki, R. Kuwahara, and K. Ohno, Phys. Rev. C **108** (2023) L011301.

[2] Z. Hajiahmadi, 8 人省略, and K. Ohno, Comp. Mat. Sci. **228** (2023) 112364.

[3] M. Khazaei, 10 人省略, K. Ohno, 3 人省略, J. Phys. Chem. C **127** (2023) 14906-14913.

[4] R. Kuwahara, K. Ohno, and T. Ohtsuki, Phys. Rev. C **109** (2024) 024609.

[5] A. Manjanath, R. Sahara, K. Ohno, and Y. Kawazoe, J. Chem Phys, **160** (2024) to appear.

Structural exploration and prediction of dielectric properties of molecular materials

Shinji TSUNEYUKI

Department of Physics, The University of Tokyo

Hongo, Bunkyo-ku, Tokyo 113-0033

In recent years, the need to calculate the dielectric properties of materials in the THz range has increased due to expectations for industrial applications. In this frequency range, changes in electronic states and polarization associated with lattice vibrations are essential, and there are many issues to be solved to treat them from first principles. Therefore, we are developing a predictive method of calculating complex permittivity using first-principles electronic structure calculation based on density functional theory, lattice dynamics calculation, molecular dynamics method, machine learning, etc. This academic year, we developed a method to calculate the complex permittivity of molecular liquids with high accuracy, with the application to polymers in mind.

Previously, we combined the lattice dynamics calculation incorporating anharmonic effects and the Born effective charges to calculate complex permittivity of crystals [1]. However, polymeric materials and molecular liquids have huge structural fluctuations that determine the dielectric constant, making it challenging to apply the above method, which starts from harmonic vibrations around the equilibrium point.

In such cases, if the time variation of the system's structure over a long period can be calculated by molecular dynamics, and if the dipole moment of the whole system at each time can be calculated, the dielectric constant is obtained from the time correlation function of the dipole moment by linear response theory. The dipole moments vary greatly depending not only on the internal structure of the constituent molecules but also on the interactions between the molecules, so they must be estimated by first-principles calculations rather than simple models such as classical fixed-charge models.

A problem here is that the computational cost of the dipole moments from first principles is very high; it is challenging to calculate the correlation function over a long period. Therefore, we developed a machine learning model that predicts the position of the Wannier center for each chemical bond from the results of short-time first-principles molecular dynamics calculations. This model is more versatile than the Wannier centroid machine learning model proposed in earlier works and

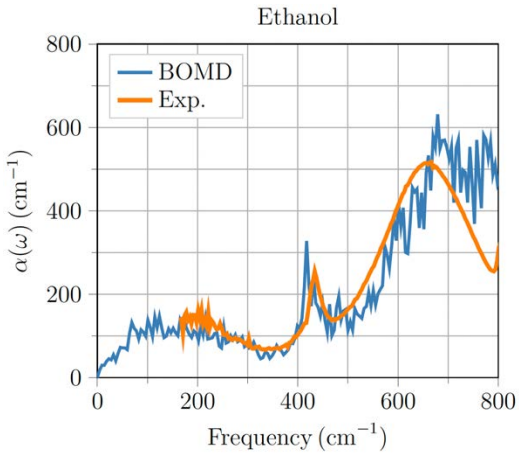

Fig.1 Infrared absorption coefficients of liquid ethanol at room temperature calculated from first principles (a blue line) and their experimental values (a smooth orange line, taken from Ref. [4]). The calculated values agree well with the experimental data by correctly evaluating the polarization due to intermolecular interactions.

can be applicable to larger molecules. By combining this model with the trajectory simulations by the classical or first-principles molecular dynamics methods, we successfully calculated the dielectric properties of liquid methanol, ethanol, propylene glycol (PG), PG dimers and 14-mers in the THz range within a realistic calculation time (see Fig.1) [2,3]. The method developed in this study will be helpful in the study of molecular or polymeric dielectric materials due to its excellent prediction capability.

This study was conducted in collaboration with JSR Corporation.

References

[1] T. Amano, T. Yamazaki, R. Akashi, T. Tadano and S. Tsuneyuki, Phys. Rev. B, 107, 094305 (2023).

[2] T. Amano, PhD Dissertation, The University of Tokyo (2024).

[3] T. Amano, T. Yamazaki and S. Tsuneyuki, to appear in Proceedings of the 34th IUPAP Conference on Computational Physics (CCP2023).

[4] E. Sani and A. Dell'Oro, Optical Materials 60, 137 (2016).

Thermal Properties of the Element and Binary Oxides toward Negative Thermal Expansion from First Principles

Yasuhide MOCHIZUKI

Department of Materials Science and Engineering,

Tokyo Institute of Technology, Ookayama, Meguro-ku, Tokyo 152-8550

Negative thermal expansion (NTE) materials have been vigorously studied for more than a century and are applied to many industrial applications such as heat resistance fillers, microdevices in light-emitting diodes (LED), large-scale integration (LSI), power semiconductors, and micropositioners in the telescopes. Although a tremendous amount of work on LTE and NTE materials has been dedicated so far [1], a comprehensive study showing the chemical aspects and materials-design concepts for realizing LTE and NTE behaviors is lacking. Specifically, it remains unclear as a nontrivial problem how we design LTE or NTE materials with various combinations of the elements. These fundamental uncertainties stem from unclear correlations between the thermal expansion coefficients and related parameters of crystals.

In this study, we present the systematic calculation results of thermal properties, namely, volumetric thermal expansion coefficients α_V, bulk moduli B_T, average atomic volumes V, and Grüneisen parameters γ for the 46 unary solids and 45 binary oxides through first-principles lattice-dynamics calculations using quasi-harmonic approximation (QHA). We provide a formulation of α_V based on the Mie─Grüneisen equation of states. From the analytic formulation of α_V, we thoroughly analyze the correlations between α_V, B_T, V, and γ using the calculation results.

The first-principles calculations were carried out using the projector augmented-wave (PAW) method [2] and the PBEsol functional [3] within the generalized gradient approximation as implemented in VASP [4]. The phonon dispersions were derived from the calculated force constants using PHONOPY [5]. Here, to derive the force constants, we adopted a 2×2×2 supercell for the cubic, rhombohedral, tetragonal, orthorhombic, and monoclinic structures, while a 3×3×2 supercell was used for the hexagonal structures. As an exception, we calculated the force constants of Cu_2O ($Pn\bar{3}m$) by expanding the supercell as 4×4×4 because the negative α_V were largely overestimated in the results from the 2×2×2 and 3×3×3 supercells. We did not calculate the thermal properties when a crystal structure has imaginary phonon modes because free energy calculations are unavailable. For the calculations through QHA, we isotropically

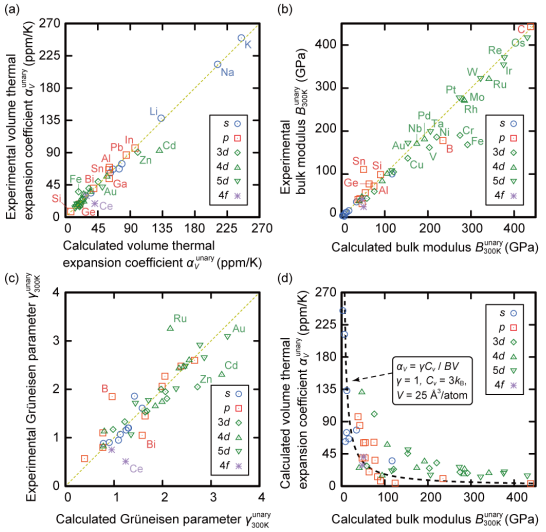

Fig. 1: Validations of the calculated (a) volumetric thermal expansion coefficients α_V, (b) bulk moduli B_T, and (c) Grüneisen parameters γ by using QHA compared to the experimental values. (d) Our calculated α_V as a function of B_T.

changed the relaxed lattice constants as −5 to +5% in the unary solids and −0.66 to +0.66% in the binary oxides. Here, in the calculations for the partially occupied 3*d* transition-metal oxides, we used the Dudarev formulation of +*U* correction with the antiferromagnetic configurations to obtain the dynamically stable phases. We applied the +*U* corrections for the on-site 3*d* electrons in V, Cr, Fe, and Ni as 3, 3, 4, and 7 eV, respectively.

We present the calculated and experimentally reported thermal expansion coefficients α_V, bulk moduli B_T, and Grüneisen parameters γ of the elements at 300 K (Figure 1a–c). The calculated and experimental values validate the predictability and accuracy of the QHA employed in this work. Additionally, Figure 1d shows that the α_V is determined mainly by the B_T, which has an inverse correlation with α_V. We also found that (i) a crystal possessing large *V* tends to have small B_T; (ii) the α_V of complex compounds tend to be large (small) when they are composed of the element with large (small) α_V; (iii) the major role of γ, which is ruled by the crystal structures and coordination environment, is the determination of the sign of α_V; (iv) the transverse-acoustic (TA) and/or low-frequency phonons are responsible for the negative thermal expansion behaviors; and (v) the NTE materials prefer the relatively large *V*, possessing negative mode Grüneisen parameters γ_{qv} [6].

References

[1] M. T. Dove and H. Fang, *Rep. Prog. Phys.* **79**, 066503 (2016).

[2] P. E. Blöchl, *Phys. Rev. B* **50**, 17953 (1994).

[3] J. P. Perdew *et al.*, *Phys. Rev. Lett.* **100**, 136406 (2008).

[4] G. Kresse and J. Furthmüller, *Phys. Rev. B* **54**, 11169 (1996); G. Kresse and D. Joubert, *ibid* **59**, 1758 (1999).

[5] A. Togo and I. Tanaka, *Scr. Mater.* **108**, 1 (2015).

[6] Y. Mochizuki, H. Koiso, K. Nagamatsu, S. Bae, T. Isobe, A. Nakajima, *J. Phys. Chem. C* **128**, 525 (2024).

Elucidating the Thermal Transport Mechanisms at Semiconductor Interfaces

Xu Bin

Department of Mechanical Engineering,

The University of Tokyo, 7-3-1, Hongo, Bunkyo-ku, Tokyo 113-8656

Semiconductor two-dimensional material heterostructures are widely used in manufacturing highly integrated, multi-interface electronic devices due to their excellent electronic, photonic, thermoelectric, and superconducting properties. However, heat dissipation at the interface between the substrate and two-dimensional material is a critical bottleneck for further device miniaturization and power-density improvement, significantly impacting device functionality, reliability, and failure thresholds. Thus, understanding the interfacial thermal transport of phonons is crucial for optimizing the performance and reliability of semiconductor-based devices.

This work combines experiments with molecular dynamics simulations to study the impact of phonon transport states on interfacial thermal transfer. Notably, during the molecular dynamics simulations, we employed a machine learning potential function to accurately describe the interactions between atoms. The time-domain thermoreflectance experimental model and the molecular dynamics simulation model are shown in Fig. 1(a) and (b), respectively.

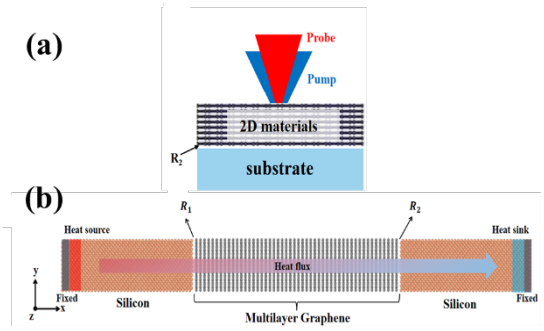

Figure 1 The thermal boundary conductance measurement schematic diagram of multilayer graphene-silicon substrate structure. (a) Non-transducer TDTR measurement setup and (b) Molecular dynamics simulation structure.

Fig. 2 shows the relationship between thermal boundary conductance and the thickness of multilayer graphene, while the inset calculates the average mean free path of graphene in the c-axis direction. The thermal boundary conductance increases with the thickness of graphene and gradually converges when the thickness reaches the average mean free path of graphene. The change in thickness dependency indicates a shift in the phonon transport state. This study bridges the gap between phonon transport mechanisms and thermal boundary conductance.

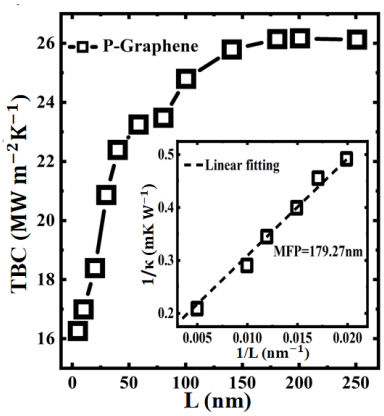

Figure 2 Thickness-dependent thermal boundary conductance of heterostructures

Reference

[1] J. Yue, S. Hu, B. Xu, R. Chen, L. Xiong, R. Guo, Y. Li, . Nian, J. Shiomi, and B. Zheng, Unraveling the mechanisms of thermal boundary conductance at the graphene-silicon interface: Insights from ballistic, diffusive, and localized phonon transport regimes, Phys. Rev. B **109**, 115302 (2024)

First-principles NEB calculations of proton tautomeric conduction pathways

Hatsumi MORI and Kaito NISHIOKA

The Institute for Solid State Physics,

The University of Tokyo, Kashiwa-no-ha, Kashiwa, Chiba 277-8581

We have been developing materials and elucidating the conduction mechanism in order to establish design guidelines for anhydrous superproton conductors, which are highly efficient proton conductors even without humidification [1-4]. Recently, we have discovered an anhydrous superproton conductor with a novel mechanism called "proton tautomerism", in which intramolecular protons are transferred in correlation with the bond recombination of π electrons. This mechanism replaced the conventional proton conduction mechanism by molecular motion with a high activation barrier and, in fact, led to the discovery of 1,2,3-triazolium dihydrogen phosphate (1,2,3-$TrzH^{+}$•$H_2PO_4^{-}$) single crystal.

The conduction mechanism of this system was investigated by ab initio Nudged Elastic Band (NEB) calculations by utilizing ISSP supercomputer. Assuming a perfect crystal, the calculated proton pathway based on proton tautomerism gave much higher activation energies than those of the experimental pathway. The ab initio molecular dynamics (MD) calculations also suggest that intermolecular proton transfer does not occur in a perfect crystal without proton defects. Therefore, proton pathways with lower barriers should be explored.

In this project, we performed ab initio NEB calculations on 1,2,3-$TrzH^{+}$•$H_2PO_4^{-}$ crystals with excess protons and proton defects in order to clarify the relationship between the conduction mechanism and proton tautomerism in this system. Then, the energy curves of single proton cycles in the crystals, namely long-range conduction pathway, were obtained.

NEB calculations for the conduction pathway with excess-proton-sites crystals have afforded the activation energy, which is good agreement with the experimental ones, unlike the case of perfect crystals. We first optimized four types of local minimum structures independently under the periodic boundary condition of a single unit cell. The transient structures obtained from the NEB calculations visually revealed the tautomerization process from the initial state to the final state. The activation energies for each of these processes involving proton tautomerism of (1,2,3-$TrzH^{+}$) assisted by ($H_2PO_4^{-}$) were estimated to be 1.048, 1.000, 0.846, and 1.034 eV. The activation energies are consistent with the experimentally obtained activation energy (~1 eV) from the temperature dependence of proton conductivity. Similarly,

for crystals with introduced proton defects, the activation energy associated with the proton tautomerism of (1,2,3-$TrzH^+$) assisted by ($H_2PO_4^-$) is consistent with the experimental value. These calculations strongly support that the proton conduction of 1,2,3-$TrzH^+$•$H_2PO_4^-$ is realized by the proton tautomerism on 1,2,3-$TrzH^+$.

References

[1] Y. Sunairi, S. Dekura, H. Mori et al., J. Phys. Soc. Jpn. **89**, 051008 (2020).

[2] Y. Hori, S. Dekura, H. Mori et al., J. Phys. Chem. Lett. **12**, 5390(2021).

[3] S. Dekura, H. Mori et al., Solid State Ionics **372**, 115775(2021).

[4] S. Dekura, M. Mizuno, H. Mori, Angew. Chem. Int. Ed. **61**, e202212872(2022).

First-principles study of phonon dynamics in all-inorganic halide perovskites

Terumasa TADANO
Center for Magnetic and Spintronic Materials, National Institute for Materials Science
Sengen, Tsukuba, Ibaraki 305-0047

All-inorganic halide perovskites $CsBX_3$(B=Sn,Pb;X=Cl,Br,I) have been studied intensively in recent years due to their unique physical properties, including high photovoltaic performance, ultralow thermal conductivity, and strong phonon damping near the structural phase transition [1]. However, elucidating and predicting these phonon-related properties of the halide perovskites quantitatively and consistently using first-principles calculations remain challenging as an accurate description of the potential energy landscape is required.

In this project, we have investigated how well the cutting-edge phonon calculation methods combined with density functional theory (DFT) predict the phonon linewidth, lattice thermal conductivity (LTC), and structure phase transition temperature (T_s) of the all-inorganic halide perovskites.

First, we calculated the renormalized phonons at the mean-field level theory, i.e., the first-order self-consistent phonon (SC1). To obtain a better one-body phonon picture, we further considered the bubble self-energy correction within the quasiparticle approximation (SC1+Bubble) following Ref. [2]. By using each renormalized one-body phonon Hamiltonian, we then calculated the phonon linewidth Γ_q by considering the three-phonon $\Gamma_q^{\rm 3ph}$ and four-phonon $\Gamma_q^{\rm 4ph}$ scattering processes. We found that the calculated Γ_q values were consistent with the experimental values only when we included the four-phonon scattering channel using the SC1+Bubble one-body Hamiltonian. However, even with the Γ_q values that were closest to the experimental linewidth, the LTC values computed using the Wigner formula underestimated the experimental values. This suggests a potential failure of the quasiparticle approximation in the Wigner theory, which is expected to be solved by employing the Kubo formula.

Second, we calculated the T_s value of the cubic-to-tetragonal phase transitions for $CsPbBr_3$ by applying the Curie-Weiss law to the temperature-dependent soft phonon frequencies. We fixed the lattice constant to the experimental value and estimated T_s using LDA, GGA (PBE, PBEsol), and meta-GGA (r^2SCAN). We found that LDA gave the lowest T_s value, which slightly underestimated the experimental value, and PBEsol T_s agreed nicely with the experimental value. On the other hand, PBE and r^2SCAN greatly overestimated T_s. Our study supports the common belief in the community that PBEsol is a better choice for predicting structure and phonon properties, but further investigation is still needed to find a best practice for the T_s prediction.

References

[1] E. Fransson *et al.*, Commun. Phys. **6**, 173 (2023).

[2] T. Tadano and W. A. Saidi, Phys. Rev. Lett. **129**, 185901 (2022).

Crystal Structure Prediction of Li-ion Solid Electrolyte Materials

Tomoki YAMASHITA
Department of Electrical, Electronics and Information Engineering,
Nagaoka University of Technology
Kamitomioka-machi, Nagaoka, Niigata, 940-2188

We have studied the structural stability of $Li_{4x}Mg_{2(1-x)}P_2O_7$ that can be a candidate material for solid electrolyte of Li-ion batteries. Crystal structure prediction simulations with CrySPY [1] and structure generation by cation substitution were performed to evaluate the phase stability of $Li_{4x}Mg_{2(1-x)}P_2O_7$. We employ the density functional theory (DFT) using the VASP code [2]. PBEsol was used as the exchange-correlation functional. We found that the structure with the same P_2O_7 framework as $Li_{2.2}Zn_{0.8}P_2O_7$ exhibits the lowest formation energy. Our results agree well with the experimental results.

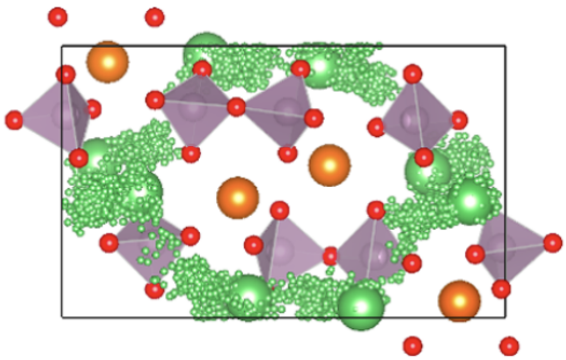

Figure 1: Li diffusion for $Li_2MgP_2O_7$. The small spheres represent the diffusion of Li.

Moreover, first-principles molecular dynamics calculations were performed for the stable P_2O_7 framework by varying the compositions of Li and Mg. Here the vasp code and PBEsol were used. The NVT ensemble was adopted for molecular dynamics calculations, and temperature control was achieved using the Nosé-Hoover [3] method, with temperatures set at 300, 700, 1000, and 1500 K. The time step for calculations was set to 2.0 fs, and the total simulation time was 30 ps.

The calculation results showed that for the $Li_4P_2O_7$ composition ($x = 1.0$), the Li atoms did not diffuse significantly. This is because the structure became too congested with Li, leaving no room for diffusion. On the other hand, in the case of $Li_2MgP_2O_7$ ($x = 0.5$), Li atom vacancies are created due to the substitution of one divalent Mg atom and two monovalent Li atoms, leading to making Li diffusion easier as shown in Fig. 1. In the $Li_{4x}Mg_{2(1-x)}P_2O_7$ system, controlling the conductivity of Li ions by substituting them with multivalent atoms is possible.

References

[1] T. Yamashita, S. Kanehira, N. Sato, H. Kino, H. Sawahata, T. Sato, F. Utsuno, K. Tsuda, T. Miyake, and T. Oguchi, Sci. Technol. Adv. Mater. Meth. **1** (2021) 87.

[2] G. Kresse and J. Hafner, Phys. Rev. B **47**, 558 (1993).

[3] W. G. Hoover, Phys. Rev. A **31**, 1695 (1985).

Response of nanographene device structures to external fields

Koichi KUSAKABE
Graduate School of Science, University of Hyogo
Kouto, Kamigori, Hyogo 5-8581

1 Introduction

To discover effective applications for quantum computation and spintronics of atomic layer materials, we are studying graphene-based quantum computation resources,[1, 2] and atomic-layer-material-based spin-electronic devices.[3] We have developed theoretical approaches to study enhanced functions of a bio-sensor made of adsorbed linkers on graphene in solvents,[4] and light-induced structural transformation of nano-scale material structures.[5]

2 New quantum computation resources by poly-PTM

We designed a two-dimensional $S = 3/2$ Heisenberg system by combining stable S=3/2 spin states on nanographene with antiferromagnetic interactions that exhibit sufficient strength. For this purpose, we have shown that the design method using poly-PTM is appropreate and much better than recent attempts by disjoint non-bonding molecular orbital method.

3 Functions and responses of atomic-layer devices

Optical experiments have confirmed that when multiple boron vacancies in hBN are selectively generated, ferromagnetically aligned magnetic moments appear. Calculations by Harfah *et al.*[3] have revealed that TMRs in excess of 400 can occur in vertical spintronics devices in which graphene is sandwiched between these magnetic hBN layers and Cu electrodes are further stacked on both sides.

Recently, optical responses of Bi_2Se_3 is detected by a pump-probe measurement method using the photoelectron emission microscope (PEEM). We analyzed the electronic local density of state at various surfaces focusing on the depth dependence from the surface.[6] The results indicate that detailed dependencies on atomic stacking are reflected in the PEEM data.

Acknowledgement

The author acknowledges strong collaboration with Dr. N. Morishita, Mr. K. Komatsu, and Prof. M. Kitatani on nanographene quantum computation resorces. He also thanks Dr. Y. Wicaksono, Dr. H. Harfah, Dr. G. K. Sunnardianto, and Prof. M. A. Majidi for fruitful collaboration on spintronics devices.

References

[1] N. Morishita, Y. Oishi, T. Yamaguchi, K. Kusakabe, Appl. Phys. Express **14**, 121005 (2021).

[2] K. Komatsu, N. Morishita, M. Kitatani, K. Kusakabe, preprint.

[3] H. Harfah, Y. Wicaksono, G. K. Sunnardianto, M. A. Majidi, and K. Kusakabe, Phys. Chem. Chem. Phys., **26**, 9733 (2024).

[4] Y. Oishi, M. Kitatani, and K. Kusakabe, Beilstein J. Org. Chem., **20**, 570 (2024).

[5] M. Nagai, Y. Higashitani, M. Ashida, K. Kusakabe, H. Niioka, A. Hattori, H. Tanaka, G. Isoyama, N. Ozaki, Commun. Phys., **6**, 88 (2023).

[6] K. Fukumoto, S. Lee, S. Adachi, Y. Suzuki, K. Kusakabe, R. Yamamoto, M. Kitatani, K. Ishida, Y. Nakagawa, M. Merkel, D. Shiga and H. Kumigashira, preprint.

HPC-based fusion of quantum simulation, experiment analysis and data-driven science

Takeo Hoshi[1,2]

[1] *National Institute for Fusion Science,*

322-6 Oroshi-cho, Toki city, Gifu Prefecture, 509-5292, Japan.

[2]*Slow Positron Facility, Institute of Materials Structure Science, High Energy Accelerator Research Organization (KEK), Oho 1-1, Tsukuba, Ibaraki, 305-0801, Japan.*

Several new features were added in 2DMAT [1-6], an open-source data-analysis software for advanced experimental measurement techniques. 2DMAT was developed by the PASUMS project at FY2020, 2021[1]. A major achievement was the efficient massively parallel computation of the population annealing Monte Carlo (PAMC) method [7]. An almost ideal parallel efficiency was found not only on the ISSP supercomputer (ohtaka) but also on the Fugaku supercomputer with upto 8×10^5 nodes, a half of the Fugaku supercomputer. We used 2DMAT for the data analysis of total-reflection high-energy positron diffraction (TRHEPD) at Slow Positron Facility, KEK [8]. The experimental setup of TRHEPD is similar to that of reflection high-energy electron diffraction (RHEED) but TRHEPD reveals the surface sensitivity and was used for the determination of surface structure. 2DMAT was applied to the analysis of the three-dimensional coordinates (x, y, z) for Ge(001)-c4x2 surface structure by the Bayesian inference using PAMC. [8] The PAMC analysis, as a global search, determined the correct surface structure without any initial guess. In addition, a new algorithm was proposed for a faster computation of the forward problem of TRHEPD analysis. [9]

References

[1] https://www.pasums.issp.utokyo.ac.jp/2DMAT

[2] K. Tanaka, *et al*. (T. Hoshi), Acta. Phys. Pol. A 137, 188 (2020).

[3] T. Hoshi, *et al*. (T. Hoshi), Comp. Phys. Commun. 271, 108186 (2022).

[4] T. Hanada, *et al*., Comp. Phys. Commun. 277 108371 (2022).

[5] Y. Motoyama, *et al*. (T. Hoshi), Comp. Phys. Commun. 280, 108465 (2022).

[6] K. Tanaka, *et al*. (T. Hoshi), JJAP Conf. Series 9, 011301 (2023).

[7] K. Hukushima, Y. Iba, AIP Conf. Proc. 690, 1604 (2003).

[8] https://www2.kek.jp/imss/spf/eng/

[9] S. Kudo *et al.*, (T. Hoshi), Comp. Phys. Commun. 296, 109029 (2024).

Computational Design of Novel Functional Materials and Catalysts for Energy-related Applications

Tetsuya TAKETSUGU

Department of Chemistry, Faculty of Science

Hokkaido University, N10W8, Kita-ku, Sapporo 060-0810

The main goal of this project is to develop a number of innovative real functional materials for energy and environment-related applications using computational approach. The density functional theory (DFT) methods as implemented in the VASP and Quantum Espresso software packages were used. The following main results were achieved:

1) Electrocatalytic activity of Au electrodes decorated by the size selected h-BN nanosheet (BNNS) for the oxygen reduction reaction (ORR) was investigated. It was demonstrated that the overpotential is reduced by all the BNNS modifications, and the smaller the size, the smaller the overpotential for ORR, i.e., the larger the ORR activity, in this size range. Our theoretical analysis of the change in free energy (Fig. 1) reveals that the ORR active sites are located at the edges of BNNS islands adsorbed on Au(111). The decrease in size of BNNS islands results in an increase in the number of the catalytically active sites and, hence, in the increase in the catalytic activity of the BNNS/Au(111) system.

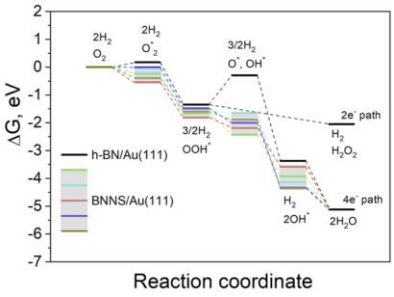

Fig. 1: Free energy diagram ORR calculated for the pristine h-BN monolayer on the Au(111) surface (black line) and small OH-terminated BNNS on Au(111) [1].

We have also explored the activity of the h-BN-based model catalyst for the methanol decomposition reaction. It was found that the methanol decomposition pathway consists of three-step processes (Fig.2). We found that the methanol interaction with the oxidized boron site leads to the H-transfer reaction and this is a crucial condition to initiate the decomposition reaction.

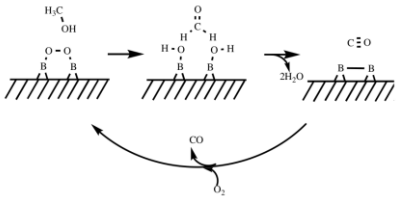

Fig. 2: Methanol decomposition over metal-free catalyst with >B-O-O-B< active sites.

2) Using the extensive large-scale DFT calculations we have modeled complicated molecular rotations in the newly developed molecular crystal consisting of triaryltriazine molecular rotor confined in a bulky crystalline phase (Fig. 3). We have demonstrated that the phenylene units of the crystalline rotors display two different and interconvertible correlated molecular motions [2] and it is possible to switch between these intermolecular geared rotational motions via a thermally induced crystal-to-crystal phase transition.

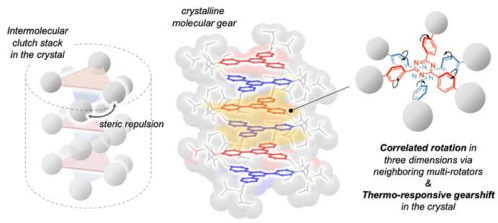

Fig. 3: A Steric-Repulsion-Driven clutch stack of triaryltriazines [2].

3) We performed a systematic investigation on the formation mechanism of complex organometallic oligomers on Cu(111) surface via bonding of phenanthroline derivatives by multiple Cu atoms (Fig. 4). Our DFT calculations revealed the important role of the Cu adatoms in the linking of enantiomers of the chiral oligomers [3]. This finding may help to increase the variety of organometallic nanostructures on surfaces.

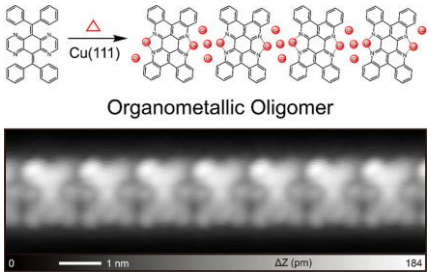

Fig. 4: Organometallic oligomer on Cu(111) surface [3].

4) Using large-scale DFT calculations we have investigated the mechanism of molecular passivation for improving the performance and operation stability of halide perovskite solar cells (HPSCs) [4]. We reveal discernible effects of diammonium molecules onto Methylammonium-free perovskites.

References

[1] H. C Dinh, G, Elumalai, H. Noguchi, A. Lyalin, T. Taketsugu, and K. Uosaki, J. Chem. Phys. **158**, 134713 (2023).

[2] M. Jin, R. Kitsu, N. Hammyo, A. Sato-Tomita, M. Mizuno, A. S. Mikherdov, M. Tsitsvero, A. Lyalin, T. Taketsugu, and H. Ito, J. Am. Chem. Soc. **145**, 27512-27520 (2023).

[3] K. Sun, K. Sugawara, A. Lyalin, Y. Ishigaki, K. Uosaki, O. Custance, T. Taketsugu, T. Suzuki, and S. Kawai, ACS Nano **17**, 24355-24362 (2023).

[4] D. B. Khadka, Y. Shirai, M. Yanagida, H. Ota, A. Lyalin, T. Taketsugu, and K. Miyano, Nat. Commun. **15**, 882 (2024).

First-Principles Molecular-Dynamics Study of Structural and Electronic Properties of Disordered Materials under Extreme Conditions

Fuyuki SHIMOJO

Department of Physics, Kumamoto University, Kumamoto 860-8555

To investigate the structural and dynamic properties of covalent liquids and glasses, such as SiO_2, calculations on a large number of atoms are required to reproduce their disordered atomic arrangement. However, accurate first-principles molecular dynamics (FPMD) simulations are limited for rather small systems because of the high calculation cost. One of solutions would be to use machine-learning interatomic potential based on artificial neural networks (ANN) trained from the results of FPMD simulations.

It has been known that the ANN calculations for enlarged systems are prone to instability when training data are insufficient. In the case of SiO_2 glass, we have found that potential averaging and active learning are useful to avoid computational instability efficiently [1]. The FPMD data were prepared with a system of 144 (48Si + 96O) atoms under periodic boundary conditions. We generated two models of the glass states at pressures of 0 and 60 GPa. For each pressure, simulations of liquid states were performed at several thousand kelvin, and subsequent calculations were carried out to 300 K by gradually lowering temperature. For the MD simulations with ANN potentials, a system of about 30,000 atoms was used. Figure 1 shows the comparison of partial pair distribution functions between the ANN-potential and FPMD calculations at aombient conditions. The profiles are in agreement with each other, indicating that the glass state of SiO_2 was succesfully reproduced using the fairly large system.

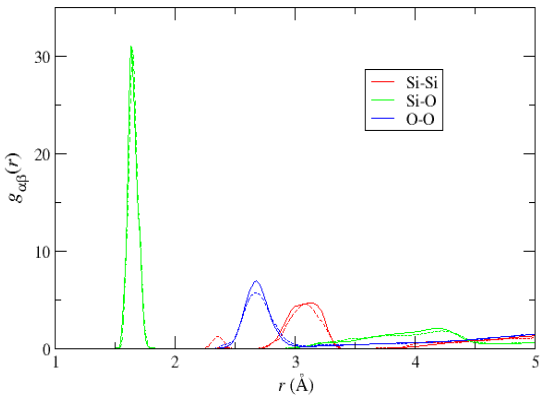

Fig. 1: Partial pair distribution function of SiO_2 glass at ambient conditions. The solid and dashed lines show the ANN-potential and FPMD calculations, respectively.

References

[1] D. Wakabayashi *et al.*, J. Phys. Soc. Jpn. **92**, 074002 (2023).

[2] E. Ryuo, *et al.*, Phys. Rev. B **96**, 054206 (2017)

Thermal Conductivity calculation with machine-learning interatomic potential for multi-component heterogeneous materials II

Kohei Shimamura

Department of Physics,

Kumamoto University, 2-39-1 Kurokami, Chuo-ku, Kumamoto 860-8555

The thermal conductivity calculation method based on the Green-Kubo (GK) formula can be applied to any materials, but require highly accurate interatomic potentials due to its high computational cost. Machine-learning interatomic potentials (MLIPs) constructed by training first-principles molecular dynamics data satisfy the high accuracy and low computational cost, so the combination with the GK formula has become applicable to many materials.

However, for materials with complex interactions, such as multi-component systems, the accuracy of the heat flux included in the GK formula is problematic. Since the heat flux cannot be the training target for MLIPs, an unphysical heat flux that depend on the training method are mixed in. This unphysical heat flux should not analytically affect the total thermal conductivity, but numerically it can cause errors to not only the total but also partial conductivities. For example, differences in the initial parameters of the machine learning models can cause variations in the obtained thermal conductivities.

To prevent heat flux bloat due to the unphysical heat flux, we proposed a training method using heat flux regularization [1]. The heat flux regularization works to reduce the heat flux as much as possible during training. The heat flux consists of atomic energy, atomic force, atomic pressure, and atomic velocity. Since these can be used during training, the heat flux can actually be defined during training. The intensity adjustment of this regularization can be determined by ensuring that both the regularization term and the root mean square errors of training targets (e.g. total potential energy, (total atomic) force, and total pressure) take small values.

The regularization would improve the accuracy of partial thermal conductivities such as atomic thermal conductivities and components in frequency space, which have been difficult in the thermal conductivity calculation based on the GK formula, and would be useful in the elucidation for the origin of thermal conductivity.

References

[1] K. Shimamura, *et al.*: Comp. Phys. Commun. **294**, 19258 (2024).

First-Principles Calculations of Altermagnetic Materials

Kunihiko Yamauchi
Center for Spintronics Research Network, Osaka University, Toyonaka, Osaka 560-8531, Japan

We have studied altermagnetic materials by means of first-principles DFT calculations using VASP and Wannier90 codes. Altermagnetism is a new type of magnetism that exhibits SOC-free spin splitting and some properties common to ferromagnetism despite the compensated magnetization. Previously, we have investigated the spin-split bandstructure and the anomalous Hall effect in perovskite $CaCrO_3$ [1]. This year, we focused on MnTe, in which the large spin splitting ($\Delta E \sim 1$ eV) appears in the bandstructure with a high Neel temperature ($T_N = 307$ K). In collaboration with the micro ARPES measurement, we found that the bandstructure in the antiferromagnetic phase exhibits the strongly anisotropic spin splitting of the bands associated with the time-reversal-symmetry breaking and provided a direct experimental evidence for the altermagnetic spin splitting [2]. When the Mn spins lie in the hexagonal ab plane, C_{3z} symmetry is broken but antiunitary C'_{2d} symmetry is kept to relate the up-spin and down-spin states as shown in Fig. 1. The spin-splitting bandstructure shows the good agreement with the ARPES result.

In addition, we worked on a hydrogen-induced metal-insulator transition in $SmNiO_3$ [3] and newly found a charge-ordered structure. We also studied 2D magnetic materials and confirmed that the Goodenough-Kanamori-Anderson rules stand in monolayer transition-metal chlorides, in which the d_{xy} and $d_{x^2-y^2}$ orbital states play an important role in the super-exchange interaction [4].

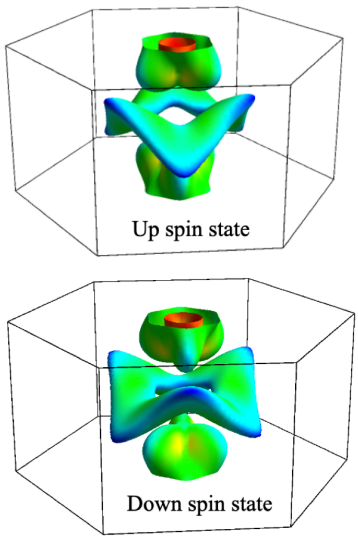

Figure 1: Iso-energy surfaces of the bandstructure at $E = E_F - 0.5$ eV for up-spin and down-spin states in altermagnetic MnTe.

References

[1] Thi Phuong Thao Nguyen and Kunihiko Yamauchi, Phys. Rev. B **107**, 155126 (2023).

[2] T. Osumi, S. Souma, T. Aoyama, K. Yamauchi, A. Honma, K. Nakayama, T. Takahashi, K. Ohgushi, and T. Sato, Phys. Rev. B **109**, 115102 (2024).

[3] Kunihiko Yamauchi and Ikutaro Hamada, Phys. Rev. B **108**, 045108 (2023).

[4] Thi Phuong Thao Nguyen and Kunihiko Yamauchi, J. Phys. Soc. Jpn. **93**, 034710 (2024).

Quantum transport theory based on large-scale first-principles electron transport calculations

NOBUHIKO KOBAYASHI
Department of Applied Physics, University of Tsukuba
1-1-1 Tennodai Tsukuba Ibaraki 305-8573

Quantum transport theory based on large-scale first-principles electron transport calculations is important from the viewpoint of materials science and technology. We have developed the nonequilibrium Green's function (NEGF) method and the O(N) time dependent wave-packet diffusion (TD-WPD) method on the basis of the density functional theory (DFT). By using these methods, we have investigated quantum transport properties of materials.

We have developed a Simulation code for Atomistic Kohn-sham Equation (SAKE) for the ab-initio electron transport calculation based on the DFT and NEGF formalism. [1] We have applied the method to analysis of electron transport in crystalline thin film of organic semiconductors. We reveal transport properties reflected by band dispersion and current characteristics due to good contact with organized electrode interface.

We developed the O(N) TD-WPD method for the quantum transport calculation of huge systems of up to 100 million atoms a decade ago, and have been applied organic semiconductors. [2] It is possible to calculate the conductivity and the mobility of the system with micron-order lengths at room temperature at the atomistic levels, and also to analyze the transport properties of materials weakly bonded by van der Waals interactions. The electron and hole mobilities of the pentacene thin-film are calculated taking the effect of intramolecular vibrations on both the partially dressed polaron and the dynamic disorder into consideration by using TD-WPD method. It is demonstrate that electron mobility in high-mobility organic semiconductors is indeed limited by polaron formation. [3]

We have also succeeded in O(N) thermoelectric transport calculation such as Seebeck coefficient and power factor. Different from a conventional method using the electric conductivity spectrum, it obtains the coefficients directly from the correlation function between heat and electric current based on linear response theory. We apply the methodology to a two-dimensional system and confirm that the calculated results are consistent with those obtained by the conventional method. The proposed methodology provides an effective approach to evaluate the thermoelectric performance of micron-scale materials based on quantum mechanics from an atomistic viewpoint. [4]

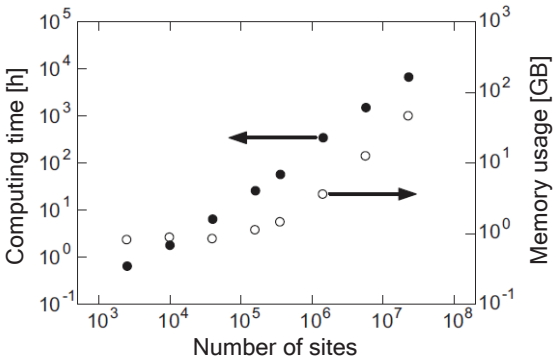

Figure 1: O(N) thermoelectric transport calculation using TD-WPD method.

References

[1] H.Takaki, N.Kobayashi, K.Hirose, *J. Phys.: Condens. Matter.* 32 325901(2020)

[2] H. Ishii, S. Obata, N. Niitsu, S. Watanabe, H. Goto, K. Hirose, N. Kobayashi, T. Okamoto, and J. Takeya, *Sci. Rep.* 10, 2524 (2020)

[3] H. Sato, S. A. Abd. Rahman, Y. Yamada, H. Ishii and H. Yoshida *Nat. Mater.* 21, 910 (2022).

[4] H. Ishii, N. Kobayashi, K. Hirose *J. Phys. Condens. Matter.* 36 (2024).

First-principles electron dynamics simulations for attosecond and nonlinear optical phenomena

Shunsuke SATO

Center for Computational Sciences

University of Tsukuba, Tsukuba, Ibaraki 305-8577, Japan

We have studied light-induced electron dynamics in solids using time-dependent density functional theory. This year, we developed a novel analysis technique for light-induced electron dynamics and nonlinear optical phenomena based on the microscopic current density, as reported in Ref. [1].

We further performed first-principles simulations on attosecond transient spectroscopy for bulk cobalt in order to investigate the transient optical properties of magnetic systems. Employing an intense femtosecond laser pulse as a pump pulse and an attosecond XUV pulse as a probe pulse, we computed the transient absorption spectra of bulk cobalt. As a result of the first-principles calculations, we observed a sharp reduction in photoabsorption around the absorption edge. We also analyzed the electron and spin density dynamics and found that the majority-spin electrons are ejected from the region close to cobalt atoms by the laser excitation, while the minority-spin electrons accumulate around the atom region. Consequently, the local spin polarization on the cobalt atoms is reduced, leading to a decrease in the exchange splitting of the core states of cobalt. Furthermore, this reduction in exchange splitting causes a blue shift in the absorption edge, resulting in a sharp reduction in photoabsorption around the edge.

This finding indicates that light-induced ultrafast spin dynamics can be investigated via attosecond transient absorption spectroscopy by focusing on photoabsorption around the absorption edge. Furthermore, since it relies on the local spin polarization of the atoms with the absorption edge, an element-specific spin dynamics detection can be realized on the attosecond timescale. We have summarized the results and submitted a manuscript to a journal.

References

[1] Shunsuke A. Sato, “"Frequency-resolved Microscopic Current Density Analysis of Linear and Nonlinear Optical Phenomena in Solids", J. Phys. Soc. Jpn. 92, 094401 (2023).

Exploring the mechanism of catalytic activity and degradation of electrodes

Minoru Otani

Center for Computational Sciences, University of Tsukuba, 1-1-1 Ten-nodai, Tsukuba, Ibaraki 305-8577, Japan

Improving energy conversion and storage technologies from renewable and sustainable sources is a significant issue in avoiding fossil fuel utilization. For this purpose, a physical understanding of electrochemical reactions at an electrode/solution interface plays a role in extracting the high electric power from low environmental impact energy sources.

Recently, a rhombohedral Boron mono-sulfide combined with a graphene nano-plate (r-BS+G) was experimentally found to be a promising material of an electrochemical catalyst for an oxygen evolution reaction (OER) in an alkaline medium [1]. We carry out the hybrid solution method based on the density functional theory and the classical solution theory (ESM-RISM) [2] to understand the catalytic mechanism at the interface between the r-BS(0001) surface and one molar KOH aqueous solution (1M-KOH(aq)). ESM-RISM enables us to control the electrode potential by varying the thermally averaged solvation structure. We apply ESM-RISM to the r-BS/1M-KOH(aq) with various surface defects because the previous experiment suggested the defect at the basal surface plays a role in the catalytic center of r-BS+G [1].

By the analysis of the change in the Gibbs free energy for the four-step OER intermediates, we found that the boron vacancy at the subsurface (V_{B2}) is considered one of the possible catalytic centers because of the low free energy barrier and stable surface structure for the OER intermediates. To understand the role of the electronic structure of V_{B2}, we applied bias voltage with the equilibrium potential of OER in the alkaline solution to the interface. The positive excess surface charge is induced at the r-BS electrode with V_{B2}, and it can attract the OH- ion, which triggers OER in alkaline media. Thus, V_{B2} has a favorable electronic structure for the OER catalyst [3].

References

[1] L. Li, S. Hagiwara, C. Jiang, H. Kusaka, N. Watanabe, T. Fujita, F. Kuroda, A. Yamamoto, M. Miyakawa, T. Taniguchi, H. Hosono, M. Otani, T. Kondo, Chem. Eng. J. **471**, 144489 (2023).

[2] S. Hagiwara, S. Nishihara, F. Kuroda, and M. Otani, Phys. Rev. Materials **6**, 093802 (2022).

[3] S. Hagiwara, F. Kuroda, T. Kondo, and M. Otani, ACS Appl. Mater. Interfaces, **43**, 50174 (2023).

First-principles calculations of exchange coupling constants dependent on magnetic short-range order

Tomonori TANAKA
Department of Materials Science and Engineering, Tokyo Institute of Technology
Nagatsuta-cho, Yokohama 226-8502

Exchange coupling constants (J_{ij}) in the classical Heisenberg model are widely used to understand finite temperature magnetism including thermal equilibrium properties and magnetic moment dynamics. A commonly used method to calculate these parameters is the one based on the magnetic force theorem (MFT), which utilizes the expression of energy change due to infinitesimal rotations of magnetic moments [1]. The validity of this expression is, however, questionable when the angles between magnetic moments become larger. Moreover, extending the MFT to include magnetic short-range order, a major temperature effect, is quite difficult.

In this project, we present a calculation method for J_{ij} with higher accuracy and extendability. In contrast to the previous perturbative method, we directly calculated the energy change resulting from small tilts of magnetic moments by using non-collinear density functional theory (DFT) with a large supercell. Exchange coupling parameters can be evaluated by fitting the energy changes to the Heisenberg model. The DFT calculations were performed within the GGA-PBE functional using PAW method as implemented in VASP.

Figures 1 (a) and (b) show the calculated J_{ij} of bcc Fe and bcc Co, respectively. The results of our method agree well with those of MFT in bcc Fe. On the other hand, there is a large difference in the J_{ij} on the first nearest neighbor between our method and MFT in the case of bcc Co. We carried out the same calculations for fcc systems and obtained the same trend. The mechanism of the deviation from the results of MFT is under consideration. Our results, however, clearly demonstrate the importance of non-perturbative calculation of J_{ij} for quantitative finite-temperature magnetism. We will further develop this method for more magnetic parameters in wide magnetic models, such as the Dzyaloshinskii-Moriya interaction.

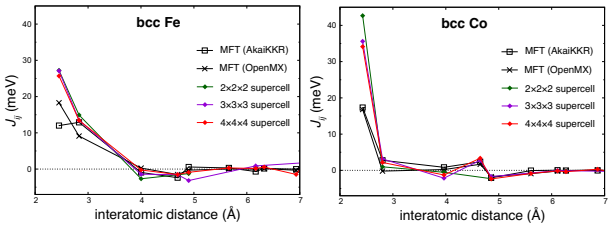

Figure 1: Exchange coupling constants as a function of interatomic distance of bcc Fe and bcc Co. Different supercells are used to check supercell-size dependence. Exchange coupling constants calculated by MFT using OpenMX[2] and AkaiKKR[3] are also shown for comparison.

References

[1] A. I. Liechtenstein *et al.*: J. Magn. Magn. Mater. **67**, 65-74 (1987).

[2] A. Terasawa *et al.*: J. Phys. Soc. Jpn. **88**, 114706 (2019).

[3] H. Akai: J. Phys.: Condens. Matter **1**, 8045 (1989).

Machine learning prediction of Lewis acidity of supported oxide single-atom catalysts

Kyoichi SAWABE
Graduate School of Engineering, Nagoya University, Chikusa, Nagoya 464-8603

Feature selection is crucial in constructing machine learning (ML) prediction models, but there is no definitive method. Eliminating multicollinearity is effective for feature selection, with the Variance Inflation Factor (VIF) serving as an indicator. However, in practical ML workflows, multiple VIFs often tend towards infinity, leading to arbitrariness in feature selection. To address this issue, we have developed the Feature selection by Random screening using VIF (FRV) method.

Figure 1 shows multiple linear regression (MR) models of the ionization energy (IE) of various transition metals as an example of this FRV method extracting high-quality features. In the case of (a), features were simply selected in order of strong correlation with IE and extracted by cross-validation. On the other hand, in the case of (b), features were extracted using the FRV method. By eliminating multicollinearity, the FRV method provides more accurate results.

Additionally, we adopt the FRV method for the ML prediction of CO adsorption energy on single-atom catalysts (SAC) using TiO_2 substrates. Slab units with n ($n = 2 - 6$) layers were used as models of TiO_2 surfaces. Three polymorphic structures of rutile, anatase, and brookite TiO_2 were used. To perturb the electronic structures of CO adsorption sites, a Ti atom with five coordinates on the TiO_2 surface was replaced with transition metals (Mn, Fe, Co, Ni, Ru, Rh, Pd, Re, Os, Ir, Pt). In this way, we have obtained the DFT energies of CO adsorption. The VASP program was used for spin polarization DFT calculations.

Figure 2a shows the results of Gradient Boosting Regression (GBR) prediction using features from the FRV method. The RMSE values for the training and test data are 0.033 and 0.151, respectively, showing good performance. However, there are outlier predictions in the test results. Therefore, to further improve the prediction, feature selection based on the chemical interactions (FC) was added. As a result, as shown in Figure 2b, the outlier elements are eliminated, and the test RMSE is improved to 0.126. This suggests that features suitable for ML models with good accuracy and generalization can be obtained by the FRV + FC method.

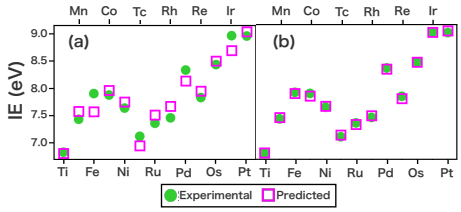

Figure 1: Experimental values versus predicted values of ionization energy (IE) for each metal by MR models. Refer to the text for the difference between (a) and (b).

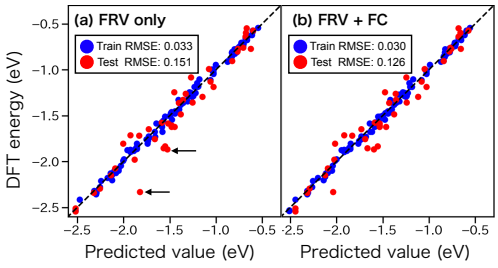

Figure 2: GRB prediciton of CO adsorption energy. The points indicated by the arrows are outlier data.

Ab-initio research on nano particles, and surfaces and grain boundaries of magnetic materials

Yasutomi TATETSU

Meio University, Biimata, Nago, Okinawa 905-8585

Recent advancements in chemical synthesis techniques have enabled precise control over nanoparticles, leading to the discovery of novel functional materials with unique properties. This targeted approach is particularly exciting for researchers seeking materials with both thermodynamic stability and instability, depending on the desired application. Teranishi's group at Kyoto University synthesized a new *Z*3-type Fe(Pd, In)$_3$ crystal structure by introducing indium as a third element into *L*1$_2$-FePd$_3$ [1].

In previous study, we conducted theoretical calculations for the *Z*3- and *L*1$_2$-type Fe–Pd–M systems where M represents Zn, Cd, Hg, Ga, In, Tl, Ge, Sn, and Pb. Conventional cells were chosen as 1 × 1 × 1 and √2×√2 × 1 for the *Z*3- and *L*1$_2$-type Fe–Pd–M systems, respectively, so the numbers of atoms in these unit cells can be the same for comparing the energy difference between these systems easily. When Cd, Hg, In, Tl, and Pb were introduced at the Pd site, we found that the Z3-type structure demonstrated higher stability than the *L*1$_2$-type structure. In contrast, the *Z*3-type structure was not stable when adding Zn, Ga, Ge, and Sn.

This year, we investigated the accuracy of neural network potentials [3] by comparing the formation energies calculated with OpenMX and Matlantis [4]. We conclude that the trends in the formation energies observed in these materials can be also seen in the results obtained using the Preferred Potential version 5.0.0 in Matlantis. However, there are inconsistencies in the formation energies calculated for materials containing heavy elements using these two methods. Further investigations will be needed by comparing some results calculated with VASP, as the Preferred Potential was referenced to a large number of calculations using VASP.

References

[1] K. Matsumoto *et al.*, Nat. Commun., **13**, 1047 (2022).

[2] S. Takamoto, et al., Nat Commun., 13, 2991 (2022).

[3] Matlantis (https://matlantis.com/), software as a service style material discovery tool.

GGA-SCAN failure for copper oxides and related superconductors

Noriyuki Egawa,[1] Soungmin Bae,[2] Hannes Raebiger[1]

1) Department of Physics, Yokohama National Universtiy, Yokohama

2) Institute of Materials Research, Tohoku University, Sendai

SCAN is a promising meta-GGA functional for strongly correlated systems [1], which has shown to open up band gaps for Mott insulators [2] and cuprate superconductors [3-5] without tunable parameters. However, SCAN has also shown to *overcorrect* the localization of carriers by opening band gaps where there should be none, predicting unphysical symmetry breakings and magnetizations [6]. Such localization errors can be corrected by $+U$ type corrections, and indeed, SCAN+U has been shown to improve oxidation enthalpies for various transition metal oxide systems, but copper oxides appear to exhibit some pathological failure [7-8]. We investigate the reliability of SCAN and SCAN+U for copper oxides and Yttrium-based cuprates, namely, $YBa_2Cu_3O_{7-\delta}$ (YBCO).

YBCO is a particularly interesting superconductor due to its high transition temperatures and the multivalence of copper. Copper in YBCO occupies two different lattice sites (Cu_{edge} and Cu_{plane} shown in Figure 1), and in $YBa_2Cu_3O_7$ (YBCO7) copper on ether site is in the Cu^+ state, whereas in $YBa_2Cu_3O_6$ (YBCO6) Cu_{edge} is in the Cu^{2+} state, and Cu_{plane}

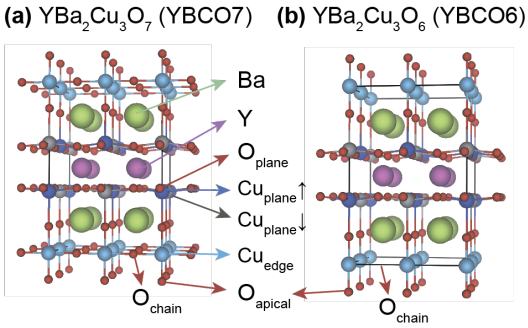

Figure 1. Lattice structures of (a) $YBa_2Cu_3O_6$ (YBCO6) and (b) $YBa_2Cu_3O_7$ (YBCO7). The arrows of Cu atoms indicate the local magnetic moments in antiferromagnetic configurations. Three oxygen sites O_{plane}, O_{chain}, O_{apcial} and two copper sites Cu_{plane} and Cu_{edge} in YBCO7 and YBCO6 are indicated.

is in the Cu^+ state. YBO6 can be formed by removing all of the oxygen in the so called *chain site* O_{chain}, but it has been recently observed that close to optimal doping, oxygen vacancies are formed not only at O_{chain} site, but also at the apical site O_{apical} [9]. We test the reliability of SCAN by investigating the formation of these different oxygen vacancies as well as the thermochemical stability of copper oxides CuO and Cu_2O.

We carry out density-functional calculations using the VASP package using PBE+U, SCAN, and SCAN+U functionals. For lattice parameters, all tested functionals show excellent agreement with experiment. We then

turn our attention to the thermochemical stability of CuO and Cu_2O by plotting their formation enthalpies in the chemical potential phase space ($\Delta\mu_O$, $\Delta\mu_{Cu}$) shown in Figure 2. $\Delta\mu_O$ and $\Delta\mu_{Cu}$ are defined by thermochemical stability conditions $\Delta H_f(CuO) = \Delta\mu_{Cu} + \Delta\mu_O$ and $\Delta H_f(Cu_2O) = \Delta\mu_{Cu} + 2\Delta\mu_O$, where $\Delta H_f(CuO)$ and $\Delta H_f(Cu_2O)$ are the formation enthalpies of the respective compounds. The zero values of $\Delta\mu_O$ and $\Delta\mu_{Cu}$ correspond to the formation of the elemental reference phase (O_2 gas and bulk copper), so the compounds are only stable in the negative quadrant of the ($\Delta\mu_O$, $\Delta\mu_{Cu}$) phase space. As seen in Figure 2, the relative stabilities of CuO and Cu_2O are well described by PBE+*U*, whereas SCAN and SCAN+*U* fail to stabilize Cu_2O at any value of the *U* parameter. This is caused by an overstabilization of $Cu^{2+}(d^9)$ against $Cu^{+}(d^{10})$ by SCAN, which becomes even worse in SCAN+*U*. We further find that this overstabilization is also translated to YBCO, where SCAN and SCAN+*U* excessively stabilize the oxygen vacancies in the apical site, associated with the oxidation of copper into $Cu^{2+}(d^9)$.

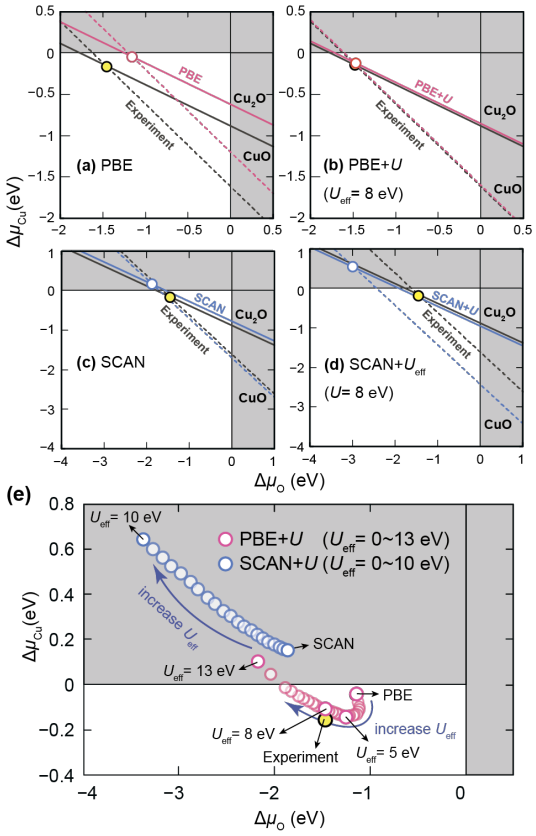

Figure 2. The phase stabilities with (a) PBE, (b) PBE+U (U_{eff} = 8 eV), (c) SCAN, and (d) SCAN+U (U_{eff} = 8 eV). The circles denote crossings where CuO and Cu_2O coexist. (e) The U_{eff} parameter dependence of the crossings predicted by PBE+U and SCAN+U functionals.

References

[1] J. Sun, A. Ruzsinszky and J. P. Perdew, *Phys. Rev. Lett.*, 2015, **115**, 036402.

[2] Y. Zhang et al., *Phys. Rev. B*, 2020, **102**, 045112.

[3] C. Lane et al., *Phys. Rev. B*, 2018, **98**, 125140.

[4] Y. Zhang et al., *Proc. Natl. Acad. Sci. U. S. A.*, 2020, **117**, 68-72.

[5] K. Pokharel et al., *npj Comput. Mater.* , 2022, **8**.

[6] Y. Zhang, W. Zhang and D. J. Singh, *Phys. Chem. Chem. Phys.*, 2020, **22**, 19585-19591.

[7] G. S. Gautam and E. A. Carter, *Phys. Rev. Mater.*, 2018, **2**, 095401.

[8] O. Y. Long, G. S. Gautam and E. A. Carter, *Phys. Rev. Mater.*, 2020, **4**, 045401.

[9] S. T. Hartman et al., *Phys. Rev. Mater.*, 2019, **3**, 114806.

Microscopic structure of water/CeO_2 interface

Akira NAKAYAMA

Department of Chemical System Engineering,

The University of Tokyo, Tokyo 113-8656, JAPAN

The structural properties, dynamical behaviors, and ion transport phenomena at the interface between water and cerium oxide are investigated by reactive molecular dynamics (MD) simulations employing neural network potentials (NNPs). The NNPs are trained to reproduce the density functional theory (DFT) results, and DFT-based MD (DFT-MD) simulations with enhanced sampling techniques and refinement schemes are employed to efficiently and systematically acquire training data that include diverse hydrogen-bonding configurations caused by proton hopping events. The water interfaces with two low-index surfaces of (111) and (110) are explored with these NNPs, and the structure and long-range proton and hydroxide ion transfer dynamics are examined with unprecedented system sizes and long simulation times. Various types of proton hopping events at the interface are categorized and analyzed in detail. Furthermore, in order to decipher the proton and hydroxide ion transport phenomena along the surface, a counting analysis based on the semi-Markov process is formulated and applied to the MD trajectories to obtain reaction rates by considering the transport as stochastic jump processes. Through this model, the coupling between hopping events, vibrational motions, and hydrogen bond networks at the interface are quantitatively examined, and the high activity and ion transport phenomena at the water/CeO_2 interface are unequivocally revealed in the nanosecond regime.[1]

In this work, the CP2K program package[2] was used for DFT-MD simulations, and the PLUMED program[3] was employed to perform the enhanced sampling simulations. The DeePMD-kit was used to construct NNPs.

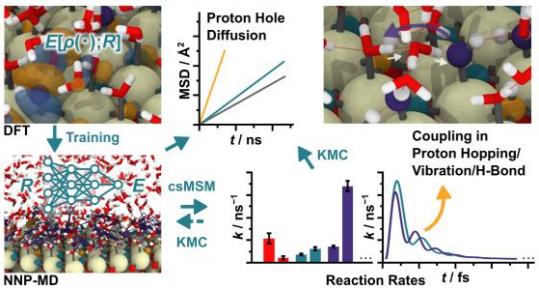

References

[1] T. Kobayashi, T. Ikeda, and A. Nakayama, Chem. Sci. **15**, 6816 (2024).

[2] T.D. Kühne, et al., J. Chem. Phys. **152**, 194103 (2020).

[3] G.A. Tribello, et al., Phys. Commun. **185**, 604 (2014).

Search for high temperature superconductivity in hydrides

Takahiro ISHIKAWA
Department of Physics, The University of Tokyo
7-3-1 Hongo, Bunkyo-ku, Tokyo 113-0033

Lanthanum hydride (La-H) shows superconductivity at 260 K at 170 GPa [1, 2]. Recently, it was reported that the superconducting critical temperature T_c was further increased to 550 K by repeatedly cooling and heating the sample [3]. The large enhancement of the superconductivity has been speculated to be caused by the reaction of La-H with contaminants in the sample chamber of the diamond anvil cell. Dominant candidates for the contaminants are nitrogen (N) and boron (B), which originate from ammonia borane, NH_3BH_3, used as a hydrogen-source material for the synthesis of La-H.

In this study, assuming that La-H reacted with N, we searched for stable and metastable phases in the La-N-H system at 20 GPa using an evolutionary construction scheme of a formation-energy convex hull [4]. At each generation, first, we quickly optimized a few thousand structures created by the scheme using universal neural network potentials on Matlantis [5], and extracted only a few ten structures showing that the enthalpy difference to the hull is less than 4.4 mRy/atom. Next, for the extracted structures, we performed structural optimization based on the density functional theory with the Quantum ESPRESSO (QE) code [6] using the ISSP supercomputer and updated the convex hull. We repeated this process up to the 20th generation. For the stable compounds, we calculated the electron-phonon coupling constant λ and the logarithmic averaged phonon frequency $\omega_{\log}$ with the QE code using the ISSP supercomputer and evaluated T_c from the Allen-Dynes formula [7]. As the results of the exploration, we found that La_2NH_2 shows the highest T_c value of 14.4 K at 20 GPa [8, 9], whereas further exploration is required to obtain concrete evidence of the high-T_c superconductivity at 550 K reported earlier.

References

[1] M. Somayazulu *et al.*: Phys. Rev. Lett. **122**, 027001 (2019).

[2] A. P. Drozdov *et al.*: Nature **569**, 528 (2019).

[3] A. D. Grockowiak *et al.*: Front. Electron. Mater. **2**, 837651 (2022).

[4] T. Ishikawa and T. Miyake: Phys. Rev. B **101**, 214106 (2020).

[5] Matlantis (https://matlantis.com/), software as a service style material discovery tool.

[6] P. Giannozzi *et al.*: J. Phys.: Condens. Matter **21**, 395502 (2009).

[7] P. B. Allen and R. C. Dynes: Phys. Rev. B **12**, 905 (1975).

[8] T. Ishikawa and S. Tsuneyuki: Proceeding of of CCP2023 (Accepted).

[9] T. Ishikawa *et al.*: Phys. Rev. B **109**, 094106 (2024).

Stable Structure Exploration of $K_2NdNb_5O_{15}$ and Phase Transition Mechanism Analysis Based on First-Principles Calculations

Hodaka ABE, Sou YASUHARA

School of Materials and Chemical Technology,

Tokyo Institute of Technology, Ookayama, Meguroku, Tokyo 152-8550

Antiferroelectric (AFE) materials have attracted considerable attention for applications in energy-storage dielectric capacitors. While numerous studies have reported perovskite-type AFEs with high energy storage properties, there have been very few reports on non-perovskite-type AFEs so far. To expand exploration range of AFEs, it is important to understand the mechanism of antiferroelectricity in non-perovskite compounds. Herein, we focused on $K_2NdNb_5O_{15}$ with a tungsten bronze (TB)-type structure. While our experimental study has reported AFE properties of Ta-substituted $K_2NdNb_5O_{15}$ at room temperature [1], the origin of the antiferroelectricity is still unclear. In this study, we investigated the mechanism of AFE phase transition in $K_2NdNb_5O_{15}$ using first-principles phonon calculations.

To deduce phase transition pathway from the high-symmetry structure, we calculated phonon dispersion curves of the $K_2NdNb_5O_{15}$ with the aristotype *P*4/*mbm* structure. First-principles phonon calculations were carried out using VASP and ALAMODE. Phonon dispersions of $K_2NdNb_5O_{15}$ at finite temperature were calculated based on self-consistent phonon (SCP) theory [2].

Figure 1 shows calculated phonon dispersion curves of $K_2NdNb_5O_{15}$ with the *P*4/*mbm* structure. We found that the phase transition behavior can be understood more clearly by focusing on a temperature dependence of phonon frequency obtained by SCP calculations rather than analyzing imaginary frequency modes calculated under the harmonic approximation. By comparing the temperature dependence of phonon frequencies, the most significant softening behavior is observed for the lowest frequency mode at the Z(0, 0, 1/2) point. The soft mode at the Z point is related to NbO_6 octahedral tilting, indicating that the high-symmetry structure can be stabilized by tilt displacement of NbO_6 octahedra.

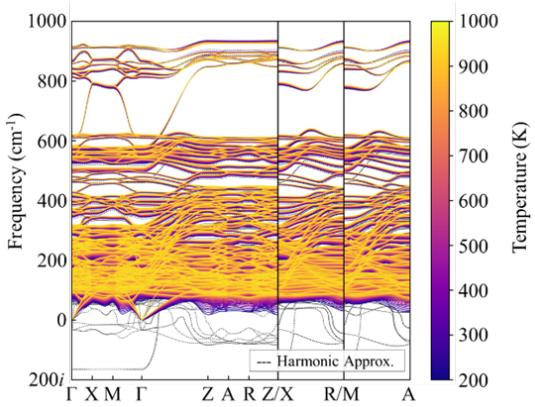

Fig. 1 Phonon dispersion curves of $K_2NdNb_5O_{15}$ with the aristotype *P*4/*mbm* structure calculated using harmonic approximation (dashed lines) and SCP theory (solid lines).

References

[1] H. Abe, S. Yasuhara, T. Tsurumi and T. Hoshina: J. Ceram. Soc. Jpn. **131**[7], 189(2023).
[2] T. Tadano and S. Tsuneyuki: Phys. Rev. B, **92**, 054301 (2015).

Investigation on a mechanism of ferroelectricity in a wurtzite-type $LiGaO_2$

Sou YASUHARA

School of Materials and Chemical Technology,

Tokyo Institute of Technology, Ookayama, Meguroku, Tokyo 152-8550

Since a discovery of ferroelectricity in a wurtzite-type structure of Sc doped AlN in 2019[1], the structure haves gathered much attention. Exploring new material is necessary for understanding the polarization switching mechanism, therefore, we have started to investigate new wurtzite-type ferroelectric materials. We now focus on $LiGaO_2$ with a distorted wurtzite-type structure, which distortion is originated from the difference of ionic radii between Li^+ and Ga^{3+}. In this study, we carried out first principles calculations for evaluating a polarization switching in $LiGaO_2$.

The density functional theory calculations were carried out using the projector augmented wave method as implemented in the VASP. The modified Predew-Burke-Ernzerhof generalized gradient approximation was utilized as an exchange correlation functional. The k-point mesh was 8×8×8. The cutoff energy and convergence energy were 550 eV and 1.0×10^{-7} eV, respectively. The barrier height energy of a polarization switching was evaluated by performing a nudged elastic band (NEB) method.

The calculation result of NEB in non-doped $LiGaO_2$ is shown in Fig. 1, in which the calculated results of AlN and ZnO are also shown (the energy was standardized by the total number of atoms). The barrier heigh energy (E_b) of polarization switching in AlN and ZnO are 0.257 eV and 0.135 eV, respectively. That in $LiGaO_2$ is 0.182 eV, indicating that the material is more favor to the polarization switching than that in AlN. We have revealed effectiveness of chemical doping to reduce the E_b value in $LiGaO_2$ as same as that in AlN or ZnO. Further investigations are kept going to understand the new ferroelectric material of $LiGaO_2$.

References

[1] S. Fichtner, N. Wolff, F. Lofink, L. Kienle, and B. Wagner, J. Appl. Phys. **125**, 114103 (2019).

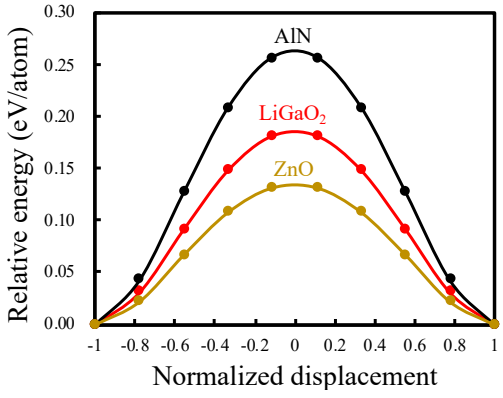

Fig. 1 The calculation results of NEB.

First-principles calculations for molecular junction

Tatsuhiko OHTO

Graduate School of Engineering,

Nagoya University, Furo-cho, Chikusa-ku, Nagoya, Aichi 464-8603

Enhancing hydrogen production is key to achieving a carbon–neutral world. Among the various technologies available, using renewable energy for water electrolysis stands out as a leading method for creating green hydrogen. Because fresh water only represents a minuscule 0.01 % of our planet's water reserves, seawater electrolysis is a potential solution to resolve this limitation and attain sustainable hydrogen production. Nevertheless, electrolysis of seawater in its neutral state demands stringent reaction conditions, making it imperative to thoughtfully design the electrodes, particularly the anodes. This study presents the development of highly durable, noble-metal-free, high-entropy alloy anodes suitable for neutral seawater under highly fluctuating power operation. Using high-throughput DFT calculations, we assessed the Gibbs free energy of the oxygen evolution reaction (OER) intermediates (H*, OH*, O*, and OOH*) and adsorption energy of a chlorine intermediate (Cl*) under an applied potential of 1.23 V on a 9 elements high entropy alloy (9eHEA). DFT calculations reveal that the oxidized surface (passivation layer) of the anode prevents Cl− adsorption, helping to protect the catalytically active sites and prevent catalyst degradation.

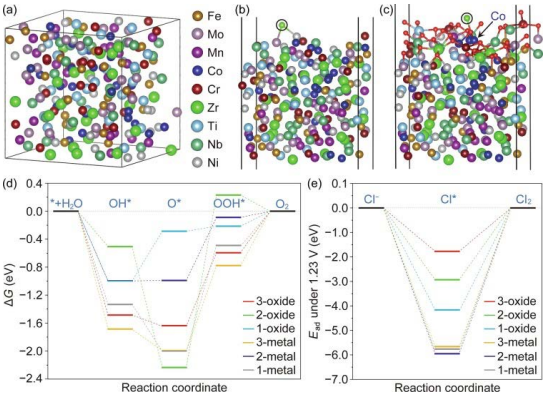

Fig. 1: (a) Model of 9eHEA without oxidation. Models of 9eHEA (b) without oxidation and (c) with oxidation with a chlorine intermediate on structure 3. Black circles indicate Cl intermediates on catalytically active sites. Red spheres represent O atoms. An arrow presents an initial adsorption side of Cl on Co. (d) Gibbs free energy profiles for the OER with oxidation under an applied potential of 1.23 V. (e) Adsorption energies of the chlorine intermediate under an offset of 1.23 eV with and without oxidation.

References

[1] F. Shiokawa et al. Chem. Eng. J. **479**, 147862 (2024).

Theoretical analysis of anion intercalation process into cathode conductive carbon

Atsuo YAMADA

Department of Chemical System Engineering,

The University of Tokyo, Bunkyo-ku, Hongo, Tokyo 113-8656

5 V-class cathode materials for high-voltage Li-ion batteries have been developed, but long-term stable operation has not been achieved. The reduced cycle stability is mainly attributed to the unintended anion intercalation into a cathode conductive carbon [1]. Herein, we theoretically investigated the insertion process of PF_6^- anion into the graphite layer in EC-based electrolyte.

The ESM-RISM method was adopted to evaluate the activation energy for the anion insertion into the graphite. The simulation cell is composed of graphite electrode ($C_{252}(PF_6)_9H_{36}$) and the 1 M $LiPF_6$/EC electrolyte. The activation energy was obtained by computing the grand potential (Ω) at each point while moving a PF_6^- anion from the electrolyte side (r = 20 Å) to the electrode interior (r = 0 Å). All the calculations were conducted with Quantum Espresso code.

The Ω profile of PF_6^- anion insertion into the graphite is shown in Fig.1. The activation energy was estimated to be 0.37 eV at the equilibrium potential, considerably smaller than that of Li^+ (0.6 eV) [2]. Notably, Ω increased as N_{EC} decreased from r = 10 Å, suggesting a significant contribution of PF_6^- desolvation process to the activation barrier. Therefore, the further exploration of solvent species that increase the desolvation energy of the anion is crucial to suppress the anion insertion into the cathode conductive carbon.

References

[1] S. Ko, Y. Yamada, A. Yamada, *Joule*, **5**, 998 (2021).

[2] J. Haruyama, T. Ileshoji, M. Otani, *J. Phys. Chem. C*, **122**, 9804 (2018).

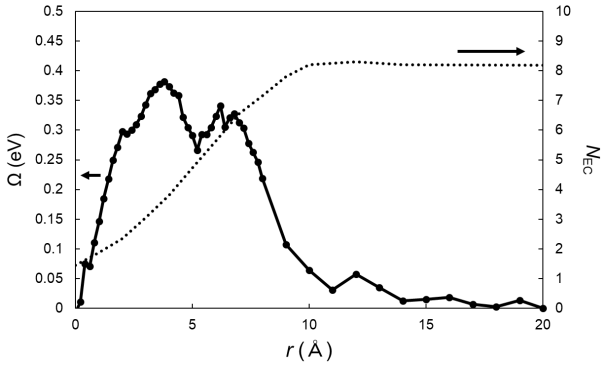

Figure 1 The variation of the ground potential (Ω, left axis) and solvent coordination number around the anion (N_{EC}, right axis) along the insertion process of the PF_6^- anion into the graphite in 1 M $LiPF_6$/EC electrolyte.

Extension of finite temperature calculation with random-phase sates to general variational wave functions

Toshiaki IITAKA

Center for Computational Science,

RIKEN, 2-1 Hirosawa, Wako, Saitama, 351-0198 JAPAN

Calculation of thermal average of an observable A of a closed quantum many-body system in its thermal equilibrium at an inverse temperature is one of the most important problems in computational physics. It has, however, two major computational difficulties. The number of quantum states to be included and the dimension of each quantum state vector are both exponentially increases as the temperature and the system size increases, respectively. Each difficulty has been independently attacked using *random state method* [1, 2] and *variational wave function*, respectively.

Thermal average of observable A at inverse temperature β is calculated using *random state* $|\Phi\rangle$ as

$$\langle A\rangle = \frac{tr[e^{-\beta H}A]}{Z} = \frac{\langle\langle\langle\Phi|A|\Phi\rangle\rangle\rangle}{Z}$$

where

$$Z(\beta) = tr[e^{-\beta H}] = \langle\langle\langle\Phi|\Phi\rangle\rangle\rangle$$

is the *partition function* and the double bracket indicates statistical average over random states. The *thermal state* is defined by the imaginary time evolution of the random state.

$$|\Phi(\beta)\rangle = e^{-\beta H/2}|\Phi\rangle$$

Thermal energy E and specific heat C are expressed as

$$E(\beta) = \langle H\rangle$$

and

$$C(\beta) = k_B\beta^2\left[\langle E^2\rangle - \langle E\rangle^2\right].$$

Variational wave function is a point on a manifold embedded in the Hilbert space,

$$|\psi(w)\rangle = \sum_{\boldsymbol{\sigma}} c(w,\boldsymbol{\sigma})|\boldsymbol{\sigma}\rangle$$

which is parameterized with variational parameters, $w = \{w_i\}$, whose number is much less than the dimension of the Hilbert space.

Thermal state has been introduced in some variational wave functions such as MPS and PEPS [3-7] as

$$\left|\Psi(\beta;w)\right\rangle = e^{-\beta H/2}\left|\Psi(w)\right\rangle$$

where $\left|\Psi(w)\right\rangle$ is a variational wavefunction with random parameters w.

In this project, the above formulation was extended to general form of variational wavefunctions for 2D spin lattice system whose coefficients $c(w,\boldsymbol{\sigma})$ are linear with respect to each parameter w such as in String-Bond States and Entangled Plaquette States [8]. The imaginary time evolution was calculated with stochastic reconfiguration[3, 9]. The program is written with NetKet [10] library and parallelized with respect to initial random states, Markov chains, and plaquettes.

References

[1] T. Iitaka, and T. Ebisuzaki, Phys. Rev. Lett. **90**, 047203 (2003).

[2] T. Iitaka, and T. Ebisuzaki, Phys. Rev. E **69**, 057701 (2004).

[3] K. Takai *et al.*, J Phys Soc Jpn **85**, 034601 (2016).

[4] S. Garnerone, T. R. de Oliveira, and P. Zanardi, Phys. Rev. A **81**, 032336 (2010).

[5] T. Iitaka, arXiv:2006.14459 (2020).

[6] A. Iwaki, A. Shimizu, and C. Hotta, Phys. Rev. Res. **3**, L022015 (2021).

[7] S. Goto, R. Kaneko, and I. Danshita, Phys. Rev. B **104**, 045133 (2021).

[8] I. Glasser *et al.*, Physical Review X **8**, 011006 (2018).

[9] S. Sorella, Phys. Rev. Lett. **80**, 4558 (1998).

[10] G. Carleo *et al.*, SoftwareX **10**, 100311 (2019).

Analysis of phonon-assisted ionic transport in solid electrolytes

Susumu FUJII
Division of Materials and Manufacturing Science, Osaka University
Yamadaoka, Suita, Osaka, 565-0871
Nanostructures Research Laboratory, Japan Fine Ceramics Center
Mutsuno, Atsuta, Nagoya 456-8587

Exploration for solid electrolytes that exhibit high ionic conductivity at room temperature is one of the important issues in the development of all-solid-state batteries. The relationship between phonons and ionic conduction has been investigated extensively, to design fast ionic conductors based on the insights from lattice dynamics [1].

Recently, fast alkali-ion conduction has been reported in the series of antiperovskite compounds M_3XCh, where M is Li or Na, X is H or F, and Ch is S, Se, or Te [2, 3]. Interestingly, the frequency of a specific phonon mode in the antiperovskites, which corresponds to the rotation of an XM_6 octahedron (Fig. 1), has a linear correlation with the migration energy barrier of alkali ions via vacancy and interstitial sites. The softness of a specific phonon mode that enhances ionic conduction may guide the development of fast ionic conductors. However, the influence of anharmonicity at finite temperature and the existance of point defects on the rotational phonon mode is still unclear, inhibiting the understanding of underlying mechanisms behind ionic conduction.

In this study, to reveal the relationship between phonons and ionic conduction in M_3XCh antiperovskites, anharmonic effects on the frequency of the rotational phonon mode has been investigated by self-consistent phonon (SCPH) theory implemented in ALAMODE code [4]. In addition, the influence of M ion vacancy has been calculated by band unfolding method implemented in Phonopy code [5] (Fig. 1). The computational resources were almost spent on the first principles molecular dynamics simulations, which were to obtain the atomic displacements and forces for estimating fourth-order force constants necessary in the SCPH calculations.

The calculations based on the SCPH theory showed the increase in frequency (hardening) of the rotational phonon mode with increasing temperature. The magnitude of hardening depends on the compounds. The linear relationship between the frequency and migration energy barrier is more evident by considering the anharmonic effect at 300 K, excluding the compounds that contain large anions.

The band unfolding calculations for large supercells including an M ion vacancy also showed that the frequency of rotational phonon mode is not significantly varied by the vacancy. This behavior is still observed in the projected band dispersions for the M ions adjacent to the vacancy.

These results demonstrate that the frequency of the rotational phonon mode is the good indicator of fast ionic conduction in the series of antiperovskites, even considering anharmonic effects.

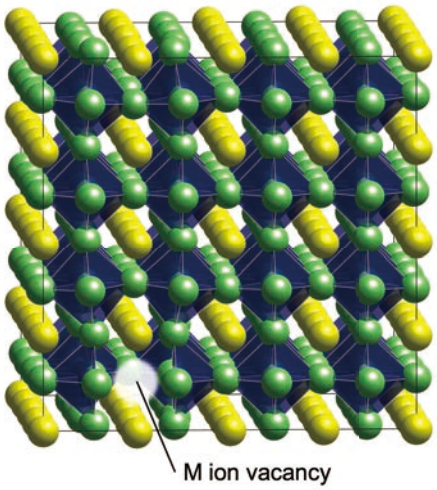

Figure 1: An example of vacancy models for the band unfolding calculations.

References

[1] S. Muy, R. Schlem, Y. Shao-Horn, and W. G. Zeier, Adv. Energy Mater. **11**, 2002787 (2021).

[2] S. Gao, T. Broux, S. Fujii, C. Tassel, H. Kageyama et al., Nat. Commun. **12**, 201 (2021).

[3] S. Fujii, S. Gao, A. Kuwabara, H. Kageyama et al., J. Am. Chem. Soc. **143**, 10668 (2021).

[4] T. Tadano, and S. Tsuneyuki, Phys. Rev. B **92**, 054301 (2015).

[5] A. Togo, L. Chaput, T. Tadano, I. Tanake, J. Phys. Condens. Matter **35**, 353001 (2023).

Analysis of mechanical properties of alloy materials using first-principles and molecular dynamics calculations

Naoki UEMURA

The Nagamori Institute of Actuators, Kyoto University of Advanced Science,

18, Yamanouchi-Gotandacho, Ukyo-word, Kyoto, 615-8577

The mechanical properties of structural materials, including strength, ductility, and toughness, as well as hydrogen embrittlement, which are causes of degradation of structural materials, have been studied using DFT and MD simulations.

In the year, the slip properties of a magnesium alloy with crystal structures called Long-Period Stacking-Ordered (LPSO) were investigated. This alloy is reported to exhibit a yield strength of more than 600 MPa [1]. Experimental studies have indicated that the basal slip is predominant, while the prismatic slip occurs as a non-basal slip [2–4]. We evaluated the slip system of Mg–Zn–Y alloys with LPSO structures by creating slab models for the basal and prismatic planes and obtaining stacking fault (SF) energies by DFT calculations [5]. The DFT calculation code used was the package VASP, which is implemented in the ISSP supercomputers.

Here we report the SF energies of the prismatic planes for two models with different initial crystal structures of 10H LPSO structure in Mg–Zn–Y alloys (Fig. 1). The difference between the two initial structures is that one of the two solute clusters in the unit cell is shifted relative to the other by (1/2, 1/2) in the ab plane. We found no difference in the SF energies of the prismatic slip of these two crystal structures. This result is consistent with previous studies showing that the long-range interactions of solute clusters are very small [6].

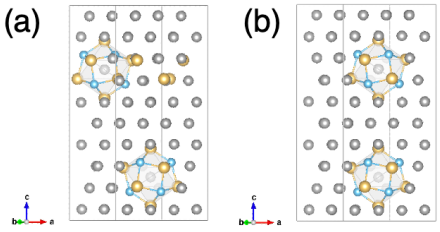

Fig. 1: Crystal structures of 10H LPSO in Mg–Zn–Y alloys. The gray, blue, and yellow spheres are magnesium, zinc, and yttrium, respectively.

References

[1] Y. Kawamura *et al*., Mater. Trans. **42** (2001) 1172–1176.

[2] K. Hagihara *et al*., Mater. Trans. **52** (2011) 1096–1103.

[3] K. Hagihara *et al*., Mater. Trans. **54** (2013) 693–697.

[4] K. Hagihara *et al*, Acta Mater. **109** (2016) 90–102.

[5] N. Uemura, S. Singhaneka, and R. Matsumoto, submitted.

[6] T. Murakami *et al*., Comput. Mater. Sci. **153** (2018) 297–302 .

Two-dimensional structures for non-layered materials

Shota ONO
Institute for Materials Research, Tohoku University, Sendai 980-8677, Japan

Two-dimensional (2D) materials have been studied extensively due to their intriguing properties and potential applications. 2D materials are usually exfoliated from layered materials that consist of atomically thin layers vertically stacked via van der Waals (vdW) forces. On the other hand, 2D materials created from non-layered materials have also been synthesized experimentally.

In this project, we have studied non-vdW 2D materials using Quantum ESPRESSO package. First, we investigated the structural properties of 2D strontium titanate ($SrTiO_3$) [see Fig. 1(a)] [1]. This is constructed by stacking SrO, TiO_2, and SrO monolayers, and the chemical formula is Sr_2TiO_4. We have shown that the TiO_6 octahedral rotations emerge with a rotation angle twice that in the 3D bulk. The rotation angle decreases when the film thickness is increased. Using the molecular dynamics (MD) simulation, we have demonstrated that the cubic-like phase appears above 1000 K [see Fig. 1(b) and 1(c)]. Such a phase transition temperature is higher than of 3D bulk. The effect of octahedral rotations on the electronic properties is also discussed.

We have also explored fluorite-type (CaF_2-type) materials in the 2D limit [2]. The crystal structures of fluorite-type materials are extracted by using Materials Project database and pymatgen code. More than 30 monolayers truncated from the surface have negative formation energy and they are dynamically stable. In addition, several monolayers are identified to exhibit negative Poisson's ratio. The present work has provided novel non-vdW materials in the 2D limit.

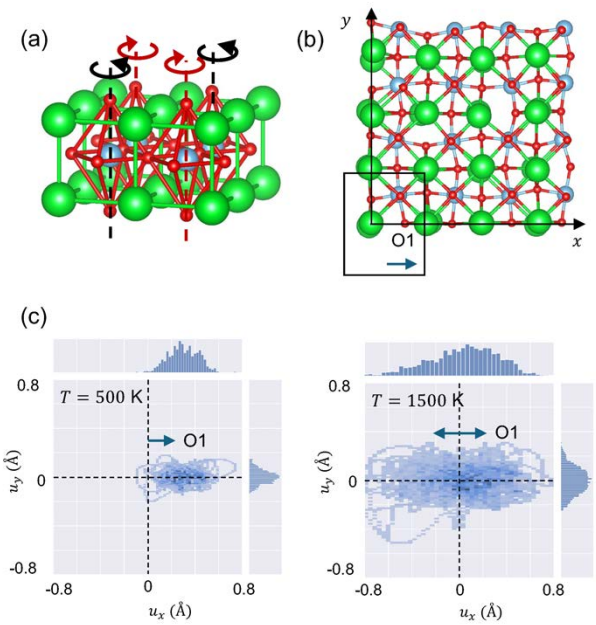

Figure 1: (a) 2D $SrTiO_3$ monolayer. The TiO_6 octahedra are elongated along the out-of-plane direction and rotate around the z axis. (b) Atomic distribution of 2D $SrTiO_3$ monolayer after a MD simulation of 5 ps for 500 K. The O1 atom shifts in the x direction. (c) The displacement distribution of O1 atom within the x-y plane at 500 K (left) and 1500 K (right).

References

[1] S. Ono and Y. Kumagai: J. Phys. Soc. Jpn. **92**, 114601 (2023).

[2] S. Ono and R. Pawar: *in preparation.*

Surface Bain distortion

Shota ONO
Institute for Materials Research, Tohoku University, Sendai 980-8677, Japan

This project is motivated by the recent experiment of bending silver (Ag) nanowires [1]: the structural transformations from fcc to bcc to hcp to fcc structures are observed by bending the Ag nanowire. The fcc-bcc transformation has been explained by tetragonal Bain distortion [see Fig. 1(a)]. However, bcc Ag has been observed only near the surface [1]. In addition, bcc-structured fcc metals are known to be unstable at ambient condition. Therefore, the realization of bcc Ag is questionable.

In this project, we study the effect of surface on the Bain distortion. The DFT calculations are performed by using Quantum ESPRESSO, and the slab models are constructed by using Atomic Simulation Environment (ASE). Through the surface Bain distortion, fcc is transformed into "body-centered tetragonal (bct) structure", followed by a reoriented fcc structure [see Fig. 1(b)]. The bct phase is thermodynamically stable only when a fixed boundary condition is imposed, implying that such a metastable phase must be surrounded by fcc ground state [see Fig. 1(c)]. The present work has extended the Bain distortion concept to apply the surface systems and indicated that the surface could play an important role in phase transitions [2].

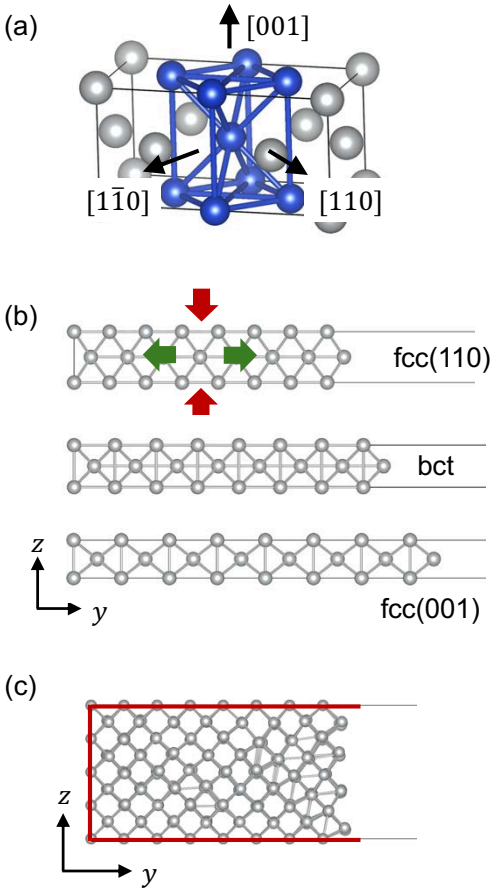

Figure 1: (a) Tetragonal unit cell in the fcc structure. A compression along the z-axis induces a transformation from fcc ($c/a = \sqrt{2}$) to bcc ($c/a = 1$) structure. (b) The surface Bain distortion of the Ag nanowire. The bct phase appears due to the free-boundary condition along the y-axis. (c) Atomic distribution of Ag nanowire in the bct phase after a molecular-dynamics simulation of 1.5 ps. Atoms on the boundary (red) are fixed during the simulation. Without the boundary condition, the bct phase is unstable [2].

References

[1] S. Sun *et al.*,: Phys. Rev. Lett. **128**, 015701 (2022).

[2] S. Ono and K. Tamura: Comp. Mater. Sci. **237**, 112920 (2024).

Study on structural elementary excitations at semiconductor surfaces and interfaces

Hiroyuki KAGESHIMA
Graduate School of Natural Science and Technology, Shimane University
1060 Nishi-Kawatsucho, Matsue, Shimane 690-8504

In this project, we have been focused on physical properties of structural elementary excitations, such as point defects and precursors, of semiconductor surfaces and interfaces [1, 2, 3]. In this year, we have focused on the physical properties of SiO self-interstitial in SiO_2 [4] and of hBN island on Cu(111) [5]. The calculations were performed based on the first-principles calculation. Program package PHASE/0 was employed [6].

The oxidation of Si is a seemingly simple phenomenon in which Si reacts with O to form Si oxide. However, when one looks at this phenomenon on an atomic scale, an interesting and complex atomic transport phenomenon occurs. O diffuses and moves through the Si oxide film as if it were sewing through the gaps between the atomic bonds of Si and O while maintaining the shape of O_2 molecules. The O_2 decomposes at the interface and breaks into Si atoms to form Si oxide, which induces a large volume expansion and distortion at the interface. The reaction of this distortion causes the Si atoms to move around in the oxide film in a complex manner, resulting in structural deformation of the oxide film and release of the distortion.

The problem is the reaction of this distortion. Roughly speaking, the oxide film seems to be able to deform freely as if it were a gas in a high-temperature environment, but the oxidation temperature is about 700°C to 1000°C, much lower than the melting point of silicon oxide, 1710°C. Therefore, the oxide film should be considered as a solid, and the reaction of strain is thought to induce various defects and set them in motion. The most fundamental of these defects are point defects, and because O is scarce in the oxide film near the interface, O vacancies and interstitial Si are the key points. But considering that compressive stress is applied, interstitial Si is considered to be the most important.

We have been focusing our attention on this point. We have shown from the first-principles calculations that the transport process of interstitial Si in the near-interface oxide film can be constructed by assuming only three fundamental atomic processes (O vacancy transport, Si coordination number conversion, and ACBD bond order conversion). The metastable structures at that time and their energy landscapes are also identified by the first-principles calculations [3]. Finally, the transition structures and barrier heights for each fundamental atomic process are identified [4]. Furthermore, we succeeded in determining the details of the energy landscape of the entire transport process and the maximum barrier height. The values are consistent with the experiment. The climbing image-nudged elastic band method (CI-NEB method) was applied in this calculation.

The hBN growth process on Cu surfaces is also a seemingly simple phenomenon in which B and N precursors aggregate to form hBN islands. However, since this is a binary system of B and N, the shape of the hBN island

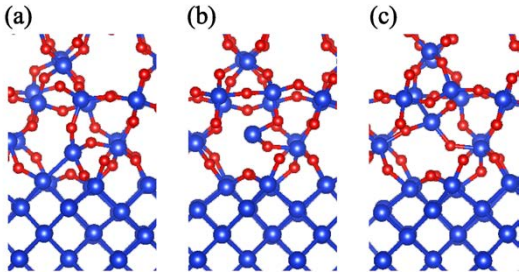

Figure 1: Fundamental processes of Si coordination number conversion. (a) 4-coordinated Si becomes (b) 2-coordinated Si and then returns to (c) 4-coordinated Si.

can change depending on the balance of the number of B and N atoms. The balance between the number of B and N atoms depends on the chemical potential. Therefore, we investigated the relationship between island size, island shape, and chemical potential by the first-principles calculations [5]. Two van der Waals force correction methods, vdwDF2-b86r and D3, were used in the study to confirm the quantitative nature of the relationship.

The basic framework of hBN islands on the Cu surface is the six-membered ring of BN. When the island size is small, only equilateral triangular islands can be formed in principle. However, as the island size increases, equilateral triangular islands are formed only when the chemical potential is extreme, otherwise ribbon-like square islands are formed. Ribbon-shaped islands have both B-only and N-only edges of equal length, which seems to be the origin of the stability of such shaped islands. In fact, the B and N at the edges interact strongly with the Cu substrate, and this interaction may be responsible for the shape of the islands.

These results are interesting when compared to the results for hBN islands that are not on the Cu surface and are completely freestanding. In freestanding islands, islands with B-only edges are unstable and do not form. Moreover, islands in which the six-membered ring is not the basic framework also become stable. In other words, when the interaction between the Cu substrate and the edge atoms of the island is eliminated, the stability and shape of the island become completely foreign.

The importance of the interaction between the edge atoms of the island and the Cu substrate becomes even clearer when looking at the cross-sectional shape of the island: for B-only edges, the distance from the Cu substrate becomes shorter due to the interaction, and the cross-section of the island becomes arched. On the other hand, the N-only edge does not have such a short distance from the Cu substrate, and thus the cross-section of the island is relatively flat. However, the distance to the Cu substrate does not necessarily indicate the strength of the interaction. In fact, when the energy of the edge is evaluated, the N-only edge is more stable than the B-only edge. In other words, the interaction with the Cu substrate is stronger for the N-only edge. This may be related to the fact that N prefers to be more negatively charged and B and Cu prefers to be more positively charged.

References

[1] H. Kageshima, Y. Yajima, K. Shiraishi, and T. Endoh, Jpn. J. Appl. Phys. **58** (2019) 111004 (11 pages).

[2] K. Yata and H. Kageshima, Jpn. J. Appl. Phys., **60** (2021) 035504 (6 pages).

[3] H. Kageshima, T. Akiyama, and K. Shiraishi, Matter. Sci. Semicon. Process. **162** (2023) 107527 (7 pages).

[4] H. Kageshima, T. Akiyama, and K. Shiraishi, Jpn. J. Appl. Phys., 63 (2024) 04SP08 (5 pages).

[5] R. Imamura and H. Kageshima, Jpn. J. Appl. Phys., 63 (2024) 04SP39 (11 pages).

[6] https://azuma.nims.go.jp

First-Principles Investigation of Energy-Conversion Processes in Biological and Material Systems

Takatoshi Fujita
National Institutes for Quantum Science and Technology
Anagawa, Inage-ku, Chiba 263-8555

We have developed a multi-scale computational methodology to investigate the exciton dynamics in complex molecular systems based on large-scale excited-state calculations [1] and open quantum system approaches. Recently, we have extended the method to calculating various time-resolved spectroscopic signals, including pump-probe and two-dimensional spectroscopy. Our multi-scale computational framework enables us to explore the relationship among the electronic structure, quantum dynamics of an exciton or a charge carrier, and the time-resolved spectroscopic signals in realistic material or biological systems. This year, we have applied our approaches to studying photo-energy conversion processes in the organic solar cell and the natural photosynthetic system.

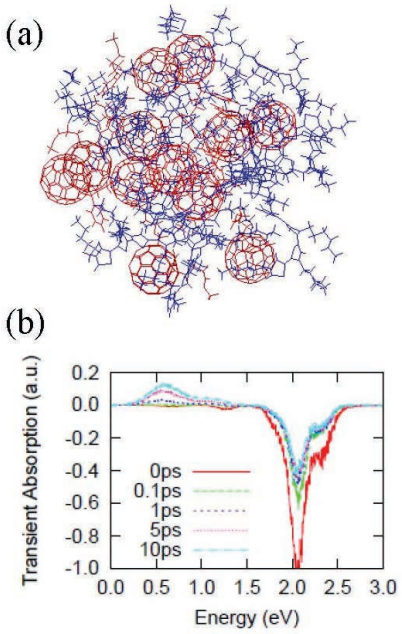

Figure 1: (a) The amorphous structure of P3HT(blue) and PCBM(red) prepared using molecular dynamics simulations. (b) The simulated transient absorption spectra, which show the negative signal at 2.1 eV of stimulated emission plus ground-state bleaching contributions and the positive signal of excited-state absorption at around 0.5–0.9 eV.

As an application [2], we have investigated the charge separation dynamics and pump-probe spectroscopy in the amorphous P3HT/PCBM blend (Fig.1(a)). The P3HT/PCBM blends have been widely studied as typical model systems as organic bulk heterojunction solar cells. To simulate quantum dynamics and time-resolved spectroscopy, the model Hamiltonian for single-excitation and double-excitation manifolds was derived on the basis of fragment-based excited-state calculations within the GW approximation and the Bethe-Salpeter equation. We explore the energetics of the electron-hole separation and the linear absorption spectrum. Then, we investigated the quantum dynamics of exciton and charge carriers; in addition, we compared it with the pump-probe transient absorption spectra (Fig.1(b)). In particular, we introduced the pump-probe excited-state absorption (ESA) anisotropy as a spectroscopic signature of charge carrier dynamics after exci-

ton dissociation. We found that the charge separation dynamics correlate well with the anisotropy dynamics of the pump-probe ESA spectra after charge-transfer excitation. The present study provides the fundamental information for understanding the experimental spectroscopy signals by elucidating the relationship between the excited states, the exciton and charge carrier dynamics, and the time-resolved spectroscopy.

As another application, we considered the charge-separation dynamics in the photosystem II-reaction center (PSII-RS) (Fig.2 (a)). Despite extensive experimental studies, the charge-separation pathway (Fig.2(b)) in the PSII-RC is still controversial. In this study, we have investigated the excited-state dynamics in the PSII-RC using fragment-based excited-state calculations, wavepacket propagation, and time-resolved spectroscopy. To improve the accuracy of the quantum dynamics method, we have applied the empirical thermal correction method, in such a way that the wavepacket propagation provides the correct thermal equilibrium state in the long-time limit. Based on the thermal-corrected wavepacket approaches, we have suggested that the ESA anisotropy dynamics can become a sensitive probe of the charge-separation pathways. The developed computational methods will also be applied to other light-harvesting systems in collaboration with the experimental group [3].

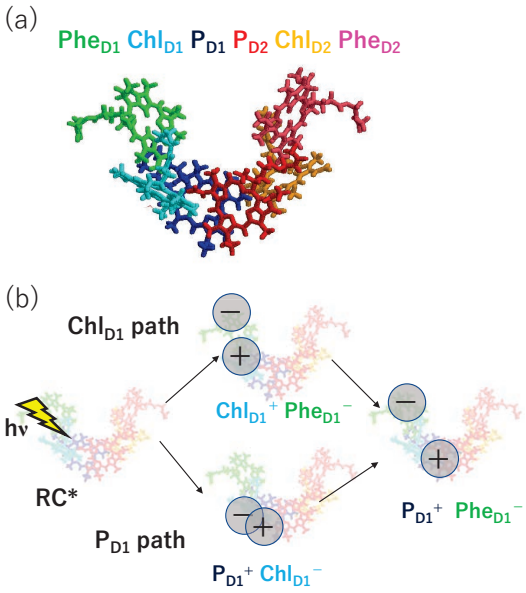

Figure 2: (a) The pigments complex in the PSII-RC (PDB ID: 3wu2), which consists of special-pair chlorophylls (P_{D1} and P_{D2}), accessory chlorophylls (Chl_{D1} and Chl_{D2}), and pheophetyns ($Pheo_{D1}$ and Phe_{D2}) (b) Two charge-separation pathways in the PSII-RC.

References

[1] T. Fujita, Y. Noguchi, J. Phys. Chem. A **125** (2021) 10580.

[2] T. Fujita, T. Hoshi, J. Phys. Chem. B **127** (2023) 7616.

[3] M. Tsubouchi, N. Ishii. Y. Kagotani, R. Shimizu, T. Fujita, M. Adachi, R. Itakura, Opt. Express **31** (2023) 6890.

Ab-initio simulation of electron energy distribution in an insulator excited by an intense laser pulse

Yasushi SHINOHARA[1,2]

[1]*Photon Science Center,*

The University of Tokyo, Hongo, Bunkyo-ku, Tokyo 113-8656.

[2]*NTT Basic Research Laboratories,*

NTT Corporation, 3-1 Morinosato Wakamiya, Atsugi, Kanagawa 243-0198.

We have investigated responses of insulators exposed to strong light fields via time-dependent density-functional theory (TDDFT) [1]. When the field strength of light is comparable to the material's internal strength, the material exhibits extremely nonlinear responses that cannot be described by perturbative series. The only viable option to describe these responses is a direct solution of the time-dependent Kohn-Sham equation in real-time. The SALMON-TDDFT code [2] provides opportunities for solving the Kohn-Sham equation for crystalline solids, molecules, and atoms. We used system B at SCC-ISSP.

To simulate subsequent phenomena after the strong field excitation, we need to consider multi-physical nature of spatiotemporal evolution beyond electron quantum degree of freedom such as thermalization over whole subsystems, energy/momentum flows in microscopic spatial range, phase transition and so on. We propose an electron energy distribution after excitation to bridge from TDDFT to a more macroscopic theoretical framework. The electron distribution is obtained by projecting the time-dependent orbitals $\psi_{c\boldsymbol{k}}(t)$ onto the ground state orbitals $\phi_{b\boldsymbol{k}}$:

$$f_{b\boldsymbol{k}}(t) = \sum_{c} |\langle \phi_{b\boldsymbol{k}} | \psi_{c\boldsymbol{k}}(t) \rangle|^2.$$

The occupation $f_{b\boldsymbol{k}}$ at crystal momentum $\boldsymbol{k}$ is interpreted as particle (hole) distribution for b belongs to a conduction (valence) band. We obtain laser-excited (LE) particle/hole distributions as

$$f_p^{\mathrm{LE}}(E) = \sum_{b(\in \mathrm{val.})\boldsymbol{k}} f_{b\boldsymbol{k}}(t = t_{\mathrm{end}})\, \delta(E - \epsilon_{b\boldsymbol{k}}),$$

$$f_h^{\mathrm{LE}}(E) = \sum_{b(\in \mathrm{cond.})\boldsymbol{k}} f_{b\boldsymbol{k}}(t = t_{\mathrm{end}})\, \delta(E - \epsilon_{b\boldsymbol{k}}),$$

where $\epsilon_{b\boldsymbol{k}}$ is the eigenvalue of the initial Kohn-Sham Hamiltonian. We obtain particle and hole effective temperatures, T_p, T_h, as characteristics of the distribution by fitting such that the particle (hole) distribution gives minimum error to a Fermi-Dirac distribution $f(E, \mu, T)$ at the effective temperature:

$$\arg\min_{T} \left(\int dE \left| f_{p/h}^{\mathrm{LE}}(E) - f\left(E, \mu_{p/h}, T\right) \right| \right) = T_{p/h},$$

where chemical potential is determined by a fact that energy integrals of the distribution give the same value, namely number of particle/hole conservation.

We perform TDDFT simulation for α-quartz with a driving field that have 1.60 eV, 13 fs pulse duration. The temperature depending on peak intensity are presented in Fig. 1. The Keldysh parameter, a characteristic value whether tunneling picture is valid or not, is equal to unity when the intensity is equal to 10 TW/cm^2. The temperatures monotonically increase as a function of the peak intensity. The sum of temperatures, interpreted as the averaged kinetic energy of the particle-hole pair, is 17.8 eV at 100 TW/cm^2. The value is close to the ponderomotive energy 19 eV evaluated with the reduced effective mass of 0.3. This coincidence invokes that kinetic energy gain is understood as free particle-hole motion after the tunneling ionization.

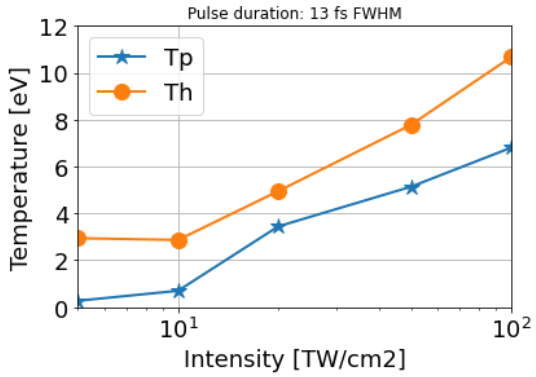

Fig. 1: Evolution of particle- and hole-temperatures.

References

[1] Erich Runge and E. K. U. Gross, Phys. Rev. Lett. **52**, 997 (1984).

[2] https://salmon-tddft.jp/, M. Noda, S.A. Sato, et al., Computer Physics Communications. **235**, 356 (2019).

Nanoscale properties and CO_2 fixation of cement-based materials : ab initio molecular dynamics simulations

Ikumi Kanemasu and Satoshi Ohmura

Department of Civil and Environmental Engineering,

Hiroshima Institute of Technology, saeki-ku, HIroshima 731-5193

The production of cement is responsible for about 8% of man-made CO_2 emissions. Therefore, CO_2 fixation technology for cementitious materials is attracting attention as a way to achieve carbon neutrality. In this project, the reaction mechanism of CO_2 with cementitious materials, specifically calcium silicate hydrate C-S-H has been reproduced using ab inito molecular dynamics simulations. Owing to its structural similarity with calcium-silicate-hydrate (C-S-H), formed by cement hydration, tobermorite is one of the main models used to simulate and study cement. First, in this study, the atomic-scale mechanism of deformation in crystalline and amorphous 11Å tobermorite under uniaxial tension and compression has been investigated using molecular dynamics (MD) simulations based on CLAYFF force field. Based on the stress-strain relationships of the uniaxial tensile and compressive deformation obtained from the MD simulations, crystalline 11Å tobermorite shows heterogeneous mechanical properties in three directions of deformation. For the amorphous state, no difference in mechanism appears depending on the direction of deformation in both tension and compression [1, 2]. Next, ab initio molecular dynamics simulations based on DFT are used to reproduce the adsorption of CO_2 on C-S-H. Figure 1 shows the atomic configurations of the adsorption process of CO_2 on C-S-H obtained from the simulation. In this process, $CaCO_3$-like structure is observed.

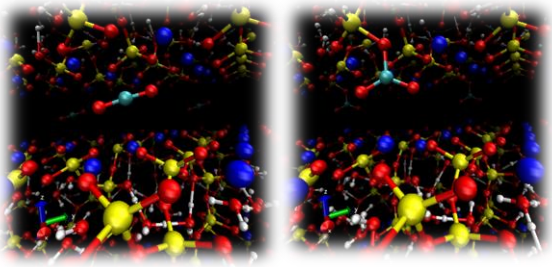

Fig. 1: Absorption process of CO2 on C-S-H.

References

[1] I Kanemasu S. Ohmura and N. Takeda, Cement Science and Concrete Technology **77** 9-16 (2023).

[2] I Kanemasu and S. Ohmura, Springer Proceedings in Physics. accepted (2023) for CCP 2023

Bowing of Energy Gap Curve for InAsSb Calculated Using VASP Based on Hybrid Density Functional Theory

Hiroki I. FUJISHIRO and Akira ENDOH

Department of Applied Electronics,

Tokyo University of Science, Niijuku, Katsushika, Tokyo 125-8585

High electron mobility transistors (HEMTs) are one of the fastest transistors for future terahertz electronics [1]. InAsSb is the most promising candidates for the channel layer of high-speed HEMTs [2] since InAsSb has the lightest electron effective mass in the III-V compound semiconductors [3]. The experimental bandgap energy E_g values for $InAs_xSb_{1-x}$ significantly lower than the linear interpolation between the E_g values for InAs and InSb, reaching a minimum at InAs content x of about 0.35. The E_g value for $InAs_{0.35}Sb_{0.65}$ is about 0.10 eV, which corresponds to the far infrared region. In this work, we obtained the energy gaps between Γ and L valley $E_{\Gamma\text{-L}}$ and between Γ and X valley $E_{\Gamma\text{-X}}$ for $InAs_xSb_{1-x}$ using Vienna Ab initio Simulation Package (VASP) based on the method in the local density approximation.

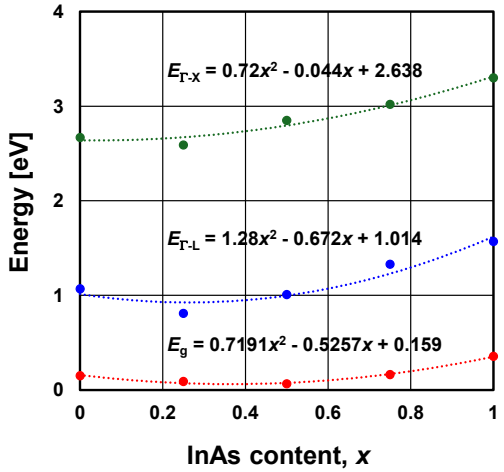

Fig. 1: InAs content x dependence of energy gaps E_g, $E_{\Gamma\text{-L}}$ and $E_{\Gamma\text{-X}}$ for $InAs_xSb_{1-x}$.

We used the hybrid coefficient of the density functional [4]. The hybrid functional is constructed by the mixing of a fraction α of the Fock exchange with a fraction $1-\alpha$ of the PBE (Perdew-Burke-Ernzerhof) exchange. The exchange-correlation energy E_{xc} can be expressed by

$$E_{xc} = \alpha E_x + (1-\alpha)E_x^{PBE} + E_c^{PBE}, \quad (1)$$

where E_x is the Fock exchange, E_x^{PBE} is the PBE exchange, and E_c^{PBE} the PBE correlation [4]. We obtained the E_g values, which are closest to the literature ones by using $\alpha = 0.21$ for InSb and $\alpha = 0.24$ for InAs. For $InAs_xSb_{1-x}$, we used linearly interpolated α values as a function of As content x, i.e., 0.2175 for $InAs_{0.25}Sb_{0.75}$, 0.225 for $InAs_{0.5}Sb_{0.5}$, and 0.2325 for $InAs_{0.75}Sb_{0.25}$ [5]. Figure 1 shows the InAs content x dependence of energy gaps E_g, $E_{\Gamma\text{-L}}$ and $E_{\Gamma\text{-X}}$ for $InAs_xSb_{1-x}$. Closed circles are the calculated values. $E_{\Gamma\text{-L}}$ and $E_{\Gamma\text{-X}}$ have

their minimum values at x = 0.25. The dashed lines in Fig. 1 indicate the fitting results by quadratic equations. The fitting equations are shown in Fig. 1. The x-dependent $E_{\Gamma\text{-L}}$ and $E_{\Gamma\text{-X}}$ curves show downwardly convex dependencies, which show similar trends to E_g [3]. The x-dependence of $E_{\Gamma\text{-L}}$ and $E_{\Gamma\text{-X}}$ obtained in this work can be applied to Monte Carlo (MC) device simulation under higher electric field where the electron intervalley transition occurs.

Acknowledgment

This work was partly supported by JSPS KAKENHI Grant Number 21K04158.

References

[1] H.-B. Jo *et al.*, Tech. Dig. 66th IEDM, no. 8-4, On-line, US, Dec. 2020.

[2] J. Zhang *et al.*, IEEE Access **7**, 102710 (2019).

[3] O. Borelo *et al.*, Phys. Rev. B **8**, 3794 (1973).

[4] T. Garwood *et al.*, Infrared Physics & Technology, 2017.

[5] H. I. Fujishiro *et al.*, Activity Report 2020, p. 128.

First-principles calculations on the electronic states of novel organic semiconductors with extended hydrogen-bonding networks

Shun DEKURA

Institute of Multidisciplinary Research for Advanced Materials (IMRAM), Tohoku University, 2-1-1 Katahira, Aoba-ku, Sendai 980-8577

The control of the molecular arrangement in organic semiconductors is important to optimize transport properties. However, conventionally, changes in molecular structure had been inevitable for the modulation of molecular arrangement. We have recently succeeded in controlling the molecular arrangement using sulfonated BTBT (= **H_2BTBTDS**) and simple amine species (**R–NH_2**) by changing only the **R–NH_3^+** cations without modulating the chemical structure of **BTBTDS^{2-}**.[1] On the other hand, the conventional evaluation of the transfer integrals between isolated molecules is insufficient for such organic semiconductors with extended hydrogen-bonding networks. In this study, we performed first-principles band calculations, and calculated the maximally localized Wannier functions (MLWFs) and the corresponding transfer integrals between MLWFs with periodic boundary condition.[2]

The first-principles band calculations were performed by using Quantum Espresso (version 6.8) for the experimentally obtained crystal structures. We employed SG15 ONCV pseudopotentials (verion 1.2) with plane-wave basis sets and GGA-PBE functional. Reasonable band structures for four types of **BTBTDS^{2-}** salts. Based on the band structures, MLWFs were calculated for HOMO- and LUMO-derived bands, respectively, by using RESPACK program. The obtained MLWFs were consistent with the shape of HOMO and LUMO calculated on the neutral semiconductor molecule, not protonated cationic state, which emphasize the importance of our approach considering periodic boundary condition. The calculated transfer integrals were also consistent with the experimentally obtained hole mobilities. The results shows that our approach is efficient to predict transport properties of hydrogen-bonded organic semiconductors.

References

1) R. Akai, K. Oka, S. Dekura, H. Mori, N. Tohnai, Bull. Chem. Soc. Jpn. **95**, 1178 (2022).

2) R. Akai, K. Oka, S. Dekura, K. Yoshimi, H. Mori, R. Nishikubo, A. Saeki, N. Tohnai, J. Phys. Chem. Lett. **14**, 3461 (2023)

First-principles study of defects in GaN

Kaori SEINO
Department of Materials Science and Engineering, Kyushu Institute of Technology
Sensui-cho, Tobata, Kitakyushu, Fukuoka 804-8550

GaN devices are the preferred candidates for next-generation power electronics. While silicon is the conventional material for power electronics, GaN offers superior physical properties such as high electron mobility, wide bandgap, and excellent thermal conductivity. Therefore, GaN devices provide much higher performance and energy savings compared to traditional silicon-based devices. One of the key technologies for high-performance GaN power devices is selective doping for *p*-type GaN using ion implantation. Recently, high-quality *p*-type GaN was achieved by Mg ion implantation with ultra-high-pressure annealing [1]. Ion implantation is advancing as an experimental technique, but theoretical efforts using first-principles calculations are necessary for atomic-scale understanding of Mg impurities in GaN. Thus far, there have been numerous investigations into various defects in GaN by first-principles calculations.

In this project, properties of defects in GaN, particularly Mg impurities in GaN, were studied by first-principles calculations. We focused on the atomic diffusion of a Mg atom in GaN here because it is crucial to understanding Mg ion implantation. We investigated the vacancy mechanism which is one of the fundamental diffusion mechanisms, using models that consist of a complex of a Mg substitutional to Ga (Mg_{Ga}) and a Ga vacancy (V_{Ga}). In the vacancy mechanism, the Mg atom migrates to the vacancy site in a complex of Mg_{Ga} and V_{Ga} (Mg_{Ga}-V_{Ga}). Thus, we analyzed diffusion processes using models as shown in Fig. 1.

We performed calculations using the hybrid approximation of Heyd-Scuseria-Ernzerhof (HSE) as implemented in the VASP code. We prepared 360-atom wurzite supercells and considered spin polarization. For the calculations of diffusion processes, we performed two approaches: using total energy surfaces and implementing the nudged-elastic-band (NEB) scheme [2]. In the NEB calculations, seven intermediate structures were employed in the reaction pathways, and parallel calculations were performed on 21 nodes in the System B. A detailed discussion will be presented elsewhere [3].

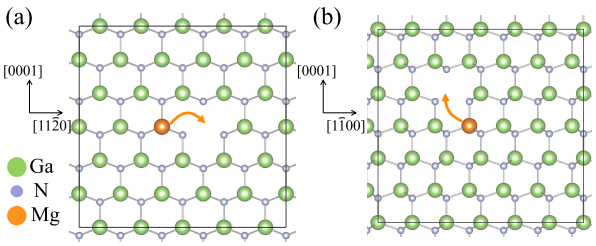

Figure 1: Schematic illustrations of the diffusion of an Mg substitutional impurity via the vacancy mechanism (a) perpendicular and (b) parallel to the c-axis.

References

[1] H. Sakurai *et al.*: Appl. Phys. Lett. **115**, 142104 (2019).

[2] G. Henkelman and H. Jónsson: J. Chem. Phys. **113**, 9978 (2000).

[3] K. Seino, A. Oshiyama, and K. Shiraishi: to be published.

Development of Stretchable Electret Materials for Energy Harvesting with the Aid of Machine Learning

Yucheng ZHANG, Yuhan Gu, Rui WANG, Kuniko SUZUKI, and Yuji SUZUKI

Department of Mechanical Engineering

The University of Tokyo, Hongo, Bunkyo-ku, Tokyo 113-8656

Electret is a dielectric material with quasi-permanent charges and can trap charges stably for decades. Vibrational electret energy harvester (VEEH) can generate electricity efficiently from kinetic energy via electrostatic induction.

CYTOP (Cyclic Transparent Optical Polymer, AGC Chemicals) shown in Fig. 1 is one of the best polymer electret materials. Recently, we utilized quantum chemical analysis for evaluating the charge trap of CYTOP electrets [1, 2]. It is found that although the repeat-unit number of CTX-A is above 1000, the trapped charge is localized at the amide bond, which is formed by a dehydration reaction between the carboxyl end group and the amine.

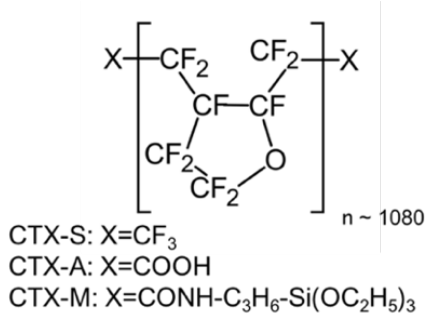

Fig. 1. Chemical structure of CYTOP series.

This result encouraged us to move further to search for a new end group in large chemical databases, aimed at designing a better polymer electret based on CYTOP CTX-A after the dehydration reaction. It is also shown that the solid-state ionization potentials (IPs) computed by the density functional theory (DFT) with the polarizable continuum model (PCM) agree well with the trends of the surface charge density and charge stability measured by the wet experiments [3, 4]. Then, the deep learning model named MEGNet [5] is employed for rapid screening of the PubChem database. We have discovered that CTX-A/BAPP (1,4-Bis(3-amino-

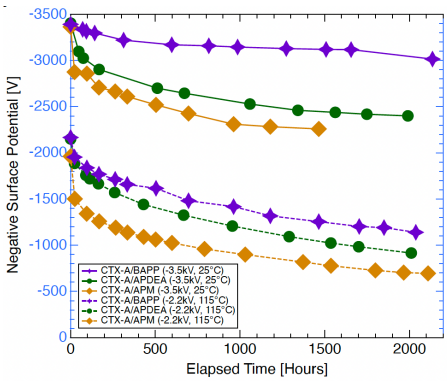

Fig. 2 Surface potential decay of different CYTOP electrets for negative/positive charging.

propyl)piperazine is one of the best candidates. Figure 2 shows the surface potential for 15 μm-thick films after charging to -3.5 kV and -2.2 kV. It is found that CTX-A/BAPP is superior to our previous materials including CTX-A/APDEA [2] in terms of charge stability. The charge-decay time constant at 80 ºC is as long as 150 years (now shown).

Based on these findings, we are now working on quantum chemical analysis of strechable electret based on fluorinated elastomer FFKM as shown in Fig. 3. Unlike CYTOP, the choice of cross linker is crucial for both higher elasticity and higher surface charge density. In addition, the molecular structure of the cross-linked structure is much bigger than CYTOP, which makes the computational cost of DFT too expensive.

All the quantum chemical calculations are made with the software GAUSSIAN [6] at the DFT level with the CAM-B3LYP functional, while PCM is combined for solid-state analysis due to the solvation effect correction.

In CYTOP cases, the 6-31+G(d,p) basis set is used and the molecule configuration is optimized with DFT. We spent a lot of effort on the systematic investigation of the simulation accuracy for different basis sets to reduce the computational cost. Finally, we found that we can get accurate solid-state IP even if we use an unoptimized molecule configuration and the 6-31+G(d,p) basis set, while the CPU time becomes at least 10 times smaller. Now, a series of DFT is made for searching a new cross-linker for a deeper charge trap in FFKM.

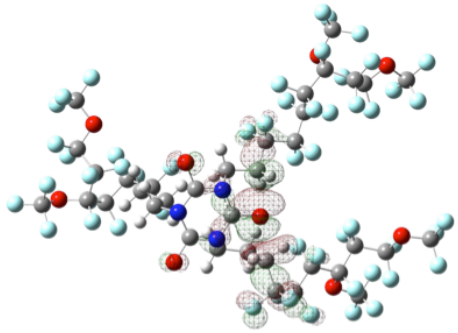

Fig. 3. Preliminary DFT results of cross-linked FFKM with TAIC.

This work was partially supported by JSPS KAKENHI 22KK0054. The calculations are performed with SGI ICE XA ISSP system B with 1 node (24 CPUs).

References

[1] Kim S., et al., J. Phys. Chem. B, Vol. 124, No. 46, pp. 10507-10513 (2020).

[2] Zhang, Y., et al., Appl. Phy. Lett., 118, 223904 (2021).

[3] Mao, Z., et al., IEEE Conf. Electr. Insul. Dielectr. Phenom., pp. 667-670 (2021).

[4] Mao, Z., et al., Adv. Mater., 2303827, (2023).

[5] Wang, R., et al., Transducers ’23, pp. 1284-1287 (2003).

[6] Frisch, M., et al., “Gaussian 09, Rev. A. 1,” Gaussian, Inc. Wellingford, CT, (2009).

Theoretical analysis of the role of neutral molecules in metal hydride ionic conductors

DOS SANTOS, E. C.

Advanced Institute for Materials Research (WPI-AIMR)

Tohoku University, Sendai, Japan 980-8577

Efficient energy storage material is vital for sustainable society establishment. Currently, lithium-ion battery is widely applied for electrical storage devices, but their cost and safety cannot satisfy large-scale applications. Fortunately, all-solid-state batteries (ASSBs) are promising alternatives with mechanical flexibility, safety, variety, and high energy density. In particular, the addition of neutral molecules is prone to promote the battery performance of multivalent closo-type metal hydrides (CTMHs), which have significant influences on the local structure of the electrolytes, thereby mixtures and multiple-phase systems are commonly obtained.

We investigate the role of neutral molecules in metal hydride ionic conductors using parallel computer simulations. The density functional calculations and molecular dynamics simulation were conducted using VASP and AIMD, respectively. Theoretical studies elucidate the structure of the closo-type boron hydrides, and a global optimization strategy is applied to generate unveiled structures. After a single system test, the individual phase effect of the CTMH complex mixtures is obtained. The global optimization and metadynamics were utilized to identify stable crystal phases of $MgB_{12}H_{12}.nH_2O$ and $ZnB_{12}H_{12}.nH_2O$ (n = {0, 6, 12}), first-principles kinetics and molecular dynamics were employed for ion diffusion kinetics, such as H_2O, NH_3, NH_3BH_3, and THF. After that, scaling relations were proposed to predict the ion diffusion performance of CTMH candidates. Based on theoretical calculations, a database was established to evaluate all possible descriptors that scale with the activation energy of the materials. The following descriptors were also evaluated: cation vacancy-free energy, number of neutral molecules in the cell, cell volume, and electronegativity of the system. Combined with the obtained scaling relations and database, new materials candidates will be selected for further evaluation.

This project analyzed local atomistic environments of the neutral molecules and diffusion of the metal ion, which strengthens the importance of CTMHs and promotes their industrial application. Furthermore, the structure performance relations (i.e., scaling relations) are established to predict new CTMH

materials candidates for battery electrolytes. Based on theoretical calculations, a database was established to evaluate all possible descriptors that scale with the activation energy of the materials. The following descriptors were also evaluated: cation vacancy-free energy, number of neutral molecules in the cell, cell volume, and electronegativity of the system. Combined with the obtained scaling relations and database, new materials candidates will be selected for further evaluation. However, obtaining SSEs with high ionic conductivity is challenging due to the complex structural information and the less-explored structure-performance relationship. This project developed a database containing typical SSEs from available experimental reports. The acquired data includes the SSE materials consisting of mono- and divalent cation components (e.g., Liþ, Naþ, Kþ, Agþ, Ca2þ, Mg2þ, and Zn2þ) and various anions (e.g., halide, hydride, sulfide, and oxide). This database provides essential guidelines for the design and development of high-performance SSEs in ASSB applications. According to machine learning and feature analyses, this database provides an opportunity to explore diverse SSE materials, which also proposes reliable structure-performance relationships. Overall, this dynamic database accelerates the discovery of novel SSEs materials with improved electrochemical performance and guides the design of optimal solid-state electrolytes. Importantly, the online surface of this database is user-friendly with dynamic updates (namely, the DDSE). This database covers critical performance indicators (i.e., ionic conductivity and ionic diffusion activation energy) of SSE materials in a wide range of temperatures.

Overall, this dynamic database accelerates the discovery of novel SSEs materials with improved electrochemical performance and guides the design of optimal solid-state electrolytes.

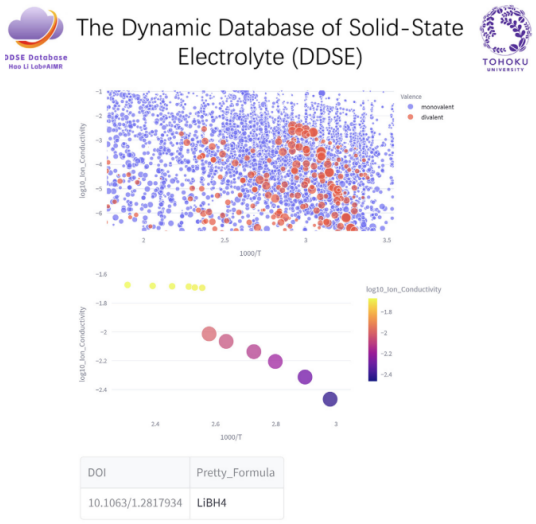

Fig. 1. Example of the online interface of the latest version of DDSE.

References

[1] Guo, Z., Yu, Y., Li, C., **Campos dos Santos, E.**, Wang, T., Li, H., Xu, J., Liu, C. and Li, H., *Angew. Chem. Inter. Edit.*, 2024,*63*, 202319913

[2] Yang, F., **Dos Santos, E.C.**, Jia, X., Sato, R., Kisu, K., Hashimoto, Y., Orimo, S.I. and Li, H., *Nano Materials* Science. 2023, DOI: 10.1016/j.nanoms.2023.08.002.

Theoretical study of oxygen-evolution reactions by first-principles calculations

Yuta TSUJI

Faculty of Engineering Sciences,

Kyushu University, 6-1, Kasuga-koen, Kasuga, Fukuoka, 816-8580, Japan

Water electrolysis devices, which can produce hydrogen either directly from solar power or from an external power source, are very attractive as a solution to the growing global demand for energy and the associated environmental problems. However, the slow reaction rate of the oxygen evolution reaction (OER) occurring at the anode of these electrolyzers has hindered the widespread use of such technologies. Therefore, the development of efficient and stable OER catalysts has been actively investigated: IrO_2 is considered the best OER electrocatalysts [1]. The high activity is also known to depend on the surface index, in the following order: $IrO_2(100) > IrO_2(110)$.

In this study, we performed ab initio calculations of the OER catalytic activity of IrO2 with various surface structures and theoretically predicted the order of catalytic activity.

Three density functional methods (PBE, RPBE, and optPBE) implemented in VASP were used to compare the activity of IrO_2 with (110), (100), and (101) surfaces (Fig. 2). The PBE and optPBE results are found consistent with the experimental results [2], but the RPBE one was found to be inconsistent with the expected.

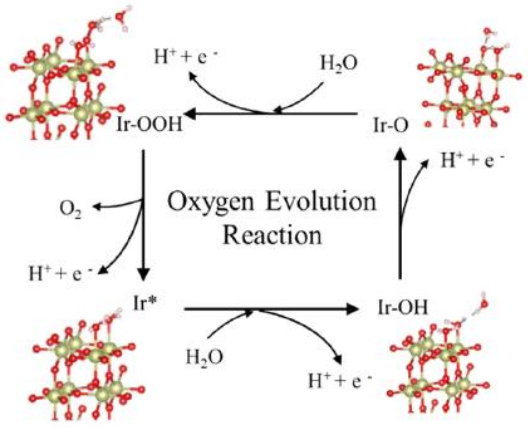

Fig. 1 Mechanism of OER.

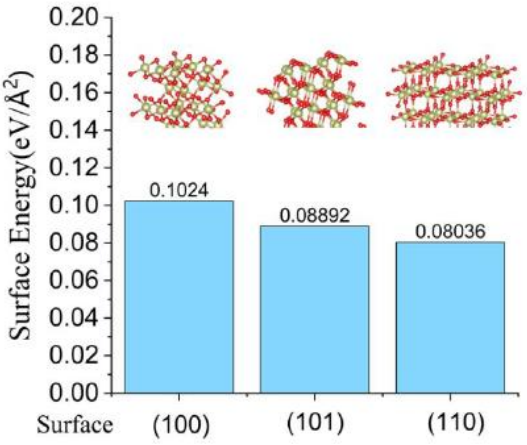

Fig. 2 Surface energies of three different surfaces of IrO_2.

References

[1] T. Reier, M. Oezaslan, P. Strasser, ACS Catalysis **2**, 1765 (2012).

[2] L. G. V. Briquet, M. Sarwar, J. Mugo, ChemCatChem **9**, 1261 (2017

Electronic state analysis on molecular thin film surface

Kaori Niki

Graduate school of science

Chiba University, Yayoi-cho, Inage-ku, Chiba 263-8522

Introduction

In photoelectron spectroscopy, significant advances in detectors have been made since around 2015, allowing measurements in all directions in wavenumber space in a short time. This method is called wave number resolved photoelectron spectroscopy. Recently, structural changes of Copper(II)phthalocyanine (CuPc) adsorbed on $TiSe_2$ surface were observed under laser irradiation. It was suggested that the electron transition from the $TiSe_2$ surface to CuPc induces the structural deformation due to the change in charge distribution. In this study, ground-state and Molecular Dynamics (MD) performed to calculate the electronic state during adsorption.

Method

We performed density functional theory (DFT) calculations using the Vienna Ab Initio Software Package (VASP) version 5.4.4 [1,2]. The exchange correlation effects were described by the spin-polarized generalized gradient approximation (GGA) within the Perdew-Burke-Ernzerhof (PBE) formalism [3]. We used a 8×8×1 $TiSe_2$ slab with lattice constants a = b = 3.53 Å, c = 20.0 Å, α = β = 90° and γ = 120°, and a plane-wave basis set with the projector augmented wave (PAW) approach with an energy cutoff of 380 eV. The Brillouin zone integration was performed on a Monkhorst-Pack of 18×18×1 grid of k-points. The energy convergence criterion chosen for the self-consistency cycle was 1×10^{-7} eV. To account for Fermi surface broadening, temperature parameter σ for Methfessel-Paxton smearing was applied. So far, we have found the parameter set (Hubbard parameter = 3.9 eV and σ = 0.01 eV), which reproduces the experimental results [4]. We used these parameters for the MD simulation of the CuPc / $TiSe_2$ structure. After relaxing the geometries at 0 K, the systems were brought up to 654 K by repeated velocity rescaling using the spin-polarized PBE+U DFT-D3 functional at the Γ-point. Then 5 ps microcanonical MD trajectories were generated with a 1 fs time step.

Results

MD calculations of the structures of CuPc and CuPc+ on $TiSe_2$ show that CuPc and CuPc+ are bent, which reflect the structures under light irradiation.

Using this structures, we succeeded in reproducing the X-ray photoelectron spectroscopy (XPS) calculations by using the original photoelectron intensity calculation

software.

Conclusion

By performing MD calculations using VASP, we clarified structural changes and substrates with increasing temperature by irradiation.

References

[1] G. Kresse and J. Hafner, Phys. Rev. B **47**, 558 (1993).

[2] G. Kresse and D. Joubert, Phys. Rev. B **59**, 1758 (1999).

[3] J. P. Perdew, K. Burke, and M. Ernzerhof, Phys. Rev. Lett. **77**, 3865 (1996).

[4] B. Singh *et. al.*, Phys. Rev. B **95**, 245136 (2017).

Modeling of the Ammonia Decomposition Reaction on Iron-based Material Surfaces

Peijie FENG, Minhyeok LEE, and Yuji SUZUKI

Department of Mechanical Engineering, School of Engineering,

The University of Tokyo, 7-3-1 Hongo, Bunkyo-ku, Tokyo 113-8656

Ammonia is considered a promising next-generation green energy carrier, but employing ammonia directly as a fuel is challenging because of its low flammability and the potential for NOx emissions [1]. Currently, research on ammonia-related reaction kinetics primarily focuses on DeNOx applications, leading to models that often lack robustness in environments devoid of oxygen, where thermal decomposition predominates [2].

Our previous study [3] revealed a mutual interaction between ammonia and iron-based materials: ammonia thermally decomposes on iron-based materials, converting them into iron nitride. This iron nitride, in turn, facilitates the thermal decomposition of ammonia more significantly than pure iron does. To understand the dynamics of the nitriding process in conjunction with thermal decomposition, molecular dynamics that can simulate chemical reactions is preferred.

However, there is a lack of an iron-nitrogen molecular dynamics force field capable of accurately representing both crystalline iron/iron nitride and molecular ammonia, along with other gas-phase products. Furthermore, existing force fields predict energies and forces poorly, particularly at high temperatures where thermal decomposition occurs.

To address these challenges, we embarked on conducting *ab initio* molecular dynamics (AIMD) using the Vienna Ab initio Simulation Package (VASP) via the supercomputer system at ISSP. This allowed us to generate a series of training trajectories, along with related energies/forces. The target crystal systems are listed in Table 1. Subsequently, DeepMD-kit [4] is incorporated to construct a machine learning interatomic force field (MLFF) for running MD simulations using the ISSP system C.

Figure 1a demonstrates that the MLFF, even with a limited amount of input data, significantly outperforms the conventional Modified Embedded Atom Method (MEAM) force field, exhibiting lower errors and virtually no bias compared to Density Functional Theory (DFT) results. The capability of transfer learning and extrapolation by the MLFF is evidenced in Fig. 1b, which assesses the MAE and RMSE

Table 1. AIMD calculate systems.

		Space Group	Crystal system	Magnetic	N %	N wt%	Exp. Observed	MD Atoms Fe:N	Minimum Size	Short AIMD 500~1000fs
01	Fe (mp12)	Im3-m	Cubic	o	0.00%	0.00%	o	250:0	15.0Å	**1000,500K**
02	Fe (mp-136)	$P6_3/mmc$	Hexagonal	x	0.00%	0.00%	o	288:0	13.0Å	**1000,500K**
03	Fe (mp-150)	Fm3-m	Cubic	x	0.00%	0.00%	o	108:0	10.9Å	**800**,500K
04	Fe8N (mp-555)	I4/mmm	Tetragonal	o	11.11%	3.03%	o	432:54	16.7Å	**1000,500K**
05	Fe4N (mp-535)	Pm3-m	Cubic	o	20.00%	5.88%	o	256:64	14.8Å	**1000,500K**
06	Fe3N (mp-1804)	$P6_322$-	Hexagonal	o	25.00%	7.69%	o	384:128	15.9Å	**1000,500K**
07	Fe12N5 (mp-27908)	P3-1m	Trigonal	o	29.41%	9.43%	o	288:120	12.7Å	**1000,500K**
08	Fe2N (mp-248)	P3-1m	Trigonal	o	33.33%	11.11%	o	216:108	12.7Å	**1000,500K**
09	Fe2N (mp-21476)	Pbcn	Orthorhombic	o	33.33%	11.11%	o	162:81	12.7Å	**1000,800,500K**
10	FeN (mp-6988)	F4-3m	Cubic	o	50.00%	20.00%	o	150:150	11.7Å	**1000,500K**
11	FeN (mp-12120)	$P6_3/mmc$	Hexagonal	o	50.00%	20.00%	o	256:256	16.8Å	**1000,500K**

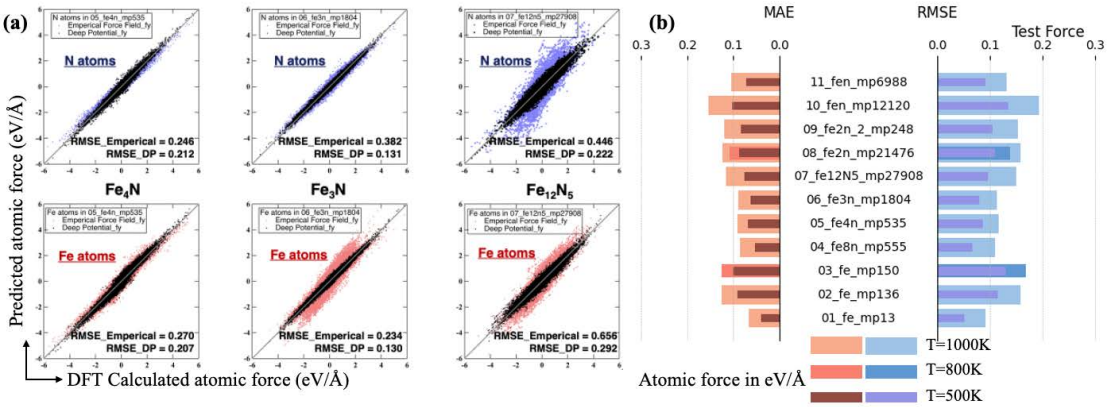

Figure 1. Testing result of force predictions using the trained MLFF. DP denotes MLFF from DeepMD, Emperical denotes the force predicted from the only available MEAM classical force field [5]. (a) Comparing the force prediction between MLFF and Emperical, using DFT calculated force as grouped truth. (b) Mean average error (MAE) and root-mean-square error (RMSE) of atomic forces in the test dataset.

through k-fold cross-validation. This evaluation was achieved by entirely omitting the training data for one system, thereby implying that the MLFF, without being trained on such a system, can predict it with an average error of less than 0.2eV/Å.

In conclusion, the MLFF surpasses the classical MEAM force field in performance and shows great promise for accurately predicting the potential energy surface of chemical reactions, assuming the MLFF is trained with well-curated DFT data. The capability of the MLFF to predict forces accurately along reaction pathways will be verified in future studies.

References

[1] M.V. Manna, P. Sabia, R. Ragucci, M. de Joannon, Fuel **264**, 116768 (2020).
[2] P. Glarborg, H. Hashemi, and P. Marshall, Fuel Commun. **10**, 100049 (2022).
[3] P. Feng, M. Lee, D. Wang, Y. Suzuki, Int. J. Hydrog. Energy **48**, 75 (2023).
[4] H. Wang, L. Zhang, J. Han, E. Weinan. Comput. Phys. Commun. **228**, 178 (2018).
[5] B. Lee, T. Lee, S. Kim, Acta. Mater. **54**, 17 (2006)

First-principles study of surface atomic structure and chemical properties of intermetallic compounds

Kazuki Nozawa

Department of Physics and Astronomy, Kagoshima University,

1-21-35, Korimoto, Kagoshima 890-0065

Trace-amount Pt-doped $Al_{13}Fe_4$ is considered a promising model system for investigating single-atom catalysis, as the doped Pt atoms are dispersed by occupying a specific atomic site[1]. Although it was reported that the conversion of the doped system for the hydrogenation of C_3H_4 is higher than that of the non-doped system, details, including the surface structure, are still unclear.

Thus, this year, we investigated the surface structure of trace Pt-doped $Al_{13}Fe_4$ using first-principles calculations. We used the VASP code for the calculation. The unit cell contains 102 atoms (Al:78, Fe:24) occupying 20 inequivalent crystallographic sites. First, we evaluated the formation enthalpy by replacing one of the crystallographic sites with Pt, corresponding to approximately 1 atom % doping. Then, we composed the convex hull using the obtained formation enthalpy to determine the thermodynamically stable phase. The results indicate that doped Pt prefers to substitute the Fe(1) site as experimentally reported for a 0.2 atom % doped system[1]. The crystal structure of $Al_{13}Fe_4$ is described by alternatively stacking two atomic layers, the flat layer and the puckered layer, along the [010] direction. We performed simulated cleavage calculations[2] by extending the simulation cell in this direction to obtain a stable surface structure. The puckered layer is divided into two parts during the cleavage process, and the obtained most stable surface is composed of the incomplete puckered layers and the flat layer exposed between the incomplete puckered layers. The doped Pt atom is situated in the flat layer, most of which is exposed to the surface. Therefore, the doped Pt atoms can be worked as a catalytically active site. Further studies on the catalytic properties of this surface are ongoing.

References

[1] T. Yamada et al., J. Am. Chem. Soc. **140**, 3838 (2018).

[2] M. Kračji and J. Hafner, Phys. Rev. B 84, 115410 (2011).

[3] S. Iwado, Master Thesis (Kagoshima University, 2024).

Prediction of properties of organic ferroelectrics and piezoelectrics by first-principles calculation

Shoji ISHIBASHI
National Institute of Advanced Industrial Science and Technology (AIST)
Tsukuba, Ibaraki 305-8568

For the 2,5-dihydroxybenzoic acid (DHBA) crystal, two possible switching mechanisms have been noted recently [1]. One is a flip-flop (FF) motion of hydroxy groups, and the other is inter-molecular proton transfer (PT). In Fig.1, structural snapshots of hydroxy groups in both the processes together with Berry phase variation [2]. λ and λ' are parameters to describe the FF and PT processes, respectively. $\lambda = +1$ and $\lambda' = +1$ correspond to the same target ferroelectric structure. The polarization-inverted structure in the PT process is described as $\lambda' = -1$ and its phase differs by 2π from that of $\lambda = -1$ reflecting the proton movements at the hydroxy groups. The Berry phase variation shows that the sign of the polarization-vector component differs between the two processes. The direct piezoelectric coefficient is evaluated, adjusting the polarization-vector component to be positive, from its change upon applying stress. The converse piezoelectric coefficient is evaluated by adjusting the sign of the electric-field component to be the same as that of the polarization-vector component. On the other hand, small structural changes are expected under a stress or an electric field. The change in polarization as a vector is uniquely defined and independent of the switching mechanism. Hence, the switching modes can be distinguished.

Using the QMAS code, we have performed computational simulations of the direct and converse piezoelectric effects for DHBA and also for Hdabco-ReO_4. By comparison with the experimental results, it is concluded that DHBA employs the FF process for its switching mechanism, whereas Hdabco-ReO_4 adopts the PT process.

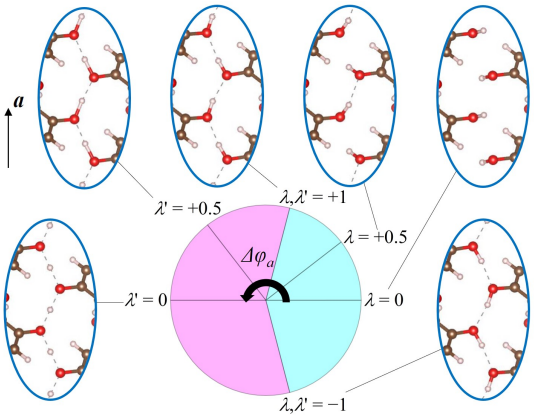

Figure 1: Berry phase variation ($\Delta\phi_a$) and structural snapshots of hydroxy groups during ferroelectric switching in the FF (λ) and PT (λ') processes for DHBA (S. Ishibashi, R. Kumai, and S. Horiuchi, Sci. Rep. **13**, 8810 (2023), DOI: 10.1038/s41598-023-34923-0).

References

[1] Y. Shimoi, S. Tsuzuki, R. Kumai, M. Sotome, and S. Horiuchi, J. Mater. Chem. C **10**, 10099 (2022).

[2] S. Ishibashi, R. Kumai, and S. Horiuchi, Sci. Rep. **13**, 8810 (2023).

Development of First-principles Codes for Evaluation of Physical Properties Through Local Berry Phases

Naoya YAMAGUCHI
Nanomaterials Research Institute (NanoMaRi), Kanazawa University
Kakuma-machi, Kanazawa, Ishikawa 920-1192

This year we continued to develop the calculation code for the coefficients of the magnetic thermoelectric effects, the anomalous Hall and Nernst effects [1], as a code for the evaluation of the physical properties of the local Berry phase method. First, we performed applied calculations on the subject of Heusler alloy systems to investigate their defect effects. When expanding the system using supercells, the computational cost increases due to the larger number of atoms, but in addition, there is the problem of increasing the number of degenerate points that induce numerical instability due to the folding of the Brillouin zone. To avoid that numerical instability, we tried devising various calculation methods for the Berry curvature evaluation routine and found that the most robust results were obtained by approximating with the minor determinant. The implementation is already MPI parallelized for k points. It will also be extended to a combined version of the modified tetrahedron method, and the improved calculation code will be evaluated through trial application calculations in the future.

We have also developed a calculation method to decompose the anomalous Hall and Nernst conductivity into the contributions of each layer in layered materials. By unitary transformation of the Bloch wavefunctions, we constructed hybrid Wannier functions localized only in the direction orthogonal to the plane of each layer, formulated a method for finding the anomalous Hall conductivity at the Wannier center, and implemented the code with the MPI parallelization for the k-points. Using this, it was confirmed that the even-layered antiferromagnetic $MnBi_2Te_4$ is an axion insulator exhibiting a surface anomalous Hall effect, where the conductivity is $1/2$ in e^2/h units at the surface. The computational model was based on the structure of odd-layered $MnBi_2Te_4$ used in last year's study [2], which was an interlayer antiferromagnetic magnetic structure. Such a calculation method for "layer anomalous Hall conductivity" is expected to be applied to a wide range of systems, including two-dimensional stacking materials and artificial superlattices.

As an application of the code developed last year for the evaluation of magnetic thermoelectric properties [1], we predicted the anomalous Nernst coefficient in Cr-doped Bi_2Se_3 which is a Chern insulator [3]. The code was also used in a theoretical study of the mechanism of the giant magnetic thermoelectric effect induced by the van Hove singularities [4].

Furthermore, in the case of tight-binding models or atomic basis set, we developed a method to avoid many eigenvalue problems by combining a highly efficient Berry phase calculation routine developed last year when implementing the electric field application method [5] with the density matrix based on that basis.

The development of the above calculation codes was done while implementing them in the first-principles calculation code OpenMX [6].

References

[1] H. Sawahata, N. Yamaguchi, S. Minami, F. Ishii, Phys. Rev. B **107**, 024404 (2023).

[2] Y. Morishima, N. Yamaguchi, H. Sawahata, F. Ishii, Appl. Phys. Express **16**, 043003 (2023).

[3] R. Syariati, V. Saraswati, H. Sawahata, N. Yamaguchi, F. Ishii, Jpn. J. Appl. Phys. **63**, 01SP26 (2024).

[4] K. Shibata, N. Yamaguchi, H. Sawahata, F. Ishii, J. Phys. Soc. Jpn. **92**, 124704 (2023).

[5] N. Yamaguchi, F. Ishii, Comput. Phys. Commun. **280**, 108487 (2022).

[6] http://openmx-square.org.

Oxygen and hydroxyl groups on Pt Nanoparticles

Takehiko SASAKI and Yasumasa IMAI

Department of Complexity Science and Engineering, Graduate School of Frontier Sciences, The University of Tokyo, Kashiwa-no-ha, Kashiwa, Chiba 277-8561

In order to elucidate and improve the operation of fuel cells (PEFC), it is important to elucidate the electrochemical cycle on the surface of platinum nanoparticles and the adsorption state on the electrode surface. We determined the structures of various oxygen adsorption states on the surface of platinum nanoparticles and the free energy for the electrochemical process of oxygen and OH adsorption reactions.

The Pt nanoparticles to be calculated are Pt nanoparticles composed of 586 atoms of the cuboctahedron type corresponding to the actual catalyst particle size range of 2.5 nm. DFT calculations were conducted using VASP. The unit cell has a volume of 22.13×44.26×33.19 ($Å^3$) and contains 215 Pt atoms and oxygen atoms. After optimization of this unit cell, cuboctahadral nanoparticle is obtained by symmetry operation. The structure optimization calculation was performed by allowing the relaxation of the first and second neighbors of oxygen atoms and hydroxyl groups. The energy cutoff was 400 eV and the k-point mesh was 3x2x2. For each structures free energy change (ΔG) for electrochemical adsorption process was calculated following previous studies [1,2]. The obtained relationship as a function of electrochemical potential is shown in Fig. 1. From this figure the major species on Pt nanoparticles can be assigned as the one with the negative largest ΔG value upon sweeping the electrochemical potential. This information is used for the analysis of *in-situ* XANES.

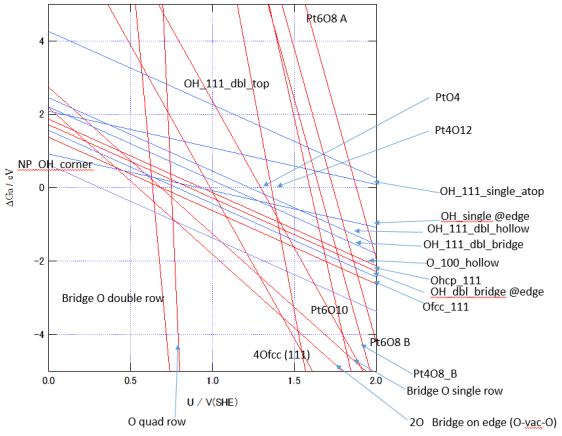

Fig. 1 ΔG for surface oxygen and hydroxyl groups on Pt cluster as a function of electrochemical potential.

References

[1] J.K. Norskov et al. , J. Phys. Chem. B **108**, 17886 (2004).

[2] R. Jinnouchi et al., Catal. Today **262**, 100 (2016).

Finite-temperature electronic transport of CoSi alloys with transition metals (Fe, Cr, Mn, Ni) using KKR-CPA method

Ho Ngoc NAM

Department of Materials Process Engineering,

Nagoya University, Furu-cho, Chikusa, Nagoya 464-8603

Most state-of-the-art thermoelectric materials are semiconductors, whereas metallic materials are abundant but have received less attention due to their typically low Seebeck coefficients and high thermal conductivity values. CoSi, an intermetallic compound with a high power factor, has recently attracted significant curiosity as a potential metallic candidate. However, theoretical studies on electronic transport in CoSi using Boltzmann's approach within relaxation time approximation suggested significant deviations compared to experimental observations, especially electrical resistivity [1]. Accordingly, the efficiency in the treatment of phonon scattering or the lack of vertex correction could be reasons.

To handle these issues, in FY2023, we employed a superior approach using the Korringa-Kohn-Rostoker Green's function method combined with the coherent potential approximation (KKR-CPA) to gain insight into the electronic transport properties of CoSi. In addition, to improve its electrical conductivity, we alloyed this material with transition metals.

In particular, by taking into account both scatterings of random chemical species and thermal-induced atomic displacements as well as the vertex correction, the electrical resistivity of CoSi observed in experiments could be quantitatively reproduced [2]. It also reveals the effect of antisite disorders on resistivity in a low-temperature range. Alloying CoSi with several transition metals (i.e., Fe, Cr, Mn, Ni) at various concentrations reveals significant changes in states of conduction electrons for specific dopants (Fig. 1) and successfully improved the system's conductivity (~25%) with Ni dopant.

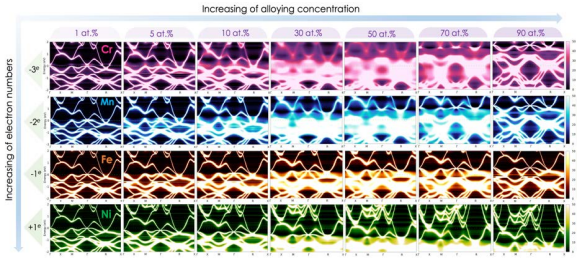

Fig. 1: Room temperature Bloch spectral function of $Co_{1-x}M_xSi$ (where M = Fe, Cr, Mn, Ni) at different alloying concentrations.

References

[1] H. N. Nam, K. Suzuki, A. Masago, H. Shinya, T. Fukushima, and K. Sato: Jpn. J. Appl. Phys. **62** (2023), 020904.

[2] H. N. Nam, Q. M. Phung, K. Suzuki, H. Shinya, A. Masago, T. Fukushima, and K. Sato: J. Mater. Chem. A **12** (2024), 451-459.

Simulations of small cluster of CeO_2

Akira Yoko

Advanced Institute for Materials Research,

Tohoku University, Katahira 2-1-1, Aoba-ku, Sendai, Miyagi 980-8577

We have studied the synthesis and characterization of CeO_2 nanoparticles. CeO_2 nanoparticles have great performance as catalyst or oxygen carrier when the surface is well controlled [1,2].

Recently, it was found that the catalytic activity of CeO2 nanoparticles had clear particle size dependence, which is not explained by the surface area increase. The origin of the catalytic performance enhancement was studied experimentally, and lattice distortion was raised as the potential origin of the high performance. The lattice distortion was caused because of the decrease in particle size, and that affects the activity of oxygen in CeO_2 nanoparticles [1,2].

In addition, we have recently achieved precise control of CeO_2 nanoparticles using continuous flow hydrothermal method. CeO_2 nanoparticles ranging from 1 nm to 9 nm were synthesized just by changing residence time based on the precursor chemistry and the elucidation of the organic modification mechanism. Interesting physical properties such as ferromagnetism and luminescent were emerged for these CeO_2 nanoparticles, and further study of these new materials are required. In this study, small clusters of CeO_2 were studied in terms of the structure and structural distortion. Without any vacancies, particles distorted because of the surface effects and surface construction with Ce and O with polarity (Fig. 1). Further simulations are necessary to elucidate new properties of those clusters.

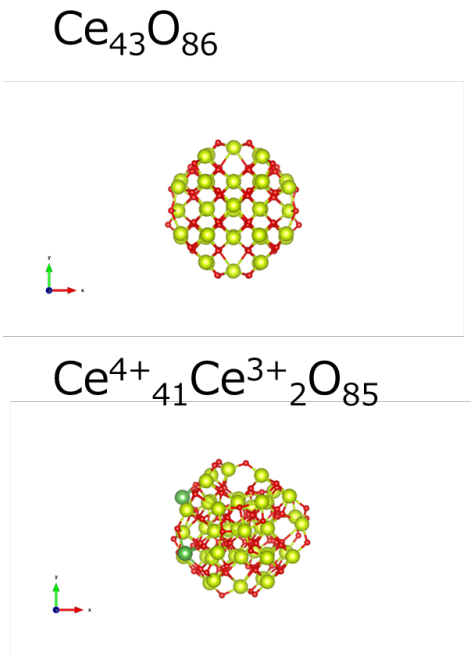

Fig. 1 Example of the simulated clusters

References

[1] X. Hao, et.al., Small, 14(42), 1802915 (2018).

[2] X. Hao, et.al., Acta Materialia, 203, 116473 (2021)

Machine learning study on static structure of light metals alloys based on *ab initio* molecular dynamics

Akihide KOURA

Technical division, Kumamoto University, Kumamoto 860-8555, Japan

It is important to investigate the microscopic mechanism of amorphization of $Mg_xZn_yY_{1-x-y}$ alloy, which is expected to be the material for vehicles and airplanes due to its light mass and strength. It is considered that the Zn_6Y_8 cluster is related with the toughening, however, the detail of the clustering mechanism during amorphization process is not clear. In this project, we focused on the concentration of $Mg_{0.816}Zn_{0.008}Y_{0.111}$ alloy to clarify the structure and dynamics of the liquid and amorphous state based on the *ab initio* molecular dynamics (AIMD) simulations. Furthermore, to decrease the calculation time, we also employ the artificial neural network [1] to make machine learning interatomic potential (MLIP) from the data of the AIMD simulations. Here, we employed the QXMD code for AIMD and MD simulations [2]. To construct the MLIP, we also used the Aenet package [1].

Figure 1 shows partial radial distribution functions $g_{\alpha\beta}(r)$ of liquid state of the Mg alloy at 1000 K. The red dashed line shows $g_{\alpha\beta}(r)$ obtained from AIMD consisting of 288 (232 Mg, 24 Zn, and 32 Y) atoms. The black and green lines correspond to those from MD simulations using different MLIPs consisting of 2304 (1856 Mg, 192 Zn, and 256 Y) atoms. Due to the small number of Zn and Y atoms, training was difficult as shown by the green line, however, averaging several MLIPs makes MD simulation robust as indicated by the black line, of which correlation functions are in good agreement with those by AIMD simulations. While, there was still room for improvement on the learning about small number of atoms.

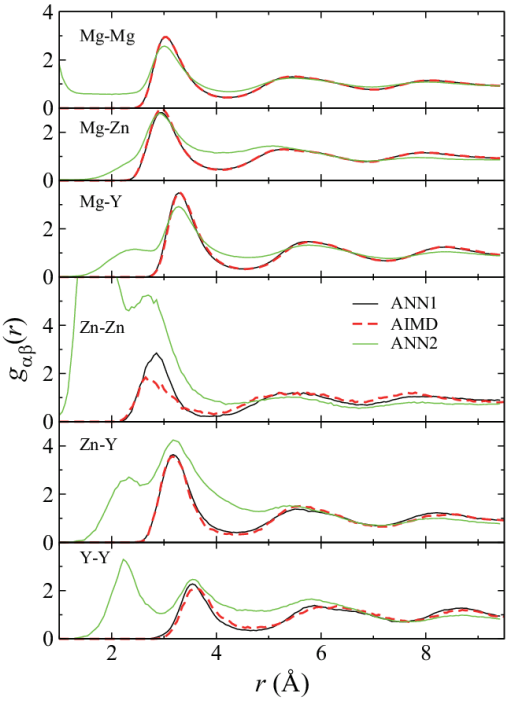

Fig.1: Partial radial distribution functions $g_{\alpha\beta}(r)$. The red dashed line shows the result of the AIMD simulation. The black and green solid lines indicate that of MLIP-MD simulations.

References

[1] N. Artrith and A. Urban, Comput. Mater. Sci. **114**, 135 (2016).

[2] F. Shimojo, *et al.*, SoftwareX **10**, 100307 (2019).

Study on the Removal Mechanism of Copper Oxide Processing by Catalyst-Referred Etching Method

Pho Van BUI, Daisetsu TOH, Kouji INAGAKI, Yoshitada MORIKAWA

Graduate School of Engineering,

Osaka University, 2-1 Yamada-oka, Suita, Osaka 565-0871

Polishing is an extremely important technique used in the finishing processes for optical and semiconductor surfaces and determines the performance of the final products. To produce smooth surface without introducing any crystallographically damaged surface, only pure chemical etching method is desired. Recently, catalyst-referred etching (CARE) method using Pt catalyst and water (as an etchant) has been proposed [1]. CARE can planarize SiC and various crystalline semiconductor materials to atomically smooth surfaces [2,3]. The main role of the catalyst is to dissociate water molecules and to stabilize the five-fold coordinated states.

Recently, transition metal oxide processing has raised much attention thanks to its importance in electronic device fabrication. Cu is commonly used as a lead in electronics thanks to its excellent electrical conductivity. In the processing, Cu is oxidized and is planarized to the desired surface quality. Experimental results have indicated that a Copper oxide layer could be planarized via CARE with a Pt catalyst. Thus, it is important to understand the removal mechanism to fully develop this technique for the practical application of CARE. Thus, density functional theory (DFT+U) based calculations for CuO(100) and CuO(111) (Fig. 1) have been performed in this study. The calculations were performed by the first-principles approach using the STATE-senri program package. The first-principles simulations were based on the generalized gradient approximation (GGA) with the Perdew-Burke-Ernzerhof (PBE) functional. Ion cores were replaced by ultrasoft pseudo-potentials for the Cu, H, O, and Pt atoms. Valence wave functions and charge densities were expanded in the plane wave basis sets with cut-off energies of 25 and 225 Ry, respectively. To calculate the reaction pathway, the climbing image nudged elastic band method was adopted.

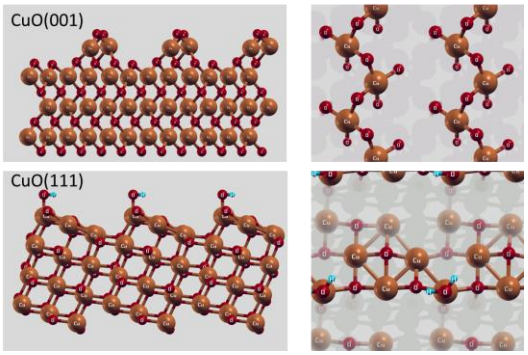

Fig. 1: Side and top views of the CuO(001) and CuO(111) slab models.

In the first step of calculations, the interaction

of the stepped CuO(001) and CuO(111) with water molecules is investigated. For the CuO(001), the first water molecule adsorption and first Cu-O bond dissociation required no activation barrier. By introducing one more water molecule, there is no required activation barrier too. However, the dissociation barrier for the Cu-O bond required an activation barrier of approximately 1.18 eV. The obtained results are summarized in Fig. 2.

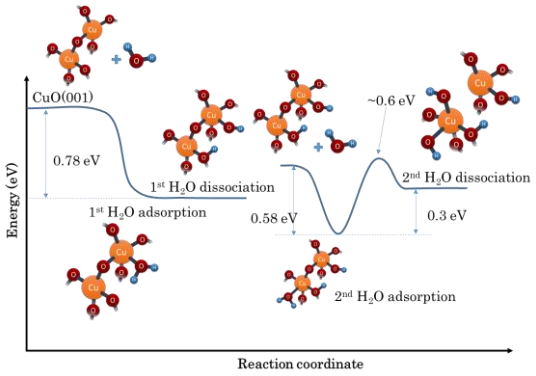

Fig. 2: Water adsorption and dissociation on the stepped CuO(001) surface.

For the CuO(111) surface, the first water molecule adsorption and dissociation required an activation barrier of 0.42 eV (Fig. 3).

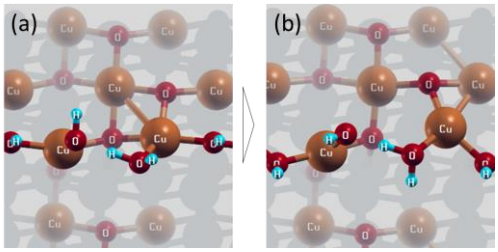

Figure 3: First water molecule adsorption and dissociation on the CuO(111) surface: (a) Adsorbed state and (b) Dissociated state.

In the next step of study, we tried to put a Pt(111) slab model on top of the CuO model to investigate the catalytic effects of Pt to the etching of CuO (Fig. 4).

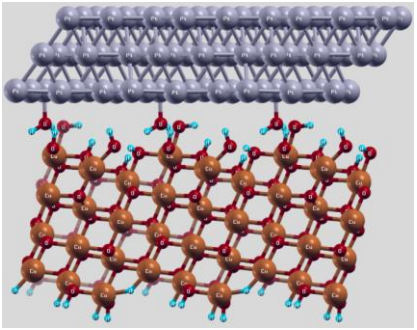

Fig. 4: Pt-CuO model

In the Pt-CuO model, due to the complexity of the interface interaction, some modifications to the code is required. Thus, we will try to solve this problem by implementing Vanderwal correction to DFT+U in the near future.

In summary, by using simplified models of CuO, the interaction of CuO with water was investigated. Without Pt catalyst, the chemical reaction of water with CuO is difficult to occur. However, by implementing Pt slab model, the calculation of the Pt-water-CuO system did not go well due to the complicated interaction between the two solid interfaces.

References

[1] H. Hara, Y. Sano, H. Mimura, K. Arima, K. Kubota, K. Yagi, J. Murata, and K. Yamauchi, J. Electron Mater. **35**, L11 (2006).

[2] D. Toh, P.V. Bui, N. Kidani, S. Matsuyama, Y. Sano, Y. Morikawa, and K. Yamauchi, K. Rev. Sci. Instrum. **90**, 045115 (2019).

[3] A. Isohashi, P.V. Bui, D. Toh, S. Matsuyama, Y. Sano, K. Inagaki, Y. Morikawa, and K. Yamauchi, Appl. Phys. Lett. **110**, 201601 (2017.

Transport study of graphene and carbon nanotubes

Yoshitaka FUJIMOTO
School of Engineering, Kyushu University
Moto-oka, Fukuoka-city, Fukuoka 819-0395

Carbon-based materials like carbon nanotubes (CNTs) and graphene are one of the most promissing device materials in electronics and sensors. The doping of heteroatom to graphene and CNTs is reported to modify their electronic structures. In addition, the adsorption properties of the carbon-based materials are reported to be improved by doping with heteroatoms [1]. Actually, it has been reported that the boron-doped graphene can strongly bind with harmful NO_x molecules [2, 3]. Furthermore, the B-doped CNTs can adsorbe the toxic CO molecule and the conductivity of the B-doped CNTs is largely changed by the adsorption of the CO molecule, suggesting the possibility to fabricate the toxic CO sensors [3, 4]. However, in the previous study, the calculation of the transport property has been performed with only a single dopant in the CNT. In the real systems, CNTs might have many defects [5]. Here, we investigate the effects of the molecular adsorption on the electronic transport of the nanotube with a defect density.

We here exmaine the adsorption properties of various molecules including environmentally toxic molecules on the B-doped (14,0) CNTs. Table 1 shows the adsorption energy and the binding distance between the molecule and the B atom in the B-doped CNTs. It is found that the CO and O_2 molecules are adsorbed with relatively large adsorption energies as well as short binding distances. It is also found that the B atoms in the B-doped CNTs protrude from the tube surface when CO and O_2 molecules are adsorbed on the B-doped CNTs. On the other hand, the CO_2 and N_2 molecules weakly bind with relatively small adsorption energy and long binding distances. In addition, the adsorption energy of the CO molecule on the B-doped (14,0) CNT is smaller than those on the B-doped (8,0) and (10,0) CNTs.

We here investigate how the introduction of the B atom and the adsorption of molecules affect the electronic transport of (14,0) CNTs. The (14,0) CNT is a semiconductor with a band gap of about 0.46 eV. The conductance spectrum of the pristine CNT shows a quantized value and step-like structures. It is found that the pristine (14,0) CNT possesses the conductance of 2 G_0 ($G_0 = 2e^2/h$) near the valence-band and the conduction-band edges.

When a B atom is doped to the semiconducting CNTs, the acceptor states appear near the valence-band maximum, and the Fermi energy of the B-doped CNT relatively moves toward the valence bands. Therefore, the B-doped CNT should act as a *p*-type semiconductor. When a CO molecule is adsorbed to the B-doped CNT, the conductance spectrum largely changes: the adsorption of the CO molecule overall reduces the conductance of the B-doped CNTs. When the O_2 molecule is adsorbed, the conductance spectrum of the B-doped CNTs overall reduces as well. However, the slope of conductance spectrum of the O_2-adsorbed B-doped CNT between $E = 0$ and -0.5 eV is different from that of the CO-adsorbed one.

In summary, the effects of doping and adsorption of molecules on energetics and electronic transport of B-doped (14,0) CNTs have been examined based on the first-principles electronic transport study. The CO and O_2 molecules are adsorbed on the B-doped CNTs with relatively large adsorption energies, while CO_2 and N_2 molecules are weakly adsorbed with long binding distances. The calculation of the electronic conductance of the (14,0) CNTs has been carried out. It is found that the electronic conductance of the CNTs changes

Table 1: Adsorption energy E_a (eV) and distance d (Å) from the B atom for each molecule adsorbed on B-doped (14,0) CNT.

	CO	CO_2	O_2	N_2
E_a	−0.30	−0.01	−0.20	−0.21
d	1.54	2.62	1.66	3.37

largely by the introduction of the dopant atom and the adsorption of the molecules. Thus, the B-doped CNT is a useful material to selectively detect toxic CO and common O_2 molecules.

References

[1] Y. Fujimoto and S. Saito, Chem. Phys. **478**, 55 (2016).

[2] Y. Fujimoto and S. Saito, Jpn. J. Appl. Phys. **58**, 015005 (2019).

[3] Y. Fujimoto and S. Saito, Appl. Surf. Sci. Adv. **1**, 100028 (2020).

[4] Y. Fujimoto and S. Saito, J. Electrochem. Soc. **169**, 037512 (2022).

[5] Y. Fujimoto, J. Electrochem. Sci. Eng. **12**, 431 (2022).

Interactions between impurities and vacancy-helium complexes in metallic materials

Kazuhito Ohsawa

Institute for Applied Mechanics, Kyushu University,

Kasuga-koen 6-1, Kasuga, Fukuoka 816-8580

Introduction

Tungsten (W) and Iron (Fe) are important materials for plasma facing materials (PFMs) used in fusion reactors. Vacancy (V) nucleated under the irradiation circumstance in the metallic materials are considered to be trap sites of a large amount of helium (He) atoms. According to first-principle calculations, more than 30 He atoms can be accommodated in the vacancy. So, the effects of the vacancy-helium (V-He) complexes, vacancy trapping one or multiple He atoms, on the metallic materials were investigated in the present works. In particular, we focused on the interactions between the V-He complexes and typical impurities in the metallic materials. For example, rhenium (Re) is produced in W specimen by nuclear transmutation in the neutron irradiation circumstance. Besides, cupper (Cu) precipitation in Fe causes the embrittlement of steal. In the present work, we investigated interactions between impurities Re and Cu and V-He complexes in W and Fe specimen, respectively. The simulations will contribute to the study of radiation damage formation.

Simulation method

Binding energy E_b between impurity X and V-He complex was estimated in terms of first-principle calculations.

$$E_b = E[M_{m-1}VHe_n] + E[M_{m-1}X] - E[M_{m-2}VHe_nX(k)] - E[M_m], \quad (1)$$

where E is cohesive energy of supercell. For example, the supercell $M_{m-1}VHe_n$ is composed of m-1 metals (M), one vacancy (V), and n He trapped in the vacancy. Impurity located at k-th nearest neighbor site from the V-He complex is expressed by X(k), as shown in Fig. 1. Then, $E[M_m]$ indicates cohesive energy of perfect crystal. A large simulation cell composed of 5x5x5 bcc lattice was used. The cut-off energy of plane wave was 500eV.

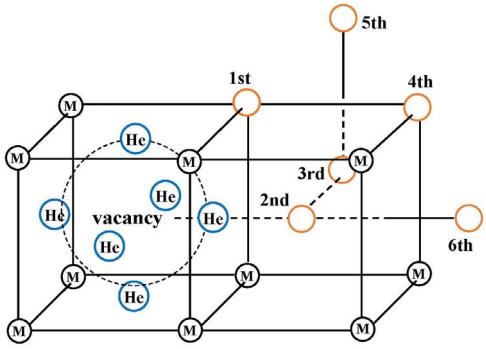

Fig. 1 Schematic view of k-th nearest neighbor site from V-He complex.

Results and discussion

We estimated binding energies of impurities Re and Cu to V-He complexes in W and Fe, respectively. The number of He atoms trapped in the vacancy is assumed to be 0, 1, and 6 in the present simulations.

According to Fig. 2, first and second nearest neighbor sites from the V-He complexes in W are energetically favorable for Re. Therefore, attractive interaction supposed to act between Re and W vacancy. Actually, Re precipitation has been reported to be observed on the inner surface of void in W specimen, which is good agreement with the present simulations. The binding energies of Re to V-He complex are almost independent of the number of He atoms trapped in the W vacancy, that is, Re does not appear to interact with He.

In the case of Cu in Fe, attractive interaction also acts between Cu and Fe vacancy, as shown in Fig. 3. The first nearest neighbor site from Fe vacancy is energetically most favorable for Cu, which consistents with the fact that Cu does not dissolve in Fe at all. However, the binding energies of Cu to V-He complex definitely depend on the number of He atoms trapped in the Fe vacancy. As the number of He atoms trapped in the Fe vacancy increases, the binding energy increases. So, there appears to be an interaction between Cu and He. However, He does not chemically bond with other elements because it is rare gas. So, we come up with a hypothesis to explain the present results. He atoms expand the Fe vacancy and create a strain filed around it. Cu only interact with the strain field and is not directly bound to the He atoms. It has been proposed that the presence of He atoms in metallic materials can be replaced by an appropriate strain field. The adequate examination for this hypothesis is an issue for the future. The difference between Re and Cu is supposed to be due to their solubility in the matrix. Re is partially soluble in W. On the contrary, Cu is completely insoluble in Fe.

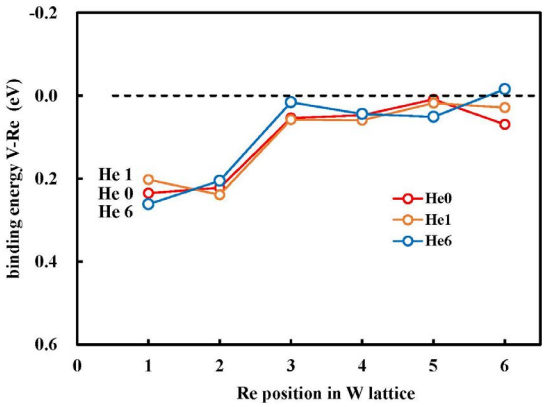

Fig. 2 Site dependence of binding energy of impurity Re to V-He complexes in W.

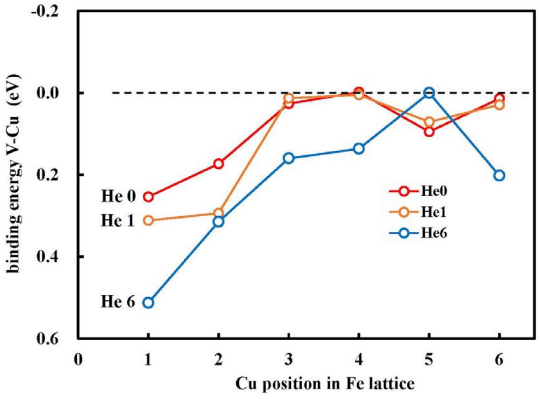

Fig. 3 Site dependence of binding energy of impurity Cu to V-He complexes in Fe.

Structure search for the T phase of silicene on the Ag(111) surface by Gaussian process regression

Yuji HAMAMOTO

Department of Precision Engineering, Graduate School of Engineering

Osaka University, Yamada-oka, Suita, Osaka 565-0871

Silicene [1], a silicon analog of graphene, has drawn growing attention from the viewpoint of a future application to ultrathin semiconductor devices. However, its charge carrier mobility is much smaller than graphene, possibly due to the nontrivial buckled structures of the honeycomb lattice, which are often observed simultaneously. Thus, identifying the buckled structures is crucial for the development of silicene-based devices. The density functional theory (DFT) is a powerful method to study the stabilities of materials, but its application to silicene has been limited to the systems whose structures can be inferred from experimental results. Consequently, there remain unidentified structures, one of which is the so-called T phase observed as less-ordered protrusions in silicene grown on Ag(111).

To investigate the stable structures of silicene on Ag(111) exhaustively and efficiently, we here adopt a structure search method based on an evolutionary algorithm and the Gaussian process regression [2]. Our results demonstrate that the method can reproduce not only the well-known stable structures but also metastable structures that have not received attention so far [3]. Especially, the $\sqrt{13} \times \sqrt{13}R19.1°$ type-I phase exhibits several metastable structures close in stability to the most stable ones as shown in Fig. 1. The metastable structures are characterized by monomer, dimer, and trimer protrusions. We have concluded that the coexistence of such metastable structures is the origin of the T phase observed experimentally.

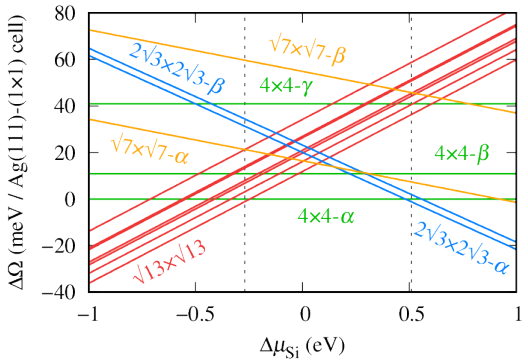

Fig. 1: Phase diagram of silicene on Ag(111).

References

[1] K. Takeda and K. Shiraishi, Phys. Rev. B **50**, 14916 (1994).

[2] M. K. Bisbo and B. Hammer, Phys. Rev. Lett. **124**, 086102 (2020).

[3] Y. Hamamoto, T. N. Pham, M. K. Bisbo, B. Hammer, and Y. Morikawa, Phys. Rev. Materials **7**, 124002 (2023).

Phase equilibrium of high entropy alloys and shape memory alloys

Yoko Yamabe-Mitarai

Frontier Science Graduate School,

The University of Tokyo, Kashiwa-no-ha, Kashiwa, Chiba 277-8561

High-entropy alloys (HEAs) comprise multiple elements with near-atomic composition and have high configurational entropy of constituent elements. HEAs have been attracted as new-generation structural and functional materials since this new paradigm was proposed in 2004 [1]. Most HEAs have a single face-center-cubic (fcc), body-center-cubic (bcc) structures, or their mixtures. Due to the limited slip system, the hexagonal-close-pack (hcp) structure is expected to be a high-temperature material. Significant solid-solution hardening is also expected for HEAs. Then, we are applying to find HEAs with hcp structure experimentally and by using DFT calculation. Phase stability of alloys was experimentally investigated, and a few alloys were found to be a hcp structure [2]. A supercell model with 128 atoms was used to indicate the solid solution phase. Special Quasirandom Structure was used to simulate random atomic position. The internal coordinates was optimized using Quantum Expresso (QE). The total energy, density of states, and electron charge density were calculated on the optimized coordinates. The results indicated that some specific bonding was very strong, and the strong bonding is expected to improve strength. This topic was presented in master's thesis and is now preparating a paper.

As the second topic, HEAs are applied for high-temperature shape memory alloys (SMAs). Several potential martensite phases are expected to be formed in HE-SMAs. The formation energy of each possible martensite phase was calculated. The results indicated that the most stable martensite phase changed depending on alloy composition.

The third topic is the adhesion behavior of the oxide layer on Ni to understand the stability of the protective oxide layer. We found that some alloying elements drastically decreased interfacial energy, improving the adhesion between Ni and the oxide layer. We submitted one paper related to this topic.

References

[1] B. Cantor et. al., A. J. B. Vincent, Mater. Sci. Eng. A, **375-377**, 213 (2004). [2] Y, Yamabe-Mitarai et. al., JALCOM, **911**, 164849 (2022)

Reaction Analysis in Solid Catalysts by DFT Calculations and Informatics

Tatsuya JOUTSUKA

Department of Materials Science and Engineering, Ehime University, 3 Bunkyo-cho, Matsuyama, Ehime 790-8577, Japan.

Center for Sustainable Energy and Environmental Engineering, Ehime University, 3 Bunkyo-cho, Matsuyama, Ehime 790-8577, Japan.

Focusing on the selectivity of zirconia-catalyzed methanol synthesis, we calculated adsorption and reaction energies to clarify the reaction mechanism. [1] In addition, polaron transfer rate constants in bulk titanium dioxide (TiO_2) and $SrTiO_3$ were calculated by the constrained density functional theory (CDFT) method. Then, the electronic structure calculation was used to elucidate the photocatalytic reaction mechanism and crystal plane selectivity in photocatalysts.

A zirconia-based solid solution catalyst $InZrO_x$ was prepared by substituting In with Zr, which has high catalytic activity. The correlation between the binding strength of the substituted elements and adsorbates (reactants, products, and intermediates) and methanol synthesis capacity was clarified. The DFT calculations employed Vienna Ab initio Simulation Package (VASP) program We conducted a Density Functional Theory (DFT) study on the formation of CH_4 on $InZrO_x$, analyzing the free energy surface and density of states (DOS). Our findings indicate a potential reaction pathway, emphasizing the transfer of the methyl group with a competitive activation barrier, aligning well with experimental data. Additionally, our study suggests that the decomposition of CH_3OH may also play a role in CH_4 production. The adsorption of a methyl group occurs exclusively on the $InZrO_x$ catalyst due to the superior overlap of DOS between the adsorbate and substrate compared to the $ZnZrO_x$ catalyst. We are now analyzing a series of solid solution catalysts in combination with machine learning. Furthermore, by integrating experimental and computational approaches, we elucidated the surface structure of CuO/t-ZrO_2. [2-3] Unlike other Cu^{2+}-containing catalysts, this catalyst is rich in highly reducible Cu^{2+} species. X-ray absorption spectroscopy and density functional theory calculations notably revealed that these Cu^{2+} species adopt a square-planar [CuO_4] configuration. Our findings suggest that these highly active [CuO_4] species are crucial in facilitating the coupling reaction.

Additionally, we calculated the polaron

transfer rate constants in bulk TiO_2 and $SrTiO_3$ (Fig. 1) using the Constrained Density Functional Theory (CDFT) method along several directions, such as the [101] direction in TiO2, with the CP2K program package. Our results show that the CDFT method provides a more accurate evaluation of the potential energy profile compared to the frequently used linear interpolation of structures for bulk TiO_2. Subsequently, we examined the $SrTiO_3$ (001) and (110) surfaces to understand polaron transfer at these surfaces. Currently, we are investigating the relationship between oxygen vacancies and electron polarons to further elucidate the photocatalytic mechanism, employing the CP2K program package.

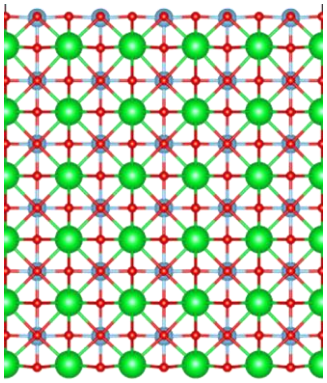

Fig. 1: Bulk $SrTiO_3$.

References

[1] Shohei Tada,* Yurika Ogura, Motohiro Sato, Akihiro Yoshida, Tetsuo Honma,e Masahiko Nishijima, Tatsuya Joutsuka,* Ryuji Kikuchi*, Phys. Chem. Chem. Phys., 26, 14037-14045 (2024).

[2] Shohei Tada,* Tatsuya Joutsuka* and Masaru Kondo,* ChemCatChem, in press.

[3] Masaru Kondo,* Tatsuya Joutsuka,* Kakeru Fujiwara, Tetsuo Honma, and Shohei Tada,* Catal. Sci. Technol., 13 (7), 2247-2254 (2023).

Materials exploration using materials informatics

Yosuke HARASHIMA
Graduate School of Science and Technology, Nara Institute of Science and Technology
Takayama-cho, Ikoma, Nara 630-0192

The 5th Strategic Energy Plan in Japan has been established, making the realization of a decarbonized society independent on fossil fuels the most crucial challenge for future development. The hydrogen energy generated from solar energy using photocatalysts (green hydrogen) is one of the promissing candidate. The purpose of this study is to establish a scheme controling impurity-induced property to improve the visible-light photocatalytic production of hydrogen, and then, to obtain novel photocatalytic compounds. We combined first-principles calculations and experiments by using informatics technique. Material searching space was determined on the basis of expert experiences. This study expands the searching space significantly by utilizing information science, thereby pioneering new research in photocatalytic material development. In particular, we construct a high-accuracy predictive by combining dynamic Monte Carlo simulation of the calcination processes with experimental data of hydrogen evolution rate (HER). This research not only addresses the energy issue with hydrogen-generating photocatalysts but also has spillover effects for carbon-neutral petrochemical synthesis from CO_2 and green hydrogen.

Performance of photocatalysts depend strongly on their calcination processes. In this study, the calcination process is explained by three features: temperature elevation speed, calcination temperature, and calcination time. Figure 1 illustrates the schematics. Products are obtained from reactants through a calcination process. This process also produces lattice defects. The HER, R, should be proportional to the amounts of products, ρ_{p}, and defects, ρ_{d}.

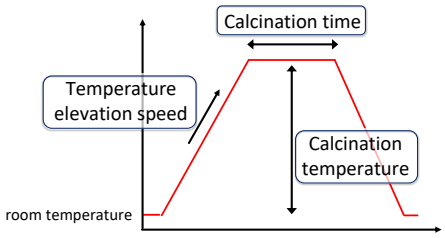

Figure 1: Schematic picture of a calcination process and its features: temperature elevation speed, calcination temperature, and calcination time.

$$R = a_{\mathrm{p}}\rho_{\mathrm{p}} + a_{\mathrm{d}}\rho_{\mathrm{d}}. \tag{1}$$

The coefficients $a_{\mathrm{p,d}}$ are determined such that the prediction reproduces experimental data of HER. $\rho_{\mathrm{p,d}}$ are calculated by dynamic Monte Carlo simulation for given calcination process.

Dynamic Monte Carlo simulation is a computational technique used to model the evolution of systems over time. The time taken for state transitions, τ, is calculated as follows.

$$\tau = -\frac{1}{W}\ln X, \tag{2}$$

where X is a random number with a range $0 < X \leq 1$, and W denotes a transition rate

$$W = \frac{1}{C}\min\left\{1, \exp\left(-\frac{\Delta E}{k_{\mathrm{B}}T}\right)\right\}. \tag{3}$$

C is a time constant, which is determined by regression. We demonstrated the scheme considering $SrTiO_3$ and optimized the calcination process to improve HER.

First principles study on the band structures of high entropy superconductors

Hidetomo USUI

Department of Applied Physics, Shimane University,

1060 Nishikawatsu-cho, Matsue, Shimane 690-8504

High-entropy (HE) compounds have attracted much attention not only from a mechanical point of view but also from the perspective of functional materials.[1,2] We have investigated the electronic structure of a HE compound MTe, which exhibits robustness of its superconductivity against external pressures[3, 4, 5]. This year, we calculated the electronic band structure of HE compounds constructed from the same or different groups in the periodic table. We used the VASP and WIEN2k packages within the PBE-exchange correlation functional with spin-orbit coupling included. We used a 2×2×2 supercell, and the site arrangement of *M* atoms is calculated using the special-quasi random structure implemented in Alloy Theoretic Automated Toolkit. The density of states of $Pb_{11}Ag_{11}Bi_{10}Se_{16}Te_{16}$ and $Ge_{10}Sn_{11}Pb_{11}Se_{16}Te_{16}$ in the rock salt structure is shown in Fig. 1. It is found that elements within the same group can strongly influence the band structure near the Fermi level ($Ge_{10}Sn_{11}Pb_{11}Se_{16}Te_{16}$). In contrast, elements from other groups tend to control the band structure near the Fermi level. The superconducting transition temperature exhibits the same behavior under pressure in (Pb,Ag,Bi)Te and (Ge,Sn,Pb)Te.[5] Therefore, our findings suggest that the electronic band structure is not a major factor in the pressure-dependent superconducting properties.

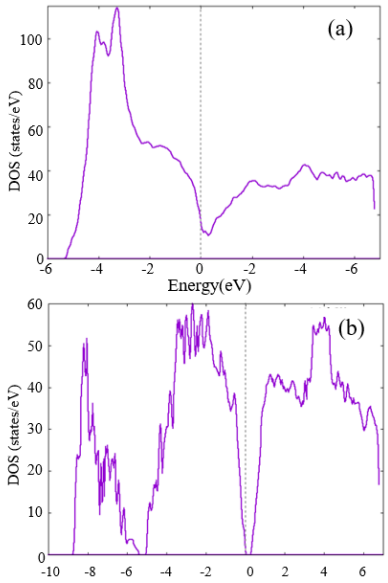

Fig. 1: The density of states of (a) $Pb_{11}Ag_{11}Bi_{10}Se_{16}Te_{16}$, (b)$Ge_{10}Sn_{11}Pb_{11}Se_{16}Te_{16}$.

References

[1] B. Jiang *et al.*, Science **371**, 830 (2021).

[2] P. Koželj *et al.*, Phys. Rev. Lett., **113,** 107001 (2014).

[3] Md R. Kasem *et al.*, Sci. Rep **12**, 7789 (2022).

[4] Y. Mizuguchi *et al.*, Mater. Today Pnys. **32**, 101019 (2023).

[5] R. Matsumoto *et al.*, J. Alloys Compd. **983**, 173906 (2024).

First-principles study of anomalous Nernst effect in topological materials

Susumu MINAMI, Takahiro SHIMADA
Department of Mechanical Engineering and Science,
Kyoto University, Nishikyo-ku, Kyoto 615-8540

The anomalous Nernst effect (ANE) is a thermoelectric (TE) effect stemming from the spontaneous magnetic order of materials, enabling the realization of flexible and efficient TE power generation modules due to the direction of the TE voltage compared to the conventional Seebeck effect [1]. Recent discoveries of topological materials that achieve a large ANE from exhibiting unique band structures (Weyl nodes, nodal lines) are promising candidate materials for TE devices based on the ANE [2]. In this research project, to elucidate the origin of the giant anomalous Nernst effect in topological magnetic materials and their characteristic electronic states, analysis of the anomalous Nernst effect and electronic states in topological magnetic materials will be conducted using first-principles calculations.

We evaluate the anomalous Nernst effect while considering in-plane lattice strain induced by epitaxial strain in the nodal-line semimetal $Co_3Sn_2S_2$. The first-principles calculations are employed the VASP package [3,4]. From the obtained Bloch states, we construct Wannier basis by using Wannier90 code [5] to evaluate transverse thermoelectric conductivity α_{xy}. The effects of the nucleus and electrons were expressed by the projector-augmented wave (PAW) method. A $24 \times 24 \times 24$ k-point mesh with the Monkhorst–Pack scheme was used for Brillouin zone sampling of the primitive cell. The generalized-gradient approximation was adopted for the exchange-correlation functional. The out-plane lattice constant and atomic configuration under each in-plane strain is optimized to satisfy the maximum force of below 0.01 eV/Å based on the conjugate gradient algorithm.

Figure 1 shows the temperature dependence of α_{xy} at several in-plane strain conditions. We find that the transverse thermoelectric conductivity α_{xy} is about 1.5 $AK^{-1}m^{-1}$ at 150 K, which is consistent with experimental results [6]. Moreover, α_{xy} reaches 2.2 $AK^{-1}m^{-1}$ with 3% in-plane compressive strain condition. We clarified that the in-plane compressive strain improves α_{xy} about 1.5 times more than no strain condition. As a future perspective, we investigate the enhancement mechanism of transverse TE conductivity α_{xy} by strain engineering for several topological magnets.

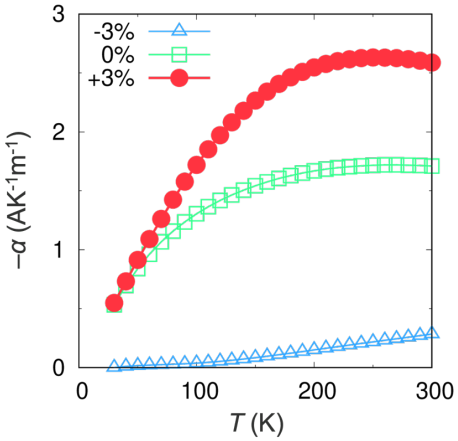

Fig. 1: Temperature dependence of transverse thermoelectric conductivity α_{xy}. Triangle, square, circle line points represent in-plane 3% tensile strain, no strain, 3% compressive strain condition, respectively.

References

[1] M. Mizuguchi and S. Nakatsuji, Sci. Tech. Adv. Mater **20**, 262 (2019).

[2] S. Nakatsuji, R. Arita, Annu. Rev. Condns. Matter Phys. **13**, 119 (2022).

[3] G. Kresse, and J. Hafner, Phys. Rev. B **47,** 558 (1993).

[4] G. Kresse, and J. Furthmüller, Phys. Rev. B **54**, 11169 (1996).

[5] G. Pizzi, et al., J. Phys.: Condens. Matter **32**, 165902 (2020).

[6] Guin, S. N. et al., Adv. Mater. **31**, 1806622 (2019).

Computational Carrier Mobility Estimation of Organic Semiconductors

Toshihiro SHIMADA

Division of Applied Chemistry, Faculty of Engineering,

Hokkaido University, Kita 13 Nishi 8, Kita-ku, Sapporo, Hokkaido 060-8628

Compared to simple p- and n-type organic field-effect transistors, it is very difficult to achieve high performance in ambipolar transistors because both HOMO–HOMO and LUMO–LUMO interactions in the crystal must be large and multidimensional. We synthesized some organic molecules with fused aromatic rings, determined the crystal structures experimentally, and calculated electronic structure including the interaction between p-electron systems between the molecules. We used VASP for the first principle band strucutre calculation using ISSP-B and -C systems for the computation. Theoretical calculations using the obtained molecular arrangement suggested that there are two-dimensional interactions for both HOMO–HOMO and LUMO–LUMO.[1]

From the calculation of TPCPA and TPDPP (shown in Fig. 1), it was found that TPCPA type 1 crystal had nearly one electronic structure for electrons, while TPCPA type 2 and TPDPP had two dimensional structures both for electrons and holes, that shows ambipolar characteristics. The experimental mesurement of FET was successfully performed for TPDPP, resulting in the confirmation of ambipolar characteristics.

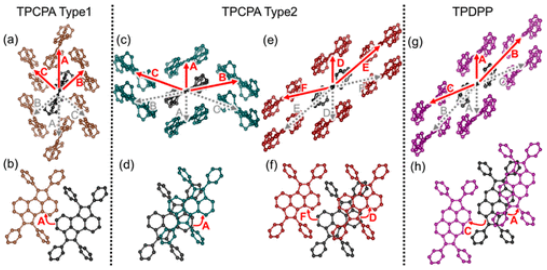

Fig. 1: Crystal structure and intermolecular interactions (arrows with A,B,C) of molecules TPCPA (two polymorphisms in crystal structure) and TPDPP. The molecular interactions were estimated from calculations using the experimentally determined crystal structures.

References

[1] H. Tanoguchi, T. Yuki, S. Yokokura, T. Yanase, J. Mingoo, H. Ito, T. Nagahama, T. Shimada, ACS Appl. Electron. Mater. 5, 6626 (2023).

[2] T. Yuki, S. Yokokura, M. Jin, H. Waizumi, S. Yokokura, T. Nagahama, T. Shimada, Cryst. Growth Des. 24, 1849 (2024).

Calculation of Formation Energies of $P_2Ir_2O_7$ and Related Compouds by DFT in relation to Thin Film Growth Experiments

Toshihiro SHIMADA

Division of Applied Chemistry, Faculty of Engineering,

Hokkaido University, Kita 13 Nishi 8, Kita-ku, Sapporo, Hokkaido 060-8628

Topological materials including Weyl semimetals (WSM) are gathering much attention recently from the expectation of possible spintronics applications. We are growing epitaxial thin films of WSM, such as pyrochlore $Pr_2Ir_2O_7$ (PIO) by molecular beam epitaxy. From the experimental structural evaluation and physical property measurement of the thin films, we consider impurity phases are sometimes included in the sample depending on the growth conditions. In order to understand the mechanism, we conducted DFT calculation of the related materials (IrO_2, PrO_2, Pr_2O_3, Pe_3IrO_7, PIO, PIO_WB(Weberite structure; *Ccmm*), PIO_DF(defect fluorite structure; $Fm\bar{3}m$) using ISSP supercomputer system. The crystal structures are shown in Fig. 1 adopted from Ref [1]. We used VASP with GGA-PBA with the cut-off Energy 650eV. The functional for Pr was Pr_3[2].

.

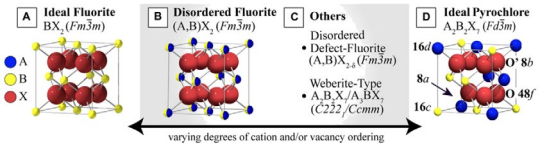

Fig. 1: Materials considered [1]

The result is shown in Fig. 2.

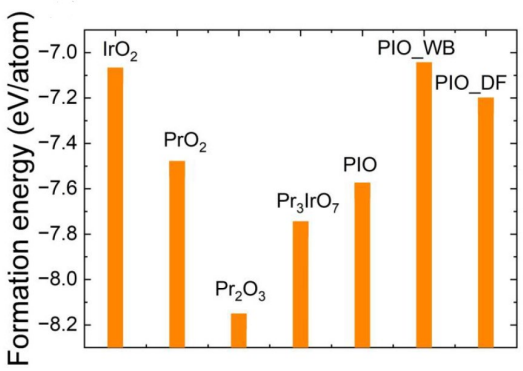

Fig.2: Formation energies from DFT.

The result is useful to optimize the thin film growth conditions for PIO.

References

[1] J.L. Wardini et al., Front. Chem. 9, 743025 (2021).

[2] G. Lan et al., Acta Mater. 91, 304 (2015).

Calculation of chemical shift of X-ray photoelectron binding energy of hydrogen-containing functional groups generated on fluoropolymer surface

Yuji OHKUBO, Misa NISHINO, and Kouji INAGAKI

Graduate School of Engineering, Osaka University, 2-1 Yamadaoka Suita, Osaka 565-0871

Polytetrafluoroethylene (PTFE) has both much low relative dielectric constant and dielectric loss tangent, so it is considered as a suitable dielectric substrate of high-frequency printed wiring boards. However, PTFE has low adhesion property, so adhering PTFE to Cu is difficult. We have achieved generation of oxygen-containing functional groups and adhesion strength of 0.98 N/mm between PTFE and Cu when PTFE was He-plasma-treated at over 200℃ under atmospheric pressure[1]. However, it is difficult to experimentally measure the exact value of the chemical shift in the X-ray photoelectron spectroscopy (XPS) spectra of the functional groups formed on the PTFE surface. Therefore, it is necessary to determine the exact values of chemical shifts of the functional groups formed on the plasma-treated PTFE surface using first-principles calculations to accurately identify the functional groups formed on the PTFE surface. In this study, we calculated the C1s core level binding energies of normal-chain-type molecules comprising C, F, O, and H. We deconvoluted the experimentally obtained C1s-XPS spectra using the calculated values to identify the chemical species generated on plasma-treated PTFE surfaces.

The C1s core level binding energy was calculated by the Δself-consistent field (ΔSCF) method. The energy difference between the ground state molecule and the molecule with a core hole was also calculated by this method using the Gaussian 09 software package. The geometry was optimized using the Hartree–Fock method, and ccpVDZ was used as the basis function. The SCF calculation of a molecule with a core hole was converged by direct minimization. Fluorine-based molecules were used as the computational models of polymers. These molecules were cut into small molecules from the –(CF_2–CF_2)*n*– chain, a component of PTFE. As the model of the as-received PTFE, CF_3–CF_2–CF_2–CF_2–CF_3 was used. CF_3–CF_2–CF_2–O–CF_3, CF_3–CF_2–O–C(=O)–CF_2–CF_3, CF_3–CF_2–CFOH–CF_2 –CF_3, CF_3–CF_2–C(=O)–CF_2–CF_3, and CF_3–CF_2–CF=CF–CF_3 were used as the models of oxygen-containing functional groups generated by plasma treatment. Furthermore, the molecules with F substituted by H were also calculated. It is difficult to accurately calculate the absolute experimental

C1s core level binding energies, but the relative C1s core level binding energies in various chemical environments can be well reproduced by ΔSCF calculations[2]. Therefore, we shift the calculated C1s core level determined by taking the energy difference between the experimentally observed C1s binding energy (Eexp) of 292.5 eV[3] in –(CF_2–CF_2)n– and the calculated value (EΔSCF) of 299.97 eV. To compare with experimental values, we subtracted Δ (7.47 eV) from the calculated C1s binding energies of all chemical species investigated in this study. The calculation error in this study originates from the incompleteness of the basis set, the neglect of the electron correlation energy in the Hartree–Fock approximation, the vacuum surrounding the model molecules, and the approximation of the model molecules as small molecules. The constant shift removes the error from the vacuum surrounding the model molecules.

Table 1 shows the calculated C1s core level binding energies of molecules with the oxygen-containing functional groups in the CF_2– and CH_2– chains. **Fig. 1** shows the deconvolution results of the C1s-XPS spectra of the plasma treated PTFE surfaces using the calculated values. The large peak near 286.4 eV was not reproduced using only these peaks because the smallest C1s core level binding energy ofmolecules with the oxygen-containing functional group in the CF_2– chain was 289.3 eV. Therefore, by adding the calculated values of the functional group in the CH_2– chain, we were able to reproduce the peak near 286.4 eV. This result indicated that the F atoms were substituted by the H atoms on the PTFE surface by plasma treatment.

Table. 1. Calculated C1s core level binding energies of molecules with oxygen-containing functional groups in the CF_2– and CH_2– chains.

No.	Molecule	E_{cal} [eV]
①	CF_3–CF_2–$\underline{C}F_2$–O–CF_3	294.1
②	CF_3–CF_2–$\underline{C}F_2$–CF_2–CF_3	292.5
③	CF_3–CF_2–O–$\underline{C}$(=O)–CF_2–CF_3	291.9
④	CF_3–CF_2–$\underline{C}$FOH–CF_2–CF_3	291.4
⑤	CF_3–$\underline{C}F$–(CF–(CF_3)$_2$)–CF_3 (Crosslinking)	290.7
⑥	CF_3–CF_2–$\underline{C}$(=O)–CF_2–CF_3	290.4
⑦	CF_3–CF_2–$\underline{C}F$=CF–CF_3	289.3
⑧	CH_3–CH_2–O–$\underline{C}$(=O)–CH_2–CH_3	289.3
⑨	CH_3–CH_2–$\underline{C}$(=O)–CH_2–CH_3	287.6
⑩	CH_3–CH_2–$\underline{C}H_2$–O–CH_3	286.2
⑪	CH_3–CH_2–$\underline{C}$HOH–CH_2–CH_3	286.1
⑫	CH_3–CH_2–$\underline{C}H_2$–CH_2–CH_3	284.6
⑬	CH_3–$\underline{C}H$–(CH–(CH_3)$_2$)–CH_3 (Crosslinking)	284.5
⑭	CH_3–CH_2–$\underline{C}H$=CH–CH_3	284.3

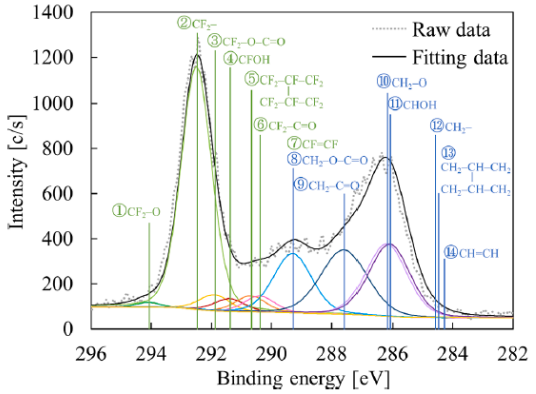

Fig. 1. Deconvolution results of C1s-XPS spectra of plasma treated PTFE surfaces using oxygen containing functional groups only in the CF_2– and CH_2– chains.

References

[1] M. Nishino et al., *RSC adv.*, **13** (2023) 25895–25903.

[2] E. A. Hoffmann et al., *J. Polym. Sci. Part A Polym. Chem.*, 42 (2004) 551–556.

[3] G. Beamson et al., *J. Chem. Educ.*, **70** (1993) A25.

Theoretical study of work function and band gap of double-perovskite

Kazume NISHIDATE
Graduate School of Science and Engineering, Iwate University
4-3-5 Ueda, Morioka, Iwate, 020-8551

Double perovskite Ba_2PrBiO_6 exhibits photo catalytic activity in the visible light range with the observed optical band gap of ∼1.0 eV. On the other hand, density functional theory (DFT) calculations predict a larger bulk band gap of 2.0 eV even with the standard Perdew-Burke-Ernzerhof (PBE) functional, which is known to underestimate the band gap of semiconductors. Much larger bulk band gap of 3.13 eV is predicted with a hybrid functional treatment for the exchange correlation, which generally gives better descriptions for them. This discrepancy between experiment and theory implies the presence of unknown mechanism which effectively reduces the band gap of Ba_2PrBiO_6 and thereby gains the sensitivity to the visible light. The first finding is that the surface band gaps of Ba_2PrBiO_6 calculated using an appropriate hybrid functional are smaller than the bulk band gaps and are 2.49 eV and 2.85 eV for the Pr-Bi and Ba-O polar surfaces, respectively. We also find that work function is quite sensitive to the surface structures and its accurate calculations are essential to show that the reduction and oxidation levels are fit to the gap region. When a substitutional defect Pr_{Bi}, in which Bi is substituted by Pr, is introduced into the Pr-Bi polar surface, surface band gap is further reduced to 0.93 eV, being very close to the experimental value. For the Ba-O polar surface, similar reduction to 1.59 eV is found but not substantial as compared to the Pr-Bi polar surface. These narrow surface band gaps may be the origin of the photo activity of Ba_2PrBiO_6 in the visible light region.

We also performed Born-Oppenheimer molecular dynamics simulations to clarify the reactivity of the polar surfaces to water. Adsorption of the second H_2O molecule generates two other hydroxyl groups with the help of the one oxygen atom at the subsurface. No more hydroxyl group is formed by the adsorption of the third H_2O molecule. On the other hand, H_2O molecule adsorbed on the Pr-Bi surface can be diffused on the surface. When two H_2O molecules were successively placed on the Pr-Bi surface, only the first H_2O molecule was adsorbed. This adsorption generates two hydroxyl groups as in the Ba-O case. However, the second H_2O molecule is not decomposed into the hydroxyl group but makes a weak bond with the surface (stage II). Then the H_2O molecule starts to diffuse on the surface (stage III). The different behaviors against the adsorptions may originate in the exposed oxygen atoms.

References

[1] K. Nishidate, M. Matsukawa, A. Matsushit, Y, Li, D. C. Roy, and M. Hasegawa,: Surf. and Int. **24**, 103914 (2024).

[2] Y. Li and K. Nishidate: Int. J. Hydro. Eng. **51**, 1471 (2024) .

Unique patterns in simulated scanning tunneling microscopy images of graphene nanoribbons

Junhuan LI, Kenta ARIMA

Graduate School of Engineering, Osaka University, Yamada-oka, Suita, Osaka 565-0871

Previously, we successfully validated the presence of a rectangular-like lattice in nanographene observed experimentally by simulating scanning tunneling microscopy (STM) images of armchair-edged graphene nanoribbons (AGNRs) [1]. However, the origin of this unique lattice remains to be explored.

Calculations were performed by STATE (Simulation Tool for Atom TEchnology) package. The band structures of 39-AGNR (where 39 is the width measured by the number of rows of carbon atoms across the AGNR) was shown in Figure 1.

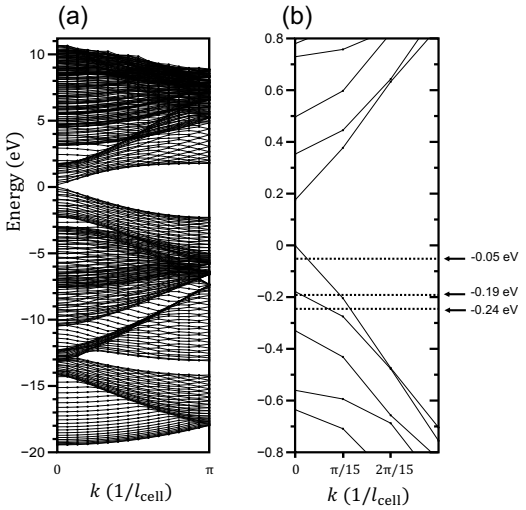

Fig. 1: Band structures of 39-AGNR.

Based on Figure 1b, we selected three different sample biases (represented by three dotted lines and arrows) for calculating the STM images. The larger the absolute value of the sample bias, the more eigenvalues in the band structure are included in the calculation. As shown in Figure 2, only the calculation results for the smallest sample voltage reveal the rectangular-like lattice [2].

This work has been performed on System B of the Supercomputer Center, the Institute for Solid State Physics, the University of Tokyo.

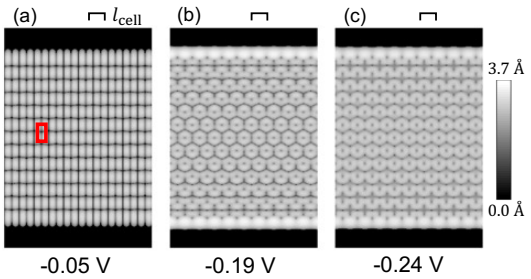

Fig. 2: Simulated STM images of 39-AGNR at different sample biases.

References

[1] J. Li et al., Phys. Rev. B **103**, 245433 (2021).

[2] J. Li et al., Phys. Rev. Res. **6**, 013252 (2024).

Acceleration of DFT calculation code by using GPU

Masao OBATA

Institute of Science and Engineering, Kanazawa University, Kanazawa, Ishikawa 920-1192

Electronic structure calculations based on density functional theory (DFT) and the Kohn-Sham (KS) approach, promising tools for analyzing and predicting the physical properties of materials, are widely used in various fields of material science. Accelerating the DFT code is crucial for promoting such investigation and will expand the application range of DFT calculations. For the speedup of DFT calculation, we considered utilizing GPUs and verified the efficiency of GPU in DFT calculation. Since the data transfer bottleneck between CPU and GPU is a well-known issue, we introduced a simple strategy to minimize data transfer called data GPUization [1]. In the data GPUization concept, we focused on large amounts of data in the DFT calculation, such as wave functions. We implemented GPU calculations in all the operations that handle such large data in the iterative procedure of DFT. As a result, large data transfers are no longer necessary in an iterative procedure. The concept of data GPUization focuses on the data size of variables as well as computational cost. Such a concept effectively reduces data transfers, especially in iterative calculations.

In our research, we implemented GPU calculation in our homemade DFT code, which employed a plane-wave basis with an ultrasoft pseudopotential scheme. The implementation was done using OpenACC and the GPU-accelerated math library provided by NVIDIA HPC SDK. We tested our implementation using ISSP System C (CPU: AMD EMPY 7763, GPU: NVIDIA A100) and compared the computational time with and without GPUs. The performance ratio between 1 CPU core and 1 GPU is around 247 (495 in the case of Tensor Core usage). We used a magnetic 224 atoms (5264 KS orbitals) system for the benchmark. The computational time in one DFT (Car-Parrinello) step was significantly reduced from 5206s in CPU to 49s in GPU without data GPUization. However, the transferred data size was 137GB in one DFT step, accounting for 60% of computational time. The computational time of the data GPUization version was 15s.

Although it was confirmed that using GPUs based on data GPUization drastically accelerates calculations, data GPUization requires large data to be constantly maintained in GPU memory; therefore, one of the future issues is overcoming GPU memory depletion.

References

[1] C. Pardede, M. Obata et al., proceedings of CCP 2023, accepted.

Leakage of surface/interfacial electrons of topological insulators

Ken-ichi Shudo

Fac. Sci/Eng, Yokohama Nat'l Univ.

Tokiwadai 79-5, Hodogaya-ku, Yokohama 240-8501

We have measured the electronic states of Bi_2Se_3, a typical topological insulator, by means of metastable atom electron spectroscopy (MAES), which exclusively detects the leak of electrons from a solid surface into the vacuum. An experimental result is shown in Fig.1. To interpret the spectra, we calculated a slab system of the material, using Vienna ab initio simulation package (VASP). The results of the calculated dispersion showed inconsistency due to the complicated band structure. The band shape depends on the approximation method or the LDA/GGE density functionals. We now measure MAES finely with varied conditions, and will compare them with the calculational results.

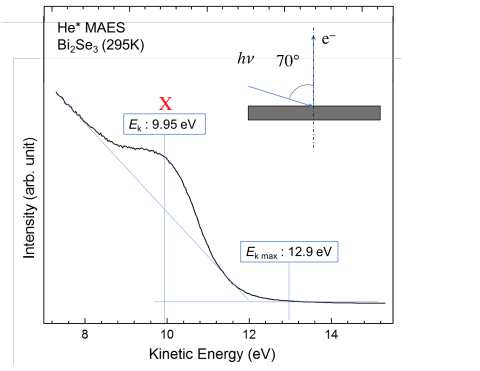

Fig. 1 MAES of Bi_2Se_3 with He* irradiation.

At the same time, we perform calculations of electronic states to elucidate the spin-dependent band structure of metal-organic framework (MOF) of metal-injected porphyrin-derivatives (the project continues from year 2022). At the pore of the porphyrin-core Fe atom is introduced, and the local spin moment remains. The spin state is correlated the linkage-legend (Cu) of MOF. The computational results account for our experimental photo-absorption spectra in magnetic circular dichroism (MCD). However, we noticed that there is intermixing of orbital angular moment and spin angular moment, and found inconsistency between the experimants and calculation in the work-function of the two-dimensional Fe-dosed porphyrin MOF layer. Currently the details are examined still.

Our group has started analysis of bend-symmetry of single crystal of pure Ti, on which optical higher harmonic generation occurs. We assume now that the asymmetry of the optical results originates from the bond strength of the fermi surface in terms of mechanical asymmetry.

Renormalized charge-spin fluctuations from first principles

Ryosuke AKASHI
National Institutes for Quantum Science and Technology

The first-principles calculation for superconductors have recently much advanced with efficient numerical implementations of the first-principles Eliashberg theory [1, 2, 3] and density functional theory for the superconductors (SCDFT [4, 5, 6]). For the phonon-mediated superconductors, those methods enabled non-empirical evaluation of the screened Coulomb interaction, which strongly suppresses the Cooper pairing, and accurate estimation of the resulting transition temperature $T_{\rm c}$. Further extensions of the framework have also been gradually conducted, toward materials regime with intermediately strong correlations.

A representative correlation effect that may become more appreciable in the regime is the spin-fluctuation effect. Recently, Essenberger and colleagues [7] have proposed a method to include the spin fluctuations in the first-principles superconducting calculation with the newly developed exchange-correlation kernel for the SCDFT. We have examined the accuracy in 3d and 4d elemental metals, V and Nb [8]. For those systems, we found that the calculations without the spin fluctuation yield values of $T_{\rm c}$ larger than the experimental values. The spin fluctuation included by the Essenberger formalism suppresses those too much: Although the deviation from the experimental observations is mitigated, the resulting values are too low. This oversuppressing phenomenon is thought to be due to the breakdown of the original formalism, which is based on the adiabatic local density approximation and presumably overestimate the strength of the fluctuation in the vicinity of the magnetic phase transition.

In this project, we have attempted to "renormalize" the strength of the spin fluctuation using the formally exact adiabatic connection formula [9]

$$E_{\rm xc} = E_{\rm x} - \frac{1}{2}\int_0^1 d\lambda \int \frac{d\omega}{2\pi} dr dr' \times \frac{\chi_\lambda[n](r,r';i\omega) - \chi_{\lambda=0}[n](r,r';i\omega)}{|\mathbf{r}-\mathbf{r}'|}. \quad (1)$$

Here, χ_λ denotes the response function for the ground state of the Hamiltonian with interaction scaled by λ: $H = H_0 + \lambda U$, where the external potential in H_0 is tuned so that the ground-state charge density n is constant against λ. The functional derivative with respect to the charge and spin densities gives us exact equations for the spin and charge susceptibilities [10].

We have tested a one-shot method, where we insert the ALDA susceptibilities in the right hand side of the derived equations and evaluated them once. At this point, however, the numerical calculations suffer from instability due to multiple Green's functions entering the equations. Efficient and reliable calculation of the formula is to be pursued in later projects.

We also explored electronic structure in nearly uniform electron model [11]. We analyzed interactions of three plane-wave branches in this model, which occur at linear regions formed by the intersections of the Bragg planes. We found that the band critical lines and Dirac nodal lines are generally formed in the close vicinity of those intersection lines.

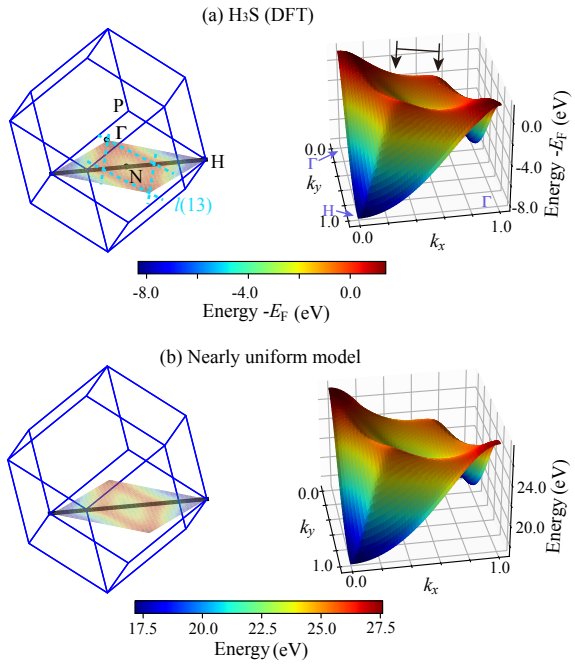

Figure 1: Structure of the valence band that is responsible for the divergence of DOS in H_3S. (a) Result with the first-principles calculation. Arrows on the right indicate the flat region that has dominant contribution to the total DOS. (b) Result with the nearly uniform electron model, with only three model parameters. See Ref. [11] for more details.

Further, we pointed out that the diverging van Hove singularity in a high-temperature superconductor H_3S is well explained by this mechanism. Figure 1(a) shows the energy eigenvalues of the band that is responsible for the DOS singularity, calculated from first principles. In the left panel, we depict the position of the intersection that is the origin of the linearly extended band critical point. By tuning the interaction matrix elements at this intersection, we successfully reproduced the band structure by the nearly uniform model as shown in panel (b). This result clarifies that the apparently anomalous electronic structure in H_3S is actually explained as an example of the general nearly uniform electron theory. The first-principles calculations were performed using Quantum Espresso [12] with norm conserving pseudopotentials from *Pseudo dojo* [13].

References

[1] G. M. Eliashberg, Zh. Eksp. Teor. Fiz. **38**, (1960) 966.

[2] A. B. Migdal, Zh. Eksp. Teor. Fiz. **34**, (1958) 1438.

[3] A. Sanna, J. A. Flores-Livas, A. Davydov, G. Profeta, K. Dewhurst, S. Sharma, and E. K. U. Gross, J. Phys. Soc. Jpn. **87**, (2018) 041012.

[4] M. Lüders, *et al.*, Phys. Rev. B **72** (2005) 024545.

[5] M. A. L. Marques, *et al.*, Phys. Rev. B **72** (2005) 024546.

[6] A. Sanna, C. Pellegrini, and E. K. U. Gross, Phys. Rev. Lett. **125**, (2020) 057001

[7] F. Essenberger *et al.*, Phys. Rev. B **90** (2014) 214504.

[8] K. Tsutsumi, Y. Hizume *et al.*, Phys. Rev. B **102**, (2020) 214515.

[9] D. C. Langreth and J. P. Perdew, Solid State Commun. 17, (1975) 1425.

[10] Y. Hizume, unpublished.

[11] R. Akashi, arXiv:2306.04238.

[12] P. Giannozzi *et al.*, J. Phys. Condens. Matter **29**, (2017) 465901.

[13] G. Pizzi *et al.*, J. Phys. Condens. Matter **32**, (2020) 165902.

Theoretical investigation for systemataising surface diradical

Kohei TADA[1, *]

Department of Materials Engineering Science, Graduate School of Engineering Science, Osaka University, Toyonaka, Osaka 560-8531, Japan

Diradical state is that with two open-shell electrons in pseudo-degenerate orbitals. The state is important for understanding the physical properties originating from strongly correlated intra-/intermolecular electrons [1]. Strongly correlated electrons are the origin of various material functions; hence, novel molecular function will be achieved by immobilising the diradical molecules on surfaces. However, the diradical state of surface-adsorbed molecules (= surface diradical) has not been well studied due to the lack of theoretical and experimental techniques.

In this project, a systematic investigation was performed on the interaction of s- and p-diradical molecules with alkaline-earth metal oxide surfaces. Diradical molecule models with s-orbitals were Au, Ag and Cu dimers with inter-atomic distance where the s-orbitals are pseudo-degenerating. This system was investigated using system B, ohtaka. For the p-orbital diradicals, a real diradical molecule, p-benzyne, was employed. This calculation was performed on system C, kugui. Used programme was VASP. Correction based on the approximated spin projection method to density functional theory calculation with plane-wave basis (AP-DFT/plane-wave) [2,3], which is a recently developed scheme, was used for the analysis of the diradical states.

Diradical character, *y*, is a feature value for diradical molecules, and can be utilised to *in silico* design [1]. The effect of surface-adsorption on diradical character (Δy) can be classified into three effects [4], as shown in Fig. 1: namely, the effect of molecular distortion caused by adsorption (Δy_{dis}), the effect of inter-molecular interactions (Δy_{coh}), and the effect of molecule-surface interaction (Δy_{surf}). Table 1 summarises Δy values of the p-benzyne adsorption models. Details of the calculated models can be found in the cited article [4]. The absolute values of Δy_{surf} are the largest among three effects. The reason why the *y* values of p-benzyne is reduced by the molecule-surface interaction is as following:

(1) Although the computational model is constructed as a physically adsorption of p-benzyne, a slight orbital correlation between the surface ions and the molecule occurs. This causes delocalisation of singly occupied C sp2 orbital to the aromatic ring.

(2) Intramolecular charge polarisation is induced by the charges of the surface ions, and

the spin density is reduced due to the enhanced contribution of the closed-shell resonance structure.

The present study explicitly shows that diradical character of real diradical molecule can be modulated even in weakly adsorbed states, such as physisorption. The results were published from *Physical Chemistry Chemical Physics*, and the paper was selected as the front cover and hot article [4].

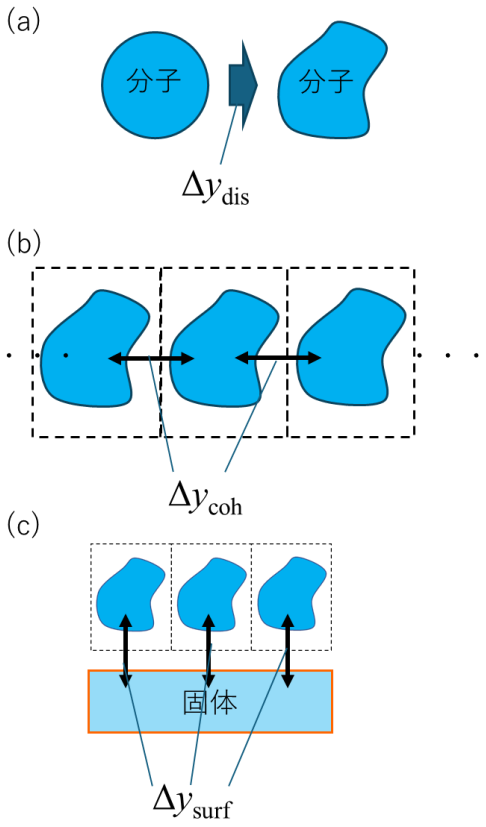

Fig. 1: Schematic views of Δy_{dis} (a), Δy_{coh} (b), and Δy_{surf} (c).

Table 1: Estimated (Δy), (Δy_{dis}), (Δy_{coh}), and (Δy_{surf}) of p-benzyne adsorption models [4]. Negative value indicates the y value of p-benzyne is reduced by the adsorption.

Model	Δy	Δy_{dis}	Δy_{coh}	Δy_{surf}
A	–0.8	+0.2	+0.8	–1.8
B	–5.7	–0.1	–0.6	–5.0
C	–6.0	–0.8	+0.6	–5.7
D	–11.1	–0.7	+0.6	–11.0
E	–5.5	–1.8	+0.6	–4.4

References

[1] T. Stuyver, B. Chen, T. Zeng, P. Geerlings, F. De Proft, R. Hoffinann, Chem. Rev. **119**, 11291 (2019).

[2] K. Tada, H. Ozaki, K. Fujimaru, Y. Kitagawa, T. Kawakami, M. Okumura, Phys. Chem. Chem. Phys. **23**, 25024 (2021).

[3] K. Tada, H. Koga, M. Okumura, S. Tanaka, Chem. Phys. Lett. **701**, 103 (2018).

[4] K. Tada, T. Kawakami, Y. Hinuma, Phys. Chem. Chem. Phys. **25**, 29424 (2023)

* Previous affiliation is National Institute of Advanced Industrial Science and Technology (AIST).

Photoexcited Carrier Dynamics in the CO_2 Photoreduction on Monoclinic-ZrO_2 Surface

Keisuke Hara and Yasuo Izumi

Graduate School of Science,

Chiba University, Yayoi-cho, Inage-ku, Chiba 263-8522

In this report, we evaluated the contribution of photoexcited electrons in the CO_2 photoreduction process occurred on the monoclinic-ZrO_2 photocatalytic surfaces. While exploring the reaction pathway through the ground state has already been done [1], the clarification of the role of excited electrons is indispensable because it directly describes the essence of photocatalytic process.

Although the final steps in the reaction mechanism normally differ among the catalysts, the onset steps often follow the mechanism in which CO_2 adsorbs on the surface, and photoexcited electrons are injected into CO_2 from the substrate. In these early stages of photocatalytic reaction pathway, the reaction can be classified into two types: Type I where excited electrons are injected into the adsorbed CO_2, forming a CO_2 anion radical and Type II where proton addition first takes place, forming an OC^+OH species. Therefore, in ZrO_2, which exhibits higher photocatalytic activity in the CO_2 reduction compared to transition metal oxides, this study elucidates whether Type I or Type II occurs predominantly over ZrO_2 photocatalyst.

Density Functional Theory (DFT) calculations were performed using the Vienna Ab initio Simulation Package (VASP) version 6.4.1.The projector-augmented wave method was employed at the DFT-D3 level to incorporate the van der Waals interaction. The generalized gradient approximation RPBE exchange-correlation functional was used for series of calculations including AIMD, with the cutoff set at 500 eV and adding Hubbard *U* parameter (4.0 eV for Zr). To further track the behavior of the photoexcited electrons, we conducted ab initio Non-Adiabatic Molecular Dynamics (NAMD) calculations. NAMD calculations are based on time-dependent Kohn-Sham theory combined with a fewest-switches surface hopping algorithm in the classical Path approximation [2, 3].

A series of calculations confirmed that adsorbed CO_2 on the pristine surface followed a Type II reaction pathway. In clear contrast, when CO_2 adsorbed at oxygen vacancies, the reaction step followed a Type I pathway. When CO_2 adsorbed at the oxygen vacancy, it bent upon adsorption, reducing the energy level of LUMO and LUMO+1 toward lower direction compared to straight configuration. The LUMO+1 level of bent CO_2 lay just below the Conduction Band Minimum of ZrO_2 and, hence, the excited

electrons were likely to relax to the LUMO+1 level. As the result, within 500 fs, 55% of the photoexcited electrons were injected into the LUMO+1 level of CO_2 after the photoexcitation (Figure 1, the line of CO_2 LUMO+1).

In contrast, there are the energy levels of CO_2 adsorbed on the pristine surface (not shown). The energy of these levels negligibly changed with the initial 500 fs. Even when photoexcited electrons were injected, these electrons quickly relaxed to the lower energy levels of ZrO_2 conduction band; the excited electrons could not be trapped for a long time. Thus, the ability of CO_2 to trap the excited electrons within its molecular orbital(s) was responsible for the formation of CO_2 anion radicals.

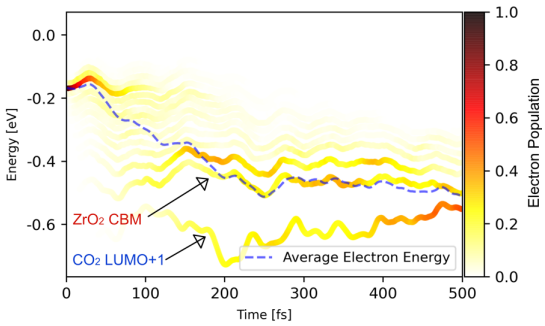

Figure 1. Time course of the relaxation of excited electrons in energy domain. The color strips indicate the normalized electron distribution at each energy state, and the blue dotted line represents the averaged electron energy.

As a future challenge, it is necessary to perform similar calculations on the other typical transition metal oxides, e.g. TiO_2 and In_2O_3, for photocatalyst to elucidate how the initial stages of the CO_2 photoreduction reaction impact on the overall photocatalytic reaction. Furthermore, it is important to clarify whether the rate of electron injection into the molecular orbitals of CO_2 dominates the reduction activity.

References

[1] Hara, K., Nozaki, M., Hirayama, R., Ishi, R., Niki, K., Izumi, Y., *J. Phys. Chem. C,* 2023, 127, 4, 1776–1788

[2] Akimov, A.V., Prezhdo, O.V., *J. Chem. Theory Comput.* 2013, 9(11), 4959–4972.

[3] Zheng, Q., Chu, W., Zhao C, *et al*., *WIREs Comput Mol Sci*. 2019, 9, e1411.

Ab initio path-integral molecular dynamics calculation of high pressure phases of ice

Jun TSUCHIYA
Geodynamics Research Center, Ehime University
Bunkyo-cho, Matsuyama, Ehime 790-8577

Determining the structures and physicochemical properties of water ice (H_2O) is fundamental across various scientific disciplines like physics, chemistry, earth and planetary sciences. Although numerous experimental and theoretical studies have been performed on the twenty known crystalline polymorphs of ice, their physical and chemical properties are not yet fully understood. A key challenge lies in the elusive nature of hydrogen, the lightest atom, with its extreme mobility and significant quantum effects posing difficulties for the experimental and theoretical investigations.

At high pressures, the behavior of ice becomes particularly complex. Previous studies indicate that in the ice VII to ice X transition, hydrogen shifts from a static to dynamically disordered state, eventually reaching symmetric hydrogen bonding states. In dynamically disordered hydrogen state, hydrogen atoms oscillate between two minima between oxygen atoms due to thermal and quantum vibrational effects. Recently, we have begun to study the structural, elastic, and vibrational properties of the high-pressure phases ice using ab initio path integral molecular dynamics (PIMD) calculations, in order to clarify the nuclear quantum effects (NQEs) on these properties (Figure 1) [1] .

The radial distribution function (RDF) of ice VII under pressure highlights the enhanced appearance of dynamically disordered hydrogen states at lower pressures in PIMD than in AIMD due to NQEs. Furthermore, a comparison of PIMD and AIMD calculations under similar conditions reveals the significant influence of NQEs on the elastic constants. At the transition from static to dynamically disordered hydrogen states, the elastic constants increase non-linearly at room temperature and high pressure around 40 GPa under the influence of NQEs. We found that the NQEs contribute significantly to the increase in the elastic constants of the dynamically disordered phases (about 20% at 300 K and 70 GPa). This study shows that NQEs have a significant influence on macroscopic properties such as elasticity even at room temperature.

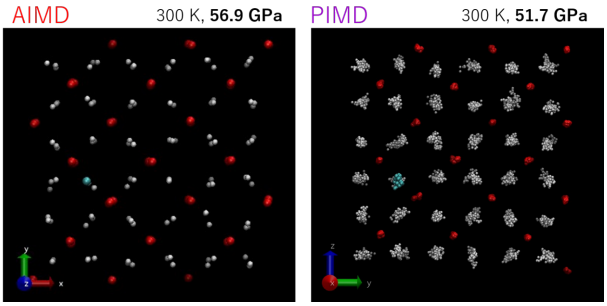

Figure 1: The snapshots of the AIMD (left) and PIMD (right) simulation of ice VII at high pressure condition.

References

[1] J. Tsuchiya, M. Shiga, S. Tsuneyuki, E.C. Thompson, preprint [arXiv:2307.14214].

First-principles study of electron interactions in transiton metal oxides

Hirofumi Sakakibara

Advanced Mechanical and Electronic System Research Center(AMES), Faculty of Engineering, Tottori University, 4-10 Koyama-cho, Tottori, Tottori 680-8552, Japan

In the history of condensed matter physics, one of the biggest topics is about cuprate high-T_c superconductors. Several theoretical studies have shown that the cuprates have ideal electronic structure for superconductivity triggered by spin-fluctuation and/or Mott physics. Theoretically, the cuprates may be described by a two-dimensional single-orbital Hubbard model on the half-filled square lattice, and this situation enhances *d*-wave superconductivity. Here, the term of the Hubbard model means a model that only onsite interaction U and the hopping integrals between the nearest neighbor sites are considered. The reason why the cuprates are recognized as ideal is that U/t value, a measure of electron correlation, is almost optimized for T_c. This implies that there are few rooms for improvement for materials described by single-orbital Hubbard models.

However, bilayer Hubbard models are theoretically investigated as candidates that go beyond the single orbital Hubbard model [1]. In bilayer models, the key value is the strong interlayer coupling $t_\perp$ and the Heisenberg exchange interaction $J{\sim}4t_\perp^2/U$. Namely, the Cooper pair is formed between different layers. Nakata et al. predicted a possibility that strong $t_\perp$ and paring is realized by the $d_{3z^2-r^2}$ orbitals spread along interlayer direction in a Ruddlesden-popper type bilayer nickelate $La_3Ni_2O_7$ [2]. In 2023, Sun et al. have reported that $La_3Ni_2O_7$ exhibit superconductivity with $T_c \sim 80$ K after structural transition under pressure of $P = 10{\sim}20$ GPa [3]. Inspired by these theory and experiment, we have started several theoretical works and collaborations between theoretical-experimental investigation.

We have modeled the electronic structure of $La_3Ni_2O_7$ using a combination between a first-principles calculation in local density approximation and the maximally localized Wannier method [4]. The figure 1 shows the electronic structure and the schematic picture of the constructed four-orbital Hubbard model, which contains the $d_{x^2-y^2}$ and $d_{3z^2-r^2}$ orbitals. By adopting the fluctuation exchange approximation (FLEX) to the model, we have obtained the green's function of dressed particles with self-energy triggered by spin- and charge-fluctuations. We have obtained an eigenvalue λ, which can be used as

a measure of T_c, plugging the green's function into the linearized Eliashberg equation. We have judged that λ~0.6 of $La_3Ni_2O_7$ is as high as that of cuprates ($\lambda \sim 0.5-0.8, T_c \sim 40-135$ K) and this explains the experimental observed T_c (~ 80 K) [5]. The superconducting gap function, which is obtained as an eigen function of linearized Eliashberg equation, can be regarded as a spin-fluctuation mediated *s*-wave superconductivity in which the sign is inverted between bonding and anti-bonding bands formed by the $d_{3z^2-r^2}$ orbitals [5].

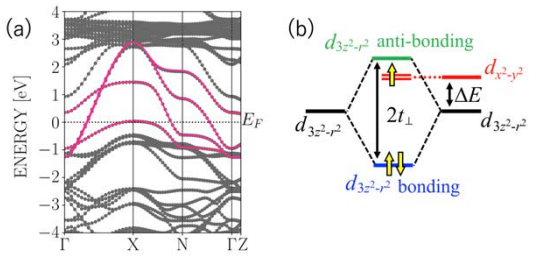

Fig. 1: (a) First-principles electronic structure (gray) and four-orbital model (magenta) of $La_3Ni_2O_7$. (b) shows a schematic picture of the model

Based on the analysis method, we have also investigated $La_4Ni_3O_{10}$, a trilayer member of Ruddlesden-popper type nickelates, in a collaboration with experimental group of Prof. Takano from NIMS. In this collaboration, we theoretical group predicted that $La_4Ni_3O_{10}$ can structurally transit to tetragonal symmetry as in $La_3Ni_2O_7$ by performing first-principles structural optimization and phonon calculation [6]. By performing FLEX calculation as the case of $La_3Ni_2O_7$, we have obtained λ of $La_4Ni_3O_{10}$ about 0.4, which means that a $La_4Ni_3O_{10}$ can exhibit a superconductivity with $T_c \sim 20$ K [6]. After the calculation, Takano's experimental group have found that the $La_4Ni_3O_{10}$ exhibit superconductivity with $T_c \sim 23$ K [6]. This means that our theoretical analysis predicted the superconductivity of $La_4Ni_3O_{10}$ before the experimental discovery.

To summarize, by using first-principles calculations, we have modeled the pressurized state of two Ruddlesden-popper type nickelates, $La_3Ni_2O_7$ and $La_4Ni_3O_{10}$, to investigate superconductivity. The superconducting nature may be the spin-fluctuation mediated *s*-wave superconductivity with pairs formed between different layers. The eigenvalue λ in FLEX explains the experimental T_c.

References

[1] R. T. Scalettar, J. W. Cannon, D. J. Scalapino, and R. L. Sugar, Phys. Rev. B **50**, 13410 (1994).

[2] M. Nakata, D. Ogura, H. Usui, and K. Kuroki, Phys. Rev. B **95**, 214509 (2017).

[3] H. Sun et al., Nature (London) **621**, 493 (2023).

[4] N. Marzari and D. Vanderbilt, Phys. Rev. B **56**, 12847 (1997).

[5] H. Sakakibara, N. Kitamine, M. Ochi, K. Kuroki, Phys Rev. Lett. **132**, 106002 (2024).

[6] H. Sakakibara et al., Phys. Rev. B **109**, 144511 (2024).

Electronic Structure and the Fermi surface of ReO_3

Takahiro Maehira
Faculty of Science, University of the Ryukyus, Nishihara, Okinawa 903-0213

Rhenium trioxide is an inorganic compound with the formula ReO_3. It is a red solid with a metallic luster that resembles copper in appearance. It is the only stable trioxide of the Group 7 elements. Rhenium trioxide exhibits extremely low electrical resistance not found in ordinary metal oxides. They are also similar to metals in that their resistance decreases as the temperature decreases. At around 78 K, it exhibits conductivity comparable to silver, which the highest electrical conductivity of any metal[1, 2]. ReO_3-type structures can be described as ABX_3 perovskites in which the A-cation site is unoccupied. They therefore have the general composition BX_3, where B is normally a cation and X is a bridging anion. The chemical diversity of such structures is very broad, ranging from simple oxides and fluorides, such as WO_3 and AlF_3, to more complex systems in which the bridging anion is polyatomic, as in the Prussian blue-related cyanides such as $Fe(CN)_3$ and $CoPt(CN)_6$. We studied cubic ReO_3 with a space group of Pm3m. The calculation for the energy band structures was carried out by using the OpenMX code(`http://www.openmx-square.org/`).

First, we discuss the calculated results for ReO_3 as shown in Figure 1, in which we depict the energy band structure along the symmetry axes in the Brillouin zone, which is shown in Figure 1, in the energy region from -25.0 to 25.0 eV. The Fermi level E_F is at 0.0 eV. for ReO_3 and indicated by dashed lines in Figure 1. With respect to the energy band structure near E_F, we emphasize that there is always hybridization between the Re 5d and O 2p states in ReO_3.

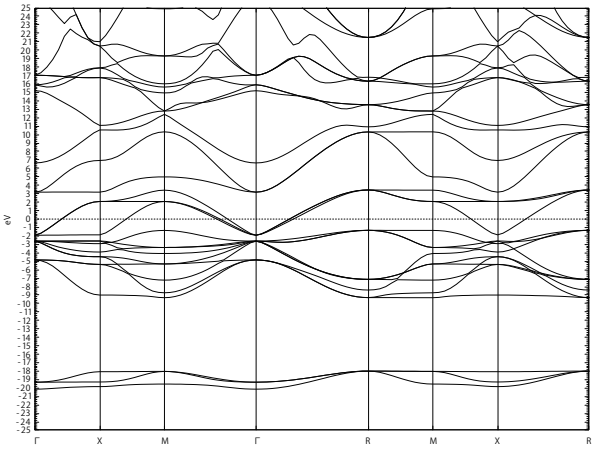

Figure 1: The energy band structure for ReO_3. E_F indicates the position of the Fermi level.

The total number of holes is equal to that of electrons, which represents that ReO_3 is a compensated metal. Since the lowest twelve bands are fully occupied, as shown in Figure 1, the next three bands are partially occupied, while higher bands are empty. This compound is compensated metal because of having two chemical units in the unit cell.

We move to discuss the Fermi surface of ReO_3. Three bands cross the E_F, therefore ReO_3 has three Fermi surfaces in Figure 2. The 13th, 14th and 15th bands construct the Fermi surface. The color on the Fermi surface illustrates the distribution of the Fermi velocity components. Fermi surfaces for ReO_3 centered at the Γ points, respectively. The 13th band construct large hole sheet centered at the Γ point and multiply connected with six arms along $\langle 100 \rangle$ direction, as shown Figure 2(a). The 14th band construct electron sheet cen-

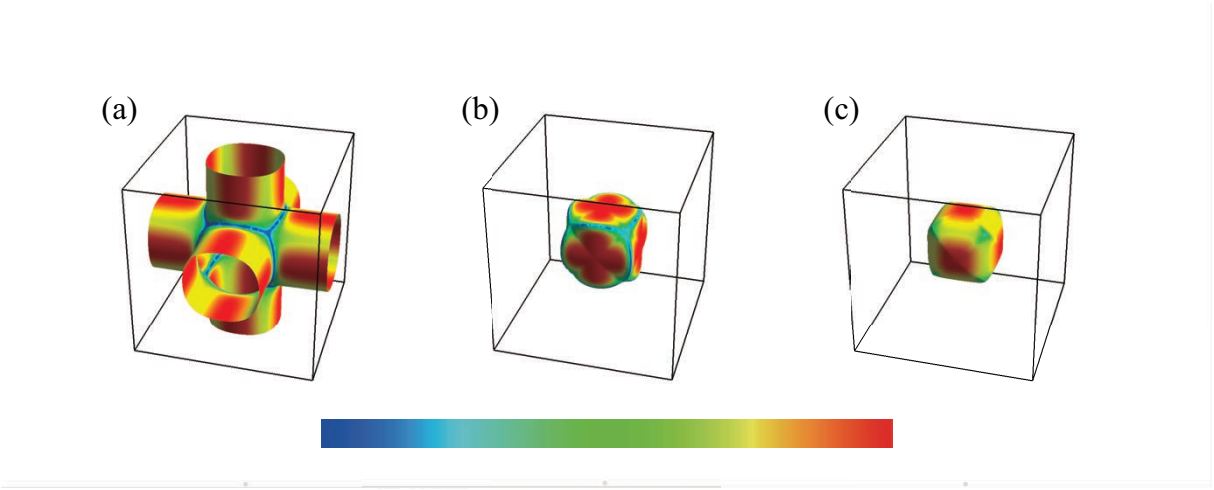

Figure 2: Calculated Fermi surfaces of ReO_3 for (a) 13th band hole sheet, (b) 14th band electron sheet, and (c) 15th band electron sheet. Colors indicate the Fermi velocity components on the Fermi surface. Red-shift indicate the increase of the Fermi velocity components. The center of the Brillouin zone is set at the Γ point.

tered at the Γ point and its shape is almost cubic, as shown Figure 2(b). The 15th band construct small electron sheet centered at the Γ point and its shape is almost cubic, as shown Figure 2(c).

The calculated total density of states (DOS) for ReO_3 is shown in Figure 3, in the energy region from -25.0 to 25.0 eV. The total density of states for ReO_3 is shown by the solid black line and the s, p, d and f states are shown by the solid color lines, respectively. This figure tells us that the DOS of the d states is higher than that of the f states at the Fermi level.

We have applied the band calculation of the electronic structure of ReO_3 based on the itinerant electrons by assuming a non-magnetic phase. We found that the hybridization between Re $5d$ and O $2p$ states occurs near E_F. The Fermi surfaces for ReO_3 are composed of one hole sheet and two electron sheets. The Fermi surface in the 13th band is multiply connected with the arms so some open orbits are expected to pass along the arms in some range of angles. We analyzed the existence of the open orbits in the ⟨100⟩ directions on the Fermi surface for ReO_3.

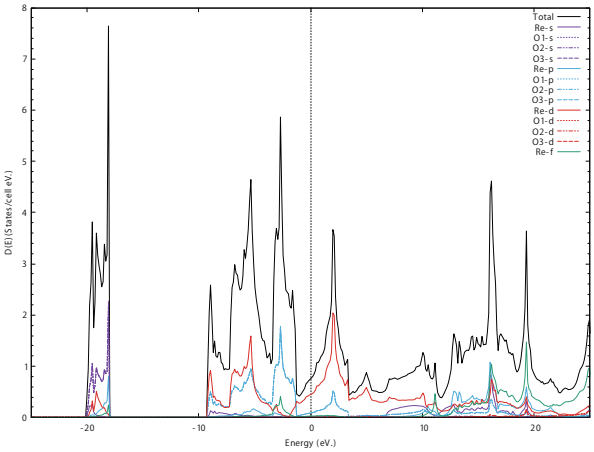

Figure 3: The density of states for ReO_3. E_F indicates the position of the Fermi level shown by the dashed line.

References

[1] A. Ferretti, D. B. Rogers, J. B. Goodenough: J. Phys. Chem. Solids **26** (1965) 2007.

[2] T. P. Pearsall, C. A. Lee: Phys. Rev. B. **10** (1947) 2190.

Theoretical Study on Electronic Properties in New Nanoscale Surfaces and Interfaces

Katsuyoshi KOBAYASHI
Department of Physics, Ochanomizu University
2-1-1 Otsuka, Bunkyo-ku, Tokyo 112-8610

We theoretically studied the magnetic structure of V_5Se_8 monolayers. V_5Se_8 is a layered material composed of VSe_2 layers and V intercalant layers. It is known that bulk V_5Se_8 has an antiferromagnetic structure at low temperatures. However, ferromagnetic behavior has been observed in a recent experiment of V_5Se_8 thin films [1]. We studied the magnetic sturtcure of V_5Se_8 monolayers by a density functional method in 2023. We used the program package VASP for density-functional calculations.

First we calculated the magnetic structure of bulk V_5Se_8. It is established that the V atoms of the intercalant layer have magnetic moments, and the magnetic moments in the VSe_2 layers are zero or negligible. The experimental value is 1.2 μ_B. The calculated values are 1.79 and 1.57 μ_B by GGA and LDA, respectively. Though the calculated values are larger than the experimental one, the LDA calculation better reproduces the experimental one. They are calculated at the experimental lattice constant. The lattice constant is better reproduced by GGA than LDA. The deviation from the experimental value is 0.9 % by GGA and -2.2 % by LDA. The minus sign means contraction.

Next we calculated the magnetic structure of a V_5Se_8 monolayer. Figure 1 shows the atomic structure of the V_5Se_8 monolayer studied in our calculation. First both the structural optimization and magnetic structure calculation were performed using GGA. It was found that a ferromagnetic structure has the lowest total energy among various magnetic structures considered in our calculation. In addition to the V atoms in the intercalant layers, those in the VSe_2 layers also have magnetic moments. This seems a surface effect.

The structural optimization and magnetic structure calculation also were performed using LDA. In this case the nonmagnetic structure has lower energy than magnetic ones. This result arises from the short interlayer distances optimized by LDA. Figure 2 shows the magnetic moment calculated as a function of the interlayer distance. When the interlayer distance is short, the energy gain due to exchange interaction is relatively reduced, which favors the nonmagnetic state. Since the bulk lattice constant is better reproduced by GGA, it seems better to use GGA for structural optimization and LDA to estimate magnetic moments.

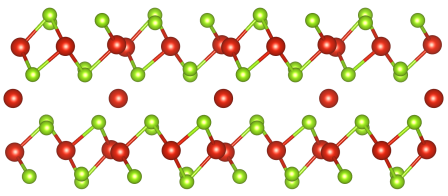

Figure 1: Atomic structure of a V_5Se_8 monolayer.

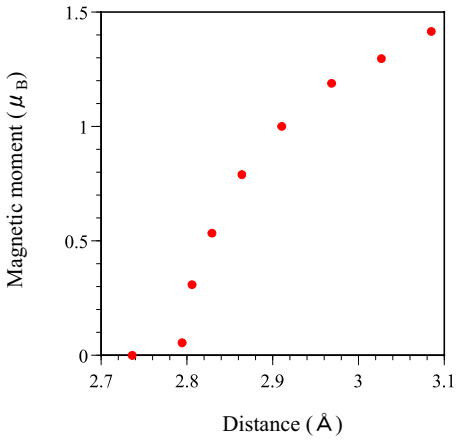

Figure 2: Magnetic moment of V atoms in the intercalant V layer of the V_5Se_8 monolayer calculated by LDA as a function of the distance between a V atom in the intercalant V layer and its nearest neighbor V atom in the VSe_2 layer. The distances optimized by LDA and GGA are 2.74 and 3.03 Å, respectively. The bulk distance is 2.95 Å.

References

[1] M. Nakano *et al.*: Nano Lett. **19** (2019) 8806.

Electronic stress tensor density analysis for material surfaces

Masahiro FUKUDA

Institute for Solid State Physics,

The University of Tokyo, Kashiwa-no-ha, Kashiwa, Chiba 277-8581

The electronic stress tensor density is a fundamental local physical quantity which is defined as the space-space components of the energy momentum tensor in the framework of quantum field theory. Since a half of the trace of the electronic stress tensor is related with the total energy of the system under the virial theorem, the analysis of the electronic stress tensor gives mechanical aspect of the chemical bond [1]. On the other hands, the material surface is important concept to discuss chemical reactivity, molecular absorptions, and force spectroscopy of atomic force microscopy. The surface defined by the zero kinetic energy density play a role as an electronic interface. The boundary surface of the positive-to-negative reversal of the kinetic energy density is consistent with the concept of the surface of materials in classical theory.

In this research, we revealed that the energy density constructed from the electronic stress tensor at the materials surface represents localization of the electronic charge density. We also found that the physical quantity expressed as the electron number density derivative of the energy density corresponds to the regional chemical potential, and its value at the material surface allows us to visualize areas prone to chemical bonding, such as dangling bonds and π -bonds. This should lead to a better understanding of the experimental observation of AFM images using atomic attractive force. This analysis of regional chemical potentials is also expected to lead to the development of a method for predicting crystal growth processes occurring on the surface of materials due to molecular adsorption, etc., from the electronic steady state before the reaction.

We are currently working on the evaluation of regional chemical potentials using post-process calculations for the electronic structure of 2D materials [2] and surface materials [3] obtained by DFT calculations using OpenMX [4].

References

[1] A. Tachibana, New Aspects of Quantum Electrodynamics, Springer, 2017.

[2] M. Fukuda and T. Ozaki, Phys. Chem. Chem. Phys., **26**, 3367 (2024)

[3] R. Zhang *et. al*., arXiv:2403.17427 [cond-mat.mtrl-sci]

[4] OpenMX, http://www.openmx-square.org

Search and realization of novel electronic properties of surfaces and interfaces and of nanostructures

Takeshi INAOKA
Department of Physics and Earth Sciences, Faculty of Science, University of the Ryukyus, 1 Senbaru, Nishihara, Okinawa 903-0213

Using the van-der-Waals density functional theory, we have been investigating the electronic structure of x-form phthalocyanine (Pc) crystals and the iodine (I) doping effect on this structure. We employ the program package 'Vienna Ab initio Simulation Package' (VASP) [1-4] on system B (ohtaka) in the present study.

The Pc is a planar π-conjugated macrocyclic molecule which can include an atom of various species at its center position. The x crystal is constituted of a square-lattice arrangement of molecular chains with double period and with molecular planes normal to the stacking direction. Doped iodine I atoms can enter one-dimensional open channels between these molecular chains.

(A) x-SiPc and x-SiPcI crystals

Although the synthesis of x-SiPc crystals is still in its infancy, we chose Si for center atoms, because we found that SiPc molecules (monomers) have Si p_z derived orbitals right above the LUMO, which may overlap each other in the x-form stacking.

Last academic year, we elucidated the following points:
(1) Because Si atomic chains dimerize, Si p_z orbitals cannot form metallic bands.
(2) The staggering angle becomes 40°, because H_2-like bonding orbitals are created between laterally neighboring molecular planes.
(3) I doping decreases the band occupancy from half-filling, as is observed experimentally as the Mott insulator-metal transition.
(4) If we assume equally spaced I atomic chains, they form metallic bands with an effective-mass ratio of 0.15.

This academic year, we examined the stability of equally spaced I atomic chains. We calculated the force working on an I atom when it is displaced in the chain-axis direction and the electronic structure is optimized with atom positions fixed. We found that the restoring force operates on each I atom displaced. The arrangement of x-SiPc chains act to create equally spaced I atomic chains.

According to X-ray analysis, the I atoms, whose average positions are equally spaced, have elongated temperature factors along the chain axis. This is interpreted as indicating that I atomic chains are trimerized without interchain correlations. Therefore, we analyzed the stability of trimerized I atomic chains in x-SiPcI crystals. We considered crystals with six-fold period in the stacking direction, and performed structure optimaization assuming formation of trimers. The result is exhibited in Fig. 1. This trimerization turned out to lower the total energy by 58.6 meV per unit cell. The I-I bond length in each trimer is 3.00Å, and the distance between neighboring trimers is 3.58Å. The

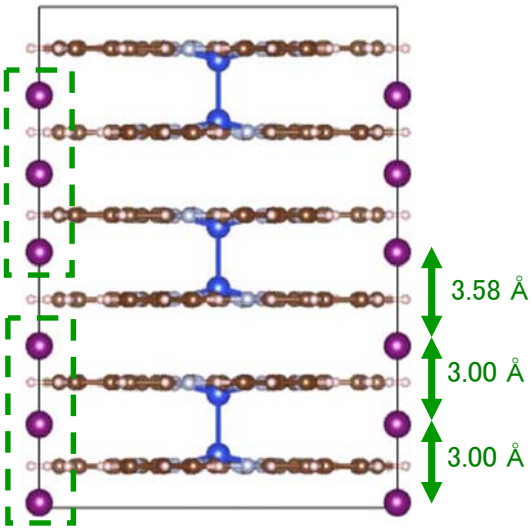

Fig. 1 Side view of the x-SiPcI crystal structure with trimerized I atomic chains.

trimerization induces a band gap at E_F, which prevent I atomic chains from making metallic bands. The SiPc chains operate to create equally space I atomic chains, while the I atoms try to form trimerized chains. These effects compete with each other, but the trmirization effect is larger.

(B) LiPc chian

In preparation for next year's study of x-LiPc and x-LiPcI crystals, we analyzed the electronic structure of a single x-LiPc chain. This molecular chain has a double period in the stacking direction, and two molecules in a primitive unit cell are stacked face-to-face with a staggering angle of 45°. Figure 2 exhibits the band dispersions on the Γ-Z line. A pair of the bands b185 and b186 are formed by band folding at E_F at the Z point. The bands b185～b190 with significant dispersions originate from π electrons. Figure 3 show the electron-density distributions (isosurfaces) of those two states at E_F which are formed by π electrons. The orbital of each state is localized to one of the two molecules in the unit cell, and each state is occupied by one electron, namely, an unpaired electron. Although our band theory cannot treat Mott insulators directly, presence of these unpaired electrons strongly suggests appearance of Mott insulators, as is observed experimentally [5]. By chemical I doping and dedoping, Teruya et al. successfully converted insulators of x-LiPc to metals of x-LiPcI and vice versa reversibly [5].

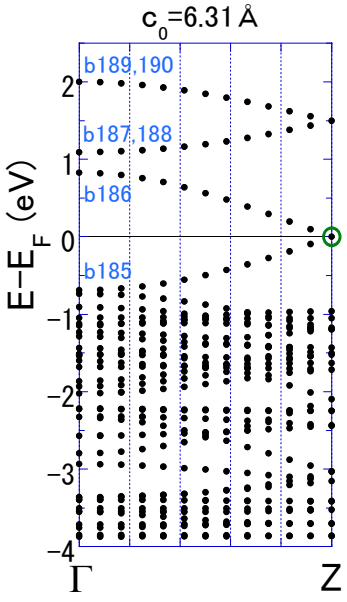

Fig. 2 Band dispersions on the Γ-Z line of a single x-LiPc chain. The green circle represents the two degenerate states at E_F.

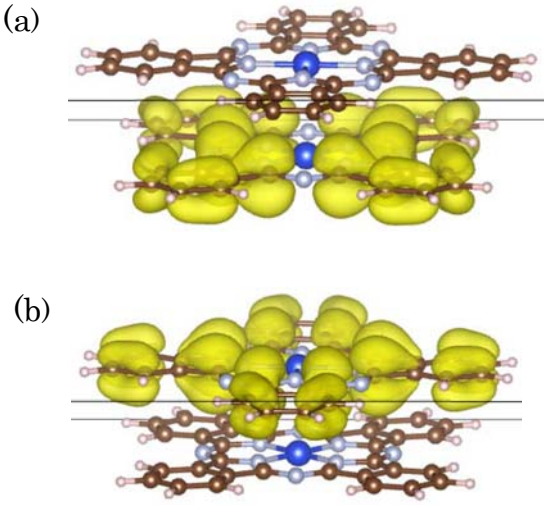

Fig. 3 Electron-density distributions (isosurfaces) of the two degenerated states at E_F at the Z point, as marked by the green circle in Fig. 2.

Next academic year, we examine the electronic structure of x-LiPc and x-LiPcI crystals and the I doping effect. We will be able to elucidate how I doping affects the band structure, and induce the insulator-metal transition, and what the electron states of I atomic chains are like.

References

[1] G. Kresse and J. Hafner: Phys. Rev. B **47**, 558-561 (1993).
[2] G. Kresse and J. Furthmüller: Comput. Mat. Sci. **6**, 15-50 (1996).
[3] P. E. Blöchl: Phys. Rev. B **50**, 17953 (1994).
[4] J. Klimeš, D. R. Bowler, and A. Michaelides: Phys. Rev. B **83**, 195131 (2011).
[5] R. Teruya et al.: Angew. Chem. Int. Ed. **61**, e202206428 (2022).

First-principles study on designing magnetic tunnel junctions from a viewpoint of Néel temperature

Katsuhiro Tanaka
Department of Physics, University of Tokyo, Hongo, Bunkyo-ku, Tokyo 113-0033

Mn_3Sn, an antiferromagnet with non-collinear spin texture, is a promising candidate for realizing the antiferromagnetic spintronics devices. Its magnetic structure, which is tightly connected to the topological electronic structure, has caused experimental observations of the tunnel magnetoresistance (TMR) effect [1] as well as the anomalous Hall and anomalous Nernst effects [2] in antiferromagnets. Studies on the ferromagnetic materials have suggested that thermal fluctuations at the interface between magnetic materials and insulators will depress the TMR effect also in the antiferromagnetic systems. Hence, from an application point of view, we believe that it is essential to enhance the Néel temperature of Mn_3Sn, which is typically 420 K. In this numerical study, we aim to search for suitable elemental substitutions that will increase the Néel temperature in Mn_3Sn.

First-principles calculations in random substitution systems were performed using the coherent potential approximation (CPA). We built a classical spin Hamiltonian for each doping system as follows:

$$\mathcal{H} = -2\sum_{i<j} J_{ij}(n_i, n_j)\boldsymbol{s}_i \cdot \boldsymbol{s}_j. \qquad (1)$$

Here, $J_{ij}(n_i, n_j)$ is the exchange coupling constants between i-th and j-th up to a cutoff length $2a$, where a is the lattice constant depending on the constituent elements. The normalized classical spin moment at the $i(,j)$-th site is denoted by $\boldsymbol{s}_{i(,j)}$. The dependence of the coupling constants on the kinds of the atoms n_i and n_j were calculated based on first principles calculation using the Korringa-Kohn-Rostoker (KKR) Green function method and the Liechtenstein formula [3] in the paramagnetic local moment disordered states, which has been implemented on the AkaiKKR code [4, 5].

Conducting the naive Monte Carlo (MC) simulations on the above Hamiltonian, we determined the Néel temperature from the peak of the magnetic heat capacity. Each MC simulation runs 100,000 MC steps for relaxation and 100,000 MC steps for the calculation of the magnetization for 5–10 atomic arrangements constructed with different random number sequences.

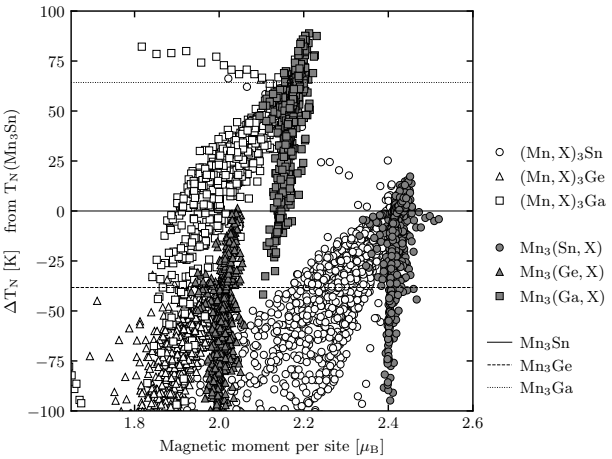

Figure 1: Variation of the Néel temperature of Mn_3Sn, Mn_3Ge, and Mn_3Ga with chemical substitution estimated by first-principles calculations.

By using the above methodology, we confirmed that the calculated Néel temperatures for Mn_3Sn, Mn_3Ga, and Mn_3Ge, which have

similar crystal and magnetic structures, semi-quantitatively reproduce the relative values of the experimental measurements. Furthermore, we carried out comprehensive calculations on systems with approximately 60 different elements substituted at levels ranging from 0–20% in the base materials. These calculations identified elements that contribute to an increase in the Néel temperature upon substitution (Fig. 1) [6].

References

[1] X. Chen, T. Higo, K. Tanaka *et al.*, Nature **613**, 490 (2023).

[2] S. Nakatsuji *et al.*, Nature **527**, 212 (2015); M. Ikhlas *et al.*, Nature Phys **13**, 1085 (2017); S. Nakatsuji and R. Arita, Annu. Rev. Condens. Matter Phys. **13** (2022).

[3] A. I. Liechtenstein *et al.*, J. Magn. Magn. Mater. **67**, 65 (1987).

[4] AkaiKKR (Machikaneyama, private version). http://kkr.issp.u-tokyo.ac.jp/

[5] T. Fukushima *et al.*, Phys. Rev. Materials **6**, 023802 (2022).

[6] Y. Toga, K. Tanaka *et al.*, in preparation.

Ab-initio MD simulation for molten $RbAg_4I_5$

Shuta TAHARA[1] and Yuki KANAE[2]

[1]*Department of Liberal Arts and Sciences,*

Chukyo University, 101-2 Yagoto Honmachi Showa-ku, Nagoya, Aichi 466-8666

[2]*Department of Physics and Earth Sciences, Graduate School of Engineering and Science,*

University of Ryukyus, 1 Senbaru Nishihara-cho, Nakagami-gun, Okinawa 903-0213

We have been carried out experimental and theoretical studies with an interest in the diffusion mechanism of Ag ions diffusing in solids, such as AgI and $RbAg_4I_5$ and its molten phases [1-3]. In our earlier studies using classical MD, we succeeded in roughly reproducing the characteristics of the structure factor $S(Q)$ obtained experimentally, but there was a problem that the accuracy was somewhat low for short range distribution. Therefore, we carried out first-principles MD simulations using Quantum Espresso software and the supercomputers ohtaka and kugui in an attempt to derive a more accurate structural model. Fig 1 shows comparisons of the $S(Q)$ of molten $RbAg_4I_5$. The present FPMD results well reproduce the experimental data, including the high wavenumber side of S(Q), indicating that the short-range order is well reproduced. In addition, a characteristic distribution of connected Ag ions was observed in the derived structural model.

We reported these results in the conference held by the molecular simulation society of Japan.

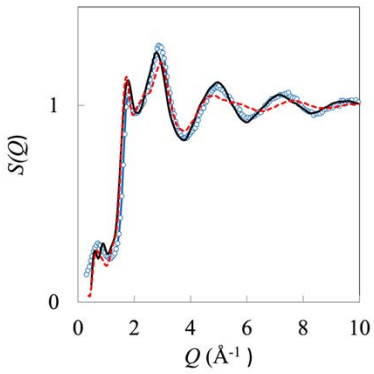

Fig. 1: Structure factors of molten $RbAg_4I_5$. Open circles [1], red dotted curve [1], and black curve indicate experimental data, classical MD, and FPMD of this study, respectively.

References

[1] S. Tahara and T. Fukami, J. Phys. Soc. Jpn. **84**, 024602 (2015).

[2] S. Tahara et al., J. Chem. Phys. **143**, 044509 (2015).

[3] S. Tahara, et al., EPJ Web conf. **151**, 03006 (2017).

A Moiré Model of Si(111)-√7×√3-In Surface

Kazuyuki UCHIDA

Kyoto Sangyo University, Kamigamo-Motoyama, Kyoto, 603-8555

Using ab-initio calculations based on the density functional theory, we have successfully constructed a new superstructure model for the Si(111)-√7×√3-In surface [1-4]. The model explains the long-range image observed in STM experiments [5] and the band structure obtained by ARPES experiments [6], being more effective than the previous model [7,8] which only replicated the ARPES experiment. We have also shown that the arrangement of bright spots in the STM image can be interpreted as a one-dimensional moiré. The calculations were conducted using the RSDFT program package [9,10] combined with a band-unfolding tool.

References

[1] J. Kraft, S. L. Surnev, and F. P. Netzer, Surface Science 340, 36 (1995).

[2] T. Zhang, P. Cheng, W. -J. Li, Y. -J. Sun, G. Wang, X. -G. Zhu, K. He, L. Wang, X. Ma, X. Chen, Y. Wang, Y. Liu, H. -Q. Lin, J. -F. Jia, and Q. -K. Xue, Nat. Phys. 6, 104 (2010).

[3] T. Uchihashi, P. Mishra, M. Aono, and T. Nakayama, Phys. Rev. Lett. 107, 207001 (2011).

[4] S. Yoshizawa, T. Kobayashi, Y. Nakata, K. Yaji, K. Yokota, F. Komori, S. Shin, K. Sakamoto, and T. Uchihashi, Nature Commun. 12, 1462 (2021).

[5] S. Yamazaki, Y. Hosomura, I. Matsuda, R. Hobara, T. Eguchi, Y. Hasegawa, and S. Hasegawa, Phys. Rev. Lett. 106, 116802 (2011).

[6] E. Rotenberg, H. Koh, K. Rossnagel, H. W. Yeom, J. Scha ̈fer, B. Krenzer, M. P. Rocha, and S. D. Kevan, Phys. Rev. Lett. 91, 246404 (2003).

[7] J. W. Park and M. H. Kang, Phys. Rev. Lett. 109, 166102 (2012).

[8] K. Uchida and A. Oshiyama, Phys. Rev. B 87, 165433 (2013).

[9] J. -I. Iwata, D. Takahashi, A. Oshiyama, B. Boku, K. Shiraishi, S. Okada, and K. Yabana, J. Comput. Phys. 229, 2339 (2010).

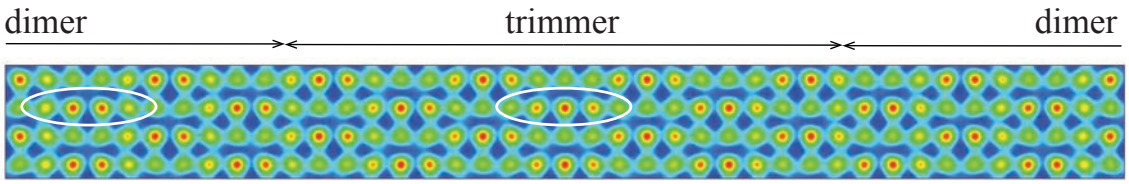

Fig.1： An STM image simulated for the new model proposed in this work.

Electronic band structures and Raman-spectra of intermediate states between $MoSe_2$ and Janus-MoSeS

Masaaki MISAWA
Department of Intelligent Mechanical Engineering, Fukuoka Institute of Technology
3-30-1 Wajiro-higashi, Higashi-ku, Fukuoka 811-0295

Janus-TMDC, which is obtained by substituting a chalcogen element on only one side of transition metal dichalcogenides (TMDCs), has attracted much attention as a functional material with the potential to lead to new electronics technologies. While various structures based on Janus-TMDC have been proposed for electronics applications, there are still many unknowns regarding how the physical properties change during the elemental substitution process. In this study, we performed first-principles simulations of the electronic band structure and evolution of Raman spectra during the synthesis of Janus-MoSeS by elemental substitution of $MoSe_2$[1]. The first-principles calculations based on density functional theory were conducted using the Vienna Ab initio Simulation Package (VASP)[2]. The Raman spectra were simulated using Phonopy[3] with Phonopy-Spectroscopy package[4].

To compute electronic band structure, the Janus $MoSe^bSe^t_{1-x}S^t_x$ (x = 0, 0.25, 0.50, 0.75 and 1.00) structures were prepared by replacing certain Se atoms with S atoms in a $2\times2\times1$ supercell of the crystalline unit cell. As a result of the calculation, we obtained the bandgap energies of 1.532, 1.520, 1.536, 1.595 and 1.652 eV for x = 0, 0.25, 0.50, 0.75 and 1.00, respectively. Note that the obtained bandgap energies for $x = 0$ and 1.00 are consistent with experimental bandgap energies very well. In an experimental result of photoluminescence (PL) spectra, it was observed that the PL peak shifts slightly to the lower energy side at the beginning of the elemental substitution, and then transfer to the higher energy side. Our calculations clearly explain this experimental PL transition.

In addition, we performed simulations of Raman spectra. In the experiment, it was observed that the A_1 mode, which characterizes $MoSe_2$, disappeared immediately with the progress of elemental substitution, and the $^1A_1$ mode, which characterizes Janus-MoSeS, is appeared. During this process, an unknown peak appeared around 260 cm^{-1}, which exists only in intermediate states and is not found in $MoSe_2$ or MoSeS. Our simulation results show that a peak appears at 258.1 cm^{-1} in the structure of $x = 0.5$, indicating a complex mode in which S and Se are intricately correlated.

This year, we also conducted first-principles calculations about the self-limiting growth mechanism of TMDC nanoribbons[5].

References

[1] H. Suzuki *et al.*: Nano Lett. **23**, 4533 (2023).

[2] G. Kresse and D. Joubert: Phys. Rev. **59**, 1758 (1999).

[3] A. Togo: JPSJ **92**, 012001 (2023).

[4] J. M. Skelton *et al.*: Phys. Chem. Chem. Phys. **19**, 12452 (2017).

[5] H. Suzuki *et al.*: ACS Nano **17**, 9455 (2023).

Lattice thermal conductivity calculation of iridium oxide $Ca_5Ir_3O_{12}$

Shoya Kawano

Department of Electrical and Electronic Engineering, Kyushu Institute of Technology, Kitakyushu, Fukuoka, 804-8550

We have studied the title compound, Ca5Ir3O12, which has attracted attention due to its strong spin-orbit interaction (SOI) [1]. This compound exhibits antiferromagnetic ordering below 7.8 K, undergoes a second order phase transition at 105 K, and displays non-linear conductivity along the c-axis. Further exploring its properties, we have conducted investigations into the thermal conductivity using synchrotron X-ray studies of lattice vibrations. To compare with these experiments, we have performed calculations using this supercomputing system.

We conducted calculations on the phonon lifetimes of $Ca_5Ir_3O_{12}$ using force constants determined through density functional theory (DFT) calculations performed with the Quantum ESPRESSO (QE) code [2] and the ALAMODE code [3] for phonon calculations. These calculations involved determining force constants that enabled us to compute phonon dispersion and phonon lifetimes.

We performed calculations using a 1×1×3 supercell. For the finite displacement and random displacement approaches, displacement distances of 0.02 Å and 0.04 Å were respectively employed. The random displacement approach was utilized to calculate the anharmonic terms of the force constants, for which 20 random structures were used. In QE code, we employed norm-conserving pseudopotentials generated by the ONCVPSP (Optimized Norm Conserving Vanderbilt Pseudopotential) code, sourced from PseudoDojo [4]. The Perdew-Burke-Ernzerhof type exchange-correlation function was used. We set a Γ-point-centered 4×4×3 k-point sampling for the supercell calculations. The energy cutoff for the wave function was 96 Ry, with a convergence criterion for the electronic self-consistency loop set at 10^{-10} Ry, and Gaussian smearing method with a smearing width of 0.002 Ry was used. We included the SOI effect.

Figure 1 displays the phonon dispersion relation for $Ca_5Ir_3O_{12}$, which is consistent with our studies conducted using synchrotron radiation experiments and calculations. The slope of the dispersion relation (dE/dk) corresponds to the phonon group velocity. The region from Γ to A shows a high slope, indicating a high group velocity.

We estimated the phonon lifetimes for $Ca_5Ir_3O_{12}$; most lifetimes are short, averaging around 0.5 ps. Long-lived phonons are

primarily found near ω = 0, contributing significantly to the thermal conductivity. When compared to phonon lifetimes obtained from our synchrotron radiation experiments, the results are consistent. The calculated thermal conductivities in the a-axis and c-axis directions are 0.09 W/mK and 0.69 W/mK, respectively, which align with experimentally observed values of approximately 1 W/mK. The very short phonon lifetimes contribute to the low thermal conductivity. Furthermore, the high group velocity in the Γ-A direction contributes to the anisotropy in thermal conductivity.

For the density functional calculations for each displacement, we used the F16CPU of system B with 2048 parallel computing cores using MPI. For the thermal conductivity calculation, a hybrid MPI/OpenMP parallelization approach was employed using the F16CPU of system B.

[1] K. Matsuhira *et al*. *J*. *Phys*. *Soc*. *Jpn*. **87**, (2018).

[2] https://www.quantum-espresso.org

[3] https://alamode.readthedocs.io

[4] http://www.pseudo-dojo.org

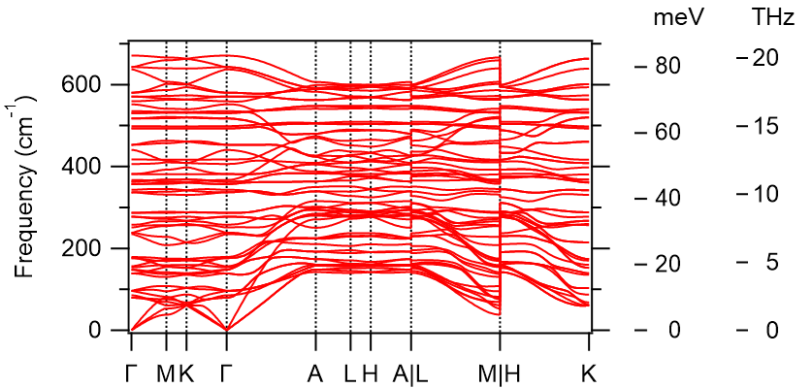

Fig. 1 Phonon dispersion of $Ca_5Ir_3O_{12}$ with SOI.

Activation barrier investigation for methane dissociation on Ni nanoparticle doped CeO_2

Takaya FUJISAKI

Faculty of Materials for Energy

Shimane University, 1060 Nishikawazu, Matsue, Shimane 690-0823

Introduction

In the world of renewable energy, biomass stands out as an important resource. It can produce methane through a process called anaerobic fermentation. This methane can then be used as a carrier for hydrogen, which is great for fuel cells because they're really good at making electricity. Recent research has shown that we can use biomass, like waste from shrimp farming, to make methane as seen in Fig. 1 [1][2]. This opens up the possibility of using money made from shrimp farming to help pay for fuel cells, which is good for both industries and helps make energy production more sustainable.

Getting hydrogen from methane efficiently is significantly important for making these fuel cell systems work well. That's why scientists are working hard to improve a process called dry reforming of methane (DRM). They've found that using a catalyst called CeO_2 loaded with tiny nickel particles could be a game-changer for how we use methane in fuel cells. This study dives deep into understanding how methane and carbon dioxide break apart during the DRM reaction to make the process more efficient.

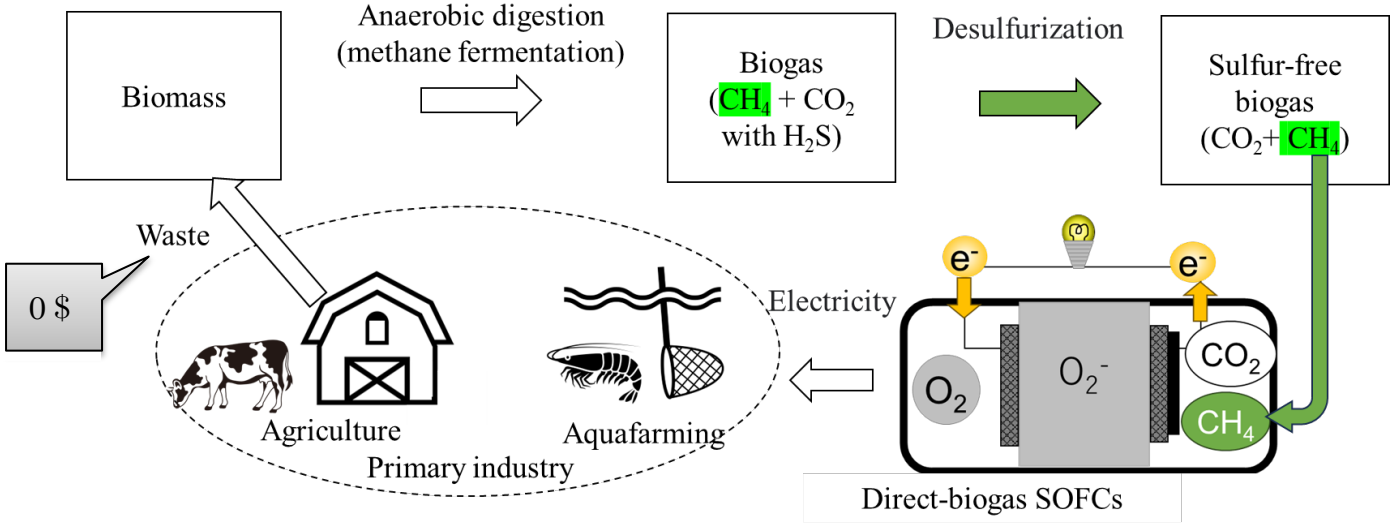

Fig.1 Schematic of combined biomass and fuel cell system

Analytical Methods

This study used a method called density functional theory (DFT) to figure out how hard it is for methane and carbon dioxide to break apart. They used a computer program called Vienna ab initio simulation package (VASP) to look at different setups of nickel nanoparticles on surfaces made of CeO_2. Then, they used a method called the nudged elastic band (NEB) to calculate how hard it is for methane and carbon dioxide to break apart for each setup. To make sure the computer results were accurate, they also did real experiments using a special catalyst made of nickel and CeO_2. By measuring how much hydrogen was made and how much methane was used up, they got a good idea of how fast the reactions were happening.

Results and Discussion

Fig. 2 shows the activation barrier of methine dissociation (left) and transition state (TS) of methane (right). The study found out some interesting things about how methane breaks apart. It turns out that it's easier for methane to break apart when the nickel particles have more positive charge. They also found that breaking apart carbon dioxide is harder than breaking apart methane during the DRM reaction. This means that how fast carbon dioxide breaks apart might control how fast the whole reaction happens. The study suggests that if we can find ways to make the nickel particles even more positively charged, we might be able to speed up the whole process even more, which would be great for making fuel cells more efficient.

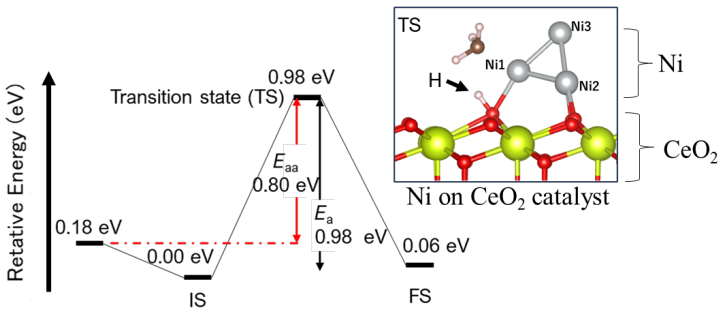

Fig.2 Ni on CeO_2 catalyst for making H_2

.

Acknowledgments

We extend our gratitude to The Institute for Solid State Physics, The University of Tokyo for providing access to their supercomputer facilities and for their invaluable support and guidance throughout this research endeavor.

References

[1] Y. Shiratori et al., Fuel Cells **19**, 346-353 (2019).

[2] P. H. Tu et al., Fuel Cells, 1-11 (2024).

Compression behavior of Xe in silica melt

Daisuke WAKABAYASHI

Photon Factory, Institute of Materials Structure Science,

High Energy Accelerator Research Organization (KEK), Tsukuba 305-0801

Noble gasses are believed to have the same abundance as the ancient Earth and planetary atmospheres because of their chemical inertness. However, it is known that the abundance of Xe in the current Earth's atmosphere is significantly lower compared to primitive meteorites. The lack of Xe in the Earth's atmosphere, known as "missing Xe," has long been studied as a major mystery in the field of geochemistry. Xe is heavier and relatively more chemically reactive among noble gases. It is hypothesized to form compounds under high temperature and pressure, remaining trapped in the deep Earth since its formation, but the detailed process remains unresolved. In this study, the behavior of Xe in magma under high temperature and pressure is simulated to elucidate its potential entrapment in the deep Earth.

Our previous experimental and theoretical studies have confirmed structural changes in the network of SiO_4 tetrahedra constituting silica glass under high pressure [1-2]. The structural change in the network is expected to affect the behavior of Xe significantly. In this project, ab-initio molecular dynamics simulations were conducted for Xe in silica glass under high pressure conditions up to 10 GPa, where the network structural changes occur.

Ab-initio calculations were carried out with a system of 145 atoms (48Si + 96O + 1Xe) under periodic boundary conditions using the QXMD code [3]. First, simulations were performed on the system without a Xe atom for more than 10 ps at 3,000 K. Then, a Xe atom was added to a void in the final atomic configuration, and subsequent calculations were performed for more than 10 ps. These calculations were conducted under the pressure conditions of 0, 3, 6, and 10 GPa.

The structure and behavior of the main component, SiO_2, remained unchanged regardless of the presence of Xe. The network structure composed of SiO_4 tetrahedra changed with pressure, leading to the collapse of voids.

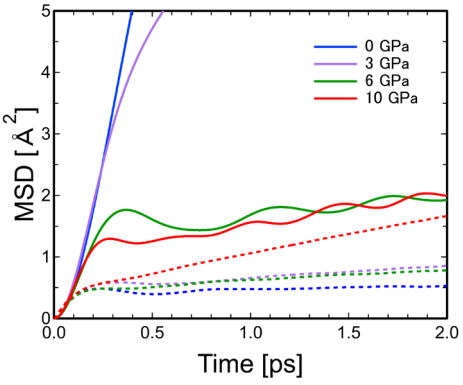

Fig. 1. Pressure dependence of mean square displacement of Xe in SiO_2 glass. Dotted lines represent the data of Si.

The mean square displacement of Xe is shown in Fig. 1, together with that of Si for reference. Figure 1 shows that the diffusion of Xe is significantly inhibited at pressures above 6 GPa, strongly suggesting that Xe is trapped within the network of SiO_2 glass and unable to move. The atomic configuration of Xe at 6 GPa and 3,000 K is shown in Fig. 2. Indeed, it is evident that Xe is confined within a narrow void. This observation is in agreement with previous experiments on silicate melt [4].

The bonding properties were estimated with a population-analysis method. The overlap population between Xe and other atoms suggests that Xe does not have a strong bonding with them. Xe becomes trapped within the network not due to chemical bonding, but simply because the network narrows as a result of the structural changes.

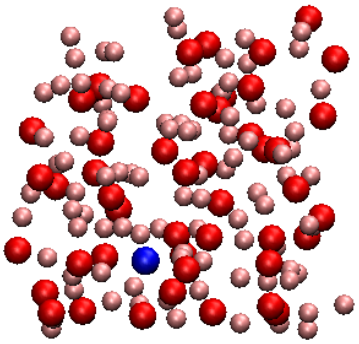

Fig. 2. Atomic arrangement of Xe in SiO2 glass at 6 GPa and 3,000 K (red: Si; pink: O; blue: Xe).

References

[1] D. Wakabayashi, N. Funamori, T. Sato, and T. Taniguchi, Phys. Rev. B **84**, 144103 (2011).

[2] E. Ryuo, D. Wakabayashi, A. Koura, and F. Shimojo, Phys. Rev. B **96**, 054206 (2017).

[3] F. Shimojo, S. Fukushima, H. Kumazoe, M. Misawa, S. Ohmura, P. Rajak, K. Shimamura, L. B. Oftelie, S. Tiwari, R. K. Kalia, A. Nakano, and P. Vashishta, Software X **10**, 100307 (2019).

[4] C. Leroy, C. Sanloup, H. Bureau, B. C. Schmidt, Z. Konôpková, and C. Raepsaet, Earth Planet. Sci. Lett. **484**, 103 (2018).

Analyses of diamond surface processes by machine-learning based potentials

Kouji INAGAKI

Graduate School of Engineering, Osaka University

Yamadaoka 2-1, Suita, Osaka 565-087

In this study, the wear process of diamond tools during the machining of ferrous materials has been analyzed using first-principles calculations. It was found that the reaction barrier for the Fe atoms to break into the C-C bonds is relatively low, and the fracture strength is lower than that of the C-C bonds. We attributed that this phenomenon is the cause of wear. In order to clarify the wear process directory by simulation, it takes much of computational cost. Machine learning techniques (MLP) is applied.

Since the reaction of Fe atom and C-C bond takes a five-folded structure in the path, we chose a graph-neural-network (GNN) based MLP. As a first step in our research, we generated a MLP to analyze the diffusion process of H on the Si surface, which we had previously identified. This is appropriate as a test calculation because Si adopts a five-folded structure in this reaction process. We employed Nequip application to form GNN-MLP, and succeeded in constructing the MLP using 1090 Si(001) 4x4 models as training data set with a Loss function of 0.008.

References

[1] K. Inagaki, K. Arima, The 84th JSAP Autumn Meeting 2023 20p-A202-5.

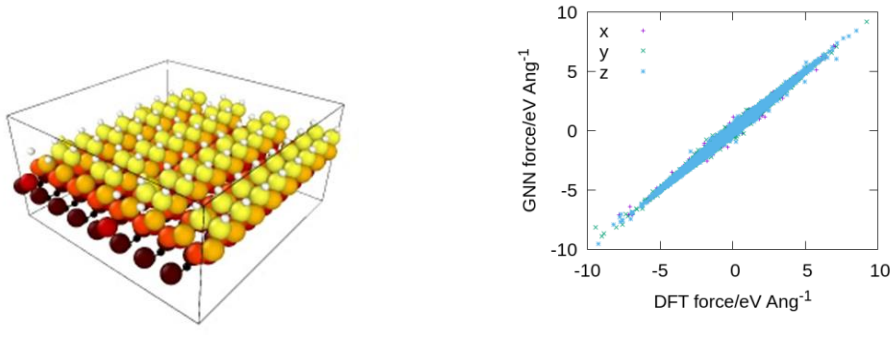

(a) (b)

Fig. 1: Training of machine learning potential. (a) Training data: One of the 1090 samples of Si (001) 4x4 6 layer model with surface 2x1 structure terminated by single H atoms with an excess H atom and bottom 16 dihydride. (b) Trained example. Loss function (defined in eqn. (9) in https://rdcu.be/dG4Zh) value is 0.008.

Reactivity analysis of high entropy alloys for catalyst informatics

Yoyo HINUMA

National Institute of Advanced Industrial Science and Technology (AIST)

1-8-31, Midorigaoka, Ikeda, Osaka 563-8577

High entropy alloys (HEAs) are a new class of metallic materials that contrast conventional alloy materials with few principal elements. HEAs consist of more than five near-equimolar components that are mixed to form single-phase solid solutions with high mixing entropy instead of (mostly) ordered intermetallic phases. Various unique synergistic effects result from such mixtures, such as high configuration entropy, lattice distortion, sluggish diffusion, and cocktail effects, resulting in peculiar characteristics including high mechanical strength, good thermal stability, and superior corrosion resistance.

Transition metal elements, especially late transition metal elements, are typically used in HEAs. The huge combination of elements makes brute-force searching impossible, and the question of which elements to use will always linger. This study considered five-component HEAs out of 12 late transition metal elements, which are Fe, Co, Ni, Cu, Zn, Ru, Rh, Pd, Ag, Ir, Pt, and Au. The activity of CO_2 adsorption, an important step in CO_2 hydrogenation, was investigated using first-principles density functional theory calculations. A CO_2 molecule was adsorbed on (111) surface sites of fcc-structure HEAs.

HEAs could be categorized into “binding”, “less binding”, or “inconclusive” HEAs. There were 27, 23, and 10 HEAs each, respectively, within 60 randomly chosen HEAs. “Binding” HEAs have low CO_2 adsorption energy positions of less than -0.08 eV, which is difficult to attain with elementary substances or binary alloys. These low adsorption energy, or more active, sites are found near top positions, whereas CO_2 does not adsorb near top “high symmetry” sites in “less binding” HEAs. HEAs containing Ru had a higher ratio of “binding” HEAs [1]. Calculating CO_2 adsorption energies could be a useful tool to check whether a specific HEA is “binding” or “less binding” prior to conducting extensive experiments.

References

[1] Y. Hinuma et al.: STAM Methods. 3 (2023) 2161807.

DFT calculations of HCOOH molecules in the pore of porous metal organic films on Cu(111)

Noriyuki Tsukahara

National Institute of Technology, Gunma College,

Toribamachi 580, Maebashi, Gunma, 371-0845, Japan

In this study, the adsorption structures of atoms and molecules that are trapped in a pore of porous organometallic thin films are investigated, and the interaction between the thin film and the adsorbed molecules is unveiled by DFT calculations.

A porous thin film obtained by adsorbing 1,3,5-tris(pyridyl)benzene (TPyB) molecules on Cu(111) is used as a host film. This film is formed when a Cu atom supplied from the substrate connect to two TPyB molecules, and hexagonal pores are periodically arranged. Formic acid is used as guest molecules.

Fig. 1 (a) shows an STM image of formic acid in the pores. A bright protrusion appears next to the two-coordinated Cu atom, and a zigzag chain is observed from the protrusion. Although the zigzag chain is observed in the adsorption structure of formic acid on Cu(111), the bright protrusion adjacent to the two-coordinated Cu originate from the unique adsorption structure in the pore.

Fig. 1(b) shows adsorption structures of an HCOOH molecule that is adjacent to two-coordinated Cu and the flat Cu(111) surface obtained by DFT calculation. The adsorption energy is larger for HCOOH adjacent to the two-coordinated Cu (-0.60 eV) compared to HCOOH on Cu(111) (-0.51 eV). For charge transfer between the substrate+film and the HCOOH molecule, charge transfer with the substrate decreases and that with the two-coordinated Cu increases when the HCOOH molecule is adjacent to the two-coordinated Cu. Therefore, the two-coordinated Cu provides new stable adsorption sites for HCOOH molecules.

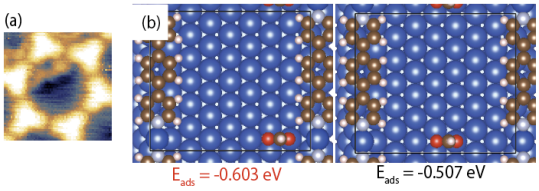

Fig. 1 (a) An STM image of HCOOH molecules in a pore of the metal-organic film on Cu(111). (b) Schematic drawings of a HCOOH molecule with two-coordinated Cu on Cu(111).

First-principles calculations of optical response to double-pulse lasers

Mizuho ONO[1], Hiroki GONOME[2]

[1]*Graduate School of Engineering,*

Tohoku University, Aoba-ku, Sendai, Miyagi 980-0845

[2]*Graduate School of Science and Engineering,*

Yamagata University, Jonan, Yonezawa, Yamagata 992-8510

Femtosecond laser pulses have very high peak intensities and can be used for nonlinear processing in wide-gap semiconductors and other applications. In recent years, material modification by multiple laser pulses has been proposed to avoid damage to optical elements [1]. Although a certain amount of energy must be applied for such material modification, it is generally difficult to predict the nonlinearity of the material. Therefore, in this study, the optical response of materials under double-pulse irradiation was verified using real-time time-dependent density functional theory. For silicon carbide, a typical wide-gap semiconductor, we examined the response to the second pulse for two systems: one in which the electrons remain in a non-equilibrium state after the first pulse and the other in which they form a thermal equilibrium state, i.e., a Fermi-Dirac distribution. Figure 1 shows the results of the induced current calculations. In the equilibrium system, a current with a threefold component was observed in addition to the laser's center frequency of 3.10 eV. In the non-equilibrium system, in addition to the 3.10 eV frequency, a current with a split threefold component was observed. Figure 2 shows the time evolution of the energy. The currents in the basic and threefold frequency components were higher in the equilibrium state, while the absorbed energy was higher in the nonequilibrium state.

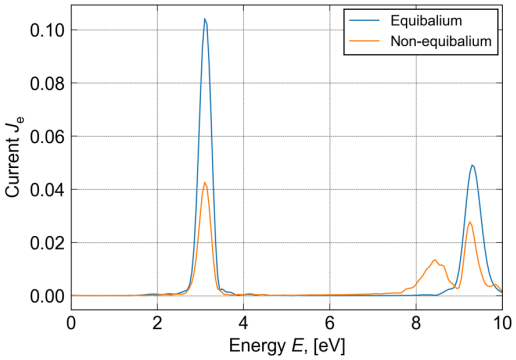

Figure 1 : Fourier components of electric current.

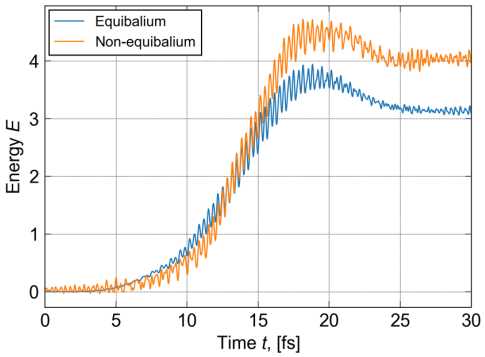

Figure 2 : Time series of internal energy.

References

[1] T. Otobe, T. Hayashi and M. Nishikino, Appl. Phys. Lett. **111**, 171107 (2017).

Structure-Performance Relationship Analysis for Catalysts

Hao LI

Advanced Institute for Materials Research (WPI-AIMR),

Tohoku University, Sendai 980-8577, Japan

The Hao Li Lab at WPI-AIMR aims to streamline catalyst search by focusing on developing precise catalysis theory for designing and understanding promising catalysts, thus bypassing the experimental trial-and-error process. In this ISSP project, we utilize *ab initio* calculations (e.g., density functional theory, DFT), multi-scale modeling, data science, and machine learning to facilitate catalyst design and comprehension. Numerous accomplishments from this project have been featured in top-tier journals like the Journal of the American Chemical Society, Nature Communications, and Angewandte Chemie International Edition.

An outstanding illustration from this project involves the investigation of pH-dependent oxygen reduction reaction (ORR) performance on single-atom catalysts (SACs) [1]. Initially, linear scaling relations were discerned among the binding energies of ORR adsorbates on different types of SACs (Fig. 1). Subsequently, we conducted pH-dependent microkinetic modeling and identified intriguing pH-dependent behaviors on SACs (Fig. 2), which align excellently with our subsequent experimental validations (Fig. 3).

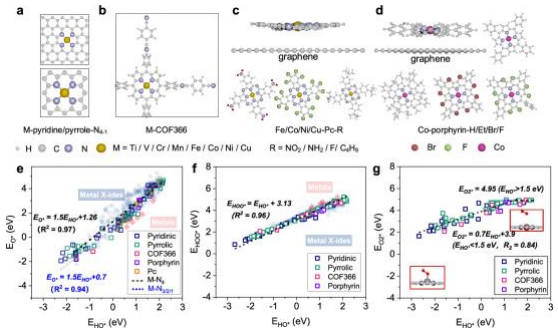

Fig. 1: Figure 1. Linear scaling relations are found in M–N–C catalysts with different atomistic environments.

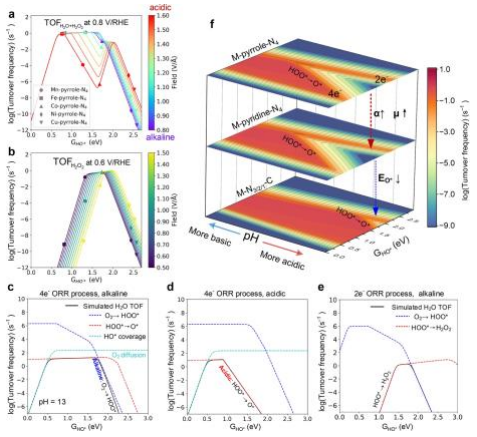

Fig. 2: Microkinetic ORR volcano models of M–N–C SACs and rate-determining analyses.

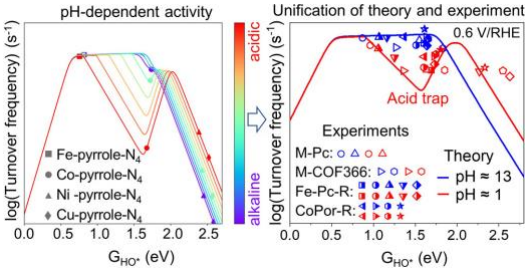

Fig. 3: Experimental validation on the derived pH-dependent volcano model for SAC ORR.

Another notable achievement is the development of an active machine-learning model for dynamic simulation and growth mechanisms of carbon on metal surfaces [2]. We designed an active learning framework to accurately fit a machine learning force field, replacing expensive DFT calculations (Fig. 4). This framework involves sampling data from various structures and utilizes on-the-fly validation and data acquisition to iteratively enhance the accuracy of the machine learning force field. The modeling results were compared with actual DFT results for validation.

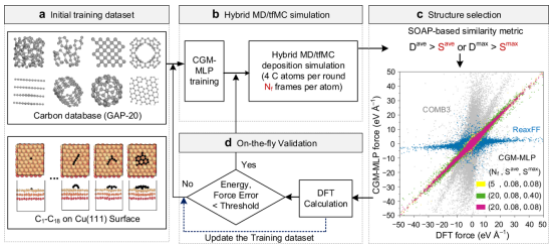

Fig. 4: The workflow of the development of on-the-fly fitting employed for this project.

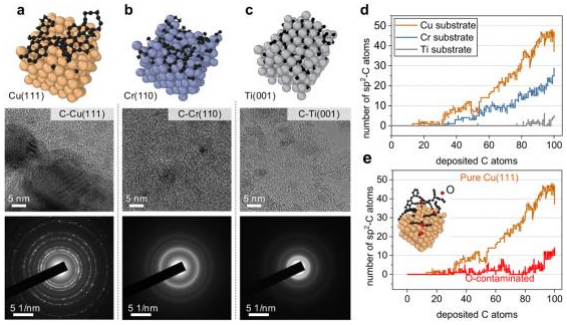

Fig. 5: Comparison between theory and experiments regarding the carbon forms on Cu, Cr, and Ti surfaces.

Utilizing the machine learning force field developed previously, we conducted extensive simulations on Cu(111), Cr(110), and Ti(001) surfaces, revealing distinct carbon behaviors on each surface. These findings demonstrate excellent agreement with subsequent experimental observations (Fig. 5). Another significant research outcome involves unraveling the structure-activity relationship for CO_2 electroreduction over SnO_2 using a standardized research paradigm [3]. We devised a workflow that integrates surface state analysis, surface reconstruction analysis, microkinetic modeling, and experimental validation (Fig. 6).

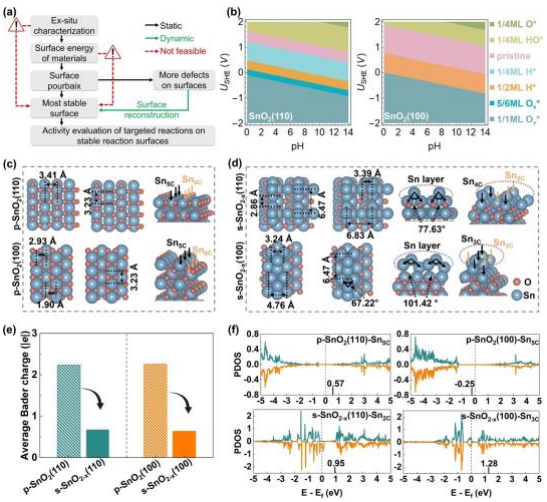

Fig. 6: Developed workflow for surface state analysis and structural dynamic evolution for CO_2 electroreduction using SnO_2.

In summary, we have successfully achieved the proposed objectives of this project, including the analysis of key reactions such as ORR and carbon behavior on catalysts. Moving forward, our future studies will focus on further developing this framework to enable more precise catalysis design, building upon our foundation in precise catalysis theory development.

❖ Besides, based on the generous

support of this ISSP project, we also have published other papers in 2023-2024, which are shown in Refs. [4-30].

References

1) D. Zhang, Z. Wang, F. Liu, P. Yi, L. Peng, Y. Chen, L. Wei*, and **H. Li***, J. Am. Chem. Soc., **2024**, 146, 3210–3219 (Cover Article).

2) D. Zhang*, P. Yi, X. Lai, L. Peng*, and **H. Li***, . Nat. Commun., **2024**, 15, 334.

3) Z. Guo, Y. Yu, C. Li, E. C. D. Santos, T. Wang, H. Li, J. Xu*, C. Liu*, and **H. Li***, Angew. Chem. Int. Ed., **2024**, 136, e202319913 .

4) D. Zhang, Y. Hirai, K. Nakamura, K. Ito, Y. Matsuo, K. Ishibashi1, Y. Hashimoto, H. Yabu*, and **H. Li***, Chem. Sci., **2024**, 15, 5123-5132 (Front Cover Article).

5) H. Liu, D. Zhang, Y. Wang, and **H. Li***, Langmuir, **2024**, 40, 7632–7638.

6) Y. Zhang, T. Wang, L. Mei, R. Yang, W. Guo, **H. Li***, and Z. Zeng*, Nanomicro Lett, **2024**, In Press (Invited Paper).

7) T. Wang, Z. Guo, H. Oka, A. Kumatani*, C. Liu*, and **H. Li***, J. Mater. Chem. A, **2024**, 12, 8438-8446.

8) F. Nekouei*, T. Wang*, F. Keshtpour, Y. Liu, **H. Li**, and S. Nekouei, Appl. Catal. B., **2024**, 351, 123974.

9) D. Zhu, J. Li, Z. Zheng, S. Ye, Y. Pan, J. Wu, F. She, L. Lai, Z. Zhou, J. Chen, **H. Li**, L. Wei*, and Y. Chen*, ACS Appl. Mater. Interfaces, **2024**, 16, 16175–16185.

10) C. Li, H. Liu, T. Zhang, Z. Liu, H. Shi, J. Cui, **H. Li***, H. Li*, and C. Li*, Adv. Mater., **2024**, 2312204.

11) X. Jiang, B. Zhou, W. Yang, J. Chen, C. Miao, **H. Li**, Y. Hou, X. Xu, L. Zhu D. Lin, and J. Xu*, Proc. Natl. Acad. Sci. U.S.A, **2024**, 121, e2309102121.

12) X. Jia, Z. Yu, F. Liu, H. Liu, D. Zhang., E. C. D. Santos, H. Zheng, Y. Hashimoto, Y. Chen, L. Wei*, and **H. Li***, Adv. Sci., **2024**, 11, 2305630.

13) Q. Li, D. Zhang, J. Wu*, Y. Luo, H. Liu, M. Lu, R. Cui, W. Liang, D. Wang, P. Xi*, M. Liu, **H. Li***, and L. Huang*, Adv. Mater., **2024**, 36, 2309266.

14) W. Yan, X. Wang, M. Liu, K. Ma, L. Wang, Q. Liu, C. Wang, X. Jiang, **H. Li**, Y. Tang*, G. Fu*, Adv. Funct. Mater., **2024**, 37, 2310487.

15) H. Liu, Y. Wang, P. Tan, E. C. D. Santos, S. M. Holmes, **H. Li***, J. Pan*, C. D'Agostino*, Small, **2023**, 2308948.

16) P. Wang, K. Zhang, **H. Li***, J. Hu*, and M. Zheng*, Small, **2023**, 2308791.

17) S. Ning, M. Li, X. Wang, D. Zhang, B. Zhang, C. Wang, D. Sun, Y. Tang, **H. Li**, K. Sun,* and G. Fu*, Angew. Chem. Int. Ed., **2023**, 62, e202314565.

18) Y. Zhang, T. Wang, F. Wang, H. Zheng, Z. Zeng*, and **H. Li***, J. Mater. Chem. A, **2023**, 11, 20528-20538.

19) J. Jing*, Z. Guo, Z. Li, Y. Chen, **H. Li***, and W-Y. Li*, Chem. Eng. Sci., **2023**, 282, 119251.

20) H. Liu, D. Zhang, S. M. Holmes, C.

D'Agostino*, and **H. Li***, Chem. Sci., **2023**, 14, 9000-9009 (Front Cover Article).

21) E. C. D. Santos, R. Sato, K. Kisu, K. Sau, X. Jia, F. Yang, S. Orimo*, and **H. Li***, Chem. Mater., **2023**, 35, 5996-6004.

22) W. Yang, Z. Jia, B. Zhou, L. Chen, X. Ding, L. Jiao, H. Zheng, Z. Gao*, Q. Wang*, and **H. Li***, ACS Catal., **2023**, 13, 9695-9705.

23) W. Yang*, Z. Jia, L. Chen, B. Zhou, D. Zhang, Y. Han, Z. Gao, and **H. Li***, Chem. Commun., **2023**, 59, 10761-10764 (Invited Paper).

24) C. Li, Z. Guo, Z. Liu, T. Zhang, H. Shi, J. Cui, M. Zhu, **H. Li***, H. Li*, and C. Li*, ACS Catal., **2023**, 13, 16114-16125 (Front Cover Article).

25) J. Li, Z. Guo, J. Wu, Z. Zheng, Z. Yu, F. She, L. Lai, **H. Li***, Y. Chen*, and L. Wei*, Adv. Energy Mater., **2023**, 13, 2301743.

26) Y. Hao*, Z. Guo, H. Cheng, C. Yao, S. Cheng, L. Yi, and **H. Li***, J. Colloid Interface Sci. **2023**, 650, 1949-1957.

27) M. Li, X. Wang, K. Liu, H. Guo, M. Li, D. Sun, **H. Li**, K. Huang*, Y. Tang*, and G. Fu*, Adv. Energy Mater., **2023**, 13, 2301162.

28) Z. Guo, C. Liu, C. Sun, J. Xu*, **H. Li***, and T. Wang*, ChemCatChem, **2023**, 15, e202300669.

29) W. Yang*, L. Chen, B. Zhou, Z. Jia, Y. Liu, **H. Li***, and Z. Gao*, J. Phys. Chem. C, **2023**, 127, 13011-13020.

30) M. Li, X, Wang, K. Liu, H. Sun, K. Huang, D. Sun, Y. Tang, W. Xing, **H. Li***, and G. Fu*, Adv. Mater., **2023**, 35, 2302462 (ESI Hot & Highly Cited Paper).

3.3 Strongly Correlated Quantum Systems

Theoretical study of strongly correlated topological phenomena and its application to machine learning

Yukitoshi MOTOME

Department of Applied Physics,

The University of Tokyo, Bunkyo, Tokyo 113-8656

We have theoretically studied a variety of intriguing topological phenomena in strongly-correlated electron systems by using numerical methods including first-principles calculations, quantum many-body calculations, and machine learning (project numbers: 2023-Ca-0066 and 2023-Cb-0014). During the last fiscal year, we have achieved substantial progress on the following topics.

(i) *Development of new theoretical methods and their applications*: We proposed a new scheme for physical reservoir computing by using interacting spin systems as reservoirs [1]. In addition, inversely exploiting the framework of quantum reservoir computing, we developed a new theoretical tool to investigate the nature of quantum systems, called "quantum reservoir probing", and applied it to quantum scrambling [2] and quantum phase transitions [3]. We also applied the inverse Hamiltonian design that we developed to discover new Hamiltonians with maximized quantum entanglement [4].

(ii) *Kitaev quantum spin liquids and its realization in experiments*: We unveiled how the Kitaev spin liquid meets spin nematics in the S=1 Kitaev model with bilinear-biquadratic interactions by using the SU(3) formalism [5]. We also clarified the origin of a chiral spin liquid found in the competing region [6]. In addition, by using the pseudo-fermion functional renormalization group method, we clarified the ground-state phase diagram of the Kitaev-Heisenberg model on a three-dimensional hyperhoneycomb lattice [7]. We also revealed that the Kitaev spin liquid exhibits a peculiar inter-edge resonance [8] and spin Seebeck effect [9]. We also studied effects of dissipation in the non-Hermitian Kitaev model under a magnetic field [10]. Furthermore, we proposed new experimental platforms in heterostructures composed of van der Waals magnets [11] and ilmenite oxides [12], and rare-earth magnets [13].

(iii) *Topological properties of Weyl semimetals*: By using first-principles calculations, we unveiled magnetic, transport, and topological properties of atomically thin films of Co-based shandite [14]. We also extend the study to topological transitions in the kagome monolayer by rotating the magnetic field [15].

(iv) *Topological spin crystals as spin moire*: Extending the research until the last years, we

clarified the behavior of emergent electric fields arising from magnetic resonance in a one-dimensional chiral magnet [16]. In addition, we revealed an instability of magnetic skyrmion strings by a spin current [17]. We also wrote an article on spin moire in 日本物理学会誌 [18].

(v) *Collaborations with experimental groups*: We made fruitful collaborations on experiments for amorphous Fe-Sn thin films [19], high-field phase diagram of a chiral antiferromagnet showing quadrupole ordering [20], orbital-selective band reconstruction in $TaTe_2$ [21], the evolution of Floquet bands under circularly polarized light [22], and the noncoplanar antiferromagnetic structures in $DyTe_3$ [23].

References

[1] K. Kobayashi and Y. Motome, Sci. Rep. **13**, 15123 (2023).

[2] K. Kobayashi and Y. Motome, preprint (arXiv:2308.00898).

[3] K. Kobayashi and Y. Motome, preprint (arXiv:2402.07097).

[4] K. Inui and Y. Motome, preprint (arXiv:2402.15802).

[5] R. Pohle, N. Shannon, and Y. Motome, Phys. Rev. B **107**, L140403 (2023).

[6] R. Pohle, N. Shannon, and Y. Motome, preprint (arXiv:2404.11623).

[7] K. Fukui, Y. Kato, and Y. Motome, J. Phys. Soc. Jpn. **92**, 064708 (2023).

[8] T. Misawa, J. Nasu, and Y. Motome, Phys. Rev. B **108**, 115117 (2023).

[9] Y. Kato, J. Nasu, M. Sato, T. Okubo, T. Misawa, and Y. Motome, preprint (arXiv:2401.13175).

[10] K. Fukui, Y. Kato, and Y. Motome, preprint (arXiv:2402.05516).

[11] L. Zhang and Y. Motome, preprint (arXiv:2310.01075).

[12] Y.-F. Zhao, S.-H. Jang, and Y. Motome, preprint (arXiv:2403.09112).

[13] S.-H. Jang and Y. Motome, preprint (arXiv:2402.18837).

[14] K. Nakazawa, Y. Kato, and Y. Motome, Commun. Phys. **7**, 48 (2024).

[15] K. Nakazawa, Y. Kato, and Y. Motome, preprint (arXiv:2402.16273).

[16] K. Shimizu, S. Okumura, Y. Kato, and Y. Motome, Phys. Rev. B **108**, 134436 (2023).

[17] S. Okumura, V. P. Kravchuk, and M. Garst, Phys. Rev. Lett. **131**, 066702 (2023) [selected as Editor's suggestion].

[18] 清水宏太郎、奥村駿、加藤康之、求 幸年: 日本物理学会誌 **78**, 314 (2023).

[19] K. Fujiwara *et al.*, Nat. Commun. **14**, 3399 (2023).

[20] T. Nomura *et al.*, Phys. Rev. B **108**, 054434 (2023).

[21] N. Mitsuishi *et al.*, Phys. Rev. Research **6**, 013155 (2024).

[22] Y. Hirai *et al.*, Phys. Rev. Research **6**, L012027 (2024).

[23] S. Akatsuka *et al.*, Nat. Commun., in press.

Analysis of *ab initio* Hamiltonians for molecular solid $(TMTTF)_2PF_6$ under pressure

Takahiro Misawa
Institute for Solid State Physics, University of Tokyo
Kashiwa-no-ha, Kashiwa, Chiba 277-8581

Organic conductors are widely studied due to the diverse physical properties that arise from the interactions of charge, spin, and lattice degrees of freedom. These interactions lead to various electronic states, including superconductivity, magnetic ordering, and charge ordering. In fact, crystals made of TMTTF molecules exhibit all these electronic states when external pressure is applied and have been the subject of active research for over 40 years. By combining these findings with results from related compounds made of TMTSF molecules, a unified pressure-temperature phase diagram has been discussed. However, there has not yet been a quantitative analysis of how external pressure impacts electron correlations in these systems, nor an understanding of what factors control the various phases under pressure.

In this project, we have performed a combined experimental and theoretical analysis of the pressure-dependent physical properties of the quasi-one-dimensional organic conductor $(TMTTF)_2PF_6$ [1]. We obtain the crystal structures under pressure by performing x-ray diffraction measurements for single crystals of $(TMTTF)_2PF_6$ with a diamond anvil cell up to 8 GPa. Based on the obtained crystal structures, we first derive the low-energy effective Hamiltonians for $(TMTTF)_2PF_6$ under pressure using Quantum ESPRESSO [2] and RESPACK [3]. We obtained the following characteristic features of the microscopic parameters in the low-energy effective Hamiltonians: (1) By applying the pressure, the transfer integrals increase, whereas the screened Coulomb interactions decrease, resulting in a drastic reduction of correlation effects. For example, the normalized onsite Coulomb interaction ($U/\bar{t}_a$) decreases from 12 at ambient pressure to 6 at 8 GPa. (2) The degree of dimerization in the intrachain transfer integrals, as the result of the decrease in structural dimerization together with the change in the intermolecular configuration, almost disappears above 4 GPa.

Then, we solve the low-energy effective Hamiltonians by using the many-variable variational Monte Carlo method [4, 5], which effectively treats electron correlation effects. We find that the charge ordering is substantially suppressed above 1 GPa while the spin ordering survives up to higher pressure. This theoretical result is consistent with the temperature dependence of the resistivity under pressure.

Changes in the electronic states of molecular solids under pressure have been studied as a typical example of pressure effects on strongly correlated electron systems. The present study demonstrates that recent advances in high-pressure experimental and computational tech-

niques now enable a quantitative microscopic analysis of physical properties under pressure.

References

[1] M. Itoi, K. Yoshimi, H. Ma, T. Misawa, *et al.*, arXiv:2403.13816.

[2] P. Giannozzi *et al.*, J.of Phys.: Cond. Matt. **29**, 465901 (2017).

[3] K. Nakaramu *et al.*, Comp. Phys. Comm. **261**, 107781 (2021).

[4] T. Misawa *et al.*, Comp. Phys. Comm. **235**, 447 (2019).

[5] https://www.pasums.issp.u-tokyo.ac.jp/mvmc/en/

On the relation between artificial neural networks and tensor networks

Yusuke NOMURA

Institute for Materials Research (IMR), Tohoku University,

2-1-1 Katahira, Aoba-ku, Sendai 980-8577, Japan

Accurate representation of quantum states is a grand challenge in computational physics. Recently, a new method based on artificial neural networks has been introduced. This is an attempt to describe the quantum many wave functions using artificial neural networks and approximate quantum states with high precision using a much smaller number of parameters than the actual dimension of the wave function.

This artificial neural network method is complementary to tensor network methods [1]. Both artificial neural networks and tensor networks have the property of universal approximation in the limit of infinite hidden degrees of freedom and bond dimensions, respectively. However, they are currently being developed independently.

In this project, we try to develop a more compact and efficient quantum state representation formalism by exploring a new network formalism that combines artificial neural networks and tensor networks. As a first step, in this fiscal year, we have tried to investigate the relation between the two types of networks.

In more detail, we performed a supervised learning to learn the relation between spin configurations σ and amplitude of wave function $\psi(\sigma)$ for one-dimensional quantum spin systems. The training data was generated using a small system size that allows for exact diagonalization [set of σ and $\psi(\sigma)$]. Then, we compare the representative ability between restricted Boltzmann machines (RBM) and matrix product states (MPS) by performing supervised learning of quantum states. It is well known that MPS is a very efficient ansatz for representing quantum states for one-dimensional systems. Surprisingly and interestingly, the performance of RBM is comparable to MPS when the number of parameters is the same between the two architectures.

This indicates that artificial neural networks have an excellent ability to represent quantum states. In the future, we will investigate the possibility of combining artificial neural networks with tensor networks to better represent quantum states.

References

[1] Y. Nomura, J. Phys.: Condens. Matter **36** 073001 (2024)

Long-time simulation for strongly-correlated quantum systems

Masatoshi IMADA
Research Institute for Sicence and Engineering, Waseda University,
3-4-1 Okubo, Shinjuku-ku, Tokyo, 169-8555
Department of Engineering and Applied Sciences, Sophia University.
7-1 Kioi-cho, Chiyoda-ku Tokyo, 102-8554

In this report, we review recent progress in development of the algorithm and its benchmark examined for forecast of the long-time behavior of the quantum many-body dynamics by utilizing short-time reliable quantum-dynamics data [1]. For the purpose of this challenging long-time forecast, here, the dynamic mode decomposition (DMD) employed in the field of fluid dynamics [2,3] has been employed. The DMD is advantageous in its simplicity and versatility. The dominant part of the computational cost is primarily scaled by that of singular value decomposition (SVD) of a certain matrix constructed from the short-time data.

This method has enabled accurate predictions of the quantum many-body dynamics at nearly one order of magnitude longer time than the range of utilized short-time training data even when the long-time behavior exhibits complex features such as multiple oscillations and power-law decay to a nonzero constant. The benchmark was performed by taking the transverse-field Ising models as model systems.

For more realistic situations, the method has applied to noisy input data as well. The DMD prediction has turned out to be still accurate when the noise level is within a few percent of the noiseless part. Furthermore, systematic and statistical errors of the DMD prediction have also been estimated in this work, which shows essentially slow growth of the estimated error ensuring the reliability of the forecast at nearly one order longer time than the time of input training data.

The findings indicate that the DMD is equally a promising tool for the dynamics of other quantum many-body systems that are difficult to simulate by conventional direct numerical simulations by the time evolution of the many-body wave functions. The DMD is powerful and versatile even at quantum critical points with temporary long-ranged quantum fluctuations characteristic of the growing quantum entanglement. Because of the versatile nature of the algorithm, the method is also expected to be applicable to the time series of experimental data in quantum many-body systems, which is left for future studies.

This review of the activity is based on the results achieved by Ryui Kaneko collaborated with Yoshiyuki Kabashima, Tomi Ohtsuki and the author. The project was financially supported by MEXT KAKENHI, Grant-in-Aid for Transformative Research Area (Grant No. JP22H05111 and No. JP22H05114). and also supported by MEXT under the grant number JPMXP1020230411.

References

[1] R. Kaneko, M. Imada, Y. Kabashima and T. Ohtsuki: arXiv:2403.19947.

[2] C. W. Rowley, I. Mezić, S. Bagheri, P. Schlatter, and D. S. Henningson, J. Fluid Mech. **641**, 115 (2009).

[3] P. J. Schmid: J. Fluid Mech. **656**, 5 (2010).

Development of Variational-Wave-Function Spectroscopy for Quantum Materials

Youhei YAMAJI
Research Center for Materials Nanoarchitectonics, National Institute for Materials Science
Namiki, Tsukuba-shi, Ibaraki 305-0044

It is known that direct observation of quantum entanglement in many-body systems is difficult. Currently, detailed analysis on signatures of the entanglement in spectroscopy measurements has been conducted on one-dimensional quantum spin chains, which are the simplest yet exhibit macroscopic quantum entanglement [1]. Thus, it is desirable to explore numerical spectroscopy flexibly applicable to complicated quantum materials.

Variational wave function methods provide a promising foundation for numerical spectroscopy. However, there had been a difficulty: As discussed in the literature [2], it is difficult to find a concise representation of the summation of two variational wave function. Once we design a variational wave function, we can define a subspace of the many-body Hilbert space, $\mathcal{J}$. However, it is not easy to find $|\psi_3\rangle \in \mathcal{J}$ that satisfies $|\psi_3\rangle = c_1|\psi_1\rangle + c_2|\psi_2\rangle$ $(c_1, c_2 \in \mathbb{C})$ for $|\psi_1\rangle$, $|\psi_2\rangle \in \mathcal{J}$. For example, it is formidable for the subspace $\mathcal{J}$ spanned by variational wave functions implemented in an open source software, mVMC [3].

A simple solution is, instead of taking summation, taking inner products, such as $\langle\psi_1|\psi_2\rangle$, and expectation values, $\langle\psi_1|\hat{O}|\psi_2\rangle$, of a given operator $\hat{O}$ among the bases. While it is again not easy because of large statistical noise in sampling for $\langle\psi_1|\psi_2\rangle$, an efficient sampling has been proposed [4] and implemented [5].

To simulate whole inelastic neutron scattering spectra, the order of $N_{\rm s}^2$ bases, where $N_{\rm s}$ is the number of electrons, are required. Angle resolved photoemission spectroscopy simulation requires more bases.

Then, the bottleneck of the method is the memory and computational costs for the generalized eigenvalue problems defined by the nonorthogonal basis set. During the maintenance of reasonable statistics to estimate the inner products, which favor the flat MPI model, we need to utilize relatively small memory per process. In the present study, to reduce memory costs and to reach $N_{\rm s} > 100$, we implemented the LOBCG [6] method and a block-type variation of the Sakurai-Sugiura method [7].

References

[1] For example, P. Laurell, *et al.*: Phys. Rev. Lett. **127**, 037201 (2021).

[2] For example, W.-L. Tu, *et al.*: Phys. Rev. B **103**, 205155 (2021).

[3] T. Misawa, *et al.*: Comput. Phys. Commun. **235**, 447 (2019).

[4] T. Li and F. Yang: Phys. Rev. B **81**, 214509 (2010).

[5] For example, K. Ido, *et al.*: Phys. Rev. B **101**, 075124 (2020).

[6] A. V. Knyazev: SIAM J. Sci. Comput. **23**, 517 (2001).

[7] T. Sakurai and H. Sugiura: J. Comput. Appl. Math. **159**, 119 (2003).

Many-body topological phases in strongly correlated electron systems

Kota IDO

Institute for Solid State Physics,

The University of Tokyo, Kashiwa-no-ha, Kashiwa, Chiba 277-8581

The Kondo lattice model is one of the fundamental models for strongly correlated electron systems [1]. This model has been originally considered an effective model for heavy fermion systems, but recently, for van der Waals heterostructure systems [2]. In this model, the competition between the RKKY magnetic effective interaction and the formation of the Kondo singlet gives birth to enriched intriguing states such as the Kondo insulator, non-Fermi liquids, and exotic superconducting states.

As one of them, the magnetic topological insulator has been discussed in the last decade [3-5]. Previous studies mentioned that the magnetic topological insulator stabilizes as the ground state at quarter filling in the classical limit [4] or within spin-wave approximation [5]. However, the role of quantum effects beyond the spin-wave approximation, including the formation of the Kondo singlet, is still an enigmatic problem.

In this study [6], we investigate the ground states of the spin 1/2 Kondo lattice model on the triangular lattice at quarter filling. As a quantum many-body solver, we employ the variational Monte Carlo (VMC) method [7]. We find that a noncoplanar magnetic ordered state becomes the ground state in the intermediate coupling region. To identify the topological property of the ground states, we propose an efficient VMC method for calculating the many-body Chern number based on Resta's polarization approach [8,9]. Using this method, we find that the noncoplanar magnetic state has indeed the non-trivial many-body Chern number. Our results shed light on not only a further pathway to realize correlated magnetic topological insulators but also an efficient analysis of the many-body topological states in strongly correlated electron systems.

References

[1] H. Tsunetsugu, M. Sigrist, and K. Ueda, Rev. Mod. Phys. **69** 809 (1997).

[2] V. Vaňo, et al., Nature **599**, 582 (2021).

[3] I. Martin and C. D. Batista, Phys. Rev. Lett. **101** 156402 (2008).

[4] Y. Akagi and Y. Motome, J. Phys. Soc. Jpn. **79** 083711 (2010).

[5] Y. Akagi, M. Udagawa, and Y. Motome, J. Phys. Soc. Jpn. **82** 123709 (2013).

[6] K. Ido and T. Misawa, arXiv:2310.07094.

[7] T. Misawa et al., Comput. Phys. Commun. **235** 447 (2019).

[8] R. Resta, Phys. Rev. Lett. **80** 1800 (1998).

[9] B. Kang, W. Lee, and G. Y. Cho, Phys. Rev. Lett. **126** 016402 (2021).

Magnetically ordered states on the hexagonal quasiperiodic tilings

Akihisa Koga
Department of Physics, Tokyo Institute of Technology, Meguro, Tokyo 152-8551

Quasiperiodic systems have attracted considerable interest since the discovery of the Al-Mn quasicrystal. Recently, electron correlations in quasicrystals have been actively studied after quantum critical behavior was observed in the Au-Al-Yb quasicrystal. In addition, long-range ordered states have been reported such as superconductivity in the Al-Zn-Mg quasicrystal, and ferromagnetically ordered states in the Au-Ga-R (R = Gd, Tb, Dy) quasicrystals. These studies have stimulated theoretical investigations on electron correlations and the spontaneously symmetry breaking states in quasicrystals.

We have introduced golden-mean hexagonal and trigonal quasiperiodic tilings, using a generalization of de Bruijn's grid method [1]. In this work, we have demonstrated the structural properties and substitution rules of the H_{00} and $H_{\frac{1}{2}\frac{1}{2}}$ tilings, where the subscript refers to the tunable grid-shift parameters. These structural properties are distinct from those for the Penrose, Ammann-Beenker, and Socolar tilings. One of the important points is the existence of the sublattice imbalance. However, they are still rooted in the physical world of experimentally observed trigonal and hexagonal quasiperiodic systems. It is therefore desirable to study magnetic properties on quasiperiodic systems with sublattice imbalances.

In this project, we have clarified magnetic properties of the Hubbard model on the H_{00} and $H_{\frac{1}{2}\frac{1}{2}}$ tilings and have studied the macroscopically degenerate states with $E = 0$ in the tight-binding model, which should play an important role for magnetic properties in the weak coupling limit [2, 3, 4]. We have clarified that two extended states appear in one of the sublattices, while confined states appear in the other. Furthermore, we have obtained the fraction of the confined states in terms of Lieb's theorem, considering magnetism in the weak coupling limit. We also have discussed how magnetic properties are affected by electron correlations in the half-filled Hubbard model.

References

[1] S. Coates, A. Koga, T. Matsubara, R. Tamura, H. R. Sharma, R. McGrath, and R. Lifshitz, arXiv:2201.11848.

[2] A. Koga and S. Coates, *Phys. Rev. B* **105**, 104410 (2022).

[3] T. Matsubara, A. Koga, and S. Coates, *J. Phys.: Conf. Ser.* **2461**, 012003 (2023).

[4] T. Matsubara, A. Koga, and S. Coates, *Phys. Rev. B* **109**, 014413 (2024).

Magnetic-field control of non-Abelian anyons in Kitaev quantum spin liquids

Joji NASU
Department of Physics, Tohoku University
Sendai 980-8578

The Kitaev model has been widely studied as a quantum many-body model that possesses a quantum spin liquid in its ground state [1], and a proposal for realizing this model in transition metal compounds has been made [2]. In this model, elementary excitations behave as if a spin is split into two independent quasiparticles: a Majorana fermion and a vison. Moreover, when a magnetic field is applied, each vison is accompanied by Majorana zero modes, leading to non-Abelian anyons. These non-Abelian anyons are potential computational elements in topological quantum computing, and thus, theoretical proposals for their temporal and spatial control are highly needed. However, observing, generating, and controlling these quasiparticles remain challenging. In this research project, we investigate the real-time dynamics of quasiparticles in the Kitaev quantum spin liquid in large clusters to clarify how to control visons with Majorana zero modes.

In the present study, we calculate the time evolution of the Kitaev quantum spin liquid in the presence of an excited vison using time-dependent mean-field theory. In this method, time evolution is computed based on the von Neumann equation for a time-dependent density matrix [3, 4]. To evaluate the commutation relations between the Hamiltonian and density matrices, we use the MKL library with thread parallelization. This approach is effective for computations involving larger matrices, which are required in the present real-space calculations with larger lattice clusters.

We apply the time-dependent local magnetic field to an excited vison and calculate the time evolution of the system. We find that a vison can follow a local field sweeping through the system. We also confirm that a Majorana zero mode always accompanies the vison even while it moves by following a time-dependent local field [5]. We reveal optimal conditions for the local field to control a non-Abelian anyon, which is determined by interactions between the fractional quasiparticles of the Kitaev model. Furthermore, we demonstrate creating and annihilating visons by applying local magnetic fields in addition to vison manipulations.

References

[1] A. Kitaev, , Ann. Phys. (NY) **303**, 2 (2003).

[2] G. Jackeli and G. Khaliullin, Phys. Rev. Lett. **102**, 017205 (2009).

[3] J. Nasu, and Y. Motome, Phys. Rev. Research **1**, 033007 (2019).

[4] T. Minakawa, Y. Murakami, A. Koga, and J. Nasu, Phys. Rev. Lett. **125**, 047204 (2020).

[5] C. Harada, A. Ono, and J. Nasu, Phys. Rev. B **108**, L241118 (2023).

Electronic and phonon states and superconductivity of multi-band low-carrier systems based on first-principles and quantum many-body calculations

Yoshiaki ŌNO

Department of Physics,

Niigata University, Ikarashi, Niigata 950-2181

We have studied the effects of ionizations induced by proton and ^{12}C radiation and molecular conformational changes in DNA. This year, we calculated the stable structure, band dispersion, and wave function of DNA under the condition that one and two electrons per 10 base pairs are ionized by radiation corresponding to 10 and 20 percent hole doped cases using the first-principles calculation software OpenMX and discussed the relationship between the energy dependence of each incident radiation type and the molecular conformational change of DNA [1].

We have also studied the superconductivity in the two-band Hubbard model (so-called *d-p* model) on the basis of the dynamical mean-field theory (DMFT), in which the irreducible vertex function Γ has no k-dependence and then only the s-wave superconductivities with the spin-singlet even-frequency pairing and the spin-triplet odd-frequency pairing are possibly realized. In the previous DMFT studies, both the singlet and triplet superconductivities have not been observed in the one-band Hubbard model. On the other hand, in the two-band Hubbard model, the singlet and/or triplet superconductivities have been found to be realized. However, the explicit results of the pair (superconducting) susceptibilities which show divergence as the temperature approaches the superconducting transition temperature T_c were not shown there. This year, we calculated the singlet and triplet pair susceptibilities by solving the Bethe-Salpeter equation and determine T_c in the two-band Hubbard model on a Bethe lattice with infinite connectivity. We obtained the phase diagrams of T_c for the singlet and triplet superconductivities as functions of doping, on-site Coulomb interaction and charge-transfer energy [2].

References

[1] T. Sekikawa, Y. Matsuya, B. Hwang, M. Ishizaka, H. Kawai, Y. Ōno, T. Sato, and T. Kai, Nucl. Instrum. Methods Phys. Res. B **548**, 165231 (2024).

[2] Y. Inokuma, and Y. Ōno, J. Phys. Soc. Jpn. **93**, 043701 (2024).

Designing and evaluating quantum many-body chaos

Masaki TEZUKA

Department of Physics, Kyoto University, Kitashirakawa, Sakyo-ku, Kyoto 606-8502

The Sachdev-Ye-Kitaev (SYK) model is a model of fermions with independently random all-to-all four-point interactions obeying the Gaussian distribution. The model can be solved in the sense of random coupling average in the limit of large number of fermions, and the Lyapunov exponent, defined by the out-of-time ordered correlation functions, realizes the universal upper bound at low temperatures.

Previously, we studied a "sparse" version of the SYK model, in which the number of non-zero interaction terms is reduced to the order of the number of fermions. While it had been known that the sparse model reproduces essential features of the original SYK model for Gaussian random couplings [1], we analyzed the spectral statistics of a further simplification, in which the magnitude of the nonzero couplings is set to be a constant [2]. This simplification is an improvement in the sense that the spectral correlation is stronger and thus closer to the random-matrix universality for the same number of non-zero couplings, compared to the Gaussian random case.

Towards quantum simulation of such models, we considered another simplification of the SYK model: a model of Pauli spin operators with all-to-all 4-local interactions, obtained by replacing Majorana fermions in the SYK model with spin operators. From the numerical analysis using the ISSP Supercomputer, we observed a striking quantitative coincidence between this spin model and the SYK model, which suggests that this spin model is strongly chaotic [3].

We also studied the quantum error correction (QEC) capabilities of the unitary time evolution according to various time-independent Hamiltonians by the Hayden-Preskill protocol. An unknown quantum state thrown into a quantum many-body system can or cannot be decoded, with the knowledge of the initial state of the system and the time evolution, by accessing only a part of the system after time evolution, depending on whether the Hamiltonian of the system is scrambling the quantum information. We compared the error estimate, obtained by the decoupling approach, against the one for random unitary evolutions obeying the circular unitary (Haar) ensemble. For the sparse SYK model, the QEC error estimate approaches the Haar value within a short time if the spectral statistics is random-matrix like. In the presence of two-fermion interactions, departure from the Haar value is observed before the Fock space localization. On the other hand, for quantum spin chains often studied in the context of chaotic dynamics, scrambling is not observed in this sense and the QEC error estimate remains large in the long-time limit [4].

References

[1] S. Su *et al.*, arXiv:2008.02303; A. M. Garcia-Garcia *et al.*, Phys. Rev. D **103**, 106002 (2021).

[2] M. Tezuka, O. Oktay, E. Rinaldi, M. Hanada, and F. Nori, Phys. Rev. B **107**, L081103 (2023).

[3] M. Hanada, A. Jevicki, X. Liu, E. Rinaldi, and M. Tezuka, J. High Energ. Phys. in press (arXiv:2309.15349).

[4] Y. Nakata and M. Tezuka, Phys. Rev. Research **6**, L022021 (2024).

Magnetization plateau and anomaly induced by spin-lattice coupling in pyrochlore antiferromagnets

Hidemaro SUWA
Department of Physics, University of Tokyo, Tokyo 113-0033

Frustrated magnetic systems inherently exhibit macroscopic degeneracy, which can be lifted by various perturbations, leading to diverse magnetic phenomena. Among these, spin-lattice coupling plays a pivotal role in stabilizing magnetization plateaus, particularly in spinel magnetic compounds. In this context, lattice modes intertwined with spin degrees of freedom are effectively modeled using simplified phonon approaches. Here, bond phonons encapsulate magnetostriction effects resulting from spin-lattice interactions, whereas site phonons are instrumental in elucidating the long-range magnetic order of real materials.

Despite their utility, these models fall short in fully accounting for the behaviors observed in certain systems, such as chromium spinel oxides that manifest pyrochlore antiferromagnetic properties. Although bond and site phonon models successfully reproduce the experimentally observed half-magnetization plateau in pyrochlore systems, they fail to capture the high-field magnetization anomaly prevalent in many chromium spinel oxides, which is arguably considered an indicator of potential magnon-bound states.

To address these discrepancies and enhance our understanding of the magnetization process in chromium spinel oxides and other related frustrated systems, a more sophisticated spin-lattice model is necessary. Our research adopts a combined spin-lattice model that amalgamates both bond and site-phonon effects. By tracing out lattice degrees of freedom, we derive an effective spin model that includes higher-order interactions, such as biquadratic and three-body spin interactions. This model introduces an additional parameter representing the relative contributions from bond and site phonons, aiming to provide a more accurate depiction of experimental observations, including magnetostriction, long-range magnetic order, and specific heat behavior.

Using the Monte Carlo method, enhanced by an advanced update scheme[1], we examined the proposed spin-lattice model within a pyrochlore lattice framework. The simulations were performed on ISSP System B in the class C project (2023-Ca-0112) in an MPI parallel computation using up to eight nodes simultaneously. Our simulations, calibrated with optimal parameters for various chromium spinel oxides, successfully replicate the half-magnetization plateau and specific heat measurements. Moreover, the model predicts a magnetization anomaly under high magnetic field conditions, suggesting a complex magnetic ordering not previously found. Our findings offer a novel perspective on the high-field magnetic anomaly and contribute to a broader understanding of the pyrochlore antiferromagnet.

References

[1] M. Gen and H. Suwa, Phys. Rev. B **105**, 174424 (2022).

Phtoinduced transient absorption spectrum in two-leg-ladder Mott insulator with strong dimer correlation

Takami TOHYAMA
Department of Applied Physics, Tokyo University of Science, Katsushika, Tokyo 125-8585

Photoinduced nonequilibrium states in the Mott insulators reflect the fundamental nature of competition between itinerancy and localization of the charge degrees of freedom. The spin degrees of freedom will also contribute to the competition in a different manner depending on lattice geometry. There is a spin gap in a two-leg-ladder Mott insulator. The spin gap is ascribed to an energy to break spin-singlet dimer predominately formed along the rung. Because of spin dimer formation, dimer-dimer correlation is also strong. Under the presence of dimer-dimer correlation, photoexcited doublon and holon tend to form a localized exciton not to break spin dimers. Such localized exciton formation appears in optical absorption as a large peak at a high frequency slightly above the on-site Coulomb energy [1]. Therefore, it is interesting to clarify how the localized exciton contributes to photoexcitation.

To answer this question, in this project we investigate pulse-excited states of the half-filled two-leg Hubbard ladder using the time-dependent density-matrix renormalization group (tDMRG) and time-dependent exact diagonalization (tED) based on the Lanczos technique [2]. Our tDMRG makes use of the Legendre polynomial for the calculation of time-evolution operator. We use two target states at a given time t and $t + \Delta t$ to construct a basis set that can express wavefunctions in the time-dependent Hilbert space. With the two-target tDMRG procedure, we can calculate time-dependent physical quantities with high accuracy even when the Hamiltonian varies rapidly with time.

From our tDMRG and tED simulations, we find that strong monocycle pulse inducing quantum tunneling gives rise to anomalous suppression of photoinduced in-gap weight, leading to negative weight [2]. This is in contrast to finite positive weight in an extended Hubbard chain [3]. Examining multipulse pumping for states above the Mott gap, we attribute the origin of this anomalous behavior of in-gap spectral weight to photoinduced localized exciton that reflects strong spin-singlet dimer correlation in the ground state. We note that so-called Majumdar-Ghosh chain having single-dimer ground state does not show in-gap negative weight.

This contrasting behavior can be confirmed if one applies a monocycle terahertz pulse to a one-dimensional Mott insulator such as Sr_2CuO_3 and a two-leg ladder Mott insulator such as $La_6Ca_8Cu_{24}O_{41}$, increases pulse strength, and observes how in-gap weight evolves with the strength.

References

[1] K. Shinjo, Y. Tamaki, S. Sota, and T. Tohyama: Phys. Rev. B **104**, 205123 (2021).

[2] T. Tohyama, K. Shinjo, S. Sota, and S. Yunoki, Phys. Rev. B **108**, 035113 (2023).

[3] K. Shinjo, S. Sota, and T. Tohyama: Phys. Rev. Res. **4**, L032019 (2022).

Nonlinear response in correlated materials

Robert PETERS

Department of Physics,

Kyoto University, Kyoto, 606-8502

The research on nonlinear phenomena in correlated materials advanced in two stages. On the one hand, (1) we analyzed the nonlinear Edelstein effect in correlated materials using a perturbative technique, and (2) we made significant progress in analyzing responses using time evolution. On the other, we (3) were able to calculate the time evolution of a quantum skyrmion driven by a magnetic field gradient using neural networks.

1) We developed a method to study the nonlinear spin response using single-particle Green's functions. We then explored the effect of correlations on this nonlinear Edelstein effect using the dynamical mean-field approximation. We found that correlations can enhance the effect in static electric fields. We also explored the optical version of the effect, i.e., the build-up of a static spin polarization in a time-dependent electric field, and we identified a delicate interplay between the lifetime of excitations and renormalization that can enhance or suppress the Edelstein effect. [1]

(2) We studied the non-equilibrium dynamics of correlated systems and analyzed the response to an external electric field. Here, we perturbatively included fluctuations in the calculations using a correlation expansion. We demonstrated that for a noninteracting system, the Green's function technique mentioned above and the time evolution yield identical results. Then, we demonstrated in an interacting Rice-Mele model that the biexciton transition strongly enhances the response whenever the frequency of the incident light matches the exciton energy. [2]

(3) We used neural network quantum states on ISSP's GPU to calculate the time-dependent wave function of a large two-dimensional quantum spin model hosting quantum skyrmions. We demonstrated that the quantum skyrmion is driven by a magnetic field gradient. We furthermore observed the merging of two quantum

skyrmions through the formation of an exceptional spin configuration. This merging is accompanied by a large build-up of entanglement. [3]

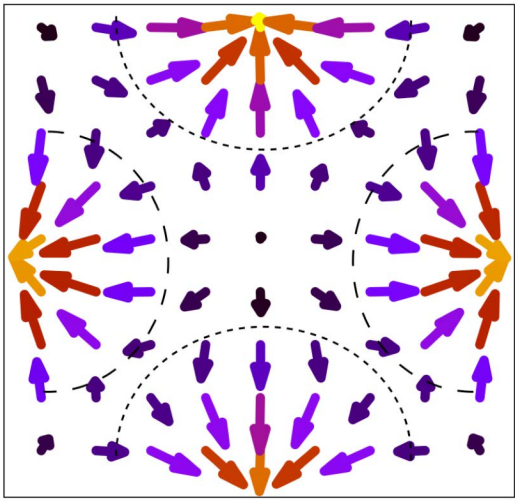

Figure 1:Ground state with two quantum as calculated by neural network quantum states

References

[1] "Nonlinear Edelstein Effect in Strongly Correlated Electron Systems" Jun Ōiké, Robert Peters; arXiv:2403.17189

[2] "Two-particle correlation effects on nonlinear optical responses in the one-dimensional interacting Rice-Mele model" Akira Kofuji and Robert Petersl Phys. Rev. B 109, 155111

[3] "Quantum skyrmion dynamics studied by neural network quantum states" Ashish Joshi, Robert Peters, Thore Posske; arXiv:2403.08184

Research of Three-Channel Kondo Effect Emerging from Tb and Tm Ions

Takashi HOTTA
Department of Physics, Tokyo Metropolitan University
1-1 Minami-Osawa, Hachioji, Tokyo 192-0397

Inspired by the discovery of three-channel Kondo effect emerging from Ho ions for the case of Γ_5 triplet ground state [**?**], we have attempted to find the three-channel Kondo effect also from Tb and Tm ions for the same case of the Γ_5 triplet ground state.

First let us explain the model Hamiltonian. It is convenient to define one f-electron state by the eigenstate of spin-orbit and crystalline electric field (CEF) potential terms. We find Γ_7 doublet and Γ_8 quartet from $j = 5/2$ sextet whereas we find Γ_6 doublet, Γ_7 doublet, and Γ_8 quartet from $j = 7/2$ octet under the cubic CEF potential. Then, we include the Γ_7 and Γ_8 conduction electron bands. Note that we consider only the hybridization between the conduction and $j = 7/2$ electrons. The model Hamiltonian is given by

$$\begin{aligned} H &= \sum_{\boldsymbol{k},\mu,\tau} \varepsilon_{\boldsymbol{k}} c^\dagger_{\boldsymbol{k}\mu\tau} c_{\boldsymbol{k}\mu\tau} + \sum_{\boldsymbol{k},\mu,\tau} V (c^\dagger_{\boldsymbol{k}\mu\tau} f_{b\mu\tau} + \text{h.c.}) \\ &+ nE_f + \sum_{j,\mu,\tau} (\lambda_j + B_{j,\mu}) f^\dagger_{j\mu\tau} f_{j\mu\tau} \\ &+ \sum_{j_1\sim j_4} \sum_{\mu_1\sim\mu_4} \sum_{\tau_1\sim\tau_4} I^{j_1 j_2, j_3 j_4}_{\mu_1\tau_1\mu_2\tau_2,\mu_3\tau_3\mu_4\tau_4} \\ &\times f^\dagger_{j_1\mu_1\tau_1} f^\dagger_{j_2\mu_2\tau_2} f_{j_3\mu_3\tau_3} f_{j_4\mu_4\tau_4}, \end{aligned} \tag{1}$$

where $\varepsilon_{\boldsymbol{k}}$ is the dispersion of conduction electron with wave vector $\boldsymbol{k}$, $c_{\boldsymbol{k}\mu\tau}$ is the annihilation operator of a conduction electron, $f_{j\mu\tau}$ is the annihilation operator of a localized f electron in the bases of (j, μ, τ), j is the total angular momentum, $j = 5/2$ and $7/2$ are denoted by "a" and "b", respectively, μ distinguishes the cubic irreducible representation, Γ_8 states are distinguished by $\mu = \alpha$ and β, while the Γ_7 and Γ_6 states are labeled by $\mu = \gamma$ and δ, respectively, τ denotes the pseudo-spin, which distinguishes the degeneracy concerning the time-reversal symmetry, V denotes the hybridization between f electron in the μ orbital and conduction electron of the μ band, n is the local f-electron number at an impurity site, and E_f is the f-electron level to control n.

As for the spin-orbit term, we obtain $\lambda_a = -2\lambda$ and $\lambda_b = (3/2)\lambda$, where λ is the spin-orbit coupling of f electron. We set $\lambda = 0.212$ and 0.326 eV for Tb and Tm ions, respectively. Concerning the CEF potential term for $j = 5/2$, we obtain $B_{a,\alpha} = B_{a,\beta} = 1320B^0_4/7$ and $B_{a,\gamma} = -2640B^0_4/7$, where B^0_4 denotes the fourth-order CEF parameter for the angular momentum $\ell = 3$. For $j = 7/2$, we obtain $B_{b,\alpha} = B_{b,\beta} = 360B^0_4/7 + 2880B^0_6$, $B_{b,\gamma} = -3240B^0_4/7 - 2160B^0_6$, and $B_{b,\delta} = 360B^0_4 - 3600B^0_6/7$. In the following calculations, we use the parametrization as $B^0_4 = Wx/15$ and $B^0_6 = W(1 - |x|)/180$ for $\ell = 3$, where x specifies the CEF scheme for the $O_{\rm h}$ point group, while W determines the energy scale of the CEF potentials. In this work, we set $W = 10^{-3}$ eV and treat x as the parameter to control the CEF ground state.

For the Coulomb interaction terms, we do not show the explicit forms of I here, but they are expressed by the four Slater-Condon parameters, F^0, F^2, F^4, and F^6. These values should be determined from experimental results, but here we simply set the ratio as

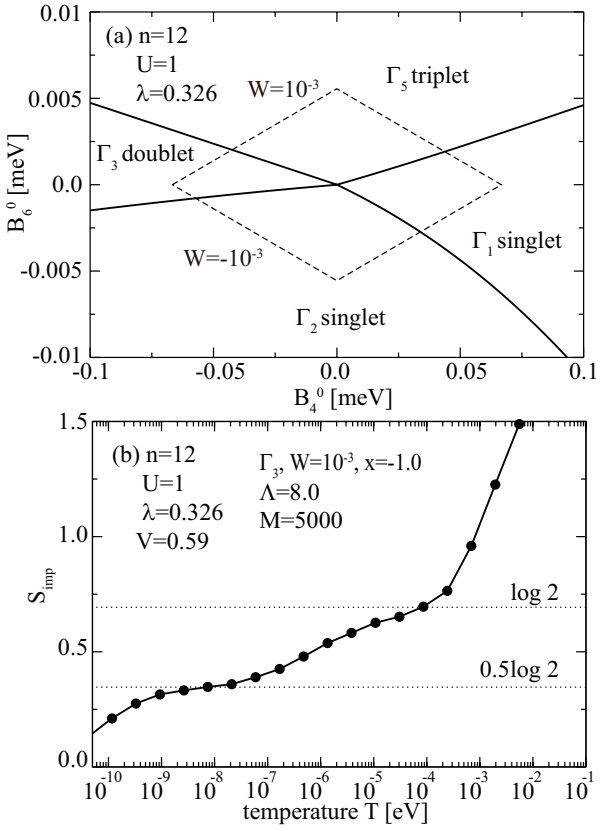

Figure 1: (a) Local CEF ground-state phase diagram on the (B_4^0, B_6^0) plane for $n = 12$ with $U = 1$ and $\lambda = 0.326$. The dashed rhombus denotes the trajectory of $B_4^0 = Wx/15$ and $B_6^0 = W(1 - |x|)/180$ for $-1 \le x \le 1$ with $W = \pm 10^{-3}$. (b) Entropy vs. temperature for $x = -1$, $W = 10^{-3}$, and $V = 0.59$ for the case with the local Γ_3 ground state.

$F^0/10 = F^2/5 = F^4/3 = F^6 = U$, where U indicates the Hund's rule interaction among the f orbitals. In this work, we set $U = 1$ eV.

In the present report, we show only the results for the Tm ion. Results for the Tb ion will be shown elsewhere. First we consider the local CEF ground-state phase diagram for $n = 12$. The ground-state multiplet for $B_4^0 = B_6^0 = 0$ is characterized by the total angular momentum $J = 6$. Under the cubic CEF potentials, the tre-dectet of $J = 6$ is split into four groups as one Γ_1 singlet, one Γ_2 singlet, one Γ_3 doublet, one Γ_4 triplet, and two Γ_5 triplets. Then, we obtain four kinds of local ground states for $n = 12$, as shown in Fig. 1(a). Roughly speaking, the Γ_5 triplet appears widely for $B_6^0 > 0$, whereas the Γ_2 singlet is found for $B_6^0 < 0$. In the region of $B_6^0 \approx 0$ and $B_4^0 > 0$, the Γ_1 singlet is stabilized. For $B_4^0 < 0$, we find the Γ_3 doublet.

The three-band Anderson model is analyzed with the use of a numerical renormalization group (NRG) method. We introduce a cut-off Λ for the logarithmic discretization of the conduction band. Due to the limitation of computer resources, we keep M low-energy states. Here we use $\Lambda = 8$ and $M = 5,000$. In the NRG calculation, the temperature T is defined as $T = D\Lambda^{-(N-1)/2}$, where D is half the conduction band width, which is set as 1 eV, and N is the number of renormalization steps.

The appearance of the three-channel Kondo effect from Ho ion is characterized by a residual entropy $S_{\rm imp}$ of $\log \phi$ with the golden ratio $\phi = (1 + \sqrt{5})/2$ for the local Γ_5 triplet ground state [**?**]. Thus, we have tried to find the residual entropy $\log \phi$ from the Tm ion in the parameter space corresponding to the local Γ_5 triplet ground state, but we could not find any signals of $\log \phi$ for the case of $n = 12$. It is inevitable to conclude that the three-channel Kondo effect does not appear for the Tm ion.

However, it is interesting to report the discovery of $S_{\rm imp} = \log \sqrt{2}$, which is characteristic of the two-channel Kondo effect. In Fig. 1(b), we show the f-electron entropy for $x = -1$, $W = 10^{-3}$, and $V = 0.59$. In this figure, we find the signal of the residual entropy of $\log \sqrt{2}$, although we did not perform the fine tuning of the CEF parameters to obtain the residual entropy even at extremely low temperatures. Thus, we conclude that for the case of $n = 12$, the two-channel Kondo effect is found even in the three-band Anderson model.

References

[1] T. Hotta, J. Phys. Soc. Jpn. **90**, 113701 (2021).

Studies on unconventional superconductivity in multilayer nickelates

KAZUHIKO KUROKI
Department of Physics, Osaka University
1-1 Machikaneyama, Toyonaka, Osaka, 560-0043, Japan

Several studies in the past have shown that the superconducting T_c in the bilayer Hubbard model can be higher than that of the d-wave superconducting state in the single-orbital Hubbard model [1, 2]. Therefore, realizing the bilayer Hubbard model in actual materials can be considered as a path toward finding new high temperature superconductors. The present author proposed that a double layer Ruddlesden-Popper compound $La_3Ni_2O_7$ can be a good candidate for realizing the bilayer Hubbard model that satisfies the above-mentioned conditions [3]. In this material, for which the Ni $3d$ electron configuration is $d^{7.5}$, the $3d_{3z^2-r^2}$ orbitals are elongated in the z (out-of-plane) direction so that $t_\perp$ between the layers is much larger than the in-plane hoppings between the neighboring $d_{3z^2-r^2}$ orbitals, and also the $d_{3z^2-r^2}$ orbitals are nearly half-filled. Hence the $d_{3z^2-r^2}$ portion of the electronic structure appears to be favorable for superconductivity from the above-mentioned viewpoint of the bilayer model, although deviation from the ideal model arises due to the presence of the Ni $3d_{x^2-y^2}$ bands, which are nearly quarter-filled, overlapping and hybridizing with the $d_{3z^2-r^2}$ bands. In this context, a recent experimental finding that $La_3Ni_2O_7$ exhibits high T_c superconductivity with a highest T_c of about 80 K under pressure above 14 GPa [4] is certainly intriguing.

Inspired by this experiment, we theoretically revisited the possibility of superconductivity in $La_3Ni_2O_7$ by constructing a four-orbital model that takes into account the crystal structure at high pressures, and applying fluctuation exchange approximation to the model. We find that $s\pm$-pairing superconductivity, which is somewhat similar to that of the bilayer Hubbard model, can take place with high T_c that is consistent with the experimental observation[6].

We have also performed density matrix renormalization group studies in a two-orbital Hubbard[7] and t-J ladder[8] models that mimic the electronic state of $La_3Ni_2O_7$. Our calculation shows that both the interchain, intraorbital pair correlation within both $d_{3z^2-r^2}$ and $3d_{x^2-y^2}$ orbitals exhibit slow, power law decay, which are enhanced by both the interlayer coupling and Hund's coupling. More interestingly, the interorbital pair correlation also exhibits a slow decay comparable to the intraorbital ones, and this occurs even in the absence of Hund's coupling, for which the pairing glue mediated by Hund's coupling is absent.

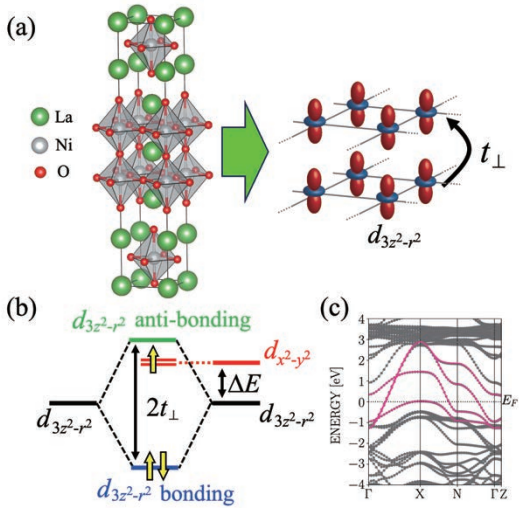

FIG. 1. (a)Crystal structure drawn by VESTA [5], (b)an energy diagram of e_g orbitals in our bilayer model, and (c) the first-principles band structure of $La_3Ni_2O_7$ are shown. In the right side of panel (a), schematic figure of the bilayer model of the $d_{3z^2-r^2}$ orbitals is depicted. In the panel (c), Wannier-interpolated band structure (pink lines) of the four-orbital model is superposed on the first-principles band structure (grey lines). The definition of the energy level offset ΔE and $t_\perp$, key parameters of this study, are indicated in the panel (b) and (a), respectively.

Following the study on the bilayer $La_3Ni_2O_7$, we further studied the possibility of superconductivity in a trilayer Ruddlesden-Popper nickelate $La_4Ni_3O_{10}$ under pressure. Through DFT calculations, we found that a structural phase transition from monoclinic to tetragonal takes place around 15 GPa. Using the tetragonal crystal structure, we have theoretically investigated the possibility of superconductivity, where a combination of fluctuation exchange approximation and linearized Eliashberg equation is applied to a six-orbital model constructed from first principles band calculation. The obtained results suggests that $La_4Ni_3O_{10}$ may also become superconducting under high pressure with T_c comparable to relatively low T_c cuprates, although it is not as high as $La_3Ni_2O_7$[9]. This theoretical expectation was confirmed from experiments on polycrystalline samples[9].

[1] K. Kuroki, T. Kimura, and R. Arita, Phys. Rev. B **66**, 184508 (2002).
[2] V. Mishra, D. J. Scalapino, and T. A. Maier, Sci. Rep. **6**, 32078 (2016).
[3] M. Nakata, D. Ogura, H. Usui, and K. Kuroki, Phys. Rev. B **95**, 214509 (2017).
[4] H. Sun, M. Huo, X. Hu, J. Li, Z. Liu, Y. Han, L. Tang, Z. Mao, P. Yang, B. Wang, J. Cheng, D.-X. Yao, G.-M. Zhang, and M. Wang, Nature (2023).
[5] K. Momma and F. Izumi, J. Appl. Crystallogr. **44**, 1272 (2011).
[6] H. Sakakibara, N. Kitamine, M. Ochi, and K. Kuroki, Phys. Rev. Lett. **132**, 106002 (2024).
[7] T. Kaneko, H. Sakakibara, M. Ochi, and K. Kuroki, Phys. Rev. B **109**, 045154 (2024).
[8] M. Kakoi, T. Kaneko, H. Sakakibara, M. Ochi, and K. Kuroki, (2023), arXiv:2312.04304.
[9] H. Sakakibara, M. Ochi, H. Nagata, Y. Ueki, H. Sakurai, R. Matsumoto, K. Terashima, K. Hirose, H. Ohta, M. Kato, Y. Takano, and K. Kuroki, Phys. Rev. B **109**, 144511 (2024).

Theoretical Study for Mixed-sequence Oligomer Salt Modeling Doped PEDOT Family

Tomoko FUJINO

Institute for Solid State Physics,

The University of Tokyo, Kashiwa-no-ha, Kashiwa, Chiba 277-8581

Organic conductors are divided into two categories: low-molecular-weight and polymer-based materials. Low-molecular-weight materials have well-defined structures but limited control over conductivities. Conductive polymers, on the other hand, have highly conjugated systems but are difficult to control due to their structural inhomogeneity.

To bridge this gap, oligomer-based conductors were developed as intermediate materials. These conductors are made of oligo(3,4-ethylenedioxythiophene), oligoEDOT, and are modeled after the doped PEDOT family 1–4]. The conductivities of these materials were studied by considering counter anion variations, lengths of oligomer donor, and band fillings. Through the study, oligoEDOT analogs were developed with tunable room temperature conductivities by several orders of magnitude, including a metallic state above room temperature [4]. The electronic structural insights were evaluated by first-principles calculations (QUANTUM ESPRESSO, RESPACK, and H-wave packages; Ohtaka, Supercomputer center, ISSP), and it was revealed that the range of Coulomb repulsion between carriers, $\boldsymbol{U}_{\mathbf{eff}}$, is the dominant factor that determines the relationship between the structures and conductivities [5]. The oligoEDOT conductor systems have a unique feature of widely variable $\boldsymbol{U}_{\mathbf{eff}}$, differentiating these systems from strongly electron-correlated systems.

References

[1] R. Kameyama, T. Fujino*, S. Dekura, M. Kawamura, T. Ozaki, and H. Mori*, Chem. Eur. J. **27**, 6696 (2021).

[2] R. Kameyama, T. Fujino,* S. Dekura, and H. Mori,* Phys. Chem. Chem. Phys. **24**, 9130 (2022).

[3] R. Kameyama, T. Fujino, S. Dekura, S. Imajo, T. Miyamoto, H. Okamoto, H. and Mori,* J. Mater. Chem. C **10** (9), 7543 (2022).

[4] K. Onozuka, T. Fujino,* R. Kameyama, S. Dekura, K. Yoshimi, T. Nakamura, T. Miyamoto, T. Yamakawa, H. Okamoto, H. Sato, T. Ozaki, and H. Mori,* J. Am. Chem. Soc. **145**, 15152 (2023).

[5] T. Fujino,* R. Kameyama, K. Onozuka, K. Matsuo, S. Dekura, K. Yoshimi, and H. Mori,* Faraday Discuss. **250**, 348 (2024).

Analyses of magnetic properties in the Hubbard models.

Atsushi Yamada
Department of Physics, Chiba University
Chiba 263-8522, Japana, Chiba 277-8581

Exotic states like a spin liquid state has attracted a lot of interest. Foe example, spin liquid may be realized in geometrically frustrated systems like the charge organic transfer salts κ-(BEDT-TTF)$_2$X[1] and Cs_2CuCl_4.[2] Hubbard model on the an-isotropic triangular lattice is a simple theoretical model of these compounds. Some theoretical groups, including us have studied that model, and idntified a possible candidates of spin liquid state in this model.[3, 4] A spin liquid could arise also in the intermediate coupling region of strongly correlated systems between a semimetal and ordered state, because in this case a correlation-driven insulating gap might open before the system becomes ordered. This possibility might be realized in the half-filled Hubbard model on the honeycomb lattice, where a semi-metal is realized at $U = 0$.

We have studied the magnetic and metal-to-insulator transitions in this model by variational cluster approximation.[6] The 10-site and 16-site clusters are used in our study as a reference system. Parts of numerical calculations were done using the computer facilities of the ISSP. Our results rule out the existence of the spin liquid in this model. Our results agree with recent large scale Quantum Monte Carlo simulations.[5]

We are currently improving our program using MPI technique so that we will be able to study a larger cluster size system compared to our previous studies[4] and more memory-intensive states like superconductivity.

References

[1] Y. Shimizu, K. Miyagawa, K. Kanoda, M. Maesato, and G. Saito, Phys. Rev. Lett. **91**, 107001 (2003); Y. Kurosaki, Y. Shimizu, K. Miyagawa, K. Kanoda, and G. Saito, Phys. Rev. Lett. **95**, 177001 (2005).

[2] R. Coldea, D.A. Tennant, A.M. Tsvelik, and Z. Tylczynski, Phys. Rev. Lett. **86**, 1335 (2001); R. Coldea, D.A. Tennant, and Z. Tylczynski, Phys. Rev. Lett. **68**, 134424 (2003).

[3] T. Yoshioka, A. Koga, and N. Kawakami, Phys. Rev. Lett. **103**, 036401 (2009); P. Sahebsara and D. Sénéchal, Phys. Rev. Lett. **100**, 136402 (2008); L.F. Tocchio, H. Feldner, F. Becca, R. Valenti, and C. Gros, Phys. Rev. B **87**, 035143 (2013); L.F. Tocchio, C. Gros, R. Valentí, F. Becca, Phys. Rev. B **89**, 235107 (2014).

[4] A. Yamada, Phys. Rev. B **89**, 195108 (2014); Phys. Rev. B **90**, 235138 (2014).

[5] S. Sorella, Y. Otsuka, and S. Yunoki, Sci. Rep. **2**, 992 (2012); F. F. Assaad and I. F. Herbut, Phys. Rev. X **3**, 031010 (2013); F. Parisen Toldin, M. Hohenadler, F. F. Assaad, and I. F. Herbut, Phys. Rev. B **91**, 165108 (2015).

[6] A. Yamada, Int. J. Mod. Phys. B **30**, 1650158 (2016).

Stripes and Charge-ordered ground state and its coexistence with superconductivity in correlated electron systems

Takashi YANAGISAWA
National Institute of Advanced Industrial Science and Technology (AIST)
1-1-1 Umezono, Tsukuba, Ibaraki 305-8568, Japan

1 Introduction

Our numerical research is based on the optimized variational Monte Carlo method[1]. We use the optimized many-body wave function which is improved by multiplying by off-diagonal exponential operators given by $e^{-\lambda K}$ and $e^{-\alpha D}$ (K and D are the kinetic operator and the double occupancy operator, respectively). The Gutzwiller-Jastrow wave function with the doublon-holon correlation operators are also employed. We have investigated the ground-state phase diagram of the two-dimensional Hubbard model[2, 3] and the two-dimensional three-band (d-p) model[4].

We carried out parallel computations in Monte Carlo calculations. In order to reduce statistical errors, we performed ~ 500 parallel calculations. Parallel computing is very essential to reduce Monte Carlo statistical errors.

The many-body wave function is written in the form $\psi^{(1)} = \exp(-\lambda K)P_G\psi_0$, where K denotes the kinetic energy part (non-interacting part) of the Hamiltonian and $P_G = P_G(g)$ is the Gutzwiller operator to control the double occupancy with the variational parameter g. ψ_0 indicates a trial wave function which is usually taken as the Fermi sea, the BCS wave function or the state with some magnetic (or charge) orders. We can improve the wave function systematically by multiplying by operators P_G and $e^{-\lambda K}$ repeatedly. We can consider $\psi^{(2)} = \exp(-\lambda' K)P_G(g')\psi^{(1)}$ for different variational parameters λ' and g'. This wave function is a very good many-body wave function because the ground-state energy is lowered greatly and the ground-state energy is lower than those that are evaluated by any other wave functions. We also employ the Jastrow-type wave function which is written as $\psi_J = P_G P_Q P_J \psi_0$ where P_J indicates a nearest-neighbor number correlation operator and P_Q controls the nearest-neighbor doublon-holon correlation.

2 Charge-ordered state coexisting with superconductivity in the Hubbard model

We have carriedi out a variational Monte Carlo simulation to examine the ground state in the optimal region of the two-dimensional Hubbard model on a square lattice. We can show that striped states are stable near the 1/8-doping region when t'/t is negative and U/t is large[5]. The one-particle state ψ_0 for stripe states are given by the eigenstate of the following Hamiltonian

$$H_{tri} = -\sum_{ij\sigma} t_{ij} c^{\dagger}_{i\sigma} c_{j\sigma} + \sum_{i\sigma} (\rho_i - \mathrm{sgn}(\sigma) m_i) n_{i\sigma}, \tag{1}$$

with $\rho_i = \rho \cos(\mathbf{Q}_c \cdot (\mathbf{r}_i - \mathbf{r}_0))$ and $m_i = m \sin(\mathbf{Q}_s \cdot (\mathbf{r}_i - \mathbf{r}_0))$. Here ρ and $m \equiv \Delta_{AF}$ are variational parameters. Two incommensurate wave vectors $\mathbf{Q}_c$ and $\mathbf{Q}_s$ characterize the charge and spin configurations, respectively. We set $\mathbf{Q}_c = 2\mathbf{Q}_s$. $\mathbf{r}_0$ denotes the position of the domain boundary. The vertical stripe is represented by $\mathbf{Q}_s = (\pi \pm 2\pi\delta, \pi)$ where δ stands for the incommensurability which defined as the inverse of the antiferromagnetic order in the x-direction. The charge modulation period is given by $\mathbf{Q}_c$.

We consider the case $t' = 0$. In this case, when U is as large as $U = 18t$, the antiferromagnetic state does not become stable[2] and thus a charge-ordered state can be stable in stead of stripes. This charge-ordered state can be called the nematic state. An important question is whether the charge-ordered state coexists with superconductivity. In the real space representation, the superconducting (SC) order parameter is assigned for each bond connecting two lattice points i and $i+\hat{\mu}$ where $\hat{\mu}$ indicates the unit vector in the μ-th direction. For d-wave pairing, we take the SC order parameter as $\Delta_{i,i+\hat{x}} = \Delta_s$ and $\Delta_{i,i+\hat{y}} = -\Delta_s$, where Δ_s is a real constant showing te magnitude of the SC order parameter. We can generalize this in several ways. For example,

$$\begin{aligned} \Delta_{i,i+\hat{x}} &= \Delta_s(\beta + (1-\beta)|\cos(\varphi(\mathbf{r}_i) - \pi/4)|), \\ \Delta_{i,i+\hat{y}} &= -\Delta_s(\beta + (1-\beta)|\cos(\varphi(\mathbf{r}_i))|), \end{aligned} \tag{2}$$

where β is a real constant in the range of $0 \leq \beta \leq 1$ and $\varphi(\mathbf{r}_i) = \mathbf{Q}_c \cdot (\mathbf{r}_i - \mathbf{r}_0)$. Δ_{ij} indicates the pure d-wave symmetry for $\beta = 1$ and is called the oscillating d-wave symmetry for $\beta = 0$.

We found that the charge-ordered state and superconductivity indeed coexist with each other when the doping rate $x =$ is near $1/8$ where we set $\delta = 1/8$[6]. In Fig. 1, we show the ground-state energy as a function of the superconducting order parameter Δ_s where we put $m = \Delta_{AF} = 0$ and $\rho = 0.01$. The d-wave state with charge nematic order is most stable for $U/t = 18$, $t' = 0$ and $x = 0.109375$.

3 Summary

We examined the ground state of the two-dimensional Hubbard model by using the advanced optimized variational Monte Carlo method. In the strong coupling region where U is ias large as or greater than the band width, the inhomogeneous state is stabilized when the doping rate x is is near $x = 0.125$. For $t' = 0$, the charge-ordered state is realized without magnetic order. The charge-ordered state can coexist with superconductivity as shown in Fig. 1.

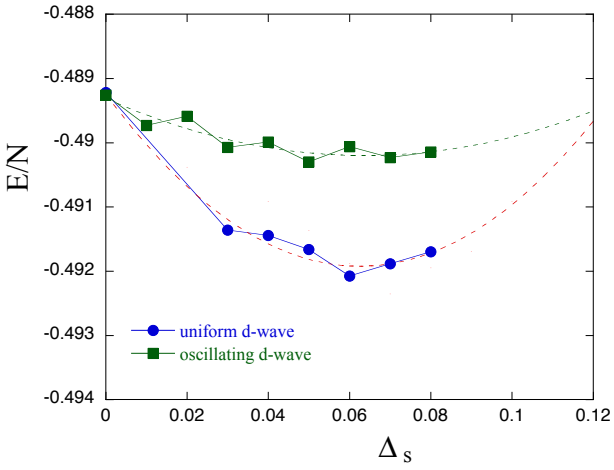

Figure 1: The ground-state energy as a function of the superconducting order parameter Δ_s for $N_e = 228$ (near 1/8-doping) on a 16×16 lattice, where we set $U = 18t$ and $t' = 0$. We employed the parameters given as $\Delta_{AF} = 0$, $\rho = 0.01$ and $\delta = 1/8$, We introduced the charge order parameter as $\rho = 0.01t$ for which the ground-state energy has a minimum. The circles show the energy for the uniform d-wave symmetry ($\beta = 1$) and the squares show that for the oscillating d-wave symmetry ($\beta = 0$).

References

[1] T. Yanagisawa et al., J. Phys. Soc. Jpn. 67, 3867 (1998).
T. Yanagisawa, Phys. Rev. B75, 224503 (2007) (arXiv: 0707.1929).

[2] T. Yanagisawa, J. Phys. Soc. Jpn. 85, 114707 (2016).
T. Yanagisawa, J. Phys. Soc. Jpn. 88, 054702 (2019).
T. Yanagisawa, Condensed Matter 4, 57 (2019).

[3] T. Yanagisawa, Phys. Lett. A403, 127382 (2021).

[4] T. Yanagisawa et al., EPL 134, 27004 (2021).

[5] M. Miyazaki, T. Yanagisawa, Phys. Lett. A448, 128276 (2022).

[6] T. Yanagisawa et al, preprint.

Many-body quantum simulations based on multi-scale space-time ansatz

Hiroshi SHINAOKA
Department of Physics, Saitama University, Saitama 338-8570

We have worked on the following topics in collaboration with co-workers.

(1) Parallelization quantics tensor train

We have implemented Julia libraries (TensorCrossInterpolation.jl, QuanticsGrids.jl) [1] for tensor cross interpolation and quantic tensor train [2,3]. A critical step toward practical calculations is parallelization of the algorithm. We have implemented a prototype parallelized code based on quantics tensor train in Julia. The code is still experimental and to be benchmarked on a HPC system.

(2) Hidden covalent insulator and spin excitations in SrRu2O6

We applied the density functional+dynamical mean-field theory to study the spin excitation spectra of SrRu2O6. We used DCore [4] and ALPS/CT-HYB [5]. After computing a self-consistent solution, we solved the Bethe-Salpeter equation to compute the dynamical susceptibility.

We found a good quantitative agreement with experimental spin excitation spectra. Depending on the size of the Hund's coupling J_H, the system chooses either the Mott insulator or covalent insulator state when magnetic ordering is not allowed. We found that the nature of the paramagnetic state has a negligible influence on the charge and spin excitation spectra.

(3) Comparative study of variational quantum circuits for quantum impurity models

We have developed compact ansatz for solving quantum impurity models using variational quantum circuits [7]. Our approaches are based on two ideas. First, we employed a compact physics-inspired ansatz, *k*-unitary cluster Jastrow ansatz, developed in the field of quantum chemistry. Second, we eliminated largely redundant variational parameters of physics-inspired ansatz associated with bath sites based on physical intuition. We benchmarked the new ansatzes and found that the compact anstazes outperform the original ansatz in terms of the number of variational parameters.

(4) Classical Monte Carlo simulation of J_1-J_2 *XY* Kagome antiferromagnet

We investigated the J_2-T phase diagram of the J_1-J_2 *XY* Kagome antiferromagnet using extensive classical Monte Carlo simulations based on non-local loop updates and replica-exchange Monte Carlo method [8]. Our code is implemented in Julia and use MPI parallelization. The obtained phase diagram

features Berezinskii-Kosterlitz-Thouless transitions of $q = 0$, $\sqrt{3} \times \sqrt{3}$ magnetic orders, and octupole orders, in addition to finite-temperature phase transitions of both ferrochiral and antiferrochiral long-range orders. We found a nontrivial first-order transition for antiferromagnetic $J_2/J_1 < 0$.

References

[1] https://tensor4all.org/

[2] H. Shinaoka, M. Wallerberger, Y. Murakami, K. Nogaki, R. Sakurai, P. Werner, and A. Kauch Phys. Rev. X **13**, 021015 (2023).

[3] M. K. Ritter, Y. N. Fernández, M. Wallerberger, J. von Delft, H. Shinaoka, and X. Waintal, Phys. Rev. Lett. **132**, 056501 (2024).

[4] H. Shinaoka, J. Otsuki, M. Kawamura, N. Takemori, K. Yoshimi, SciPost Phys. **10**, 117 (2021).

[5] H. Shinaoka, E. Gull, P. Werner, Comput. Phys. Commun. **215**, 128 (2017).

[6] D. Csontosová, H. Shinaoka, A. Hariki, and J. Kuneš, PRB **108**, 195137 (2023).

[7] R. Sakurai, O. J. Backhouse, G. H. Booth, W. Mizukami, and H. Shinaoka, Phys. Rev. Res. **6**, 023110 (2024).

[8] F. Kakizawa, T. Misawa, H. Shinaoka, PRB **109**, 014439 (2024).

Nonequilibrium dynamics in quantum systems driven by optical electric fields

Atsushi ONO
Department of Physics, Tohoku University, Sendai 980-8578

Research on controlling quantum systems through light irradiation has been actively pursued. We have conducted numerical simulations of the real-time dynamics of quantum systems driven by optical electric fields and explored the possibility of new classes of photoinduced phase transitions and ultrafast phenomena [1, 2], focusing on magnetic materials.

Among various magnetic structures, spin textures such as magnetic skyrmions have attracted interest owing to their intriguing transport and optical responses due to emergent fields. These noncoplanar magnetic structures are characterized by spin scalar chirality and are known to be stabilized by antisymmetric interactions such as the Dzyaloshinskii–Moriya interaction in systems with broken spatial inversion symmetry. However, limited studies have been conducted on the optical control of spin textures in centrosymmetric systems.

In a paper [1], we conducted numerical analyses of the real-time dynamics induced by terahertz electric fields in a ferromagnetic Kondo lattice model on a triangular lattice with spatial inversion symmetry. We numerically solved coupled equations of the von Neumann equation for electrons and the Landau–Lifshitz–Gilbert equation for localized spins. We found that, when a linearly polarized electric field is applied to the ground state of the ferromagnetic metallic phase, the ferromagnetic order melts within a time scale of approximately several hundred femtoseconds, followed by the emergence of a scalar chiral state after several picoseconds. Furthermore, it was revealed that the handedness of circular polarization controls the sign of chirality in this nonequilibrium scalar chiral state, as shown in Fig. 1. This photoinduced magnetic order is stabilized by the nonequilibrium distribution of electrons driven by the electric field and does not require antisymmetric interactions. This suggests that centrosymmetric itinerant magnets could be a promising platform for the ultrafast optical control of spin textures.

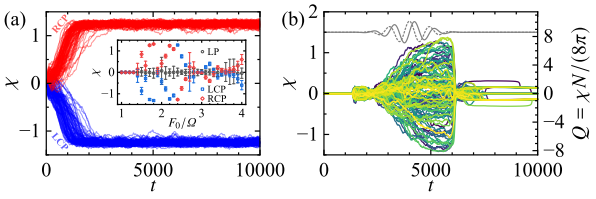

Figure 1: Temporal profiles of scalar chirality under (a) a circularly polarized continuous wave and (b) a linearly polarized pulse, for different spin configurations in the initial states, adapted from Ref. [1]. The inset in (a) shows the time-averaged chirality in the steady states as a function of the optical amplitude.

References

[1] A. Ono and Y. Akagi: Phys. Rev. B **108**, L100407 (2023).

[2] S. Imai and A. Ono: Phys. Rev. B **109**, L041303 (2024).

Theoretical study of BCS-BEC crossover in solid-state materials

Hiroshi WATANABE
Research Organization of Science and Technology, Ritsumeikan University
1-1-1 Noji-Higashi, Kusatsu-shi, Shiga 525-8577

In fermion systems with attractive interactions, the pairing mechanism of superconductivity (SC) or superfluidity is described by the Bardeen-Cooper-Schrieffer (BCS) theory in a weak interaction regime, while it is described by the Bose-Einstein condensation (BEC) in a strong interaction regime. They are smoothly connected in the intermediate regime, which is called BCS-BEC crossover. Recently, the possibility of BCS-BEC crossover in real materials has been reported in 2D gated semiconductor Li_xZrNCl, iron-based superconductor $FeSe_{1-x}S_x$, and 2D molecular superconductor κ-$(ET)_4Hg_{2.89}Br_8$. In strongly-correlated electron systems, it is much more difficult to identify the BCS-BEC crossover than in simple Fermi gas systems because of the unconventional (non-s-wave) gap symmetry and competition with various magnetic and/or charge orderings. To clarify the nature of BCS-BEC crossover in strongly-correlated electron systems, we study the extended Hubbard model for the κ-ET system [1, 2], which shows SC, several magnetic and/or charge orderings, and also the spin-liquid phase depending on the variety of anion layers. The hopping integral t_{ij}, on-site Coulomb interaction U, and the intersite Coulomb interaction V_{ij} are estimated from first-principles calculation. The ground state properties are analyzed with a variational Monte Carlo method. The system size for the calculation is N=24×24=576 unit cells (and thus 576×2=1152 molecules in total) and the computation has been done mainly with the system B at the ISSP Supercomputer Center.

In the non-doped case, the system undergoes a first-order transition from SC to Mott insulator with increasing U/t_{b1}, where t_{b1} denotes the largest hopping integral. This transition can be seen from the abrupt vanishing of the superconducting correlation function $P_{\rm SC}$. On the other hand, for the 5.5% hole-doped case, $P_{\rm SC}$ shows dome-shaped behavior with respect to U/t_{b1}, suggesting the BCS-BEC crossover (Fig. 1). Since the Mott insulator disappears with hole doping, SC survives in a large U/t_{b1} region at which the crossover realizes. These behaviors are consistent with the measured $T_{\rm c}$ and it suggests the occurrence of the BCS-BEC crossover in the κ-ET system.

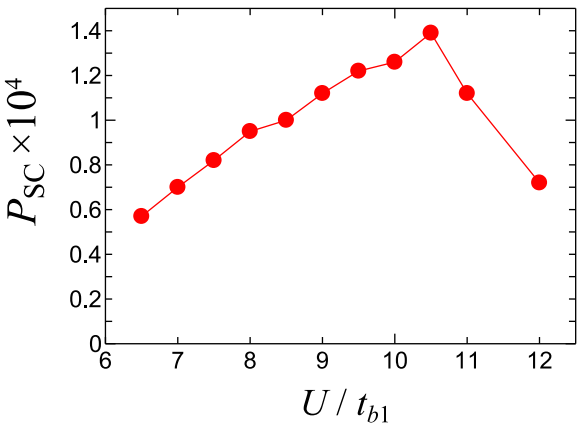

Figure 1: U/t_{b1} dependence of the superconducting correlation function $P_{\rm SC}$ of the extended Hubbard model with 5.5% hole doping.

References

[1] H. Watanabe, H. Seo, and S. Yunoki, J. Phys. Soc. Jpn. **86**, 033703 (2017).

[2] H. Watanabe, H. Seo, and S. Yunoki, Nat. Commun. **10**, 3167 (2019).

Compensated Ferrimagnetism with Colossal Spin Splitting in Organic compound $(EDO\text{-}TTF\text{-}I)_2ClO_4$

Akito Kobayashi[a], Taiki Kawamura[a], Kazuyoshi Yoshimi[b], Kenichiro Hashimoto[c], and Takahiro Misawa[b]

[a] *Department of Physics, Nagoya University, Nagoya 464-8602*

[b] *Institute for Solid State Physics, University of Tokyo, Kashiwa, Chiba 277-8581, Japan*

[c] *Department of Advanced Materials Science, University of Tokyo, Kashiwa, Chiba 277-8561, Japan*

Conventionally, it has been thought that collinear antiferromagnets, in which the spins are aligned antiparallel, do not exhibit unusual transport phenomena such as the generation of spin currents. However, recent theoretical research has revealed the existence of mysterious antiferromagnets, such as altermagnets and compensated ferrimagnets, which exhibit unique transport phenomena such as the anomalous Hall effect and spin current generation[1, 2, 3]. However, research on compensated ferrimagnetic materials has been limited to inorganic compounds such as alloys, and there have not been many examples of their implementation.

In this research, we discovered a simple method to realize compensated ferrimagnetism by using organic compounds with dimer structure. Specifically, we showed a simple design guideline that a compensated ferrimagnetic material can be realized if an antiferromagnetic order occurs in an organic compound in which two different dimers exist (Fig. 1). Furthermore, we also pointed out the possibility that compensated ferrimagnetism could be realized in the recently synthesized organic compound $(EDO\text{-}TTF\text{-}I)_2ClO_4$ using this mechanism. It was known that in this material, originally equivalent dimers become non-equivalent at low temperatures due to anion ordering. Using a strongly correlated first-principles calculation method, we analyzed the ordered phase that can theoretically be realized at low temperatures. As a result, we showed that the ground state is a compensated ferrimagnet[4]. This discovery sheds new light on the study of compensated ferrimagnets and shows that organic compounds provide an ideal stage for realizing compensated ferrimagnets.

References

[1] M. Naka et al., Nat. Commun. **10**, 1, (2019)

[2] H. van Leuken et al., Phys. Rev. Lett. **74**, 1171 (1995)

[3] S. Semboshi et al., Sci. Rep. **12**, 10687 (2022)

[4] T. Kawamura et al., Phys. Rev. Lett. **132**, 156502 (2024)

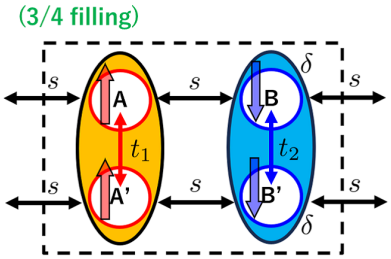

Figure 1: A non-equivalent dimer model that produces the compensated ferrimagnetism

Emergent inductance arising from a ferromagnetic domain wall under AC current

Kyohei Kado and Fumitaka Kagawa
Department of Physics,
Tokyo Institute of Technology, Tokyo 152-8551

The so-called "emergent inductor" describes a functionality that arises from the spin Berry phase associated with the interplay between flowing conduction electrons and an underlying magnetic texture [1]. Under the application of an AC electric current, the magnetic texture deforms in an AC manner as a result of a spin-transfer-torque (STT) effect. The flowing conduction electrons thus perceive a time-dependent U(1) gauge field, giving rise to an oscillating emergent electric field (EEF), which is described by:

$$e_i(r,t) = \frac{\hbar}{2|e|}\boldsymbol{m}(\boldsymbol{r},t) \cdot [\partial_i \boldsymbol{m}(\boldsymbol{r},t) \times \partial_t \boldsymbol{m}(\boldsymbol{r},t)], \quad (1)$$

where e (>0) is the elementary charge, $\boldsymbol{m}(\boldsymbol{r},t)$ is the unit vector of the local magnetic moment at position r and time t, and ∂_i (i = x, y, z) and ∂_t denote the spatial and time derivatives, respectively. As described in Eq. (1), changes in the magnetic texture in space and time are both essential for the emergence of an EEF. Even if the applied current density is weak and the magnetic texture is in the so-called pinned regime, the magnetic texture can elastically deform as a result of the STT effect by the current, I. Thus, under an AC current, $\partial_t \boldsymbol{m}(\boldsymbol{r},t)$ is finite in proportion to dI/dt, and an EEF may appear in an AC manner. Remarkably, it has been theoretically revealed that the AC-current-induced pinned dynamics of a helical magnetic texture1 give rise to an EEF with inductive characteristics (i.e., positive reactance) as a linear response to the applied AC current. Such a material showing the inductive response of the EEF is denoted an emergent inductor. Later, the close relationship between the emergent inductive reactance and the current-induced increase in magnetic-texture energy was also revealed. This new principle for inductive responses has drawn immediate attention from an application perspective because the inductance was inversely proportional to the sample cross-section size and therefore was presumed to be advantageous in terms of miniaturization over existing solenoid inductors.

In this study, we numerically investigated the emergent inductance due to a ferromagnetic domain wall under the application of an AC current. By referring to Landau-Lifshitz-Gilbert equation, we tracked the time evolution of the

spin texture under the current and calculated the emergent electric field from Eq. (1). The frequency dependence of the emergent inductance is shown in Fig. 1, in which L_1 and L_2 denote the real and imaginary parts of the emergent inductance, respectively.

We found that the Debye-like relaxation behaviour is obtained for the case of the intrinsic pinning (Fig. 1), whereas a resonance type is obtained for the case of the extrinsic pinning (not shown). The value of emergent inductance arising from single DW is on the order of 1 fH. Given that the detection limit in the inductance measurements is on the order of 1-10 nH, the required number of the domain walls is estimated to be 10^3-10^4.

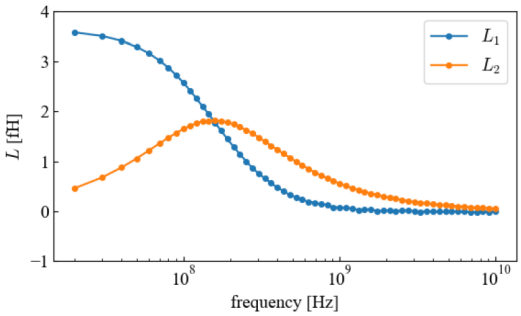

Fig. 1: Frequency dependence of the emergent inductance.

We used kugui and conducted micromagnetic simulation using MuMax3 respectively.

References

[1] N. Nagaosa, Jpn. J. Appl. Phys. **58**, 120909 (2019).

Theoretical study of thermoelectric properties in Heusler compounds using weak-coupling approaches

Kazutaka NISHIGUCHI
Graduate School of System Informatics, Kobe University
Rokkodai-Cho, Nada-Ku, Kobe 657-8501

Ferromagnetic fluctuations in Heusler alloy Fe_2VAl

Heusler compound Fe_2VAl is one of promising thermoelectric materials, which exhibits large power factor $P = \sigma S^2$ with σ and S being the electrical conductivity and Seebeck coefficient, respectively. On the other hand, the thermal the dimensionless figure of merit $ZT = \sigma S^2 T/\kappa$ is not so large yet reflecting its large thermal conductivity κ. Recently, it is experimentally observed in doped Fe_2VAl (i.e., $Fe_2V_{0.9}Cr_{0.1}Al_{0.9}Si_{0.1}$ and $Fe_{2.2}V_{0.8}Al_{1-y}Si_y$) as a weekly ferromagnetic material that ferromagnetic fluctuations enhance the thermoelectric properties such as S and P around the Curie temperature ($T_c = 285$ K). [1] It is not only a desirable property for practical use in realistic (room) temperatures, but also a fundamental and intriguing quantum phenomena where quantum fluctuations and thermoelectric effects are entangled by electron correlations.

Motivated above, we have studied electronic properties of Fe_2VAl using first-principles calculations based on the density functional theory (DFT) within the generalized gradient approximation (GGA). We performed DFT calculations with the Perdew–Burke–Ernzerhof (PBE) exchange-correlation functional for solids (PBEsol) and the projector augmented wave (PAW) method using The Vienna Ab Initio Simulation Package (VASP) [2] and Quantum ESPRESSO package (QE). [3]

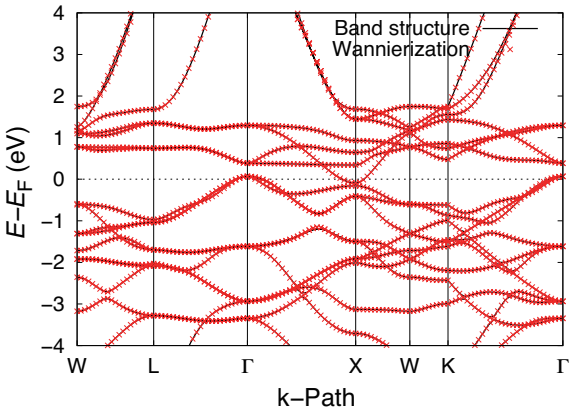

Figure 1: DFT band structure and Wannierization of Fe_2VAl.

Using the maximally localized Wannier functions, we could construct a low-energy effective model from the first- principles bands around the Fermi level. The effective model is composed of the Fe-3d, V-3d, and Al-2sp3 Wannier orbitals, namely, 19 orbitals. The DFT and structure and Wannier orbitals are shown in Fig. 1.

Furthermore, the obtained 19-orbital effective model was investigated using the random phase approximation (RPA). Figure 2 shows the total spin and charge susceptibility along the k-point path. It is clear that the spin fluctuations are dominant compared to the charge ones. Also, the obtained spin susceptibility has a peak at $q = (0, 0, 0)$, which reflects the ferromagnetic instability. This is consistent with the fact that Fe_2VAl exhibits the weak ferromagnetism.

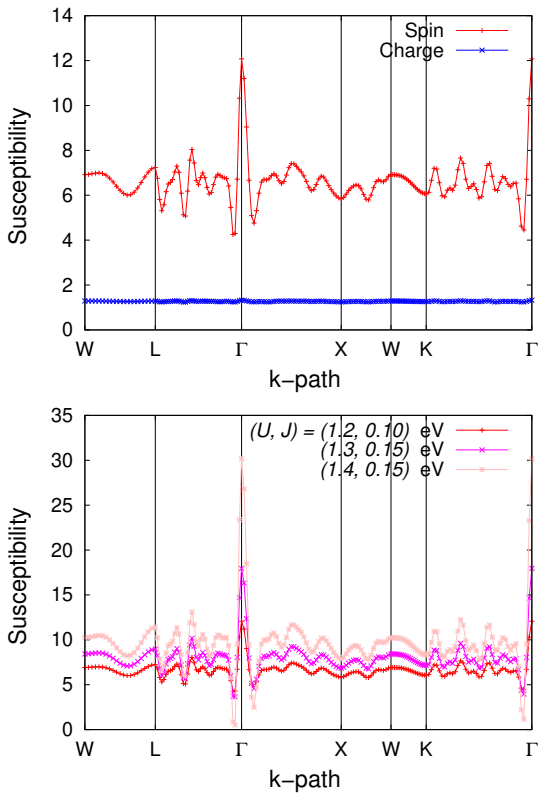

Figure 2: (Top) Total spin and charge susceptibility. (Bottom) Interaction dependence of the spin susceptibility. These are displayed along the k-point path.

Calculation conditions

We have performed the DFT calculations using the hybrid (MPI+OpenMP) parallel computing, where the parallelization over bands and k-points is used by VASP version 6.4.2 and QE version 7.2.

References

[1] N. Tsujii, A. Nishide, J. Hayakawa, and T. Mori: Sci. Adv. **5**, eaat5935 (2019).

[2] G. Kresse *et. al.*: Phys. Rev. B **47**, 558 (1993); Phys. Rev. B **49**, 14251 (1994); Computational Materials Science **6** (1996) 15–50; Phys. Rev. B **54**, 11169 (1996).

[3] P. Giannozzi *et. al.*: J. Phys.: Condens. Matter **21**, 395502 (2009) ; J. Phys.: Condens. Matter **29**, 465901 (2017) ; J. Chem. Phys. **152**, 154105 (2020).

[4] I. Souza, N. Marzari, and D. Vanderbilt: Phys. Rev. B **65**, 035109 (2001) ; A. A. Mostofi *et. al.*: Comput. Phys. Commun. **178** (2008) 685–699; A. A. Mostofi *et. al.*: Comput. Phys. Commun. **185** (2014) 2309–2310; G. Pizzi *et. al.*: J. Phys.: Condens. Matter **32**, 165902 (2020).

Calculating the Electronic Structure of Oxyhalides: Insights into their Optical Transitions

Takayuki MAKINO

University of Fukui, Bunkyo, Fukui, Fukui 910-8557

Bismuth oxychloride (BiOCl) is an oxyhalide compound with potential photocatalytic and optoelectronic applications. However, creating a flat surface has been challenging due to its low symmetry. Sun *et al.* successfully grew epitaxial layers of BiOCl with a flat surface and high crystallinity using a mist chemical vapor deposition method. This potentially facilitates the detailed characterization of their optical properties. [1,2]

Oxyhalides are classified as indirect-type semiconductors with an energy gap of approximately 2.9 eV. The optical response at the band-edge region of indirect semiconductors is considered weak, especially in the case of thin films. A recent report suggested that the formation of heterostructures between oxyhalides could turn an indirect-type into a direct-type semiconductor. This opens up possibilities for observing strong optical transitions even at the indirect-band-edge region. However, the grade suitable for detailed optical characterization having an atomically flat surface is only available in the form of thin films. This has discouraged researchers from studying the spectroscopic study of the indirect-type semiconductors at the band-edge region.

We conducted the optical characterization of BiOCl thin film on STO substrate by using a photoreflectance spectroscopy. We published a full paper [3] reporting the results of the optical characterization. In that article, it was necessary to display the energy-band structure for the clarification of the involved optical transition. That is why we calculated it despite several precedented theoretical works. The next paragraph is devoted to the description of the calculation procedure.

To calculate the band structures of BiOCl, we used the plane wave basis set PWscf package of Quantum ESPRESSO, an ab-initio density functional theory program with the plane wave basis, and a pseudopotential method. In addition to calculating band dispersion, QE can also perform structural optimization calculations, eigenfrequencies, and dielectric constants. First-principles calculations within the framework of density functional theory (DFT) is performed to analyze the structural and electronic properties of BiOCl. In this calculation, we neglected the contribution from $SrTiO_3$. For the atomic coordinates of BiOCl, the structure that has been adopted in the previous DFT calculations,

consistent with the experimental results, was adopted. To find the influence of the electron density on the exchange correlation energies of ions, we have used the LDA functional, which belongs to the class of Methfessel-Paxton functionals. The Brillouin zone (BZ) was integrated using an 8×8×8 centered Monkhorst-Pack k-point grid. As a precaution, it is necessary to adopt a value for which the cutoff energy converges. Our cutoff energy is $10^{(-8)}$ Ry. The Bi, Cl, and O atoms are represented by norm-conserving pseudopotentials, and the kinetic energy and charge density cutoffs are chosen to be 50 and 400 Ry, respectively. Methfessel-Paxton smearing of the Fermi-Dirac distribution, with a smearing width of 0.02 Ry.

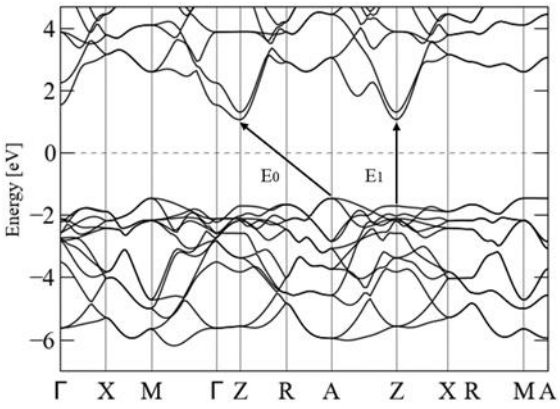

Fig. 1: Electronic structure of BiOCl.

References

[1] K. T. Drisya, S. Cortés-Lagunes, A.-L. Garduño-Jiménez, R. N. Mohan, N. Pineda-Aguilar, A. C. Mera, R. Zanella, and J. C. Durán-Álvarez, J. Environ. Chem. Eng. **10**, 108495 (2022).

[2] Z. Sun, D. Oka, and T. Fukumura, Chem. Commun. **56**, 9481 (2020).

[3] T. Nishiwaki, T. Makino, Z. Sun, D. Oka, T. Fukumura: Jpn. J. Appl. Phys, **63**, 02SP09 (2024).

Band Engineering and Electron Correlation Effects in Artificially Stacked Systems

Toshikaze KARIYADO

Research Center for Materials Nanoarchitectonics,

National Institute for Materials Science, Tsukuba, Ibaraki 305-0044

It is known that a zigzag edge of graphene hosts a flat edge band dispersion that leads to edge magnetization due to the large density of states [1,2]. On the other hand, it is also known that a proper edge decoration to a zigzag edge removes the flat band and the edge magnetization [3,4]. From these, we expect that partial completion of the edge decoration can be used to control magnetism at the graphene edge, for instance, to have a localized spin-1/2 state at the edge.

To demonstrate this idea, we investigated electronic and magnetic properties of some graphene nanoflakes with partially completed decorations at the edge (Inset of Fig. 1). We have done structural relaxations and band calculations based on the density functional theory using Quantum Espresso and OpenMX packages. Since the investigated flakes have large number of atoms, we need large computational resources. Both packages are nicely parallelized for large scale calculations, and OpenMX package is designed to handle large number of atoms. Note that the hydrogenation at the edge is applied terminated by hydrogen in actual calculations for stability.

Figure 1 shows a typical (Kohn-Sham) energies obtained in the spin density functional theory calculation. The result indicates that there appears a localized spin-1/2 state at the upper middle part of the flake in the inset of Fig. 1. It is an interesting future work to extend the same idea to variety of flake structures, to see spin-spin interaction when there are multiple localized states.

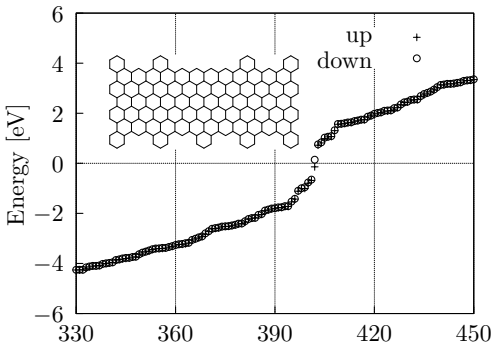

Fig. 1: Spin resolved energy spectrum.

References

[1] M. Fujita *et al.*, J. Phys. Soc. Jpn. **65**, 1920 (1996).

[2] G. Z. Madga *et al.*, Nature **514**, 608 (2014).

[3] D. J. Klein and L. Bytautas, J. Phys. Chem. A **103**, 5196 (1999).

[4] A. Narita et al., Nature Chem. **6**, 126 (2014).

3.4 Cooperative Phenomena in Complex Macroscopic Systems

Low-rank approximations for tensor decomposition and their application to critical phenomena

Naoki KAWASHIMA

Institute for Solid State Physics,

University of Tokyo, Kashiwa-no-ha, Kashiwa, Chiba 277-8581

Many of classes of data are labeled with multiple indicators. In that sense, they can be considered as tensor-type data. Compression of tensor type data has a lot in common with information extraction, classification, and restoration. Therefore, it is a technology with extremely high social needs. In recent years, research on critical phenomena using tensor networks (TN) has been actively conducted in the field of computational statistical mechanics. In handling tensor type-data, the low-rank approximation is a technique of the crutial importance. In this project, we aim at developing a low-rank approximation method that approximates tensor-type data, with an eye toward application to general data processing, and we are applying this to critical phenomena in classical and quantum spin models.

The core ingredient in our method is the tensor ring decomposition using "nuclear norm regularization". This method is being actively discussed among data science researchers, and has been applied to image compression, image classification, etc. [1] Previously, this method is applied to the TN renormalization group (TNRG), and it evaluates critical phenomena more stably with a simpler procedure than conventional methods. In the nuclear norm regularization we introduce the kernel norm, which is the sum of singular values, as a penalty term. A similar method could be constructed by using the sum of squares of singular values or mutual information as a penalty term instead of the nuclear norm. However, the nuclear norm is a sum of first powers, similar to LASSO, which has been frequently used in regression analysis, etc. In LASSO, and in our method as well, the optimal solution is such that some parameters (in our case, singular values) are exactly zero. Therefore, it naturally converges to a low-rank solution in our case. In addition, because the shape of the cost function around the optimal solution is not flat, we can expect the calculation to converge quickly. In this project, we improve upon this method to study two types of systems; critical phenomena in 2D classical statistical mechanics models and one-dimensional quantum spin systems, and critical phenomena in 3D classical statistical mechanics models. In the school year 2023, we obtained the following results:

(A) Benchmark calculations of 2D Ising model by the new method shows a clear advantage over the any previously-known TNRG methods and also over similar methods with milder cost functions based on mutual information. (Reported partially in [2], but shall be fully discussed in its revised version.)

(B) Some pilot calculation was carried out on the 3D Ising model, which produced promising results on the accuracy and the stability in the scaling dimensions. (The result will be fully discussed elsewhere.)

(C) Some other application of TN methods were carried out for dynamical properties of 2D quantum systems and exploring the phase diagram of a system that shows order-by-disorder physics. Since this part have been already published formally, we will discuss these further below.

In [3], we proposed a method for obtaining elementary excitations from unknown ground states. For this purpose, so-called diagrammatic summation is necessary while the code that realizes such computation is usually rather messy demanding a large amount of human labor. To solve this problem, we extended the scheme that we previously proposed for taking the diagrammatic summation using the generating-function. With the ansatz of the form of a one-particle excitation, we show that the excited state can be computed efficiently in this formalism. The dynamical structure factor of the system can be also computed. We carried out benchmark calculation on the spin-1/2 transverse-field Ising model and Heisenberg model on the square lattice, which exhibits good agreement with known results with reasonable accuracy. We then studied the spin-1/2 J1-J2 model on the same lattice and investigated the dynamical properties of the putative gapless spin liquid phase.

In [4], we studied the simplest quantum lattice spin model for the two-dimensional (2D) cubic ferromagnet by means of mean-field analysis and tensor network calculation. While both methods give rise to similar results in detecting related phases, the 2D infinite projected entangled-pair state (iPEPS) calculation provides more accurate values of transition points. Near the phase boundary, moreover, our iPEPS results indicates the easy-axis softening, implying an emergence of continuous U(1) symmetry.

References

[1] Q. Zhao, et al, arXiv:1606.05535.

[2] Kenji Homm and Naoki Kawashima, arXiv:2306.17479.

[3] Wei-Lin Tu, Laurens Vanderstraeten, Norbert Schuch, Hyun-Yong Lee, Naoki Kawashima, and Ji-Yao Chen, Physical Review X5, 010335 (2024)

[4] Wei-Lin Tu, Xinliang Lyu, S. R. Ghzanfari, Huan-Kuang Wu, Hyun-Yong Lee and Naoki Kawashima, Physical Review B 107, 224406 (1-14) (2023)

Large-scale Molecular Simulation of Soft Materials using All- Atom and Coarse-Grained Models

Wataru SHINODA
Research Institute for Interdisciplinary Science, Okayama University
3-1-1 Tsushima-naka, Kita-ku, Okayama 700-8530

We have used molecular simulations to study several biomolecular self-assemblies and soft materials, including highly concentrated Li-salt electrolytes. Significant progress in developing the SPICA force field (FF) has been the improvement of the protein model[1]. Our new protein model (SPICA FF ver2) overcomes the shortcomings found in the previous force field, where intrinsically disordered proteins (IDPs) were simulated as too compact in the dimension in an aqueous solution, and protein binding on the lipid membrane surface was over-stabilized. These issues were commonly found in many FFs, including all-atom FF, so we introduced protein secondary structure-dependent nonbonded interaction parameters to the backbone segments and re-optimize almost all nonbonded parameters for amino acids. The improved FF effectively replicates the radius of gyration observed in multiple IDPs, the binding sensitivity of numerous peripheral membrane proteins, and the dimerization-free energies of various transmembrane helices. Additionally, the updated model demonstrates enhanced consistency with experimental findings regarding the free energy of peptide association in aqueous environments.

Coarse-grained molecular dynamics (CG-MD) simulations using non-polar water models cannot correctly describe electrostatic screening effects owing to the hydration of ionic segments and thus cannot appropriately describe molecular events involving water channels and pores through lipid membranes. To overcome this issue, we developed a protein model in the pSPICA FF, in which a polar CG water model showing the proper dielectric response was adopted.[2] The developed CG model significantly improved the transfer free energy profiles of charged side chain analogues across the lipid membrane. Application studies on melittin-induced membrane pores and mechanosensitive channels in lipid membranes demonstrated that CG-MDs using the pSPICA FF correctly reproduced the structure and stability of the pores and channels. Furthermore, the adsorption behavior of the highly charged nona-arginine peptides on lipid membranes changed with salt concentration, indicating the pSPICA FF is also useful for simulating protein adsorption on membrane surfaces.

The above-mentioned large-scale CG-MDs have been carried out using System B with highly parallelized software such as LAMMPS and GROMACS. We also have done a series of MD simulations at the atomistic level using our polarizable model to investigate the Li-ion dynamics in solvated Li-salts, mostly using System C, which produced several papers this year[3, 4, 5, 6].

References

[1] T. Yamada, et al., J. Chem. Theory Comput. **19**, 8967 (2023).

[2] Y. Miyazaki and W. Shinoda, J. Chem. Inf. Model. **64**, 532 (2024).

[3] S. Ikeda, et al., J. Phys. Chem. C, **127**, 13837 (2023).

[4] S. Tsuzuki, et al., J. Phys. Chem. B, **127**, 6333 (2023).

[5] K. Shigenobu, et al., J. Phys. Chem. B, **127**, 10422 (2023).

[6] T. Sudo, et al., J. Phys. Chem. C, **127**, 12295 (2023).

Molecular Dynamics Analysis on Ultrasonic Cavitation

Yuta ASANO

Institute for Materials Research,

Tohoku University, Katahira, Aoba-ku, Sendai, Miyagi 980-8577

When a liquid is subjected to powerful ultrasonic waves, numerous bubbles are repeatedly generated and collapsed. This phenomenon is called ultrasonic cavitation. A high-temperature and high-pressure field is generated locally associated with the bubble collapse. Since ultrasonic cavitation is a highly safe and environmentally friendly technology, its application exists in broad fields, including food, medicine, biotechnology, and chemistry. Therefore, it is crucial to unveil the underlying mechanisms of ultrasonic cavitation. However, ultrasonic cavitation is a highly intricate phenomenon that causes many bubbles to continuously form, grow, and collapse under highly nonequilibrium conditions, and its mechanism is not fully comprehended.

In FY2023, we focused on elucidating soundwave propagation in a bubbling liquid, because its characteristics constitute an essential part of ultrasonic cavitation. The large-scale molecular dynamics (MD) simulation is applied to the analysis of soundwave propagation [1]. The MD simulation is promising for directly analyzing the effects of the interaction between bubbles, thermal and mass transport through the gas-liquid interface and phase transition.

The fluid is modeled by the Lennard-Jones (LJ) system. The system is a rectangular parallelepiped with the dimension of $L_x \times L_y \times L_z = 5000 \times 250 \times 250$. The periodic boundary conditions are applied to y- and z-directions. Since the soundwave propagates x-direction, the oscillating and stationary walls are placed at both boundaries. The liquid density is 0.6 with the total number of particles is about 200 million in total. MD simulations are performed by LAMMPS (Large-scale Atomic/Molecular Massively Parallel Simulator).

The bubbly liquid is generated using the depressurized method [2]. A non-condensable gas is added to the liquid to control the bubble distribution. Since the non-condensable gas affects the cavitation process and suppresses the Ostwald ripening [3], its addition can control the bubble distribution. The liquid with non-condensable gas is modeled by the binary LJ fluid. The maximum volume fraction of the non-condensable gas is up to 10%.

Figure 1 shows the bubbly liquid obtained by the depressurization. Only low-density areas are depicted for visibility. Although the liquid

has no bubbles at the boiling point (Fig. 1(a)), After the depressurization, the bubbles appear in the liquid. When the small depressurization, large bubbles distribute sparsely (Fig. 1(b)). As for the large depressurization, various sizes of bubbles distribute densely (Fig. 1 (c)). The bubbly liquid with non-condensable gas is also generated (Fig. 2). The bubbles become finer with the concentration of non-condensable gas.

When sound waves are propagated in a bubbly liquid, scattering, and absorption by the bubbles impede the propagation of the sound waves. In the pure liquid, the large bubble strongly attenuates the soundwave. The attenuation increases with the number of bubbles. As for the liquid with non-condensable gas, since the bubble distribution gradually changes with the concentration of the non-condensable gas, the attenuation is gradually varied. Fig. 3 shows the waveform of liquid with non-condensable gas with and without bubbles. Note that the wavelength also decreases due to the bubble. Although the addition of impurity increases the attenuation due to the viscosity increase, we found that increasing the concentration causes a larger propagation length. Therefore, the bubble distribution, especially its average radius, plays the dominant role in the soundwave propagation. More detailed analyses can reveal the mechanism of a drastic decrease in sound speed and the origin of dispersion in bubbly liquids.

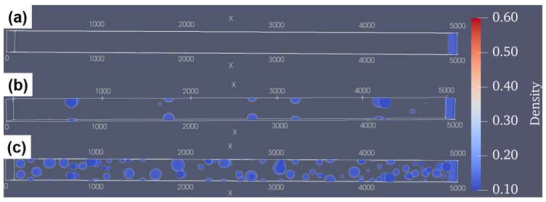

Fig. 1: (a) Pure liquid at boiling point, and (b, c) bubbly liquid.

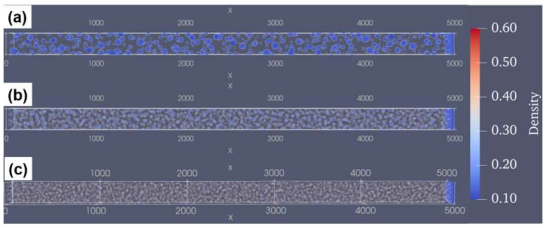

Fig. 2: Bubbly liquid with non-condensable gas with the concentration of (a) 1%, (b) 5%, and (c) 10%.

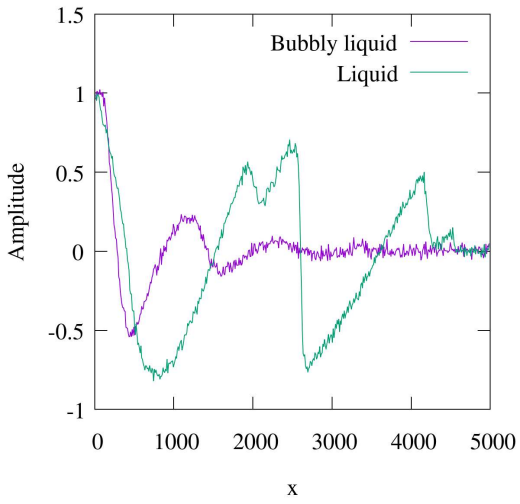

Fig. 3: The waveform of liquid and bubbly liquid with the non-condensable gas of 5%.

References

[1] Y. Asano, H. Watanabe, and H. Noguchi, Phys. Rev. Fluids **7**, 064302 (2022).

[2] H. Watanabe, M. Suzuki, H. Inaoka, N. Ito, J. Chem. Phys. **141**, 234703 (2014).

[3] S. Tsuda, S. Takagi, Y. Matsumoto, Fluid Dyn. Res. **40**, 606 (2008)

Energy spectrum analysis on a red blood cell model

Tetsuya YAMAMOTO and Hiroshi WATANABE
Faculty of Science and Technology, Keio University
Yokohama, Kanagawa 223-8522, Japan

We investigated the fluctuation behavior of the red blood cells (RBCs). RBCs are the main blood component, transporting oxygen and carbon dioxide. RBCs can deform so they can pass through capillaries with diameters less than half their radius, and elucidating their physical properties is essential for health. While RBCs have been studied theoretically and experimentally, recent developments in computational power allow us to perform direct blood flow simulations. With computer simulations, we can directly verify the behavior of fluids containing many plastic deformable objects, which is challenging to handle theoretically and elucidate microscopic properties that are difficult to observe experimentally. Modeling red blood cells is necessary to perform numerical simulations of them. Several types of red blood cell modeling exist, one of which is the particle-based method proposed by Fedosov et al. [1]. This model includes two-, three-, and four-body forces. The model parameters were determined to reproduce the mechanical properties determined by the experiment. Still, due to limitations in the accuracy of the experiments, the estimates of these parameters were ambiguous. To address this problem, we proposed a new method of determining the model parameters precisely from the fluctuations of the RBC membrane [2].

We adopted the dissipative particle dynamics (DPD) to achieve the isothermal environment. After thermalization with the DPD thermostat, we turned off the thermostat and continued the simulation under the isoenergetic environment. We observed the time evolutions of the potential energies and obtained their spectra with the temporal Fourier transform. Reflecting the microscopic nature of the model, multiple peaks appeared in the spectra. We performed the same simulation, with the model parameters changed from their original values, and observed the spectra to determine where each peak originated. If the peaks shifted, we can determine that they originated from the changed model parameters. We then found that some peaks originated from the two-body interaction, and others originated from the volume conservation laws. As an experimentally observable quantity, we also investigated the spectrum of the gyration radius of the RBC. The results show that a characteristic peak also appears in the spectra and that the peak position is sensitive to parameter changes. Compared to previous methods for studying the response of red blood cells to a static external field, our method using spectra is expected to allow more precise determination of model parameters because of the sharp parameter dependence of the peak positions of the spectra.

References

[1] A. Fedosov, B. Caswell, and G. E. Karniadakis, Comput. Methods Appl. Mech. Eng. **199**, 1937–1948 (2010).

[2] T. Yamamoto and H. Watanabe, J. Chem. Phys. **159**, 234119 (2023).

Tensor Netowkr Study on $S = 1$ Bilinear-Biquadratic Kitaev model

Tsuyoshi OKUBO
Institute for Physics of Intelligence, University of Tokyo
7-3-1 Hongo, Bunkyo-ku, Tokyo 133-0033

The $S = 1/2$ honeycomb lattice Kitaev model has been extensively studied as a model for investigating the properties of two-dimensional spin liquids [1, 2]. Similarly, Kitaev models with higher S are also believed to have spin liquid ground states. However, unlike the $S = 1/2$ case, Kitaev models with higher S are not exactly solvable, making numerical analysis crucial. In spin systems with higher S, in addition to conventional magnetic order, the nematic order, which is absent in $S = 1/2$ spin systems, can also be stabilized. Recently, the competition between Kitaev and other interactions have been analyzed using semiclassical approximations [3]. However, due to the limitations of these approximations, Kitaev spin liquid could not be precisely treated, and the phase structure near the spin liquid has not been sufficiently analyzed.

To elucidate the competition between the $S = 1$ Kitaev spin liquid and nematic order, we analyzed bilinear-biquadratic (BBQ) Kitaev model [3] this year. The Hamiltonian of the BBQ-Kitaev model is given as

$$\hat{H}_{\mathrm{BBQ-K}} = \sum_{\gamma=x,y,z} \sum_{\langle i,j\rangle_\gamma} \hat{H}_{\langle i,j\rangle_\gamma}, \tag{1}$$

$$\hat{H}_{\langle i,j\rangle_\gamma} = J_1 \hat{\boldsymbol{S}}_i \cdot \hat{\boldsymbol{S}}_j + J_2 \left(\hat{\boldsymbol{S}}_i \cdot \hat{\boldsymbol{S}}_j\right)^2 + K \hat{S}_i^\gamma \hat{S}_j^\gamma. \tag{2}$$

Here, $\langle i, j\rangle_\gamma$ denotes the nearest neighbor pair on a γ bond. J_1, J_2, and K are the coupling coefficients for the Heisenberg, biquadratic, and Kitaev interactions, respectively. To analyze the phase structure of the BBQ-Kitaev model, we employed the infinite projected entangled pair state (iPEPS) method, which can directly calculate the ground state of an infinitely large system. To optimize the tensors in iPEPS, we used imaginary time evolution combined with the truncation of the bond dimension by the simple update. The calculation of the physical quantities was performed by the corner transfer matrix renormalization group method. The entire calculation was done using TeNeS [4], which supports MPI and OpenMP hybrid parallelization.

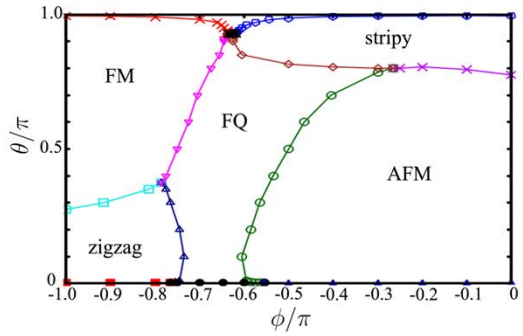

Figure 1: Phase diagram of the BBQ-K model in the region of $0.0 \leq \theta/\pi \leq 1.0$ and $-1.0 \leq \phi/\pi \leq 0.0$. FQ stands for the ferro-quadrupolar phase, and in the vicinity of $\phi/\pi = 0$ and 1, we observed an extended spin liquid phase. (Adapted from Ref. [5])

In Fig. 1, we show the phase diagram of the BBQ-Kitaev model for $J_2 < 0$ [5]. We represented the interaction coefficients with two parameters θ and ϕ as $(J_1, J_2, K) \equiv (\sin\theta\cos\phi, \sin\theta\sin\phi, \cos\theta)$. We found that

the BBQ-Kitaev model has a rich phase structure, including both ferro and anti-ferro Kitaev spin liquids, the quadrupolar order, and several magnetic orders. Interestingly, there is a direct phase transition between the ferro-quadrupolar (FQ) ordered and the Kitaev spin liquid phases. Note that both phases are characterized by the absence of magnetic order. In this sense, we can consider that such direct transition is induced by quantum fluctuations, and there is no classical counterpart.

In addition to this point, in the case of ferro Kitaev spin liquid, we observed an extension of the spin liquid phase around $\phi = \arctan(2) \simeq -0.648\pi$, where the BBQ interaction is reduced into the pure quadrupolar interaction, without Heisenberg interaction. This result indicates that the ferro Kitaev spin liquid is robust against the quadrupolar interaction. This would be useful not only for the search for Kitaev spin liquids in real compounds but also for understanding the nature of general spin liquids.

References

[1] A. Kitaev, Ann. Phys. **321** (2006) 2.

[2] Y. Motome and J .Nasu, J. Phys. Soc. Jpn. **89** (2020) 012002.

[3] R. Pohle, N. Shannon, and Y Motome, Phys. Rev. B **107** (2023) L140403 .

[4] Y. Motoyama, T. Okubo, K. Yoshimi, S. Morita, T. Kato and N. Kawashima, Comput. Phys. Commun. **279**, (2022) 108437.

[5] T. Mashiko and T. Okubo, arXiv:2403.11490.

Numerical simulations of fluctuating hydrodynamics: renormalized correction of shear viscosity

Hiroyoshi NAKANO
Institute for Solid State Physics, University of Tokyo
Kashiwa-no-ha, Kashiwa, Chiba 277-8581

In the intermediate regime between microscopic and macroscopic scales, conventional deterministic hydrodynamics often fails to accurately capture certain phenomena since the influence of thermal noises becomes profoundly significant, as represented by the Brownian motion. Fluctuating hydrodynamics is an extension of conventional fluid mechanics to describe this intermediate regime. The fundamental equation of motion of d-dimensional fluids was proposed in 1959 as follows [1]:

$$\frac{\partial \rho}{\partial t} = -\nabla \cdot (\rho \boldsymbol{v}) \tag{1}$$

$$\rho \left[\frac{\partial \boldsymbol{v}}{\partial t} + (\boldsymbol{v} \cdot \nabla)\boldsymbol{v} \right] = -\nabla p + \eta_0 \nabla^2 \boldsymbol{v} + \left[\zeta_0 + \left(1 - \frac{2}{d} \right) \eta_0 \right] \nabla(\nabla \cdot \boldsymbol{v}) - \nabla \cdot \boldsymbol{\Pi}^{\mathrm{ran}} \tag{2}$$

with

$$\left\langle \Pi_{ij}^{\mathrm{ran}}(\boldsymbol{r}, t) \Pi_{mn}^{\mathrm{ran}}(\boldsymbol{r}', t') \right\rangle = 2 k_B T \delta^d(\boldsymbol{r} - \boldsymbol{r}') \delta(t - t') \left[\eta_0 \left(\delta_{im}\delta_{jn} + \delta_{in}\delta_{jm} \right) + \left(\zeta_0 - \frac{2}{d}\eta_0 \right) \delta_{ij}\delta_{mn} \right] \tag{3}$$

where $\rho(\boldsymbol{r}, t)$ is density field, $\boldsymbol{v}(\boldsymbol{r}, t)$ is velocity field, $p(\boldsymbol{r}, t)$ is pressure field, and $\Pi_{ij}^{\mathrm{ran}}(\boldsymbol{r}, t)$ is random stress tensor field. η_0 and ζ_0 are shear and bulk viscosity, respectively. This formulation is reasonable within the principles of nonequilibrium statistical mechanics, as pioneered by Onsager. Indeed, it has been applied to various fields. A prominent example is the transport phenomena in low-dimensional fluids, where fluctuating hydrodynamics leads to the renormalized correction of observed transport coefficients due to the nonlinear coupling of fluctuations [2]. However, so far, such nonlinear phenomena have been examined primarily through theoretical approaches such as renormalization group theory and mode-coupling theory. No studies have yet attempted to directly simulate fluctuating hydrodynamics Eqs. (1), (2), and (3). Therefore, the validity -particularly the quantitative validity- of these theoretical results remains unclear.

In this study, we performed the numerical simulation of Eqs. (1), (2), and (3) in two dimensions [3] under the nearly incompressible condition and examined the divergence of the observed viscosity.

We focus on the Couette flow setup (the left panel of Fig. 1), where the fluid is confined between two parallel walls moving in opposite directions at speeds of $\pm v_0/2$. Then, we observe the noise-averaged velocity profile $\langle v^x(\boldsymbol{x}) \rangle$ and shear stress profile $\langle \sigma^{xy}(\boldsymbol{x}) \rangle$ to study the observed viscosity η defined by

$$\langle \sigma^{xy}(\boldsymbol{x}) \rangle = \eta \frac{\partial \langle v^x(\boldsymbol{x}) \rangle}{\partial y} \tag{4}$$

This observed viscosity η differs from the theoretical viscosity η_0. In the right panel of Fig. 1, we present the variation of $\eta - \eta_0$ with respect to η_0, showing that $\eta - \eta_0$ is small for large η_0 and converges to the finite value as η_0 approaches 0. We further compare our simulation

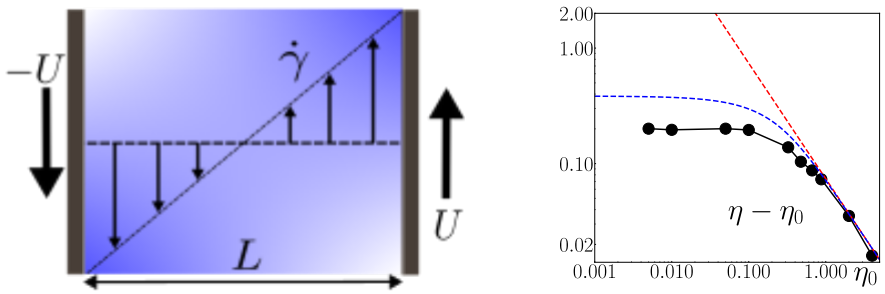

Figure 1: (Left) Couette flow setup. (Right) Variation of $\eta - \eta_0$ with respect to η_0. The black, red, and blue curves, respectively, represent the results of our simulation, the simple perturbation theory, and the theory of Forster, Nelson, and Stephen [2].

results against two previous theoretical results developed for Eqs. (1), (2), and (3), which are depicted as red and blue lines in the right panel of Fig. 1. We can see that for sufficiently large η_0, our simulation results are in good agreement with both the simple perturbation theory and Forster's theory [2]. However, as η_0 decreases, both theories deviate from the simulation results.

The previous theories rely on perturbation methods and have limitations in the treatment of nonlinear effects. Thus, our simulation results suggest that a more precise theory is necessary for small η_0 to enable quantitative analysis.

References

[1] D. Landau and E. M. Lifshitz, Fluid Mechanics (Pergamon Press, Oxford, 1959).

[2] D. Forster, D. R. Nelson, and M. J. Stephen, Phys. Rev. A **16** 732 (1977)

[3] I. Srivastava *et al.* Phys. Rev. E **107**, 015305 (2023)

Basic and applied studies on protein structure and function

Koji OOKA[1], Masataka YOSHIMURA[2], Nao SATO[2], Runjing LIU[2], Kaho KOTANI[2], Shinya INOUE[2], Sae KATO[2], Shun NAGAI[3], Shunji SUETAKA[2], and Munehito ARAI[1,2,3]

[1]College of Arts and Sciences, [2]Department of Life Sciences, Graduate School of Arts and Sciences, and [3]Department of Physics, Graduate School of Science, The University of Tokyo, Komaba, Meguro, Tokyo 153-8902

Proteins have recently been used in industry and medicine. These proteins perform biological functions such as binding and catalysis through dynamic motions after folding into specific globular structures. Therefore, it is important to elucidate the mechanisms of protein folding to facilitate their application. In addition, the theoretical design of proteins has recently received considerable attention. Thus, we have studied the folding mechanisms of proteins, the functional motions of proteins, and the theoretical design of novel useful proteins.

To theoretically predict protein folding mechanisms, we have developed a statistical mechanics theory that can accurately predict the free energy landscape of proteins, called the WSME-L model [1]. This theory represents a significant advance in the field because it can be applied to any protein, regardless of the presence or absence of disulfide bonds or the shape of the protein. The program is written in C++ and Python. In addition, we have used this theory to design mutants with altered protein folding pathways. Since the WSME-L model requires the three-dimensional structure of a protein to predict its free energy landscape, we predicted the structures of various mutants using localcolabfold, which can perform protein structure prediction using AlphaFold 2 in a local environment [2]. We are also trying to extend the WSME-L model to predict free energy landscapes for protein-protein interactions, protein-small molecule interactions, and enzymatic reactions.

Protein-ligand interactions are essential for the function of many proteins. To study the interaction between a cyanobacterial photoreceptor protein AnPixJg2_BV4 and biliverdin, we performed molecular dynamics simulations of the protein-ligand complex. The model structure was built using AmberTools22 with the ff14SB force field [3]. Simulations were performed using GROMACS 2022.4 [4] for 2 μs in triplicate (total of 6 μs). We found that amino acid substitutions in the protein altered its interaction with biliverdin, which in turn affected the stability of the complex [5].

Enzymes are widely used in the industrial production of useful substances. Therefore, it is necessary to develop efficient methods to

improve enzymes. Using the physics-based protein design software Rosetta (versions 3.8 and 3.13) [6], we are developing a universal method that can generally improve the activity of various enzymes. Our strategy is to reduce the height of the free energy barrier for the rate-limiting step in the enzyme reaction cycle. We have applied this method to enzymes such as dihydrofolate reductase (DHFR) and aldehyde deformylating oxygenase (ADO). Experimental verification showed that we succeeded in improving the turnover rate of DHFR by ~5-fold by a single amino acid substitution. Activity measurements of ADO mutants are in progress.

Protein-protein interactions have attracted attention as drug targets. However, the interaction surface is generally broad and shallow, making it difficult to inhibit with small molecules, and the development of inhibitors using peptides with a broad interaction surface is promising. We have previously designed two types of peptide inhibitors that bind to each of the two transcription factor binding sites on KIX, targeting the interaction between the KIX domain of CBP and transcription factors involved in various diseases such as leukemia [7,8]. By linking these two peptide inhibitors, we designed a bivalent chimeric peptide inhibitor that simultaneously inhibits both binding sites. We modeled the linker structure using Rosetta and then designed a linker sequence that could improve the binding ability to the target using ProteinMPNN [9], a deep learning-based amino acid sequence design software. The structures of designed proteins were predicted using localcolabfold. Experiments showed that the designed chimeric peptide binds KIX with more than 2,000-fold higher affinity compared to the isolated peptide inhibitors. Thus, our methods may be useful in the design of inhibitors of protein-protein interactions.

References

[1] K, Ooka, and M. Arai: Nat. Commun. **14**, 6338 (2023).

[2] M. Mirdita, K. Schütze, Y. Moriwaki, L. Heo, S. Ovchinnikov, and M. Steinegger: Nat. Methods, **19**, 679-682 (2022).

[3] D. A. Case, et al.: AMBER 2022. University of California, San Francisco (2022)

[4] S. Pall, C. J. Smith, B. Hess, E. Lindah: SoftwareX, **1–2**, 19-25 (2015).

[5] T. Suzuki, M. Yoshimura, M. Arai, and R. Narikawa: J. Mol. Biol. **436**, 168451 (2024).

[6] J. K. Leman, et al.: Nat. Methods, **17**, 665 (2020).

[7] S. Suetaka, Y. Oka, T. Kunihara, Y. Hayashi, and M. Arai: Sci. Rep. **12**, 816 (2022).

[8] N. Sato, S Suetaka, Y Hayashi, and M Arai: Sci. Rep. **13**, 6330 (2023).

[9] J. Dauparas, et al.: Science, **378**, 49-56 (2022).

Spin Nematic Phase of 2D Ferromagnetic Dimer Systems

Tôru SAKAI[1,2], Hiroki NAKANO[1], Masaru Hashimoto[1], Tomoki Houda[1]Rito FURUCHI[1], and Tokuro SHIMOKAWA[3]

[1] *Graduate School of Science, University of Hyogo, Kouto, Kamigori, Hyogo 678-1297, Japan*

[2] *National Institute for Quantum Science and Technology, SPring-8, Kouto, Sayo, Hyogo 679-5148, Japan*

[3] *Theory of Quantum Matter Unit, Okinawa Institute of Science and Technology Graduate University, Onna-son, Okinawa 904-0495, Japan*

1 Field-Induced Spin Nematic Phase of Quantum Spin Systems

The spin nematic phase is one of interesting topics in the field of the condensed matter physics. Using the numerical exact diagonalization analysis the field induced spin nematic phase is investigated in several low-dimensional quantum spin systems.

1.1 $S = 1/2$ Delta Spin Chain

The magnetization process of the S = 1/2 delta chain with the anisotropic ferromagnetic interaction is investigated using the numerical diagonalization of finite-size clusters[**?**]. It is found that the spin nematic liquid phase appears in higher magnetization region, as well as the SDW liquid one in lower region.

1.2 $S = 1/2$ Bond-Alternating Chains

The S = 1/2 ferromagnetic-antiferromagnetic bond-alternating spin chain with the anisotropy on the ferromagnetic exchange interaction in magnetic field is investigated using the numerical diagonalization and the density matrix renormalization group analyses[**?**]. It is found that the nematic-spin-dominant Tomonaga-Luttinger liquid phase is induced by the external magnetic field for sufficiently large anisotropy. The phase diagram with respect to the anisotropy and the magnetization is presented.

1.3 $S = 1/2$ Distorted Diamond Chain

The magnetization process of the S = 1/2 distorted diamond quantum spin chain with the Ising-like anisotropic ferromagnetic interaction is investigated using the numerical diagonalization method[**?**]. Two kinds of wide magnetization plateaux are found at 1/3 of the saturation magnetization based on the Haldane-like mechanism and the N´ eel-like mechanism, respectively. Apart from the magnetization plateaux, there appear the conventional Tomonaga-Luttinger liquid (TLL) phase and the two-magnon TLL phase. The latter phase is composed of the nematic TLL phase and the SDW TLL phase. The phase diagram with respect to the ferromagnetic interaction anisotropy parameter versus the magnetization is presented.

1.4 2D Ferromagnetic Dimer System

The $S = 1/2$ two-dimensional Shastry-Sutherland system with the ferromagnetic dimers is investigated using the numerical diagonalization[**?**]. It is found that the field induced spin nematic phase would appear, as well as the magnetization jump due to the spin flop transition.

References

[1] T. Sakai, R. Furuchi, H. Nakano and K. Okamoto, SciPost Physics Proceedings **11**, 011 (2023)

[2] R. Nakanishi, T. Yamada, R. Furuchi, H. Nakano, H. Kaneyasu, K. Okamoto, T. Tonegawa and T. Sakai, JPS Conf. Proc. **38**, 011156 (2023).

[3] M. Hashimoto, T. Houda, R. Furuchi, H. Nakano, K. Okamoto and T. Sakai, New Physics: Sae Mulli. **73**, 1127 (2023)

[4] T. Sakai, in preparation.

Novel Magnetization PLateau of the Spin Ladder System

Tôru SAKAI[1,2], Hiroki NAKANO[1], Masaru Hashimoto[1], Tomoki Houda[1]Rito FURUCHI[1], and Tokuro SHIMOKAWA[3]

[1] *Graduate School of Science, University of Hyogo, Kouto, Kamigori, Hyogo 678-1297, Japan*

[2] *National Institute for Quantum Science and Technology, SPring-8, Kouto, Sayo, Hyogo 679-5148, Japan*

[3] *Theory of Quantum Matter Unit, Okinawa Institute of Science and Technology Graduate University, Onna-son, Okinawa 904-0495, Japan*

1 Translational Symmetry Broken Magnetization Plateau of the One-Dimensional Quantum Spin Systems

We investigate the $S = 1$ antiferromagnetic quantum spin chain with the exchange and single-ion anisotropies in a magnetic field, using the numerical exact diagonalization of finite-size clusters, the level spectroscopy analysis, and the density matrix renormalization group (DMRG) methods[1]. It is found that a translational symmetry broken magnetization plateau possibly appears at the half of the saturation magnetization, when the anisotropies compete with each other. The level spectroscopy analysis gives the phase diagram at half the saturation magnetization. The DMRG calculation presents the magnetization curves for some typical parameters and clarifies the spin structure in the plateau phase.

2 Novel Magnetization Plateau of the S=2 Antiferromagnetic Chain with Anisotropies

The magnetization plateau of the S = 2 antiferromagnetic chain with interaction and single ion anisotropies is investigated using the numerical diagonalization of finite-size clusters and some size scaling analyses[2]. The previous level spectroscopy analysis indicated that two different magnetization plateau phases appear at half of the saturation magnetization. One is due to the large-D mechanism and the other is due to the Haldane one. In the present study the phase diagram is extended to wider region of the anisotropies. As a result we find another half magnetization plateau phase, where the translational symmetry is spontaneously broken.

3 Magntization Plateau due to Competing Anisotropies

The magnetization process of the $S = 1/2$ ferromagnetic and antiferromagnetic bond-alternating chain with competing anisotropies

is investigated using the numerical diagonalization of finite-size systems[3]. It is found that when the easy-plane and easy-axis anisotropies are introduced at the ferromagnetic and antiferromagnetic bonds, respectively, the system possibly exhibits the 1/2 magnetization plateau with the spontaneous translational symmetry breaking. The phase diagrams with respect to the two anisotropies are presented.

The magnetization plateau based on the same mechanism is revealed to occur in the $S = 1/2$ spin ladder system with the ferromagnetic rung interaction in the presence of the competing anisotropies[4].

References

[1] T. Sakai, K. Okamoto, K. Okunishi, M. Hashimoto, T. Houda, R. Furuchi and H. Nakano, Phys. Rev. B **108**, 174435 (2023).

[2] T. Yamada, R. Nakanishi, R. Furuchi, H. Nakano, H. Kaneyasu, K. Okamoto, T. Tonegawa and T. Sakai, JPS Conf. Proc. **38**, 011163 (2023).

[3] T. Sakai, M. Hashimoto, T. Houda, R. Furuchi, H. Nakano, K. Okamoto and K. Okunishi, New Physics: Sae Mulli. **73**, 1131 (2023).

[4] T. Sakai, M. Hashimoto, T. Houda, R. Furuchi, H. Nakano, K. Okamoto and K. Okunichi, in preparation.

Rotational diffusion of water molecules on phospholipid bilayers

Yuji HIGUCHI
Research Institute for Information Technology, Kyushu University
Motooka Nishi-ku, Fukuoka 819-0395

By molecular simulations, we have revealed the dynamics of water on semicrystalline polymers [1] and on phospholipid bilayers [2], changes in ion distribution on phospholipid bilayers [3], and transport dynamics of phase-separated domains on phospholipid bilayers induced by electric fields [4]. This year, we studied the water dynamics around osmolytes by density-functional tight-binding molecular dynamics (DFTB-MD) simulations using DFTB+ [5] on systems B and C.

The experiments suggested that the dynamics of water around osmolytes influence protein stability. However, the relationship between osmolytes and water dynamics remains unclear at the molecular level. We perform DFTB-MD simulations to reveal the different rotational dynamics of water molecules around 15 osmolytes. In Fig. 1, a positive correlation is found between the rotational relaxation time $\langle\tau\rangle$ and our proposed normalized parameter $N_{\mathrm{HB}}/N_{\mathrm{NN}}$, which is obtained by dividing the number of hydrogen bonds between water molecules by the number of nearest neighbor water molecules. The rotational dynamics of water molecules slow down when the value of the normalization parameter in the second layer from the osmolyte increases, indicating that the second hydration shell is important for the rotational dynamics of water molecules. We expect that our simulation results contribute to understanding the water dynamics around organic molecules and the long-range structure of water molecules.

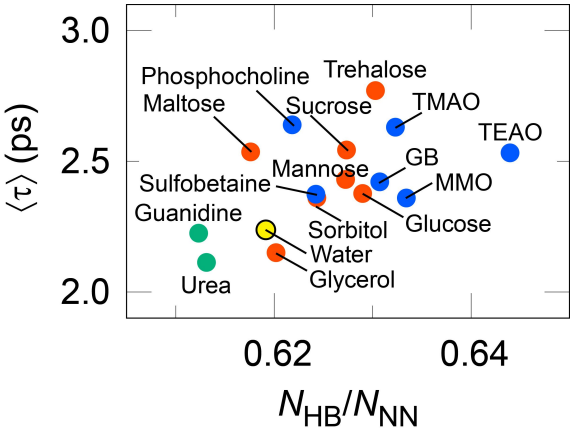

Figure 1: The average rotational relaxation time of water for 15 osmolyte solutions versus the normalized parameter.

References

[1] T. Kokuzawa, S. Hirabayashi, Y. Ikemoto, J. Park, R. Ikura, Y. Takashima, Y. Higuchi, and G. Matsuba: Polymer **298**, 126922 (2024).

[2] M. K. Rahman, T. Yamada, N. L. Yamada, M. Hishida, Y. Higuchi, and H. Seto: Struct. Dyn. **10**, 044701 (2023).

[3] Y. Higuchi, K. Bohinc, J. Rečsčič, N. Shimokawa, and H. Ito: Soft Matter **19**, 3640 (2023).

[4] H. Ito, N. Shimokawa, and Y. Higuchi: J. Phys. Chem. B **127**, 8860 (2023).

[5] B. Hourahine, et al.: J. Chem. Phys. **152**, 124101 (2020).

Molecular dynamics simulations for engineering tensile properties of carbon nanotube yarns

Go Yamamoto and Redha A. Ramadhan

Department of Aerospace Engineering, Tohoku University,
6-6-01 Aramaki-Aza-Aoba, Aoba-ku, Sendai 980-8579, Japan

Carbon nanotubes (CNTs) are an innovative material with significant potential for a wide range of applications, including, but not limited to, the development of lightweight composite materials or superconductors. An individual CNT demonstrates an exceptional degree of tensile strength [1]. CNTs are commonly employed in yarn structures, where several CNT strands are arranged and aligned together. CNT yarns, on the other hand, have a lower tensile strength than individual CNTs due to the different parameters of the yarn [2]. This study aimed to investigate the effect of different structural parameters on the mechanical properties of CNT yarns.

The simulation was performed using LAMMPS. Results from tensile loading simulations with structure modifications were gathered from sixty MD simulations and used as the data for the parametric study. The models were generated using High-throughput MD (HTMD), a Python-based tool [3], which allowed for the control of CNT variables. Fig. 1 shows the blue outer regions on both ends of every MWCNT in the yarn, assigned as the fixed parts where the tensile load was applied, while the red part was assigned as the mobile parts where the atoms were unconstrained and used for stress calculation. The number of CNTs in the yarn varied between 1, 3, and 7, while the number of walls ranged from 2 to 5. Both armchair and zigzag types of CNT chirality were simulated. The twist angle was also investigated by varying the yarn twist between 0° – 30° with 5° steps. Sixty CNT yarn models with different structures were simulated with the MD simulation. It was found that the parameters for the CNT yarn that yield a higher tensile strength are the armchair-type CNT with a small diameter, a large number of walls, crosslink density higher than approximately 1%, and a low twist angle.

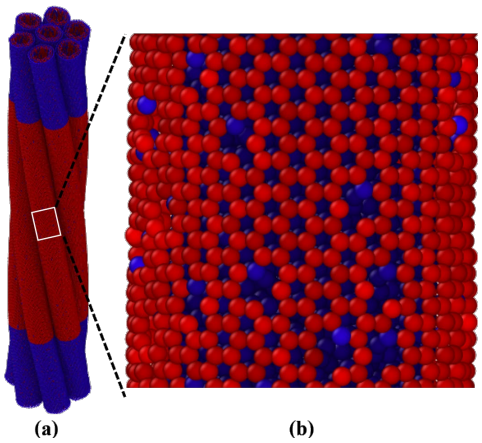

Fig. 1: View of a full 7-MWCNT yarn model with 10° twist angle, showing the blue fixed parts on both ends of the MWCNTs, and the red mobile parts on the middle of the MWCNTs.

References

[1] B. Peng, M. Locascio, P. Zapol, S. Li, S.K. Mielke, G.C. Schatz, and H.D. Espinosa, H. D. Nat. Nanotechnol. **3**, 626 (2008).

[2] K. Koziol, J. Vilatela, A. Moisala, M. Motta, P. Cunniff, M. Sennett, and A. Windle, Science **318**, 1892 (2007).

[3] Y. Xiang, K. Shimoyama, K. Shirasu, and G. Yamamoto, Nanomaterials **10**, 2459 (2020).

Quantum-classical hybrid simulations for sensor materials based on quantum state tomography

Wataru Mizukami

Center for Quantum Information and Quantum Biology, Osaka University, Osaka 560-0043, Japan

Quantum computers have made significant advancements in recent years, and the field of computational materials science is considered to be its promising application area. Nevertheless, a quantum computer alone is not capable of easily performing meaningful calculations. Quantum-classical hybrid algorithms, where quantum computers handle limited tasks and classical computers handle the rest, are crucial for applying quantum computers to real-world problems. Our research focuses on developing and applying such hybrid algorithms to simulate actual materials, particularly sensor materials.

This year, we applied a methodology based on quantum state tomography to calculate the properties of molecules and materials. The Variational Quantum Eigensolver (VQE), a representative quantum-classical hybrid algorithm for fermionic systems, has been extensively researched but faces issues such as low noise tolerance and high sampling costs. To address these issues, we developed several methods that reconstruct the quantum state on a classical computer through tomography. These methods allow us to combine accurate classical algorithms like Coupled Cluster (CC) and Auxiliary Field Quantum Monte Carlo (AFQMC) with quantum computing. We validated the AFQMC with our tomography method on chemical reaction systems, achieving chemical accuracy within 1 kcal/mol compared to the state-of-the-art classical algorithm CBS-QB3. We also developed QC-CBT-TCC, which connects with CC, and verified its effectiveness.

Furthermore, we developed a method for applying quantum machine learning (QML) to cheminformatics. At this moment, owing to constraints on available qubits, compact descriptors are highly desirable for QML. We exploited universal neural network potentials (NNPs) to generate such descriptors. Using intermediate information from well-trained NNPs as descriptors enables the creation of compact yet highly accurate descriptors, comparable to the state-of-the-art FCHL descriptor in predicting NMR chemical shifts. We also created QML models using these descriptors, paving the way for constructing practical QML models for molecules/materials.

Study on Johari-Goldstein relaxation mode in glass-forming liquids

Takeaki ARAKI[a] and Makina SAITO[b]

[a]*Department of Physics, Kyoto University, Sakyo-ku, Kyoto 606-8502*

[b]*Department of Physics, Tohoku University, Sendai Miyagi 980-8578*

Johari-Goldstein (JG) relaxation, also known as slow β relaxation, is a relaxation phenomenon observed in supercooled liquids and glasses [1-2]. It plays a significant role in impacting various properties, including but not limited to the impact strength of the materials, particularly below the glass transition temperature. However, despite its importance, the precise physical mechanism underlying JG relaxation remains elusive. This challenge arises primarily due to the inherent difficulties in both experimental observation and numerical simulation of this phenomenon.

In our study, we delved into the Johari-Goldstein mode in both ionic glass CKN and metallic glasses. We carried out molecular dynamics simulations of 2376 molecules up to 12msec for the ionic glass CKN, and 32000 atoms interacting through EAM potentials for metallic glass ZrCuAl, with LAMMPS.

Our simulations unveiled the intricate microscopic dynamics characterizing the JG mode. Specifically, we observed that a subset of particles undergoes thermally activated jump motions, a hallmark behavior of the JG mode. Remarkably, these jump motions triggered a collective local relaxation among neighboring particles that were conventionally assumed to be immobile. This collective relaxation, involving both jumping and non-jumping particles, played a pivotal role in the stress relaxation of the entire glass structure [3].

By bridging findings from gamma ray quasi-elastic scattering experiments with the computational insights, our work provides a deeper understanding of the underlying mechanisms governing the JG mode in diverse glassy materials, thereby advancing our knowledge of their structural dynamics.

References

[1] G. P. Johary and M. Goldstein, J. Chem. Phys. **53**, 2327 (1970).

[2] K. L. Ngai, Relaxation and diffusion in complex systems, Springer, Berlin, 2011.

[3] M. Saito, T. Araki, Y. Onodera, K. Ohara, M. Seto, Y. Yoda and Y. Wakabaashi, submitted.

Topological and mechanical properties of colloidal gels

Koichi HIRATA and Takeaki ARAKI

Department of Physics,

Kyoto University, Kitashirakawa-oiwake cho, Sakyo-ku, Kyoto 606-8502

We numerically investigated the aggregation dynamics and resulting network structures of colloidal gels using slippery diffusion-limited cluster aggregation (DLCA) model. In this model, bonds are irreversibly formed upon the particle contacts, but the angles among them are not fixed unlike the conventional DLCA. This allows clusters to be deformed in the process of aggregation. We carried out Brownian dynamics simulations of 10648 particles with a code we have developed. By characterizing the aggregation dynamics and using reduced network scheme, our simulation revealed two distinct branching structure formation routes depending on the particle volume fraction ϕ. In lower volume fraction systems $\phi \leq 8\%$, the deformations of small-size clusters proceed prior to the percolation.

When the Maxwell criterion is satisfied and the clusters become mechanically stable, the formation of the branching structure is nearly completed. After forming the branching structures, they aggregate and form larger percolating network. Then, the aggregation proceeds through the elongation and straightening of the chain parts of the network.

In higher volume fraction systems (ϕ>8%), on the other hand, the clusters percolate and fine and homogeneous branching structure is formed at the early stage of the aggregation. In aging stage, it collapses into denser and more heterogeneous structure, and becomes more stable. Our quantitative analyses on the branching structure will shed light on a new strategy for describing the network formation and elasticity of colloidal gels.

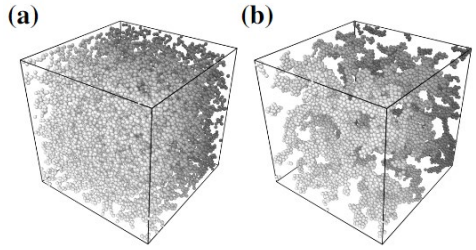

Fig. 1: Snapshots of the simulated gel structure at the final state of (a) DLCA and (b) the slippery DLCA.

References

[1] S. Babu, *et al.*, Eur. Phys. J. E **27**, 297 (2008).

[2] M. Gimperlein *et al.*, arXiv:2312.11156 [cond-mat] (2023).

Physical origin of forming ferroelectric nematic phase

Matheus DE MELLO and Takeaki ARAKI

Department of Physics,

Kyoto University, Kitashirakawa-oiwake cho, Sakyo-ku, Kyoto 606-8502

The nematic phase is a distinct state among liquid crystal phases, characterized by the alignment of rod-like molecules along a preferred direction. In the ordinary nematic phase, the preservation of head-tail symmetry prevents the manifestation of ferroelectricity, which has been not discovered for a long time. It was not until 2017 that the experimental realization of two distinct low molecular weight compounds exhibiting ferroelectricity marked a significant breakthrough. Despite extensive studies, the physical mechanism underlying the emergence of ferroelectricity in nematic liquid crystals remains elusive. This study aims to explore and understand the unique properties and underlying mechanisms of this phase.

Our investigation focuses on systems composed of DIO. Utilizing Gaussian16, we obtained the electric charge distribution to assign the partial charge on each atom. Subsequently, employing GROMACS, we conducted molecular dynamics simulations of 1000 DIO molecules. To elucidate the roles of electrostatic interaction, we also carried out simulations of 2048 DIO molecules without the electric charges.

Our simulations reveal spontaneous polarization in the charged DIO, albeit with the polarization degree smaller than the experimental observations. We attribute this weaker ferroelectricity to computational limitations, as molecular motions are quite slow within the simulation time. On the other hand, spontaneous polarization is not observed in the chargeless system, indicating the electrostatic interaction promotes polarization, in contrast to ordinary nematic phases.

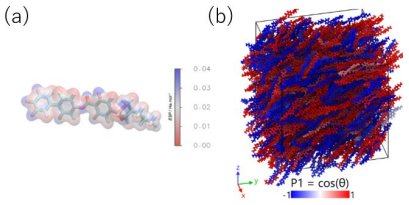

Fig. 1: (a) Electrostatic isopotential of DIO. (b) Snapshot of the DIO system at 330K.

References

[1] H. Nishikawa, *et al*., Adv. Matter. **29**, 1702354 (2017).[2] R. J. Mandle, *et al*., Phys. Chem. Chem. Phys. **19**, 11429 (2017).

Simulation of Quantum Many-Body Systems by Tensor Network and Sampling

Synge TODO
Department of Physics, University of Tokyo, Tokyo, 113-0033

We developed novel numerical methods by combining Monte Carlo, tensor network algorithms, and other optimization techniques. We investigated topological quantum phase transitions in strongly correlated many-body systems and optimization of quantum operations in quantum computing.

Negative Sign Problem in Quantum Monte Carlo Methods

The quantum Monte Carlo method for quantum many-body systems is a widely used computational technique. However, a negative sign problem arises in some quantum lattice models, and the statistical error increases exponentially at low temperatures. To address this problem, we redefine the negative sign problem as an optimization problem by integrating the basis transformation and the reweighting method. In particular, we found that assuming a frustration-free system simplifies the optimization function and effectively reduces the negative sign. Numerical simulations confirm that the proposed method performs well for spin systems for which analytical solutions exist and for frustration-free systems for which solutions are unknown.

Effective Dimension in Long-Range Interacting Systems

In quantum critical phenomena, long-range interactions are of interest in that the effective dimension of the system can be varied by controlling the anisotropy in space and time by the decay rate of the interaction. However, comprehensive and accurate numerical analysis remains challenging due to the extensive search space with additional degrees of freedom governing the interaction and strong finite-size effects. We have shown that the problem can be significantly improved by automatically adjusting the parameters of the model under the guiding principle of "setting the correlation ratio in the spatial/temporal axes to the same and optimal value," and have also successfully determined the universality class boundary for the quantum phase transition of the one-dimensional transverse-field Ising model (Fig. 1).

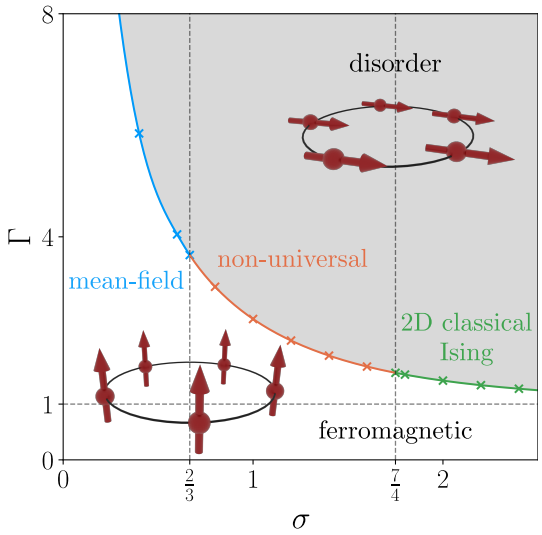

Figure 1: Ground-state phase diagram of long-range interacting transverse-field Ising chain.

Quantum Monte Carlo in Continuous Space Systems

For interacting bosons such as He^4, it is difficult to sample physical quantities related to quantum statistics, such as the superfluid

density and condensate fraction. Conventional Monte Carlo updates cannot change the path winding number. We incorporate the path-integral quantum Markov-chain Monte Carlo method for continuous-space many-body systems with exchange Monte Carlo and population annealing developed for simulations of spin glass systems. By slowly turning on the interaction in different imaginary-time slices and moving from a non-interacting system to a fully interacting one, we confirm that updates to the winding number can be achieved quickly.

Application of the Grassmann tensor network to lattice fermion systems

The tensor renormalization group approach has been applied to the simulation of lattice field theories at finite density for over a decade. We construct a Grassmann tensor network representing the partition function of 1+1-dimensional SU(2) Yang-Mills theory coupled with staggered fermion on a square lattice. The gauge group integration is discretized using a random sampling method, and the Grassmann integral of staggered fermion fields is written as the trace of a Grassmann tensor network by introducing auxiliary Grassmann fields. Since the theory has massive internal degrees of freedom, the bond dimension of the initial tensors is at least in the order of 10^2. So, performing accurate TRG calculations with these initial tensors is difficult. We introduce an efficient initial tensor compression scheme. After that, the Grassmann bond-weighted tensor renormalization group algorithm is applied to contract the Grassmann tensor network composed of the compressed tensors. Physical quantities such as the number density and the fermion condensate in the thermodynamic limit can be computed by finite differences in the partition function.

Noise Model Estimation Based on Syndrome Statistics of Surface Codes

The surface code attracts attention as a practical error correction code in quantum computation. Although the decoding algorithm for surface codes can improve performance by using information from noise models, additional measurements are required because the noise model information must be prepared in advance by tomography. Estimating the noise model based on the results of syndrome measurements obtained during the decoding process can prevent performance degradation without additional quantum computation. We have developed a method combining a tensor network simulator for surface code with Monte Carlo techniques to estimate noise model parameters beyond the Pauli noise. We have successfully estimated various noise models, including a time-varying amplitude-decaying noise model, and have also confirmed that using the estimated results improves the performance of decoding algorithms (Fig. 2).

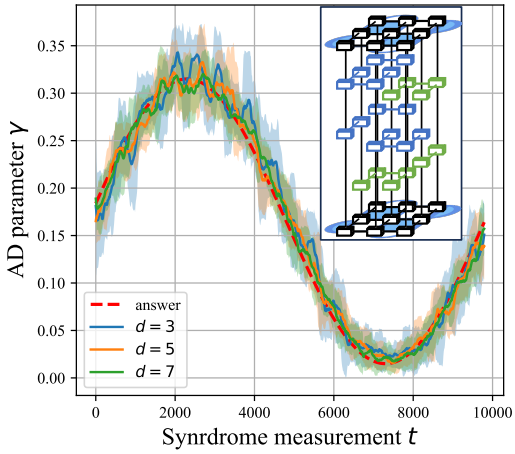

Figure 2: Estimation of time-varying noise models based on syndrome statistics.

Efficient sampling simulation of the soft modes significantly contribute to protein properties

Hiroshi Kono, Kazuhiro Takemura, Duy Tran, Wijaya Tegar, Hao Thai Nguyen, Ting-yi Chu, Shinji Ikizawa, Sari Hagimoto, Tatsuhiro Kimizono, Yusei Ito, Akio Kitao

School of Life Science and Technology,

Tokyo Institute of Technology, Ookayama, Meguro-ku, Tokyo 152-8550

Almost all organisms, including humans, require sugars such as glucose as an energy source. Therefore, many organisms possess the ability to uptake sugars into their bodies, and one of the proteins responsible for this function is SGLT. SGLT (Sodium Glucose Cotransporter) is a protein that transports glucose and sodium simultaneously. Through this mechanism, it performs secondary active transport by utilizing the potential generated by the sodium concentration gradient between the intracellular and extracellular spaces to uptake glucose from the extracellular to the intracellular space. In humans, six isoforms of SGLT have been discovered so far, each with strict sugar selectivity [1]. For example, while SGLT1 transports both glucose (Glc) and galactose (Gal), SGLT2 transports only Glc and not Gal. The recognition mechanism that can distinguish specifically between Glc and Gal, which structurally have minor differences, has been the subject of research. However, studies approaching the principles of selectivity by observing dynamics using molecular dynamics (MD) simulations have not been extensively conducted. The objective of this study is to elucidate the dynamic mechanism at the atomic level by which SGLT recognizes monosaccharides such as Glc and Gal. Generally, substrate transport by transporters involves steps where the substrate approaches from one side of the cell membrane, binds to a binding site located inside the membrane, and then, through structural changes, a pathway opens to the opposite side for the substrate to move across. In the fiscal year 2023, as the first stage of the research, detailed investigation of interactions in the binding state located inside the membrane and simulations of dissociation from the binding state to the extracellular side were conducted.

We performed normal molecular dynamics (MD) simulations for 1 μs using the complex of Glc or Gal with SGLT1 as the initial structure（PDB: 7wmv）. The protein force field was AMBER19SB [2], the force field for Glc and Gal was GLYCAM06 [3], and the water model used was OPC [4]. After that, we next conducted dissociation simulations of the glycans from the bound state using the Parallel Cascade Selection Molecular Dynamics (PaCS-MD) simulation [5-

7]. In this study, we performed 60 MD parallel runs for 100 ps per PaCS-MD cycle. The ranking and selection of structures of each cycle was based on the inter-center of mass distance of the protein and the ligands. PaCS-MD stopped when center of mass distance reached 7.5 nm.

Prior to PaCS-MD, classical 1 μs MD simulations were conducted five times each for Glc and Gal. Analysis of hydrogen bonding between the protein and the ligand revealed significant differences in the number of hydrogen bonds between W291 and Glc or Gal. W291 formed more hydrogen bonds with Gal than Glc as shown in Figure 1. These differences in hydrogen bonding suggest that the difference in affinity between Glc and Gal in SGLT1 may be due to this.

Furthermore, dissociation simulations to the extracellular side were performed using PaCS-MD, with 20 trials each for Glc and Gal. Dissociation was observed 20 times for Glc and 16 times for Gal. Calculations of the binding free energy ΔG_O using Markov State Modelling yielded values of -11.1 kcal/mol for Glc and -9.6 kcal/mol for Gal in Figure 2. This difference corresponds to the difference in binding affinity K_m for Glc/Gal in SGLT1 measured experimentally, suggesting that selectivity occurs at the binding step.

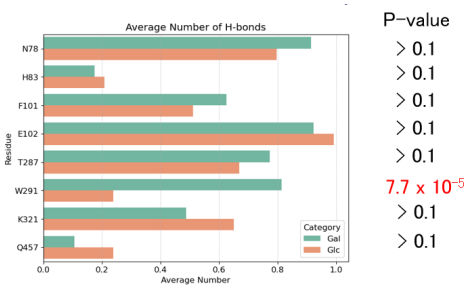

Figure 1. Comparison of the number of hydrogen bonds formed between each residue and Glc/Gal.

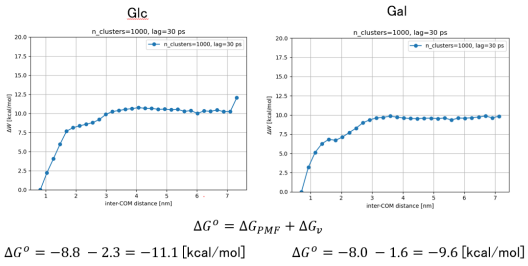

Figure 2. Free energy landscape along the center of mass distance and standard binding free energy.

References

[1] L. Han et al., Nature 601, 274 (2022).

[2] C. Tian et al., J. Chem. Theory Comput. 16, 528 (2020).

[3] K. N. Kirschner et al., J. Comput. Chem. 29, 622 (2008).

[4] S. Izadi et al., J. Phys. Chem. Lett 5, 3863 (2014).

[5] D P Tran et al., J. Chem. Theory Comput. 14, 404 (2018).

[6] D. P. Tran, A. Kitao, J. Phys. Chem. B 123, 2469 (2019).

[7] S. Ikizawa et al., J. Phys. Chem. B 128, 3631 (2024).

Improvement of analysis for relaxation of fluctuations by the use of Gaussian process regression

Y. Ozeki and Y. Osada

Graduate School of Informatics and Engineering, The University of Electro-Communications

We investigate an improvement for the numerical estimations of critical exponents due to non-equilibrium relaxation (NER) of fluctuations. [1] The numerical derivative which is necessary to estimate the asymptotic exponent of relaxation is improved as a smooth function by the use of the Gaussian process regression and kernel method. [2]

To estimate critical exponents in the NER method [**?**]ome relaxation functions are calculated at the transition temperature, which are numerically estimated usually; the order parameter $m(t)$ as well as the dimensionless susceptibility $f_{mm}(t) \equiv N\left(\frac{\langle m^2\rangle_t}{\langle m\rangle_t^2}-1\right)$, and another dimensionless correlation function, $f_{me}(t) \equiv N\left(\frac{\langle me\rangle_t}{\langle m\rangle_t\langle e\rangle_t}-1\right)$, where m and e represent the order parameter and the energy per site, N is the number of sites, and $\langle\cdots\rangle_t$ denotes a dynamical average at time t. At the critical point, these functions are expected to show algebraic behaviors asymptotically as

$$m(t)\sim t^{-\lambda_m},\quad f_{mm}(t)\sim t^{\lambda_{mm}},\quad f_{me}(t)\sim t^{\lambda_{me}}. \tag{1}$$

The dynamical exponents are related with the conventional critical exponents as

$$\lambda_m=\frac{\beta}{z\nu},\quad \lambda_{mm}=\frac{d}{z},\quad \lambda_{me}=\frac{1}{z\nu} \tag{2}$$

If the above dynamical functions are estimated numerical by Monte Carlo simulations, one can define the following logarithmic derivative

$$\lambda_m(t)\equiv-\frac{\partial\log m(t)}{\partial\log t}, \tag{3}$$

which would approaches λ_m as $t\to\infty$. We call this function the local exponent of λ_m Similarly, other local exponents

$$\lambda_{mm}(t)\equiv\frac{\partial\log f_{mm}(t)}{\partial\log t},\quad \lambda_{me}(t)\equiv\frac{\partial\log f_{me}(t)}{\partial\log t}, \tag{4}$$

are defined, which would approach λ_{mm} and λ_{me}, respectively.

Previously, to evaluate conventional critical exponents, we first calculate the functions $m(t)$, $f_{mm}(t)$ and $f_{me}(t)$ numerically for a finite system up to a maximum observation time $t_{\max}$ due to Monte Carlo simulations. The system size N is chosen so that the size dependence does not appear in the calculated functions up to $t=t_{\max}$. This provides the analysis corresponding to an infinite system. Then, the local exponents defined in Eqs. (3)-(4) are evaluated by numerical derivative for a finite interval of time, and are extrapolated to obtain the dynamical exponents (2) providing conventional critical exponents ν,β,z.

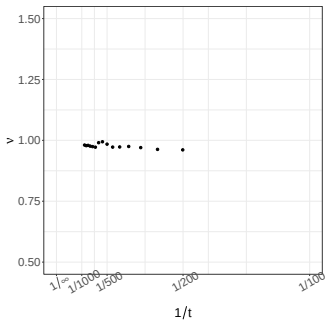

Figure 1: The local exponent $\nu(t)$ for the 2D Ising model plotted as a function of $1/t$ evaluated by the previous analysis using the numerical derivative.

The above method is efficient and reliable in the numerical evaluation of critical exponents. However, there has been a kind of difficulty in the extrapolation scheme of local exponents. Numerically evaluated local exponents are obtained in discrete time, and are sometimes not smooth functions because of the numerical derivative on simulated values. Thus, the extrapolation of them to $t\to\infty$ cannot be done systematically and yields unstable results. To overcome this difficulty, we applied Gaussian process regression and the kernel method as in the dynamical scaling analysis which has been used successfully. This improvement enables comparison of exponents at multiple critical points of various systems. This will greatly advance the discussion of universality.

As an example, we show a result for the ferromagnetic Ising model in two dimensions. The cal-

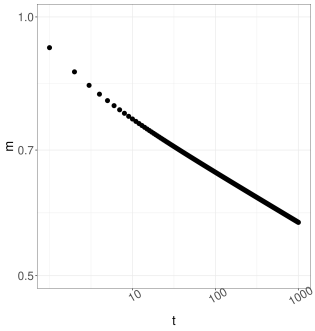

Figure 2: The relaxation of order parameter $m(t)$ for the 2D Ising model plotted in a double-logarithmic scale.

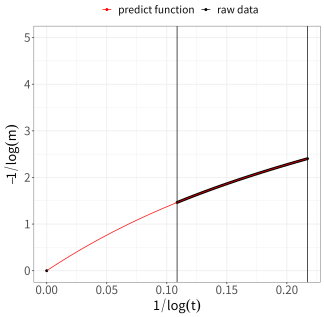

Figure 3: The result of interpolation for $-\log m(t)$ as a function of $\log t$. The black points indicate the interval where the numerical data exist, and the red ones indicate out of that.

culation is carried out at the exact transition temperature $T = 2,2691853$ on 501×500 lattice; 10^7 samples are used for averaging; the observation is made for $10^2 \leq t \leq 10^4$ MCS. The relaxation functions $m(t)$, $f_{mm}(t)$ and $f_{me}(t)$ are calculated. First, we show the result obtained by the previous analysis using the numerical derivative; in Fig.1, the resulting local exponent of ν defined by

$$\nu(t) \equiv \frac{\lambda_{mm}(t)}{d\ \lambda_{me}(t)} \tag{5}$$

is plotted. As pointed out above, the data point is discrete and is not smooth.

In the present method, we interpolate the relaxation data using the Gaussian process regression and the kernel method. In Fig.2, the numerical data for $m(t)$ is plotted with a double-logarithmic scale. The result of interpolation for $-\log m(t)$ as a function of $\log t$ is shown in Fig.3, where we use the fact that the curve reaches the origin $(0, 0)$. At least the interval where the numerical data exist, the obtained smooth curve is much precise and can be differentiate at any point. Then, we evaluate the

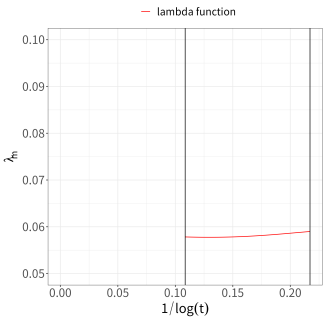

Figure 4: The local exponent $\lambda(t)$ evaluated by the differentiation of the curve shown in Fig.3.

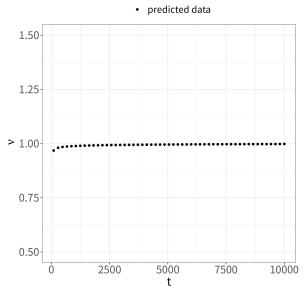

Figure 5: The extrapolation of local exponent $\nu(t)$ evaluated by the present method.

local exponent $\lambda(t)$ as a smooth curve in this interval (shown in Fig.4). and the extrapolation can be performed. The same procedure is made for other relaxation functions $f_{mm}(t)$ and $f_{me}(t)$. In Fig.5, the resulting extrapolation is performed for $\nu(t)$ by the use of the Shanks transformation. [3] We obtain $\beta = 0.1250(4)$ and $\nu = 1.000(2)$ in this demonstration, while $\beta = 1/8$ and $\nu = 1$ are known as exact values. It is shown that the present method works well.

References

[1] Y. Ozeki and N. Ito, *J. Phys.: Math. Theor.* **40** R149 (2007).

[2] Y. Echinaka and Y. Ozeki, *Phys. Rev.* E**94** 043312 (2016).

[3] D. Shanks, *J. Math. and Phys.* **34** 1 (1955).

The Anderson transitions in quasi-periodic systems

TOMI OHTSUKI[1]
TOHRU KAWARABAYASHI[2]
KEITH SLEVIN[3]
1) Dept. Phys., Sophia University, Chiyoda-ku, Tokyo 102-8554, Japan
2) Dept. Phys., Toho University, Miyama 2-2-1, Funabashi 274-8510, Japan
3) Dept. Phys., Osaka University, Toyonaka, Osaka 560-0043, Japan

Random quantum systems, lacking translational and rotational symmetries, display time reversal, chiral, and particle-hole symmetries, classifying them into ten symmetry classes. Significant research has focused on the Wigner-Dyson classes identified in the 1950s and 1960s. Recent advancements in experimental techniques have shifted focus to the quasi-periodic potentials. Random potentials cause wave function localization in one-dimensional systems, while quasi-periodic potentials result in both localization and delocalization. The impact of quasi-periodicity in higher-dimensional systems is an active research topic [1-3].

We study three-dimensional systems where the translational invariance is broken by quasi-periodic potentials. We analyzed system size dependence of conductance and used finite-size scaling to estimate critical points and exponents, covering orthogonal, unitary, and symplectic Wigner-Dyson classes. The results showed that critical exponents match those in random potential systems, indicating that the universality classes remain the same in the case of quasi-periodicity. We also note the shifts of the critical strength of potential (V_c) due to the violation of time reversal and spin rotation symmetries are consistent with the weak localization theory.

Furthermore, we employed a three-dimensional convolutional neural network (CNN) for wave function analysis (Figure 1). Initially trained on the Anderson localization model, the CNN was adapted to assess wave functions under quasi-periodic potentials, differentiating between localized and delocalized states.

References

1. S. Sakai, R. Arita, Tl Ohtsuk: Physical Review B **105**, 054202 (2022)
2. S. Sakai, R. Arita, Tl Ohtsuk: Physical Review Research **4**, 033241 (2022)
3. X. Luo, T. Ohtsuki, Physical Review B **106**, 104205 (2022).

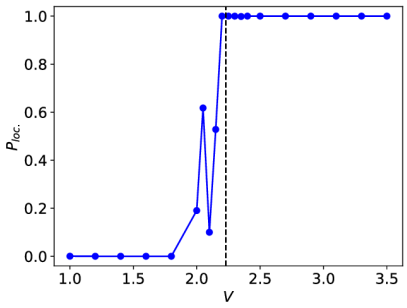

Figure 1: Probability of localization ($P_{\rm loc}$) for wave functions in quasiperiodic systems as a function of quasiperiodic potential strength (V) , as predicted by a convolutional neural network trained on the localized/delocalized wave functions from the disordered Anderson model. The critical point (V_c) is marked by the vertical dashed line. Each data point's probability is the average of 10 samples. The analysis focuses on a wave function near E=0 within a cubic system of linear size L=42. Taken from Ref. [3].

Molecular dynamics simulation of protein aggregation

Hisashi Okumura

Exploratory Research Center on Life and Living Systems,

Institute for Molecular Science, Okazaki, Aichi 444-8585

When protein concentration increases due to aging or other reasons, they aggregate and cause various diseases. For example, Alzheimer's disease is considered to be caused by aggregates of amyloid-beta (Aβ) peptide, and polyglutamine disease by aggregates of polyglutamine. Aβ peptide usually consists of 40 or 42 amino acid residues. Aβ peptide with 40 residues is referred to as Aβ40, and that with 42 residues is referred to as A42. We have performed molecular dynamics (MD) simulations to understand the aggregation and disaggregation mechanisms of Aβ peptides. In this fiscal year, we performed large-scale MD simulations of Aβ peptide aggregation.

We performed all-atom MD simulations of 32 Aβ40 and Aβ42 peptides in explicit water solvent for 1.8 μs. All of the Aβ peptides were placed discretely in the initial conditions. MPI/OpenMP hybrid parallelization was used to execute the large jobs. We observed Aβ peptides aggregated with repeating aggregation and disaggregation. They finally formed large oligomers, as shown in Fig. 1. We revealed structural changes in the aggregation process, inparticular forcusing on the aspect ratio of the oligomers and secondary structure.

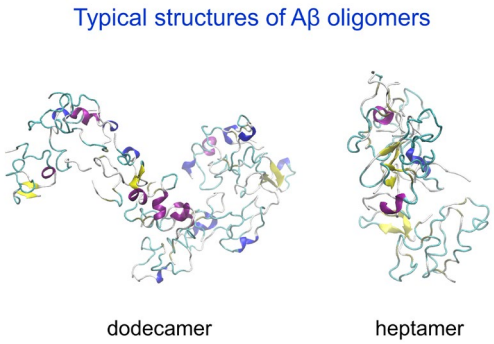

Fig. 1 Typical conformations of amyloid-β (Aβ) oligomers obtained by molecular dynamics simulations.

We found that the relatively large oligomers tend to have a long aspect ratio. It means that small oligomers are relatively spherical, but tend to extend in one way as they get larger. In addition, the oligomers of Aβ42 formed more β-hairpin and intermolecular β-sheet structures than those of Aβ40. We are now trying to reveal the reason for these structural features.

It isn't easy to clarify the growth process of Aβ oligomers at the molecular level by wet experiments. However, MD simulation can reproduce it as if it had been seen. We believe that elucidating the initial process of Aβ aggregation at the molecular level through this study will provide important knowledge for developing future therapies.

Thermal effects on quantum frustrated magnetisms

Tokuro Shimokawa

Theory of Quantum Matter Unit, Okinawa Institute of Science and Technology Graduate University, Onna 904-0495, Japan

Investigating the effects of thermal fluctuations in quantum frustrated magnets is crucial for developing our understanding of quantum spin liquids. $Ca_{10}Cr_7O_{28}$ (CCO) [1] is a quantum spin liquid candidate that can be described by the S=1/2 bilayer breathing kagome (BBK) Heisenberg model. Here, we examine the importance of thermal fluctuations by focusing on the J_1-J_2 classical honeycomb-lattice Heisenberg model corresponding to the classical system of this S=1/2 BBK model.

To do this, we employ classical Monte Carlo simulations, utilizing a hybrid parallelization approach combining the heat-bath method, over-relaxation method, and replica exchange method. We investigate the ordering behavior of the honeycomb lattice model in a finite-temperature magnetic field with a focus on the several J_2/J_1 parameter values. Physical quantities, including specific heat, magnetic susceptibility, equal-time structure factor, and chirality, are examined to identify the presence of a Skyrmion lattice state with sublattice structure and other additional multiple-q states [2].

We also report on the investigation of the static and dynamic properties of the S=1/2 J_A-J_B-J_C honeycomb-lattice Heisenberg model, which is believed to be important for understanding the quantum spin liquid behavior in different honeycomb-lattice material $Cu_2(pymca)_3(ClO_4)$ [3]. The investigations were carried out using quantum Monte Carlo simulations based on ALPS application [4] and exact diagonalization. Our results demonstrate the realization of a quantum paramagnetic state in this material, and suggest that focusing on dynamic properties is crucial for experimentally identifying this state [5].

References

[1] C. Balz, *et al.* Nat. Phys. **12** 942 (2016).

[2] T. S., *et al*, in preparation

[3] Z. Honda, *et al*, J. Phys. Soc. Jpn. **84**, 034601 (2015).

[4] A. Albuquerque, *et al*, J. Magn. Magn. Mater. **310**, 1187 (2007).

[5] T. S., Ken'ichi Takano, Zentaro Honda, Akira Okutani, and Masayuki Hagiwara, Phys. Rev. B **106**, 134410 (2022).

Numerical study on low-energy states of quantum spin systems

Hiroki NAKANO
Graduate School of Science, University of Hyogo
Kouto, Kamigori, Hyogo 678-1297, Japan

The difficulty in accurately estimating physical quantities is due to the many-body problems researchers encounter in condensed matter physics. The quantum spin system is a typical problem. In studying a quantum spin system, numerical approaches have been widely and effectively used. Computational studies have provided us with valuable information about the target systems.

Three methods have been successfully employed in the field of quantum spin systems. The traditional one is the numerical-diagonalization method. The quantum Monte Carlo (QMC) simulation is the second method. The third method is the density matrix renormalization group (DMRG) method. Although each of these methods has benefits, they also have drawbacks. QMC simulations are capable of handling systems that are significantly larger, regardless of their spatial dimensions. On the other hand, the negative sign problem with this approach prevents us from accurately evaluating physical quantities in frustrated systems. When the spatial dimension of a target system is one, however, the DMRG method is very useful, regardless of whether or not the target system includes frustration. Regrettably, this method is still in progress for cases where the spatial dimension is larger than one. Regardless of the presence of frustrations or the spatial dimension, the numerical diagonalization method can be applied to various systems. However, the method is limited to treating systems with very small sizes. In order to overcome this drawback of the numerical diagonalization method, we developed a hybrid-type parallelized code of Lanczos diagonalization[1]. This code enables us to treat various large systems that have not been treated yet using this method. As a primary approach in this project, we utilize this method to examine various quantum spin systems.

In 2023, this project reported our achievement concerning the Shastry-Sutherland model, namely, the $S = 1/2$ Heisenberg antiferromagnet on the orthogonal dimer lattice [2]. In this study, we successfully carried out Lanczos diagonalizations of this system up to 48 sites. Within Lanczos-diagonalization studies, this size was treated for the first time to the best of our knowledge. Note here that the largest treated matrix dimension is 32,247,603,683,100. The properties of this model are determined by the ratio of two interaction amplitudes denoted by $r = J_2/J_1$, where J_1 denotes the amplitude of the Heisenberg interaction at the orthgonal dimer and J_2 denotes the amplitude of interaction forming the square lattice. Our result concerning the edge of the exact-dimer phase for the 48-site system is $r = 0.67542$. From the comparison between the 44- and 48-site systems, our conclusion for the edge of the exact-dimer phase is

$$r = 0.6754(2). \tag{1}$$

This result was compared with the result obtained in electron spin resonance measurements under high pressure and high field[3]

and discussed the difference between the experimental and theoretical results from the viewpoint of Dzyaloshinski-Moriya interactions that are not taken into account in the theoretical model. Our studies contribute much to our deeper understandings of the quantum magnetism. Further investigations would clarify nontrivial quantum effects in these systems.

References

[1] H. Nakano and A. Terai: J. Phys. Soc. Jpn. **78**, 014003 (2009).

[2] H. Nakano and T. Sakai: JPS Conf. Proc. **38**, 011166 (2023).

[3] T. Sakurai, Y. Hirao, K. Hijii, S. Okubo, H. Ohta, Y. Uwatoko, K. Kudo, and Y. Koike: J. Phys. Soc. Jpn. **87**, 033701 (2018).

Multiscale simulations for complex flows

Yohei MORII and Toshihiro KAWAKATSU

Department of Physics,

Tohoku University, Sendai, Miyagi 980-8578

We have developed a platform for multiscale simulations on complex flows named MSSP (Multi-Scale Simulation Platform for complex flows), where a macroscopic flow simulator based on smoothed particle hydrodynamics (SPH) and microscopic molecular dynamics simulators embedded in each of SPH particles are coupled [1]. In the present project, we studied the Marangoni effect of surfactant adsorbed on an oil/water interface. For this purpose, we implemented an evaluation method of surface tension and a diffusion process of microscopic molecules between adjacent SPH particles. We prepared an oil droplet in a water matrix and injected a micellar solution of surfactant (Fig.1), where the micelles are regarded as deformable objects and show viscoelastic response to external flow field.

In Figs.2 and 3, we show the simulation results using 10,000,000 micelles on MSSP for the system shown in Fig.1 [2]. We can successfully observe the deformation of oil droplet caused by the Marangoni effect.

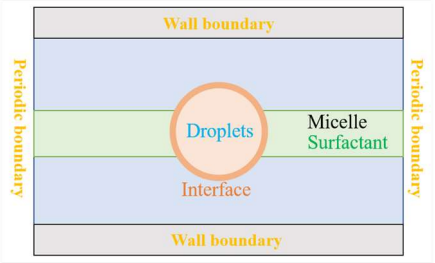

Fig. 1: Setting of the simulation system.

Acknowledgement

The computation in this work has been done using the facilities of the Supercomputer Center, the Institute for Solid State Physics, the University of Tokyo.

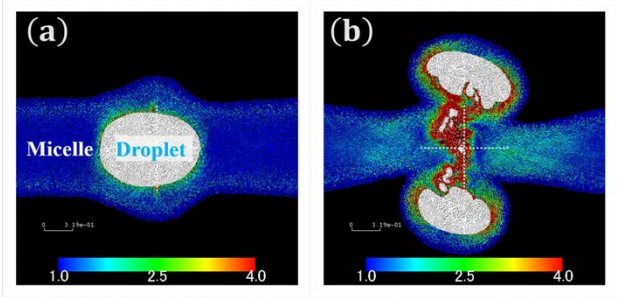

Fig.2 Configurations of micelles around the droplet for (a) low and (b) high affinity of surfactant to the interface.

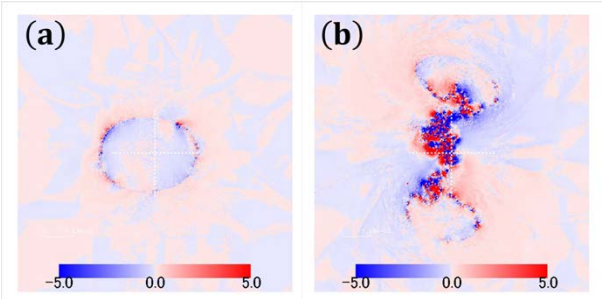

Fig.3 Distribution of vorticity.

References

[1] Y.Morii and T.Kawakatsu, Phys. Fluids, **33**, 093106 (2021).

[2] Y.Morii and T.Kawakatsu, *in preparation*.

Search for magnetic skyrmion by machine learning

Satoru Hayami
Graduate School of Science, Hokkaido University, Sapporo 060-0810, Japan

A topological spin texture, which shows distinct physical phenomena from conventional ferromagnetic and antiferromagnetic spin textures, has been extensively studied in both theory and experiment. Among them, a magnetic skyrmion characterized by a topologically-nontrivial swirling spin texture has been a central subject in topological magnetism since its discovery in 2009. Although a skyrmion crystal phase consisting of a periodic array of the magnetic skyrmion in a crystal has been observed in various materials, its stabilization conditions in terms of the lattice structure and magnetic interactions have not been fully elucidated. In the project with number 2023-Ca-0002, we have numerically investigated the stabilization mechanism of magnetic skyrmion crystal phases by considering various situations. We have presented the main results this year below.

(i) Anisotropic spin model and multiple-Q states in cubic systems: We have constructed an effective spin model with magnetic anisotropic interactions in cubic systems [1]. By considering the symmetry conditions to possess the Dzyaloshinskii-Moriya interaction and symmetric anisotropic interaction in momentum space, we have classified the nonzero anisotropic interactions at high-symmetry wave vectors in both centrosymmetric and noncentrosymmetric cubic space groups. We have also demonstrated that the obtained anisotropic spin model exhibits the instability toward a variety of multiple-Q states including the hedgehog-antihedgehog crystal.

(ii) Skyrmion crystals in noncentrosymmetric cubic magnet: Cases of O, T, and $T_{\rm d}$: We have investigated the low-temperature magnetic phase diagrams of the spin model in three noncentrosymmetric cubic point groups, O, T, and $T_{\rm d}$ [2]. By performing the simulated annealing, we discussed the similarity and difference of the phase diagrams in each point group. We have found that the instability toward the skyrmion crystal is different for the point groups (O, T) and $T_{\rm d}$ according to the different nature of the Dzyaloshinskii-Moriya interaction; the skyrmion crystal is stabilized only for the point groups (O, T), while that is not for $T_{\rm d}$. Meanwhile, we have clarified that the skyrmion crystal phase can appear in the case of the point group $T_{\rm d}$ once the effect of the uniaxial strain lowering the symmetry to $D_{\rm 2d}$ is introduced.

(iii) Antiferro skyrmion crystal phases in a synthetic bilayer antiferromagnet under an in-plane magnetic field: We have investigated the possibility of stabilizing the antiferro skyrmion crystal without the uniform scalar chirality in synthetic layered antiferromagnets [3]. By considering the centrosymmetric bilayer structure with the staggered Dzyaloshinskii-Moriya interaction, we have found that the antiferro skyrmion crystal is induced in an external magnetic field. We summarized four conditions to stabilize the antiferro skyrmion crystal in the ground state: (1) the staggered DM interaction, (2) the easy-plane single-ion anisotropy, (3) the interlayer exchange interaction, and (4) the in-plane magnetic field. Additionally, we have shown that the ferri-type skyrmion crystal is stabilized next to the antiferro skyrmion crystal.

(iv) Magnetic bubble crystal in tetragonal magnets: We have investigated the stabilization mechanisms of a magnetic bubble crystal, which consists of a superposition of double-Q sinusoidal waves, in centrosymmetric tetragonal magnets [4]. We constructed the magnetic-field-temperature phase diagrams while changing the easy-axis magnetic anisotropic two-spin interaction by the efficient steepest descent method. We found that there are two key ingredients in addition to the easy-axis two-spin magnetic anisotropy to realize the bubble crystal: the high-harmonic wave-vector interaction and the biquadratic interaction. We showed that the bubble crystal phase tends to appear in the high-temperature region of the skyrmion crystal phase for a moderate easy-axis anisotropic two-spin interaction; they are transformed into each other by changing the temperature. In addition, we showed that the bubble crystal remains stable in the zero-temperature limit for the large high-harmonic wave-vector interaction or biquadratic interaction in addition to the large easy-axis anisotropic two-spin interaction.

(v) Multiple-Q dipole–quadrupole instability in spin-1 triangular-lattice systems: We have investigated the multiple-Q instability in the classical $S = 1$ model with magnetic dipole and electric quadrupole degrees of freedom on a triangular lattice [5]. By systematically performing the simulated annealing for the effective models with various multipole–multipole interactions, we have found that four out of the fifteen models show the triple-Q ground states. These triple-Q states are stabilized as a consequence of the interplay between the dipole and quadrupole interactions, which requires neither single-ion magnetic anisotropy nor higher-order mode–mode couplings. We have also discussed the effect of the hexagonal crystalline electric field and the appearance of charge disproportionation.

(vi) Hybrid skyrmion and antiskyrmion phases in polar C_{4v} systems: We have examined the role of the Dzyaloshinskii-Moriya interaction at low-symmetric wave vectors in noncentrosymmetric magnets [6]. We have analyzed the effective spin model on the polar square lattice, which is derived from the Kondo lattice model in the weak-coupling regime, by performing the simulated annealing. We have found that the direction of the Dzyaloshinskii-Moriya vector affects the formation of the skyrmion crystals as well as the helicity of the spiral wave. We have shown that the rhombic skyrmion crystal is realized when the Dzyaloshinskii-Moriya vector lies in the $\langle 100 \rangle$ direction, while the square skyrmion crystal is realized for other cases. Furthermore, we have shown that the anti-type skyrmion crystal is also realized depending on the direction of the Dzyaloshinskii-Moriya vector, which provides another root to realize the anti-type skyrmion crystal even under polar symmetry.

References

[1] R. Yambe and S. Hayami, Phys. Rev. B **107**, 174408 (2023).

[2] S. Hayami and R. Yambe, Phys. Rev. B **107**, 174435 (2023).

[3] S. Hayami, J. Phys. Soc. Jpn. **92**, 084702 (2023).

[4] S. Hayami and Y. Kato, Phys. Rev. B **108**, 024426 (2023).

[5] S. Hayami and K. Hattori, J. Phys. Soc. Jpn. **92**, 124709 (2023).

[6] S. Hayami, Phys. Rev. B **109**, 054422 (2024).

Dzyaloshinskii transition in a classical Heisenberg model of a chiral magnet

Yoshihiko NISHIKAWA
Department of Physics, Kitasato University
Sagamihara, Kanagawa, Japan, 252-0373

We have studied a classical Heisenberg model of a chiral magnet on a three-dimensional cubic lattice [1] with a clock perturbation. The Hamiltonian of the system is

$$H(\{\boldsymbol{S}_i\}) = -J_{\parallel} \sum_{\langle i,j\rangle_{\parallel}} \boldsymbol{S}_i \cdot \boldsymbol{S}_j - J \sum_{\langle i,j\rangle_{\perp}} \boldsymbol{S}_i \cdot \boldsymbol{S}_j - \boldsymbol{D} \cdot \sum_{\langle i,j\rangle_{\parallel}} \boldsymbol{S}_i \times \boldsymbol{S}_j - \delta \sum_i \cos\left(N_\delta \arctan\left(\frac{S_{i,z}}{S_{i,x}}\right)\right), \quad (1)$$

where $\boldsymbol{S}_i$ is a classical Heisenberg spin, $\boldsymbol{D} = D\boldsymbol{e}_y$ with $D > 0$, $\delta > 0$, and $N_\delta = 3$. The first and second summations run over pairs of neighboring spins with $\boldsymbol{r}_{ij} = \boldsymbol{r}_j - \boldsymbol{r}_i \parallel \boldsymbol{D}$ and $\boldsymbol{r}_{ij} = \boldsymbol{r}_j - \boldsymbol{r}_i \perp \boldsymbol{D}$, respectively. We fix $J_{\parallel}^2 + D^2 = 2J$. The Dzyaloshinskii–Moriya interaction, the third term in the Hamiltonian, induces a helical structure into the system at low temperature with its axis parallel to $\boldsymbol{D}$. If we set the boundary condition in the y direction to be periodic, the system is forced to have a commensurate helical structure in the y direction even when it does not naturally favor that winding number. This could make finite-size corrections significantly large. The boundary condition in the y direction is thus set open, while those in the x and z directions are periodic in our simulation. The last term, although it looks unfamiliar, stands for a N_δ-state clock perturbation: When $\arctan(S_{i,z}/S_{i,x}) = 2\pi n/N_\delta$ ($n \in \mathbb{Z}$), it gains an energy. Thus our system is a model of chiral magnet with a clock perturbation. The linear length of the lattice is L for the x and z directions and $L_y = 8L$ for the y direction.

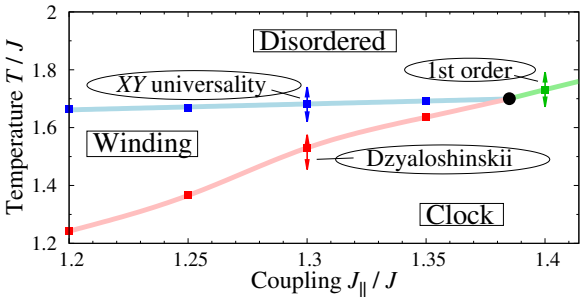

Figure 1: Phase diagram of the system. Depending on $J_{\parallel}/J$, the system has three qualitatively different phase transition: XY-type continuous transition, first-order transition, and Dzyaloshinskii transition.

This model can be seen as an effective classical model of the J-Q model [2], a quantum spin model for studying the deconfined quantum criticality (DQC), with a chiral perturbation. A recent work [3] has argued that a field breaking the chiral symmetry of the system is a relevant perturbation for the putative DQC point, and has shown that it indeed induces a qualitatively different phase transition between the *helical valence-bond* (HVB) and the valence-bond solid (VBS) phases. Motivated by their work, we study the phase transitions in the effective classical model and discuss its detailed characterization.

We show the phase diagram of the model in Fig. 1. When $J_{\parallel}/J < 1.38$, the system has two phase transition when decreasing temper-

ature. The one at lower temperature, dubbed as *Dzyaloshinskii transition* [4], separates the winding phase, in which the system has a clear helical structure, and the clock phase with a homogeneous magnetization. This corresponds to the HVB-VBS transition found in the JQ model, and we focus on it in the following.

We define the winding number per spin

$$w = \frac{1}{L_y} \sum_k \theta_{k+1} - \theta_k, \tag{2}$$

where $\theta_k = \arctan(\boldsymbol{m}_{k,z}/\boldsymbol{m}_{k,x})$ with

$$\boldsymbol{m}_k = \frac{1}{L}^2 \sum_i \delta_{i_y,k} \boldsymbol{S}_i. \tag{3}$$

Here, i_y indicates the y component of the position of spin i and δ is the Kronecker delta. We then calculate the free energy of the system as a function w

$$f(w) = -\frac{\beta^{-1}}{8L^3} \log \int d\boldsymbol{S} \delta(w(\boldsymbol{S}) - w) \exp(-\beta H) \tag{4}$$

using the replica-exchange Wang-Landau [5] and multicanonical simulations [6] at a fixed temperature. Our results clearly show that, in the vicinity of the transition, the free energy has many minima while at high temperature it is convex and simple, see Fig. 2. Each minimum corresponds to a helical structure with a certain number of winding, and transition between them needs a subextensive but $O(L^2)$ free energy. The number of minima grows as L_y, suggesting, at $L \to \infty$ and $L_y \to \infty$, the system has an infinite number of free-energy minima. This clearly characterizes the peculiar nature of the phase transition: Despite its continuous nature, the system has an infinite number of locally stable states at the transition, realizing an interesting counterexample to the Ginzburg-Landau-Wilson picture for conventional critical points. We will further discuss the dynamical properties of the Dzyaloshinskii transition in future work.

This work was done in collaboration with Jun Takahashi.

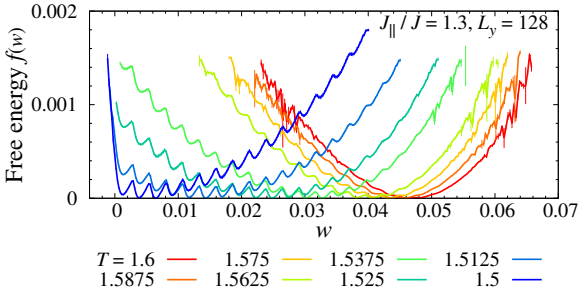

Figure 2: Free energy of the system as a function of the winding number w. See main text for its definition.

References

[1] Y. Nishikawa and K. Hukushima, Physical Review B **94**, 064428 (2016)

[2] A. W. Sandvik, Physical Review Letters **98**, 227202 (2007).

[3] B. Zhao, J. Takahashi, and A. W. Sandvik, Physical Review Letters **125**, 257204 (2020).

[4] I. E. Dzyaloshinskii, JETP **19**, 960 (1964).

[5] F. Wang and D. P. Landau, Physical Review Letters, **86**, 2050 (2001); T. Vogel *et al.*, Physical Review Letters, **110** 210603 (2013).

[6] B. A. Berg, T. Neuhaus, Physical Review Letters, **68**, 9 (1992).

Dynamics in Active Cyclic Potts Model

Hiroshi NOGUCHI
Institute for Solid State Physics, University of Tokyo

Various spatiotemporal patterns have been observed in nonequilibrium active systems. Many phenomena are well-captured by a description in terms of nonlinear but deterministic partial differential equations. However, noise effects are not understood so far. We focused on the effects of thermal fluctuations, since they are significant on a molecular scale.

We simulated the nonequilibrium dynamics of a Potts model with three cyclic states ($s = 0$, 1, and 2) [1]. The neighboring sites of the same states have an attraction to induce a phase separation between different states, and they have a cyclic state-energy-difference in the rock–paper–scissors manner. It is a model system for chemical reactions on a catalytic surface or molecular transport through a membrane. For the reaction case, the three states are reactant, product, and unoccupied sites. For the transport case, the molecule can bind to both surfaces and flip between these two states. In a cyclically symmetric condition, we found two dynamic modes: homogeneous cyclic mode and spiral wave mode. At a low cycling energy h between two states, the homogeneous dominant states cyclically change as $s = 0 \to 1 \to 2 \to 0$ via nucleation and growth, as shown in Fig. 1(a). In contrast, spiral waves are formed at high energy h, as shown in Fig. 1(b). The waves are generated from the contacts of three states and rotate around them.

For large systems, a discontinuous transition occurs from these cyclic homogeneous phases to spiral waves, while the opposite transition is absent. Conversely, these two modes can temporally coexist for small systems, and the ratio of the two modes continuously changes with increasing h. The transition from the homogeneous cyclic to spiral wave modes occurs by the nucleation of the third state during the domain growth, while the transition to the homogeneous cyclic mode occurs through the disappearance of three-state contacts. With increasing system size, the former rate increases but the latter rate exponentially decreases. The transition character is changed by these size dependencies.

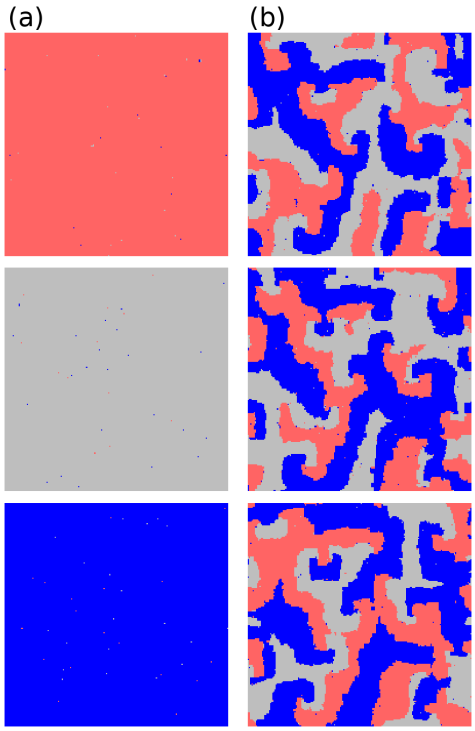

Figure 1: Sequential snapshots of active cyclic Potts model. (a) Homogeneous cyclic mode at $h = 0.8$. (b) Spiral wave mode at $h = 1.1$. The states, $s = 0$, 1 and 2, are displayed in gray, blue, and red colors, respectively.

References

[1] H. Noguchi, F. van Wijland, and J.-B. Fournier, J. Chem. Phys. 161, 025101 (2024).

All-Atom Molecular Dynamics Simulation Study of Polymer Dynamics in Nanoporous Materials

Nobuhiko HOSONO

Department of Applied Chemistry, Graduate School of Engineering, The University of Tokyo, 7-3-1 Hongo, Bunkyo-ku, Tokyo 113-8656

Metal–organic frameworks (MOFs) are crystalline compounds with numerous nano-sized pores capable of encapsulating molecules ranging from small gas molecules to extremely long polymers, as demonstrated by previous research [1]. Specifically, experiments and MD simulations have elucidated that polymer chains with elongated structures thread into the pores of MOFs from their termini, gradually uncoiling their entangled conformations [2]. Recently, we experimentally discovered that the polymer infiltration rate and diffusion pathways within the pores significantly vary depending on the chemical structure of the polymer chains [3]. In this study, we conducted all-atom MD simulations of this polymer diffusion process to gain molecular-level insights into the mechanism behind the polymer structure's influence on diffusivity in MOF nanopores.

We utilized the LAMMPS package for the all-atom MD simulation and selected a typical pillared-layer type MOF, $[Zn_2(1,4\text{-ndc})_2(ted)]_n$ (ndc = naphthalenedicarboxylate, ted = triethylenediamine). To examine the effect of substitution groups on the PEG chain, we also designed and used a PEG with a phenyl group at the middle of the chain. Initial structures were constructed by placing guest PEG molecules in contact with the (001) surface of the MOF. The MD simulations were conducted at 393 K for 100 ns with MPI process (Figure 1). The infiltration process of the PEG chains within the MOF nanopores was tracked, and diffusion kinetics and pathways were investigated. Results clearly indicate differences in diffusion pathways as well as diffusion rates between unsubstituted PEG and phenyl-substituted PEG. We observed that even minor structural alterations on the polymer chain significantly influence the diffusion process and infiltration behavior of polymers within the MOF nanopores. This phenomenon holds promise for new polymer separation applications.

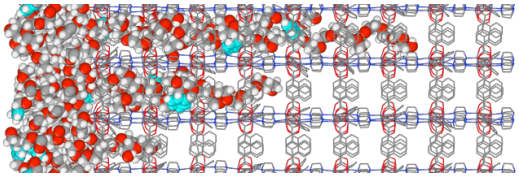

Figure 1. A snapshot of the MD

References

[1] N. Oe, N. Hosono, and T. Uemura, Chem. Sci. **12**, 12576 (2021).

[2] T. Uemura *et al.*, J. Phys. Chem. C **119**, 21504 (2015).

[3] N. Mizutani *et al.*, J. Am. Chem. Soc. **142**, 3701 (2020).

Dynamic friction of macroscopic objects

Michio OTSUKI

Graduate School of Engineering Science,

Osaka University, Machikaneyama, Toyonaka, Osaka 560-8531

Amontons-Coulomb law of friction states that the friction coefficient does not depend on the shape of objects or the relative velocity between two objects in contact. However, the phenomenological explanation of the law is based on the adhesion of microscopic asperities at friction interface and implicitly assumes the uniformity of the stress field. A recent study has revealed that the static friction coefficient depends on the shape of the 3D rectangle block, which indicates the breakdown of the law, due to the nonuniform stress field [1].

In this study, we conducted simulations on static friction of grooved objects and hysteresis friction of viscoelastic objects using finite element method with parallel computing. The computational size is 500,000 nodes and billions of time steps, which takes 50 hours using our in-house code compiled with the Intel Fortran compiler and 1,700 MPI processes on the CPU servers.

First, we investigated the friction of a 3D grooved block on substrate using finite element simulation [2], as shown in Fig. 1. The results show that the static friction coefficient decreases with increasing groove width and depth. A theoretical analysis based on a simplified model reveals that the static friction coefficient is related to the critical area of the slow precursor slip. The decrease in the effective viscosity leads to the decrease in the friction coefficient.

We also investigated the hysteresis friction of viscoelastic objects, as shown in Fig. 2. The results show that the friction coefficient depends on the relative velocity between objects and takes different peaks at certain velocities depending on the viscosity. We also find that the type of deformation changes in high velocity region depending on the viscosity.

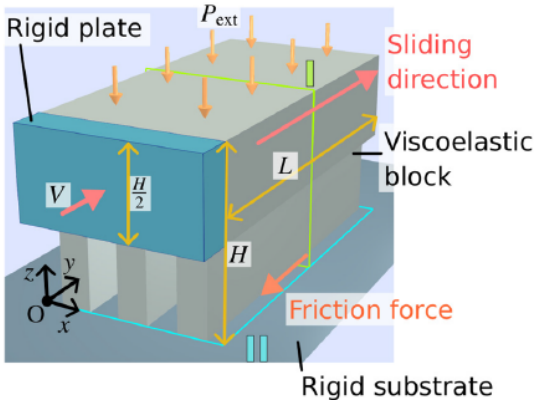

Fig. 1: Schematic of the grooved block [2].

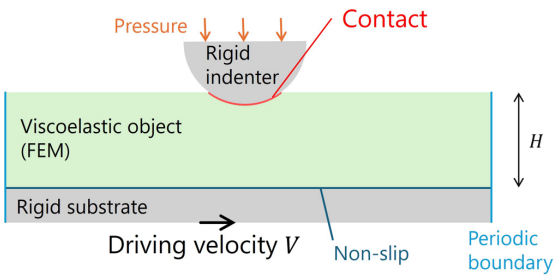

Fig. 2: Schematic of the grooved block.

References

[1] W. Iwashita, H. Matsukawa, and M. Otsuki, Sci. Rep. **13**, 2511 (2023).

[2] W. Iwashita, H. Matsukawa, and M. Otsuki, Tribol. Lett. **72**, 25 (2024).

Development of calculation methods for time correlation functions requiring long time computations

Takahiro MURASHIMA

Department of Physics, Tohoku University

Aramaki-aza-Aoba, Aoba-ku, Sendai, Miyagi 980-8578

Melts composed of polymers have long relaxation times, and various physical properties are correlated for long periods of time. To efficiently perform the calculation of the correlation function requiring long computation time in molecular dynamics (MD) simulations, it is necessary to develop an efficient method for calculating the correlation function and to accelerate the speed of MD simulations. For an efficient method of computing correlation functions, we have the multiple-tau method [1] developed by Ramirez et al. I extended the algorithm to calculate various physical quantities and improved it to run the correlation functions for each molecule in parallel. The developed program is packaged in a form that can be run on LAMMPS [2]. For speeding up MD simulations, GPUs are utilized. Specifically, I developed a hybrid simulation method in which MD simulations are performed by HOOMD-blue [3] and correlation function calculations are performed by LAMMPS. These improvements enable the computation of long-time time-correlation functions to be performed more efficiently than before. Figure 1 shows the mean-square displacement of the middle particle in a polymer chain with length N. The appearance of a region of $t^{1/4}$ [4], characteristic of entangled polymer chains with $N \geq 100$, indicates that our method computed correctly. This result is in preparation for submission to a journal.

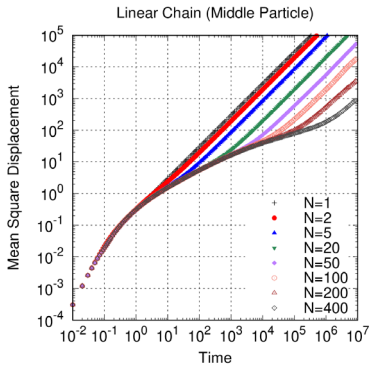

Fig. 1: Mean square displacement of the middle particle in a linear chain composed of N particles.

References

[1] J. Ramirez et al., *J. Chem. Phys.* **133**, 154103 (2010).

[2] S. Plimpton, *J. Comput. Phys.* **117**, 1 (1995).

[3] J. Anderson et al., Comput. Mater. Sci. **173**, 109363 (2020).

[4] M. Doi, S. F. Edwards, The Theory of Polymer Dynamics, Oxford (1986)

Supersolid in Bose-Hubbard model with titled dipole interactions

Takafumi SUZUKI

Graduate School of Engineering,

University of Hyogo, Shosha, Himeji, Hyogo 670-2280

We have used ISSP supercomputer resources for the following two topics: (1) supersolid states in two-dimensional hard-core bosonic Hubbard model with dipole interactions and (2) dynamical properties of the extended honeycomb-lattice Kitaev-Γ model.

(1) Superolid in Bose-Hubbard model with titled dipole interactions

For realizing supersolid [1,2], many efforts have been made so far. Experimentally ultracold atomic gases trapped in optical lattices are promising stages for realizing the supersolid. Theoretically frustrated interactions are significant to stabilize the supersolid states in lattice Bose-Hubbard models. The authors in ref. [3] have investigated the ground-state phase diagram of the two-dimensional bosonic Hubbard model with the dipole-dipole interactions by the mean-field (MF) approach and infinite entangled-pair-state (iPEPS) calculations. When the dipole axis is tilted on the two-dimensional lattice plain and the cut-off distance for the dipole-dipole interactions is restricted, the MF approach and iPEPS calculations predicted that several supersolid phases appear in between solid phases with different commensurate fillings.

In this project, we investigated the ground-state phase diagram of this model by quantum Monte Carlo (QMC) calculations. To characterize the nature of each phase appeared, we applied not only conventional finite-size-scaling approaches but also a machine-learning assisted approach. In the machine-learning assisted approach, we prepare the multi-convolutional neural network (mCNN) that was trained by magnetization snapshots obtained from classical Monte Carlo simulations or the several Ising models. The snapshots include several ordered phases, such as ferromagnetic, Neel, stripe, and up-up-down (down-up-up) ordering, which are possible ordered phase in the target quantum model. We checked the accuracy of the mCNN for the hard-core Bose Hubbard model on the triangular lattice, where the supersolid state arises in a low temperature. We confirmed that the mCNN network quantitatively predicts the phase transition temperature for the emerging the 1/3 (2/3) solid order and is not affected by the emergence of the superfluidity.

By utilizing the mCCN, we classified phases of the Bose-Hubbard model with tilted dipole interactions. We find that the QMC results reproduce the phase diagram obtained by the MF approach and iPEPS calculations [3]. By changing the cut-off distance for the long-range dipole interactions, we further investigate the phase diagram.

(2) Dynamical properties of the extended S=1 honeycomb-lattice Kitaev-Γ model

In this project, we have investigated ground states and dynamical properties of the extended S=1 Kitaev-Γ model on a honeycomb lattice by the numerical exact diagonalization and density-matrix-renormalization-group approaches. In the previous study, we focused on the S=1/2 case and investigated the effect of anisotropy of the interaction; we connect the spin chain model and the isotropically interacting model on the honeycomb lattice by tuning the interactions [4]. We clarified that the Tomonaga-Luttinger liquid (TLL) appearing in the spin chain limit [5] persists for the finite interchain interactions and it becomes a proximate Tomonaga-Luttinger liquid (pTTL), which is analogous to sliding TLL [6]. In addition, the phase diagram near the isotropically interacting limit includes characteristic natures; (1) when K is ferromagnetic and Γ is antiferromagnetic, the three-fold degenerated phase whose phase boundary is characterized by the first order transition appears in $1/6 < K/|\Gamma| < 1$ and otherwise, the model is located at the phase boundary between the pTLL-like (almost one-dimensional) state and dimerized phase. In this

project, we have investigated the S=1 case. We found that the three-fold degenerated phase is also confirmed in the S=1 case.

References

[1] G. V. Chester, Phys. Rev. A **2**, 256 (1970).
[2] A. J. Leggett, Phys. Rev. Lett. **25**, 1543 (1970).
[3] H. -K. Wu and W. -L. Tu, Phys. Rev. A **102**, 053306 (2020).
[4] M. Gohlke, J. C. Pelayo, and T. Suzuki, arXiv:2212.11000.
[5] W. Yang, et al., Phys. Rev. Lett. 124, 147205 (2020) and W. Yang, A. Nocera, and I. Affleck, Phys. Rev. Research 2, 033268 (2020).
[6] R. Mukhopadhyay, C. L. Kane, and T. C. Lubensky, Phys. Rev. B **64**. 045120 (2001).

Analyses on the Potential-dependent Dynamics of Ionic Liquid Electrolytes Forming Electric Double Layers Facing the Electrodes

Ken-ichi FUKUI

Department of Materials Engineering Science, Graduate School of Engineering Science, Osaka University, Machikaneyama, Toyonaka, Osaka 560-8531

Electric double layer-organic field effect transistor (EDL-OFET) using an ionic liquid (IL) as a gate dielectric has attracted much attention, because EDL formed at IL/semiconductor interface reduces the operating voltage for accumulation of carriers at the interface [1]. Thus, the response of interfacial IL to the potential change of the gate voltage is important for device performance. However, details of solvation structure and dynamics of ionic liquids at the interfaces are still not clear. In this study, we performed classical molecular dynamics (MD) simulation to investigate the local structure of interfacial IL and its response to the potential change of C_n-DNBDT-NW crystalline single-layer (semiconductor) film, whose interfaces were recently analyzed by interfacial spectroscopy [1].

All MD simulations were conducted by classical MD package of GROMACS-5.0.7. A simulation cell (7.3 × 7.9 nm^2 in-plane) contains 800 ion pairs of EMIM-FSI as IL and a single C_n-DNBDT-NW layer. To reproduce the potential dependent behavior of the IL at the interface, hole charges were uniformly distributed on the atoms constituting the HOMO of C_n-DNBDT-NW and corresponding ions were removed to maintain the cells neutral. Local structures of the IL at the interface depending on the interfacial potential were evaluated from 20 ns MD trajectories at 400 K after 4.0 ns equilibration run.

At the potential of zero charge (PZC) without any apparent change at the C_9-DNBDT crystalline film, the anions and cations showed a checkerboard-like local structure in the region of 3 Å from the film surface. (Fig. 1a). At -1.0 V, the anions were more strongly localized on the crystal film surface, while keeping the character of the checkerboard structure (Fig. 1c). In the region from 3 Å to 6 Å from the C_9-DNBDT film surface, the cations were dominant at both of PZC and -1.0 V (Fig. 1c and d). These characteristics were common when the alkyl chain length (C_n) was changed from 1 to 8. Angle distribution analyses at the interfaces showed an interesting feature that the interfacial EMIM cation was aligned its imidazolium ring more perpendicular to the surface of hole injected films with even chain numbers (C_n).

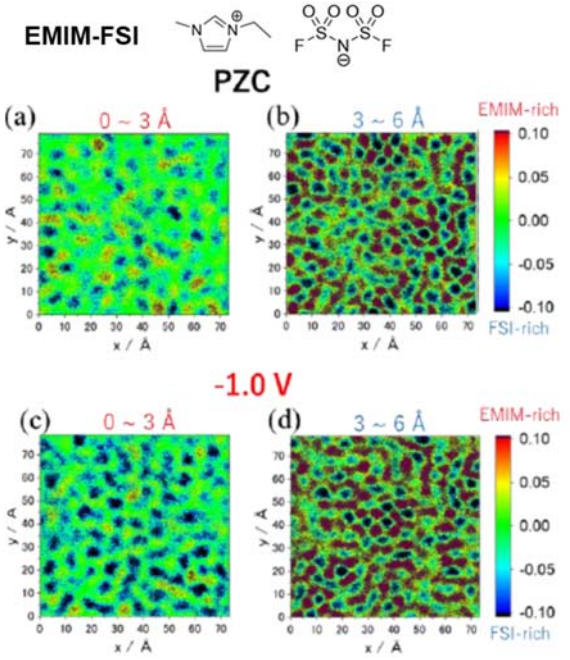

Fig. 1 2D distribution of cations (red) and anions (blue) at the IL / C_9-DNBDT-NW interface.

Reference

[1] T. Okamoto, et al. *J. Am. Chem. Soc*. **142**, 9083 (2020).

[2] Tanabe, K. Fukui, and coworkers, *Commun. Chem.* **4**, 88 (2021).

Molecular dynamics simulation for chemical reactions in multicomponent systems of thermosetting resins

Yutaka Oya

Department of Materials Science and Technology,

Tokyo University of Science, Niijuku, Katsushika-ku, Tokyo 125-8585

We quantitatively evaluated the damage of thermosetting resins using molecular dynamics (MD) simulations. To achieve this goal, we needed to address two challenges related to the "changes in polymer topology," which are typically difficult to simulate using conventional classical molecular dynamics methods. The first challenge is reproducing the chemical reactions of thermosetting resins. The second is to mimic the dissociation of covalent bonds induced by mechanical loading. Thermosetting resins form dense crosslinked structures through chemical reactions between the base resin and curing agent. In the previous year, we focused on creating these crosslinked structures and developed MD methods to reproduce the mechanical properties of multicomponent epoxy systems. In this year, we have developed an algorithm in MD for bond dissociation and quantitatively evaluated the stress-strain curves of epoxy resins and entropy as a measure of damage. Below, we describe the overview of our approach.

In this study, DGEBA was used as the base resin and 44-DDS as the curing agent for epoxy resin. The base resin has two epoxy groups at both ends, while the curing agent has two primary amine groups at both ends as well. The primary amine groups react with the epoxy groups to form secondary amines, and further reaction of the secondary amines with epoxy groups results in tertiary amines. Branching formed by such sequential reactions spreads throughout the system, leading to the formation of a crosslinked structure. By reproducing such chemical reactions, a crosslinked structure shown in Figure 1 was obtained. This crosslinked structure has a curing degree of 0.83, showing good agreement with previous research results [1].

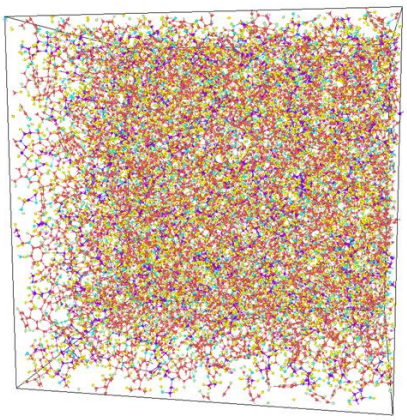

Figure 1. Crosslinked structure formed by chemical reaction.

A uniaxial tensile test was conducted on the obtained crosslinked structure for the stress-strain relationship. The strain rate was set to 5.0 × 10^9, and a pressure of 1 atm was applied in perpendicular to the tensile direction. The system temperature was set to T = 300K. During the uniaxial tensile test, internal covalent bonds were broken. In this study, a distance-based covalent bond dissociation algorithm was introduced to evaluate internal damage. Specifically, each covalent bond was eliminated when its length exceeded 1.1 times the natural length. Furthermore, a very short NVT relaxation (10fs) was introduced after covalent bond dissociation to alleviate sudden forces acting on the atoms.

Figure 2 depicts the stress-strain curve, entropy generation, and bond dissociation obtained from the uniaxial tensile simulation. Incorporating covalent bond dissociation, the maximum strength is reached at around 6 percent strain, and fracture occurs at 15 percent strain. In contrast, in conventional MD simulations without considering covalent bond dissociation, the system continues to deform without a decrease in stress. From the stress-strain curve, the resulting entropy generation is evaluated as shown in Figure 2 (b), indicating an increase in

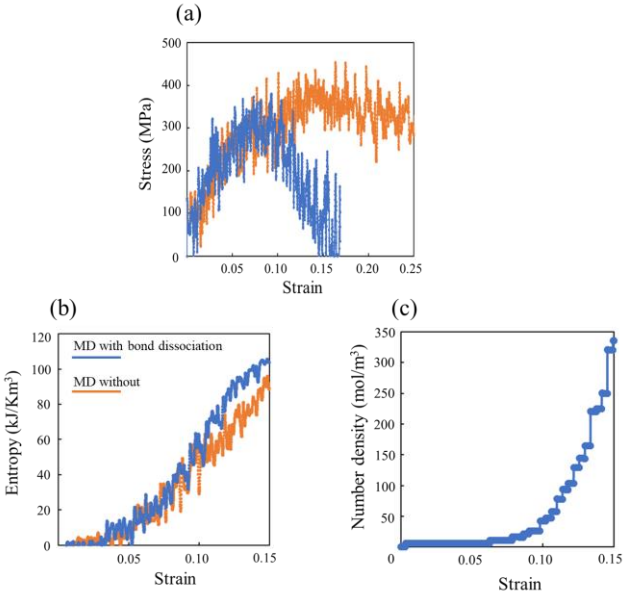

Figure 2. (a) Stress-strain curves with and without bond dissociations, (b) Entropy generation, and (c) Number density of dissociated covalent bonds.

entropy due to covalent bond dissociation. The results of the number of bond dissociation, as depicted in Figure 2 (c), show a strong positive correlation with the increase in entropy. In summary, these findings underscore the importance of covalent bond dissociation in reproducing the mechanical properties of thermosetting resins.

Fig. 1: Supercomputer System B at SCC-ISSP.

References

[1] Carla E. Estridge, *Polymer* 141 (2018), 12-20.

New Monte Carlo approach: Kondo vs Kitaev

Masahiko G. YAMADA
Department of Physics, School of Science, University of Tokyo
Hongo, Bunkyo-ku, Tokyo 113-0033

We developed a new Monte Carlo method called an infinite product expansion (iPE) method [1]. This iPE method is applicable to both Kondo lattice models and Kitaev models for classical/quantum spin systems as an "order N" method for the finite-temperature calculation of quantumness.

For example in the case of the weight of Monte Carlo becomes $W \propto \det\cosh\frac{\beta(H-\mu)}{2}$ for a Hamiltonian H with a chemical potential μ. We can expand this as $\det\cosh\frac{\beta(H-\mu)}{2} = \det\prod_{n=1}^{\infty}\left\{1+\left[\frac{\beta(H-\mu)}{\pi(2n-1)}\right]^2\right\}$. In this way, we can use the sparsity of the Hamiltonian (H matrix) to accelerate the Monte Carlo drastically, down to orders $O(N^2)$ or even $O(N)$.

We apply this new massive-scale Monte Carlo approach (iPE) to reveal two topological phenomena. First to reveal a new topological excitation of the Kondo lattice model, and second to reveal a new topological phase of the Kitaev model Larger N calculations enabled by the massive parallelization will give us a further insight into the physics of topology in both a spin liquid and a localized spin picture.

For Kitaev models, many new topological phase transitions, even inside exactly solvable regions can be expected in its phase diagram. Specifically, a larger N simulation may discover a new Berezinskii-Kosterlitz-Thouless transition inside the Kitaev model, which is always difficult to prove because of the logarithmic correction.

For Kondo cases, there are many more. Topological excitations like skyrmions, hedgehogs, Hopfions are expected, and we are now exploring such possibilities in large (real-space) systems of Kondo lattice models. Rich variety of phase diagrams can newly be investigated by our new approach (iPE).

References

[1] M. G. Yamada, Y. Akagi, and M. Udagawa: to appear.

Kinetics of phase transition and polyamorphism

Kazuhiro FUCHIZAKI
Department of Physics, Ehime University, Matsuyama 790-8577

Nowadays, it is generally known that a kind of intermediate-length scale order is developed in a metastable amorphous state compared to the corresponding stable liquid phase. In FY2023, as sufficient structural data were stored, we examined the structural similarities and differences between the liquid phases of SnI_4 and their amorphous states.

The ambient-pressure crystalline phase CP-I of SnI_4 was found to undergo pressure-induced amorphization at around 15 GPa on compression [1], and the amorphous state was named Am-I, which transforms with a discontinuous density decrease to another amorphous state Am-II on the return way to CP-I. Recently, we recognized that Am-I could be further classified into two structures depending on pressure: the high-density state Am-IH, composed of dissociated tin and iodine atoms, and the relatively low-density state Am-IL [2]. The transition between these states occurs continuously from 14 to 18 GPa [2].

Meanwhile, Liq-II, the stable liquid phase for CP-I and Am-II, undergoes a liquid–liquid transition (LLT) to Liq-I at 1.5 GPa and 970 K [3]. This LLT is associated with a subtle change (0.3-0.4 g/cc) in density [4]. No molecular dissociation has been confirmed in Liq-I up to 3.4 GPa, the highest pressure attained thus far. Therefore, the structural comparison here is restricted to Liq-II/Am-II and Liq-I/Am-IL.

Liq-II and Am-II have similar structures; they consist of randomly oriented molecules with perfect tetrahedral symmetry T_d. Similar structural factors characterize them; their snapshot aspects can only be distinguished by the degree of crowding, i.e., the density of molecules.

As far as the length scale of the order of a molecule is concerned, the situation in Liq-I and Am-IL is again said to be similar. The symmetry of molecules is locally broken; the symmetry is lowered from T_d to C_{3v} or C_{2v} [2, 5]. (The author speculates that the symmetry lowering is not a result but the trigger of the transition [5]. Introducing the two different length scales by symmetry lowering can facilitate the induction of compressional (dilatational) density waves.) However, a difference between Liq-I and Am-IL has been recognized for the structure beyond the intermediate length scale. Am-IL's structure factor does have a bump at 4.4 $Å^{-1}$, which is missing in Liq-I's. The origin of this intermediate length-scale order remained unanswered except that it is ascribable to the spatial correlation between iodine atoms [2].

To answer this problem, reverse Monte Carlo (RMC) simulations [6] were conducted again, but with an increased system size of 8000 SnI_4 units, compared to the previous one with 2744 units [2], to gain better statistics. Although the densities were available, the initial configurations of units used as input to the RMC simulations were prepared using molecular dynamics simulations.

In order to interpret the output configurations from the RMC simulations, the formation of a metallic I_2 bond was assumed if an intermolecular distance between iodine atoms of adjacent SnI_4 units fulfills the following two criteria simultaneously: i) the distance is less than 3.1 Å [7] and ii) the units

on both sides are deformed. This latter condition ii) was introduced because the molecular deformation, as examined below, could be regarded as a precursor to forming a chemical bond. Here, we call a segment satisfying the criteria a 'bond.' Such 'bonds' were found to be percolated throughout the system in Am-IL, whereas the size of clusters consisting of 'bonds' remained finite in Liq-I. Furthermore, the spatial distribution of iodine atoms belonging to a percolation cluster in Am-IL was confirmed to be responsible for the formation of the bump in the structure factor. Nonparticipating iodine atoms in a percolation cluster did not contribute to the bump. The bump thus does not emerge in the structure factor of Liq-I without a percolation cluster. A detailed report will be published in due course [8].

Finally, the relationship between molecular deformation and the possibility of 'bond' formation was examined based on quantum chemical considerations [9]. The related computations were not performed using ISSP supercomputers, and the results are kept concise. Two SnI_4 molecules could have a chance to form a physical 'bond' with a lifetime of the order of 0.1 ps when they approach closely within 10 Å. Interestingly, the 'bond' formation was induced by the deformation of molecules to C_{3v} or C_{2v} structures depending on their mutual orientations. However, the formation of a chemical bond has not yet been confirmed within available computation times.

References

[1] Y. Fujii, M. Kowaka, and A. Onodera: J. Phys. C **18**, 789 (1985).

[2] K. Fuchizaki *et al.*: J. Phys.: Condens. Matter **33**, 365401 (2021).

[3] K. Fuchizaki *et al.*: J. Chem. Phys. **135**, 091101 (2011).

[4] K. Fuchizaki, N. Hamaya, and Y. Katayama: J. Phys. Soc. Jpn. **82**, 033003 (2013).

[5] K. Fuchizaki, T. Sakagami, and H. Iwayama: J. Chem. Phys. **150**, 114501 (2019).

[6] O. Gereben and L. Pusztai: J. Comput. Chem. **33**, 2285 (2012).

[7] K. Takemura *et al.*: Z. Kristallogr. Cryst. Mater. **219**, 749 (2004).

[8] K. Fuchizaki: to be presented in 61st EHPRG, 1–6 September 2024, Thessaloniki, Greece; to be published.

[9] M. J. Frisch *et al,*: GAUSSIAN 09 Revision E.01, Gaussian, Inc., Wallingford, CT, 2009.

Physical properties of crosslinked polymer networks through network topology analysis

Katsumi HAGITA,[1] and Takahiro MURASHIMA[2]

[1]*Department of Applied Physics, National Defense Academy, Yokosuka 239-8686*

[2]*Department of Physics, Tohoku University, Sendai 980-8578*

To elucidate the topological effect on the physical/mechanical properties of the tetra-arm end-link gel/rubber, it is desirable to establish model approaches using coarse-grained MD (CGMD) simulations of the Kremer-Grest model and/or realistic approaches using all-atom MD (AAMD) simulations. There is a large gap in computational cost between CGMD and AAMD, and effective connections between them are also desired.

To develop a statistical approach to evaluate macroscopic properties of hydrogels from AAMD simulations, we studied poly(ethylene glycol) (PEG) hydrogels that show "negative energetic elasticity" [1]. In the analysis for experimental data, we estimated the linear relation $G = A\,(T - T_E)$ between shear modules (G) and temperature (T) where G was estimated from the relation $G = \sigma_{XY}/\gamma$ between shear stress (σ_{XY}) for each shear strain (γ). Here, T_E is an indicator of a negative energetic elasticity. In AAMD simulations, because statistical errors in σ_{XY} are significant, errors in G are also significant and make difficult to confirm the relation $G = A\,(T - T_E)$. We proposed a statistical approach [1] considering numerous datasets (σ_{XY}, γ, T) based on the multivariate regression of the equation $\sigma_{XY} = A\gamma\,(T - T_E)$ in a narrow temperature range using fitting parameters A and T_E. We confirmed the feasibility of the obtained T_E values via a statistical error analysis [1].

To investigate diamond lattice structures with artificial irresolvable entanglements, we developed a method to obtain initial configurations of AAMD simulations by converting configurations obtained by CGMD simulations. In the CGMD simulations, the diamond lattice structures with the artificial irresolvable entanglements were generated in four steps as follows. (i) The box size of the periodic boundary condition (PBC) with the number density $\rho = 0.85$ of the melt without solvent is set to $L_{pbc,\rho=0.85}$, and the system is expanded by a = 1.0, 1.2, 1,4, 1,6, 1,8, and 2.0 times $L_{pbc,\rho=0.85}$. (ii) Equilibrium relaxation calculations were performed in which the chains were treated as a phantom chain by setting the excluded volume to 0 with the cos-type non-bonding interactions. (iii) A push-off operation restored the excluded volume and returned the phantom chain to the KG chain.

(iv) The PBC box size was decreased to $L_{pbc,\rho=0.85}$ for $a > 1.0$ and was rest for $a = 1.0$. The networks of KG model were converted to the networks of AA model by mapping from a KG bead to a carbon (or oxygen) atom. Then, water molecules were introduced in the gaps of the PEG network to achieve a target PEG concentrations c [g/L].

Figure 1 (a) summarized the stresses at strain of 5.0 and clarified the anisotropy of network. These behaviors were consistent with the primitive path analysis of the backbone of the PEG network. Figure 1 (b,c) shows stress–strain curves of various entangled networks of KG model (without solvent) under the elongation rate of 0.0001 and shear strain rate of 0.0001. We found that the expansion coefficient a characterizes the elastic behavior. For $a = 1.0$, rapid increases of stresses were observed due to highly entangled structure. On the other hand, the stress–strain curves at $a = 1.8$ and 2.0 were close to a diamond lattice structure which has no entanglement. A future challenge will be to utilize this knowledge in the evaluation of actual material systems.

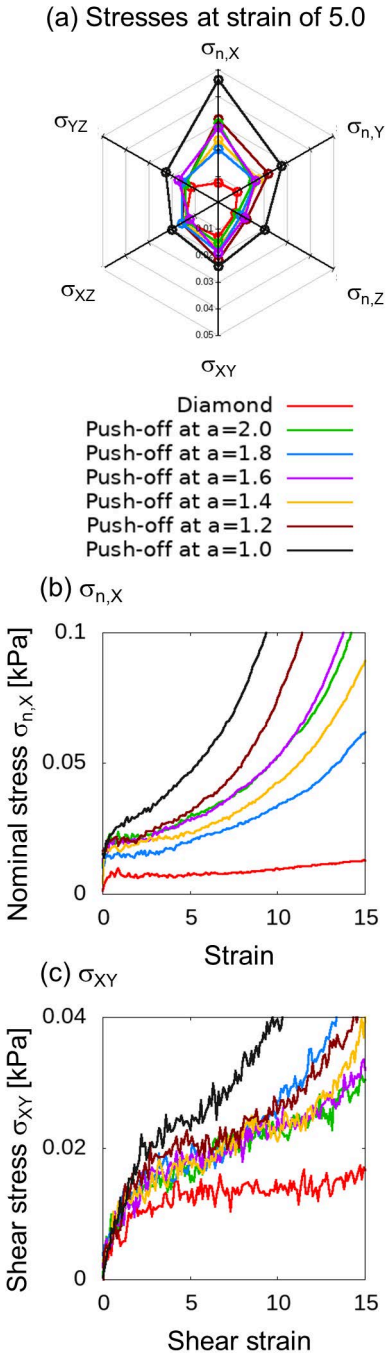

Fig. 1: Stresses of randomly entangled networks generated from a diamond lattice using a push-off procedure under different expansion coefficient a.

References

[1] K. Hagita, S. Nagahara, T. Murashima, T. Sakai, N. Sakumichi, Macromolecules **56**, 8095-8105 (2023).

Frustration and randomness in the honeycomb-lattice spin systems

Chitoshi YASUDA
Department of Physics and Earth Sciences, Faculty of Science, University of the Ryukyus, Okinawa 903-0213, Japan

Honeycomb-lattice magnets have gotten a lot of attention recently. These include the honeycomb-lattice Kitaev model, in which the ground state is a quantum spin liquid, and the combination of metal complexes and ferdadylradicals, in which several types of randomly coexisting interactions exist. A new quantum spin liquid was found from experiments on a solid helium thin film. The low density of the film predicts that the helium atoms form a honeycomb lattice. In this project, we conducted two studies on the honeycomb lattice, (1) the site-dilution effects on the antiferromagnetic Heisenberg model, and (2) the multiple-spin exchange model describing well the magnetism of solid helium.

The ground-state phase diagram of the spin $S = 1/2$ and $S = 1$ antiferromagnetic (AF) Heisenberg model on a honeycomb lattice, which is composed of bond-alternating chains and interchain interactions, is investigated by the quantum Monte Carlo simulation with the continuous-imaginary-time loop algorithm [1]. The phase diagram is parametrized by the intrachain alternating coupling constant α and the interchain coupling constant J'. The ground state becomes the dimerized spin-gapped state or the AF long-range ordered state depending on the parameters α and J'. In the dimerized state realized for small α and J', the finite correlation lengths are found to become relatively smaller than those of the square lattice [2]. The difference would be related to the difference in coordination number. The site-dilution-induced AF long-range order (LRO) has been also investigated in the honeycomb-lattice systems. As in the square-lattice systems [3], the results suggest that the LRO is induced at infinitesimal concentrations of dilution. However, its evaluation was more difficult than for the square-lattice systems. Specifically, the temperature that can be regarded as absolute zero has been lowered. We expect that the result could be due to the shortness of the correlation length of the pure system.

The multiple-spin exchange model is difficult to analyze due to its complexity. In this project, thermodynamic properties of ferromagnetic and AF states are investigated by using the molecular-field (MF) theory and the Green's function method. Within the MF approximation, we investigated the temperature dependences of magnetization and susceptibility, and obtained results suggesting that ferromagnetic and AF correlations are suppressed by the six-body exchange. In the Green's function method, which incorporates spin correlations rather than the MF approximation, we could have a formulation in which temperature fluctuations suppress magnetic orders.

References

[1] S. Todo and K. Kato, Phys. Rev. Lett. **87**, 047203 (2001).

[2] M. Matsumoto, C. Yasuda, S. Todo, and H. Takayama, Phys. Rev. B **65**, 014407 (2001).

[3] C. Yasuda, S. Todo, M. Matsumoto, and H. Takayama, Phys. Rev. B **64**, 092405 (2001).

Application of tensor networks in tensor data analysis

Kenji Harada
Graduate School of Informatics, Kyoto University
Kyoto 606-8501, Japan

In the fields of condensed matter and statistical physics, tensor networks have gained attention as a representation format for various many-body problems. These include ground states of quantum systems and nonequilibrium stationary distributions in time-evolving systems.

Various applications have proposed data science as a representation method for tensor data. For instance, an innovative approach to efficiently represent high-dimensional data distributions is a generative model that uses tensor networks[1, 2]. In this research project, we aim to further explore the application of tensor networks in the generative modeling.

Here, we consider a generative model based on a quantum state [1, 2]. Following the Born rule, we define $p(\mathbf{x})$ as the square of the amplitude of a wave function: $p(\mathbf{x}) = \frac{|\psi(\mathbf{x})|^2}{Z}$, where $\psi(\mathbf{x})$ is a wave function and Z is the normalization factor.

Two different approaches, MPSs [1] and balance TTNs [2], have been proposed for defining the wave function in generative modeling. The number of indexes of a tensor in the balance TTN is equal to that in the MPS. However, the difference lies in the topology of the network. In the TTN, all physical indexes x_i are connected, and there is no loop structure. Therefore, an MPS is a specialized type of TTN. It has been shown in [2] that the performance depends heavily on the network topology of TTNs.

We propose a new algorithm to optimize the network structure of a TTN for generative modeling. Various strategies can be employed to select a better local network structure [3]. Our network optimization technique enhances the performance of generative modeling with TTNs.

We applied our method to diverse data, including randomly generated data, stock price volatilities of companies embedded in stock indices, handwritten text images, and artificial data with stochastic dependencies. We aimed to examine the characteristics of these datasets. For example, through optimization, we discovered a network with topological coupling corresponding to the original dependencies of many data with stochastic dependencies, such as Bayesian networks.

References

[1] Zhao-Yu Han, Jun Wang, Heng Fan, Lei Wang, and Pan Zhang. Unsupervised Generative Modeling Using Matrix Product States. *Phys. Rev. X*, 8(3):031012, 2018.

[2] Song Cheng, Lei Wang, T. Xiang, and Pan Zhang. Tree tensor networks for generative modeling. *Phys. Rev. B*, 99(15):155131, 2019.

[3] Kenji Harada, Tsuyoshi Okubo, and Naoki Kawashima. Network optimization of tree generative models. in preparation.

The Study on Superionic Conduction and Phase Transition by Disordering of Complex Hydride

Ryuhei Sato

Advanced Institute for Materials Research,

Tohoku University, 2-1-1 Katahira, Aoba-ku, Sendai 980-8577, Japan

To improve ionic conductivity, it is important to understand the mechanism of many-body problems such as "concerted motion of ions" and "the coupling of transport ions with lattice vibrations and counterion rotation". So far, we have worked on physical properties related to ion conductivity, such as the mechanism elucidation of concerted transport mechanisms [1] and the role of neutral molecules in the bulk [2] and so on [3]. This year, the relationship between anion rotation and ion migration was analyzed by the trajectory of molecular dynamics simulations for $LiCB_9H_{10}$ having rotational complex anions ($CB_9H_{10}^-$).

Figure 1(a) shows an Arrhenius plot of Li diffusion coefficient obtained during machine learning potential molecular dynamics (MLP-MD) simulations. To improve the accuracy, MLP was reconstructed from the one used in the previous year. As a result, we succeeded in reproducing not only high-temperature (HT) phase but also the unknown low-temperature (LT) phase, although we slightly overestimated phase transition temperature. The diffusion coefficient increases by nearly two orders of magnitude before and after the phase transformation, confirming the large effect of anion rotation. The structure of the LT phase is shown in the fig. 1(b).

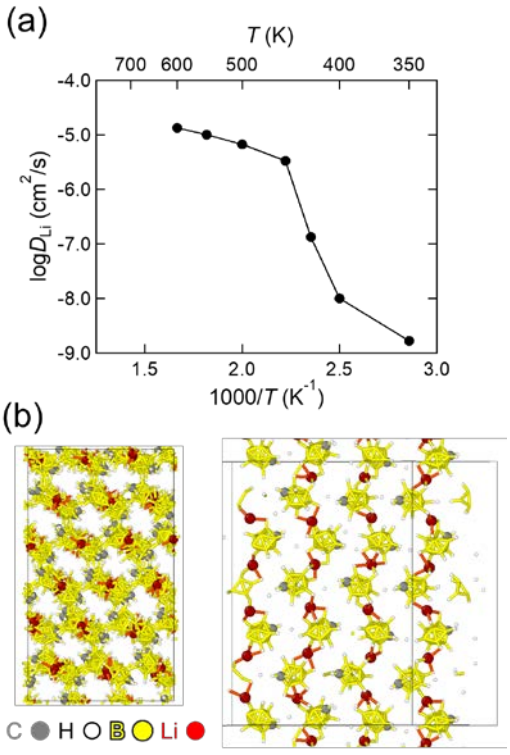

Fig. 1(a) Li diffusivity Arrhenius plot during MLP-MD simulation (b) Low T phase of $LiCB_9H_{10}$ obtained from MLP-MD simulation

It consists of a one-dimensional chain-like

structure of CB_9H_{10} and Li ions. Li connects only in the opposite direction to the C atom of $CB_9H_{10}^-$ due to the positive charge of C atom in this cluster. This strong site selectivity of Li for $CB_9H_{10}^-$ prevents Li ions from migration within LT phase since complex anion hardly rotates at low temperatures. Whereas, once complex anions are thermally activated and rotates, Li ion migrates along with the rotation of these anions. In fact, the site selectivity is maintained even in HT phase, and Li is transported by the paddle-wheel mechanism.

Figure 2 shows a plot of the connectivity of Li ions during MLP-MD simulations for $LiCB_9H_{10}$ obtained from graph theory. The vertical axis represents the number of Li atoms in the bond chain, while the horizontal axis shows the cut-off radius value at which two Li atoms are regarded to be bonded. The probability density in each state is as shown in the color scale. As confirmed by the results for T = 300 K in the grey scale color map, short Li-Li bonds with a cut-off radius below 4.5 Å was not observed during MLP-MD simulation for LT phase at 300K. On the other hand, dimers or trimers with Li-Li distances below 4.5Å are identified in HT phase. This shows the stronger interaction between Li ions during Li migration, suggesting concerted motion of Li ions occur via these dimers or trimers with the help of anion rotation.

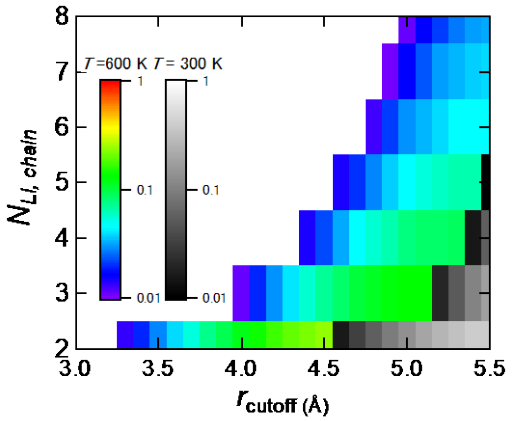

Fig. 2 Time-averaged probability density distribution of the number of Li ions in bonded chain determined from graph theory. The horizontal axis is the cut-off radius within which Li ions are regarded as bonded. The distribution for each cut-off radius is normalized so that the sum of the distributions for each cut-off radius is 1.

References

[1] R. Sato et. al. *J. Chem. Phys.*, 158 (2023) 144116.

[2] E. Santos, R. Sato, et. al., *Chem. Mater.*, 35 (2023) 5996.

[3] F. Yang, E. Santos, X. Jia, R. Sato, K. Kisu, Y. Hashimoto, S. Orimo. H. Li, *Nano Mater. Sci.*, in press.

Study of ground states and excitations in frustrated quantum magnets using MPS-based simulations

Matthias GOHLKE
Theory of Quantum Matter Unit, Okinawa Institute of Science and Technology
1919-1 Tancha, Onna-son, Okinawa 904-0495

Competing interactions—or frustration—between the constituents of a many-body system have proven to be an origin of exotic phases of matter. A famous example in this context are quantum spin liquids (QSL), that do not exhibit conventional magnetic order of spin-dipolar moments, but rather are defined by emergent gauge fields, fractionalized excitations, and topological order. A topical example in this context are Kitaev-like frustrated magnets, that exhibit a bond-dependent spin-exchange resulting in exchange frustration and, for certain choices of parameters, can result in a QSL ground state. Part of the computational resources provided by ISSP has been used to study the related anisotropic Kitaev-Γ model [see (I)].

On the other hand, ordering of higher moments like spin-quadrupoles may occur as well. Unlike spin-dipolar order, spin-quadrupolar order is defined by a director—an arrow without a head—in close analogy to the rods of nematic order and liquid crystals. Thus, spin-quadrupolar order is also named quantum spin nematic (QSN). Part of the resources have been used to study the QSN phase stabilizing in a frustrated ferromagnet with external magnetic field [see (II)].

(I) Extended QSL in an Anisotropic Kitaev-Γ Model. The characterization of quantum spin liquid phases in Kitaev materials has been a subject of intensive studies over the recent years. Most theoretical studies have focused on isotropic coupling strength in an attempt to simplify the problem. We, instead, have focused on an extended spin-1/2 Kitaev-Γ model on a honeycomb lattice with an additional tuning parameter that controls the coupling strength on one of the bonds [1], allowing us to connect the limit of isolated Kitaev-Γ chains, which is known to exhibit an emergent $SU(2)_1$ Tomonaga-Luttinger liquid (TLL) [2], to the two-dimensional model. We find that the critical properties of the TLL persist for finite inter-chain coupling, and a quantum paramagnetic phase which we call the proximate TLL stabilizes in analogy to *sliding Luttinger liquids*. This proximate TLL differs from the Kitaev spin liquid [1] in that Z_2 fluxes are not conserved.

Moreover, we have investigated the region of parameter space near the antiferromagnetic Kitaev coupling, were we find several long-range magnetically ordered phases [3], see Fig. 1.

(II) QSN in a Spin-$\frac{1}{2}$ Frustrated Ferromagnet. Here, we focus on a quantum magnet with spin-$\frac{1}{2}$ degrees of freedom. Such magnets can only exhibit a QSN states if two spin-$\frac{1}{2}$ are combined into an effective spin-1 [4].

Experimentally, the nature of such a ground state is intrinsically difficult to verify, due to the lack of probes that couple directly to the spin-quadrupole moments. Instead, it is necessary to examine the dynamics of a QSN: A continuous symmetry for the director of a spin-quadrupole remains, that give rise to a gapless Goldstone mode [6].

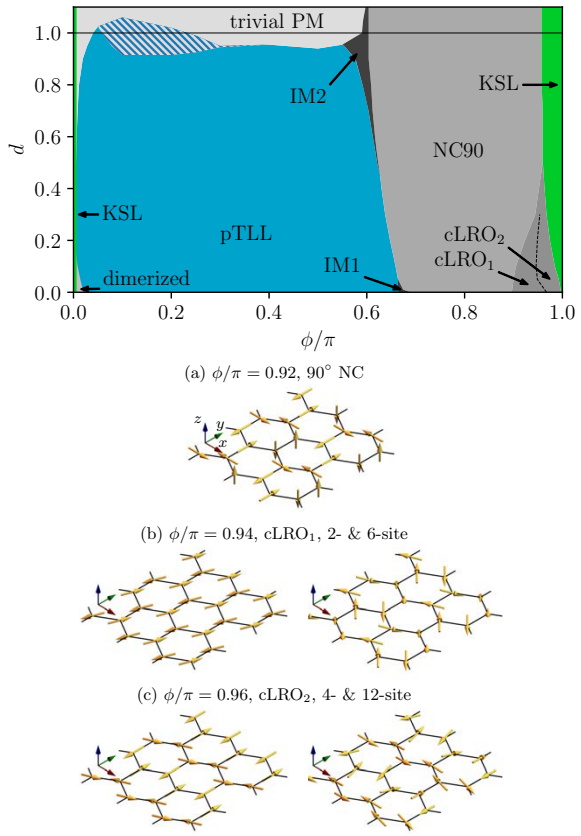

Figure 1: Extended phase diagram of the anisotropic KΓ model with illustrations of the long range magnetically ordered phases.

Here, we study the square-lattice frustrated J_1-K model [4], with dominant ferromagnetic Heisenberg exchange J_1 between nearest neighbor spins, cyclic ring-exchange K around squares, and h_z the Zeeman coupling to a magnetic field along the z-axis. Using iDMRG and the matrix product states (MPS) framework as well as a recently developed exact diagonalization (ED) method near saturation [5], we confirm the existence of the QSN phase in an extended range of $K/|J_1|$. Overall we find a good agreement between high-field ED on symmetric clusters and iDMRG.The QSN phase is sandwiched between high-field polarized and 4-sublattice AF phase. Additional phases (Neél, vector-chiral) occur for large K.

As reported previously, we have identified a gapless mode at an incommensurate wave vector coinciding with a set of eigenvalues in the MPS transfer matrix (TM) spectrum. Consequently, we have been able to study its behaviour with respect to an external magnetic field, system size and geometry, without having to invoke costly time-evolution simulations. Momentum information is contained through the complex phase of the TM eigenvalues, and momentum along the circumference being a well defined quantum number as long as translation symmetry remains. In essence, we find linear dependence of the wave vector with the magnetization, but also a dependence on the cylinder circumference. The latter makes an extrapolation to the 2D thermodynamic limit difficult. Consequently, we are trying to elucidate its physical origin. A publication is currerntly in preparation [7].

All MPS-related simulations have been carried out using TenPy [8]. TenPy makes use of Cython and calls heavily optimized Lapack and Blas routines matrix operations, e.g. singular value decomposition.

References

[1] M. Gohlke, J. C. Pelayo, T. Suzuki, arXiv:2212.11000 (2022). *To be published as a Letter in PRB. See also report by T. Suzuki.*

[2] Yang et al. Phys. Rev. Lett. **124**, 147205 (2020).

[3] M. Gohlke, J. C. Pelayo, T. Suzuki, *in preparation.*

[4] A. Andreev and I. Grishchuk, Sov. Phys. JETP **60** (1984) 267.

[5] H. Ueda, S. Yunoki, and T. Shimokawa, Comp. Phys. Comm. **277** (2022) 108369.

[6] R. Shindou, S. Yunoki, and T. Momoi, Phys. Rev. B **87**, (2013) 054429.

[7] M. Gohlke, T. Shimokawa, J. Sonnenschein, N. Shannon, *in preparation.*

[8] J. Hauschild, and F. Pollmann, SciPost Phys. Lect. Notes 5 (2018).

Towards understanding ground-state properties of multilayered superconductors using the variational Monte Carlo method

Ryui KANEKO
Research Institute for Science and Engineering, Waseda University
Shinjuku, Tokyo 169-8555, Japan

It is indispensable to understand the trend of layered cuprate superconductors through studying their effective Hamiltonians derived by first-principles calculations [1]. In particular, single-layer models focusing on each CuO_2 layer have been obtained for $CaCuO_2$, $Bi_2Sr_2CuO_6$ (Bi2201), $Bi_2Sr_2CaCu2O_8$ (Bi2212), and $HgBa_2CuO_4$, and their superconducting correlations that depend on doping levels have been extensively calculated [2] using the many-variable variational Monte Carlo method [3]. We previously found that it is crucial to enhance the on-site Coulomb repulsion over the nearest-neighbor hopping substantially and to sufficiently reduce the long-range Coulomb repulsion compared to the on-site repulsion for the purpose of increasing the superconducting order parameter, which correlates with the superconducting transition temperature [2].

The number of layers should also contributes to the stability of the superconducting state. However, in the analysis regarding the number of layers, the effective Hamiltonians include many long-ranged parameters that hinder the ground-state search. Thus, the effects of layers still need to be thoroughly verified using highly accurate numerical methods. Typically, in quasi-2D systems with intense interlayer hopping and interactions, an increase in spatial dimensionality is known to enhance magnetic ordering in general. The effective model under such conditions differs from a simple single-layer model. Whether the superconducting state can prevail over this magnetic state in a global parameter space is a crucial question. For this purpose, it is essential to solve models with two or more layers with high accuracy. So far, it has only been confirmed that the superconducting order parameters are comparable between single-layer and two-layer effective Hamiltonians at specific doping concentrations for Bi2212 [2].

In this study, using the many-variable variational Monte Carlo method [3], we investigate the ab initio three-layer effective Hamiltonian derived in the first-principles calculations [4] corresponding to $HgBa_2Ca_2Cu_3O_{8+\delta}$ (Hg1223), which has the highest transition temperature at ambient pressure among any mercury-based cuprate superconductors currently available. We first estimate the difference in chemical potential between the inner and outer layers, which reproduces the orbital filling of the GW calculation, at 20% hole doping.

Calculations regarding whether the superconducting state can prevail over magnetic and charge ordered states with long-period structure [5] are under way.

Acknowledgement

The author thanks Jean B. Morée for providing him with the ab initio results of Hg1223.

References

[1] J.-B. Morée, M. Hirayama, M. T. Schmid, Y. Yamaji, and M. Imada, Phys. Rev. B **106**, 235150 (2022).

[2] M. T. Schmid, J.-B. Morée, R. Kaneko, Y. Yamaji, and M. Imada, Phys. Rev. X **13**, 041036 (2023).

[3] T. Misawa, S. Morita, K. Yoshimi, M. Kawamura, Y. Motoyama, K. Ido, T. Ohgoe, M. Imada, T. Kato, Comp. Phys. Commun., **235**, 447 (2019).

[4] J.-B. Morée, Y. Yamaji, and M. Imada, arXiv:2312.16402.

[5] K. Ido, T. Ohgoe, M. Imada, Phys. Rev. B **97**, 045138 (2018).

Quantum entanglement dynamics in free boson systems by computing the matrix permanent

Ryui KANEKO
Research Institute for Science and Engineering, Waseda University
Shinjuku, Tokyo 169-8555, Japan

The time evolution of entanglement has been measured in experiments with ultracold atomic systems in optical lattices [1, 2], and it is crucial to verify how well numerical simulations on classical computers can reproduce it. However, numerical simulations of long-term evolution in soft-core bosonic systems are incredibly challenging, with conventional methods based on exact diagonalization or matrix product states being limited to dozens of sites for calculating entanglement dynamics [3]. Recently, we provided an analytical solution for the time evolution of Renyi entanglement entropy after quenching to a noninteracting bosonic system starting from an insulating state. Numerical evaluation of this entanglement entropy requires computing the permanent of matrices, which increases exponentially with the matrix size $2n$ or twice the number of particles n, namely, $O(2n \times 2^{2n})$ [4]. We numerically demonstrated that one could compute entanglement dynamics for systems of about 50 sites at half filling within realistic timeframes [4].

In this study, we focus on the unexplored area of spatial 2D systems, which would help us understand how the propagation of quantum information changes with dimensionality. As a simple example of a 2D system, we consider the Bose-Hubbard model on a square lattice. Starting from a charge-density-wave insulating product state at half filling, which is realized for sufficiently large interactions, we compute the time evolution of the Renyi entanglement $S_2(t)$ of the states at each time t after quenching the system to $U = 0$, where U is the interaction parameter. The formulas

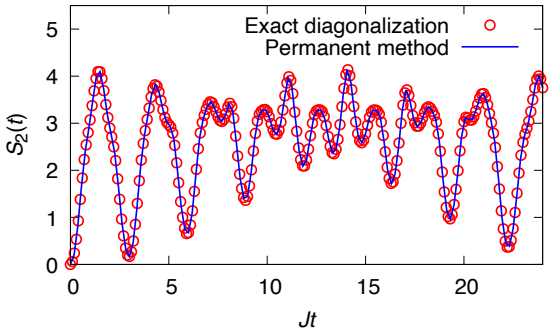

Figure 1: Time evolution of Renyi entanglement for 4×3 sites with open boundary conditions. The initial state is chosen as the staggered charge-density-wave state ($010101\cdots$ type) at half filling. We calculate entanglement entropy when the system is divided into two regions of 2×3 sites.

$$S_2(t) = -\ln \mathrm{perm} A(t), \tag{1}$$

$$A(t) = \begin{pmatrix} Z(t) & I - Z(t) \\ I - Z(t) & Z(t) \end{pmatrix} \tag{2}$$

give the Renyi entanglement [4], where I is the identity matrix and $Z(t)$ is a matrix constructed from the time-dependent single-particle correlation function obtained from the noninteracting Hamiltonian and the initial insulating product state. While obtaining $Z(t)$ from the diagonalization of matrices written in quadratic form is easy, the computational cost of $\mathrm{perm} A(t)$ is exponentially high. Considering the price of computing the permanent from

previous studies [4–7], it is likely that calculations for about 7×7 sites are feasible.

$S_2(t)$ does not need to be sequentially computed as a function of time, and it can be calculated in parallel for any time t. One can also parallelize the computation of the permanent itself. As a benchmark, we computed $S_2(t)$ quenched from the staggered charge-density-wave state ($010101\cdots$ type) at half filling for small systems (4×3 sites) with time steps of $\Delta Jt = 3/16$ (J: hopping) and for $Jt \in [0, 24]$ (see Fig. 1), confirming good agreement with exact diagonalization results. Computing $S_2(t)$ for larger systems is a future task.

References

[1] R. Islam et al., Nature **528**, 77 (2015).

[2] A. M. Kaufman et al., Science **353**, 794 (2016).

[3] S. Goto and I. Danshita, Phys. Rev. B **99**, 054307 (2019).

[4] D. Kagamihara et al., Phys. Rev. A **107**, 033305 (2023).

[5] A. Neville et al., Nat. Phys. **13**, 1153 (2017).

[6] J. Wu et al., Natl. Sci. Rev. **5**, 715 (2018).

[7] P.-H. Lundow and K. Markström, J. Comput. Phys. **455**, 110990 (2022).

Cell Division Plane Prediction

Yuuki Matsushtia, Katsuyoshi Matsushita, Koichi Fujimoto
Graduate School of Integrated Sciences for Life, Hiroshima University
Kagamiyama, Higashi-Hiroshima, Hiroshima 739-0046

Cell division is one of the indispensable cellular properties in the developmental process. In particular, plant cells cannot move, and therefore, the direction of the cell division determines the plant shape. One of the simple determination principles for cell division is Errera's rule [1]. The rule states that the division plane forms likely a soap film. This rule indicates that the division plane takes the smallest-area curved plane in the given shape of a mother cell under a constraint of daughter cell volumes. Based on this rule, the physical model of phase boundary under volume constraints of two phases can simulate this rule. The simulation is analytically solvable in the case of simple mother-cell shapes[2, 3], but the analytical solution hardly applies to realistic mother-cell shapes. To solve this hardness of analysis, a numerical simulator has been recently developed based on the phase field model and applied to various predictions of plant developments [4].

The calculation cost of the phase field model is very high and, therefore, can only accept cases with a few cells. A simpler calculation model is necessary for the prediction of long-time plant development yielding a large number of cells. To overcome this issue, Moukhtar *et al.* [6] used the cellular Potts model [5]. Using the Monte Carlo method, the model relatively reduces calculation costs by optimizing energy. In this model, the failure of orientation determination has been reported because of the lattice anisotropy effect. As an improvement to avoid this failure, a modification using the Hamiltonian term of the Crofton formula of interface area was proposed instead of the Potts Hamiltonian. The calculation introduces a complicated evaluation in the area of the division plane. Therefore, the model is inefficient for extending the cases, including the cell polarity or cytoskeleton configuration dependence. For further development of the division plane prediction, we should consider a more straightforward way of this method.

To reduce the anisotropy effect of this model, we considered the second and third neighbor interactions of the cellular Potts model. The long-range interaction has been reported to reduce the effect [5]. We developed the simulator for these long-range interactions and sufficiently succeeded in determining the division planes in simple shapes. We further applied the simulator to predict the division plane of the embryo of the Arabidopsis. We collaborated with biological experimentalists and obtained realistic mother cell shapes. We confirmed the correctness of the prediction using the simulator and now attempt to apply this method to various experimental conditions.

References

[1] L. Errera, Botanische Centralblatt **34**, 395, (1888).

[2] S. Besson J. Dumais, Proc. Natl. Acad. Sci. USA **108**, 6294 (2010).

[3] N. Kamamoto, T. Tano, K. Fujimoto, M. Shimamura, J. Plant Res. **134**, 457 (2021).

[4] C. Ishikawa, *et al.*, Proc. Natl. Acad. Sci. USA **120**, e2210632120 (2023).

[5] F. Graner and J. Glazier, Phys. Rev. Lett. **69**, 2013 (1992).

[6] J. Moukhtar, *et al.* PLoS Comput Biol **15**, e1006771 (2019).

Calculation of ordered structures, dynamics and optical properties of soft materials

Hiroki MATSUKIYO and Jun-ichi FUKUDA

Department of Physics, Kyushu University, Motooka 744, Nishi-ku, Fukuoka 819-0395

This year we have studied the dynamics of active matter systems, particularly focusing on the behavior of polar active fluids under geometrical confinements [1]. The behavior of polar active fluids can be described by a continuum equation, the Toner-Tu-Swift-Hohenberg (TTSH) equation. Several previous studies on the simulation based on the TTSH equation employed the non-slip boundary condition and did not describe the "edge current" (the unidirectional flow along the boundary), which had been observed in experiments. In ref. [1], we have proposed a new numerical method to calculate the TTSH equation under a slip boundary condition and successfully realized the edge current, see FIG.1. Furthermore, we have discovered the temporal oscillation of the edge current direction. To investigate the relation between the frequency of the oscillation and the parameters in the TTSH equation, we have performed simulations for many sets of parameter values, see FIG.2. The large number of threads of System B, Ohtaka, made it possible for us to perform the simulations in parallel for a large number of combinations of parameter values.

References

[1] Hiroki Matsukiyo and Jun-ichi Fukuda, arXiv:2312.08788. (to be published in Physical Review E)

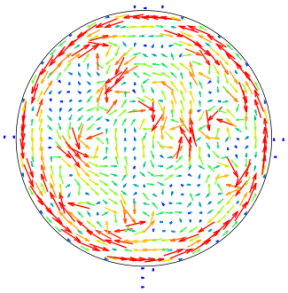

FIG.1: A typical snapshot of the velocity filed.

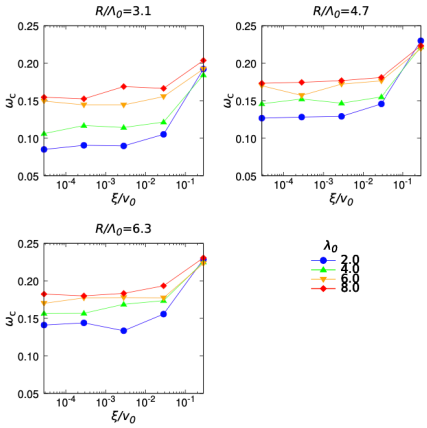

FIG.2: The relation between the characteristic frequency ω_c of the edge current oscillation and the parameters in the TTSH equation (ξ is the drag coefficient, λ_0 is the advection strength and R is the radius of the circular domain).

Dynamics of monitored quantum systems with symmetry

Yohei FUJI
Department of Applied Physics, University of Tokyo, Tokyo 113-8656

Many-body quantum states subject to frequent measurements undergo a measurement-induced phase transition, at which various critical scaling properties described by conformal field theory emerge [1, 2]. Such phase transitions typically occur between a volume-law entangled state, dominated by unitary dynamics, and an area-law entangled state, dominated by measurements. When the dynamics preserves some symmetry, measurement-induced transitions can also occur between area-law entangled states, in closed analogy to equilibrium phase transitions between ordered and disordered phases. However, the role of symmetry for universal properties at measurement-induced phase transitions is still largely unexplored.

In this study, we consider measurement-induced phase transitions in (2+1)-dimensional quantum circuits consisting of competing projective measurements. Measured operators in the circuits constitute a (2+1)-dimensional quantum Ising model and its plaquette extensions, as shown in Fig. 1, and thus preserve a global or subsystem $\mathbb{Z}_2$ symmetry. Since these circuits are written solely in terms of the measurements of Pauli operators, an efficient numerical algorithm based on the stabilizer formalism is available to access systems with $O(10^3)$ spins. We found that a measurement-induced transition between area-law entangled states takes place when the measurements of bond (XX) or plaquette $(XXXX)$ operators competes with those of single-site Pauli Z operators. While

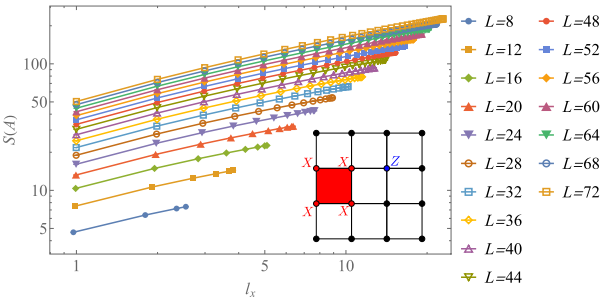

Figure 1: Entanglement entropy $S(A)$ at the measurement-induced transition in the plaquette Ising circuit. We consider an $L \times L$ system on a torus and its bipartition into $l_x \times L$ and $(L - l_x) \times L$ cylindrical subsystems.

the quantum Ising circuit exhibits critical properties expected for a three-dimensional percolation transition as previously reported, the plaquette Ising circuit shows somewhat unusual scaling properties as exemplified in algebraic growth of the entanglement entropy. We are currently trying to understand the role of the subsystem $\mathbb{Z}_2$ symmetry to those critical properties.

References

[1] A. C. Potter and R. Vasseur, Entanglement Dynamics in Hybrid Quantum Circuits, arXiv:2111.08018.

[2] M. P. A. Fisher, V. Khemani, A. Nahum, and S. Vijay, Random Quantum Circuits, Annu. Rev. Condens. Matter Phys. **14**, 335 (2023).

A Large-Scale Molecular Dynamics Simulation Study on the Shape of an Ice Crystal Grown from Water Including Air Molecules

Hiroki NADA

Faculty of Engineering, Tottori University, 4-101 Koyama-Minami, Tottori 680-8552

Elucidating the growth kinetics of ice from water in the presence of air molecules is of importance for understanding ice particle formation in nature. In this project, a molecular dynamics (MD) simulation was conducted to investigate the shape of an ice crystal grown from water in which air molecules were dissolved.

The simulation was performed using a system in which an ice crystal grew freely in all directions perpendicular to the crystal's *c*-axis [1]. The system used contained a cylindrical ice crystal at the center, and the remainder of the system corresponded to liquid water including air molecules. The numbers of H_2O and air molecules in the system were 17540 and 100, respectively. In this study, we specially focused on the effects of N_2 and CO_2 molecules on the growth shape of an ice crystal. To elucidate those effects, for comparison, the simulation was also performed for a pure H_2O system.

A modified version of six-site model of H_2O [2] was used to estimate the intermolecular interaction between a pair of H_2O molecules. Temperature and pressure were maintained at 265 K and 1 atm, respectively. TraPPE N_2 and CO_2 models were used to estimate the interaction acting on air molecules [3]. The MD simulation was carried out with DL_POLY 2.20, using System B of ISSP Supercomputer Center.

The effect of air molecules on the growth rate of the ice crystal was different between N_2 and CO_2 molecules. N_2 molecules bound to the interface between the growing ice crystal and water and lowered the growth rate of the ice crystal. However, CO_2 molecules did not stably bind to the interface and, hence, did not significantly change the growth rate. In addition, the growth shape of the ice crystal was also different between N_2 and CO_2 molecules.

References

[1] H. Nada: Cryst. Growth. Des. **11** (2011) 3130.

[2] H. Nada: J. Chem. Phys. **145** (2016) 244706.

[3] J. J. Potoff and J. I. Siepmann: AIChE J. **47** (2001) 1676.

A Large-Scale Metadynamics Simulation Study on the Binding Conformations of Ionic Polymers at a Geometrically Rough Surface of Calcium Carbonate Crystal

Hiroki NADA

Faculty of Engineering, Tottori University, 4-101 Koyama-Minami, Tottori 680-8552

The control of calcium carbonate crystal growth by additives is essential to biomineralization, scale inhibition, and materials technology. In this project, molecular dynamics (MD) simulations based on the metadynamics (MTD) method (hereafter, MTD simulation) were conducted to elucidate the stable binding conformations of a polymaleic acid (PMA_n, $\{(CO_2CHCHCO_2)^{2-}\}_n$, n=5–10) and a polyacrylic acid (PAA_n, $\{(CH_2CHCO_2)^{-}\}_n$, n=10–20) at a calcite (104) surface having a geometrically rough structure, which appears during calcite growth.

The simulation system was a rectangular parallelepiped in which a calcite slab was placed at its center such that its (104) planes, at which steps having kinks at their edges were formed, were perpendicular to the *z*-axis [1]. A liquid water phase containing the additive was placed at one of the two (104) planes. Following our previous studies [1, 2], the interactions within calcite were estimated with a model proposed by Raiteri et al., and the potential parameters for were determined using the general AMBER force field. The interaction between pairs of water molecules was estimated using the TIP3P model. The MTD simulation was carried out with DL_POLY 2.20, in which PLUMED 1.3 was implemented to permit combination with the MTD method, using System C of ISSP Supercomputer Center.

For all the additives examined, a free energy surface (FES) obtained using the x- and y-components of the distance between two C atoms at the sides of the additive's main chain as collective variables indicated several local minima, suggesting the existence of several different stable binding conformations. For all the stable binding conformations emerged, the main chain of the additive was distorted, and most of the carboxyl O atoms were exposed to the water phase. The binding stability was higher for PMA_n than for PAA_n, when they had the same number of carboxyl groups.

References

[1] H. Nada: J. Phys. Chem. C **118** (2014) 14335.

[2] H. Nada: Langmuir **14** (1996) 136.

Structural formation of non-spherical colloidal particles

Takamichi TERAO

Department of Electrical, Electronic and Computer Engineering,

Gifu University, Yanagido 1-1, Gifu, 501-1132

In colloid science, theoretical studies have focused on patchy particles, exploring how their behavior is influenced by orientation-dependent attractions [1]. These studies characterize systems of charged patchy particles, which feature a heterogeneous surface charge distribution, by the interplay between electrostatic attraction and repulsion. However, systematic research on non-spherical charged patchy particles is lacking, and several unresolved issues persist.

In this study, a computer modeling is employed to treat non-spherical charged patchy particles in molecular dynamics simulations. The model arranges several small particles with both positive and negative charges on the surface of a rotating ellipsoid, treating the entire assembly as a single patchy particle. These small particles are categorized into three groups: those at both ends of the long axis are assigned a negative charge, while the remaining particles receive a positive charge. Although this method of modeling patchy particles as a set of small particles is computationally demanding, it allows for the accurate replication of a wide range of patchy particle properties.

Molecular dynamics simulations were performed on a system of non-spherical charged patchy particles confined between parallel planes. Figure 1 displays a typical snapshot of the system, with the areas representing the patchy particles highlighted in white. Under these conditions, the patchy particles were observed to aggregate randomly. It was also confirmed that various structures of non-spherical patchy particles appear in different conditions.

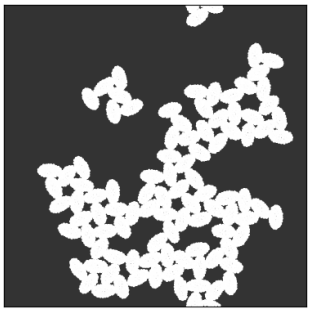

Fig. 1: Snapshot of non-spherical patchy particles

References

[1] E. Bianchi, J. Largo, P. Tartaglia, E. Zaccarelli, and F. Sciortino, Phys. Rev. Lett. **97**, 168301 (2006).

Comparison of superconducting properties in quasicrystals and approximant crystals

Nayuta TAKEMORI
Department of Physics, Graduate School of Science, Osaka University
1-1 Machikaneyama,Toyonaka,Osaka 560-0043

Quasicrystals are characterized by an unusual crystal structure that lacks translational symmetry and displays unconventional point group symmetry, such as 5-fold rotational symmetry. This has implications for superconductivity in materials with such structures, which has garnered significant attention recently. Specifically, non-BCS-type s-wave weak coupling superconductivity in quasicrystals, predicted in 2017, involves Cooper pairs with finite center-of-mass momentum, representing a novel form of exotic superconductivity [1]. In 2018, bulk superconductivity was experimentally confirmed in Al-Mg-Zn quasicrystals and their 1/1 approximants. The temperature dependence of the electronic specific heat in these materials was found to be consistent with the theoretical predictions, although the jump in specific heat is about 10-20% smaller than expected from BCS theory due to the absence of a Fermi surface and coherence peaks [2].

In this work, we investigate the results of a theoretical analysis of the attractive Hubbard model using Bogoliubov-de Gennes mean-field theory. The previous works [1, 2] suggests that quantitative differences in specific heat jumps may exist between quasicrystals and approximants with periodic approximation. However, it remained unknown to what extent the specific heat jump in approximants differs from that in quasicrystals. Motivated by this, we also investigate Penrose approximants and compare their superconducting properties with those of quasicrystals and regular periodic systems. We demonstrate that the peculiar superconducting properties of quasiperiodic systems do not appear in the case of approximants which exhibit locally similar structures to those of quasicrystals (Table 1).

References

[1] Shiro Sakai, Nayuta Takemori, Akihisa Koga, and Ryotaro Arita. Superconductivity on a quasiperiodic lattice: Extended-to-localized crossover of cooper pairs. *Phys. Rev. B*, 95:024509, Jan 2017.

[2] Nayuta Takemori, Ryotaro Arita, and Shiro Sakai. Physical properties of weak-coupling quasiperiodic superconductors. *Phys. Rev. B*, 102:115108, Sep 2020.

[3] Michael Tinkham. *Introduction to superconductivity*. Courier Corporation, 1996.

	Penrose (OBC)				Socolar (OBC)	Square (PBC)		Penrose approx (PBC)		BCS
	1591	4181	11006	ext	5289	2500	10000	1/1	4/3–3/2	
$\frac{2E_g^0}{T_c}$	3.35	3.38	3.38	3.38	3.37	3.46	3.45	3.42	3.45	3.52
A_1	1.61	1.63	1.69	1.70	1.66	1.70	1.70	1.68	1.67	1.74
$\frac{\Delta C}{C_{\rm en}}$	1.13	1.21	1.21	1.21	1.19	1.40	1.39	1.41	1.45	1.43

Table 1: The ratio of the superconducting gap at zero temperature to the critical temperature (top), a coefficient in the temperature dependence of the superconducting gap near the critical temperature (middle), and the jump of the specific heat (bottom) obtained in Penrose tiling of 1591, 4181 and 11006 sites, as well as its extrapolated value and those for square lattice of 2500 and 10000 sites. Universal values in the conventional continuum BCS theory [3] are added in the rightmost column.

Numerical study of dynamical structure factors based on spinon operator representation of Heisenberg antiferromagnets

Yoshiyuki Fukumoto
Department of Physics and Astronomy, Faculty of Science and Technology, Tokyo University of Science, 2641 Yamazaki, Noda, Chiba 278-8510

In recent years, a lot of interests have been focused on low-energy excitations of frustrated magnetically ordered systems [1]. The trigger was a high-resolution neutron scattering experiment on the $S = 1/2$ triangular-lattice system $Ba_3CoSb_2O_9$ [2], which clearly observes a continuous band that is thought to be a composite excitation of spinons in addition to magnon excitations. The magnon spectrum is significantly deformed from the calculation results of the linear spin-wave theory. It looks as if it is being pushed by the continuous band.

In order to understand this experimental observation, Zhang *et al.* performed theoretical calculations using the fermion representation of the spin operator, for which each site is constrained to have one fermion. They made a mean-field approximation corresponding to the equal-amplitude resonating valence bond (RVB) state, and construct a single-particle state using the mean-field Hamiltonian under a staggered magnetic field that stabilizes the magnetic 120-degree structure. A ground state and particle-hole excited states are created from these one-particle states. They argued that the structure of the spinon continuum is closely related to the roton minimum of the magnon spectrum, and also discovered an amplitude mode consisting of two bound spinons that cannot be captured by the spin wave approximation. However, the constraint condition for the fermion representation is treated within the RPA approximation. Thus, it is desired to perform calculations that accurately handle the constraint.

In this study, we strictly handle the constraint conditions and calculate the ground state and the dynamic structure factors, with taking into account the particle-hole excited states, by using the variational Monte Carlo (VMC) method, where we have introduced a method called reweighting to use a common sample to calculate all matrix elements [4].

The ground state calculations were performed for a system of up to 288 sites, and the energy at the thermodynamic limit was estimated by extrapolating the system size. Our result of ground state per site is $E/JN = -0.5407(2)$. Although our result is lower than previous VMC studies, $E/JN = -0.532(1)$ [5], and the spin-wave approximation, $E/JN = -0.538(2)$, but it is higher than the result of the series expansion method, $E/JN = -0.5502(4)$ [6], which shows that there is room for further improvement in variational functions. It is desirable to introduce longer valence bonds into the variational function. We also calculated the dynamic structure factors for the 36-site system and compared them with the experimental results for $Ba_3CoSb_2O_9$ and the calculation results by Zhang *et al*, and we will perform calculations on a larger system next year.

[1] B. D. Piazza *et al.*, Nat. Phys. 11, 62, 2015.
[2] S. Ito *et al.*, Nat. Commun. 8, 235, 2017.
[3] C. Zhang *et al.*, PRB 102, 075108, 2020.
[4] T. Li *et al.*, PRB 81, 214509, 2010.
[5] C. Weber *et al.*, PRB 73, 014519, 2006.
[6] W. Zheng *et al.*, PRB 74, 224420, 2006.

Impact of direction of the Dzyaloshinskii-Moriya vector on the magnon dispersion of the q=0 state in kagome-lattice systems

Yoshiyuki Fukumoto
Department of Physics and Astronomy, Faculty of Science and Technology, Tokyo University of Science, 2641 Yamazaki, Noda, Chiba 278-8510

A magnon is an elementary excitation from a magnetically ordered state. The linear spin wave (LSW) theory is a standard calculation method of magnon dispersion relations. However, through research using neutron scattering experiments of $S = 1/2$ Heisenberg antiferromagnets on triangular lattices and kagome lattices [1-3], it has been found that the LSW results require very large correction factors for $S = 1/2$ frustrated systems [4,5].

Kogure *et al.* used the series expansion method based on the linked-cluster algorithm [6] to study the magnon dispersion relation of the kagome system $Cs_2Cu_3SnF_{12}$ with $q = 0$ order [5]. Their model Hamiltonian consisted of the nearest-neighbor exchange and Dzalosinsky-Moriya (DM) interactions, where the direction of the DM vector was perpendicular to the kagome plane. As a result, it was revealed that the band width of the magnon spectrum in the series expansion is less than half of the LSW, and its shape is also significantly changed. It was also revealed that the correction for the LSW is larger for the kagome lattice than for the triangular lattice. As the magnitude of the DM vector is chosen as $0.12J$, where $J = 20.7$ meV is the exchange parameter, the magnon spectrum by the series expansion can be compared with the experimental result for $Cs_2Cu_3SnF_{12}$. However, there remain quantitative discrepancies: one of them is that the experimental value of the excitation gap at the M point is 8.3 meV, whereas the calculation gives a smaller value of 6.2 meV.

In this study, we consider the case where the direction of the DM vector is tilted from the kagome plane, and investigate how this affects the calculated results of the magnon spectrum. Then, the interaction matrix elements become to be complex numbers, so we need to rewrite the calculation program accordingly. In particular, the matrix S, in a transformation matrix e^S used to construct the effective Hamiltonian, changes from a real antisymmetric matrix to a skew-Hermitian matrix. We confirmed that our program correctly satisfies the conditions for the order in which cluster weights are generated [6].

As a result of calculations up to seventh order, it was found that the DM vector component parallel to the kagome plane has almost no effect on the excitation energy around the M point. Another interaction that should be considered is the second-neighbor exchange interaction J_2, which was estimated to be $J_2 \simeq -0.1J$ in a previous study [2]. This ferromagnetic second-neighbor interaction has a frustrating effect on the $q = 0$ state. Next year, we plan to investigate the influence of ferromagnetic J_2 on magnon dispersion. Since the number of clusters increases significantly with the introduction of second-neighbor interactions, more computational resources are required.

[1] S. Ito *et al.*, Nat. Commun. 8, 235, 2017.
[2] T. Ono *et al.*, JPSJ 83, 043701, 2014.
[3] M. Saito *et al.*, PRB 105, 064424, 2022.
[4] W. Zheng *et al.*, PRB 74, 224420, 2006.
[5] S. Kogure *et al.*, JPSJ 92, 113703, 2023.
[6] M. P. Gelfand *et al.*, JSP 59, 1093, 1990.

Ground-State Phase Diagram of an Anisotropic $S=3/2$ Chain: Triatic TLL and Nematic TLL Phases

Takashi Tonegawa

Kobe Univ., Osaka Metropolitan Univ., and Univ. of Hyogo

The purpose of this report is to explore the ground-state phase diagram of an anisotropic $S=3/2$ chain system by using mainly numerical methods. We express the Hamiltonian which describes this system as

$$\mathcal{H} = \sum_{j=1}^{N} \left\{ S_j^x S_{j+1}^x + S_j^y S_{j+1}^y + \Delta S_j^z S_{j+1}^z + D\left(S_j^z\right)^2 \right\}, \tag{1}$$

where S_j^α ($\alpha = x$, y, z) is the α-component of the $S = 3/2$ operator at the j-th site; Δ and D are, respectively, the XXZ-type anisotropy parameter of the nearest-neighbor interactions and the on-site anisotropy parameter; N, being assumed to be even, is the total number of spins in the system. Hereafter, we denote the z-component of the total spin by $M\left(=\sum_{j=1}^{N} S_j^z\right)$, where $M=0$, ±1, ±2, $\cdots$, $\pm 2N/3$.

In this report we numerically determine the ground-state phase diagram as accurately as possible. Estimating the phase boundary lines, we analyze the energy eigenvalues of the Hamiltonian $\mathcal{H}$, which are calculated by the use of the exact-diagonalization (ED) method. The resultant phase diagram is shown in Fig. 1. In spite of the present simple system, this phase diagram is rather rich and consists of five kinds of phases; these are the triatic Tomonaga-Luttinger liquid (tTLL), nematic Tomonaga-Luttinger liquid (nTLL), $XY1$ (XY1), Néel (N), and ferromagnetic (F) phases.

Let us now discuss how to numerically determine the phase boundary lines shown in Fig. 1. We denote, respectively, by $E_0(N,M)$ and $E_1(N,M)$, the lowest and second-lowest energy eigenvalues of the Hamiltonian $\mathcal{H}$ under the periodic boundary condition ($S_{N+1}^\alpha \equiv S_1^\alpha$) within the subspace of N and M. We have numerically calculated these energies for finite-size systems with up to $N=14$ spins by using the ED method. The ground-state energy of the finite-N system is given by $E_0(N,3N/2)$ in the F region and by $E_0(N,0)$ in the other regions. We introduce here the following energy differences,

$$\Delta_{00}(N) = E_1(N,0) - E_0(N,0)\,, \tag{2}$$

$$\Delta_{10}(N) = E_0(N,1) - E_0(N,0)\,, \tag{3}$$

$$\Delta_{20}(N) = E_0(N,2) - E_0(N,0)\,, \tag{4}$$

$$\Delta_{30}(N) = E_0(N,3) - E_0(N,0)\,. \tag{5}$$

In the following way, we estimate the finite-size critical values of Δ (or D) for various values of D (or Δ) for each phase transition. Then, the phase boundary line for the transition is obtained by connecting the results for the $N\to\infty$ extrapolation of the finite-size critical values.

The tTLL state is the TLL state which accompanies the three-magnon bound state, while in the $XY1$ state no magnon bound state accompanies. These lead to the following fact. In the ground-state magnetization curve for a given finite-size system, the magnetization increases stepwisely with increasing the magnitude of the external magnetic field applied along the z-axis; the first step occurs from the $M=0$ to the $M=3$ state in the tTLL phase, while it occurs from the $M=0$ to the $M=1$ state in the $XY1$ phase. From these arguments, it is easy to see that the finite-size critical values for the phase transition between the tTLL and $XY1$ phases are calculated by solving

$$\Delta_{30}(N)/3 = \Delta_{10}(N)\,. \tag{6}$$

numerically. Similarly, the nTLL state accompanies the two-magnon bound state, and in this state the first step in the ground-state magnetization curve for a finite-size system occurs from the $M=0$ to the $M=2$ state. Therefore, the finite-size critical values for the phase transition between the nTLL and $XY1$ phases can be estimated from

$$\Delta_{20}(N)/2 = \Delta_{10}(N)\,. \tag{7}$$

The above arguments imply that the equation from which the finite-size critical values for the phase transition between the tTLL and nTLL phases is given by

$$\Delta_{30}(N)/3 = \Delta_{20}(N)/2\,. \tag{8}$$

The tTLL-Néel, nTLL-Néel', and $XY1$-Néel' phase transitions are of the Berezinskii-Kosterlitz-Thouless type [1] with accompanying the spontaneous translational-symmetry breaking. Therefore, the phase boundary lines can be accurately estimated by the level spectroscopy method developed by Okamoto and Nomura [2]. Considering

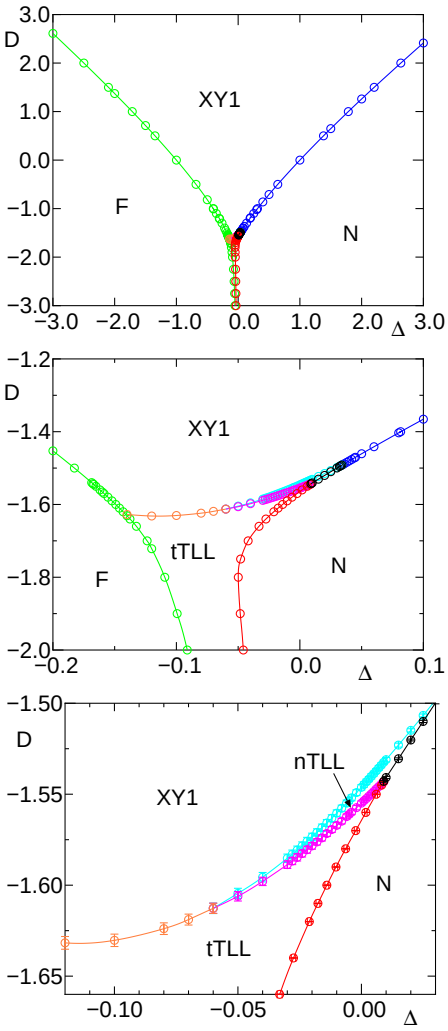

Figure 1: Ground-state phase diagram on the Δ versus D plane obtained in the present work. The topmost figure is the whole view, and the middle and bottom figures are, respectively, the enlarged views near the tTLL and nTLL regions.

the above discussions related to the magnon bound states, we can obtain the equations from which the finite-size critical values for these three phase transitions; they are, respectively,

$$\Delta_{30}(N)/3 = \Delta_{00}(N)\,, \tag{9}$$
$$\Delta_{20}(N)/2 = \Delta_{00}(N)\,, \tag{10}$$
$$\Delta_{10}(N) = \Delta_{00}(N)\,. \tag{11}$$

It is apparent that the finite-size critical values for the phase transition between the F and $XY1$ phases and that between the F and tTLL phases, both of which are of the first order, are calculated from

$$E_0(N, 3N/2) = E_0(N, 0)\,. \tag{12}$$

Finally we discuss the binding energy, $E_{3\mathrm{mbe}}(N)$,

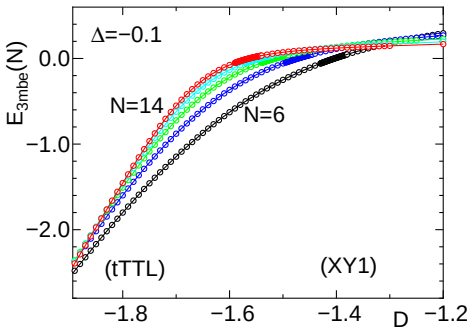

Figure 2: Dependence $E_{3\mathrm{mbe}}(N)$ ($N=6$, 8, 10, 12, 14) on D for $\Delta=-0.1$.

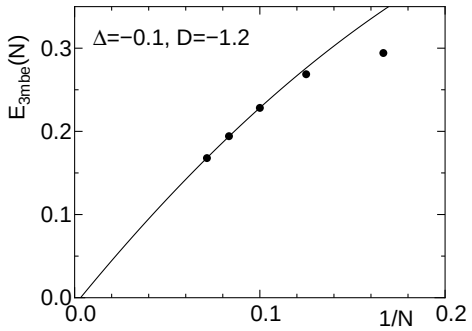

Figure 3: Dependence $E_{3\mathrm{mbe}}(N)$ on $1/N$ for $\Delta=-0.1$ and $D=-1.2$. The solid line represents the fitting to a quadratic function of $1/N$, where the data for $N=10$, 12, 14 are used.

of three magnons give by

$$E_{3\mathrm{mbe}}(N) = \Delta_{30}(N) - 3\Delta_{10}(N)\,. \tag{13}$$

It should be noted that this equation is closely related to Eq. (6). Figure 2 shows the dependence of $E_{3\mathrm{mbe}}(N)$ on D for $\Delta=-0.1$ in the region including the critical value of the tTLL-$XY1$ transition point, $D=D_c=-1.630\pm0.003$. We see from this figure that in the tTLL region ($D<D_c$), the values of $E_{3\mathrm{mbe}}(N)$ are negatively finite for finite N's as well as for the $N\to\infty$ limit, while in the $XY1$ region ($D>D_c$), they are positively finite for finite N's and vanish for the $N\to\infty$ limit (see Fig. 3). These results are consistent with the well-known fact that the transverse two-spin correlation function $\langle {S_1}^+ S^-_{1+j}\rangle$ decays exponentially and algebraically in the tTLL and $XY1$ states, respectively.

Invaluable discussions with T. Hikihara, K. Okamoto, and T. Sakai are gratefully acknowledged.

[1] Z. L. Berezinskii, Sov. Phys. JETP **34**, 610 (1971); J. M. Kosterlitz and D. J. Thouless, J. Phys. C **6**, 1181 (1973).
[2] K. Okamoto and K. Nomura, Phys. Lett. A **169**, 433 (1992).

Finite-size scaling analysis with bond-weighted tensor renormalization group

Satoshi MORITA
Graduate School of Science and Technology, Keio University
Yokohama, Kanagawa 223-8522

Tensor network (TN) methods are attracting much attention as powerful tools in various fields including quantum many-body physics, quantum computation, and machine learning. In the classical statistical physics, the state sum in the partition function can be represented in the form of TN. However, the contraction of a large TN still requires an exponentially large computational effort. One of solutions to this problem is the real-space renormalization group. The tensor renormalization group (TRG) method and its variants calculate a coarse-grained tensor by information compression using the singular value decomposition [1, 2]. Since one step of renormalization doubles the system size, these methods can calculate the partition function approximately in logarithmic time for the system size. Recently, Adachi, et al. have proposed the bond-weighted TRG (BWTRG) method, which improves the accuracy of TRG by introducing a bond weight and distributing it appropriately [3].

Recently, we have proposed an algorithm to calculate higher-order moments of physical quantities based on the higher-order TRG (HOTRG) [4]. We introduce an impurity tensor which represents a physical quantity. With the appropriate update rule, a coarse-grained impurity tensor containing multiple impurities can be generated to calculate the higher-order moments of the physical quantity. We have succeeded to estimate the critical exponents and the critical temperature based on the finite-size scaling analysis of the squared magnetization and distinguish the weakly first-order and continuous phase transitions in the Potts model.

In this study, we generalize this impurity method to BWTRG. Unlike HOTRG, BWTRG involves tensor decomposition, making it difficult to construct consistent update rules for the impurity tensor. Therefore, we propose to place an impurity at a bond rather than a site, and successfully derive the update rule for the impurity matrix on a bond. BWTRG can smoothly improve accuracy from TRG by tuning the hyperparameter, Our impurity method also holds this property. We investigate how the accuracy of the finite-size scaling analysis depends on this hyperparameter. We find that the accuracy of the critical point decays with the power of the bond dimension and its exponent smoothly changes with the hyperparameter. The error decays most quickly at the value of the hyperparameter expected to be optimal in BWTRG.

References

[1] M. Levin and C. P. Nave, Phys. Rev. Lett. **99**, 120601 (2007).

[2] Z. Y. Xie, J. Chen, M. P. Qin, J. W. Zhu, L. P. Yang, and T. Xiang, Phys. Rev. B **86**, 1 (2012).

[3] D. Adachi, T. Okubo, and S. Todo, Phys. Rev. B **105**, L060402 (2022).

[4] S. Morita and N. Kawashima, Comput. Phys. Commun. **236**, 65 (2019).

Structure analysis of Sb/Bi heterostructure on Si(111) by Total-Reflect High-Energy Positron Diffraction with 2DMAT

D. Iwasawa, H. Abe, T. Takeda, M. Shoji,

I. Mochizuki[A], K. Wada[A], T. Hyodo[A] and A. Takayama

Department of Physics, Waseda University, Ohkubo, Shinjuku-ku, Tokyo 169-8555

[A]IMSS, KEK, Oho, Tsukuba, Ibaraki 305-0801

Introduction

Since the experimental demonstration of topological insulators, they have actively been investigated due to their intriguing fundamental properties and potential applications in spintronics devices and quantum computations. Recently a lot of studies focusing on topological phase transitions have been performed in various materials, and topological phase transitions by epitaxial strain at the interface are very useful from the viewpoint of applications because they do not require any external field environment and are compatible with surface sensitive experimental technique.

Group-V semimetal bismuth (Bi) and antimony (Sb) turn from being topologically trivial to nontrivial by slight lattice strain. For Bi, the phase transition to a topological semimetal induced by 0.4%–1% lattice strain has theoretically been predicted [1]. Various theoretical predictions have also been reported for ultrathin Sb films. For instance, freestanding Sb(111) films with less than 4 BL have been reported to be topologically trivial, however several calculations predicted that the topological phase transition can be induced by tuning structural parameters [2]. To observe and discuss the details of the topological phase transition in Sb ultrathin films experimentally, it is necessary to fabricate Sb thin films on substrates with a larger lattice constant and to analysis and determine the atomic structure.

In this work, we have performed structure analysis of ultrathin Sb films on Bi(111) using by total-reflect high-energy positron diffraction (TRHEPD). A structural analysis of Bi was carried out first, followed by a stacked Sb structure. The TRHEPD experiment consists of measuring a series of the diffraction patterns for a fixed incident azimuthal direction at various glancing angles θ. Here, the rocking curve is defined as the diffraction intensity of the (00) spot plotted as a function of θ. In the structural analysis, the experimental rocking curves are compared with those calculated for various structural models. For analysis, calculations of the rocking curves for TRHEPD were performed by the structure-analysis program 2DMAT [3].

Results and discussion

Figure 1(a) shows the rocking curves of Bi(111) thin film for 10BL measured under the many-beam (MB) condition. In the MB condition, the beam is incident along a symmetric direction, thus the rocking curve in the MB condition essentially gives the information on the atomic positions in the in-plane and out-of-plane direction. Here, we considered a structural model with the Bi interlayer distance and the in-plane lattice constant as parameters. The results of the analysis showed that the structure shown in Fig. 1(b) reproduced the experimental results best; the in-plane lattice constant is 4.38 Å, and the

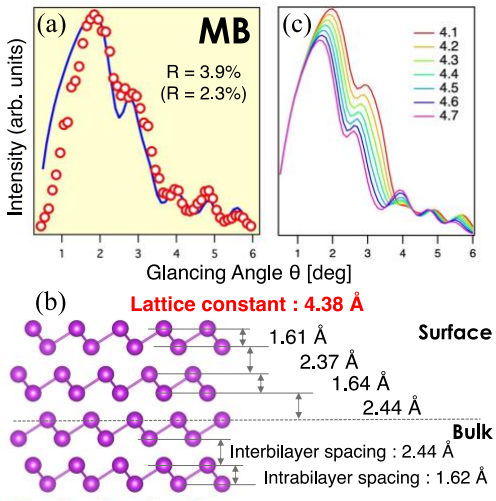

Fig. 1: Experimental measured rocking curves under MB condition for Bi thin films (10 BL) with calculated curves with the structure model in (b). (c) Dependence of the rocking curve on the in-plane lattice constant.

layer distances correspond well with the results of previous studies. We also calculated rocking curves under the OB condition with several in-plane lattice constant [Fig. 1(c)]. One sees the shape of the rocking curve changed significantly in response to the value of the in-plane lattice constant, and we found the experimental results are not reproduced by the lattice constant of bulk Bi (4.54 Å). This result suggest that the Bi is a topologically non-trivial.

Next we have performed structure analysis of ultrathin Sb films (2 BL) on Bi(111). By electron diffraction, we have confirmed that Sb thin film grows on Bi with different lattice constant. However, no moiré pattern was observed in electron diffraction, so it is not possible to construct a structural model assuming a long-period structure. Therefore we have performed TRHEPD measurement under the one-beam (OB) condition. In the OB condition the beam

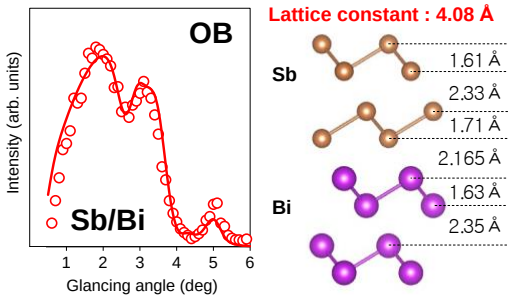

Fig. 2: (Left) Experimental measured rocking curves under OB condition and (right) determined structure model for Sb/Bi heterostructure.

is incident along an off-symmetric direction. The Rocking curve in the OB condition essentially gives the information on the atomic positions in the out-of-plane direction and atomic density in layer. In this analysis, the lattice constant of Sb relative to Bi 1 BL was estimated by calculating the density of Sb. Figure 2 shows the rocking curves of Sb/Bi heterostructure measured by TRHEPD and determined structure model. As a result of the analysis, the in-plane lattice constant of Sb thin films on Bi was estimated to be 4.08 Å. This value corresponds with that estimated from electron diffraction. For more detailed structure determination, a heterostructure model will be constructed from this estimate in the future, and the structure will be analyzed in a giant lattice system.

References

[1] T. Hirahara, *et al.*, Phys. Rev. Lett. **109** (2012) 227401.

[2] Z.-Q. Huang, *et al.*, New J. Phys. **16** (2014) 105018.

[3] Y. Motoyama, *et al.*, Computer Physics Communications, **280** (2022) 108465.

Theoretical proposals of novel superconducting phenomena in strongly correlated systems with multi-degrees of freedom

Shuntaro SUMITA
Department of Basic Science, The University of Tokyo, Meguro, Tokyo 153-8902

We have studied an interplay between incommensurate magnetism and superconductivity. The target material is CrAs, in which an incommensurate helimagnetic state is realized at ambient pressure, whereas the magnetic order is suppressed and superconducting phase transition occurs by applying pressure [1]. We performed the first-principles calculations for the paramagnetic state of CrAs by using the Quantum ESPRESSO [2, 3], and found that some of the Fermi surfaces are located near the R–S line, which is the Brillouin zone boundary (π, π, k_z) for the space group $Pnma$ of CrAs. Since an electronic state on this line behaves as an anomalous pseudospin that does not couple to a Zeeman field because of the nonsymmorphic symmetry [4], we expect that the property induces novel features for both magnetism and superconductivity.

We designed an effective tight-binding model reproducing the Fermi surfaces around the R–S line, and introduced Hubbard and exchange interactions. We are now analyzing the Ginzburg–Landau theory construct from the microscopic model to understand the interplay between magnetism and superconductivity. The detailed results will be presented in the future [5].

As another project, furthermore, we have studied spin parity effects in an one-dimensional antiferromagnetic chain with an easy-plane anisotropy under a transverse magnetic field. To understand the ground-state property, we performed numerical exact diagonalization for $S = 1/2, 1, ..., 5/2$, using the QuSpin package [6]. Also, we obtained entanglement spectra of the ground state by the density matrix renormalization group analyses using `ITensors.jl` [7]. We discovered that spin parity effects clearly appear as finite-size effects in the magnetization curve when the anisotropy is sufficiently large [8].

References

[1] W. Wu *et al.*, Nat. Commun. **5**, 5508 (2014).

[2] P. Giannozzi *et al.*, J. Phys. Condens. Matter **21**, 395502 (2009).

[3] P. Giannozzi *et al.*, J. Phys. Condens. Matter **29**, 465901 (2017).

[4] Y. Yu *et al.*, arXiv:2310.00838.

[5] S. Sumita and D. F. Agterberg, in preparation.

[6] P. Weinberg and M. Bukov, SciPost Phys. **2**, 003 (2017); *ibid.* **7**, 020 (2017).

[7] M. Fishman *et al.*, SciPost Phys. Codebases 4 (2022); *ibid.* 4-r0.3 (2022).

[8] S. Sumita, A. Tanaka, and Y. Kato, arXiv: 2402.19311.

Tensor-network-based finite-size scaling of critical phenomena

Atsushi Ueda, Haruki Shimizu, and Masaki Oshikawa

Institute for Solid State Physics,

The University of Tokyo, Kashiwa-no-ha, Kashiwa, Chiba 277-8581

We have investigated critical phenomena in one-dimensional quantum and two-dimensional classical systems utilizing the tensor-network-based approaches. Extending our previous finite-size scaling studies of the energy spectrum under periodic boundary conditions, we have clarified the effects of the finite bond dimensions in the tensor-network renormalization calculations [1]. The finite bond dimensions induce a finite correlation length; finite-size scaling analyses using the systems smaller than the correlation length give extremely accurate results.

In order to extend our success to boundary critical phenomena, we have developed conformal perturbation theory of finite-size energy spectrum for open boundary conditions [2]. A systematic understanding for open boundary conditions has previously been missing, primarily due to the complexity introduced by both bulk and boundary perturbations. We observed that the optimal system size to be used for finite-size scaling is not always simply given by the number of lattice sites, because of the boundary perturbations. This subtlety has been largely ignored in prior studies, allowing us to provide new insights into accurate finite-size scaling analyses. Large-scale DMRG simulations, performed on the ISSP supercomputer, were indispensable for verifying our theory.

Furthermore, these simulations enabled us to propose an efficient method for computing universal properties on unorientable manifolds [3]. While extending this approach to higher dimensions is not straightforward—due to the increased computational costs associated with contracting higher-dimensional tensors—the use of the ISSP supercomputer has facilitated efficient parallelization of these processes. Consequently, we have been able to explore new physical phenomena in two-dimensional systems, such as anyonic chiral spin liquids [4] and three-dimensional criticality [5], which have previously posed significant challenges.

References

[1] A. Ueda and M. Oshikawa, Phys. Rev. B **108**, 024413 (2023).

[2] Y. Liu, H. Shimizu, A. Ueda, and M. Oshikawa, e-print arXiv:2405.06891 (2024).

[3] H. Shimizu and A. Ueda, e-print arXiv:2402.15507 (2024).

[4] K. Ohmori, A. Ueda, and K. Inamura in preparation.

[5] A. Ueda and S. Akiyama in preparation.

Second harmonic generation induced by dynamics of pinned superconducting vortex

Yusuke MASAKI
Department of Applied Physics, Tohoku University
Sendai, Miyagi 980-8579

Recently, Nakamura *et al.* reported the giant second harmonic generation (SHG) from thin film superconductors in which transport current was applied [1]. The mechanism of the SHG has been attributed to the pinned vortex dynamics driven by the THz irradiation.

This year, we focused on the numerical simulation of the time-dependent Ginzburg–Landau equation coupled with the Maxwell equations to study the photo-driven dynamics of the superconducting vortex. Our setup includes a single vortex pinned in the center of the system. The external electric field has the gaussian form with the central frequency (driving frequency) $\omega_{\rm ext}$.

Our main results are as follows. Figure 1(a) shows the Fourier spectra of the total current induced by the external field. The orange (blue) curve labeled "$B_j = 0.05$" ("$B_j = 0.0$") is the one in the presence (absence) of the transport current, while the black dashed curve is the Fourier spectrum of the input electric field. We confirmed that application of the transport current enhances not only the SH component but also the third harmonic component. Figure 1(b) shows the $\omega_{\rm ext}$-dependence of the SH intensity. This calculation requires many-core systems. The SH intensity has a noticeable peak at around $\omega_{\rm ext} = 0.1$. We have clarifid that this peak is realized when both of the pinned vortex and the transport current exist. Corresponding peak structures appear also in the Fourier spectra of time evolution of the center of mass coordinate for the vortex. Therefore we attribute this resonant SH component to the dynamics of the pinned vortex under the transport current.

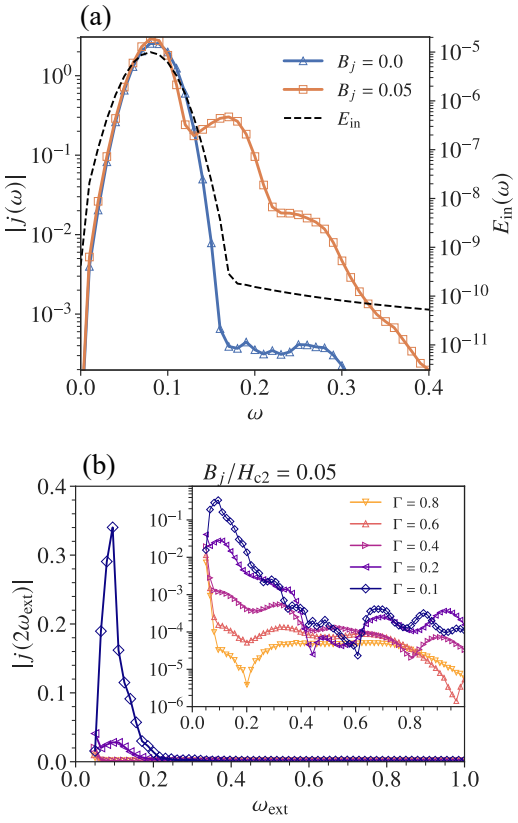

Figure 1: (a) Fourier spectra of the currents and the external field. (b) $\omega_{\rm ext}$-dependence of the SH component of the current.

References

[1] S. Nakamura *et al.*: Phys. Rev. Lett. **125**, 097004 (2020).

Equilibration and glass transition in self-propelled hard polygon systems

Masaharu ISOBE
Nagoya Institute of Technology
Gokiso-cho, Showa-ku, Nagoya, 466-8555

As the simplest models, the hard disk/sphere systems have been extensively investigated through molecular simulation for both equilibrium and non-equilibrium phenomena [1]. In this project, we focus on the equilibration and non-equilibrium phase transitions in the self-propelled hard polygon model system using modern algorithms, *i.e.*, Event-Chain Monte Carlo (ECMC) [2, 3], Newtonian Event-Chain Monte Carlo (NECMC) [4], and Event-Driven Molecular Dynamics (EDMD) [5].

Simple and efficient methods for local structural analysis in polydisperse hard disk systems

Quantifying the nearest (and higher-order) neighbors and local free volumes of particles in nonequilibrium statistical physics systems is crucial for elucidating the origins of macroscopic collective phenomena, such as glass/granular jamming transitions and various behaviors of active matter. However, conventional techniques, such as those based on a fixed-distance cutoff or the Voronoi construction, have primarily been applied to equilibrated, homogeneous, and monodisperse particle systems. In this study, we implement simple and efficient methods for local structure analysis in nonequilibrium, inhomogeneous, and polydisperse hard disk systems. We introduce an efficient and non-reciprocal method for detecting neighbors, namely, 2D SANNex, and a simple, efficient, and precise method for categorizing neighbors to enclose the local free area (NELF-A) in dense polydisperse hard disk systems [6]. We also demonstrate how these novel methods can overcome the difficulties encountered by conventional techniques and present some applications.

As an application of NELF-A, we propose an alternative method to obtain the inherent structure, which avoids the use of short-time averaged coarse-graining trajectories. The summary of the algorithm is as follows:

1. The displacement vectors from a particle position to the geometric center of the Free Volume (FV) estimated by NELF-A for each particle are drawn.
2. The positions in the entire system are updated with the displacement vectors multiplied by a scaling parameter less than unity.
3. Repeat step 2 until the positions converge toward an inherent structure.

In an equilibrium state, the positions eventually converge after the above procedure, and the isotropic shape of FV located on a triangular lattice can be observed, indicative of the inherent structure. Even in a typical non-equimolar binary mixture hard disk system, the probability density distribution obtained by the described procedure is fairly consistent with that obtained by the conventional method based on short-time averaged coarse-graining trajectories. We also confirmed the accuracy of this method by estimating pressure based on FV and comparing it with other conventional methods [7].

Phase transition in dense hard triangle systems by Newtonian Event-Chain Monte Carlo

In this study, we investigate the phase transition of hard triangle systems by increasing the packing fraction (density) through the application of two novel algorithms: (i) Newtonian Event-Chain Monte Carlo, recognized for its efficiency in translational diffusion in hard sphere systems, and (ii) XenoSweep [8], which is efficient for contact detection between rigid objects. These algorithms facilitate the equilibration of hard triangle particle systems, which have notably different shapes from hard disks. To characterize the phase transition, we focus on the diffusional characteristics and novel orientational order parameters for the hard triangle particle system, as proposed in our current study [9].

Crystallization and Motility-Induced Phase Separation in the Flow of Active Brownian Particles Around an Obstacle

In fluid dynamics, the flow around an obstacle is a classic area of study, where phenomena such as vortex formation and turbulence instability occur with the increase in the control parameter, namely, the Reynolds number. A well-known example of this is the Kármán vortex street. Previously, this phenomenon has been thoroughly investigated through numerical methods, including both direct numerical simulation (DNS) based on the macroscopic Navier-Stokes equations and molecular dynamics simulation using classical microscopic equations of motion. We focus on the phase changes of the flow composed of massive Active Brownian Particles (ABP) with the Weeks-Chandler-Andersen (WCA) repulsive force around a fixed obstacle, analyzed through large-scale molecular dynamics simulation (*HOOMD-blue v4*). We observed nontrivial flow instabilities leading to the formation of vortices, turbulence, and notably, crystallization, influenced by both the Reynolds number and the magnitude of self-propulsion velocity. Unlike the WCA system, the ABP system demonstrated crystallization through two distinct mechanisms: (i) collision-induced crystallization with the cylinder, leading to pressure-induced crystallization, and (ii) crystallization triggered by motility-induced phase separation (MIPS). In both cases, it was observed that the number density within the crystalline clusters exceeded the Alder transition point of equilibrium systems. These findings suggest that crystallization in the non-equilibrium ABP flow around a cylinder might occur through mechanisms akin to those in equilibrium systems. The roles of self-propulsion magnitude and rotational diffusion coefficient in the crystallization mechanism are summarized [10].

References

[1] M. Isobe: Mol. Sim. **42** (2016) 1317.

[2] E. P. Bernard, W. Krauth, and D. B. Wilson: Phys. Rev. E **80** (2009) 056704.

[3] W. Krauth: Front. Phys. **9** (2021) 229.

[4] M. Klement and M. Engel: J. Chem. Phys. **150** (2019) 174108.

[5] M. Isobe: Int. J. Mod. Phys. C **10** (1999) 1281.

[6] D. Mugita, K. Souno, H. Koyama, T. Nakamura, and M. Isobe: J. Chem. Phys. (2024) *in press.*

[7] D. Mugita, K. Souno, and M. Isobe: *in preparation*

[8] M. Klement, S. Lee, J. A. Anderson and M. Engel: J. Chem. Theor. Comp. **17** (2021) 4686.

[9] T. Shirai, D. Mugita, and M. Isobe: Proceedings of the 29th Symposium on Traffic Flow and Self-driven Particles, **29** (2024) 49. (in Japanese)

[10] K. Iwase and M. Isobe: *in preparation.*

Numerical Study of One Dimensional Frustrated Quantum Spin Systems

Kazuo HIDA
Professor Emeritus, Division of Material Science,
Graduate School of Science and Engineering,
Saitama University, Saitama, Saitama 338-8570

1 Model

We investigate the ground-state phases of mixed diamond chains described by the following Hamiltonian:[1]

$$\mathcal{H} = \sum_{l=1}^{L} \Big[(1+\delta)\boldsymbol{S}_l(\boldsymbol{\tau}_l^{(1)} + \boldsymbol{\tau}_{l-1}^{(1)}) + (1-\delta)\boldsymbol{S}_l(\boldsymbol{\tau}_l^{(2)} + \boldsymbol{\tau}_{l-1}^{(2)}) + \lambda \boldsymbol{\tau}_l^{(1)}\boldsymbol{\tau}_l^{(2)} \Big], \quad (1)$$

where $\boldsymbol{S}_l, \boldsymbol{\tau}_l^{(1)}$ and $\boldsymbol{\tau}_l^{(2)}$ are spin operators with magnitudes $S_l = \tau_l^{(1)} = 1/2$ and $\tau_l^{(2)} = 1$, respectively. The number of unit cells is denoted by L. The lattice structure is depicted in Fig. 1. We consider the region $\lambda \geq 0$ and $1 \geq \delta \geq -1$.

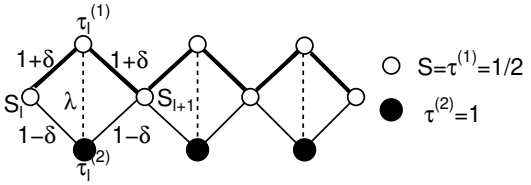

Figure 1: Structure of the diamond chain investigated in this work.

2 Numerical Results

We have carried out the numerical exact diagonalization (NED) calculation for $L = 4, 6$ and 8 and the DMRG calculation for $L = 48$. The spontaneous magnetization $m_{\rm sp}$ in each phase is calculated to obtain the ground-state phase diagram of Fig. 2.

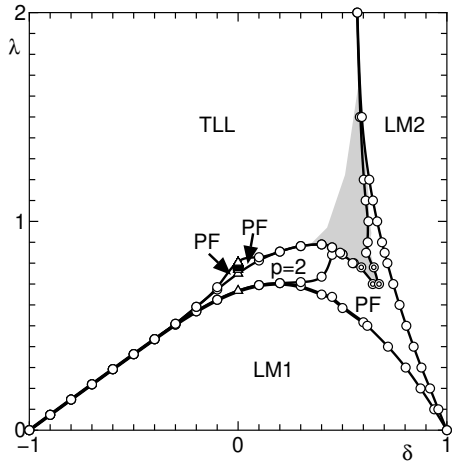

Figure 2: Ground-state phase diagram. The open circles are the phase boundaries estimated from the NED data extrapolated to the thermodynamic limit from $L = 4, 6$ and 8 by the Shanks transform. The double circles are the phase boundaries estimated from the DMRG data for $L = 48$. The triangles at $\delta = 0$ are the phase boundaries between the infinite series of QF phases determined in Ref. [5]. The deviation from the scaling relation $\Delta E \sim 1/L$ for $L = 18$ and 24 is significant in the shaded area. The curves are guides for the eye.

Two Lieb-Mattis-type quantized ferrimagnetic (QF) phases (LM1, LM2) with $m_{\rm sp} = 1$ are separated by the partial ferrimagnetic (PF) phase and nonmagnetic phase as shown in Fig. 3 for $\lambda = 0.6$.

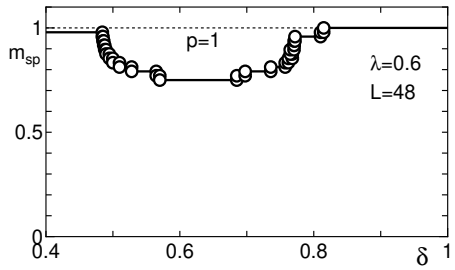

Figure 3: δ-dependence of $m_{\rm sp}$ in the ground state for $\lambda = 0.6$ calculated by the DMRG method for open chains with $L = 48$.

As for the nonmagnetic phase, the conventional Lieb-Schultz-Mattis (LSM) theorem[2] does not exclude the unique gapped phase, since the sum of the spin magnitudes in a unit cell is an integer. However, our model satisfies the condition to exclude the unique gapped phase in the recent extension of the LSM theorem to the site-reflection invariant spin chains.[3] Taking the continuity to the TLL phase in the limit $\lambda \to \infty$ and $\delta = 0$ [4] into account, the whole nonmagnetic phase is considered to be the TLL phase.

It is checked that the singlet-triplet energy gap ΔE calculated by the NED method approximately scales with the system size L as $\Delta E \sim 1/L$ as shown in Fig.4(a) for $\delta = -0.3$ and (b) for 0.3. Similar analyses are also carried out for several other values of δ. In the vicinity of the PF phase indicated by the shaded area of Fig. 2, however, the deviation from the scaling relation $\Delta E \sim 1/L$ is significant as shown in Fig. 4(c). Nevertheless, this area shrinks with the system size. Hence, it is likely that the whole nonmagnetic phase is a TLL phase.

The effect of δ on the infinite series of ferrimagnetic phases found for $\delta = 0$[5] is also investigated. It is shown that the bosonization argument supports the numerically found fragility of the ferrimagnetic phases with large spatial periodicities reported in [4].

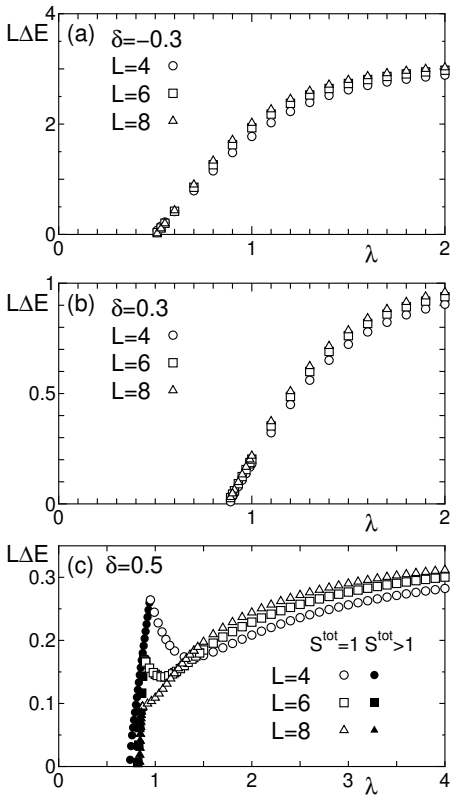

Figure 4: λ-dependence of the scaled gap $L\Delta E$ of the lowest excitations for (a) $\delta = -0.3$, (b) 0.3 and (c) 0.5 with $L = 4, 6$ and 8. The open and filled symbols are the excitations with total spin $S^{\rm tot} = 1$ and $S^{\rm tot} > 1$, respectively.

References

[1] K. Hida, J. Phys. Soc. Jpn. **93**, 044703 (2024).

[2] E. Lieb, T. Schultz, and D. Mattis, Ann. Phys. **16**, 407 (1961).

[3] Y. Ogata, Y. Tachikawa, and H. Tasaki, Commun. Math. Phys. **385**, 79 (2021).

[4] K. Hida, Activity Report 2022/Supercomputer Center, ISSP 341.

[5] K. Hida, J. Phys. Soc. Jpn. **90**, 054701 (2021).

Proposal of a quantum active particle

Manami YAMAGISHI
Department of Physics, The University of Tokyo
Kashiwa-no-ha, Kashiwa, Chiba 277-8581;
RIKEN, Hirosawa, Kashiwa, Saitama 351-0198

Naomichi HATANO
Institute of Industrial Science, The University of Tokyo
Kashiwa-no-ha, Kashiwa, Chiba 277-8581

We present a minimal model of a quantum active particle [1] as a building block of quantum active matter. Active matter is a component that takes up energy from the environment, stores it inside, converts the internal energy into kinetic energy, and thereby moves, or a collection of such components. The introduction of the idea of classical active matter enabled us to unify a variety of studies outside conventional classes of dynamics, dynamics without energy or momentum conservation, that had been investigated separately before and to understand their commonalities and universalities. Some researchers very recently tried to introduce the concept of active matter into quantum systems. Starting with a paper by Adachi *et al.* [2], the research field of quantum active matter is expanding [1, 3, 4, 5].

We propose a quantum active particle using non-unitary quantum walks in one and two spatial dimensions (1D and 2D). As a building block of quantum active matter, we start with one-particle systems, setting real-time evolution in a fully quantum range. With our quantum active particle, we have observed similarities to a classical active Brownian particle [6] and distinct quantum features at the same time. As a similarity, we observed that dynamics of our quantum active walker becomes more active in a non-trivial way when a non-Hermiticity parameter g, which corresponds to the energy take-up in classical active Brownian particles, becomes larger. As quantum features, we observed ballistic propagation of peaks (1D), particle staying on the constant energy surface (2D) and resonant transition between two energy levels (1D and 2D).

We utilized the Supercomputer at ISSP to numerically diagonalize our time-evolution operator, whose maximum size was $(70 \times 70 \times 8)^2$. By allocating arrays dynamically, we allowed our system to reach the spatial size of 70×70 (one in the x direction and the other in the y direction).

References

[1] M. Yamagishi, N. Hatano, and H. Obuse: arXiv:2305.15319 (2023).

[2] K. Adachi, K. Takasan, and K. Kawaguchi: Phys. Rev. Res. **4**, 013194 (2022).

[3] Y. Zheng and H. Löwen: arXiv:2305.16131 (2023).

[4] R. Khasseh, S. Wald, R. Moessner, C.A. Weber, and M. Heyl: arXiv:2308.01603 (2023).

[5] K. Takasan, K. Adachi, and K. Kawaguchi: arXiv:2308.04382 (2023).

[6] F. Schweitzer, W. Ebeling, and B. Tilch: Phys. Rev. Lett. **80**, 5044 (1998).

Magnetic field effect on a topological chiral order in breathing kagome antiferromagnets

Kazushi AOYAMA
Department of Earth and Space Science, Graduate School of Science, Osaka University
Machikaneyama-cho, Toyonaka-shi, Osaka 560-0043

In magnetic materials, the scalar spin chirality $\chi_{ijk} = \mathbf{S}_i \cdot (\mathbf{S}_j \times \mathbf{S}_k)$ often plays an important role. When the total chirality summed over all the elementary triangles $\chi^T = \sum_{\triangle_{ijk}} \chi_{ijk}$ is nonzero, an anomalous Hall effect of chirality origin can appear in metallic systems. Since χ_{ijk} is related to a solid angle subtended by three spins $\mathbf{S}_i$, $\mathbf{S}_j$, and $\mathbf{S}_k$, it is also relevant to topological orders where the total solid angle subtended by all the spin in the magnetic unit cell Ω takes an integer value in units of 4π. In a skyrmion crystal (SkX) state, both χ^T and $\Omega/4\pi$ take nonzero values. Previously, we theoretically demonstrated that a zero-field topological chiral order with $\chi^T \neq 0$ and $\Omega/4\pi = \pm 2$ can be realized in the following J_1-J_3 classical Heisenberg model on the breathing kagome lattice [1] :

$$\mathcal{H} = J_1 \sum_{\langle i,j \rangle_S} \mathbf{S}_i \cdot \mathbf{S}_j + J_1' \sum_{\langle i,j \rangle_L} \mathbf{S}_i \cdot \mathbf{S}_j + J_3 \sum_{\langle\langle i,j \rangle\rangle} \mathbf{S}_i \cdot \mathbf{S}_j, \quad (1)$$

where the summation $\sum_{\langle\rangle_{S(L)}}$ runs over site pairs on small (large) triangles having the nearest neighbor (NN) interaction J_1 (J_1'), and $J_3 > 0$ is the third NN antiferromagnetic interaction along the bond direction. The zero-field topological chiral order can be viewed as a miniature version of the SkX. In the work, we examine the stability of this topological chiral order against an external magnetic field H.

By performing Monte Carlo (MC) simulations for system sizes upto $L = 288$, we investigate the ordering properties of the J_1-J_3 model in a magnetic field. Here, the total number of spins N is related to L via $N = 3L^3$. In our simulations, 2×10^5 MC sweeps are carried out under the periodic boundary condition and the first half is discarded for thermalization. Our 1 MC sweep consists of 1 heatbath sweep and successive 10 overrelaxation sweeps, and observations are done at every MC sweep. The statistical average is taken over 4 independent runs starting from different random initial configurations.

It is found that the topological chiral order is relatively robust against the external magnetic field H; for $J_1'/J_1 = 0.4$ and $J_3/J_1 = 1.2$, with increasing field at $T/J_1 = 0.08$, the topological number $\langle|\Omega|\rangle/4\pi = 2$ remains unchanged until it suddenly drops down to zero at $H/J_1 \sim 2$, where $\langle\rangle$ denotes the thermal average. Interestingly, the total chirality $\langle\chi^T\rangle$ remains nonzero even in the high-field non-topological phase at $2 < H/J_1$ where $\langle|\Omega|\rangle/4\pi = 0$. A system size dependence of $\langle\chi^T\rangle$ cannot be seen for $L = 72$, 144, and 288, so that the nonzero $\langle\chi^T\rangle$ would not be due to the finite-size effect. Further analysis is going on to clarify the origin of the nonzero total chirality outside the topological phase.

References

[1] K. Aoyama and H. Kawamura, Phys. Rev. B **105**, (2022) L100407; J. Phys. Soc. Jpn. **92**, (2023) 033701.

Study on algorithms for Ising machines

Shu Tanaka

Department of Applied Physics and Physico-Informatics, Keio University

Hiyoshi, Yokohama, Kanagawa, 223-8522

In recent years, Ising machines, which are specialized computers for metaheuristics such as quantum annealing, have been vigorously developed as a highly efficient solution method for combinatorial optimization problems. Since the announcement of commercial machines by several private companies, academic institutions in Japan and abroad have been proposing Ising machines based on new concepts and new internal algorithms, and conducting research and development of Ising machines for proof-of-concept.

In this research project, we developed a new algorithm based on the knowledge of statistical mechanics to maximize the hardware performance of the Ising machine. It is expected that this research will not only provide the basic technology for the development of software for existing Ising machines, but also lead to the research and development of new Ising machines based on new concepts and new internal algorithms.

(I) Dynamical process of a bit-width reducing Ising model with simulated annealing [1]

The Ising machine has attracted attention as an efficient solver for combinatorial optimization problems, which are formulated as ground-state (minimum energy) search problems for the Ising model. Due to the limited bit width of the coefficients of the Ising machine, the Ising model must be converted to a bit width reduced (BWR) Ising model. Previous studies have shown that the bit-width reduction method, which adds auxiliary spins, theoretically makes the ground state of the BWR Ising model the same as the Ising model before bit-width reduction (the original Ising model). However, while the dynamical process is closely related to the accuracy of the solution, how the BWR Ising model progresses toward the ground state has not been elucidated. Therefore, we compared the dynamical processes of these models using Simulated Annealing (SA). The results show that there are significant differences in the dynamical processes between the models. The analysis from the viewpoint of statistical mechanics reveals that the BWR Ising model has two characteristic properties: effective temperature and slow relaxation. These properties change the temperature schedule and spin flip probability of the BWR Ising model and lead to differences in the

dynamical processes. Therefore, we have proposed SA parameters for the BWR Ising model. The proposed SA parameters are demonstrated on a square lattice Ising model. The results show that the dynamical processes of the BWR Ising model and the original Ising model are closer.

(II) Hybrid Optimization Method Using Simulated-Annealing-Based Ising Machine and Quantum Annealer [2]

Ising machines have been developed as fast and accurate solvers for combinatorial optimization problems. In this study, we investigate the performance of a hybrid optimization method that exploits the advantages of both non-quantum Ising machines and quantum annealing machines. The non-quantum Ising machine is used to improve the performance of quantum annealing. In this method, the non-quantum annealing Ising machine first solves the original Ising model multiple times as a preprocessing step. Then, the reduced sub-Ising model generated by spin-fixation is solved by the quantum annealer. The method outperforms the preprocessing SA and the quantum annealer alone in the fully coupled random Ising model.

References

[1] S. Kikuchi, N. Togawa, and S. Tanaka, IEEE Access **11**, 95493 (2023).

[2] S. Kikuchi, N. Togawa, and S. Tanaka, J. Phys. Soc. Jpn. **92**, 124002 (2023).

Relaxation process in open quantum systems

Tatsuhiko Shirai
Waseda Institute for Advanced Study, Waseda University
Nishi Waseda, Shinjuku-ku, Tokyo 169-0051

Many-body Open quantum systems have attracted much attention due to the experimental progress. Markovian dynamics, which is described by the Lindblad equations, exhibit complicated relaxation dynamics towards the steady state. The spectral gap of the Lindblad operator called the Liouvillian gap gives the asymptotic decay, but does not necessarily give a correct estimate of the relaxation time. This is due to the long timescale of the transient regime. Therefore, it is important to clarify the relaxation dynamics in the transient regime.

Here we study the relaxation dynamics of the steady-state autocorrelation function in a bulk-dissipated quantum system. To investigate a transient regime, we introduce an instantaneous decay rate $\kappa_A(t)$ that gives a rigorous upper bound of the autocorrelation function $C_A(t)$ as

$$|C_A(t)| \leq \exp\left(-\int_0^t \kappa_A(\tau)d\tau\right)|C_A(0)|, \quad (1)$$

where A is an operator. The instantaneous decay rate is defined by the symmetrized Liouvillian [1], which symmetrizes the Lindblad operator with respect to a steady-state inner product. We have used openMPI to calculate $C_A(t)$ and $\kappa_A(t)$. Figure 1 (Upper) shows the relaxation dynamics of the autocorrelation function. The decay rate in the transient regime is different from the Liouvillian gap. Figure 1 (Bottom) shows the dynamics of the instantaneous decay rate. The instantaneous decay rate in the transient regime is almost constant, which describes the decay rate of the autocorrelation function in the transient regime. We interpret the decay rate in the transient regime from the operator spreading due to the unitary time evolution [2].

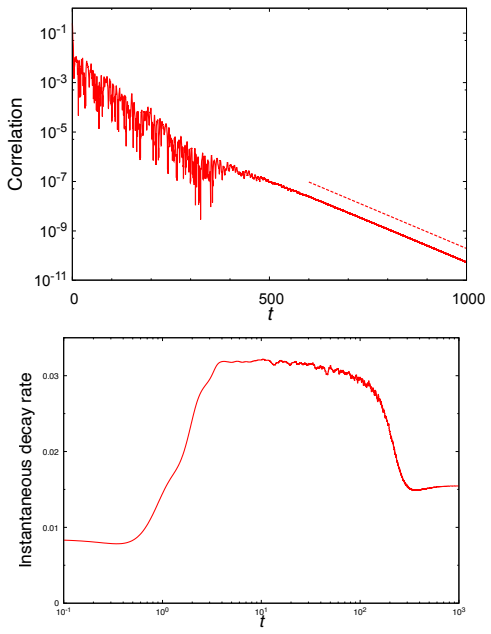

Figure 1: (Upper) Dynamics of the autocorrelation function. The dotted line indicate the decay at the rate of the Liouviilan gap (Bottom) Dynamics of the instantaneous decay rate.

References

[1] T. Mori and T. Shirai, Phys. Rev. Lett. **130**, 230404 (2023).

[2] T. Shirai and T. Mori, arXiv:2309.03485.

Analysis of Ising model in statistical-mechanical informatics

Yuya SEKI

Graduate School of Science and Technology, Keio University, Kanagawa 223-8522

We have studied properties of factorization machine with annealing (FMA) [1], which is an optimization method based on the simulated/quantum annealing method cooperated with factorization machine (FM), a machine learning model whose model equation is in the quadratic form. FMA is mainly used for discrete black-box optimization problems including integer-variable optimization problems [2]. Since a Hamiltonian is not given analytically in black-box optimization problems, we need to estimate the Hamiltonian whose ground state can be obtained by the simulated/quantum annealing method. In FMA, the Hamiltonian is estimated with training of FM. Since the model equation of FM is in the quadratic form, which is equivalent to the Ising model, the simulated/quantum annealing method can be applied to find its ground state.

This year we focused on interaction graph structure of FM and, we found that FMA with a restricted interaction graph works for certain range of optimization problems via parallel computing on the supercomputer. Since some actual annealing machines including D-Wave machines have limited structure of interaction between spins, Hamiltonian estimated by FM cannot be dealt with actual annealing machines directly. Minor embedding is commonly used to solve the problem. However, the minor embedding method requires ancilla spins to represent fully connected Ising model with a model with sparse interactions used in actual devices. The overhead of ancilla spins is problematic especially for large size systems, because the number of required spins increase quadratically with the number of spins in the original model. To overcome this problem, we proposed FMA with a restricted interaction graph structure. In our method, the interaction graph structure is constructed from the interaction structure of actual annealing devices. Since the interaction graph structures of FM and actual devices are same, no ancilla spins are necessary. We performed parallel computing with various problem instances and parameters in the proposed method. As a result, we found that our method can minimize the Hamiltonian which is generated with an assumption that the model has a sparse interaction whose degree is independent of the system size.

References

[1] K. Kitai *et al.*: Phys. Rev. Research **2** (2020) 013319.

[2] Y. Seki *et al.*: arXiv:2209.01016 (2022).

Molecular Dynamics of Stretched Polymer Chains

Koichi MAYUMI, Kosuke AOMURA

Institute for Solid State Physics,

The University of Tokyo, Kashiwa-no-ha, Kashiwa, Chiba 277-8581

The segmental dynamics of polymer chains is the molecular origin of the entropic elasticity of polymeric materials [1]. When polymer chains are stretched, the molecular dynamics of polymer chains is restricted, and chain tension is increased with stretching. In this study, we have performed full-atomistic molecular dynamics simulations of stretched polymer chains in water.

A polyethylene glycol (PEG) chain consisting of 42 monomers was placed in a simulation box filled with 68,000 water molecules. The MD simulations were performed with GROMACS version 2021.1. The PEG chain was stretched at 0, 5, 10, 30, 70, 100, and 210 kJ/(mol nm). Fig.1 shows the intermediate scattering functions of PEG in the unstretched and stretched states (0 and 10 kj/(mol nm)). The segmental motion of the stretched chain becomes slow in the stretching direction (z-direction), while the chain dynamics in the directions perpendicular to stretching (x and y directions) is accelerated by stretching. This simulation result is consistent with our quasi-elastic neutron scattering results on the segmental motion of polymer chains in stretched PEG gels [1].

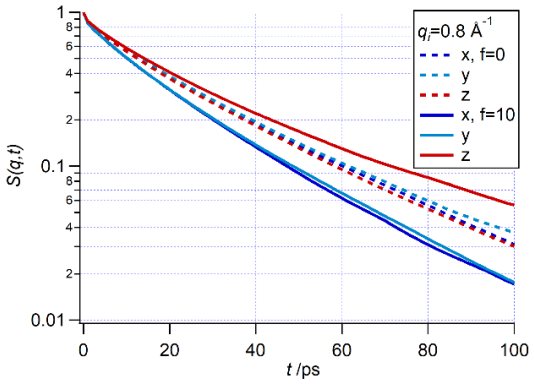

Fig. 1: Simulated intermediate scattering function of unstretched and stretched single PEG chain in water.

References

[1] M. Rubinstein, R. H. Colby, “Polymer physics”, Oxford university press (2003).

[2] K. Aomura, Y. Yasuda, T. Yamada, T. Sakai, K. Mayumi, Soft Matter, **19**, 147 (2023).

Consideration on the microscopic mechanism of the friction by the frictional force caused by magnetic structures

Hisato Komatsu
Data Science and AI Innovation Research Promotion Center, Shiga-university
Banba, Hikone, Shiga 522-8522, Japan

Microscopic mechanisms of the friction has not been understood completely, although this phenomenon itself has been known from early ages. Magnetic friction, the frictional force generated from the magnetic interaction between spin variables, has been studied to reveal this mechanism, and many types of theoretical models have been proposed[1, 2].

In the last academic year, we investigated a simplified model of the magnetic friction and consider its finite-size effect[3]. Specifically, we introduced a model composed of N Ising spin variables $\{\sigma_i\}$ interacting with each other by the following Hamiltonian:

$$H = -\frac{J(x)}{N}\sum_{i,j}\sigma_i\sigma_j = -NJ(x)m^2, \qquad (1)$$

and considered the time development of the lattice shift x under following overdamped Langevin equation:

$$\gamma N\frac{dx}{dt} = F_{\rm ex} - \frac{\partial H}{\partial x} + \sqrt{2\gamma NT}R(t). \qquad (2)$$

Here, $F_{\rm ex}$ is the external force, and we let the spin variables obey the Glauber dynamics. The coupling constant $J(x)$ is the periodic function of x. Numerical simulations using ISSP Supercomputer revealed that this system shows two different behaviors depending on the damping constant γ. When γ is small, the stick and slip states are separated as the metastable states, and the friction-velocity relation is determined by the probability that each state appears. When γ is large, on the other hand, such separation does not appear and the velocity of the magnetic body is determined by the thermal activation process. We also considered the difference of the friction-velocity relation from the Dieterich-Ruina law[4, 5], a well-known empirical law of the usual solid surfaces. However, whether such behavior is observed in the case that the magnetic body is pulled by a certain velocity was not investigated.

In this academic year, we consider the case that the magnetic body is pulled by a chain composed of n_S Voigt units, instead of the fixed external force, and investigated the relation between the frictional force and velocity of the other edge of the chain, v. The Langevin equation of x in this case is expressed as follows:

$$\begin{aligned}\gamma N\frac{dx}{dt} &= kN\left(vt + x_C - x\right) + \gamma Nv - n_S\frac{\partial H}{\partial x} \\ &\quad + \sqrt{2\gamma Nn_ST}R(t), \qquad (3)\end{aligned}$$

where k and γ mean the spring and damping constants of Voigt units, and x_C is the position of the other edge of the chain at the initial time $t = 0$. As the result of the numerical simulations using ISSP Supercomputer, the histogram of the magnetization m and the lattice shift x show that the value of m in the slip state largely changes depending on k, like Fig. 1. The effect of this difference on the friction-velocity relation should be considered in future works.

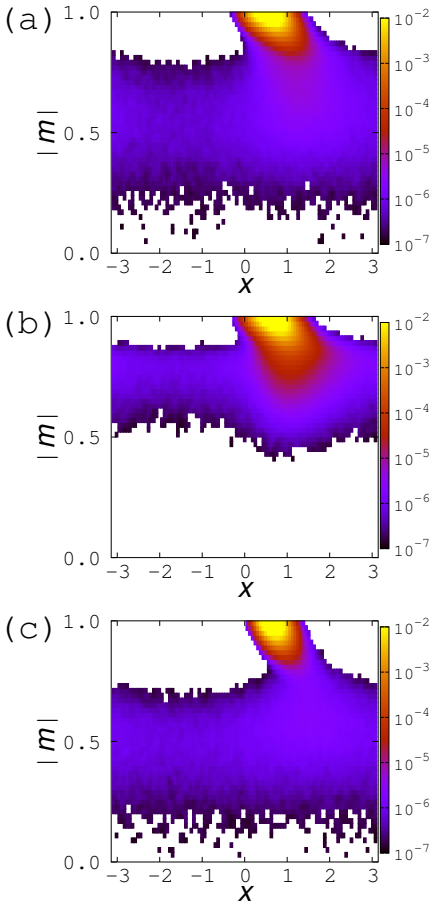

Figure 1: Examples of histograms of the magnetization m and shift of the lattice x under (a) small k and (b) large k. Graph (c) is a histogram under a fixed external force which gives the similar velocity to these two graphs.

References

[1] D. Kadau, A. Hucht, and D. E. Wolf, Phys. Rev. Lett. **101**, 137205 (2008).

[2] M. P. Magiera, L. Brendel, D. E. Wolf, and U. Nowak, Europhys. Lett. **87**, 26002 (2009).

[3] H. Komatsu, Phys. Rev. E. **108**, 034803 (2023)

[4] A. Ruina, J. Geophys. Res. **88**, 10359 (1983)

[5] J. H. Dieterich, Tectonophysics **144**, 127 (1987)

Materials informatics researches based on PHYSBO

Ryo TAMURA
International Center for Materials Nanoarchitectonics,
National Institute for Materials Science,
1-1 Namiki, Tsukuba, Ibaraki, 305-0044

PHYSBO is a Python library for fast and scalable Bayesian optimization, which was developed in "Project for advancement of software usability in materials science" by The Institute for Solid State Physics, The University of Tokyo.[**?**] Using PHYSBO, we performed some materials informatics researches. In this report, two examples are introduced.

First example is the optimization of structures of core-shell nanoparticles (CSNPs)[**?**]. To perform it, a new black-box optimization technique was developed. In this method, the structure of the CSNPs is optimized using FMQA algorithm[**?**] and their constituent materials are selected using Bayesian optimization with the optical properties of the materials as the "descriptors". Here, PHYSBO package is used to perform Bayesian optimization. Aiming for applications to i-line photolithography, we searched for CSNPs that are transparent to ultraviolet light of wavelength 355–375 nm and opaque to visible light of wavelength 400–830 nm by our proposed method. The transmittance spectra of the nanoparticles were obtained using a Mie theory calculator[**?**]. The optimized nanoparticles with the best optical properties have a multilayered structure with a radius of approximately 40 nm and an outer shell are either Mg or Pb.

Second example is a material optimization for electrocatalyst for water electrolyzers[**?**]. To perform it, we developed a new material search algorithm that accurately predicts materials properties by evolving the prediction method according to the number of data. In detail, Bayesian optimization based on PHYSBO and binary classification based on random forest classifier are combined. The random forest classification can select active materials for electrocatalyst. By our algorithm with experiments performed by human, a new material suitable for electrocatalytic materials for water electrolyzers was discovered in only one month from about 3,000 candidates. The discovered electrocatalytic material does not use any elements of platinum group and is expected to be an inexpensive electrocatalytic material to produce a large scale water electrolyzers.

References

[1] Y. Motoyama, R. Tamura, K. Yoshimi, K. Terayama, T. Ueno, and K. Tsuda, Comput. Phys. Commun. **278**, 108405 (2022).

[2] M. Urushihara, M. Karube, K. Yamaguchi, and R. Tamura, Adv. Photon. Res. **4**, 23002 (2023).

[3] K. Kitai, J. Guo, S. Ju, S. Tanaka, K. Tsuda, J. Shiomi, and R. Tamura, Phys. Rev. Res. **2**, 013319 (2020).

[4] O. Peña and U. Pal, Comput. Phys. Commun. **180**, 2348 (2009).

[5] K. Sakaushi, W. Hoisang, and R. Tamura, ACS Cent. Sci. **9**, 2216 (2023).

Theoretical study for absorption and fluorescence of firefly bioluminescence substrate analogs

Miyabi HIYAMA
Gunma University
Tenjin-cho, Kiryu, Gunma 376-8515

Firefly luciferin is a substrate for firefly bioluminescence reaction. In this year, we studied core excitation of firefly luciferin in Carbon (C) K-edge X-ray absorption spectra [1] and the free energy for the firefly luciferin analogs named "seMpai" [2] using the density functional theory (DFT) and time-dependent (TD) DFT calculations. All calculations using the computational chemistry software package, Gaussian09 [3], were performed on system B of Super Computer Center in ISSP.

C K-edge X-ray absorption spectra for firefly luciferin in aqueous solutions at pH 5, 7, and pH 10 were measured using a soft X-ray spectroscopy measurement system [1]. It was found that the C K-edge spectra for firefly luciferin have four characteristic peaks. The peak energies for pH 5 were the same as those for pH 7.

To assign these spectra, the TDDFT calculations for the core excitations of firefly luciferin anion and dianion were carried out, because the most abundant chemical species at pH 5 and 7 is knows as a firefly luciferin anion and that at pH 10 is a firefly luciferin dianion [4]. The structure of firefly luciferin dianion is deprotonated one from the hydroxy group of firefly luciferin anion.

From the assignments of C K-edge X-ray absorption spectra for firefly luciferin, it was found that the effect of deprotonation of the hydroxy group appears in the energy difference of the first and second peaks of these spectra. These results indicated that the deprotonation of the hydroxy group can be distinguished based on the soft X-ray absorption spectra.

"seMpai", is one of the firefly luciferin analogs and produces red luminescence with firefly luciferase [2]. To obtain free energies for the ground states of seMpai and its conjugate acids and bases expected to be main component in the aqueous solutions, the vibrational analysis for these chemical species were carried out. It was found that the calculations for vibrational analysis using Gaussian09 with the bases set, cc-pVTZ, were converged, but those with the larger basis set, aug-cc-pVTZ were not.

References

[1] Y. Kudo, F. Kumaki, M. Nagasaka, J-i. Adachi, Y. Noguchi, N. Koga, H. Itabashi, and M. Hiyama: J. Phys. Chem. A **128**, 611 (2024).

[2] R. Saito, T. Kuchimaru, S. Higashi, S. W. Lu,M. Kiyama, S. Iwano, R. Obata, T. Hirano, S. Kizaka-Kondoh, and S. A. Maki: Bull. Chem. Soc. Jpn. **92**, 608 (2019).

[3] Gaussian09 Revision D.01, M. J. Frisch et al.

[4] Y. Ando and H. Akiyama: J. J. App. Phys. **49**, 117002 (2010).

Application of Symbolic Regression with Alpha Zero to Find Analytical Methods in Physics

Yoshihiro MICHISHITA

Center for Emergent Matter Science (CEMS),

RIKEN, HIrosawa, Wako, Saitama 351-0198

We have studied an application of the symbolic regression with Alpha Zero[1] to find the analytical methods in physics, especially about periodically-driven systems using massive parallel computer simulations.

We proposed a framework for deriving theoretical analysis methods in physics using symbolic regression with the Alpha Zero algorithm.

In all previous studies using symbolic regression in physics, the goal was to identify the equations of unknown nonlinear dynamics, whereas in this study, the goal was to search for a basis that would facilitate theoretical analysis of the dynamics, assuming that the equations of dynamics are known.

In addition, existing studies have used genetic algorithms, Monte Carlo tree search, and regression neural networks, but Alpha Zero overcomes their weak points.

In this study [2], focusing on period-driven systems in particular, Alpha Zero "derives" the Floquet-Magnus expansion by setting "the smallness of the time dependence of the Hamiltonian after time-dependent unitary transformation" as a "measure of convenience for theoretical analysis. We have shown that Alpha Zero "derives" the Floquet-Magnus expansion. This is derived by symbolic regression, so it literally derives a table expression.

We also found that the Alpha Zero algorithm performs better than other reinforcement learning methods such as epsilon-greedy and Actor-Critic (PPO).

==========

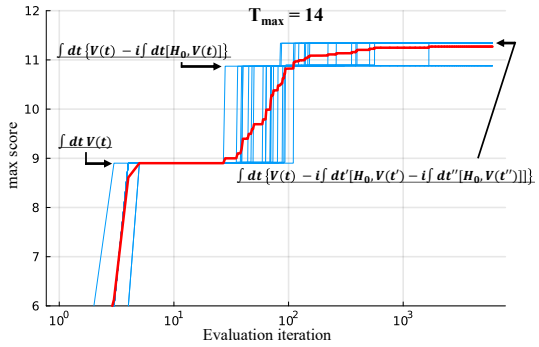

FIG: Searching dynamics by Alpha Zero for Physics.

==========

References

[1] D. Silver, et al,Science. **362**, 1140 (2018).

[2] YM, J. Phys. Soc. Jpn. **accepted**(2024).

Development of integrated interface of eigensolvers Rokko and application to quantum spin systems

Tatsuya Sakashita
Center for Quantum Information and Quantum Biology, Osaka University
1-2 Machikaneyamachō, Toyonaka, Osaka 560-0043

To establish universal exact diagonalization package for quantum lattice models including the Heisenberg-Kitaev model, we focused on developing integrated interfaces for eigensolvers, "Rokko"[1].

In Rokko, we implemented the integrated interfaces for the following types:

- Serial solvers for dense matrices (Eigen3, LAPACK)
- MPI parallelized solvers for dense matrices (EigenExa[2], ELPA[3], Elemental[4], ScaLAPACK)
- MPI parallelized solvers for sparse matrices (Anasazi in Trilinos[5], SLEPc[6]) to cover matrix representations below:
  - CRS (Compressed Row Storage)
  - Matrix-free method (the method to give matrix-vector product routines to solvers)

Rokko has the following features:

- Integrated interfaces for eigensolvers and matrices, independent of individual eigensolver libraries
- Rokko's interfaces are implemented by utilizing factory. It enables the user to dynamically select a solver.
- C, Fortran, and Python bindings of Rokko
- Automatically detecting libraries by using CMake in building Rokko
- Unit and integrated test programs by GoogleTest
- Install scripts of eigensolvers for various architectures

We prepare a paper to report design policy, software structure, and usage examples of Rokko.

References

[1] T. Sakashita, R. Igarashi, Y. Motoyama, T. Okubo, and S. Todo. Repository of Rokko. `https://github.com/t-sakashita/rokko.git`, 2012.

[2] T. Imamura, T. Hirota, and T. Fukaya. EigenExa web page. `https://www.r-ccs.riken.jp/labs/lpnctrt/projects/eigenexa/`, 2021.

[3] ELPA Consortium. ELPA (Eigenvalue soLvers for Petaflop Applications web page). `http://elpa.rzg.mpg.de`, 2013.

[4] J. Poulson. Distributed-memory dense linear algebra Elemental web page. `https://github.com/elemental/Elemental`, 2013.

[5] M. A. Heroux, R. A. Bartlett, and V. E. Howle. Trilinos Project web page. `https://trilinos.github.io`, 2003.

[6] V. Hernandez, J. E. Roman, and V. Vidal. SLEPc web page. `http://slepc.upv.es`, 2002.

Finite temperature calculations of quantum spin systems

Katsuhiro MORITA
Department of Physics and Astronomy, Faculty of Science and Technology, Tokyo University of Science, Noda, Chiba 278-8510

We conducted calculations on the finite-temperature magnetization curves for the $J_1 - J_2$ kagome lattice, with a particular focus on the 1/3 magnetization plateau [1]. For $J_2 = \pm 0.3$, the 1/3 plateau begins to melt almost symmetrically as the temperature increases. However, at $J_2 = 0$, the magnetization deviates from 1/3 starting from the left side of the plateau, displaying asymmetric melting. This confirms that asymmetric melting occurs only around $J_2 = 0$. Instead of a plateau, a slope appears at $M/M_{sat} = 1/3$, which differs on either side, suggesting a difference in the density of states.

Therefure, we calculated low-energy excitation spectra for $N = 36$ at $J_2 = 0$ and $J_2 = -0.3$ to investigate the causes of the asymmetric melting of the 1/3 plateau at $J_2 = 0$ and the symmetric melting at $J_2 = -0.3$. At $J_2 = 0$, all excitation energies for $S^z_{tot} = 7$ are greater than 0.1, whereas for $S^z_{tot} = 5$, there are 76 states with $\Delta E \leq 0.06$ as shown in Fig. 1(a). This indicates the cause of asymmetric melting. In contrast, at $J_2 = -0.3$, similar energy spectra are observed for $S^z_{tot} = 5$, 6, and 7, with excitation energies above 0.2, excluding very low excited states as shown in Fig. 1(b). These spectra differ from those at $J_2 = 0$ and indicate the symmetric melting of the 1/3 plateau.

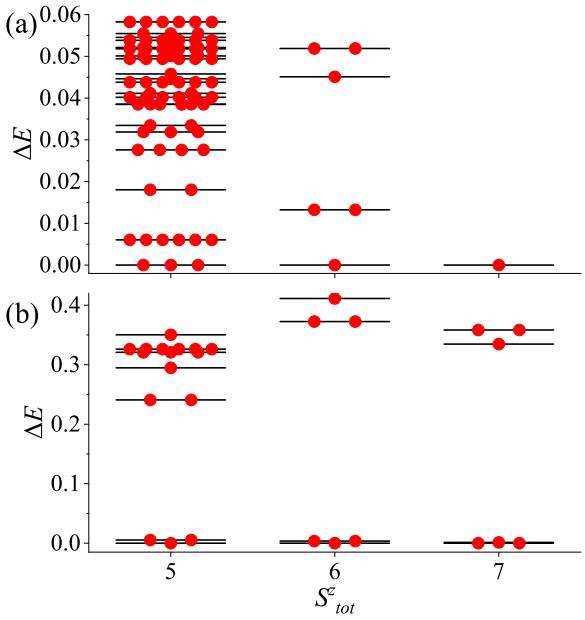

Figure 1: Low-energy excitation spectra of the $J_1 - J_2$ kagome lattice with $N = 36$ for the states with $S^z_{tot} = 5, 6$, and 7 at (a) $J_2 = 0$ and (b) $J_2 = -0.3$. The horizontal bars indicate the energy gap ΔE. The number of filled red circles represents the degeneracy. [1]

References

[1] K. Morita: Phys. Rev. B **108**, 184405 (2023).

Multiple-Q orders in two-dimensional Hubbard Models

Takashi UCHIDA
Hokkaido University of Science
4-1, 7-15, Maeda, Teine-ku, Sapporo 006-8585

In the last decade, multiple-Q orders in magnetic systems have attracted attention because they sometimes reveal nontrivial magnetic structures such as magnetic skyrmions. Typically, these structures are realized in the Dzyaloshinskii-Moriya (DM) interaction driven systems under magnetic field. The nontrivial multiple-Q orders can also be realized in inversion-symmetric systems where the DM interaction is absent [1, 2].

The purpose of the present research is to investigate the nature of the multiple-Q orders in inversion-symmetric itinerant systems. We have explored the magnetic and electronic structures of the triangular-lattice single-band Hubbard model by means of the molecular spin dynamics (MSD) method [3]. The present formulation of the MSD adopts the static approximation to the functional integral method and the isothermal molecular dynamics technique, and reduces to the generalized Hartree-Fock approximation at the ground state.

In the present work, we have performed the MSD calculation with use of the global charge neutrality condition instead of using the local charge neutrality condition [3]. This has the advantage that the charge transfer among the atoms is allowed in the magnetic structure formation. In the numerical calculations the most time-consuming process is the magnetic force calculation at each time step, where the local electronic structures are calculated in real space by means of the recursion method. We have adopted the MPI parallel calculation scheme and found it effective in saving both computing time and CPU resources.

We have performed magnetic structure calculations on a hexagonal supercell with 972 lattice points, which is embedded in a large cluster consisting of 6 such supercells, each of which are connected by the periodic boundary condition. Under zero magnetic field and the fixed value of the temperature $T/t = 0.0005$, we have explored the magnetic structures changing the Coulomb interaction strength U/t and the electron number n along the antiferromagnetic-ferromagnetic boundary. We have found that the 3Q magnetic orders are realized for $U/t < 4.0$ and $n = 1.45 \sim 1.53$ accompanying the 3Q charge density waves (CDW) with the same Q vectors as the magnetic ones. For $U/t = 4.0 \sim 4.3$ and $n \sim 1.4$, 2Q+2Q+2Q states were found to appear, which do not accompany CDWs. In both cases, the electronic density of states shows a dip at the Fermi energy, which suppress the formation of spontaneous magnetization and stabilize the multiple-Q orders.

References

[1] T. Okubo, S. Chung, and H. Kawamura: Phys. Rev. Lett. **108** (2012) 017206

[2] Y. Kakehashi: J. Phys. Soc. Jpn. **89** (2020) 094710.

[3] Y. Kakehashi, S. Akbar, and N. Kimura: Phys. Rev. B**57** (1998) 8354.

Molecular Dynamics Simulation of Graphene-nanosapcer Stacking Structure

Mingda Ding, Taiki Inoue, Yoshihiro Kobayashi

Department of Applied Physics, Osaka University, Yamadaoka, Suita, Osaka 565-0871

In this year, we studied the microstructure of graphene (Gr) and nanospacer stacking structure using molecular dynamics simulation [1].

By controlling the interlayer distance and altering interlayer interactions, it is possible to modulate the properties of multilayer Gr and induce novel physical phenomena. However, the energetically favorable AB stacking structure in multilayer Gr indicates a parabolic dispersion band structure with strong interlayer coupling. To address this issue, we introduce nanomaterials between Gr layers as nanospacers to manipulate the microstructure. The Gr stacking structures with carbon nanotube (CNT) and nanodiamond (ND) as spacers are fabricated experimentally. Raman spectroscopy confirms a decrease in interlayer interaction, while atomic force microscopy (AFM) reveals an expansion of the interlayer distance. The AFM observation finds two distinct morphologies, upper Gr suspension and interlayer adhesion, which are determined by the density of spacers. To systematically elucidate the regularities and mechanisms of nanospacer's influence on the interlayer distance of the stacking structure, MD simulation was conducted.

The MD simulation is conducted using the open-source software, LAMMPS (Large-scale Atomic/Molecular Massively Parallel Simulator). The number of atoms is 10,000~770,000, which depends on the size of the Gr layers. The AIREBO potential is used to describe the short-range interaction and the LJ interaction is used for long-range interaction between Gr layers. The dynamic relaxation is conducted to find the energy-stable structure using the velocity-Verlet method. The cases of Gr-ND with more atoms are mainly simulated in System B (Ohtaka) with 2~4 nodes and a computational time of 16~48 h. The systems of Gr-CNT are simulated in System C (Kugui) with 1 node and a computational time of 5~18 h.

We simulated stacked structures of double-layer Gr with both CNTs and NDs spacers (Fig. 1). By applying periodic boundary conditions around the structure edges, the systems with different sizes of Gr can simulate different areal densities of CNTs and NDs. Additionally, we constructed stacked structures with CNTs and NDs of varying diameters for simulation. As the size of Gr increased, i.e., a decrease in spacer areal density, there was a transition from

upper Gr suspension to interlayer adhesion. This transition is comparable with the two distinct morphologies observed experimentally. Furthermore, with an increase in nanospacer diameter, the critical areal density for the transition also increased.

The appearance of two different configurations is induced by the difference in potential energy. The configurations with minimum energy are obtained in MD simulations with the two dominant components of deformation energy and adhesion energy. The flat-suspended upper Gr results in lower deformation energy and increased adhesion energy. The significant deformation of adhered Gr increases the deformation energy, while the adhesion energy decreases to a minimum. When the inter-spacer distance is small, the sum of the energy components is lower with upper Gr suspension. The difference in adhesion energy between the two configurations increases with the size of the Gr i.e., inter-spacer distance. When the inter-spacer distance exceeds a critical value, the transition from suspension to interlayer adhesion appears.

Our study of the nanospacer insertion effect contributes to the enhanced and novel properties of multilayer Gr to facilitate functional enhancement for wider applications.

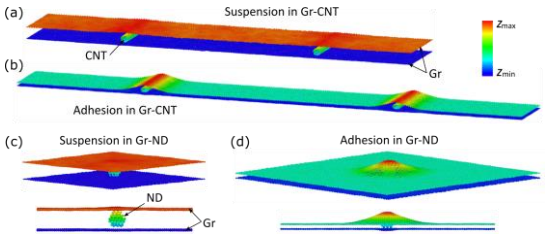

Figure 1: Deformed configuration obtained by MD simulation of graphene (Gr) and nanospacer stacking structure. (a) The Gr and carbon nanotube (CNT) stacking structure (Gr-CNT) with upper Gr suspension of larger interlayer distance. (b) The Gr-CNT with larger inter-CNT distance and interlayer adhesion. (c, d) The suspension and interlayer adhesion of Gr and nanodiamond (ND) stacking structure (Gr-ND).

References

[1] M. Ding, T. Inoue, J. I. Enriquez, H. H. Handoko, Y. Ogawa, Y. Taniyasu, Y. Hamamoto, Y. Morikawa, Y. Kobayashi, J. Phys. Chem. C **127**, 23768‑23777 (2023).

Classification of slow and fast earthquakes based on fluid pressure and porosity

Takehito SUZUKI
Department of Physical Sciences, Aoyama Gakuin University
5-10-1, Fuchinobe, Chuo-ku, Sagamihara, Kanagawa 252-5258

Two qualitatively different behaviors of earthquakes have been known. One is the fast earthquake, which we feel naturally. The other one is slow earthquakes, which generate negligible seismic waves. Although the slow earthquakes are not disastrous, they are considered to sometimes change to the fast earthquakes after several repetitions. Whether this transition occurs or not is a fatal problem to the human society, and we should clarify the condition for the transition to occur.

We employ the spring-block model and the interaction among the slip, heat, fluid pressure, and porosity. The former is widely known to generate the stick-slip behavior, which can be considered to model the earthquake cycle. The latter is also known to affect the dynamic earthquake slip behavior. First, note that the heat and pore-generation effects are related with the fluid-pressure change on the slip surface. If the heat effect is dominant, the fluid pressure increases, whereas if the pore-generation effect is dominant, the fluid pressure decreases. Moreover, if the fluid pressure on the slip surface increases, the slip is enhanced, whereas if it decreases, the slip is inhibited.

For this model, it should be emphasized that we have found that the function

$$F(u_f) = \frac{1}{2}k_p u_f^2 + \mu_{\rm stat}(\sigma_n^0 + p_0)u_f - \mu_{\rm slid}\left[\frac{1}{\gamma}\left(\sigma_n^0 + p_0 - \frac{M_0'\alpha_0}{\frac{\alpha_0}{\phi_\infty} - \gamma}\right)(1 - e^{-\gamma u_f}) + \frac{M_0'\phi_\infty}{\frac{\alpha_0}{\phi_\infty} - \gamma}(1 - e^{-\alpha_0 u_f/\phi_\infty})\right] \quad (1)$$

governs whether the slow and fast earthquakes occur (the variables are summarized in [1]). If the equation $F(u_f) = 0$ has three positive solutions, the slow earthquakes emerge, whereas if the equation has a single positive solution, the fast earthquakes emerge [1].

We obtain the phase diagram of the small and large slippages, i.e., the phase diagram of the foreshocks and mainshock, in the $p_0 - \phi_0$ plane, as follows, where p_0 and ϕ_0 describe the value of the fluid pressure and porosity at the onset of each slippage, respectively. By definition, $dF(u_f)/du_f|_{u_f=u_2} = 0$ must be satisfied, where $F(u_2)$ is the local maximum. From Eq. (1), equation $dF(u_f)/du_f = 0$ yields

$$e^{-\gamma' u_2} = \frac{k_p u_2}{\mu_{\rm slid} AS} + \frac{\mu_{\rm stat}(\sigma_n^0 + p_0)}{\mu_{\rm slid} A} - \frac{\sigma_n^0 + p_0 - A}{A}e^{-\gamma u_2}. \quad (2)$$

Therefore, using Eqs. (1) and (2), we obtain

$$\frac{1}{2}k_p u_2^2 + \left(\mu_{\rm stat}(\sigma_n^0 + p_0)S + \frac{k_p}{\gamma'}\right)u_2 - \frac{\mu_{\rm slid}}{\gamma}(\sigma_n^0 + p_0 - A)S - \frac{\mu_{\rm slid}}{\gamma'}AS + \frac{\mu_{\rm stat}}{\gamma'}(\sigma_n^0 + p_0)S + \mu_{\rm slid}(\sigma_n^0 + p_0 - A)S\left(\frac{1}{\gamma} - \frac{1}{\gamma'}\right)e^{-\gamma u_2} = 0. \quad (3)$$

When the magnitude of γu_2 is greater than the order of unity, we can neglect the $\exp(-\gamma u_2)$ term. Thus, we have a quadratic

equation, which gives the relation among u_2, p_0, and ϕ_0. By substituting the solution of this quadratic equation into Eq. (1), we obtain p_0 and ϕ_0, which are critical for inducing the phase transition, yielding

$$\begin{aligned} F(u_2) &= -\frac{k_p}{\gamma'}u_2 - \frac{\mu_{\rm stat}}{\gamma'}(\sigma_n^0 + p_0)S \\ &\quad + \frac{\mu_{\rm slid}}{\gamma'}e^{-\gamma' u_2}AS \\ &\equiv G(p_0, \phi_0) = 0. \end{aligned} \tag{4}$$

The phase diagram thus obtained is shown in Figure 1, exhibiting the numerical results obtained using several sets of (p_0, ϕ_0) for $\phi_\infty = 0.1$. The green line shows the phase boundary, $G(p_0, \phi_0) = 0$, and the red and blue symbols show that (p_0, ϕ_0) cause fast and slow earthquakes, respectively. The analytical results coincide well with the numerical ones for $\phi_\infty = 0.1$, and we can conclude that the approximation above is valid for this case. For the calculations, ISSP Supercomputer was useful.

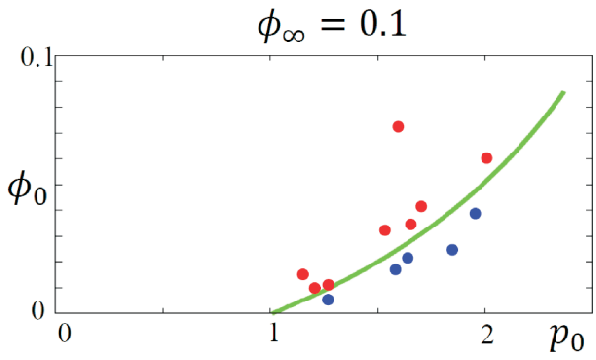

Figure 1: Boundary between the slow and fast earthquakes, denoted by the green line in the $p_0 - \phi_0$ plane obtained from Eq. (4). The value of ϕ_∞ is 0.1. The red and blue symbols show that (p_0, ϕ_0) cause fast and slow earthquakes, respectively.

References

[1] T. Suzuki, and H. Matsukawa, submitted to Rhys. Rev. E.

3.5 SCCMS Projects

Creatin of material maps by KKR Green's function method

Tetsuya FUKUSHIMA
CD-FMat, National Institute of Advanced Industrial Science and Technology (AIST)
1-1-1 Umezono, Tsukuba, Ibaraki 305-8568, Japan

The purpose of Data Creation and Utilization-Type Material Research and Development Project (Digital Transformation Initiative Center for Magnetic Materials) is to find new functional permanent magnets, soft magnets and spintronics materials by data-driven approaches. The project has placed a high priority on creating materials maps to accelerate the magnetic material developments.

In this year, we generated the magnetic property data, such as magnetization, Curie temperature, and magnetic anisotropy, in preparation for creating the material maps for 1-5 permanent magnets materials[1]. The target materials are $CeCo_5$ alloy series, where the Ce and Co atoms are replaced by the La and Co atoms, respectively. Our calculation is based on the all-electron full-potential Korringa-Kohn-Rostoker (KKR) Green's function method. The randomness of the atomic arrangement is considered by the coherent potential approximation. The spin-orbit coupling is included as the $l_z s_z$ term. The generalized gradient approximation (GGA) is used for the exchange-correlation potential. The space group of the crystal structure is $P6/mmm$, and the lattice constants of the disordered systems are determined by the Vegard rule; the lattice constants of the endpoints is optimized by the full-potential KKR method.

Figure 1 shows the calculated (a) magnetic anisotropy (K_u), (b) magnetization (M_s), (c) anisotropic field ($\mu_0 H_a$), and (d) formation energy ($E_{\rm form}$) for $Ce_{1-\alpha}La_\alpha Co_{5-x}Fe_x$. K_u is enhanced with a small amount of the Fe atoms and then is gradually decreased with the Fe atoms. The maximum value of K_u is around $x = 0.3$. M_s increases monotonically with the Fe concentration. Therefore, $CeCo_{4.7}Fe_{0.3}$, which has larger K_u and M_s compared to those of $CeCo_5$, is a candidate for new functional permanent magnets. Anisotropic magnetic field is defined by $H_a = \sqrt{2Ku/\mu_0 M_s}$. In the region of $x < 0.3$ for $CeCo_{5-x}Fe_x$, since both K_u and M_s are increased, the change of H_a is small. The formation energy is increased with the Fe concentration, leading to the instability of the 1-5 phase. However, $CeCo_{4.7}Fe_{0.3}$ has still negative formation energy, $E_{\rm from} = -0.19$ eV/f.u., and may stabilize the 1-5 phase.

Next, we consider the effect of the La doping. K_u is decreased monotonically with the La concentration, while M_s is increased. This is due to the hybridization between the Ce-4f and the transition metal 3d states, which leads to the enhancement of the occupied electrons in the minority spin states. As a result, the total magnetic moment is decreased. This mechanism is less likely to occur in the La case with the unoccupied 4f states. Therefore, the total magnetic moment is expected to be increased when Ce is replaced by La.

The Curie temperature ($T_{\rm C}$) of $CeCo_5$ estimated by the full-potential KKR calculations and mean-field approximation is 965 K, which is higher than the experimental value of 653 K. This overestimation is a general error of

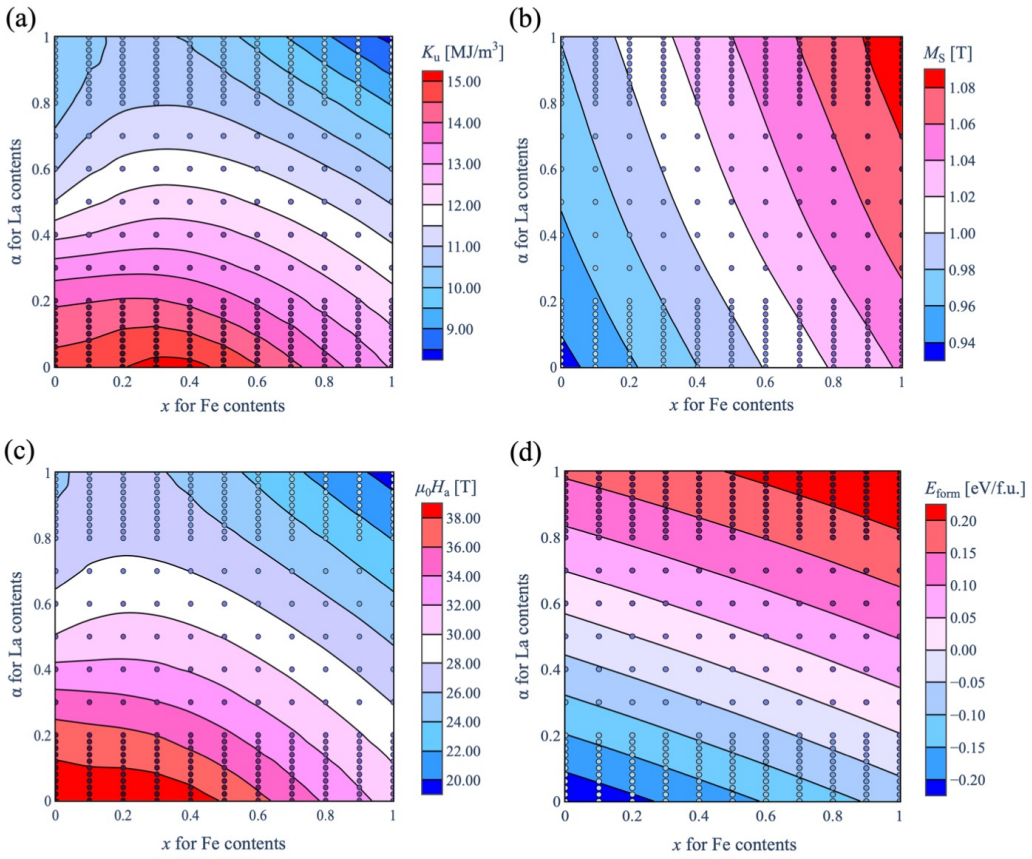

Figure 1: Calculated (a) magnetic anisotropy (K_u), (b) magnetization (M_s), (c) anisotropic field ($\mu_0 H_a$), and (d) formation energy (E_{form}) for $Ce_{1-\alpha}La_{\alpha}Co_{5-x}Fe_x$.

the mean-field approximation. The calculated T_C of $CeFe_5$ and $LaCo_5$ are 1357 K and 1176 K, respectively. These values are higher than that of $CeCo_5$. Our calculation confirms that both the Fe and La doping lead to the increase of T_C. In particular, $CeCo_{4.7}Fe_{0.3}$ has rather higher T_C of 1005 K

References

[1] H. Okumura, T. Fukushima, H. Akai, and M. Ogura, Solid State Commun. **373-374**, 115257 (2023).

First-principles study of magnetic materials

Takashi MIYAKE
CD-FMat, National Institute of Advanced Industrial Science and Technology
Umezono, Tsukuba, Ibaraki 305-8568

We have performed systematic first-principles calculations of transition metal compounds for the development of magnetic materials. This year, we focused on iron-cobalt systems. Calculations were performed by changing the composition of iron and cobalt and the lattice constants.

The calculation is based on density functional theory in the local density approximation. We use AkaiKKR which is based on the Korringa-Kohn-Rostoker Green function method. Chemical disorder is treated within the coherent potential approximation (CPA) which is the best single-site approximation for disordered alloys.

Figure 1 shows the magnetic moment of Fe-Co systems for (a) Fe, (b) $Fe_{0.8}Co_{0.2}$, (c) $Fe_{0.6}Co_{0.4}$, (d) $Fe_{0.4}Co_{0.6}$, (e) $Fe_{0.2}Co_{0.8}$, and (f) Co. The horizontal line is c/a, where c/a=1 means the bcc structure, and $c/a = \sqrt{2}$ is the fcc structure. Starting from iron in the bcc structure and increasing c/a, the magnetic moment decreases. Starting from iron in the bcc structure and increasing the cobalt concentration, the magnetic moment increases then turns to decrease, as is well-known in the Slater-Pauling curve. The calculations of the Curie temperature and other transition-metal alloys are now underway.

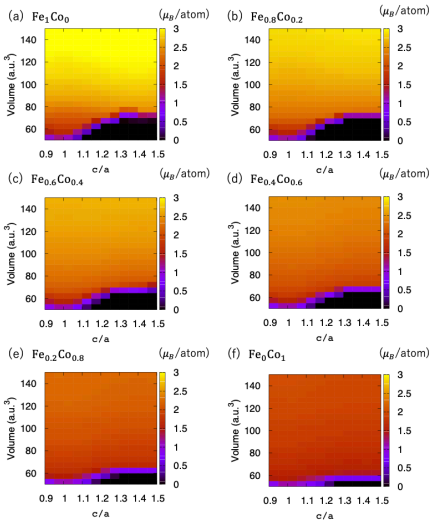

Figure 1: Magnetic moment of Fe-Co systems.

We have also carried out systematic first-principles calculation of $A_{2-x}B_xMo_3N$ in the β-Mn phase by changing A and B elements (Fig. 2). The magnetic moment is calculated, and chemical composition having high magnetic moment is proposed.

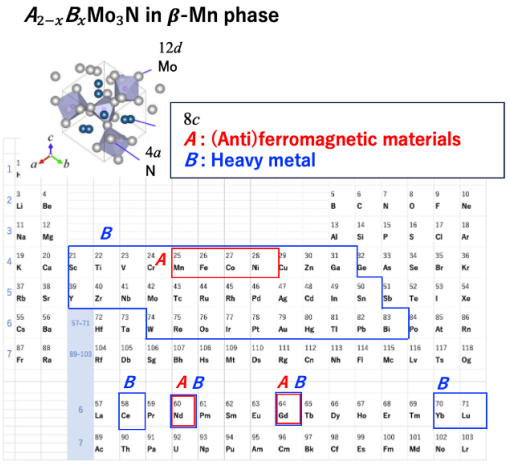

Figure 2: First-principles calculation of $A_{2-x}B_xMo_3N$ in the β-Mn phase.

Construction of NNP for Fe-Ti-N

Junping Du and Shigenobu Ogata

Department of Mechanical Science and Bioengineering,

Osaka University 1-3 Machikaneyama-cho, Toyonaka, Osaka 560-8531, Japan

We have trained a neural network potential (NNP) for the Fe-Ti-N system using the Deepkit framework [1,2]. The density functional theory (DFT) calculations were conducted to prepare the training dataset using the VASP software. The training dataset contains the designed atomic models with monoatomic, binary, and ternary elements, which were obtained using the supercomputer system "Ohtaka" at the ISSP.

Because of the low concentration of Ti and N (~1%) in the Fe-Ti-N system we studied, the matrix properties of the system are represented by the BCC-Fe. Therefore, we designed a BCC-Fe supercell model with 54 atoms. Various deformations were applied to this model and various configurations were sampled by direct molecular dynamics simulations at 0~1000 K using a NNP of Fe [3]. The configurations of vacancy, the surfaces, the γ surface, and the two-dimensional Peierls potential of the screw dislocation, were also designed. The results of the DFT calculations for these configurations constitute the BCC-Fe dataset.

Considering that B1-TiN is the precipitated phase in this system, we have taken the information on the B1-TiN phase as an important part of the dataset. We constructed a 108-atom model of B1-TiN, applied different deformations to this model as well, and conducted FPMD simulations using VASP at 200 K~1000 K, thus giving the dataset of TiN.

Since the property of the Fe/TiN interface controls the TiN precipitation process, we also designed a dataset of this interfacial system. The various configurations of Ti and N in BCC-Fe forming a solid solution were also designed to model the precipitation process.

Based on the above DFT dataset, which contains 23,866 configurations, the Fe-Ti-N NNP was successfully trained using the Deepkit framework, and root-mean-squared errors of the energy and the force are 3 meV and 12 meV/Å. For the training of NNP based on Deepkit framework, "Kugui" accelerator server was used.

References

[1] H. Wang, L. Zhang, J. Han, and W. E. **Comput. Phys. Commun. 228**, 178 (2018).

[2] J. Zeng, D. Zhang, D. Lu, P. Mo, Z. Li, Y. Chen, M. Rynik, L.A. Huang, Z. Li, S. Shi, Y. Wang, et al. **J. Chem. Phys. 159**, 054801 (2023).

[3] F.S. Meng, J.P. Du, S. Shinzato, H. Mori, P. Yu, K. Matsubara, N. Ishikawa, and S. Ogata, **Phys. Rev. Mater. 11**, 113606 (2021)

Exploration of Ferroelectric Materials using Large-scale Computations

Kazuki SHITARA

Nanostructures Research Laboratory,

Japan Fine Ceramics Center, 2-4-1 Mutsuno, Nagoya, Aichi 456-858

Recently, ferroelectricity has been reported in crystal structures other than the perovskite structure such as the wurtzite and fluorite structures. For example, ferroelectricity has been experimentally observed in AlN and ZnO which have the wurtzite structures[1]. Theoretical calculations play an important role in understanding the mechanism of ferroelectricity in such new crystal structures. In this study, we performed comprehensive first-principles calculations to obtain the guidelines for designing ferroelectric materials.

Figure 1 shows SHAP analysis results to explore the dominant factors on the energy barrier of polarization reversal. It shows the extent to which each descriptor affects the energy barrier, and provides guidance on adjusting the descriptor's value to increase or decrease the barrier energy. For example, we found that reducing the sum of boiling points of simple substances results in a smaller energy barrier. This corresponds to the fact that the boiling points of Si, C, and B, which are highly covalent, and their formal charges are high.

We applied a similar analysis to spontaneous polarization. By extracting dominant factors from a wide composition range, a reciprocal relationship is found between the spontaneous polarization and the energy barrier, which is controlled by the valence of cation and anion. Simultaneously, it is suggested that the energy barrier can be reduced while maintaining a high spontaneous polarization value by controlling ionic/covalent bonding, thereby proposing specific material design guidelines to break away from the reciprocal relationship.

References

[1] K. Ferri, *et al*., J. Appl. Phys. **130** (2021).

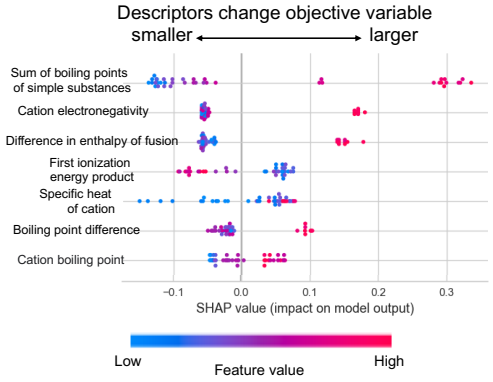

Fig. 1: Results of dominant factor analysis using machine learning (SHAP analysis)

Systematic evaluation of solubility of polypeptides in solvents by free energy calculation method using all-atom model

Kazuo YAMADA and Nobuyuki MATUBAYASI

Division of Chemical Engineering, Graduate School of Engineering Science, Osaka University, Toyonaka, Osaka 560-8531

The development of biopharmaceuticals using polypeptides, which are artificially synthesized using proteinogenic amino acids as building blocks, is anticipated in the field of pharmaceuticals. This is due to the fact that artificial polypeptides possess the advantageous property of biodegradability, whereas conventional, PEG-modified ones are often not biodegradable. Natural peptides are composed of 20 kinds of amino acids, including glycine (Gly), alanine (Ala), serine (Ser), aspartic acid (Asp), lysine (Lys), and arginine (Arg), among others. These amino acids can be combined in various ways to synthesize a vast array of artificial polypeptides. Solubility and partition coefficient in in vivo solvent environments, such as water and saline solutions, are crucial physical quantities for controlling pharmacokinetics, including absorption, distribution, metabolism, and excretion. Therefore, it is imperative to systematically explore the solubility and partition coefficient in water in connection to amino acid sequences. Given the vast number of possible amino acid sequences, computer simulation is an invaluable tool for evaluating the solubilities of peptides in water.

To analyze the solubilities at atomic resolution, we employ all-atom molecular dynamics (MD) simulation. We focus on homo-tetrapeptides as model systems and identify the intermolecular interaction components that are responsible for the solubilities. The key is the free-energy calculation. By combining MD simulation and the energy-representation theory of solvation [1,2], we obtain the free energies determining the solubilities. The solubility of a peptide molecule is determined as the difference of its solvation free energy in water from the free energy of insertion of a single molecule of the peptide into the pure solid. The insertion free energy into the solid can also be treated as a solvation free energy by viewing the inserted peptide as the solute and the other peptide molecules as the solvent. We extend the energy-representation method of solvation to the solid systems in this work.

The free energies of solvation were calculated for 15, different homo-tetrapeptides in the single-component pure solid systems and in the aqueous solutions at infinite dilution. The equilibration and sampling calculations were

performed using GROMACS 2016.4 [1], while the solvation free energies were computed using ERmod [2]. MD simulation with GROMACS were performed in parallel using GPU nodes, and ERmod was on CPU nodes.

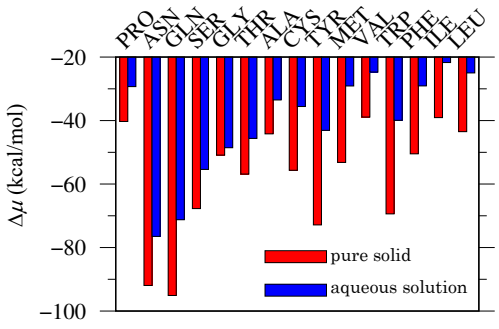

Fig. 1: Free energies of solvation $\Delta\mu$ of homo-tetrapeptides in their pure solids and aqueous solutions; the differences between the two solvation free energies provide the water solubilities of the peptides.

Figure 1 shows the free energies of solvation $\Delta\mu$ of 15 tetrapeptides. The experimentally measured solubility of a single amino acid in water is lower and more hydrophobic from left to right. Since the dissolution refers to the transfer of a peptide molecule from its solid to the aqueous solution, the solubility is given by the difference in $\Delta\mu$ between the solid and aqueous solution. It is then seen in Figure 1 that the peptide dependence of $\Delta\mu$ is parallel between the solid and aqueous solution. This means that the solubility cannot be ranked simply by the affinity of the peptide to water.

The solvation free energies were further decomposed to identify the intermolecular-interaction components determining the dependence of the solubilities into water on the peptide species. The excluded-volume component exhibited the strongest correlation with the peptide solubility of peptide, with a correlation coefficient of 0.86. The excluded-volume component is the free-energy penalty required for displacing solvent molecules from the region to which the solute molecule is to be inserted. A negative correlation was observed, with a coefficient of –0.13, for the direct interaction energy between the solute, peptide molecule and the solvent molecules against the solubility of the peptide into water. The above results indicate that the excluded-volume component is a more important factor for the solubility into water than the direct interaction energy such as the hydrogen bonding.

The effect of added salt on the solubility of model compounds were also addressed through free-energy decomposition [3]. In this case, too, the importance of the excluded-volume effect was pointed out.

References

[1] M. J. Abraham, *et. al*, SoftwareX **1-2** (2015) 19–25

[2] S. Sakuraba and N. Matubayasi: J. Comput. Chem. **35** (2014) 1592-1608

[3] S. Hervø-Hansen, D. Lin, K. Kasahara, and N. Matubayasi: Chem. Sci. **15** (2024) 477-489

First-principles study toward elucidating the proton transfer mechanism with nuclear quantum effect

Tomomi Shimazaki

Graduate School of Nanobioscience,

Yokohama City University, 22-2 Seto, Kanazawa, Yokohama 236-0027

The quantum nature of nuclei can affect various physical and chemical properties on atomic-scale systems. Especially, the proton is the lightest element, and hence it is important to deal with nuclear quantum effects to study its behavior in detail. In this study, we investigate the proton transfer mechanism in water using the first-principles path integral (PIMD) method. For comparison, we also performed simulations for D+ in heavy water (D_2O) as well as H+ in light water (H_2O). As a result, it was observed that H_3O+ tends to have a trigonal pyramidal structure in the solvent, while D_3O+ is more likely to have a planar structure, which may be due to the difference in the oxygen-oxygen structure in the first and second hydration spheres, as seen in **Fig. 1**.

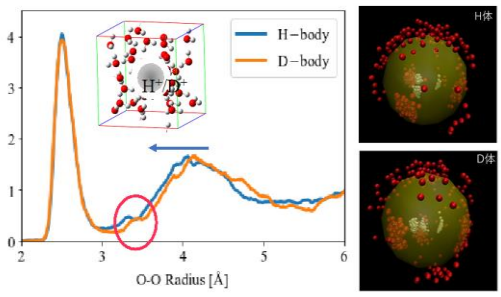

Fig 1. The structure around the proton obtained by first-principles simulation including nuclear quantum effects.

However, the first-principles PIMD method is computationally expensive and difficult to apply to large-scale models. Therefore, we tried to develop the QM/MM method. For the MM program, we employed MODYLAS, which has been used in many large-scale simulations on Fugaku. We modified the source code of MODYLAS and implemented an interface with a QM program.

On the other hand, even if the QM/MM method is used, the computational cost of the QM part is very high for large-scale simulations. Therefore, we attempted to build a prediction model for QM calculations using a machine learning (neural network) model. We confirmed that the machine learning (ML) model can give good prediction performance for test systems.[1] In the next step, we will perform QM/ML/MM simulations by incorporating the machine learning model (ML) into the QM/MM method.

[1] Tomommi Shimazaki and Masanori Tachikawa, Chem. Phys. Lett, 829, 140744, 2023.

Phonon-calculation method for magnetic random alloys

Y. Gohda[1], T. Tadano[2], T. Miyake[3], and T. Ohkubo[2]
[1]*Dept. Mater. Sci. Eng., Tokyo Tech, Yokohama 226-8502, Japan*
[2]*DXMag, National Institute for Materials Science, Tsukuba 305-0047, Japan*
[3]*CD-FMat, AIST, Tsukuba 305-8658, Japan*

Phase equilibria can be discussed from phase diagrams that are constructed from free energies of multiple phases. First-principles phonon calculations play a significant roles in evaluating free energies. Since phonon dispersions of random alloys are broadened, band unfolding techniques are necessary as same as electronic band structures.

In this project, we developed a band-unfolding method within first-principles phonon calculations using the direct method. In the original Brillouin zone of the supercell, many important details of the band structure are hidden in the spaghetti bands resulting from different modes of numerous atoms within the supercell. By unfolding the band, hidden band gaps are revealed, and it becomes easier to make qualitative comparison between different systems based on the same primitive material. The unfolding technique is implemented into the ALAMODE code [1]. In the present study, it is made possible to incorporate impurity atoms at interstitial sites. Figure 1 shows calculated band dispersions of Ti-Al alloys without and with oxygen interstitials. Ti-Al is in the ordered α_2 phase with the $D0_{19}$ structure. However, since the alloy is off-stoichiometric (stoichiometric: Ti_3Al), phonon bands become broadened even in the binary form. It is clear from the figure that interstitial oxygen makes phonon dispersion broadened further. The present method is applicable for magnetic materials, where the difference in the spin directions causes broadning of phonon dispersions. In addition, phase equilibria in permanent magnets were discussed through the CALPHAD approach with the first-principles cluster-expansion method [2].

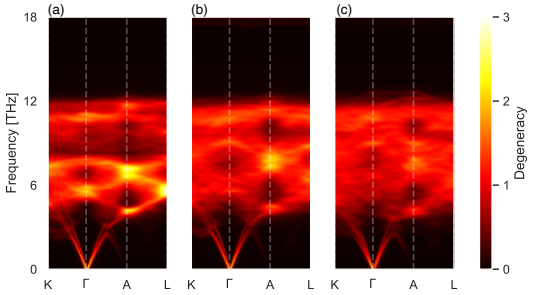

Figure 1: Changes in the effective phonon-band structure for Ti-Al alloys (at.37.5% of Al) in the α_2 phase with the $D0_{19}$ structure in (a) a binary form and with (b) 2 and (c) 5 interstitial O atoms within 64-site supercell.

[1] T. Tadano, Y. Gohda, and S. Tsuneyuki, J. Phys.: Condens. Matter **26**, 225402 (2014).
[2] S. Enomoto, S. Kou, T. Abe, and Y. Gohda, J. Alloys Compd. **950**, 169849 (2023).

3.6 Software Advancement Projects and Workshop Support

Implementation of Finite-Temperature Calculation in TeNeS

Tsuyoshi OKUBO
Institute for Physics of Intelligence, University of Tokyo
7-3-1 Hongo, Bunkyo-ku, Tokyo 133-0033

In quantum many-body problems, such as quantum spin systems and strongly correlated electron systems, the dimension of the Hilbert space increases exponentially with the number of spins or particles, making precise analysis of large systems difficult. The tensor network method, which is one technique to overcome such difficulties, represents quantum states as a network constructed by the contraction of small tensors, thereby reducing the effective degrees of freedom and enabling the computation of large systems. The infinite projected entangled pair state/infinite tensor product states (iPEPS/iTPS) is a tensor network that can directly represent the ground state of an infinitely large system. We are developing a tensor network library TeNeS based on iPEPS/iTPS [1, 2]. TeNeS supports MPI and OpenMP hybrid parallelization, and enables us to calculate the ground states of various two-dimensional lattice models.

This year, through the support of Project for Advancement of Software Usability in Materials Science (PASUMS), we have implemented the finite-temperature calculation in TeNeS. The finite-temperature calculation is essential for the analysis of the physical properties of quantum many-body systems, such as the specific heat, and magnetization. The finite-temperature calculation is performed by the imaginary time evolution of the density matrix represented by the infinite projected entangled pair operator/infinite tensor product operator (iPEPO/iTPO) [3] (See Fig. 1). Such imaginary time evolution for iPEPO/iTPO is algorithmically similar to the ground state calculation based on iPEPS/iTPS, and we can easily implement the finite-temperature calculation in TeNeS.

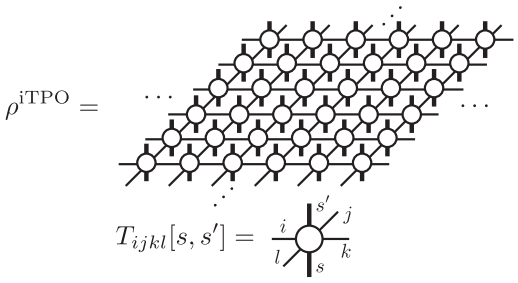

Figure 1: Tensor network diagram of a density matrix ρ represented as an iPEPO/iTPO. Vertical open legs stand for indices of local Hilbert space.

In addition to the finite-temperature calculation, we also implemented the real-time evolution of a pure state using TeNeS. The algorithm of the real-time evolution is essentially the same as the imaginary time evolution. However, usually approximation based on iPEPS/iTPS becomes less accurate for longer time evolution due to the increase of quantum entanglement. Thus, real-time evolution approximated by iPEPS/iTPS is limited to short time evolution.

The finite-temperature calculation and the real-time evolution implemented in TeNeS are useful for the analysis of the physical properties of quantum many-body systems. We hope

that TeNeS can enhance research in the field of quantum many-body systems.

TeNeS was developed with Yuichi Motoyama, Kazuyoshi Yoshimi, Satoshi Morita, Tatsumi Aoyama, Takeo Kato, and Naoki Kawashima.

References

[1] Y. Motoyama, T. Okubo, K. Yoshimi, S. Morita, T. Kato and N. Kawashima, Comput. Phys. Commun. **279**, (2022) 108437.

[2] https://github.com/issp-center-dev/TeNeS

[3] A. Kshetrimayum, M. Rizzi, J. Eisert, and R. Orús, Phys. Rev. Lett. **122**, (2019) 070502.

Development of a tool to create a database of first-principles calculations using high-throughput calculations

Kazuyoshi YOSHIMI[1], Tatsumi AOYAMA[1], Yuichi MOTOYAMA[1],
Masahiro FUKUDA[1], Kota IDO[1], Tetsuya FUKUSHIMA[2], Shusuke KASAMATSU[3],
Takashi KORETSUNE[4], Taisuke OZAKI[1]

[1]*Institute for Solid State Physics, University of Tokyo, Kashiwa-no-ha, Kashiwa, 277-8581*,
[2]*National Institute of Advanced Industrial Science and Technology,*
Tsukuba, 305-8568,
[3] *Faculty of Science, Academic Assembly, Yamagata University,*
Yamagata 990-8560
[4] *Department of Physics, Tohoku University, Sendai 980-8578*

In recent years, approaches to predicting physical properties and designing materials using machine learning (materials informatics) have become popular, in which the generation of a large amount of supervised data is essential for highly accurate prediction and design. From this perspective, databases such as MaterialsProject [1], which store crystal structures, experimental measurement results and first-principles calculations, have been developed and are actively used. On the other hand, machine learning requires the preparation of materials and physical quantities as teacher data, but in many cases the desired materials and physical quantities do not exist in existing databases. If tools and environment can be created to quickly prepare these teacher data, it will provide a research stage for the field of materials informatics and is expected to make a significant contribution to its progress.

We developed HTP tools [2] for exhaustive data generation from crystal structures using first-principles calculations under the support of "Project for advancement of software usability in materials science". Specifically, we developed a script cif2x [3] to generate input files from crystal structures for the first-principles calculation software VASP [4], Quantum ESPRESSO [5], OpenMX [6], and AkaiKKR [7]. Samples and tutorials are provided for each software to explain how to use cif2x with each software.

We also developed a tool to generate batch job scripts, moller [8], which can easily realize exhaustive calculations by bulk execution of jobs on the ISSP supercomputer. Since moller is independent of cif2x in nature, it can be used for general exhaustive calculations with various

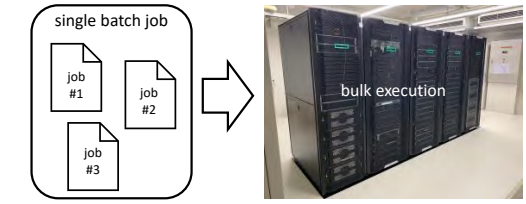

Figure 1: a series of small jobs are executed within a job of large batch classes as a bulk job execution.

solvers. Samples and tutorials are provided that apply HΦ [9] and DSQSS [10] to illustrate the implementation in bulk jobs when multiple calculation scenarios are prepared.

These two software packages, cif2x and moller, are developed as Open Source software and distributed under GPL v.3.0. They have already been pre-installed on the ISSP supercomputer systems. For future plans, we would like to create a computational materials science database using cif2x and moller. It would be interesting to make moller compatible with supercomputing systems other than ISSP supercomputer, to become a standard for exhaustive computations at HPCI. With these tools, we hope that users will make use of them to generate various databases.

References

[1] https://next-gen.materialsproject.org

[2] https://www.pasums.issp.u-tokyo.ac.jp/htp-tools/en/

[3] https://github.com/issp-center-dev/cif2x

[4] https://www.vasp.at

[5] https://www.quantum-espresso.org

[6] https://www.openmx-square.org

[7] http://kkr.issp.u-tokyo.ac.jp

[8] https://github.com/issp-center-dev/moller

[9] https://github.com/issp-center-dev/HPhi

[10] https://github.com/issp-center-dev/dsqss

Report of CCMS hands-on sessions in the 2023 fiscal year

Kota IDO

Institute for Solid State Physics,

The University of Tokyo, Kashiwa-no-ha, Kashiwa, Chiba 277-8581

In the 2023 fiscal year, Center for Computational Materials Science (CCMS) in the Institute for Solid State Physics (ISSP) held 4 hands-on sessions where the ISSP supercomputer was used [1-4]. In this report, we briefly summarize them.

Table 1 shows the list of the hands-on sessions in the 2023 fiscal year. There are 4 software used in the hands-on sessions: TeNeS, RESPACK, SALMON and 2DMAT. Development of the software except for SALMON was supported by "Project for advancement of software usability in materials science" (PASUMS) [5].

Table 1: List of CCMS hands-on sessions where the ISSP supercomputer was used in the 2023 fiscal year.

Date	Lecturer	Software
Nov. 20	T. Okubo et al.	TeNeS[6]
Jan. 11	K. Yoshimi et al.	RESPACK[7]
Fen. 22	S. Yamada et al.	SALMON[8]
Mar. 28	T. Hoshi et al.	2DMAT[9]

Features of each software are as follows. TeNeS is open-source software for performing simulations for quantum many-body systems by using tensor network methods [6]. RESPACK is a software package for *ab initio* downfolding methods [7]. SALMON is open-source software for performing *ab initio* calculations of electron dynamics in materials [8]. 2DMAT is a Python package to search an optimal result of a given optimization problem by using search algorithms combined with direct-problem solvers [9].

In all of the hands-on sessions, lecturers explained the basics of each software and gave its tutorial. Materials of some hands-on sessions are available on each official page.

References

[1] https://ccms.issp.u-tokyo.ac.jp/event/6260

[2] https://ccms.issp.u-tokyo.ac.jp/event/6293

[3] https://ccms.issp.u-tokyo.ac.jp/event/6310

[4] https://ccms.issp.u-tokyo.ac.jp/event/6432

[5] https://www.pasums.issp.u-tokyo.ac.jp

[6] https://www.pasums.issp.u-tokyo.ac.jp/tenes/en

[7] https://sites.google.com/view/kazuma7k6r

[8] https://salmon-tddft.jp

[9] https://www.pasums.issp.u-tokyo.ac.jp/2dmat/en/

Supercomputer course of Computational Materials Design (CMD®) workshop

Masaaki GESHI[1], Yoshitada MORIKAWA[2], Tomoya ONO[3]

[1]*R^3 Institute for Newly-Emerging Science Design,*
Osaka University, Machikaneyama, Toyonaka, Osaka 560-0043

[2] *Department of Precision Engineering,*
Osaka University, Yamada-oka, Suita, Osaka 565-0871

[3]*Graduate School of Engineering,*
Kobe University, Rokkodai-cho, Nada, Kobe 657-8501

The 41st Computational Materials Design (CMD®) workshop (CMD41) has been held from September 5th to September 9th and the 42nd CMD® workshop (CMD42) has been done from February 20th to February 24th. Both were held online. In this workshop we have the supercomputer course to train up human resources to advance research by using system B supercomputer of ISSP, the University of Tokyo.

In CMD41, nine participants took the supercomputer course and followed a tutorial on STATE-Senri developed by Y. Morikawa. After an introductory lecture on large-scale computing and an explanation of how to use the supercomputer of ISSP by M. Geshi, the participants started constructing computational models for their own research subjects with the help of the lecturers. Then they carried out calculations using supercomputers. Specific themes included molecular adsorption on solid surfaces, chemical reactions of molecules in solutions, chemical reactions of molecules on catalytic surfaces, reactions at solid-solid interfaces, and so on. The participants performed calculations and examined their results.

In CMD42 three participants took the supercomputer course and used the supercomputer of ISSP. They got a tutorial on RSPACE developed by T. Ono. After giving the introductory lecture of large-scale computing by M. Geshi and introducing the calculation method of electronic structures and electron conduction property using RSPACE, exercises instructed in the textbook were carried out. Then, electronic structure calculations were carried out for various molecules, and the electronic density distribution was visualized. The attendees also performed massively parallel calculations to confirm the efficiency for parallel computing. Finally, the electron conduction properties of two-dimensional materials and dialectic materials sandwiched between metallic electrodes were investigated.

4 PUBLICATION LIST

Example:

LASTNAME, Firstname [project class; # points (B), # points (C)] (Page #)

— *Project title*

1. First paper
   Names of Authors, etc.
2. Second paper
   ...

□ ISSP Joint Research Projects

○ B–E classes

AKASHI, Ryosuke [B class; 600 (B), 100 (C)] (180)

— *Renormalized charge-spin fluctuations from first principles*

1. Semiconducting Electronic Structure of the Ferromagnetic Spinel $HgCr_2Se_4$ Revealed by Soft-X-Ray Angle-Resolved Photoemission Spectroscopy
   Hiroaki Tanaka, Andrei V Telegin, Yurii P Sukhorukov, Vladimir A Golyashov, Oleg E Tereshchenko, Alexander N Lavrov, Takuya Matsuda, Ryusuke Matsunaga, Ryosuke Akashi, Mikk Lippmaa, Yosuke Arai, Shinichiro Ideta, Kiyohisa Tanaka, Takeshi Kondo, Kenta Kuroda Physical Review Letters **130**, 186402 (2023).
   DOI:10.1103/PhysRevLett.130.186402

AOYAMA, Kazushi [B class; 500 (B), 100 (C)] (342)

— *Field-induced chirality in breathing-kagome antiferromagnets*

ARAI, Munehito [C class; 6400 (B), 0 (C)] (266)

— *Development of a general method for rationally improving enzymatic activity*

— *Rational design of novel proteins for drug discovery*

1. Accurate prediction of protein folding mechanisms by simple structure-based statistical mechanical models
   K, Ooka, and M. Arai Nature Communications **14**, 6338 (2023).
   DOI:10.1038/s41467-023-41664-1

2. Crucial residue for tuning thermal relaxation kinetics in the biliverdin-binding cyanobacteriochrome photoreceptor revealed by site-saturation mutagenesis
   T. Suzuki, M. Yoshimura, M. Arai, and R. Narikawa J Mol Biol. **436**, 168451 (2024).
   DOI:10.1016/j.jmb.2024.168451

ARAKI, Takeaki [B,C class; 5200 (B), 670 (C)] (275, 276, 277)

— *Physical origin of forming ferroelectric nematic phase*

— *Study on Johari-Goldstein relaxation mode in glass-forming liquids*

— *Topological and mechanical properties of colloidal gels*

ARIMA, Kenta [B class; 800 (B), 0 (C)] (177)
— *Analysis of interface reaction between functional graphene and semiconductor surface*
— *Simulation of electronic structures of functional graphene sheets with wrinkles*

1. First-principles simulations of scanning tunneling microscopy images exhibiting anomalous dot patterns on armchair-edged graphene nanoribbons
   Junhuan Li, Kouji Inagaki, and Kenta Arima, Physical Review Research, **6**, 013252 (2024).
   DOI:10.1103/PhysRevResearch.6.013252

ARUGA, Tetsuya [B class; 400 (B), 100 (C)] ()
— *Electronic structure and conductivity of novel indium thin film on semiconductor surface*

ASANO, Yuta [E class; 16000 (B), 1550 (C)] (259)
— *Large-scale molecular dynamics simulation of ultrasonic cavitation*
— *Molecular dynamics simulation of ultrasound cavitation*

BIN, Xu [C class; 5000 (B), 650 (C)] (96)
— *Elucidating the Thermal Transport Mechanisms at Semiconductor Interfaces*
— *Thermal transport across heterojunction between 2D materials and substrate*

BUI, VANPHO [C class; 1600 (B), 0 (C)] (158)
— *Study on the removal mechanism of Copper Oxide processing in catalyst-referred etching method*

CAMPOS, Dos [C class; 2200 (B), 0 (C)] (143)
— *Exploring the Role of Neutral Molecules in All-solid-state Battery Electrolytes*

DEKURA, Shun [B,C class; 2200 (B), 100 (C)] (139)
— *First-principles calculations for phase stabilities and electronic structures of As-incorporated organoelemental materials*
— *First-principles calculations on the electronic states of novel organic semiconductors with extended hydrogen-bonding networks*
— *Unveiling the proton conduction pathways based on proton tautomerism in anhydrous molecular crystals by first-principles NEB calculations*

1. Precise Control of the Molecular Arrangement of Organic Semiconductors for High Charge Carrier Mobility
   R. Akai, K. Oka, S. Dekura, K. Yoshimi, H. Mori, R. Nishikubo, A. Saeki, N. Tohnai J. Phys. Chem. Lett. **14**, 34613467 (2023).
   DOI:10.1021/acs.jpclett.3c00334

EGAMI, Yoshiyuki [C class; 6000 (B), 300 (C)] (88)
— *First-principles electron-transport study on 2-dimensional SiC materials*
— *First-principles study on electron transport properties in molecule-adsorbed atomic layered materials*

1. GPU acceleration of conjugate gradient method obtaining Green's function for transport-property calculation
   T. Akamatsu, M. Uemoto, Y. Egami, and T. Ono, Comp. Phys. Commun. **295**, 108989 (2024).
   DOI:10.1016/j.cpc.2023.108989

FUCHIZAKI, Kazuhiro [C class; 2000 (B), 0 (C)] (305)
— *Kinetics of phase transition and polyamorphism*

1. Can weight hysteresis in a neural network judge the continuity/discontinuity of a phase transition?
   K. Nakamura and K. Fuchizaki, J. Phys. A: Math. Theor. **56**, 305002 (2023).
   DOI:10.1088/1751-8121/ace13e

FUJI, Kana [B class; 200 (B), 90 (C)] ()
— *Numerical studies on morphogenesis of organoids using a multicellular phase field model*

FUJI, Yohei [B class; 800 (B), 170 (C)] (321)
— *Dynamics of monitored quantum systems with symmetry*
— *Numerical study for stability of measurement-induced critical phenomena*

FUJII, Susumu [C class; 3000 (B), 0 (C)] (125)
— *Analysis of phonon-assisted ionic transport in solid electrolytes*

1. Discovery of unconventional proton-conducting inorganic solids via defect-chemistry-trained, interpretable machine learning
   S. Fujii, Y. Shimizu, J. Hyodo, A. Kuwabara, and Y. Yamazaki, Adv. Energy Mater., 2301892 (2023).
   DOI:10.1002/aenm.202301892

FUJIMOTO, Yoshitaka [C class; 1400 (B), 0 (C)] (160)
— *First-principles calculations of electronic transport of graphene*
— *Transport study of graphene layers*

1. Formation, structure, electronic and transport properties of nitrogen defects in graphene and carbon nanotubes
   Y. Fujimoto: submitted to Micromachine.

2. Modulation Doping and Quantum Transport in Double-Walled Boron-Nitride Nanotubes
   Y. Fujimoto and S. Saito: submitted to Physical Review Letters.

3. First-Principles Theoretical Design of Graphene-Based Field Effect Transistors
   Y. Fujimoto: Advanced Nanoscale MOSFET architectures: Current Trends and Future Perspectives, in press.

FUJINO, Tomoko [C class; 1800 (B), 400 (C)] (237)
— *Electronic structures for highly conducting oligomer conductors in single crystals*

1. Metallic State of a Mixed-sequence Oligomer Salt that Models Doped PEDOT Family
   K. Onozuka, T. Fujino, R. Kameyama, S. Dekura, K. Yoshimi, T. Nakamura, T. Miyamoto, T. Yamakawa, H. Okamoto, H. Sato, T. Ozaki, and H. Mori, J. Am. Chem. Soc. **145**, 15152 (2023).
   DOI:10.1021/jacs.3c01522

2. Single-crystalline oligomer-based conductors modeling the doped poly(3,4-ethylenedioxythiophene) family
   T. Fujino, R. Kameyama, K. Onozuka, K. Matsuo, S. Dekura, K. Yoshimi, and H. Mori, Faraday Discuss. **250**, 348 (2024).
   DOI:10.1039/D3FD00134B

FUJISAKI, Takaya [B class; 300 (B), 60 (C)] (202)
— *Search for optimal composition of reforming catalysts for high efficiency of fuel cells with direct biogas supply*

FUJISHIRO, Hiroki [C class; 2400 (B), 0 (C)] (137)
— *Strained Band-Structure Engineering for Antimonide-Based Terahertz Transistors*

FUJITA, Takatoshi [C class; 2600 (B), 0 (C)] (132)
— *First-Principles Investigation of Energy-Conversion Processes in Biological and Material Systems*

1. Ab Initio Study of Charge Separation Dynamics and PumpProbe Spectroscopy in the P3HT/PCBM Blend
   Takatoshi Fujita, Takeo Hoshi J. Phys. Chem. B 127 (2023) 7616.
   DOI:10.1021/acs.jpcb.3c02458

FUKUDA, Jun-ichi [B class; 800 (B), 180 (C)] (320)
— *Calculation of ordered structures, dynamics and optical properties of soft materials*

FUKUDA, Masahiro [B class; 400 (B), 100 (C)] (192)
— *Electronic stress tensor density analysis for material surfaces*

1. Electronic band structure change with structural transition of buckled Au_2X monolayers induced by strain
   Masahiro Fukuda, and Taisuke Ozaki, Phys. Chem. Chem. Phys., **26**, 3367 (2024)
   DOI:10.1039/D3CP03135G

Data Repository
Structural identification of silicene on the Ag(111) surface by atomic force microscopy
https://isspns-gitlab.issp.u-tokyo.ac.jp/masahiro.fukuda/root13_silicene_on_Ag111
DOI:10.1103/PhysRevB.98.195311

Atomic arrangement of Si adatom on the Silicene/Ag(111) surface
https://isspns-gitlab.issp.u-tokyo.ac.jp/masahiro.fukuda/T4_silicene_Si_adatom_on_Ag111
DOI:10.1016/j.apsusc.2023.157336

Electronic band structure change with structural transition of buckled Au_2X monolayers induced by strain
https://isspns-gitlab.issp.u-tokyo.ac.jp/masahiro.fukuda/buckled-Au2X
DOI:10.1039/D3CP03135G

FUKUI, Ken-ichi [C class; 2800 (B), 100 (C)] (301)
— *Analyses on the Potential-dependent Dynamics of Ionic Liquid Forming Electric Double Layer Facing the Electrodes*

FUKUMOTO, Yoshiyuki [B class; 800 (B), 0 (C)] (327, 328)
— *Impact of direction of the Dzyaloshinskii-Moriya vector on the magnon dispersion of the q=0 state in Kagome-lattice systems*
— *Numerical study of dynamical structure factors based on spinon operator representation of Heisenberg antiferromagnets*

1. A Series Expansion Study for Large Negative Quantum Renormalization of Magnon Spectra in the S =1/2 Kagome-Lattice Heisenberg Antiferromagnet $\{Cs_2Cu_3SnF_{12}\}$
   Singo Kogure, Masashi Takeda, Katsuhiro Morita, Yoshiyuki Fukumoto, Mutsuki Saito, and Hidekazu Tanaka: J. Phys. Soc. Jpn. 92, 113703, (2023).
   DOI:10.7566/JPSJ.92.113703

GOHDA, Yoshihiro [C class; 8800 (B), 900 (C)] (64)
— *Electron theory of magnetocrystalline anisotropy*
— *Phonon effects in phase equilibria*

1. Clarification of origin of positive excess volume of PdFe binary alloys by using first-principles calculations and HAXPES
   M. Watanabe, Y. Takagi, T. Tanaka, Y. Gohda, M. Adachi, M. Uchikoshi, T. Nakamura, M.

Takata, and H. Fukuyama, Acta Mater. **267**, 119718 (2024).
DOI:10.1016/j.actamat.2024.119718

2. Strain-induced specific orbital control in a Heusler-alloy-based interfacial multiferroics
J. Okabayashi, T. Usami, A.M. Yatmeidhy, Y. Murakami, Y. Shiratsuchi, R. Nakatani, Y. Gohda, and K. Hamaya, NPG Asia Mater. **16**, 3 (2024).
DOI:10.1038/s41427-023-00524-6

3. Unidirectional Nano-Modulated Binding and Electron Scattering in Epitaxial Borophene
S. Kamal, I. Seo, P. Bampoulis, M. Jugovac, C.A. Brondin, T. Menteş, I. Šarić-Janković, A. Matetskiy, P. Moras, P. Sheverdyaeva, T. Michely, A. Locatelli, Y. Gohda, M. Kralj, M. Petrović, ACS Appl. Mater. Interfaces 15, 57890 (2023).
DOI:10.1021/acsami.3c14884

4. Metastable Co3Mn/Fe/Pb(Mg1/3Nb2/3)O3-PbTiO3 multiferroic heterostructures
Y. Murakami, T. Usami, R. Watarai, Y. Shiratsuchi, T. Kanashima, R. Nakatani, Y. Gohda and K. Hamaya, J. Appl. Phys. 134, 224101 (2023).
DOI:10.1063/5.0180644

5. Unveiling the Origin of Large Coercivity in (Nd, Dy)-Fe-B Sintered Magnets
X. Tang, J.N. Li, H. Sepehri-Amin, A. Bolyachkin, A. Martin-Cid, S. Kobayashi, Y. Kotani, M. Suzuki, A. Terasawa, Y. Gohda, T. Ohkubo, T. Nakamura, and K. Hono, NPG Asia Mater. 15, 50 (2023).
DOI:10.1038/s41427-023-00498-5

6. Strain-induced magnetic anisotropy in Heusler alloys studied from first principles
A.M. Yatmeidhy and Y. Gohda, Appl. Phys. Express 16, 053001 (2023).
DOI:10.35848/1882-0786/accfe1

7. Subphase exploration for SmFe12-based permanent magnets by Gibbs energies obtained with first-principles cluster-expansion method
S. Enomoto, S. Kou, T. Abe, and Y. Gohda, J. Alloys Compd. 950, 169849 (2023).
DOI:10.1016/j.jallcom.2023.169849

GOHLKE, Matthias [C class; 1000 (B), 200 (C)] (313)
— *Ground state and dynamical properties of the J_1J_2K-Heisenberg model on the square lattice*

GONOME, Hiroki [C class; 3800 (B), 600 (C)] (209)
— *Study of the principle of photothermal conversion by ab initio calculations*

HAGITA, Katsumi [C class; 1400 (B), 500 (C)] (307)
— *Physical properties of crosslinked polymer networks through network topology analysis*

1. All-atom molecular dynamics simulations of poly(ethylene glycol) networks in water for evaluating negative energetic elasticity
K. Hagita, S. Nagahara, T. Murashima, T. Sakai, N. Sakumichi, Macromolecules **56**, 8095 (2023).
DOI:10.1021/acs.macromol.3c01121

HAMADA, Ikutaro [C class; 7400 (B), 500 (C)] (78)
— *Density functional theory study of adsorption and reaction of molecules on metal surfaces*

1. Oxygen Reduction Reaction on Single-Atom Catalysts From Density Functional Theory Calculations Combined with an Implicit Solvation Model
A. F. Z. Abidin and I. Hamada J. Phys. Chem. C 127, 13623 (2023).
DOI:10.1021/acs.jpcc.3c02224

2. Electronic and optical properties of the hydrogen boride sheet from the many-body perturbation theory
L. T. Ta, Y. Morikawa, and I. Hamada J. Phys.: Condens. Matter 35, 435002 (2023).
DOI:10.1088/1361-648X/ace8e3

HAMAGUCHI, Satoshi [C class; 6200 (B), 750 (C)] ()
— *Development of atomic interaction models for reactive sputtering simulation by machine learning*
— *Surface reaction analyses for atomic layer processes*

HAMAMOTO, Yuji [C class; 1200 (B), 0 (C)] (164)
— *Structure search of the T phase in silicene on the Ag(111) surface by Gaussian process regression*
1. Stability of Pd_xO_y Particles Supported on Strontium Titanate Perovskite under Three-Way Catalyst Operating Conditions: Implications for Sintering Resistance
T. N. Pham, B. A. C. Tan, Y. Hamamoto, K. Inagaki, I. Hamada, and Y. Morikawa ACS Catal. **14**, 1443 (2024).
DOI:10.1021/acscatal.3c05673

2. Machine-learned search for the stable structures of silicene on Ag(111)
Y. Hamamoto, T. N. Pham, M. K. Bisbo, B. Hammer, and Y. Morikawa Phys. Rev. Materials **7**, 124002 (2023).
DOI:10.1103/PhysRevMaterials.7.124002

HARADA, KENJI [C class; 800 (B), 500 (C)] (310)
— *Application of tensor networks in tensor data analysis*

HARASHIMA, Yosuke [C class; 1000 (B), 0 (C)] (168)
— *Materials exploration using materials informatics*
1. Finite temperature effects on the structural stability of Si-doped HfO_2 using first-principles calculations
Y. Harashima, H. Koga, Z. Ni, T. Yonehara, M. Katouda, A. Notake, H. Matsui, T. Moriya, M. K. Si, R. Hasunuma, A. Uedono, and Y. Shigeta, Appl. Phys. Lett. **122**, 262903 (2023).
DOI:10.1063/5.0153188

HARUYAMA, Jun [C class; 3000 (B), 500 (C)] (15)
— *Electrochemical reaction analysis using density functional calculation + implicit solvation model 5*
1. First-principles study of water adsorption monolayer on Pt(111): Adsorption energy and second-order nonlinear susceptibility
J. Haruyama, T. Sugimoto, and O. Sugino, Phys. Rev. Mater. **7**, 115803 (2023).
DOI:10.1103/PhysRevMaterials.7.115803

Data Repository
QE input for H20 adsorption monolayer system on Pt(111)
https://isspns-gitlab.issp.u-tokyo.ac.jp/j-haruyama/Pt111_H2O-monolayer

HATANO, Naomichi [B class; 500 (B), 100 (C)] (341)
— *Numerical Simulation of A Novel Model of Two-Dimensional Quantum Active Particle*

HAYAMI, Satoru [C class; 3400 (B), 450 (C)] (290)
— *Search for magnetic skyrmion by machine learning*
1. Anisotropic spin model and multiple-Q states in cubic systems

R. Yambe and S. Hayami Physical Review B **107**, 174408 (2023).
DOI:10.1103/PhysRevB.107.174408

2. Field direction dependent skyrmion crystals in noncentrosymmetric cubic magnets: A comparison between point groups (O, T) and $T_{\rm d}$
S. Hayami and R. Yambe Physical Review B **107**, 174435 (2023).
DOI:10.1103/PhysRevB.107.174435

3. Antiferro Skyrmion Crystal Phases in a Synthetic Bilayer Antiferromagnet under an In-Plane Magnetic Field
S. Hayami Journal of Physical Society of Japan **92**, 084702 (2023).
DOI:10.7566/JPSJ.92.084702

4. Magnetic bubble crystal in tetragonal magnets
S. Hayami and Y. Kato Physical Review B **108**, 024426 (2023).
DOI:10.1103/PhysRevB.108.024426

5. Unconventional Hall effect and magnetoresistance induced by metallic ferroaxial ordering
S. Hayami, R. Oiwa, and H. Kusunose Physical Review B **108**, 085124 (2023).
DOI:10.1103/PhysRevB.108.085124

6. Checkerboard bubble lattice formed by octuple-period quadruple-Q spin density waves
S. Hayami Physical Review B **108**, 094415 (2023).
DOI:10.1103/PhysRevB.108.094415

7. Chern insulating state with double-Q ordering wave vectors at the Brillouin zone boundary
S. Hayami Physical Review B **108**, 094416 (2023).
DOI:10.1103/PhysRevB.108.094416

8. Uniform and Staggered electric axial moment in zigzag chain
S. Hayami Physical Review B **108**, 094106 (2023).
DOI:10.1103/PhysRevB.108.094106

9. Time-reversal switching responses in antiferromagnets
S. Hayami and H. Kusunose Physical Review B **108**, L140409 (2023).
DOI:10.1103/PhysRevB.108.L140409

10. Chiral charge as hidden order parameter in URu_2Si_2
S. Hayami and H. Kusunose Journal of Physical Society of Japan **92**, 123703 (2023).
DOI:10.7566/JPSJ.92.123703

11. Multiple-q Dipole-Quadrupole Instability in Spin-1 Triangular-Lattice Systems
S. Hayami and K. Hattori Journal of Physical Society of Japan **92**, 124709 (2023).
DOI:10.7566/JPSJ.92.124709

12. Three-sublattice antiferro-type and ferri-type skyrmion crystals in magnets without the Dzyaloshinskii-Moriya interaction
S. Hayami Physical Review B **109**, 014415 (2024).
DOI:10.1103/PhysRevB.109.014415

13. Hybrid skyrmion and anti-skyrmion phases in polar C_{4v} systems
S. Hayami Physical Review B **109**, 054422 (2024).
DOI:10.1103/PhysRevB.109.054422

HIDA, Kazuo [B class; 500 (B), 100 (C)] (339)
— *Numerical Study of One Dimensional Frustrated Quantum Spin Systems*

1. Ground-State Phase Diagram of (1/2, 1/2, 1) Mixed Diamond Chains
   K. Hida, J. Phys. Soc. Jpn. **93**,044703 (2024).
   DOI:10.7566/JPSJ.93.044703

HIGUCHI, Yuji [C class; 5600 (B), 700 (C)] (272)
— *Rotational diffusion of water molecules on phospholipid bilayers*
— *Self-assembly processes of amphiphilic molecules and their structural controls*

1. Coarse-grained molecular dynamics simulation of cation distribution profiles on negatively charged lipid membranes during phase separation
   Yuji Higuchi, Klemen Bohinc, Jurij Rečsčič, Naofumi Shimokawa, and Hiroaki Ito, Soft Matter **19**, 3640 (2023).
   DOI:10.1039/d3sm00222e

2. Quasi-elastic neutron scattering reveals the relationship between the dynamical behavior of phospholipid headgroups and hydration water
   Md. Khalidur Rahman, Takeshi Yamada, Norifumi L. Yamada, Mafumi Hishida, Yuji Higuchi, and Hideki Seto, Struct. Dyn. **10**, 044701 (2023).
   DOI:10.1063/4.0000184

3. Lateral Transport of Domains in Anionic Lipid Bilayer Membranes under DC Electric Fields: A Coarse-Grained Molecular Dynamics Study
   Hiroaki Ito, Naofumi Shimokawa, and Yuji Higuchi, J. Phys. Chem. B **127**, 8860 (2023).
   DOI:10.1021/acs.jpcb.3c04351

4. Absorption of water molecules on the surface of stereocomplex-crystal spherulites of polylactides: An in-situ FT-IR spectroscopy investigation
   Tomoka Kokuzawa, Shunryu Hirabayashi, Yuka Ikemoto, Junsu Park, Ryohei Ikura, Yoshinori Takashima, Yuji Higuchi, and Go Matsuba, Polymer **298**, 126922 (2024).
   DOI:10.1016/j.polymer.2024.126922

HINUMA, Yoyo [B class; 300 (B), 0 (C)] (207)
— *Reactivity analysis of high entropy alloys for catalyst informatics*

HIRATA, Kenji [C class; 800 (B), 0 (C)] ()
— *First-principles investigation of electronic state and piezoelectric property in oxide-based phosphor*

HIYAMA, Miyabi [B class; 400 (B), 0 (C)] (351)
— *Theoretical study for absorption and fluorescence spectra of firefly bioluminescence substrate analogs*

1. Experimental and Theoretical Study for Core Excitation of Firefly Luciferin in Carbon K - Edge Spectra
   Y. Kudo, F. Kumaki, M. Nagasaka, J-i. Adachi, Y. Noguchi, N. Koga, H. Itabashi, and M. Hiyama, J. Phys. Chem. A **128**, 611 (2024).
   DOI:10.1021/acs.jpca.3c07504

HO, Ngoc [C class; 1400 (B), 400 (C)] (155)
— *Electronic and transport properties of transition metal monosilicides for thermoelectric applications: KKR-CPA calculations*

1. Insight into Scattering Mechanisms and Transport Properties of AgCuS for Flexible Thermoelectric Applications
   Nam, Ho Ngoc and Phung, Quan Manh and Suzuki, Katsuhiro and Masago, Akira and Shinya,

Hikari and Fukushima, Tetsuya and Sato, Kazunori, ACS Appl. Mater. Interfaces **15**, 43871-43879 (2023).
DOI:10.1021/acsami.3c09437

2. Exploring finite-temperature electronic transport in CoSi alloys with transition metals (Cr, Mn, Fe, and Ni) using the KKR-CPA method
Nam, Ho Ngoc and Phung, Quan Manh and Suzuki, Katsuhiro and Shinya, Hikari and Masago, Akira and Fukushima, Tetsuya and Sato, Kazunori, J. Mater. Chem. A **12**, 451-459 (2024).
DOI:10.1039/D3TA06259G

HOSHI, Takeo [C class; 3800 (B), 500 (C)] (103)
— *HPC-based fusion of quantum simulation, experiment analysis and data-driven science*

1. A fast and efficient computation method for reflective diffraction simulations
S. Kudo, Y. Yamamoto, T. Hoshi Computer Physics Communications 296, 109029 (2024).
DOI:10.1016/j.cpc.2023.109029

Data Repository
2DMAT Gallery
https://isspns-gitlab.issp.u-tokyo.ac.jp/2dmat-dev/2dmat-gallery

HOSONO, Nobuhiko [C class; 3200 (B), 450 (C)] (295)
— *All-Atom Molecular Dynamics Simulation Study of Polymer Dynamics in Nanoporous Materials*

HOTTA, Takashi [C class; 3200 (B), 0 (C)] (233)
— *Research of Three-Channel Kondo Effect Emerging from Tb and Tm Ions*

HUKUSHIMA, Koji [C class; 1200 (B), 100 (C)] ()
— *Molecular dynamics study of Chromatin molecular model*

IDO, Kota [C class; 8200 (B), 850 (C)] (223)
— *Many-body topological phases in frustrated magnets*
— *Many-body topological phases in strongly correlated electron systems*

1. Update of HΦ: Newly added functions and methods in versions 2 and 3
Kota Ido, Mitsuaki Kawamura, Yuichi Motoyama, Kazuyoshi Yoshimi, Youhei Yamaji, Synge Todo, Naoki Kawashima, Takahiro Misawa Comput. Phys. Commun. **298**, 109093 (2024).
DOI:10.1016/j.cpc.2024.109093

2. Data Analysis of Ab initio Effective Hamiltonians in Iron-Based Superconductors — Construction of Predictors for Superconducting Critical Temperature
Kota Ido, Yuichi Motoyama, Kazuyoshi Yoshimi, Takahiro Misawa J. Phys. Soc. Jpn. **92**, 064702 (2023).
DOI:10.7566/JPSJ.92.064702

3. Interface tool from Wannier90 to RESPACK: wan2respack
Kensuke Kurita, Takahiro Misawa, Kazuyoshi Yoshimi, Kota Ido, Takashi Koretsune Comput. Phys. Commun. 292, 108854 (2023).
DOI:10.1016/j.cpc.2023.108854

Data Repository
Update of HΦ: Newly added functions and methods in versions 2 and 3
https://isspns-gitlab.issp.u-tokyo.ac.jp/hphi-dev/hphi-paper2023

Interface tool from Wannier90 to RESPACK wan2respack

https://isspns-gitlab.issp.u-tokyo.ac.jp/kido902/wan2respack_paper

IITAKA, Toshiaki [C class; 2600 (B), 500 (C)] (123)
— *Extension of finite temperature calculation with random-phase sates to general variational wave functions*
— *Miscible-Immiscible Transition of Hydrous Silicate Melt*

IKEDA, Hiroaki [B class; 500 (B), 100 (C)] ()
— *Ab initio calculations of spin currents and chirality in chiral materials*

IKUHARA, Yuichi [C class; 6400 (B), 0 (C)] (87)
— *Exploring stable interface atomic structures and properties by first-principles calculations*
— *Structural analysis and property prediction of grain-boundary segregation by first-principles calculations*

IMADA, Masatoshi [E class; 14000 (B), 1500 (C)] (220)
— *Long-time simulation for strongly-correlated quantum systems*

1. Quantum criticality of bandwidth-controlled Mott transition
   Kensaku Takai, Youhei Yamaji, Fakher F. Assaad, Masatoshi Imada Phys. Rev. Res. **5**, 033186 (2023).
   DOI:10.1103/PhysRevResearch.5.033186

2. Superconductivity studied by solving ab initio low-energy effective Hamiltonians for carrier doped CaCuO2, Bi2Sr2CuO6, Bi2Sr2CaCu2O8, and HgBa2CuO4
   Michael Tobias Schmid, Jean-Baptiste More, Ryui Kaneko, Youhei Yamaji, Masatoshi Imada Phys. Rev. X **13**, 041036 (2023).
   DOI:10.1103/PhysRevX.13.041036

INAGAKI, Kouji [B class; 200 (B), 100 (C)] (206)
— *Analyses of diamond surface processes by machine-learing based potentials*

INAOKA, Takeshi [B class; 400 (B), 90 (C)] (193)
— *Search and realization of novel electronic properties of surfaces and interfaces and of nanostructures*

1. First principles study of electronic structure of x-form phthalocyanine crystals doped with one-dimensional iodine atomic chains
   T. Inaoka, submitted in J. Chem. Phys.

ISHIBASHI, Shoji [C class; 2000 (B), 0 (C)] (152)
— *Prediction of properties of organic ferroelectrics and piezoelectrics by first-principles calculations*

1. Competition of polar and antipolar states hidden behind a variety of polarization switching modes in hydrogen-bonded molecular chains
   Sachio Horiuchi, Hiromi Minemawari, and Shoji Ishibashi, Mater. Horizons **10**, 2149 (2023).
   DOI:10.1039/d2mh01530g

2. A straightforward method using the sign of the piezoelectric coefficient to identify the ferroelectric switching mechanism
   Shoji Ishibashi, Reiji Kumai, and Sachio Horiuchi, Sci. Rep. **13**, 8810 (2023).
   DOI:10.1038/s41598-023-34923-0

ISHIDA, Kunio [B class; 700 (B), 150 (C)] ()
— *Dynamics of photoinduced entanglement generation in electron-phonon systems*
— *Photoinduced entanglement generation dynamics in electron-phonon systems*

ISHII, Fumiyuki [C class; 9200 (B), 900 (C)] (62)
— *Development and applications of first-principles computational methods using Berry phase of Bloch wavefunctions*
— *First-principles calculation of van der Waals magnet*

1. First-principles study of anomalous Nernst effect in Cr-doped Bi_2Se_3
   R. Syariati, V. Saraswati, H. Sawahata, N. Yamaguchi, and F. Ishii Jpn. J. Appl. Phys. **63**, 01SP26 (2024).
   DOI:10.35848/1347-4065/acfe17

2. Thermoelectric Effect in Kagome Lattice Enhanced at Van Hove Singularities
   K. Shibata, N. Yamaguchi, H. Sawahata, and F. Ishii J. Phys. Soc. Jpn. **92**, 124704 (2023).
   DOI:10.7566/JPSJ.92.124704

ISHIKAWA, Takahiro [C class; 3000 (B), 400 (C)] (118)
— *Search for high temperature superconductivity in hydrides*

1. Evolutionary search for superconducting phases in the lanthanum-nitrogen-hydrogen system with universal neural network potential
   T. Ishikawa, Y. Tanaka, and S. Tsuneyuki Phys. Rev. B **109**, 094106 (2024).
   DOI:10.1103/PhysRevB.109.094106

2. Evolutionary Search for Superconducting Phases in the Lanthanum-Nitrogen-Hydrogen System with Universal Neural Network Potential PFP
   T. Ishikawa and S. Tsuneyuki Proceeding of CCP2023.

ISOBE, Masaharu [B class; 500 (B), 100 (C)] (337)
— *Equilibration and glass transition in self-propelled hard polygon systems*

1. Phase transition in dense hard triangle systems by Newtonian Event-Chain Monte Carlo
   T. Shirai, D. Mugita, and M. Isobe, Proceedings of the 29th Symposium on Traffic Flow and Self-driven Particles, **29**, 49 (2024).

IZUMI, Yasuo [B class; 500 (B), 100 (C)] (184)
— *Excited carrier transfer processes in the CO_2 photo reduction at semiconductor surfaces*

1. Adsorbed CO2-Mediated CO2 Photoconversion into Solar Fuel at the O Vacancy Site of Zirconium Oxide
   Keisuke Hara, Misa Nozaki, Rumiko Hirayama, Rento Ishii, Kaori Niki, and Yasuo Izumi The Journal of Physical Chemistry C, 127, 1776 (2023).
   DOI:10.1021/acs.jpcc.2c06048

JESCHKE, Harald [C class; 6400 (B), 0 (C)] ()
— *Fluctuation exchange approximation for superconductivity in FeSe intercalates*
— *Theoretical study of isoelectronic doping effects in iron-based superconductors*

JIE, Sun [C class; 1600 (B), 250 (C)] ()
— *The study of transport properties in two-dimensional materials on substrates using large-scale simulation methods based on machine learning*

JOUTSUKA, Tatsuya [C class; 1000 (B), 0 (C)] (166)
— *Reaction Analysis in Solid Catalysts by DFT Calculations and Informatics*

KADARISMAN, Hana [B class; 300 (B), 60 (C)] ()
— *First-principles calculation of diamond materials*

KAGAWA, Fumitaka [C class; 0 (B), 500 (C)] (247)
— *Numerical calculation of emergent electric field induced by current-driven non-collinear magnetic structure*

KAGESHIMA, Hiroyuki [C class; 2200 (B), 400 (C)] (130)
— *Study on physical properties of structural elementary excitations at solid surfaces and interfaces*

1. Theoretical study on island edges in CVD growth of hBN
   R. Imamura and H. Kageshima, Jpn. J. Appl. Phys. **63**, 04SP39 (2024).
   DOI:10.35848/1347-4065/ad2bbe

2. First-principles study on barrier height of silicon emission from interface into oxide during silicon thermal oxidation
   H. Kageshima, T. Akiyama, and K. Shiraishi, Jpn. J. Appl. Phys. **63**, 04SP08 (2024).
   DOI:10.35848/1347-4065/ad2bb9

KANEKO, Ryui [B class; 1000 (B), 180 (C)] (315, 317)
— *Study of quantum entanglement dynamics in free boson systems by computing the matrix permanent*
— *Variational Monte Carlo study of ground-state properties in effective models for Bi-based multilayered superconductors*

1. Dynamics of correlation spreading in low-dimensional transverse-field Ising models
   Ryui Kaneko and Ippei Danshita Phys. Rev. A 108, 023301 (2023).
   DOI:10.1103/PhysRevA.108.023301

2. Superconductivity Studied by Solving Ab Initio Low-Energy Effective Hamiltonians for Carrier Doped $CaCuO_2$, $Bi_2Sr_2CuO_6$, $Bi_2Sr_2CaCu_2O_8$, and $HgBa_2CuO_4$
   Michael Thobias Schmid, Jean-Baptiste Morée, Ryui Kaneko, Youhei Yamaji, and Masatoshi Imada Phys. Rev. X 13, 041036 (2023).
   DOI:10.1103/PhysRevX.13.041036

3. Quantum many-body scars in the Bose-Hubbard model with a three-body constraint
   Ryui Kaneko, Masaya Kunimi, and Ippei Danshita Phys. Rev. A 109, L011301 (2024).
   DOI:10.1103/PhysRevA.109.L011301

KARIYADO, Toshikaze [B class; 400 (B), 50 (C)] (253)
— *Band engineering and electron correlation effects in artificially stacked systems*

KASAMATSU, Shusuke [E class; 6000 (B), 950 (C)] (81)
— *Equilibrium/nonequilibrium electrochemistry of disordered solid-state interfaces*

1. Configuration sampling in multi-component multi-sublattice systems enabled by ab Initio Configuration Sampling Toolkit (abICS)
   Shusuke Kasamatsu, Yuichi Motoyama, Kazuyoshi Yoshimi, and Tatsumi Aoyama, Sci. Technol. Adv. Mater. Meth. **3**, 2284128 (2023).
   DOI:10.1080/27660400.2023.2284128

2. On-lattice 機械学習モデルを用いた固溶体のアンサンブルサンプリング
   笠松秀輔, アンサンブル 26 巻、p.48 (2024).

KATOW, Hiroki [B class; 400 (B), 70 (C)] ()
— *Development of First Principles methods for Light-Matter Interaction*

KAWAKATSU, Toshihiro [C class; 4000 (B), 0 (C)] (289)
— *Multiscale simulations for complex flows*

KAWAMURA, Hikaru [C class; 1800 (B), 0 (C)] ()
— *Novel order in frustrated magnets*

KAWANO, Shoya [B class; 400 (B), 0 (C)] (200)
— *Lattice thermal conductivity calculation of iridium oxide* $Ca_5Ir_3O_{12}$

KAWASHIMA, Naoki [E class; 29000 (B), 2650 (C)] (255)
— *Tensor-Network Study of Classical Random Spin Systems*

1. Generating Function for Projected Entangled-Pair States
   Wei-Lin Tu, Laurens Vanderstraeten, Norbert Schuch, Hyun-Yong Lee, Naoki Kawashima, and Ji-Yao Chen, Physical Review X 5, 010335 (2024).
   DOI:10.1103/PRXQuantum.5.010335

2. Possibility of a Topological Phase Transition in Two-dimensional RP3 Model
   Tsuyoshi Okubo and Naoki Kawashima, Journal of the Physical Society of Japan 92 114701 (2023).
   DOI:10.7566/JPSJ.92.114701

3. Ashkin-Teller phase transition and multicritical behavior in a classical monomer-dimer model
   Satoshi Morita, Hyun-Yong Lee, Kedar Damle and Naoki Kawashima, Physical Review Research 5 043061 (2023).
   DOI:10.48550/arXiv.2306.02578

4. Cubic ferromagnet and emergent U(1) symmetry on its phase boundary
   Wei-Lin Tu, Xinliang Lyu, S. R. Ghzanfari, Huan-Kuang Wu, Hyun-Yong Lee and Naoki Kawashima, Physical Review B 107, 224406 (2023).
   DOI:10.1103/PhysRevB.107.224406

KITAI, Koki [E class; 800 (B), 100 (C)] ()
— *Developing Prediction Model of Polymer Properties Based on Trajectory Data from Molecular Dynamics Simulation*

KITAO, Akio [C class; 5200 (B), 500 (C)] (280)
— *Efficient sampling simulation of the soft modes significantly contribute to protein properties*

1. 高圧による細菌べんモーターの回転制御
   畑 宏明 , 北尾 彰朗 高圧の科学と技術 33, 69 (2023).
   DOI:10.4131/jshpreview.33.69

2. Energetic and Kinetic Origins of CALB Interfacial Activation Revealed by PaCS-MD/MSM
   Tegar N. Wijaya and Akio Kitao J. Phys. Chem. B 127, 34, 7431 (2023).
   DOI:10.1021/acs.jpcb.3c02041

3. PaCS-Toolkit: Optimized Software Utilities for Parallel Cascade Selection Molecular Dynamics (PaCS-MD) Simulations and Subsequent Analyses
   Shinji Ikizawa, Tatsuki Hori, Tegar Nurwahyu Wijaya, Hiroshi Kono, Zhen Bai, Tatsuhiro Kimizono, Wenbo Lu, Duy Phuoc Tran, Akio Kitao J. Phys. Chem. B 128, 15, 3631 (2024).
   DOI:10.1021/acs.jpcb.4c01271

KOBAYASHI, Akito [B class; 400 (B), 100 (C)] (246)
— *Electron correlation-induced topological order and spatial inversion symmetry breaking in organic Dirac electron systems*

1. Compensated Ferrimagnets with Colossal Spin Splitting in Organic Compounds
   Taiki Kawamura, Kazuyoshi Yoshimi, Kenichiro Hashimoto, Akito Kobayashi, and Takahiro Misawa Phys. Rev. Lett. 132, 15, 156502 (2024).
   DOI:10.1103/PhysRevLett.132.156502

2. H-wave - A Python package for the Hartree-Fock approximation and the random phase approximation
   Tatsumi Aoyama, Kazuyoshi Yoshimi, Kota Ido, Yuichi Motoyama, Taiki Kawamura, Takahiro Misawa, Takeo Kato, Akito Kobayashi Computer Physics Communications 298, 109087 (2024).
   DOI:10.1016/j.cpc.2024.109087

KOBAYASHI, Katsuyoshi [B class; 400 (B), 100 (C)] (191)
— *Theoretical study on electronic properties of new nanoscale surfaces and interfaces*

KOBAYASHI, Nobuhiko [C class; 3400 (B), 450 (C)] (109)
— *Quantum transport theory by large scale first-principles electron transport calculations*

1. Electronic and magnetic properties of CoSb3, Cr-doped CoSb3, and related compound thin films
   K. Kobayashi, H. Takaki, M. Shimono, H. Ishii, N. Kobayashi, K. Hirose, T. Mori Jpn. J. Appl. Phys. 62 SC1046 (2023).
   DOI:10.35848/1347-4065/acb3ce

2. Asymmetrically Functionalized Electron-Deficient π-Conjugated System for Printed Single-Crystalline Organic Electronics,
   C. P. Yu, S. Kumagai, M. Tsutsumi, T. Kurosawa, H. Ishii, G. Watanabe, D. Hashizumi, H. Sugiura, Y. Tani, T. Ise, T. Watanabe, H. Sato, J. Takeya, and T. Okamoto, Adv. Sci. 10 2207440 (2023).
   DOI:10.1002/advs.202207440

3. Order-N calculations for thermoelectric power factor based on linear response theory
   H. Ishii, N. Kobayashi, K. Hirose J. Phys. Condens. Matter 36, 335903 (2024).
   DOI:10.1088/1361-648X/ad4a15

KOBAYASHI, Ryo [B class; 300 (B), 0 (C)] ()
— *Molecular dynamics analyses of electrode-electrolyte interfaces using reactive potentials*

KOBAYASHI, Yoshihiro [B class; 200 (B), 50 (C)] (356)
— *Molecular dynamics simulation of nanocarbon stacking structure*

1. Reduction of Interlayer Interaction in Multilayer Stacking Graphene with Carbon Nanotube Insertion: Insights from Experiment and Simulation
   M. Ding, T. Inoue, J. I. Enriquez, H. H. Halim, Y. Ogawa, Y. Taniyasu, Y. Hamamoto, Y. Morikawa, and Y. Kobayashi J. Phys. Chem. C **127**, 23768 (2023).
   DOI:10.1021/acs.jpcc.3c06132

KOGA, Akihisa [C class; 6000 (B), 450 (C)] (225)
— *Analyzing Ferromagnetic Order in Multi-Component Fermionic Systems using DMFT*
— *Magnetism for the half-filled Hubbard model on the two-dimensional quasiperiodic tilings*

KOMATSU, Hisato [B class; 400 (B), 90 (C)] (348)

— Consideration on the microscopic mechanism of the friction by the frictional force caused by magnetic structures

1. Transition between the stick and slip states in a simplified model of magnetic friction
   H. Komatsu, Phys. Rev. E 108 034803 (2023).
   DOI:10.1103/PhysRevE.108.034803

KOURA, Akihide [C class; 1600 (B), 0 (C)] (157)

— Machine learning study on static structure of light metals alloys based on it ab initio molecular dynamics

1. Efficient Training of the Machine-Learning Interatomic Potential Based on an Artificial Neural Network for Estimating the Helmholtz Free Energy of Alkali Metals
   S. Fukushima, K. Shimamura, A. Koura, and F. Shimojo J. Phys. Soc. Jpn. **92**, 054005 (2023).
   DOI:10.7566/JPSJ.92.054005

2. Construction of Machine-Learning Interatomic Potential Under Heat Flux Regularization and Its Application to Power Spectrum Analysis for Silver Chalcogenides
   K. Shimamura, A. Koura, and F. Shimojo Computer Physics Communications **294**, 108920 (2024).
   DOI:10.1016/j.cpc.2023.108920

3. Ab initio Molecular Dynamics of the Initial Growth of Few-Layer Graphene on a Cu-Ni(111) Catalyst
   E. B. Yutomo, F. A. Noor, T. Winata, K. Shimamura, A. Koura, and F. Shimojo J. Phys. Chem. C **127**, 19258 (2023).
   DOI:10.1021/acs.jpcc.3c04687

4. Large-scale Molecular-dynamics Simulations of SiO_2 Melt under High Pressure with Robust Machine-learning Interatomic Potentials
   D. Wakabayashi, K. Shimamura, A. Koura, and F. Shimojo J. Phys. Soc. Jpn. **92**, 074002 (2023).
   DOI:10.7566/JPSJ.92.074002

5. Atomic and electronic structures of an Ag-containing 4A zeolite
   S. Hosokawa, K. Kobayashi, A. Koura, F. Shimojo, Y. Tezuka, J. Adachi, Y. Onodera, S. Kohara, H. Tajiri, A. Chokkalingam, T. Wakihara Microporous Mesoporous Mater. **359**, 112662 (2023).
   DOI:10.1016/j.micromeso.2023.112662

6. Atomic and electronic structures on a Mordenite zeolite
   S. Hosokawa, H. Sato, Y. Tezuka, J. Adachi, K. Kimura, K. Hayashi, S, Kohara, H. Tajiri, K. Kobayashi, A. Koura, and F. Shimojo e-J. Surf. Sci. **22**, 25 (2024).
   DOI:10.1380/ejssnt.2023-063

7. Intermolecular Correlations in Liquid Lactic Acid Based on ab initio Molecular Dynamics Simulations Combined with High-Energy X-ray Diffraction Measurements
   K. Ito, H. Shimakura, S. Tahara, K. Ohara, K. Shimamura, A. Koura, and F. Shimojo J. Phys. Soc. Jpn., in press.
   DOI:10.7566/JPSJ.93.054601

KUNISADA, Yuji [C class; 6400 (B), 0 (C)] (86)

— Development of Ceramic Protective Coating for High Corrosion Resistance of Metallic Materials

1. Unveiling the Origin of Fast Hydride Ion Diffusion at Grain Boundaries in Nanocrystalline TiN Membranes
   Y. Kunisada, C. Kura, N. Sakaguchi, C. Zhu, H. Habazaki, and Y. Aoki, ACS Omega **9**, 13738 (2024).

DOI:10.1021/acsomega.3c08277

KUROKI, Kazuhiko [C class; 2600 (B), 0 (C)] (235)
— *Studies on unconventional superconductivity in nickelates*

1. Possible High T_c Superconductivity in $La_3Ni_2O_7$ under high pressure through manifestation of a nearly half-filled bilayer Hubbard model
   Hirofumi Sakakibara, Naoya Kitamine, Masayuki Ochi, and Kazuhiko Kuroki, Phys. Rev. Lett. **132**, 106002 (2024).
   DOI:10.1103/PhysRevLett.132.106002

2. Pair correlations in the two-orbital Hubbard ladder: Implications for superconductivity in the bilayer nickelate $La_3Ni_2O_7$
   Tatsuya Kaneko, Hirofumi Sakakibara, Masayuki Ochi, and Kazuhiko Kuroki, Phys. Rev. B **109**, 045154 (2024).
   DOI:10.1103/PhysRevB.109.045154

KUSAKABE, Koichi [C class; 4200 (B), 500 (C)] (102)
— *Response of nanographene device structures to external fields*

1. Terahertz-induced martensitic transformation in partially stabilized zirconia
   M. Nagai, Y. Higashitani, M. Ashida, K. Kusakabe, H. Niioka, A. Hattori, H. Tanaka, G. Isoyama, N. Ozaki, Commun. Phys. **6**, 88 (2023).
   DOI:10.1038/s42005-023-01207-y

2. Ultra-thin van der Waals magnetic tunnel junction based on monoatomic boron vacancy of hexagonal boron nitride
   H. Harfah, Y. Wicaksono, G. K. Sunnardianto, M. A. Majidi, and K. Kusakabe, Phys. Chem. Chem. Phys., **26**, 9733 (2024).
   DOI:10.1039/D4CP00218K

3. Possible bi-stable structures of pyrenebutanoic acid-linked protein molecules adsorbed on graphene: theoretical study
   Y. Oishi, M. Kitatani, and K. Kusakabe, Beilstein J. Org. Chem., **20**, 570 (2024).
   DOI:10.3762/bjoc.20.49

LEE, Minhyeok [C class; 1600 (B), 450 (C)] (149)
— *Modeling of the Ammonia Decomposition Reaction on Iron-based Material Surfaces*

LI, Hao [C class; 3800 (B), 0 (C)] (210)
— *Design of Effective Electrocatalysts by Theory and Ab Initio Computations*

MAEHIRA, Takahiro [B class; 400 (B), 100 (C)] (189)
— *Electronic Structure and Fermi surface of ReO_3*

MAKINO, Takayuki [B class; 400 (B), 90 (C)] (251)
— *Construction of ab-initio tight-binding Hamiltonian and determination of dielectric functions of rare-earth monoxides having insulating ground states*

1. Photoreflectance spectroscopy of BiOCl epitaxial thin films
   T. Nishiwaki, T. Makino, Z. Sun, D. Oka, T. Fukumura, Jpn. J. Appl. Phys., **63**, 02SP09 (2024).
   DOI:10.35848/1347-4065/ad0306

2. Evaluation of optical constants in oxide thin films using machine learning
   K. Saeki and T. Makino, Jpn. J. Appl. Phys., **62**, 081002 (2023).

DOI:10.35848/1347-4065/acea4b

MASAKI, Yusuke [B class; 500 (B), 100 (C)] (336)
— *Bosonic excitation in spatially non-uniform superconductors and superfluids*

MATSUKAWA, Hiroshi [C class; 3600 (B), 450 (C)] ()
— *Physics of Friction*

MATSUSHITA, Katsuyoshi [C class; 1000 (B), 0 (C)] (319)
— *Division Plane Inference for Cell Division based on Computatinal Physics*
— *Statistical Physical Inference for Cell Division Plane*

1. Fluctuating Collective Cell Motion with Short-Range Order due to Contact Triggering
   Katsuyoshi Matsushita, Taiko Arakaki, Kouichi Fujimoto, Proceedings of the Symposium on Traffic Flow and Self-driven Particles 29, 41 (2024).

MATSUSHITA, Yu-ichiro [E class; 8300 (B), 1100 (C)] (69)
— *Electronic structure of wide-gap semiconductors based on first-principles calculations: from power devices to quantum devices*
— *Proposal for Free Devices Based on First-Principles Calculations: From Material Exploration to Device Fabrication*

1. Atomic scale localization of KohnSham wavefunction at SiO_2/4HSiC interface under electric field, deviating from envelope function by effective mass approximation
   Hironori Yoshioka, Jun-Ichi Iwata, and Yu-ichiro Matsushita Appl. Phys. Lett. 122, 222104 (2023).
   DOI:10.1063/5.0151547

2. First-quantized eigensolver for ground and excited states of electrons under a uniform magnetic field
   Taichi Kosugi , Hirofumi Nishi and Yu-ichiro Matsushita Jpn. J. Appl. Phys. 62, 062004 (2023).
   DOI:10.35848/1347-4065/acddc0

3. Skyrmions in van der Waals centrosymmetric materials with Dzyaloshinskii-Moriya interactions
   Hung Ba Tran, Yu-ichiro Matsushita Scripta Materialia 239, 115799 (2024).
   DOI:10.1016/j.scriptamat.2023.115799

4. Exhaustive search for optimal molecular geometries using imaginary-time evolution on a quantum computer
   Taichi Kosugi, Hirofumi Nishi, Yuichiro Matsushita npj Quantum Information volume 9, 112 (2023).
   DOI:10.1038/s41534-023-00778-6

5. Channel Attention for Quantum Convolutional Neural Networks
   Gekko Budiutama, Shunsuke Daimon, Hirofumi Nishi, Ryui Kaneko, Tomi Ohtsuki, Yu-ichiro Matsushita arXiv:2311.02871
   DOI:10.48550/arXiv.2311.02871

6. Temperature and size dependence of energy barrier for magnetic flips in $L1_0$ FePt nanoparticles: A theoretical study
   Hung Ba Tran, Yu-ichiro Matsushita Scripta Materialia 242:115947(2024).
   DOI:10.1016/j.scriptamat.2023.115947

7. Systematic study on the dependence of the warm-start quantum approximate optimization algorithm on approximate solutions

Ken N. Okada, Hirofumi Nishi, Taichi Kosugi, Yu-ichiro Matsushita Scientific Reports 14, 1167 (2024).
DOI:10.1038/s41598-023-50406-8

8. First-quantized adiabatic time evolution for the ground state of a many-electron system and the optimal nuclear configuration
Yusuke Nishiya, Hirofumi Nishi, Yannick Couzini, Taichi Kosugi, Yu-ichiro Matsushita Phys. Rev. A 109, 022423 (2024).
DOI:10.1103/PhysRevA.109.022423

MAYUMI, Koichi [B class; 400 (B), 100 (C)] (347)
— *Molecular Dynamics of Polymer Chain under Deformation*

MICHISHITA, Yoshihiro [B class; 300 (B), 90 (C)] (352)
— *Machine-Learning-Assisted Exploration of Appropriate Transformation and Projections*

MINAMI, Susumu [B class; 800 (B), 170 (C)] (170)
— *First-principles study of magnetic thermoelectric effect in topological magnets*
— *First-principles study of stable interfacial structure analysis and magnetic tunnel conductance in topological magnets*

MISAWA, Masaaki [B class; 400 (B), 0 (C)] (199)
— *Phonon properties based on nanoscale structures in two-dimensional materials*

1. Intermediate State between MoSe2 and Janus MoSeS during Atomic Substitution Process
H. Suzuki, Y. Liu, M. Misawa, C. Nakano, Y. Wang, R. Nakano, K. Ishimura, K. Tsuruta, Y. Hayashi Nano Letters **23**, 4533-4540 (2023).
DOI:10.1021/acs.nanolett.3c00972

2. Self-Limiting Growth of Monolayer Tungsten Disulfide Nanoribbons on Tungsten Oxide Nanowires
H. Suzuki, M. Kishibuchi, M. Misawa, K. Shimogami, S. Ochiai, T. Kokura, Y. Liu, R. Hashimoto, Z. Liu, K. Tsuruta, Y. Miyata, Y. Hayashi ACS Nano **17**, 9455-9467 (2023).
DOI:10.1021/acsnano.3c01608

MISAWA, Takahiro [D,E class; 23000 (B), 1650 (C)] (217)
— *Analysis of ab initio Hamiltonians for molecular solid (TMTTF)$_2$PF$_6$ under pressure*
— *Comprehensive ab initio investigation of high-Tc materials using database*

1. Compensated Ferrimagnets with Colossal Spin Splitting in Organic Compounds
Taiki Kawamura, Kazuyoshi Yoshimi, Kenichiro Hashimoto, Akito Kobayashi, and Takahiro Misawa Phys. Rev. Lett. 132, 156502 (2024).
DOI:10.1103/PhysRevLett.132.156502

2. Combined X-ray diffraction, electrical resistivity, and ab initio study of $(TMTTF)_2PF_6$ under pressure: implications to the unified phase diagram
Miho Itoi, Kazuyoshi Yoshimi, Hanming Ma, Takahiro Misawa, Takao Tsumuraya, Dilip Bhoi, Tokutaro Komatsu, Hatsumi Mori, and Yoshiya Uwatoko arXiv:2403.13816.
DOI:10.48550/arXiv.2403.13816

3. Comprehensive ab initio investigation of the phase diagram of quasi-one-dimensional molecular solids
Kazuyoshi Yoshimi, Takahiro Misawa, Takao Tsumuraya, and Hitoshi Seo, Phys. Rev. Lett. 131, 036401 (2023).
DOI:10.1103/PhysRevLett.131.036401

4. Kota Ido and Takahiro Misawa
Many-body Chern insulator in the Kondo lattice model on a triangular lattice arXiv:2310.07094.
DOI:10.48550/arXiv.2310.07094

Data Repository
tmttfpf6-pdep
https://isspns-gitlab.issp.u-tokyo.ac.jp/k-yoshimi/tmttfpf6-pdep

tm-salts
https://isspns-gitlab.issp.u-tokyo.ac.jp/k-yoshimi/tm-salts

edottf
https://isspns-gitlab.issp.u-tokyo.ac.jp/k-yoshimi/edottf

MITARAI, Yoko [B,D class; 1000 (B), 0 (C)] (165)
— *Phase equilibrium of high entropy alloys and shape memory alloys*

MIZUKAMI, Wataru [C class; 5000 (B), 900 (C)] (274)
— *Quantum-classical hybrid simulations for sensor materials based on quantum state tomography*

1. Comparative study on compact quantum circuits of hybrid quantum-classical algorithms for quantum impurity models
Rihito Sakurai, Oliver J. Backhouse, George H. Booth, Wataru Mizukami, Hiroshi Shinaoka, arXiv.2312.04105
DOI:10.48550/arXiv.2312.04105

2. Solvent distribution effects on quantum chemical calculations with quantum computers
Yuichiro Yoshida, Wataru Mizukami, Norio Yoshida, J. Chem. Theory Comput. 20, 5, 1962 (2024).
DOI:10.1021/acs.jctc.3c01189

3. Universal neural network potentials as descriptors: Towards scalable chemical property prediction using quantum and classical computers
Tomoya Shiota, Kenji Ishihara, Wataru Mizukami, arXiv.2402.18433
DOI:10.48550/arXiv.2402.18433

4. Ab initio extended Hubbard model of short polyenes for efficient quantum computing
Yuichiro Yoshida, Nayuta Takemori, Wataru Mizukami, arXiv.2404.01623
DOI:10.48550/arXiv.2404.01623

MOCHIZUKI, Masahito [C class; 2200 (B), 50 (C)] (23)
— *Theoretical study on photoinduced nonequilibrium electron states in spin-orbit coupling systems and strongly correlated electron systems*

1. Theory of collective excitations in the quadruple-Q magnetic hedgehog lattices
Rintaro Eto, and Masahito Mochizuki Physical Review Letters 132, 226705 (2024).
DOI:10.1103/PhysRevLett.132.226705

MOCHIZUKI, Yasuhide [C class; 5200 (B), 500 (C)] (94)
— *Quasi-harmonic approximated and molecular dynamic calculations for phonon-induced negative-thermal-expansion materials*

1. Mechanism of Negative Thermal Expansion in Monoclinic Cu2P2O7 from First Principles
Y. Mochizuki, K. Nagamatsu, H. Koiso, T. Isobe, and A. Nakajima The Journal of Physical Chemistry Letters 15, 156 (2024).

DOI:10.1021/acs.jpclett.3c02856

2. Thermal Properties of the Element and Binary Oxides toward Negative Thermal Expansion: A First-Principles Lattice-Dynamics Study
Y. Mochizuki, H. Koiso, K. Nagamatsu, S. Bae, T. Isobe, A. Nakajima The Journal of Physical Chemistry C 128, 525 (2024).
DOI:10.1021/acs.jpcc.3c06507

3. Superlattice MAX phases with A-layers reconstructed into 0D-clusters, 1D-chains, and 2D-lattices
M. Khazaei, S. Bae, R. Khaledialidusti, A. Ranjbar, H.-P. Komsa, S. Khazaei, M. Bagheri, V. Wang, Y. Mochizuki, M. Kawamura, G. Cuniberti, S. M. Allaei, K. Ohno, H. Hosono, and H. Raebiger J. Phys. Chem. C **127**, 14906 (2023).
DOI:10.1021/acs.jpcc.3c02233

MORI, Hatsumi [C,D class; 5600 (B), 0 (C)] (98)
— *First-principles NEB calculations of proton tautomeric conduction pathways*
— *First-principles NEB calculations of proton tautomeric conduction pathways (II)*
— *First-principles NEB calculations of proton tautomeric conduction pathways(I)*

MORI, RYO [B class; 400 (B), 70 (C)] ()
— *Investigation of spin and electronic structures in surface/interface of topological insulator thin films*

MORIKAWA, Yoshitada [E class; 14000 (B), 2400 (C)] (56)
— *Theoretical study on dynamical processes in heterogeneous catalysis using density functional theory and machine learning methods*

1. The quantitative study of methane adsorption on the Pt(997) step surface as the initial process for reforming reactions
Y. H. Choi, S. E. M. Putra, Y. Shiozawa, S. Tanaka, K. Mukai, I. Hamada, Y. Morikawa, J. Yoshinobu Surf. Sci. **732**, 122284 (2023).
DOI:10.1016/j.susc.2023.122284

2. Electronic and optical properties of the hydrogen boride sheet from the many-body perturbation theory
Luong Thi Ta, Yoshitada Morikawa, and Ikutaro Hamada J. Phys.: Condens. Matter **35** 435002 (2023).
DOI:10.1088/1361-648X/ace8e3

3. Machine learning molecular dynamics simulation of CO-driven formation of Cu clusters on the Cu(111) surface
H. H. Halim, R. Ueda, and Y. Morikawa J. Phys. : Condens. Matter, **35**, 495001 (2023).
DOI:10.1088/1361-648X/acf2d8

4. First-principles Microkinetic Study of NO Reduction on Cu Catalysts
M. R. Al Fauzan, T. N. Pham, H. H. Halim, Y. Hamamoto, K. Inagaki, I. Hamada, and Y. Morikawa J. Phys. Chem. C, **127**, 19451 (2023).
DOI:10.1021/acs.jpcc.3c02820

5. DFT investigation of the oxygen reduction reaction over nitrogen (N) doped graphdiyne as an electrocatalyst: the importance of pre-adsorbed OH* and the solvation effect
Y. Wang, T. N. Pham, H. H. Halim, L. Yan, and Y. Morikawa Materials Advances, **4**, 6542 (2023).
DOI:10.1039/D3MA00502J

6. Machine-learned search for the stable structures of silicene on Ag(111)
Y. Hamamoto, T. N. Pham, M. K. Bisbo, B. Hammer, and Y. Morikawa Phys. Rev. Mater., **7**,

124002 (2023).
DOI:10.1103/PhysRevMaterials.7.124002

7. Stability of Pd_xO_y Particles Supported on Strontium Titanate Perovskite under Three-Way Catalyst Operating Conditions: Implications for Sintering Resistance
T. N. Pham, B. A. Choi Tan, Y. Hamamoto, K. Inagaki, I. Hamada, and Y. Morikawa ACS Catal., **14**, 1443 (2024).
DOI:10.1021/acscatal.3c05673

8. Origin of the Surface Facet Dependence in the Oxidative Etching of the Diamond (111) and (100) Surfaces from First-Principles Calculations
J. I. G. Enriquez, T. Yamasaki, M. Michiuchi, K. Inagaki, M. Geshi, I. Hamada, Y. Morikawa J. Phys. Chem. C, **128**, 6294 (2024).
DOI:10.1021/acs.jpcc.3c08378

MORITA, Katsuhiro [B class; 300 (B), 0 (C)] (354)
— *Finite temperature calculations of quantum spin systems*

MORITA, Satoshi [B class; 600 (B), 100 (C)] (331)
— *Study of critical phenomena by the bond-weighted tensor renormalization group method*

1. Ashkin-Teller phase transition and multicritical behavior in a classical monomer-dimer model
Satoshi Morita, Hyun-Yong Lee, Kedar Damle, and Naoki Kawashima, Phys. Rev. Research **5**, 043061 (2023).
DOI:10.1103/PhysRevResearch.5.043061

MOTOME, Yukitoshi [C,D class; 30400 (B), 1950 (C)] (215)
— *Large-scale analysis of scrambling rate by tensor quantum reservoir probing*
— *Numerical study of spin-charge coupled dynamics by machine learning potentials*
— *Theoretical study of strongly correlated topological phenomena and its application to machine learning*

1. Spin nematics meet spin liquids: Exotic quantum phases in the spin-1 bilinear-biquadratic model with Kitaev interactions
R. Pohle, N. Shannon, and Y. Motome Phys. Rev. B **107**, L140403 (2023).
DOI:10.1103/PhysRevB.107.L140403

2. Ground-State Phase Diagram of the KitaevHeisenberg Model on a Three-dimensional Hyperhoneycomb Lattice
K. Fukui, Y. Kato, and Y. Motome J. Phys. Soc. Jpn. **92**, 064708 (2023).
DOI:10.7566/JPSJ.92.064708

3. Berry curvature contributions of kagome-lattice fragments in amorphous FeSn thin films
K. Fujiwara, Y. Kato, H. Abe, S. Noguchi, J. Shiogai, Y. Niwa, H. Kumigashira, Y. Motome, and A. Tsukazaki Nat. Commun. **14**, 3399 (2023).
DOI:10.1038/s41467-023-39112-1

4. Thermally-robust spatiotemporal parallel reservoir computing by frequency filtering in frustrated magnets
K. Kobayashi and Y. Motome Sci. Rep. **13**, 15123 (2023).
DOI:10.1038/s41598-023-41757-3

5. Emergent electric field from magnetic resonances in a one-dimensional chiral magnet
K. Shimizu, S. Okumura, Y. Kato, and Y. Motome Phys. Rev. B **108**, 134436 (2023).
DOI:10.1103/PhysRevB.108.134436

6. Metallic ruthenium ilmenites: First-principles study of $MgRuO_3$ and $CdRuO_3$
S.-H. Jang and Y. Motome AIP Advances **14**, 015229 (2024).
DOI:10.1063/5.0185801

7. Magnetic, transport and topological properties of Co-based shandite thin films
K. Nakazawa, Y. Kato, and Y. Motome Commun. Phys. **7**, 48 (2024).
DOI:10.1038/s42005-024-01534-8

8. Unveiling the orbital-selective electronic band reconstruction through the structural phase transition in $TaTe_2$
N. Mitsuishi, Y. Sugita, T. Akiba, Y. Takahashi, M. Sakano, K. Horiba, H. Kumigashira, H. Takahashi, S. Ishiwata, Y. Motome, and K. Ishizaka Phys. Rev. Research **6**, 013155 (2024).
DOI:10.1103/PhysRevResearch.6.013155

9. Quantum reservoir probing of quantum information scrambling
K. Kobayashi and Y. Motome submitted to Phys. Rev. Applied

10. Possible Realization of Kitaev Spin Liquids in van der Waals Heterostructures of α-$RuCl_3$ and CrX_3 (X=Cl and I)
submitted to Phys. Rev. B

11. Spin Seebeck Effect as a Probe for Majorana Fermions in Kitaev Spin Liquids
Y. Kato, J. Nasu, M. Sato, T. Okubo, T. Misawa, and Y. Motome submitted to Phys. Rev. X

12. Magnetic field effects on the Kitaev model coupled to environment
K. Fukui, Y. Kato, and Y. Motome submitted to Phys. Rev. B

13. Quantum reservoir probing of quantum phase transitions
K. Kobayashi and Y. Motome submitted to Nature Commun.

14. Topological transitions by magnetization rotation in kagome monolayers of ferromagnetic Weyl semimetal Co-based shandite
K. Nakazawa, Y. Kato, and Y. Motome, preprint (arXiv:2402.16273) submitted to Phys. Rev. B

15. Exploring rare-earth Kitaev magnets by massive-scale computational analysis
S.-H. Jang and Y. Motome submitted to Communications Materials

16. Spin-Orbit Coupled Insulators and Metals on the Verge of Kitaev Spin Liquids in Ilmenite Heterostructures
Y.-F. Zhao, S.-H. Jang, and Y. Motome submitted to npj Quantum Materials

17. Eight-color chiral spin liquid in the S=1 bilinear-biquadratic model with Kitaev interactions
R. Pohle, N. Shannon, and Y. Motome submitted to Phys. Rev. B

MURASHIMA, Takahiro [C class; 3000 (B), 400 (C)] (298)
— *Nonequilibrium dynamics of multicyclic chains under elongational flow*

NADA, Hiroki [B,C class; 400 (B), 500 (C)] (322, 323)
— *A Large-Scale Metadynamics Simulation Study on the Binding Conformations of Ionic Polymers at a Geometrically Rough Surface of Calcium Carbonate Crystal*
— *A Large-Scale Molecular Dynamics Simulation Study on the Shape of an Ice Crystal Grown from Water Including Air Molecules*

1. Observation of hydrogen-ordered cubic ice thin films on the surface of ice Ic nanocrystals upon coarsening

A. Kouchi, T. Yamazaki, H. Katsuno, H. Nada, T. Hama, Y. Kimura Chem. Phys., **572** (2023) 111966.
DOI:10.1016/j.chemphys.2023.111966

2. Anisotropy in spinodal-like dynamics of unknown water at ice V-water interface
H. Niinomi, T. Yamazaki, H. Nada, T. Hama, A. Kouchi, T. Oshikiri, M. Nakagawa, Y. Kimura Sci. Rep., **13** (2023) 16227.
DOI:10.1038/s41598-023-43295-4

3. In situ cryogenic transmission electron microscopy observation on the formation of hydrogen-ordered hexagonal ices and its astrophysical implications
T. Yamazaki, A. Kouchi, K. Murata, H. Katsuno, H. Nada, T. Hama, Y. Kimura Monthly Notices of the Royal Astronomical Society, **527** (2024) 2858.
DOI:10.1093/mnras/stad3401

4. Chiral spinodal-like ordering of homoimmiscible water at interface between water and chiral ice III
H. Niinomi, T. Yamazaki, H. Nada, T. Hama, A. Kouchi, T. Oshikiri, M. Nakagawa, Y. Kimura J. Phys. Chem. Lett., **15** (2024) 659.
DOI:10.1021/acs.jpclett.3c03006

5. Unknown crystal-like phases formed in an imidazolium ionic liquid: a metadynamics simulation study
H. Nada, Submitted to J. Chem. Phys.

NAKAGAWA, Naoko [C class; 4200 (B), 500 (C)] (37)
— *Steady metastable states contained in heat conducting phase coexistence*

NAKAMURA, Kazuma [C,D class; 4600 (B), 0 (C)] (45)
— *Ab initio calculations for optical property of transition-metal compound interface*
— *Construction of thermal conductivity and plasma frequency database from first principles*
— *Construction of thermal conductivity database from first principles*

1. Superconductivity of barium with highest transition temperatures in metallic materials at ambient pressure
M. Mito, H. Tsuji, T. Tajiri, K. Nakamura, Y. Tang, Z. Horita Sci. Rep. **14**,965 (2024).
DOI:10.1038/s41598-023-50940-5

2. Ab initio calculation for electronic structure and optical property of tungsten carbide in a TiCN-based cermet for solar thermal applications
S. Hayakawa, T. Chono, K. Watanabe, S. Kawano, K. Nakamura, K. Miyazaki Sci. Rep. **13**, 9407 (2023).
DOI:10.1038/s41598-023-36337-4

3. Insulating Nature of Iridium Oxide Ca5Ir3O12 Probed by Synchrotron-Radiation-Based Infrared Spectroscopy
H. Hanate, S. Kawano, M. Hayashida, K. Nakamura, Y. Ikemoto, T. Moriwaki, T. Hasegawa, S. Tsutsui, K. Matsuhira J. Phys. Soc. Jpn **92**, 064705 (2023).
DOI:10.7566/JPSJ.92.064705

NAKANO, Hiroki [C class; 3800 (B), 450 (C)] (287)
— *Numerical study on low-energy states of quantum spin systems*

1. Large-Scale Numerical-Diagonalization Study of the Shastry-Sutherland Model
H. Nakano and T. Sakai, JPS Conf. Proc.38, 011166 (2023).

DOI:10.7566/JPSCP.38.011166

2. Translational symmetry broken magnetization plateau of the S=1 antiferromagnetic Heisenberg chain with competing anisotropies
T. Sakai, K. Okamoto, K. Okunishi, M. Hashimoto, T. Houda, R. Furuchi, H. Nakano, Phys. Rev. B 108, 174435 (2023).
DOI:10.1103/physrevb.108.174435

NAKANO, Hiroyoshi [C class; 7800 (B), 850 (C)] (264)
— *Analysis of microphase separation in active particle systems with self-propulsion*
— *Phase separation of active Brownian particles with Levy walks*

1. Universal properties of repulsive self-propelled particles and attractive driven particles
H. Nakano, K. Adachi Phys. Rev. Research **6**, 013074 (2024).
DOI:10.1103/PhysRevResearch.6.013074

NAKAYAMA, Akira [C class; 3000 (B), 400 (C)] (117)
— *DFT-MD and NNP-MD simulations for metal-oxide catalysis*

NASU, Joji [C class; 4200 (B), 550 (C)] (226)
— *Creation and manipulation of Majorana zero mode in quantum spin liquids*
— *Real-time dynamics of vison excitations in Kitaev spin liquids*

1. Field-driven spatiotemporal manipulation of Majorana zero modes in a Kitaev spin liquid
C. Harada, A. Ono, and J. Nasu, Phys. Rev. B **108**, L241118 (2023).
DOI:10.1103/PhysRevB.108.L241118

2. Flavor-wave theory with quasiparticle damping at finite temperatures: Application to chiral edge modes in the Kitaev model
S. Koyama and J. Nasu, Phys. Rev. B **108**, 235162 (2023).
DOI:10.1103/PhysRevB.108.235162

3. Field-direction Dependence of Majorana-mediated Spin Transport
H. Taguchi, A. Koga, Y. Murakami, J. Nasu, and H. Tsuchiura, JPS Conf. Proc. **38**, 011152 (2023).
DOI:10.7566/JPSCP.38.011152

NIKI, Kaori [C class; 1600 (B), 500 (C)] (147)
— *Electronic state analysis on molecular thin film surface*

1. Adsorbed CO2-Mediated CO2 Photoconversion Cycle into Solar Fuel at the O Vacancy Site of Zirconium Oxide
K. Hara, M. Nozaki, R. Hirayama, R. Ishii, K. Niki, and Y. Izumi J. Phys. Chem. C 2023, 127, 4, 1776 (2023).
DOI:10.1021/acs.jpcc.2c06048

NISHIDATE, Kazume [C class; 800 (B), 0 (C)] (176)
— *Theoretical study of the reactivity of H_2O molecule on the double-perovskite*

1. Surface electronic structure and photo activity of double perovskite Ba2PrBiO6: First-principles investigations
K. Nishidate et al. Surfaces and Interfaces **24**, 103914 (2024).
DOI:10.1016/j.surfin.2024.103914

NISHIGUCHI, Kazutaka [B class; 400 (B), 90 (C)] (249)
— *Theoretical study of thermoelectric properties in Heusler compounds using weak-coupling approaches*

NISHIKAWA, Yoshihiko [C class; 3800 (B), 0 (C)] (292)
— *Phase transitions in a classical chiral magnet with a clock anisotropy*

NOGUCHI, Hiroshi [C class; 3200 (B), 450 (C)] (294)
— *structure formation of biomembrane*

NOGUCHI, Yoshifumi [C class; 6400 (B), 750 (C)] (80)
— *Development of second-order GW electron-hole interaction kernel*
— *Self-interaction corrections in GW approximation*

1. Significant contributions of second-order exchange terms in GW electron-hole interaction kernel for charge-transfer excitations
   Yamada and Yoshifumi Noguchi, J. Chem. Phys. **159**, 234105 (2023).
   DOI:10.1063/5.0178723

NOMURA, Yusuke [E class; 14500 (B), 1500 (C)] (219)
— *Development and application of tensor neural network methods*

NOZAWA, Kazuki [C class; 1800 (B), 200 (C)] (151)
— *First-principles study of surface atomic structure and chemical properties of intermetallic compounds*

1. First-principles Study of Adsorption of Atomic Oxygen on PdZn(111) Surface
   K. Iwamura, Y. Otani, Y. Takahashi, Y. Ishii, and K. Nozawa Materials Transactions, accepted

OBATA, Masao [B class; 600 (B), 140 (C)] (178)
— *Analysis of magnetic materials with anisotropic crystal structures*
— *First-principles investigation on magnetic shape memory alloy*

1. Computational acceleration on density functional approach code using GPU
   C. Pardede, M. Obata, R. Majumder, I. Pardede, and T. Oda Proceedings of the 34th IUPAP Conference on Computational Physics (CCP2023), accepted

OCHI, Masayuki [C class; 8400 (B), 0 (C)] (76)
— *Development of a first-principles calculation software for a many-body wave function theory*
— *Improvement of accuracy and software development for the first-principles wave function theory*

1. Pair correlations in the two-orbital Hubbard ladder: Implications for superconductivity in the bilayer nickelate $La_3Ni_2O_7$
   T. Kaneko, H. Sakakibara, M. Ochi, and K. Kuroki Phys. Rev. B **109**, 045154 (2024).
   DOI:10.1103/PhysRevB.109.045154

2. Possible High Tc Superconductivity in $La_3Ni_2O_7$ under High Pressure through Manifestation of a Nearly Half-Filled Bilayer Hubbard Model
   H. Sakakibara, N. Kitamine, M. Ochi, and K. Kuroki Phys. Rev. Lett. **132**, 106002 (2024).
   DOI:10.1103/PhysRevLett.132.106002

ODA, Tatsuki [C class; 5600 (B), 850 (C)] (84)
— *Analyses on electronic structure and magnetic anisotropy in high-performance spintronics magnetic materials and parallelization development/application in quasi-particle self-consistent GW code*
— *Analyses on electronic/magnetic structures in high-performance spintronics magnetic materials and parallelization development/application in quasi-particle self-consistent GW code*

1. Migration of the Twin Boundary in a Modulated Martensite Phase of Magnetic Shape Memory

Alloy Ni2MnGa
Rinku Majumder, Masao Obata, Chandro Pardede, Jakub Lutinec, Ladislav Kalvoda, and Tatsuki Oda, accepted for the proceedings of CCP2023 (34th IUPAP Conference on Computational Physics).

2. Computational acceleration on density functional approach code using GPU
Chandro Pardede, Masao Obata, Rinku Majumder, Indra Pardede, and Tatsuki Oda, accepted for the proceedings of CCP2023 (34th IUPAP Conference on Computational Physics).

3. Parallelization in the code of quasi-particle self-consistent GW and electronic structure in the magnetic shape memory alloy Ni2MnGa
Ko Hyodo, Masao Obata, Jakub Lutinec, Ladislav Kalvoda, Takao Kotani, and Tatsuki Oda, accepted for the proceedings of CCP2023 (34th IUPAP Conference on Computational Physics).

OHKUBO, Yuji [B class; 800 (B), 70 (C)] (174)
— Calculation of chemical shift of X-ray photoelectron binding energy of functional groups generated on fluoropolymer surface
— Calculation of chemical shift of X-ray photoelectron binding energy of hydrogen-containing functional groups generated on fluoropolymer surface

1. Identification of chemical species on plasma-treated polytetrafluoroethylene surface by ab-initio calculations of core-energy-level shift in X-ray photoelectron spectra
Misa Nishino, Kouji Inagaki, Yoshitada Morikawa, Kazuya Yamamura, Yuji Ohkubo Applied Surface Science, 655, 159369 (2024).
DOI:10.1016/j.apsusc.2024.159369

OHMURA, Satoshi [C class; 2400 (B), 0 (C)] (136)
— Nanoscale properties and CO_2 fixation of cement-based materials : ab initio molecular dynamics simulations

1. Quantum lattice model solver $H\Phi$
D. Murayama, S. Ohmura, R. Kodama and N. Ozaki, J. Appl. Phys. **134**, 095902 (2023).
DOI:10.1063/5.0156913

2. 分子動力学法による結晶状態と非晶質状態の 11 トバモライトの局所力学特性
I. Kanemasu, S. Ohmura, N. Takeda, セメント・コンクリート論文集、**77**, 9, (2023).
DOI:10.14250/cement.77.9

3. Molecular dynamics study of uniaxial tensile and compressive behavior of crystalline and amorphous tobermorite
I. Kanemasu and S. Ohtaka, Springer Proceedings in Physics for CCP 2023. accepted

OHNISHI, Masato [C,E class; 16600 (B), 1500 (C)] (54)
— Construction of anharmonic phonon database with first-principles calculations
— Data-drive materials development using anharmonic phonon database

1. Thermoelectric power of a single van der Waals interface between carbon nanotubes
H. Hamasaki, Y. Li, M. Ohnishi, J. Shiomi, K. Yanagi, and K. Hirahara ACS Nano 18, 612 (2024).
DOI:10.1021/acsnano.3c08694

2. Thermoelectric figure-of-merit of metastable crystalline ST12 germanium allotrope
H. Meng, M. Ohnishi, Meng An, and J. Shiomi Materials Today Physics 38, 101270 (2023).
DOI:10.1016/j.mtphys.2023.101270

OHNO, Kaoru [C class; 5600 (B), 500 (C)] (91)
— *Improvement and application of all-electron mixed basis program*

1. Electron-capture decay rate of ^{7}Be encapsulated in C_{70} fullerene cage
   Tsutomu Ohtsuki, Riichi Kuwahara, and Kaoru Ohno, Phys. Rev. C **108**, L011301 (2023).
   DOI:10.1103/PhysRevC.108.L011301

2. Electronic and optical properties of C_{60}/Ti_2CT_2 and $C_{60}/Ti_3C_2T_2$ (T = F, OH, or O) Heterostructures
   Zahra Hajiahmadi, Mohammad Khazaei, Ahmad Ranjbar, Alireza Mostafaei, Sergii Chertopalov, Thomas D. Khne, Gianaurelio Cuniberti, Hamid Hosano, Hannes Raebiger, and Kaoru Ohno, Comp. Mat. Sci. **228**, 112364 (2023).
   DOI:10.1016/j.commatsci.2023.112364

3. Superlattice MAX phases with A-layers reconstructed into 0D-clusters, 1D-chains, and 2D-lattices
   Mohammad Khazaei, Soungmin Bae, Rasoul Khaledialidusti, Ahmad Ranjbar, Hannu-Pekka Komsa, Somayeh Khazaei, Mohammad Bagheri, Yasuhide Mochizuki, Mitsuaki Kawamura, Gianaurelio Cuniberti, Mehdi Vaez Alaei, Kaoru Ohno, Hideo Hosono, and Hannes Raebiger, J. Phys. Chem. C **127**, 14906-14913 (2023).
   DOI:10.1021/acs.jpcc.3c02233

4. Electron-capture decay rate of ^{7}Be in cluster and crystal forms of beryllium: A first-principles study
   Riichi Kuwahara, Kaoru Ohno, and Tsutomu Ohtsuki, Phys. Rev. C **109**, 024609 (2024).
   DOI:10.1103/PhysRevC.109.024609

OHSAWA, Kazuhito [C class; 1200 (B), 0 (C)] (162)
— *Study of interaction between radiation damage and interstitial atom*

OHTO, Tatsuhiko [C class; 3200 (B), 0 (C)] (121)
— *First-principles calculations for molecular junctions*

1. Durable high-entropy non-noble metal anodes for neutral seawater electrolysis
   Fumiya Shiokawa, Aimi Asilah Haji Tajuddin, Tatsuhiko Ohto, Yue Yu, Takeshi Fujita, Hisanori Tanimoto, Zeyu Xi, Samuel Jeong, and Yoshikazu Ito journalChem. Eng. J. 479, 147862 (2024).
   DOI:10.1016/j.cej.2023.147862

OHTSUKI, Tomi [C class; 5200 (B), 300 (C)] (284)
— *The Anderson transitions in quasi-periodic systems*

1. Anisotropic Topological Anderson Transitions in Chiral Symmetry Classe
   Z. Xiao, K. Kawabata, X. Luo, T. Ohtsuki, R. Shindou Physical Review Letters **131**, 056301 (2023).
   DOI:10.1103/PhysRevLett.131.056301

2. Singular-value statistics of non-Hermitian random matrices and open quantum systems
   K. Kawabata, Z. Xiao, T. Ohtsuki, R. Shindou PRX Quantum **4**, 040312 (2023).
   DOI:10.1103/PRXQuantum.4.040312

3. Critical behavior of the Anderson transition in higher-dimensional Bogoliubovde Gennes symmetry classes
   T. Wang, Z. Pan, K. Slevin, T. Ohtsuki Physical Review B **108**, 144208 (2023).
   DOI:10.1103/PhysRevB.108.144208

4. Irrelevant corrections at the quantum Hall transition
   K. Slevin, T. Ohtsuki physica status solidi (RRL)Rapid Research Letters **17**, 2300080 (2023).

DOI:10.1002/pssr.202300080

5. Machine learning wave functions to identify fractal phases
T. Cadez, B. Dietz, D. Rosa, A. Andreanov, K. Slevin, T. Ohtsuki Physical Review B **108**, 184202 (2023).
DOI:10.1103/PhysRevB.108.184202

6. A Stochastic Method to Compute the L2 Localisation Landscape
M. Kakoi and K. Slevin Journal of the Physical Society of Japan, **92**, 054707 (2023).
DOI:10.7566/JPSJ.92.054707

7. Time evolution of coherent wave propagation and spin relaxation in spin-orbit-coupled systems
M. Kakoi and K. Slevin Physical Review A, **109**, 033303 (2024).
DOI:10.1103/PhysRevA.109.033303

OKITSU, Kouhei [B class; 200 (B), 50 (C)] ()
— *Verification of the hypothesis concerning 'too much R-factor' of protein crystal structure analysis*

OKUBO, Masashi [B class; 500 (B), 100 (C)] ()
— *Theoretical calculation of intercalation-type electrode materials for aqueous proton rechargeable batteries*

OKUBO, Tsuyoshi [C class; 8400 (B), 850 (C)] (262, 371)
— *Study on finite temperature properties of frustrated magnets*
— *Tensor network study of quantum spin models on the honeycomb lattice.*

1. Possibility of a topological phase transition in two-dimensional RP^3 model
T. Okubo and N. Kawashima J. Phys. Soc. Jpn. **92**, 114701 (2023).
DOI:10.7566/Jpsj.92.114701

2. Spin Seebeck Effect as a Probe for Majorana Fermions in Kitaev Spin Liquids
Y. Kato, J. Nasu, M. Sato, T. Okubo, T. Misawa, and Y. Motome arXiv:2401.13175
DOI:10.48550/arXiv.2401.13175

3. Quantum phase transition between spin liquid and spin nematics in spin-1 Kitaev honeycomb model
T. Mashiko and T. Okubo arXiv:2403.11490
DOI:10.48550/arXiv.2403.11490

OKUMURA, Hisashi [C class; 4800 (B), 500 (C)] (285)
— *Molecular dynamics simulation of protein aggregation*

ONO, Atsushi [B class; 600 (B), 100 (C)] (243)
— *Nonequilibrium dynamics in quantum systems driven by optical electric fields*

1. Photocontrol of spin scalar chirality in centrosymmetric itinerant magnets
A. Ono and Y. Akagi, Phys. Rev. B **108**, L100407 (2023).
DOI:10.1103/PhysRevB.108.L100407

2. Theory for Fourier-limited attosecond pulse generation in solids
S. Imai and A. Ono, Phys. Rev. B **109**, L041303 (2024).
DOI:10.1103/PhysRevB.109.L041303

ONO, Shota [B,C class; 2500 (B), 270 (C)] (128, 129)
— *Surface Bain distortion*
— *Two-dimensional structures for non-layered materials*

1. Structural Properties of Two-Dimensional Strontium Titanate: A First-Principles Investigation
S. Ono and Y. Kumagai, J. Phys. Soc. Jpn. **92**, 114601 (2023).
DOI:10.7566/JPSJ.92.114601

2. Bain distortion of noble metal thin films that exhibit fcc, bct, and reoriented fcc structures
S. Ono and K. Tamura, Comp. Mater. Sci. **237**, 112920 (2024).
DOI:10.1016/j.commatsci.2024.112920

ONO, Tomoya [C class; 9400 (B), 850 (C)] (60)
— *Development of first-principles calculation code RSPACE and design of highly functional interface*

1. Twist p_z Orbital and Spin Moment of the Wavy-Graphene/L10-FePd Moiré Interface
H. Naganuma, M. Uemoto, H. Adachi, H. Shinya, I. Mochizuki, M. Kobayashi, A. Hirata, B. Dlubak, T. Ono, P. Seneor, J. Robertson, and K. Amemiya J. Phys. Chem. C **127**, 11481 (2023).
DOI:10.1021/acs.jpcc.2c08982

2. GPU acceleration of conjugate gradient method obtaining Green's function for transport-property calculation
T. Akamatsu, M. Uemoto, Y. Egami and T. Ono Comput. Phys. Commun. **295**, 108989 (2024).
DOI:10.1016/j.cpc.2023.108989

3. Valley filters using graphene blister defects from first principles
M. Uemoto, M. Nishiura, and T. Ono J. Phys.: Condens. Matter **36**, 095301 (2024).
DOI:10.1088/1361-648X/ad0d26

4. Density functional theory study on the effect of NO annealing for SiC(0001) surface with atomic-scale steps
M. Uemoto, N. Funaki, K. Yokota, T. Hosoi, and T. Ono Appl. Phys. Express **17**, 011009 (2024).
DOI:10.35848/1882-0786/ad1bc3

5. First-principle study of spin transport property in $L1_0$-FePd(001)/graphene heterojunction
H. Adachi, R. Endo, H. Shinya, H. Naganuma, T. Ono, and M. Uemoto J. Appl. Phys. **135**, 043902 (2024).
DOI:10.1063/5.0175047

ONO, Yoshiaki [C class; 4200 (B), 500 (C)] (227)
— *Electronic and phonon states and superconductivity of multi-band low-carrier systems based on first-principles and quantum many-body calculations*

1. Changes in molecular conformation and electronic structure of DNA under ^{12}C ions based on first-principles calculations
T. Sekikawa, Y. Matsuya, B. Hwang, M. Ishizaka, H. Kawai, Y. Ōno, T. Sato, and T. Kai, Nucl. Instrum. Methods Phys. Res. B **548**, 165231 (2024).
DOI:10.1016/j.nimb.2023.165231

2. Singlet Even-Frequency and Triplet Odd-Frequency Superconductivity in the Two-Band Hubbard Model Based on the Dynamical Mean-Field Theory
Y. Inokuma, and Y. Ōno, J. Phys. Soc. Jpn. **93**, 043701 (2024).
DOI:10.7566/JPSJ.93.043701

3. Crystal Structures and Superconducting Properties of Metallic Double-Chain Based Cuprate $Pr_2Ba_4Cu_7O_{15-\delta}$

M. Hagawa, M. Matsukawa, K. Niinuma, R. Kudo, Y. Mizushima, N. Kawarada, H. Yamamoto, K. Sano, Y. Ōno, and T. Sasaki, J. Phys. Soc. Jpn. **93**, 044705 (2024).
DOI:10.7566/JPSJ.93.044705

4. Temperature and Doping Dependence of the Singlet and Triplet Pair Susceptibilities in the Two-Band Hubbard Model Based on the Dynamical Mean-Field Theory
Y. Inokuma, and Y. Ōno, New Physics: Sae Mulli **73**, 1119 (2023).
DOI:10.3938/NPSM.73.1119

OSHIKAWA, Masaki [B class; 500 (B), 100 (C)] (335)
— *Tensor-network-based finite-size scaling of critical phenomena*

1. Finite-size and finite bond dimension effects of tensor network renormalization
A. Ueda and M. Oshikawa Phys. Rev. B **108**, 024413 (2023).
DOI:10.1103/PhysRevB.108.024413

OSHIYAMA, Atsushi [E class; 10500 (B), 1500 (C)] (58)
— *Clarification of Microscopic Mechanisms of Semiconductor Epitaxial Growth and Device-Interface Formation by Large-Scale Quantum-Theory-Based Computations*

1. Theoretical study of the influence of GaO_x interfacial layer on the GaN/SiO_2 interface property
S. Hattori, A. Oshiyama, and K. Shiraishi J. Appl. Phys. to be published (2024).

2. Microscopic mechanisms of nitrogen doping in silicon carbide during epitaxial growth
S. Yamauchi, I. Mizushima, T. Yoda, A. Oshiyama, and K. Shiraishi Appl. Phys. Exp. to be published (2024).

3. First-Principles Study of Recombination-Enhanced Migration of an Interstitial Magnesium in Gallium Nitride
Y. Zhao, K. Shiraishi, T. Narita, and A. Oshiyama Appl. Phys. Lett. to be published (2024).

OTANI, Minoru [C class; 3800 (B), 0 (C)] (111)
— *Exploring the mechanism of catalytic activity and degradation of electrodes*

1. Electrocatalytic Mechanisms for an Oxygen Evolution Reaction at a Rhombohedral Boron Monosulfide Electrode/Alkaline Medium Interface
Satoshi Hagiwara, Fumiaki Kuroda, Takahiro Kondo, Minoru Otani ACS Appl. Mater. Interfaces 15, 43, 50174 (2023).
DOI:10.1021/acsami.3c10548

2. Structural changes in the lithium cobalt dioxide electrode: A combined approach with cluster expansion and Bayesian optimization
Fumiaki Kuroda, Satoshi Hagiwara, Minoru Otani Phys. Rev. Materials 7, 115402 (2023).
DOI:10.1103/PhysRevMaterials.7.115402

OTSUKI, Michio [C class; 3000 (B), 450 (C)] (296)
— *Dynamic friction of macroscopic objects*

1. Control of static friction by designing grooves on friction surface
W. Iwashita, H. Matsukawa, and M. Otsuki Tribol. Lett. **72**, 25 (2024).
DOI:10.1007/s11249-023-01822-4

OYA, Yutaka [C class; 2400 (B), 350 (C)] (302)
— *Molecular dynamics study of microscopic damage in thermosetting polymers*

OZEKI, Yukiyasu [C class; 4800 (B), 700 (C)] (282)
— *Improvement of analysis for relaxation of fluctuations by the use of Gauss process regression*
— *Improvement of analysis for relaxation of fluctuations by the use of Gauss process regression II*

1. Dynamical scaling analysis for $\pm J$ Ising model in three dimensions
   Y. Terasawa and Y. Ozeki J. Phys. Soc. Jpn **92**, 074003 (2023).
   DOI:10.7566/JPSJ.92.074003

2. Dynamical scaling analysis and estimation of critical exponent z for continuous spin systems simulated using event-chain algorithm
   Y. Osada and Y. Ozeki J. Phys. Soc. Jpn **92**, 084004 (2023).
   DOI:10.7566/JPSJ.92.084004

PETERS, Robert [C class; 2800 (B), 800 (C)] (231)
— *Nonequilibrium dynamics of correlated quantum matter using neural networks*
— *nonlinear response in strongly correlated materials*

1. Two-particle correlation effects on nonlinear optical responses in the one-dimensional interacting Rice-Mele model
   A. Kofuji and R. Peters Phys. Rev. B 109, 155111 (2024).
   DOI:10.1103/PhysRevB.109.155111

2. Unique properties of the optical activity in noncentrosymmetric superconductors: Sum rule, missing area, and relation with the superconducting Edelstein effect
   K. Shinada and R. Peters Phys. Rev. B 108, 165119 (2023).
   DOI:10.1103/PhysRevB.108.165119

3. Quantum skyrmion Hall effect in f-electron systems
   R. Peters, J. Neuhaus-Steinmetz, and T. Posske Phys. Rev. Res. 5, 033180 (2023).
   DOI:10.1103/PhysRevResearch.5.033180

4. Ground state properties of quantum skyrmions described by neural network quantum states
   A. Joshi, R. Peters, and T. Posske Phys. Rev. B 108, 094410 (2023).
   DOI:10.1103/PhysRevB.108.094410

5. Unconventional gap dependence of high-order harmonic generation in the extremely strong light-matter-coupling regime
   A. Kofuji and R. Peters Phys. Rev. A 108, 023521 (2023).
   DOI:10.1103/PhysRevA.108.023521

6. Low-energy excitations and transport functions of the one-dimensional Kondo insulator
   R. Petes and R. Rausch SciPost Phys. 14, 166 (2023).
   DOI:10.21468/SciPostPhys.14.6.166

RAEBIGER, Hannes [C class; 3000 (B), 400 (C)] (115)
— *Carrier doping of Mott insulators: chemical trends*

1. Localized coherent phonon generation in monolayer MoSe—2— from ultrafast exciton trapping at shallow traps
   S. Bae, T. Y. Jeong, H. Raebiger, K. J. Yee, Y. H. Kim Nanoscale Horiz.**8**, 1282 (2023).
   DOI:10.1039/d3nh00194f

SAKAGUCHI, Norihito [C class; 8000 (B), 0 (C)] ()
— *Reduction of Rare Metals in Fuel Cell and Formic Acid Decomposition Catalysts*

SAKAI, Toru [C class; 5600 (B), 700 (C)] (268, 270)
— *Novel Magnetization PLateau of the Spin Ladder System*
— *Spin Nematic Phase of 2D Ferromagnetic Dimer Systems*

1. Translational symmetry broken magnetization plateau of the S=1 antiferromagnetic Heisenberg chain with competing anisotropies
   Toru Sakai, Kiyomi Okamoto, Kouichi Okunishi, Masaru Hashimoto, Tomoki Houda, Rito Furuchi, Hiroki Nakano Physical Reviw B 108, 174435 (2023).
   DOI:10.1103/PhysRevB.108.174435

2. Spin-Peierls transition to a Haldane phase
   Hironori Yamaguchi, Hiroki Takahashi, Takashi Kawakami, Kiyomi Okamoto, Toru Sakai, Takeshi Yajima, and Yoshiki Iwasaki Physical Review B 107, L161111 (2023).
   DOI:10.1103/PhysRevB.107.L161111

3. Quantum spin nematic liquid in the low-dimensional anisotropic magnets -S=1/2 delta spin chain with the anisotropic ferromagnetic interaction in magnetic field-
   Toru Sakai, Rito Furuchi, Hiroki Nakano, Kiyomi Okamoto SciPost Physics Proceedings 11, 011 (2023).
   DOI:10.21468/scipostphysproc.1

4. Nematic Tomonaga-Luttinger Liquid Phase in an S = 1/2 Ferromagnetic-Antiferromagnetic Bond-Alternating Chain
   Takashi Tonegawa, Kiyomi Okamoto, Kiyohide Nomura, Toru Sakai JPS Conference Proceedings 38, 011154 (2023).
   DOI:10.7566/JPSCP.38.011154

5. Quantum Phase Transition of the Shastry-Sutherland System and ESR Forbidden Transition
   Toru Sakai, Rito Furuchi, and Hiroki Nakano JPS Conference Proceedings 38, 011155 (2023).
   DOI:10.7566/JPSCP.38.011155

6. Field-Induced Spin Nematic Liquid of the S = 1/2 Bond-Alternating Chain with the Anisotropy
   Ryosuke Nakanishi, Takaharu Yamada, Rito Furuchi, Hiroki Nakano, Hirono Kaneyasu, Kiyomi Okamoto, Takashi Tonegawa, Toru Sakai JPS Conference Proceedings 38, 011156 (2023).
   DOI:10.7566/JPSCP.38.011156

7. Translational Symmetry Broken Magnetization Plateau of the S=2 Antiferromagnetic Chain with Anisotropies
   Takaharu Yamada, Ryosuke Nakanishi, Rito Furuchi, Hiroki Nakano, Hirono Kaneyasu, Kiyomi Okamoto, Takashi Tonegawa, Toru Sakai JPS Conference Proceedings 38, 011163 (2023).
   DOI:10.7566/JPSCP.38.011163

8. Large-Scale Numerical-Diagonalization Study of the Shastry?Sutherland Model
   Hiroki Nakano, Toru Sakai JPS Conference Proceedings 38, 011166 (2023).
   DOI:10.7566/JPSCP.38.011166

9. Numerical Study of S=1/2 Heisenberg Antiferromagnet on the Floret Pentagonal Lattice
   Rito Furuchi, Hiroki Nakano, Toru Sakai JPS Conference Proceedings 38, 011167 (2023).
   DOI:10.7566/JPSCP.38.011167

10. Field-Induced Spin Liquids in the S=1/2 Distorted Diamond Spin Chain with Anisotropic Ferromagnetic Interaction
    Masaru Hashimoto, Tomoki Houda, Rito Furuchi, Hiroki Nakano, Kiyomi Okamoto, Toru Sakai New Physics: Sae Mulli. 73, 1127 (2023).
    DOI:10.3938/NPSM.73.1127

11. Translational Symmetry Broken Magnetization Plateau of the Spin-1/2 Ferromagnetic and Antiferromagnetic Bond-Alternating Spin Chain with Competing Anisotropies
Toru Sakai, Masaru Hashimoto, Tomoki Houda, Rito Furuchi, Hiroki Nakano, Kiyomi Okamoto, Kouichi Okunishi New Physics: Sae Mulli. 73, 1131 (2023).
DOI:10.3938/NPSM.73.1131

12. Magnetization process of the antiferromagnetic quatum spin chains with the biquadratic exchange interaction
Toru Sakai AIP Advances 14, 015332 (2024).
DOI:10.1063/9.0000656

SAKAKIBARA, Hirofumi [B class; 500 (B), 0 (C)] (187)
— *First-principles study of electron interactions in transition metal oxides*

1. Monte Calro study of cuprate superconductors in a four-band d-p model: role of orbital degrees of freedom
H. Watanabe, T. Shirakawa, K. Seki, H. Sakakibara, T. Kotani, H. Ikeda, S. Yunoki, J. of Phys. Condens. Matter. 35, 195601 (2023).
DOI:10.1088/1361-648X/acc0bf

2. Possible high Tc superconductivity in La3Ni2O7 under high pressure through manifestation of a nearly-half-filled bilayer Hubbard model
H. Sakakibara, N. Kitamine, M. Ochi, K. Kuroki, Phys. Rev. Lett. 132, 106002 (2024).
DOI:10.1103/PhysRevLett.132.106002

3. Pair correlations in the two-orbital Hubbard ladder: Implications for superconductivity in the bilayer nickelate La3Ni2O7
T. Kaneko, H. Sakakibara, M. Ochi, K. Kuroki, Phys. Rev. B 109, 045154 (2024).
DOI:10.1103/PhysRevB.109.045154

4. Theoretical analysis on the possibility of superconductivity in a trilayer Ruddlesden-Popper nickelate La4Ni3O10 under pressure and its experimental examination: comparison with La3Ni2O7
H. Sakakibara, M. Ochi, H. Nagata, Y. Ueki, H. Sakurai, R. Matsumoto, K. Terashima, K. Hirose, H. Ohta, M. Kato, Y. Takano, K. Kuroki, Phys. Rev. B 109, 144511 (2024).
DOI:10.1103/PhysRevB.109.144511

SAKASHITA, Tatsuya [B class; 200 (B), 170 (C)] (353)
— *Development of integrated interface of eigensolvers Rokko and application to quantum spin systems*

SASAKI, Takehiko [C class; 1600 (B), 250 (C)] (154)
— *Study on structures and reactions of platinum nanoparticles*

SATO, Ryuhei [C class; 1200 (B), 0 (C)] (311)
— *The Mechanism Study of Superionic Conduction Induced by Complex Ion Rotation Using Persistent Diagram*

1. Explore the Ionic Conductivity Trends on B12H12 Divalent Closo-Type Complex Hydride Electrolytes
Egon Campos, dos, Santos and Ryuhei, Sato and Kazuaki, Kisu and Kartik, Sau and Xue, Jia and Fangling, Yang and Shin-ichi, Orimo and Hao, Li, Chemistry of Materials, 5996, 35, (2023).
DOI:10.1021/acs.chemmater.3c00975

2. A dynamic database of solid-state electrolyte (DDSE) picturing all-solid-state batteries
Fangling Yang and Egon, Campos dos Santos and Xue Jia and Ryuhei Sato and Kazuaki Kisu

and Yusuke Hashimoto and Shin-ichi Orimo and Hao Li, Nano Materials Science, in press
DOI:10.1016/j.nanoms.2023.08.002

SATO, Shunsuke [C class; 3800 (B), 0 (C)] (110)
— *First-principles analysis on attosecond transient absorption spectroscopy for FePt alloy*

1. Frequency-resolved Microscopic Current Density Analysis of Linear and Nonlinear Optical Phenomena in Solids
   S. A. Sato, J. Phys. Soc. Jpn. 92, 094401 (2023).
   DOI:10.7566/JPSJ.92.094401

SAWABE, Kyoichi [C class; 3400 (B), 50 (C)] (113)
— *Machine learning prediction of Lewis acidity of supported oxide single-atom catalysts*

SEINO, Kaori [C class; 2000 (B), 250 (C)] (140)
— *First-principles study of defects in GaN*

SEKI, Yuya [B class; 400 (B), 100 (C)] (346)
— *Analysis of Ising model in statistical-mechanical informatics*

1. Black-box optimization for integer-variable problems using Ising machines and factorization machines
   Y. Seki, R. Tamura, and S. Tanaka, arXiv.2209.01016
   DOI:10.48550/arXiv.2209.01016

SHIMADA, Toshihiro [B class; 800 (B), 160 (C)] (172, 173)
— *Change in the electronic structure of atomic layered, organic and magnetic materials by doping*
— *Construction of model Hamiltonian to interpret experimental results of topological* $Pr_2Ir_2O_7$

1. Pitched π-stacking crystal structure and two-dimensional electronic structure of acenaphtho[1,2-k]fluoranthene analogues with various substituents
   Yuki, Takuma; Yokokura, Seiya; Jin, Mingoo; Waizumi, Hiroki; Nagahama, Taro; Shimada, Toshihiro Crystal Growth and Design **24**, 1849 (2024).
   DOI:10.1021/acs.cgd.3c01510

2. Nearly three-dimensional Dirac fermions in an organic crystal line material unveiled by electron spin resonance
   Ryuhei Oka, Keishi Ohara, Naoya Tajima, Toshihiro Shimada, Toshio Naito Materials Advances **5**, 1492 (2023).
   DOI:10.1039/D3MA00619K

3. Single Crystal Growth of Cyclopenta-Fused Polycyclic Aromatic Hydrocarbon by the Naphthalene Flux Method:2D Ambipolar Charge Transport Properties and NIR Absorption
   Hirohiko Tanoguchi, Takuma Yuki, Seiya Yokokura, Takashi Yanase, Mingoo Jin, Hajime Ito, Taro Nagahama, and Toshihiro Shimada, ACS Applied Electronic Materials, **5** 6266 (2023).
   DOI:10.1021/acsaelm.3c01148

4. Band structure evolution during reversible interconversion between Dirac and standard fermions in organic charge-transfer salts
   Ryuhei Oka, Keishi Ohara, Kensuke Konishi, Ichiro Yamane, Toshihiro Shimada, Toshio Naito Magnetochemistry **9** , 153 (2023).
   DOI:10.3390/magnetochemistry9060153

SHIMAMURA, Kohei [C class; 3800 (B), 350 (C)] (107)
— *Thermal Conductivity calculation with machine-learning interatomic potential for multi-component heterogeneous materials II*

1. Construction of Machine-Learning Interatomic Potential Under Heat Flux Regularization and Its Application to Power Spectrum Analysis for Silver Chalcogenides
   Y. Shimamura, A. Koura, and F. Shimojo: Comp. Phys. Commun. **294**, 108920 (2024).
   DOI:10.1016/j.cpc.2023.108920

SHIMOJO, Fuyuki [C class; 3800 (B), 450 (C)] (106)
— *First-Principles Molecular-Dynamics Study of Structural and Electronic Properties of Disordered Materials under Extreme Conditions*

1. Efficient training of the machine-learning interatomic potential based on an artificial neural network for estimating the Helmholtz free energy of alkali metals
   S. Fukushima, K. Shimamura, A. Koura, and F. Shimojo J. Phys. Soc. Jpn. **92**, 054005 (2023).
   DOI:10.7566/JPSJ.92.054005

2. Large-scale Molecular-dynamics Simulations of SiO_2 Melt under High Pressure with Robust Machine-Learning Interatomic Potentials
   D. Wakabayashi, K. Shimamura, A. Koura, and F. Shimojo J. Phys. Soc. Jpn. **92**, 074002 (2023).
   DOI:10.7566/JPSJ.92.074002

3. Construction of Machine-Learning Interatomic Potential Under Heat Flux Regularization and Its Application to Power Spectrum Analysis for Silver Chalcogenides
   K. Shimamura, A. Koura, and F. Shimojo Comput. Phys. Commun. **294**, 108920 (2024).
   DOI:10.1016/j.cpc.2023.108920

SHIMOKAWA, Tokuro [C class; 4200 (B), 650 (C)] (286)
— *Thermal effects on quantum frustrated magnetisms*
— *Thermal effects on quantum frustrated magnets*

SHINAOKA, Hiroshi [B class; 600 (B), 100 (C)] (241)
— *Many-body quantum simulations based on multi-scale space-time ansatz*

1. Hidden covalent insulator and spin excitations in SrRu2O6
   D. Csontosová, H. Shinaoka, A. Hariki, and J. Kuneś Phys. Rev. B **108**, 195137 (2023).
   DOI:10.1103/PhysRevB.108.195137

2. Comparative study on compact quantum circuits of hybrid quantum-classical algorithms for quantum impurity models
   R. Sakurai, O. J. Backhouse, G. H. Booth, W. Mizukami, and H. Shinaoka Phys. Rev. Res. **6**, 023110 (2024).
   DOI:10.1103/PhysRevResearch.6.023110

3. Monte Carlo study on low-temperature phase diagrams of the J1-J2 classical XY kagome antiferromagnet
   F. Kakizawa, T. Misawa, H. Shinaoka Phys. Rev. B **109**, 014439 (2024).
   DOI:10.1103/PhysRevB.109.014439

SHINODA, Wataru [E class; 25500 (B), 2550 (C)] (257)
— *Molecular Simulation of Soft Materials using All-Atom and Coarse-Grained Force Field*

1. Fluorescence Turn-on of Tetraphenylethylene Derivative by Transfer from Cyclodextrin to Liposomes, HeLa Cells, and E. coli
   Kosuke Masuda, Riku Omokawa, Riku Kawasaki, Yuta Mise, Yousuke Ooyama, Shogo Harada,

Wataru Shinoda, Atsushi Ikeda Chem. Eur. J. 29, e2022203071 (2023).
DOI:10.1002/chem.202203071

2. Self-Assembly of Glycerol-Amphiphilic Janus Dendrimers Amplifies and Indicates Principles for the Selection of Stereochemistry by Biological Membranes
Dapeng Zhang, Qi Xiao, Mehrnoush Rahimzadeh, Matthew Liu, Cesar Rodriguez-Emmenegger, Yusuke Miyazaki, Wataru Shinoda, and Virgil Percec J. Am. Chem. Soc. 145, 7, 4311 (2023).
DOI:10.1021/jacs.3c00389

3. Liquid Structures and Ion Dynamics of Ionic Liquids Viewed from Intermolecular Interaction
Seiji Tsuzuki and Wataru Shinoda Chem. Rec. 23, e202200272 (2023).
DOI:10.1002/tcr.202200272

4. Mutation detection of urinary cell-free DNA via catch-and-release isolation on nanowires for liquid biopsy
Hiromi Takahashi, Takao Yasui, Masaki Hirano, Keiko Shinjo, Yusuke Miyazaki, Wataru Shinoda, Takeshi Hasegawa, Atsushi Natsume, Yotaro Kitano, Mikiko Ida, Min Zhang, Taisuke Shimada, Piyawan Paisrisarn, Zetao Zhu, Fumiharu Ohka, Kosuke Aoki, Sakon Rahong, Kazuki Nagashima, Takeshi Yanagida, Yoshinobu Baba Biosens. Bioelectron. 234, 115318 (2023).
DOI:10.1016/j.bios.2023.115318

5. Li-Ion Transport and Solution Structure in Sulfolane-Based Localized High-Concentration Electrolytes
Taku Sudoh, Shuhei Ikeda, Keisuke Shigenobu, Seiji Tsuzuki, Kaoru Dokko, Masayoshi Watanabe, Wataru Shinoda, and Kazuhide Ueno J. Phys. Chem. C, 127, 12295 (2023).
DOI:10.1021/acs.jpcc.3c02112

6. Lithium-Ion Dynamics in Sulfolane-Based Highly Concentrated Electrolytes
Shuhei Ikeda, Seiji Tsuzuki, Taku Sudoh, Keisuke Shigenobu, Kazuhide Ueno, Kaoru Dokko, Masayoshi Watanabe, and Wataru Shinoda J. Phys. Chem. C, 127, 13837 (2023).
DOI:10.1021/acs.jpcc.3c02155

7. Molecular Dynamics Simulations of High-Concentration Li[TFSA] Sulfone Solution: Effect of Easy Conformation Change of Sulfolane on Fast Diffusion of Li Ion
Seiji Tsuzuki, Shuhei Ikeda, Wataru Shinoda, Keisuke Shigenobu, Kazuhide Ueno, Kaoru Dokko, and Masayoshi Watanabe J. Phys. Chem. B, 127, 6333 (2023).
DOI:10.1021/acs.jpcb.3c02009

8. Complex Energy Landscapes of Self-Assembled Vesicles
Jiabin Luan, Danni Wang, Shaohua Zhang, Yusuke Miyazaki, Wataru Shinoda, and Daniela A. Wilson J. Am. Chem. Soc. 145, 15496 (2023).
DOI:10.1021/jacs.3c04285

9. HER-2-Targeted Boron Neutron Capture Therapy with Carborane-integrated Immunoliposomes Prepared via an Exchanging Reaction
Riku Kawasaki, Ayano Oshige, Keita Yamana, Hidetoshi Hirano, Kotaro Nishimura, Yamato Miura, Ryuji Yorioka, Yu Sanada, Kaori Bando, Anri Tabata, Kazuma Yasuhara, Yusuke Miyazaki, Wataru Shinoda, Tomoki Nishimura, Hideki Azuma, Takushi Takata, Yoshinori Sakurai, Hiroki Tanaka, Minoru Suzuki, Takeshi Nagasaki, Atsushi Ikeda Chem. Eur. J. 29, e202302486 (2023).
DOI:10.1002/chem.202302486

10. Improved Protein Model in SPICA Force Field
Teppei Yamada, Yusuke Miyazaki, Shogo Harada, Ashutosh Kumar, Stefano Vanni, and Wataru Shinoda J. Chem. Theory Comput. 19, 8967 (2023).
DOI:10.1021/acs.jctc.3c01016

11. Molecular Level Origin of Ion Dynamics in Highly Concentrated Electrolytes
Keisuke Shigenobu, Seiji Tsuzuki, Frederik Philippi, Taku Sudoh, Yosuke Ugata, Kaoru Dokko, Masayoshi Watanabe, Kazuhide Ueno, and Wataru Shinoda J. Phys. Chem. B, 127, 10422 (2023).
DOI:10.1021/acs.jpcb.3c05864

12. pSPICA Force Field Extended for Proteins and Peptides
Yusuke Miyazaki and Wataru Shinoda J. Chem. Inf. Model. 64, 532 (2024).
DOI:10.1021/acs.jcim.3c01611

13. Proteinlipid acyl chain interactions: Depth-dependent changes of segmental mobility of phospholipid in contact with bacteriorhodopsin
Yuichi Umegawa, Sho Kato, Sangjae Seo, Wataru Shinoda, Satoshi Kawatake, Shigeru Matsuoka, and Michio Murata Biophys. Chem. 308, 107204 (2024).
DOI:10.1016/j.bpc.2024.107204

14. Understanding the effects of ethanol on the liposome bilayer structure using microfluidic-based time-resolved small-angle X-ray scattering and molecular dynamics simulations
Masatoshi Maeki, Niko Kimura, Yuto Okada, Kazuki Shimizu, Kana Shibata, Yusuke Miyazaki, Akihiko Ishida, Kento Yonezawa, Nobutaka Shimizu, Wataru Shinoda, Manabu Tokeshi Nanoscale Adv., 6, 2166 (2024).
DOI:10.1039/D3NA01073B

15. Light-controllable cell-membrane disturbance for intracellular delivery
Wenting Huo, Koji Miki, Huiying Mu, Takashi Osawa, Harumi Yamaguma, Yuuya Kasahara, Satoshi Obika, Yoshimasa Kawaguchi, Hisaaki Hirose, Shiroh Futaki, Yusuke Miyazaki, Wataru Shinoda, Shuji Akai, Kouichi Ohe J. Mater. Chem. B, in press (2024).
DOI:10.1039/D3TB02956E

16. Linear ether-based highly concentrated electrolytes for Li-sulfur batteries
Toru Ishikawa, Shohei Haga, Keisuke Shigenobu, Taku Sudoh, Seiji Tsuzuki, Wataru Shinoda, Kaoru Dokko, Masayoshi Watanabe, Kazuhide Ueno Faraday Diss., in press (2024).
DOI:10.1039/D4FD00024B

17. Evolving Better Solvate Electrolytes for Lithium Secondary Batteries
Frederik Philippi, Maleen Middendorf, Keisuke Shigenobu, Yuna Matsuyama, Oriele Palumbo, David Pugh, Taku Sudoh, Kaoru Dokko, Masayoshi Watanabe, Monika Schnhoff, Wataru Shinoda, Kazuhide Ueno Chem. Sci., in press (2024).
DOI:10.1039/D4SC01492H

SHINOHARA, Yasushi [C class; 2400 (B), 0 (C)] (134)
— *First-principles simulations for optical absorption of dielectrics by multi-pulse laser fields*

SHIOMI, Junichiro [C class; 8000 (B), 800 (C)] (72)
— *Analysis of thermal transport in disordered systems*
— *Large-scale simulations based on machine learning for thermal transport in twisted layered materials*

1. Thermoelectric power of a single van der Waals interface between carbon nanotubes
H. Hamasaki, Y. Li, M. Ohnishi, J. Shiomi, K. Yanagi, and K. Hirahara ACS Nano 18, 612 (2024).
DOI:10.1021/acsnano.3c08694

2. Thermoelectric figure-of-merit of metastable crystalline ST12 germanium allotrope
H. Meng, M. Ohnishi, Meng An, and J. Shiomi Materials Today Physics
DOI:10.1016/j.mtphys.2023.101270

3. Modulation of interface modes for resonance-induced enhancement of the interfacial thermal conductance in pillar-based Si/Ge nanowires
Liu, Yingzhou; Liu, Yinong; Yue, Jincheng; Xiong, Long; Nian, Lei-lei; Hu, Shiqian Phys. Rev. B 108, 235426 (2023).
DOI:10.1103/PhysRevB.108.235426

4. Unraveling the mechanisms of thermal boundary conductance at the graphene-silicon interface: Insights from ballistic, diffusive, and localized phonon transport regimes
Yue, Jincheng; Hu, Shiqian; Xu, Bin; Chen, Rongkun; Xiong, Long; Guo, Rulei; Li, Yuanzhe; Nian, Lei-lei; Shiomi Junichiro; Zhen, Bo Phys. Rev. B 109, 115302 (2024).
DOI:10.1103/PhysRevB.109.115302

5. Modulating phonon transport in bilayer black phosphorus: Unraveling the interplay of strain and interlayer quasicovalent bonds
Chen, Rongkun; Hu, Shiqian; Ren, Weina; Zeng, Chunhua Phys. Rev. B 109, 165413 (2024).
DOI:doi.org/10.1103/PhysRevB.109.165413

SHIRAI, Tatsuhiko [B class; 500 (B), 0 (C)] (345)
— *Relaxation process in open quantum systems*

1. Postprocessing Variationally Scheduled Quantum Algorithm for Constrained Combinatorial Optimization Problems
T. Shirai, and N. Togawa, IEEE TQE **5**, 3101114 (2024).
DOI:10.1109/TQE.2024.3376721

SHIRAISHI, Kenji [C class; 9600 (B), 0 (C)] (67, 68)
— *First Principles Design of GaN/Insulator Interface for GaN MOSFET*
— *Theoretical Studies on New Types of Point Defects Orignated from Floating States in a-SiN towards Flash Memories Applications*

1. Theoretical study of the influence of GaOx interfacial layer on the GaN/SiO2 interface property
Shuto Hattori, Atsushi Oshiiyama, and Kenji Shiraishi J. Appl. Phys. 135, 175303 (2024).
DOI:10.1063/5.0204285

SHUDO, Ken-ichi [B class; 600 (B), 100 (C)] (179)
— *leakage of surface/interfacial electrons of topological insulators*

SUGINO, Osamu [C class; 8400 (B), 900 (C)] (71)
— *First-principles calculation of adsporption on electrode sufaces*
— *Quantum theory of electrode*

1. Magnetic phases of electron-doped infinite-layer $Sr_{1-x}La_xCuO_2$ from first-principles density functional calculations
A. N. Tatan, J. Haruyama and O. Sugino Phys. Rev. B 109, 165134 (2024).
DOI:10.1103/PhysRevB.109.165134

2. Time-dependent electron transfer and energy dissipation in condensed media
E. F. Arguelles and O. Sugino J. Chem. Phys. 160, 144102 (2024).
DOI:10.1063/5.0196143

3. Theoretical calculation and comparison of H diffusion on Cu(111), Ni(111), Pd(111), and Au(111)
Y. Kataoka, J. Haruyama and O. Sugino Phys. Rev. B 107, 205414 (2023).
DOI:10.1103/PhysRevB.107.205414

4. First-principles study of water adsorption monolayer on Pt(111): Adsorption energy and second-

order nonlinear susceptibility
J. Haruyama, T. Sugimoto and O. Sugino Phys. Rev. Materials 7, 115803 (2023).
DOI:10.1103/PhysRevMaterials.7.115803

SUMITA, Shuntaro [B class; 500 (B), 100 (C)] (334)
— *Theoretical proposals of novel superconducting phenomena in strongly correlated systems with multi degrees of freedom*

1. Anisotropy-Induced Spin Parity Effects
   Shuntaro Sumita, Akihiro Tanaka, and Yusuke Kato submitted to Phys. Rev. Lett.

SUWA, Hidemaro [C class; 3800 (B), 500 (C)] (229)
— *Novel magnetic phases emerging from spin-charge-lattice couplings*

1. Extraordinary Magnetic Response of an Anisotropic 2D Antiferromagnet via Site Dilution
   Junyi Yang, Hidemaro Suwa, Derek Meyers, Han Zhang, Lukas Horak, Zhan Zhang, Evguenia Karapetrova, Jong-Woo Kim, Philip J. Ryan, Mark P. M. Dean, Lin Hao*, and Jian Liu Nano Lett. **23** (24), 11409 (2023).
   DOI:10.1021/acs.nanolett.3c02470

2. Reducing rejection exponentially improves Markov chain Monte Carlo sampling
   Hidemaro Suwa Physica A **633**, 129368 (2024).
   DOI:10.1016/j.physa.2023.129368

SUZUKI, Takafumi [C class; 2800 (B), 400 (C)] (299)
— *Dynamical properties of the extended Kitaev-Gamma model on a honeycomb lattice 2*

SUZUKI, Takehito [B class; 200 (B), 30 (C)] (358)
— *Classification of slow and fast earthquakes based on fluid pressure and porosity*
— *Understanding of the difference of magnitude-frequency relation between the fast and slow earthquakes based on a microscopic viewpoint*

SUZUKI, Yuji [C class; 2200 (B), 0 (C)] (141)
— *Development of Stretchable Electret Materials for Energy Harvesting with the Aid of Machine Learning*

TADA, Kohei [B class; 500 (B), 100 (C)] (182)
— *Theoretical investigation for systemataising surface diradical*

1. Model calculations for the prediction of the diradical character of physisorbed molecules: p-benzyne/MgO and p-benzyne/SrO
   K. Tada, T. Kawakami, Y. Hinuma Phys. Chem. Chem. Phys. **25**, 29424 (2023).
   DOI:10.1039/D3CP02988C

TADANO, Terumasa [C class; 4600 (B), 500 (C)] (100)
— *Elucidation and prediction of thermal properties of solids using machine-learning interatomic potentials integrated with advanced phonon calculation methods*

1. Inverse-Perovskite Ba_3BO (B = Si and Ge) as a High Performance Environmentally Benign Thermoelectric Material with Low Lattice Thermal Conductivity
   X. He, S. Kimura, T. Katase, T. Tadano, S. Matsuishi, M. Minohara, H. Hiramatsu, H. Kumigashira, H. Hosono, and T. Kamiya Adv. Sci. **e2307058** (2023).
   DOI:10.1002/advs.202307058

2. Limits of the Phonon Quasi-Particle Picture at the Cubic-to-Tetragonal Phase Transition in Halide

Perovskites
E. Fransson, P. Rosander, F. Eriksson, J. M. Rahm, T. Tadano, and P. Erhart Commun. Phys. **6**, 173 (2023).
DOI:10.1038/s42005-023-01297-8

TAHARA, Shuta [B class; 400 (B), 70 (C)] (197)
— *Ionic conduction mechanism of superionic conductor $RbAg_4I_5$*

TAKAHASHI, Osamu [B class; 200 (B), 100 (C)] ()
— *Electronic structure of aqueous functional group materials*

TAKAYAMA, Akari [B class; 600 (B), 0 (C)] (332)
— *Topological phase transition in Sb/Bi heterostructure studied by TRHEPD*

TAKEMORI, Nayuta [C class; 600 (B), 250 (C)] (325)
— *Comparison of superconducting properties in quasicrystals and approximant crystals*

TAKETSUGU, Tetsuya [C class; 3800 (B), 450 (C)] (104)
— *Ab initio study on the structure and functions of nanomaterials*

TAMURA, Ryo [B class; 300 (B), 100 (C)] (350)
— *Development of prediction method for phase diagrams by machine learning*

TANAKA, Katsuhiro [B class; 400 (B), 70 (C)] (195)
— *First-principles study on designing magnetic tunnel junctions and calculating tunneling conductance*

TANAKA, Shu [B class; 400 (B), 100 (C)] (343)
— *Study on algorithms for Ising machines*

1. Dynamical process of a bit-width reduced Ising model with simulated annealing
   S. Kikuchi, N. Togawa, and S. Tanaka IEEE Access **11**, 95493 (2023).
   DOI:10.1109/ACCESS.2023.3310875

2. Hybrid Optimization Method Using Simulated-Annealing-Based Ising Machine and Quantum Annealer
   S. Kikuchi, N. Togawa, and S. Tanaka J. Phys. Soc. Jpn. **92**, 124002 (2023).
   DOI:10.7566/JPSJ.92.124002

TANAKA, Tomonori [C class; 3200 (B), 350 (C)] (112)
— *First-principles calculations of exchange coupling constants dependent on magnetic short-range order*

1. Clarification of origin of positive excess volume of PdFe binary alloys by using first-principles calculations and HAXPES
   M. Watanabe, Y. Takagi, T. Tanaka, Y. Gohda, M. Adachi, M. Uchikoshi, T. Nakamura, M. Takata, and H. Fukuyama, Acta Mater. **267**, 119718 (2024).
   DOI:10.1016/j.actamat.2024.119718

TATETSU, Yasutomi [C class; 3000 (B), 400 (C)] (114)
— *Ab-initio research on nano particles, and surfaces and grain boundaries of magnetic materials*

TEN-NO, Seiichiro [C class; 7800 (B), 850 (C)] (74)
— *First-principles analysis of artificial photosynthesis using perovskite semiconductor photocatalysts*
— *Theoretical study of visible-light-driven semiconductor photocatalysts using first-principles calculations*

TERAO, Takamichi [B class; 700 (B), 150 (C)] (324)
— *Structural formation of non-spherical colloidal particles*

1. Cluster-size distribution of ions in concentrated aqueous NaCl solutions: Molecular dynamics simulations
   Kouhei Komori and Takamichi Terao Chem. Phys. Lett. **825**, 140627 (2023)
   DOI:10.1016/j.cplett.2023.140627

2. Anomaly detection for structural formation analysis by autoencoders: application to soft matters
   Takamichi Terao Philos. Mag. **103**, 2013 (2023)
   DOI:10.1080/14786435.2023.2251408

3. Localization of waves in double-negative acoustic metamaterial multilayers with thickness disorder
   Takamichi Terao Waves Random Complex, in press (2023)
   doi10.1080/17455030.2023.2173501

TEZUKA, Masaki [C class; 3800 (B), 500 (C)] (228)
— *Development of quantum computation for bosonic systems and out-of-time-ordered correlators for quantum many-body systems*

1. A model of randomly-coupled Pauli spins
   Masanori Hanada, Antal Jevicki, Xianlong Liu, Enrico Rinaldi, and Masaki Tezuka, J. High Energy Phys. in press.

2. Hayden-Preskill Recovery in Hamiltonian Systems
   Yoshifumi Nakata and Masaki Tezuka, Phys. Rev. Research **6**, L022021 (2024).
   DOI:10.1103/PhysRevResearch.6.L022021

TODO, Synge [C class; 5200 (B), 500 (C)] (278)
— *Simulation of quantum many-body systems by tensor network and sampling*

TOHYAMA, Takami [C class; 3600 (B), 0 (C)] (230)
— *Phtoinduced transient absorption spectrum in one-dimensional Mott insulator with strong dimer correlation*

1. Controlling inversion and time-reversal symmetries by subcycle pulses in the one-dimensional extended Hubbard model
   K. Shinjo, S. Sota, S. Yunoki, and T. Tohyama Phys. Rev. B **107**, 195103 (2023).
   DOI:10.1103/PhysRevB.107.195103

2. Anomalous suppression of photoinduced in-gap weight in the optical conductivity of a two-leg Hubbard ladder
   T. Tohyama, K. Shinjo, S. Sota, and S. Yunoki Phys. Rev. B **108**, 0351133 (2023).
   DOI:10.1103/PhysRevB.108.035113

3. Spin loop-current textures in Hubbard models
   K. Shinjo, S. Sota, S. Yunoki, and T. Tohyama Phys. Rev. B **108**, 195118 (2023).
   DOI:10.1103/PhysRevB.108.195118

TONEGAWA, Takashi [B class; 700 (B), 0 (C)] (329)
— *Numerical Study of the One-Dimensional Quantum Spin Systems*

1. Nematic Tomonaga-Luttinger Liquid Phase in an S=1/2 Ferromagnetic-Antiferromagnetic Bond-Alternating Chain
   Takashi Tonegawa, Kiyomi Okamoto, Kiyohide Nomura, and Toru Sakai, JPS Conf. Proc. **38**, 011154 (2023).
   DOI:10.7566/JPSCP.38.011154

2. Field-Induced Spin Nematic Liquid of the S=1/2 Bond-Alternating Chain with the Anisotropy
Ryosuke Nakanishi, Takaharu Yamada, Rito Furuchi, Hiroki Nakano, Hirono Kaneyasu, Kiyomi Okamoto, Takashi Tonegawa, and Toru Sakai, JPS Conf. Proc. **38**, 011156 (2023).
DOI:10.7566/JPSCP.38.011156

3. Translational Symmetry Broken Magnetization Plateau of the S=2 Antiferromagnetic Chain with Anisotropies
Takaharu Yamada, Ryosuke Nakanishi, Rito Furuchi, Hiroki Nakano, Hirono Kaneyasu, Kiyomi Okamoto, Takashi Tonegawa, and Toru Sakai, JPS Conf. Proc. **38**, 011163 (2023).
DOI:10.7566/JPSCP.38.011163

TRAN, Ba [E class; 5700 (B), 1100 (C)] (82)
— *Computational screening of giant magnetocaloric materials*
— *Large-scale simulation of magnetic nanoparticle toward magnetic recording applications*

1. Dzyaloshinskii-Moriya interaction in $Nd_2Fe_{14}B$ as the origin of spin reorientation and rotating magnetocaloric effect
H. B. Tran, and Y. Matsushita Appl. Mater. Today 32, 101825 (2023).
DOI:10.1016/j.apmt.2023.101825

2. Skyrmions in van der Waals centrosymmetric materials with Dzyaloshinskii-Moriya interactions
H. B. Tran, and Y. Matsushita Scr. Mater. 239, 115799 (2024).
DOI:10.1016/j.scriptamat.2023.115799

3. Temperature and size dependence of energy barrier for magnetic flips in $L1_0$ FePt nanoparticles: A theoretical study
H. B. Tran, and Y. Matsushita Scr. Mater. 242, 115947(2024).
DOI:10.1016/j.scriptamat.2023.115947

TSUCHIYA, Jun [B class; 500 (B), 0 (C)] (186)
— *Ab initio path integral molecular dynamics investigations of the hydrous phases in the Earth's interior*

TSUJI, Yuta [B,C class; 1700 (B), 400 (C)] (145)
— *First-principles theoretical catalytic studies for C1 chemistry*
— *Theoretical study of oxygen-evolution reactions by first-principles calculations*

1. Frontier Orbital Views of Stacked Aromaticity
K. Okazawa, Y. Tsuji, and K. Yoshizawa J. Phys. Chem. A **127**, 4780 (2023).
DOI:10.1021/acs.jpca.3c00360

2. Exploring Metal Nanocluster Catalysts for Ammonia Synthesis Using Informatics Methods: A Concerted Effort of Bayesian Optimization, Swarm Intelligence, and First-Principles Computation
Y. Tsuji, Y. Yoshioka, K. Okazawa, and K. Yoshizawa ACS Omega **8**, 30335 (2023).
DOI:10.1021/acsomega.3c03456

3. Hueckel Molecular Orbital Analysis for Stability and Instability of Stacked Aromatic and Stacked Antiaromatic Systems
Y. Tsuji, K. Okazawa, and K. Yoshizawa J. Org. Chem. **88**, 14887 (2023).
DOI:10.1021/acs.joc.3c01167

4. Elucidating the Effects of Chemisorbed Water Molecules on the Adhesive Interactions of Epoxy Resin to -Alumina Surfaces
T. Uwabe, Y. Sumiya, Y. Tsuji, S. Nakamura, and K. Yoshizawa Langmuir **39**, 18537 (2023).
DOI:10.1021/acs.langmuir.3c02883

5. Ready-to-transfer two-dimensionalmaterials using tunable adhesive force tapes
M. Nakatani, S. Fukamachi, P. Sol?s-Fern?ndez, S. Honda, K. Kawahara, Y. Tsuji, Y. Sumiya, M. Kuroki, K. Li, Q. Liu, Y. Lin, A. Uchida, S. Oyama, H. Goo Ji, K. Okada, K. Suenaga, Y. Kawano, K. Yoshizawa, A. Yasui, and H. Ago Nat. Electron. **7**, 119 (2024).
DOI:10.1038/s41928-024-01121-3

TSUKAHARA, Noriyuki [B class; 200 (B), 70 (C)] (208)
— *DFT calculations of the metal-organic film and atoms/molecules captured by the film on metal surfaces*

TSUNEYUKI, Shinji [C class; 6000 (B), 0 (C)] (92)
— *Structural exploration and prediction of dielectric properties of molecular materials*

1. Evolutionary search for superconducting phases in the lanthanum-nitrogen-hydrogen system with universal neural network potential
T. Ishikawa, Y. Tanaka, and S. Tsuneyuki Phys. Rev. B 109, 094106 (2024).
DOI:10.1103/PhysRevB.109.094106

2. Crystal Structure Prediction of Multi-Phase Materials by Data Assimilation
Y. Kubo, R. Sato, Y. Zhao, T. Ishikawa and S. Tsuneyuki Springer Proceedings in Physics: CCP2023 - 34th IUPAP Conference on Computational Physics (accepted)

3. The first-principles study of THz dielectric properties with a machine learning model for dipole moment
T. Amano, T. Yamazaki, S. Tsuneyuki Springer Proceedings in Physics: CCP2023 - 34th IUPAP Conference on Computational Physics (accepted)

UCHIDA, Kazuyuki [C class; 400 (B), 0 (C)] (198)
— *First-principles Study on Superstructures of Si(111)-r7xr3-In Surface (PART II)*

UCHIDA, Takashi [B class; 200 (B), 80 (C)] (355)
— *Multiple-Q orders in two-dimensional Hubbard models*

UEHARA, MASATOMO [B class; 600 (B), 150 (C)] ()
— *Prediction of Transition Temperatures for Superconductors with Imperfect Crystal Structures Using Transition Learning*
— *Superconductor transition temperature prediction by deep learning and phonon density of states estimation by model analysis*

UEMURA, Naoki [C class; 2800 (B), 0 (C)] (127)
— *Analysis of mechanical properties of alloy materials using first-principles and molecular dynamics calculations*

1. First-principles study of generalized stacking fault energy in MgZnY alloy with long-period stacking-ordered structure
N. Uemura, S. Singhaneka, and R. Matsumoto, submitted to Mater. Trans.

USUI, Hidetomo [B class; 800 (B), 170 (C)] (169)
— *FIrst principles study on band structure of high entropy superconductors*

WAKABAYASHI, Daisuke [B class; 300 (B), 0 (C)] (204)
— *Compression behavior of xenon in silica melt*

WATANABE, Hiroshi [E class; 9500 (B), 1200 (C)] (261)
— *Dynamic properties of coarse-grained modeled red blood cells*

1. Energy spectrum analysis on a red blood cell model
   T. Yamamoto and H. Watanabe, J. Chem. Phys. **159**, 234119 (2023).
   DOI:10.1063/5.0169467

WATANABE, Hiroshi [B class; 500 (B), 100 (C)] (244)
— *Theoretical study of BCS-BEC crossover in solid-state materials*

WATANABE, Satoshi [C class; 8800 (B), 850 (C)] (65)
— *Analyses on local properties at complex structures such as surfaces, interfaces and defects via machine-learning potentials*
— *Analyses on local properties at complex structures via ab-initio-based methods*

1. Prediction of Born effective charges using neural network to study ion migration under electric fields: applications to crystalline and amorphous Li_3PO_4
   K. Shimizu, R. Otsuka, M. Hara, E. Minamitani, and S. Watanabe Sci. Technol. Adv. Mater. Methods **3**, 2253135 (2023).
   DOI:10.1080/27660400.2023.2253135

2. Electrolyte engineering for effective seawater splitting based on manganese iron chromium layered triple hydroxides as novel bifunctional electrocatalysts
   S. Pal, K. Shimizu, S. Khatun, S. Singha, S. Watanabe, and P. Roy J. Mater. Chem. A **11**, 12151 (2023).
   DOI:10.1039/D2TA09984E

3. Persistent homology-based descriptor for machine-learning potential of amorphous structures
   E. Minamitani, I. Obayashi, K. Shimizu, and S. Watanabe J. Chem. Phys. **159**, 084101 (2023).
   DOI:10.1063/5.0159349

4. ニューラルネットワークを用いた電場中でのイオン挙動計算手法の開発：アモルファスリン酸リチウム中でのイオン伝導への応用
   清水 康司, 大塚 竜慈, 渡邉 聡粉体および粉末冶金 **70**, 486 (2023).
   DOI:10.2497/jjspm.23-00043

5. Hydrogen-triggered metal filament rupture in Cu-based resistance switches
   B. Xiao, X. Yu, W. Li, Q. Li, and S. Watanabe Sci. Technol. Adv. Mater. **25**, 2318213 (2024).
   DOI:10.1080/14686996.2024.2318213

6. 機械学習ポテンシャルのアモルファス系への適用と荷電欠陥・電場応答に対する試み
   安藤 康伸, 清水 康司, 渡邉 聡分子シミュレーション学会誌""アンサンブル **26**, 40 (2024).

7. Uncovering the Dynamics of Li-Au Alloying and Li Nucleation at the Au/LiPON Interface: *In-Situ Z-Contrast and Surface Roughness Contrast Imaging via SEM*
   M. Motoyama, K. Shimizu, T. Kimura, T. Yamamoto, S. Watanabe, and Y. Iriyama ACS Central Science, submitted.

8. *Enthralling anodic protection by molybdate on high-entropy alloy based electrocatalyst for sustainable seawater oxidation*
   S. Khatun, K. Shimizu, S. Pal, S. Nandi, S. Watanabe, and P. Roy Small, submitted.

9. *Enhanced ionic conductivity through crystallization of glass-Li_3PS_4 by machine learning molecular dynamics simulations*
   K. Shimizu, P. Bahuguna, S. Mori, A. Hayashi, and S. Watanabe J. Phys. Chem. C, submitted.

10. *Representing Born effective charges with equivariant graph convolutional neural networks*
A. Kutana, K. Shimizu, S. Watanabe, and R, Asahi Machine Learning: Sci. Technol., submitted.

Data Repository
Neural network model for Born effective charges
https://github.com/shimizu00000/born-effective -charge-nn.git

YAMADA, Atsuo [C class; 2600 (B), 500 (C)] (122)
— *Analysis of novel rechargeable battery materials using first-principles calculations and neural network force field*

1. High-Voltage Electrochemical Properties of Lithium-Rich Spinel Oxides
K. Kawai, T. Sudayama, D. Asakura, J. Kikkawa, E. Watanabe, M. Okubo, A. Yamada J. Phys. Chem. C **127**, 12428 (2023).
DOI:10.1021/acs.jpcc.3c01184

YAMADA, Atsushi [C class; 800 (B), 350 (C)] (238)
— *Analyses of the superconductivity and magnetic states in Hubbard models and their applicatoins to strongly correlated electron systems.*

YAMADA, Masahiko [C class; 2000 (B), 400 (C)] (3004)
— *Parallelization and application of matrix product renormalization group*

YAMAGUCHI, Naoya [C class; 1400 (B), 500 (C)] (153)
— *Development of First-principles Codes for Evaluation of Physical Properties Through Local Berry Phases*

1. First-principles study of anomalous Nernst effect in Cr-doped Bi_2Se_3
R. Syariati, V. Saraswati, H. Sawahata, N. Yamaguchi, and F. Ishii Jpn. J. Appl. Phys. **63**, 01SP26 (2024).
DOI:10.35848/1347-4065/acfe17

2. Thermoelectric Effect in Kagome Lattice Enhanced at Van Hove Singularities
K. Shibata, N. Yamaguchi, H. Sawahata, and F. Ishii J. Phys. Soc. Jpn. **92**, 124704 (2023).
DOI:10.7566/JPSJ.92.124704

YAMAJI, Youhei [E class; 12000 (B), 1350 (C)] (222)
— *Development of variational-wave-function spectroscopy for quantum materials*

1. Quantum criticality of bandwidth-controlled Mott transition
K. Takai, Y. Yamaji, F. F. Assaad, and M. Imada, Phys. Rev. Research **5**, 033186 (2023).
DOI:10.1103/PhysRevResearch.5.033186

YAMAMOTO, Go [C class; 5200 (B), 700 (C)] (273)
— *Decreasing Topological Defects Sensitivity in Multi-Walled Carbon Nanotubes Through Interwall Coupling*
— *Machine learning-assisted high-throughput molecular dynamics simulation of high-performance CNT yarn structure*

YAMASHITA, Tomoki [C class; 4200 (B), 500 (C)] (101)
— *Crystal structure prediction of Li-ion solid electrolyte materials*

YAMAUCHI, Kunihiko [C class; 4000 (B), 0 (C)] (108)
— *First-principles calculation of anomalous Hall effect in antiferromagnets*

1. Ab initio prediction of anomalous Hall effect in antiferromagnetic CaCrO3
   Thi Phuong Thao Nguyen and Kunihiko Yamauchi, Phys. Rev. B **107**, 155126 (2023).
   DOI:10.1103/PhysRevB.107.155126

2. Hydrogen-induced insulating state accompanied by interlayer charge ordering in SmNiO3
   Kunihiko Yamauchi and Ikutaro Hamada, Phys. Rev. B 108, 045108 (2023).
   DOI:10.1103/PhysRevB.108.045108

3. GoodenoughKanamoriAnderson Rules in 2D Magnet: A Chemical Trend in MCl2 with M = V, Mn, and Ni
   Thi Phuong Thao Nguyen and Kunihiko Yamauchi, J. Phys. Soc. Jpn. 93, 034710 (2024).
   DOI:10.7566/JPSJ.93.034710

4. Antiferromagnetic topological insulator with selectively gapped Dirac cones
   A. Honma, D. Takane, S. Souma, K. Yamauchi, Y. Wang, K. Nakayama, K. Sugawara, M. Kitamura, K. Horiba, H. Kumigashira, K. Tanaka, T. K. Kim, C. Cacho, T. Oguchi, T. Takahashi, Yoichi Ando, and T. Sato Nat. Commun. 14, 7396 (2023).
   DOI:10.1038/s41467-023-42782-6

5. Observation of a giant band splitting in altermagnetic MnTe
   T. Osumi, S. Souma, T. Aoyama, K. Yamauchi, A. Honma, K. Nakayama, T. Takahashi, K. Ohgushi, and T. Sato Phys. Rev. B **109**, 115102 (2024).
   DOI:10.1103/PhysRevB.109.115102

YANAGISAWA, Susumu [C class; 6200 (B), 0 (C)] (89)
— *First-principles bandstructure calculation with electron-phonon interactions in organic semiconductor crystals*

1. Proving weak electronic interaction between molecules and substrate: a study of pentacene monolayer on graphite
   Y. Hasegawa, T. Yamaguchi, M. Meissner, T. Ueba, F. Bossolotti, S. Ideta, K. Tanaka, S. Yanagisawa, and S. Kera arXiv preprint arXiv:2304.14734 (2023).
   DOI:10.48550/arXiv.2304.14734

YANAGISAWA, Takashi [B class; 700 (B), 160 (C)] (239)
— *Numerical study of the mechanism of high-temperature superconductivity in strongly correlated electron systems*
— *Research on the mechanism of high-temperature superconductivity in strongly correlated electron systems*

1. From Resistance Minimum to Kondo Physics
   T. Yanagisawa New Physics: Sae Mulli 73, 1098 (2023).
   DOI:10.3938/NPSM.73.1098

2. Inhomogeneous charge distribution and coexistence with superconductivity in the two-dimensional Hubbard model
   T. Yanagisawa preprint

YASUDA, Chitoshi [C class; 1800 (B), 0 (C)] (309)
— *Frustration and randomness in the honeycomb-lattice spin systems*

YASUHARA, Sou [B,C class; 3200 (B), 0 (C)] (119, 120)
— *Investigation on a mechanism of Ferroelectricity in a wurtzite-type LiGaO2*
— *Stable Structure Exploration of K2NdNb5O15 and Phase Transition Mechanism Analysis Based on First-Principles Calculations*

YOKO, Akira [C class; 1400 (B), 350 (C)] (156)
— *First-principles calculations of sub-3 nm metal oxide particles*

○ A class

Since this class is for trial use, research reports are not required.
When other classes are also used, their publications are shown in the list of B–E classes.
Then, the pages of their reports and publications are given in ( ).

AKIYAMA, Ryota [A class; 100 (B), 50 (C)] ()
Band calculations of atomic-layer α-Sn on SnTe

FUJISAWA, Shuji [A class; 100 (B), 50 (C)] ()
Structure optimization of nanocellulose using DFT calculations

FUKUDA, Tuneo [A class; 100 (B), 50 (C)] ()
First-principles Study of the Phase Diagram of Si(111)-In surface structures

INUI, Koji [A class; 100 (B), 50 (C)] ()
Inverse design of Hamiltonians with target properties using automatic differentiation

KAIJU, Hideo [A class; 100 (B), 50 (C)] ()
Electronic structure analysis of spin devices using first-principles calculation
— *Electronic structure analysis of lattice-matched magnetic tunnel junctions using first-principles calculation*

KATOW, Hiroki [A class; 100 (B), 50 (C)] (390)
Development of First Principles methods for Light-Matter Interaction

KUSANO, Akane [A class; 100 (B), 50 (C)] ()
Fundamental Materials Informatics Research on Binary Systems of Materials

LI, Yanjun [A class; 100 (B), 50 (C)] ()
Study of TiO2 surface catalysis

MOTOTAKE, Yoh-ichi [A class; 100 (B), 50 (C)] ()
Ab initio molecular dynamics study of inorganic polymer

MURAMATSU, Mayu [A class; 100 (B), 50 (C)] ()
Development of a MD-FEM Coupling Analysis Method

NAKAGAWA, Takeshi [A class; 100 (B), 50 (C)] ()
Structural analysis of single layer borophene on Ni surfaces

SAKURAI, Hiroshi [A class; 100 (B), 50 (C)] ()
Development of method for reconstruction of momentum density with a sparse modeling

SATO, Taku [A class; 100 (B), 50 (C)] ()
Quantum pyrochlore magnet

TANAKA, Katsuhiro [A class; 100 (B), 50 (C)] (195, 417)
Exploring physical properties of noncollinear magnets from first-principles

TATENO, Michio [A class; 100 (B), 50 (C)] ()
Impact of pore morphology on compressive yielding in sticky spheres

TATSUMI, Toshinobu [A class; 100 (B), 50 (C)] ()
Theoretical study on molecular adsorption on metal catalyst surface

UEMURA, Naoki [A class; 100 (B), 50 (C)] (127, 420)
A benchmark test using VASP for alloy materials

WANG, Yinqiao [A class; 100 (B), 50 (C)] ()
Hyperuniform glass

YAMAMOTO, Sayoko [A class; 100 (B), 50 (C)] ()
Theoretical study of water splitting reaction by oxides

YASUHARA, Sou [A class; 100 (B), 50 (C)] (119, 120, 424)
Investigation of substitution for a wurtzite-type ferroelectric material LiGaO2

YOKOMORI, So [A class; 100 (B), 50 (C)] ()
Elucidation of electronic structure modulation effects of solid solution and element substitution in single-component molecular conductors

YUAN, Jiaxing [A class; 100 (B), 50 (C)] ()
Hydrodynamic Simulations of Soft Matter

YUHARA, Junji [A class; 100 (B), 50 (C)] ()
Structural analysis of oxide quasicrystal thin films

□ SCCMS Projects

FUKUSHIMA, Tetsuya [4000 (B), 400 (C)] (361)
— *Creating of magnetic material maps by KKR Green ' s function method*

1. First-principles Calculation of Magnetocrystalline Anisotropy of Y(Co,Fe,Ni,Cu)5 Based on Full-potential KKR Green ' s Function Method
   H. Okumura, T. Fukushima, H. Akai, and M. Ogura Solid State Communications **373-374**, 115257 (2023).
   DOI:10.1016/j.ssc.2023.115257

2. Computational Materials Design of High-Entropy Alloys Based on Full Potential Korringa-Kohn-Rostoker Coherent Potential Approximation and Machine Learning Techniques
   K. Sato, G. Hayashi, K. Ogushi, S. Okabe, K. Suzuki, T. Terai, and T. Fukushima Materials Transactions **64**, 2174 (2023).
   DOI:10.2320/matertrans.MT-MG2022012

3. Insight into Scattering Mechanisms and Transport Properties of AgCuS for Flexible Thermoelectric Applications
   H. N. Nam, Q. M. Phung, K. Suzuki, A. Masago, H. Shinya, T. Fukushima, and K. Sato ACS Applied Materials & Interfaces **15**, 43871 (2023).
   DOI:10.1021/acsami.3c09437

4. Theoretical Study on the Origin of Anomalous Temperature-dependent Electric Resistivity of Ferromagnetic Semiconductor
   H. Shinya, T. Fukushima, K. Sato, S. Ohya, and H. Katayama-Yoshida APL Materials **11**, 111114 (2023).
   DOI:10.1063/5.0165352

5. Exploring finite-temperature electronic transport in CoSi alloys with transition metals (Cr, Mn, Fe, and Ni) using the KKR-CPA method
   H. N. Nam, Q. M. Phung, K. Suzuki, H. Shinya, A. Masago, T. Fukushima, and K. Sato Journal of Materials Chemistry A **12**, 451 (2024).
   DOI:10.1039/D3TA06259G

MATUBAYASHI, Nobuyuki [2000 (B), 200 (C)] (366)
— *Systematic evaluation of solubility of polypeptides in solvents by free energy calculation method using all-atom model*

1. Free-energy decomposition of salt effects on the solubilities of small molecules and the role of excluded-volume effects
   S. Hervø-Hansen, D. Lin, K. Kasahara, and N. Matubayasi, Chem. Sci. **15**, 477 (2024).
   DOI:10.1039/d3sc04617f

MIYAKE, Takashi [2000 (B), 100 (C)] (363)
— *First-principles study of magnetic materials*

1. Towards understanding structure-property relationships in materials with interpretable deep learning
   Tien-Sinh Vu, Ming-Quyet Ha, Duong-Nguyen Nguyen, Hieu-Chi Dam, Viet-Cuong Nguyen, Yukihiro Abe, Truyen Tran, Huan Tran, Hiori Kino, Takashi Miyake and Koji Tsuda npj Comp. Materials **9**, 215 (2023).
   DOI:10.1038/s41524-023-01163-9

MORIWAKE, Hiroki [4000 (B), 400 (C)] ()
— *Computational Exploring of Novel high permittivity Materials*
— *Data-driven Exploration of High Dielectric Constant Materials*

OGATA, Shigenobu [2000 (B), 200 (C)] (364)
— *Atomistic analysis of hydrogen impact on mechanical properties of structural material and database construction*

OHKUBO, Tadakatsu [5000 (B), 500 (C)] (369)
— *Phonon-calculation method for magnetic random alloys*

1. Clarification of origin of positive excess volume of PdFe binary alloys by using first-principles calculations and HAXPES
   M. Watanabe, Y. Takagi, T. Tanaka, Y. Gohda, M. Adachi, M. Uchikoshi, T. Nakamura, M. Takata, and H. Fukuyama, Acta Mater. **267**, 119718 (2024).
   DOI:10.1016/j.actamat.2024.119718

2. Strain-induced specific orbital control in a Heusler-alloy-based interfacial multiferroics
   J. Okabayashi, T. Usami, A.M. Yatmeidhy, Y. Murakami, Y. Shiratsuchi, R. Nakatani, Y. Gohda, and K. Hamaya, NPG Asia Mater. **16**, 3 (2024).
   DOI:10.1038/s41427-023-00524-6

3. Unidirectional Nano-Modulated Binding and Electron Scattering in Epitaxial Borophene
   S. Kamal, I. Seo, P. Bampoulis, M. Jugovac, C.A. Brondin, T. Menteş, I. Šarić-Janković, A. Matetskiy, P. Moras, P. Sheverdyaeva, T. Michely, A. Locatelli, Y. Gohda, M. Kralj, M. Petrović, ACS Appl. Mater. Interfaces 15, 57890 (2023).
   DOI:10.1021/acsami.3c14884

4. Metastable Co3Mn/Fe/Pb(Mg1/3Nb2/3)O3-PbTiO3 multiferroic heterostructures
   Y. Murakami, T. Usami, R. Watarai, Y. Shiratsuchi, T. Kanashima, R. Nakatani, Y. Gohda and K. Hamaya, J. Appl. Phys. 134, 224101 (2023).
   DOI:10.1063/5.0180644

5. Unveiling the Origin of Large Coercivity in (Nd, Dy)-Fe-B Sintered Magnets
   X. Tang, J.N. Li, H. Sepehri-Amin, A. Bolyachkin, A. Martin-Cid, S. Kobayashi, Y. Kotani, M. Suzuki, A. Terasawa, Y. Gohda, T. Ohkubo, T. Nakamura, and K. Hono, NPG Asia Mater. 15, 50 (2023).
   DOI:10.1038/s41427-023-00498-5

6. Strain-induced magnetic anisotropy in Heusler alloys studied from first principles
   A.M. Yatmeidhy and Y. Gohda, Appl. Phys. Express 16, 053001 (2023).
   DOI:10.35848/1882-0786/accfe1

7. Subphase exploration for SmFe12-based permanent magnets by Gibbs energies obtained with first-principles cluster-expansion method
   S. Enomoto, S. Kou, T. Abe, and Y. Gohda, J. Alloys Compd. 950, 169849 (2023).
   DOI:10.1016/j.jallcom.2023.169849

SHIMAZAKI, Tomomi [2000 (B), 200 (C)] (368)
— *Theoretical study on proton transfer in fuel cell material based on first-principles method with nuclear quantum effect*

SHITARA, Kazuki [4000 (B), 400 (C)] (365)
— *Computational Exploring of Novel Ferroelectric Materials*
— *Computational and Data-driven Exploration of Ferroelectric Materials*

TEN-NO, Seiichiro [2000 (B), 200 (C)] (74)
— *Theoretical study of visible-light hydrogen-evolution semiconductor photocatalysts using first-principles calculations*

□ Doctor Theses

1. **AMANO, Tomohito**
   First-principles and machine learning study of anharmonic vibration and dielectric properties of materials
   The University of Tokyo, 2024-03

2. **Amran Mahfudh Yatmeidhy**
   First-principles study of multiferroic composite with strain transfer
   Tokyo Institute of Technology, 2023-09

3. **AOMURA, Kosuke**
   Molecular mechanism of strain-induced crystallization in polymer gels
   The University of Tokyo, 2024-03

4. **CAO, Ruixiao**
   Improvement of numerical algorithm for quantum dimer models
   The University of Tokyo, 2023-09

5. **CHENG, Zhizhong**
   All-day passive radiative cooling and water harvesting by hierarchical polymer films
   The University of Tokyo, 2023-04

6. **FURUCHI, Rito**
   Theoretical Study of Frustrated Magnet on Pentagonal Lattice
   University of Hyogo, 2024-03

7. **HALIM, Harry Handoko**
   The Multi-scale Simulations of the Non-equilibrium States of Cu Surfaces
   Osaka University, 2023-09

8. **HARFAH, Halimah**
   First-Principles Study on the Role of Vacancies in 2D Materials:Improving Magnetic Tunnel Junctions for Future Spintronics Applications
   Osaka University, 2024-03

9. **INOKUMA, Yusuke**
   Spin-singlet and spin-triplet superconductivity in the two-band Hubbard model based on the dynamical mean-field theory
   Niigata University, 2024-03

10. **IWANO, Akito**
    High-temperature superconductivity in bilayer Hubbard models
    The University of Tokyo, 2024-03

11. **KAWAMURA, Taiki**
    Theory of magnetism due to molecular orbital degree of freedom and electron correlation in organic conductors
    Nagoya University, 2024-03

12. **KIKUCHI, Shuta**
    Algorithms for mitigating hardware restrictions in Ising machines
    Keio University, 2024-03

13. **MATSUBAYASHI, Yukihiro**
Theoretical Study of Photoinduced Nonequilibrium Dynamics in Superconductors
Tohoku University, 2024-03

14. **MD. KHALIDUR Rahman**
Hydration water dynamics between phospholipid bilayers
The Graduate University for Advanced Studies, 2023-09

15. **NISHINO, Misa**
Osaka University 2024-03

16. **SAKURAI, Rihito**
Hybrid quantum-classical algorithms for quantum impurity problems
Saitama University, 2023-03

17. **SATO, Nao**
Development of inhibitors targeting protein-protein interactions
The University of Tokyo, 2024-03

18. **SHIMIZU, Kotaro**
Spin moire engineering and emergent electromagnetism in topological spin crystals
The University of Tokyo, 2024-03

19. **TANI, Mizuki**
Theoretical Study on the Light-Matter Interaction during the Initial Stages of Femtosecond Laser Processing
The University of Tokyo, 2024-03

20. **UEDA, Atsushi**
Renormalization group flow and fixed-point in tensor network representations
The University of Tokyo, 2024-03

21. **WANG, Yuelin**
Two-dimensional metal-free carbon nitride materials as catalysts for energy applications (CO2RR, N2RR, and ORR): A density functional theory study
Osaka University, 2023-11

22. **YAMBE, Ryota**
Symmetry-based modeling for noncoplanar spin textures: crystal-dependent and laser-induced magnetic interactions
The University of Tokyo, 2023-09

23. **ZHANG, Yucheng**
Machine-learning-based Functional Group Optimization of Amorphous Polymer Electret for Energy Harvesting
The University of Tokyo, 2023-10

□ Master Theses

1. **AIKAWA, Tatsuro**
   Ab initio calculations for piezo transport properties of cuprate superconductors
   Kyushu Institute of Technology, 2024-03

2. **AMANO, Rei**
   Exploring the Isotropic-Nematic Transition in Liquid Crystals through Random Interactions: An Analytical Study
   Kyoto University, 2024-03

3. **BODAIJI, Kazu**
   Magnetization process of a kagome antiferromagnet with $\{Y_3Cu_9(OH)_{19}Cl_8\}$-type distortion
   Tokyo University of Science, 2024-03

4. **CHONO, Toshiharu**
   Elucidation of the Photothermal Conversion Mechanism for Tungsten Carbide
   Kyushu Institute of Technology, 2024-03

5. **FUKUDA, kanaya**
   Dynamical structure factor of the triangular-lattice Heisenberg antiferromagnet using variational Monte-Carlo method with a reweighting technique
   Tokyo University of Science, 2024-03

6. **FUKUDA, Shinya**
   First-principles study of the growth mechanism of epitaxial graphene growth on SiC
   Shimane University, 2024-03

7. **FUKUYAMA, Katsuya**
   Development of neural network potential for adsorption of Pb on Ag-In-Yb quasicrystal surface
   Kagoshima University, 2024-03

8. **HANAI, Ryohei**
   Graph neural network prediction of hopping motion induced by a cavity in deeply supercooled binary hard disk systems
   Nagoya Institute of Technology, 2024-03

9. **Hanif Yuandi Widyandaru**
   First-principles Calculations of Ni/GeSe Interfaces with Antiferroelectric and Ferroelectric Polarizations
   Tokyo Institute of Technology, 2023-09

10. **HATAKEYAMA, Sanshiro**
    Theoretical analysis of photon detection mechanism in superconducting single-photon detector
    Tohoku University, 2024-03

11. **HOUDA, Tomoki**
    Theoretical Study on Anomalous Phenomena of Frustrated Magnet
    University of Hyogo, 2024-03

12. **HYODO, Ko**
    Parallelization in the code of quasi-particle self-consistent GW and electronic structure in the magnetic shape memory alloy Ni_2MnGa
    Kanazawa University, 2022-03

13. **INAGE, Daiki**
A theoretical study of material design about perovskite compounds with energetically inverted e_g orbitals
Tottori University, 2024-03

14. **ITO, Kazuki**
Friction Behavior Analysis of Crystalline Polymers Containing Fillers by Coarse-Grained Molecular Dynamics Simulation
University of Hyogo, 2024-03

15. **IWADO, Shota**
First-principles study of trace Pt/Pd/Ni-doped $Al_{13}Ni_4$ surfaces
Kagoshima University, 2024-03

16. **IWASE, Koji**
Motility-induced phase separation and crystallization in flow of active Brownian particles around an obstacle
Nagoya Institute of Technology, 2024-03

17. **KIHARA, Koki**
First-principles electrodynamics study on harmonic generation from Si nano structures
Kobe University, 2024-03

18. **KITO, Sohei**
Analysis of water adsorption/desorption phenomena and heat transfer characteristics of moisture adsorbent for the application to passive heat sink
The University of Tokyo, 2024-03

19. **KOBAYASHI, Kaito**
Reservoirs of Insight: Harnessing and Probing Nature via Computational Paradigms
The University of Tokyo, 2024-03

20. **KOBORI, Takumi**
Application of tensor network simulation for Bayesian inference of noise model from surface code's syndrome statistics
The University of Tokyo, 2024-03

21. **KOTANI, Kaho**
Development of a theoretical design method for rational improvement of enzyme activity
The University of Tokyo, 2024-03

22. **KUBO, Yuuki**
A data assimilation method to determine crystal structures in multiphase materials
The University of Tokyo, 2024-03

23. **KUDO, Yuto**
Study for Core Excitation of Firefly Luciferin
Gunma University, 2023-03

24. **LIU, Runjing**
Predicting protein folding and enzyme reactions by statistical mechanical models
The University of Tokyo, 2024-03

25. **HATTORI, Shuto**
Interaction between Mg_{Ga} and V_O in interfacial GaOx layers at GaN/SiO_2 Interfaces
Nagoya University, 2024-03

26. **HAYASHI, Kodai**
Analysis of thermal conductivity in cellulose nanofiber using molecular dynamics
The University of Tokyo, 2024-03

27. **IMAI, Yasumasa**
Structural exploration of graphene oxide by GRRM and prediction of structures of platinum nanoparticles using neural network potentials
The University of Tokyo, 2024-03

28. **LAI, Yiqing**
Thermal conductivity of nano-cellulose film with promoted alignment
The University of Tokyo, 2023-09

29. **MAEKAWA, Naoki**
Analysis of behavior of Zirconia under applied electric field using machine learning potential
The University of Tokyo, 2024-03

30. **MARUO, Yuta**
Free energies of Ti-Al alloys by cluster-expansion method
Tokyo Institute of Technology, 2024-03

31. **MIYAHIRA, Jun**
Considerations on the Spin Structure at the Edge in the Zigzag Antiferromagnetic Phase of Manganese Oxides
Tokyo Metropolitan University, 2024-03

32. **MORITA, Kyosuke**
Electronic and phonon states and superconductivity of HgTe under pressure based on the first-principles calculations
Niigata University, 2024-03

33. **MUROTA, Keisuke**
Strategies for mitigating the negative-sign problem in quantum spin systems: basis rotation and reweighting method
The University of Tokyo, 2024-03

34. **NAGAYA, Yuma**
Effect of H and Cl incorporation in a-SiN
Nagoya University, 2024-03

35. **NISHIWAKI, Tomohiro**
Photoreflectance Spectroscopy in Bismuth-Based Acid Halide Thin Films
University of Fukui, 2024-03

36. **OHISHI, Shunji**
Fabrication of $Pr_2Ir_2O_7$ Thin Films by Reactive MBE and Solid Phase Epitaxy and Their Physical Properties
Hokkaido University, 2024-03

37. **OHMOTO, Mizuho**
First-principles study on electronic structure of SiC/SiO2 interface before and after NO annealing
Kobe University, 2024-03

38. **OKAMOTO, Shumpei**
Capillary transportation of Condensate water by Micro-Groove structures
The University of Tokyo, 2024-03

39. **OMATA, Ayana**
Mechanism of CO2 photoreduction on ZrO2 surface
Chiba University, 2024-03

40. **OTSUKA, Ryuji**
Analysis of S-vacancy structure in WS_2 thin film using neural network potential
The University of Tokyo, 2024-03

41. **OZAWA, Aoi**
Numerical analysis of non-equilibrium critical phenomena in sand-pile models
The University of Tokyo, 2023-03

42. **PAYONG MASAN, Samuel Eka Putra**
Revealing the exact structure of MoSx hydrogen evolution electrocatalyst using machine-learning combined density functional theory calculations
Osaka University, 2023-09

43. **SAEKI, Kyosuke**
Extraction of Dielectric Constants Using Deep Neural Networks
University of Fukui, 2024-03

44. **SATO, Shunto**
Development of high thermally conductive cellulose nanofiber filaments
The University of Tokyo, 2024-03

45. **SANO, Ryotaro**
Theoretical study of diffusion properties of hydrogen isotopes at the α-Al_2O_3/α-Cr_2O_3 interface
Hokkaido University, 2024-03

46. **SARUYA, Ryusuke**
Development of high-dimensional neural network potential for binary alloys
Chuo University, 2024-03

47. **SHIRAI, Tomoki**
Phase transition in dense hard triangle systems by Newtonian event-chain Monte Carlo
Nagoya Institute of Technology, 2024-03

48. **SHIRATANI, Sora**
Stochastic approximation analysis of dynamical quantum critical phenomena in long-range transverse field Ising chain
The University of Tokyo, 2024-03

49. **SHOJI, Makoto**
Structural analysis of B/Al(111) using electron and positron diffraction
Waseda University, 2024-03

50. **TANIE, Kosuke**
Cyber-physical loop with dynamic Monte Carlo simulation and application for optimization of photocatalitic performance of $SrTiO_3$.
Nara Institute of Science and Technology, 2024-03

51. **TAKA, Toshiki**
Data assimilation model for first-principles and experimental data on the bandgap of perovskite metal oxides.
Nara Institute of Science and Technology, 2024-03

52. **TAKAGI, Yuta**
Theoretical analysis of SEI film formation process in cyclic phosphate electrolytes
The University of Tokyo, 2024-03

53. **TAKAHASHI, Yuki**
Structure and Stability of Oxidized PdZn (111) Surface: density functional theory study
Chuo University, 2024-03

54. **TAMAYOSE, Yudai**
Site-Dilution-Induced Antiferromagnetic Order in Honeycomb Lattice Spin Systems
University of the Ryukyus, 2024-03

55. **TANAKA, Kimiharu**
A study of electronic structure of iron-based superconductor using first-principles calculation
Tottori University, 2024-03

56. **TARUI, Shota**
Potential dependent behavior of Li+ ion in the electric double layer at ionic liquid / graphite electrode interface by MD calculation
Osaka University, 2024-03

57. **TOBITA, Rintaro**
Examination of analysis methods using machine learning for thermal conductivity of GaN containing defects
The University of Tokyo, 2024-03

58. **TSUKIYAMA, Takumi**
Feature selection based on chemical interactions for machine learning prediction of CO adsorption energy
Nagoya University, 2024-03

59. **WU, Yijia**
Analysis of suppressed thermal transport in graphite by intercalation
The University of Tokyo, 2023-09

60. **YAJIMA, Kohei**
Multifractality in monitored single-particle dynamics
University of Tokyo, 2024-03

61. **YAMADA, Teppei**
Development of a Highly Accurate Coarse-Grained Protein Model
Okayama Univesity, 2024-03

62. **YAMADA, Yuki**
Prediction of diffusion processes of H on Cu surfaces using graph-neural network
Osaka University, 2024-03

63. **YANAMOTO, Ryota**
Exploration of magnet compounds by first-principles calculations and machine learning
Tokyo Institute of Technology, 2024-03

64. **YATSU, Tokomi**
Phonons of Ti-Al-O from first principles
Tokyo Institute of Technology, 2024-03

65. **YUKI, Takuma**
Electronic Structure Calculation and Fabrication/Characterization of Organic Single Crystals
Hokkaido University, 2024-03

66. **ZHANG, Lingzhi**
Possible Kitaev spin liquids in a van der Waals material α-$RuCl_3$: *ab initio* study
The University of Tokyo, 2024-03